JAXA-SP-08-014E

JAXA Special Publication

Astrophysics with All-Sky X-Ray Observations
— 3rd international MAXI Workshop —

February 2009

Japan Aerospace Exploration Agency

MAXI Workshop Series

"All-Sky X-ray Observations in the Next Decade
A workshop for ASM and GRB missions in the X-ray band"
RIKEN, Wako, Japan, March 3-5, 1997
Eds., M. Matsuoka and N. Kawai
Seiyo Printing Co. Japan, December 1997

"MAXI Workshop on AGN Variability"
Nikko Kanaya Hotel, Nikko, Japan, March 10-11, 2001
Eds., N. Kawai, H. Negoro, A. Yoshida, and T. Mihara
Seiyo Printing Co. Japan, January 10-11, 2003

"Astrophysics with All-Sky X-Ray Observations
— 3rd international MAXI Workshop —"
RIKEN, Wako, Japan, June 10-12, 2008
Eds., N. Kawai, T. Mihara, M. Kohama, and M. Suzuki

in Japanese

"全天Ｘ線監視シンポジウム ("MAXI Symposium")"
NASDA, Tsukuba, Japan, May 19-20, 1998
Eds., T. Mihara

"全天Ｘ線観測で探るサイエンス ("Science with MAXI")"
Nihon Univ., Tokyo, Japan, March 23, 2006
Eds., T. Mihara

Contact Address:

Cosmic Radiation Laboratory
The Institute of Physical and Chemical Research (RIKEN)
2-1 Hirosawa, Wako, Saitama, 351-0198, Japan
Phone: +81-48-467-9335
Fax : +81-48-462-4640
URL : http://maxi.riken.jp/
E-mail: astrows@crab.riken.jp

ISS Science Project Office
Japan Aerospace Exploration Agency (JAXA)
2-1-1, Sengen, Tsukuba, Ibaraki, 305-8505, Japan
Phone: +81-29-868-3780
Fax : +81-29-868-3956

Organizing Committees

MAXI Advisers

Roger Blandford (Stanford)
Thierry Courvoisier (ISDC)
Andy Fabian (CAM)
Rob Fender (Southampton)
Neil Gehrels (NASA/GSFC)
Guenther Hasinger (MPE)
Katsuji Koyama (Kyoto)
Hideyo Kunieda (Nagoya)
Kazuo Makishima (Tokyo/RIKEN)
Dan McCammon (Wisconsin)
Shin Mineshige (Kyoto)
Kazuhisa Mitsuda (JAXA/ISAS)
Masaki Mori (Tokyo/ICRR)
Hiroshi Murakami (JAXA/ISAS)
Robert Petre (NASA/GSFC)
Luigi Piro (IASF)
Tadayuki Takahashi (JAXA/ISAS)
David Thompson (NASA/GSFC)

Local Organizing Committee

Ken Ebisawa (JAXA/ISAS)
Nobuyuki Kawai (Tokyo Tech) *(Chair)*
Kazuyoshi Kawasaki (JAXA)
Mitsuhiro Kohama (RIKEN)
Tatehiro Mihara (RIKEN) *(Co-chair)*
Emi Miyata (Osaka)
Hitoshi Negoro (Nihon)
Mutsumi Sugizaki (RIKEN)
Hiroshi Tomida (JAXA)
Hiroshi Tsunemi (Osaka)
Yoshihiro Ueda (Kyoto)
Shiro Ueno (JAXA)
Atsumasa Yoshida (AGU)

Sponsored by

The Institute of Physical and Chemical Research (RIKEN), Wako, Saitama
Japan Aerospace Exploration Agency (JAXA), Tsukuba, Ibaraki
Japan Society for the Promotion of Science, Tokyo
the Grants-of-Aid for Scientific Research of MEXT

Supported by

The Astronomical Society of Japan
The Physical Society of Japan

Preface

MAXI, Monitor of All-sky X-ray Image, is an X-ray all-sky monitor and the first payload on the Japanese Experiment Module Kibo - Exposed Facility (JEM-EF) of the International Space Station (ISS). The pressured module of Kibo was transported to the orbit and attached to the ISS on June 4, 2008, which occurred just before the workshop. The JEM-EF and MAXI is scheduled to be delivered to the ISS in May 2009 by the Space Shuttle Endeavour (STS-127). All the electrical and environmental tests in Japan have been completed in June 2008. On this occasion we held this workshop titled Astrophysics with All-Sky X-Ray Observations as the third international MAXI workshop. The objectives of this workshop are to inform the performance and capabilities of MAXI widely to the scientists in the world, and to discuss the MAXI's science and to maximize its scientific output.

MAXI provides an all-sky X-ray image at every ISS orbit. The sensitivity of MAXI is unprecedented as an X-ray all-sky monitor, being a few milli-Crab in a day covering most of the sky. By integrating the scans of the sky for one week, the sensitivity reaches one milli-Crab (except for the small region around the Sun). While MAXI can monitor the variability of a large number of X-ray sources at much lower flux levels than is possible with the current all-sky or wide-field missions, its science output will be greatly enhanced by the joint multi-wavelength observations with contemporary missions such as INTEGRAL, Swift, Fermi (formerly GLAST) and ground-based optical/NIR/radio and UHE gamma-ray observatories, as well as deep follow-up observation in X-ray bands by RXTE, Suzaku, XMM, and Chandra. Collaboration with future X-ray programs, such as eRosita and ASTROSAT will be also useful.

Prompt dissemination of the observational results of MAXI is planned. Once MAXI discovers an X-ray nova or a transient X-ray source, an alert will be issued immediately worldwide to encourage multi-wavelength follow-up observations. Light curves and spectra of about 1000 pre-selected X-ray sources will be also regularly delivered to the community on the web. The X-ray sky map including both point sources and diffuse emission will be delivered regularly.

The workshop was held on June 10 - 12, 2008, at Suzuki-Umetaro hall in the RIKEN Wako campus. 180 participants, including 33 foreign participants from 10 countries outside Japan, attended it. We had 41 oral presentations and 42 posters. They are summarized in this proceeding. We had a special MAXI tour to the Tsukuba space center of JAXA on June 13 to see the MAXI instrument.

This workshop was organized by RIKEN (The Institute of Physical and Chemical Research) and sponsored by the Japan Society for the Promotion of Science, RIKEN symposium, the Japan Aerospace Exploration Agency, and the Grants-in-Aid for Scientific Research of MEXT, with cooperation of the Physical Society of Japan and the Astronomical Society of Japan.

Chairs of Local Organizers
Tatehiro Mihara
Nobuyuki Kawai

Monitor of All-sky X-ray Image (MAXI)

Monitor of All-sky X-ray Image (MAXI) is an All-sky X-ray scanner mounted on the 'kibo' exposed platform of the International Space Station (ISS). MAXI consists of X-ray slit cameras with high sensitivity and continuously monitors astronomical X-ray objects over a broad energy band (0.5 to 30 keV) once every 96-minutes rotation of ISS. The red spot at the center represents the X-ray object (high energy celestial object) and also the national flag of Japan. The white long arc from the MAXI on top mimics the field of view of the slit camera.

全天X線監視装置(MAXI)ミッション

「きぼう」船外実験プラットフォームで実施される宇宙科学観測ミッションです。「全天の X 線天体を観測する装置」という意味の英語の頭文字をとって「MAXI(マキシ)」と名付けられました。MAXI は X 線を検知できる高感度のスリットカメラを搭載しており、国際宇宙ステーションが地球を 1 周する度に全天をくまなく走査します。中央にある赤い点は、X 線天体(高エネルギー天体)と日の丸を意味しています。また上部の実験装置(MAXI)から出ている内側の円弧はスリットカメラの視野をイメージしています。

Table of contents

MAXI

Accreting binaries and neutron stars

Theory of accretion

Active galactic nuclei

Gamma-ray bursts

Diffuse emission

Multiwavelength opportunities and results

Future missions

MAXI

Welcome to the Third MAXI Workshop

Masaru Matsuoka

ISS Science Project Office, Institute of Space and Astronautical Science,
JAXA- Japan Aerospace Exploration Agency,
2-1-1, Sengen, Tsukuba, Ibaraki 305-8505, Japan
E-mail(MM): matsuoka.masaru@jaxa.jp

Abstract

Welcome to the third MAXI workshop. We would like to thank so many participants from 10 leading countries with current and@future great satellites. This gives us the greatest of pleasure. @We would appreciate it entirely if you could provide recent science and useful comments to MAXI project.

Key words: welcome, MAXI WS, ASM

1. General Remarks on MAXI

MAXI is the first astronomical payload to be installed in Japanese Experiment Module (JEM) "Kibo"- Exposed Facility (EF), a component of International Space Station (ISS). Japanese modules are carried in three parts separately to ISS. The first part of Japanese modules was launched in March 2008, while the second part of them was just attached to ISS at the time of this MAXI work shop with Space Shattle,"Discovery". Now JEM Pressurized Module (JEM-PM) with experiment logistics of Japanese Experiment Module has been completed by installing these two parts in ISS. On the other hand MAXI will be carried to ISS next year with JEM Exposed Facility (JEM-EF) (see the papers on MAXI in this conference).

MAXI provides an all-sky X-ray image every ISS orbit. By scanning the sky for one month, MAXI will be able to make an all-sky image for X-ray sources stronger than one milli-Crab , excluding the bright region around the Sun. MAXI will rapidly report X-ray novae or highly variable phenomena of X-ray objects to astronomers worldwide if these objects are discovered. Furthermore, MAXI does not only provide short and long-term variability of Galactic and extra-Galactic X-ray sources, but also provides catalogues of all-sky X-ray sources every month and/or year. Moreover, MAXI provides Galactic diffuse soft X-ray map with line resolvable CCD camera.

2. A History of MAXI

MAXI has a long history with ISS project. Japanese space agency "NASDA" which is a previous name of JAXA has promoted payloads for exposed facility on ISS as well as micro-gravity experiments in pressurized module. Therefore, we have considered for about 20 years what the most suitable payload is or ISS or JEM-EF (Matsuoka et al. 1990).

As you know the ISS can not provide ideal environment and perfect condition for observational payloads because of complicated interface, uncertain schedule behind, attitude fluctuation, rigid/severe safety design, limited operation and communication resources and so forth. We have to accept such environment and condition to design scientific payload on ISS.

Nevertheless, ISS project has been promoted by international political strong power. Some pure scientists have escaped from ISS project or sometimes have been negative to ISS project because of pushing pure science budget. On the other hand, as long as ISS project is promoted, we have followed ISS to make it useful with flexible mind and without any political reason.

After comprehensive investigation we have concluded that an all sky X-ray monitor is the most suitable/reasonable payload. At that time we discussed on fundamental design of the ASM which type of ASM is the most suitable for ISS, a coded mask type or a pinhole type. At last we have arrived at an idea of an X-ray all sky image monitor by using slit cameras; that is, MAXI (Matsuoka et al.1997). Finally MAXI was approved in 1997 by NASDA and Japanese SAC (Space Activity Commission).

Now, more than ten years has already passed from beginning although we prepared ourselves for such delayed time. MAXI colleagues from beginning have gotten more than ten years as me. Some colleagues have become big professors from normal researchers and so forth. In other words MAXI team members have changed considerably, but fortunately expanded without decay from beginning to the present.

MAXI development has been advanced so much since

1997. Meanwhile, X-ray astronomy has progressed greatly with exciting results provided by several X-ray astronomy satellites. Most satellites have performed pointing observations with narrow field of views. Only the Rossi-XTE satellite which has been operated since 1995 have an X-ray ASM to monitor bright novae and Galactic variable X-ray sources.

3. Conclusion for important mission of MAXI

Although the ASM on RXTE has produced much data on X-ray novae and/or transients, we believe that what we search nova-like or variable X-ray objects is able to achieve still useful and important science, especially for weaker sources. Systematic all sky survey with non-bias is still interesting in future. Therefore, the concept of MAXI is alive and useful to answer the quests for the science of variable, transient and bursting objects over the Galaxy.

Now, MAXI is scheduled to be launched by Space Shuttle Endeavour in the middle of next year. After MAXI is mounted on JEM-EF of ISS, we will adjust data processing systems and carry out various performance observations for several months. We welcome you to participate in MAXI science and utilize its observation data.

4. Acknowledgement

Finally I would like to thank the organized committee who are all MAXI active colleagues for preparing this workshop. Special acknowledgement would be given to Dr.Kawai, Dr.Mihara, and Dr.Kohama who are involved in this WS preparation. I would also thank Mrs.Takahashi and the colleagues in RIKEN as host institute for elaborate preparation of this workshop.

Thank you very much again for your participation.

References

M.Matsuoka et al.; 1990 "An X-ray All Sky Monitor for a Japanese Experiment Module on the Space Station", "Observations in Earth Orbit and Beyond", pp463-468 (1990), ed.Y.Kondo, Kluwer Academic Publishers

M.Matsuoka et al.; 1997, "MAXI (Monitor of All-sky X-ray Image) for JEM on the Space Station", SPIE - Soc. of Photo-Opt. Instr. Eng. Vol. 3114 "EUV, X-ray and Gamma-ray Instrumentation for Astronomy VIII", pp.415-421.

Overview of JEM-EF on ISS

Kazuyoshi Kawasaki[1]
[1]Space Environment Utilization Center
TKSC, Tsukuba, Ibaraki, Japan
E-mail (KK): Kawasaki.kazuyoshi@jaxa.jp

ABSTRACT

Japanese Experiment Module "Kibo" Exposed Facility (JEM-EF) is a multipurpose experiment platform where various activities such as scientific experiments, Earth observation, engineering experiments. Those can be conducted by utilizing environment which is exposed to space characterized with microgravity, high level vacuum and vast area. MAXI will be attached to the JEM-EF ram side port (EFU#1). On ISS, JEM-EF and the Truss sites are the main facilities that allow experiments those being exposed to space environment, which many researchers are interested in. JEM-EF will be launched by STS-127(2J/A) flight in May, 2009.

The JEM-EF with its size of 6m x 5m x 4m (20ft x 16.7ft x 13.3ft) weighs approximately 4000kg (8890lb) at time of launch. Experiment payloads of JEM-EF can be exchanged by Kibo robotics arm. JEM-EF will be operated for ten years on orbit supporting exposed experiments. It will supply electric power, circulates coolant for cooling the experiment devices or collects experiment data. Standard payload envelope is assumed to be of 1.85m x 1.0m x 0.8m (6.2ft x 3.3ft x 2.7ft) and weighs 500kg (1110lb). In this paper, further detail of the JEM-EF will be presented.

1. General

The ISS (International Space Station) program has started since the middle of 1980's to build a lasting manned facility that enables various activities in the space environment.

Japan, one of major participating nations to the ISS program, will provide a space science laboratory, Japanese Experiment Module, "KIBO", aiming for implementing a wide variety of space researches on the ISS.

KIBO is composed of several modules, and the JEM-EF (Exposed Facility), one of important and unique KIBO hardware, can serve scientists, engineers, etc. with fields of experiments in the environment which is directly exposed to the space.

JEM-EF will be launched by STS-127(2J/A) flight in May, 2009.

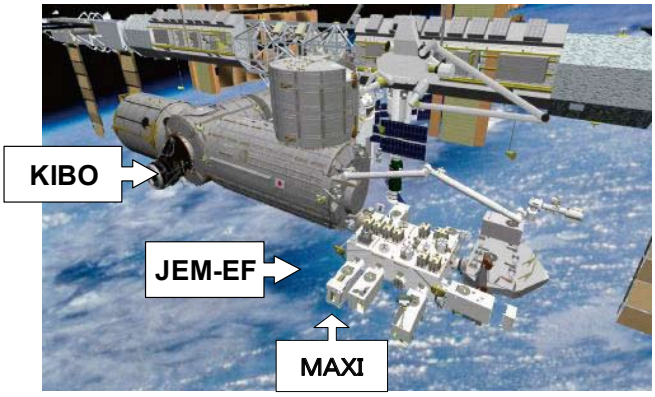

Fig.1. "KIBO" (JEM) Exposed Facility

2. JEM-EF System Characteristics

The EF is attached to the JEM-PM (KIBO Pressurized Module) via BM (Berthing Mechanism) and can accommodate other hardware such as MAXI, ICS-EF (Inter orbit Communication System - EF), ELM-ES (Experiment Logistics Module - External Section), and HTV-EP (H2A Transfer Vehicle - Exposed Pallet).

The EF receives several resources (electrical power, coolant, etc.) through the JEM-PM's BM and distributes them to the attached EF P/Ls (Payloads) for experiments. These EF P/Ls will be transported by ELM-ES (Space shuttle carrier) or HTV-EP (H2A Transfer Vehicle carrier) and will be attached to the EF port via EEU (Equipment Exchange Unit) using JEM RMS (JEM Remote Manipulator System).

By exchanging the P/L, various experiments will be possible on the EF during its operational life.

The main characteristics of the JEM-EF are:

- Dimensions : Approx. 5.7m×5.0m×3.8m
- Launch Max. Weight : 4038 kg(8902 lbs)
  [Actual measurement: 3951 kg (8711 lbs)]
- On Orbit Max. Weight : 13538 kg (29846 lbs), including 9500 kg (20944 lbs) of P/L, etc.
- Operational Life : 10 years
- Performance :
  a. Power Consumption - 562.6W
  for housekeeping
  /payload support on orbit
  b. Max. Power Usage - 11kW
  (System: 1kW, P/L: 10kW)

c. C&DH (Communication & Data Handling)
- System Local bus-2
- Payload bus-2:
  Primary & second 1ea for P/Ls
- High rate data: Total 8ch for P/Ls
- Video data: 2ch for EF system(external video camera) & 2ch for P/Ls
- Ethernet: Total 7ch for P/Ls
- Local bus P/L JEM(NASA P/L bus):
  Prim. /second. 1ea for P/Ls

d. TCS - Max. Heat Transfer: 11kW
Fluid Temperature: nominal 16-24℃
Max. Design Pressure: 12kgf/cm2 (1.18MPa / 171psi)
Flow Rate: Max.1940kg/Hr
Coolant: Fluorinert-72 (Perfluoro carbon)

e. Berthing Capability
- P/L: max.12 locations (EFU1-12) (max.10 simultaneous ops)
- ICS-EF: 2 locations (EFU7/nominal, EFU5/backup)
- ELM-ES: 2 locations (EFU10/nominal, EFU9/backup)
- HTV-EP: 2 locations (EFU10/nominal, EFU9/backup)

3. EF Subsystem Functions

The JEM-EF system consists of several subsystems such as EPS (Electrical Power System), C&DH (Communication & Data Handling), TCS (Thermal Control System), etc., and these subsystem components are replaceable as ORU (Orbital Replaceable Unit) such as R-ORU (Robotics compatible), E-ORU (EVA compatible), or other common/unique ORUs. If these subsystem components failed, they can be replaced by JEMRMS with SFA (Small Fine Arm) or EVA (Extravehicular Activity) on orbit.

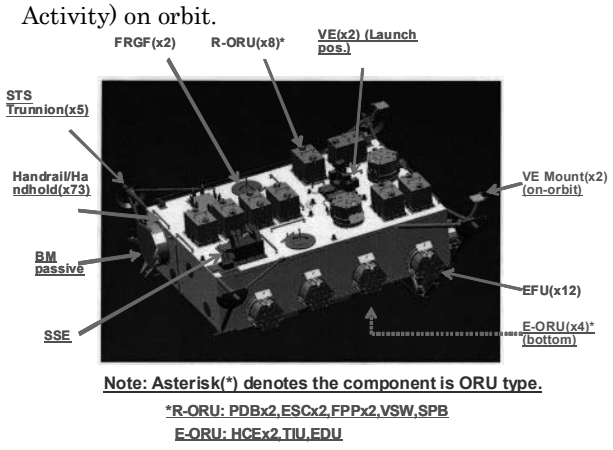

Fig.2 JEM-EF Subsystems

The JEM-EF's TCS consists of Active TCS and Passive TCS. As ATCS, there is a fluid loop system to absorb the heat, and as PTCS there are heaters, insulators, etc. to maintain the thermal condition of the JEM-EF components.

Fig.3 shows the JEM-EF fluid loop system in ATCS. The JEM-EF ATCS has:

- 2 Pumps (FPP, 1 for redundant)
- 2 Accumulators (1 for redundant)
- Flow rate control by differential pressure sensor feedback.
- Heat rejection by EF Heat Exchanger (EFHX) located outside on the JEM-PM.
- Valves that have a back pressure relief mechanisms for pressure release from the payload section when its pressure increased too high.

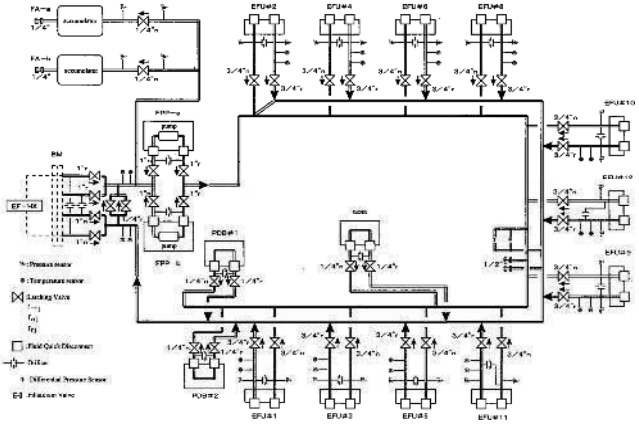

Fig.3 JEM-EF ATCS loop schematics

4. Payload Resources/Interface

4.1 Resources

The JEM-EF has 12 attachment ports for external payload and can accommodate up to 10 payloads simultaneously. Japan and U.S. shares these ports (5 for Japan, and 5 for U.S.).

Fig.4 shows the port locations and its number. Each port can accommodate 500kg class payload while the port #2, #9 and #10 can accommodate up to 2,500kg class payload. The experimental power is 3 kW (120Vdc) maximum while the port #1 and #2 has two power lines (3kW x 2). For data communication, there are Payload Bus (1553B), Ethernet, and High rate data link. The accommodation varies at each port location. The Table 1 shows the payload resources in detail.

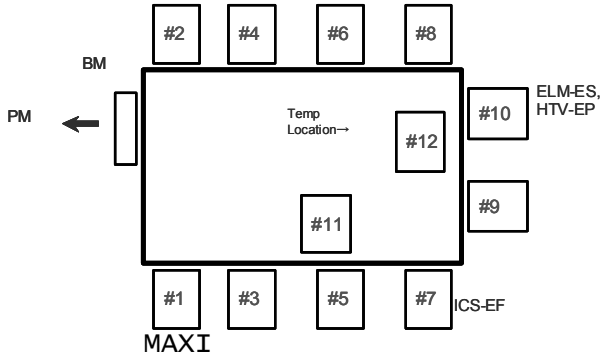

Fig.4 JEM-EF Port location for external payloads

Table 1 Payload resources

EFU #	USAGE	Max.P/L Weight (kg)	POWER 3KW BUS	POWER 100W Survival	C&DH Payload BUS	C&DH NASA local BUS	C&DH VIDEO data ×1	C&DH High rate data	C&DH Ethernet	C&DH HK data	C&DH ICS	C&DH System local BUS2	TCS 3kW Coolant
1	U	500	2	1	1R	1R	1	1	1	2R			1(6kW)
2	U	2500	2	1	1R	1R	1	1	1	2R			1(6kW)
3	U	500	1	1	1R	1R	1	1	1	2R			1
4	U	500	1	1	1R	1R	1	1	–	2R			1
5	U(ICS backup)	500	1	1	1R	1R	1	1	–	2R	1R		1
6	U	500	1	1	1R	1R	1	1	1	2R			1
7	S(ICS)	500	–	1	1R	–	–	–	–	2R	1R		–
8	U	500	1	1	1R	1R	1	1	–	2R			1
9	U(ES/EP backup)	2500	1	1	1R	1R	1	1	1	2R		1R	1
10	S(ES,EP)	2500	1	1	1R	1R	–	–	–	2R		1R	1
11	U	500	1	1	1R	1R	–	–	1	2R			1
12	U/S(P/L temp)	1350	1	1	1R	1R	–	–	1	2R			1

Usage: U(User), S(System)
1R : Single Redundancy 2R: Double Redundancy
Power(*1): Power supply is selected from either for EFU#2(one line,3kW) or EFU#12.
(*2): EFU#7 has 0.6kW power line.
Video(*3): 1ch is selected among EFU#1,#4,#5,and #8, and 1 more ch is selected among EFU#2,#3,#6, and #9.
HK: House Keeping(=Temperature/Pressure)

4.2 Interface

The attachment port on the JEM-EF has mechanical, thermal and electrical interface with attached payloads. This interface mechanism is called Experimental Exchange Unit (EEU). Fig. 4 shows the EEU. The EEU consist of two parts, one is Exposed Facility Unit (EFU) on the JEM-EF side, and the other is Payload Interface Unit (PIU) on the payload side. The EFU has an active mechanism which grapples and fixes the payload. The PIU is a passive half to be grappled by three EFU latching arms. The mechanism is designed to connect the Quick Disconnect (QD) for ATCS fluid and electrical lines securely and safely.

The PIU is a Government Furnished Equipment (GFE) and is provided to the payload developers. In addition to the PIU, the external payload must equip a FRGF (interface with Robotics Arm) and an interface with the launch carrier. Fig. 5 shows these interfaces on the MAXI, for example.

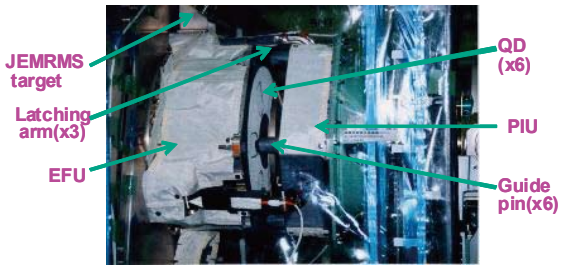

Fig.4 Experimental Exchange Unit (EEU)

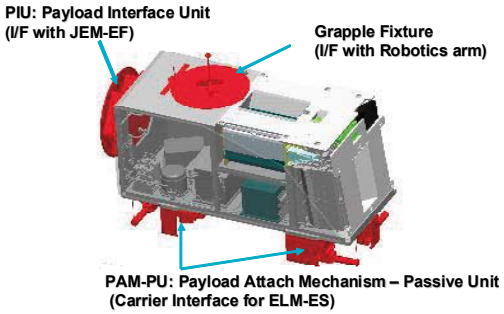

Fig.5 JEM-EF Interface on payload

5. Launch Configuration

The JEM-EF payload will be launched by the Space Shuttle or HTV. MAXI will be launched by the Space Shuttle (STS-127) along with JEM-EF and other equipment. However, after the Shuttle retirement, only the HTV-EP will be a transportation carrier. Fig. 6 shows the HTV-EP with attached payloads. The interface with the HTV-EP is different from the ELM-ES interface, which is called HTV Cargo Attachment Mechanism (HCAM).

HTV-EP will be used for the payload disposal (by de-orbit re-entry burn) after the mission. Currently there is no capability to retrieve the payload after the Shuttle retirement.

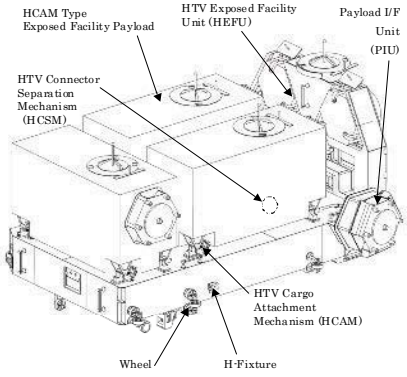

Fig. 6 HTV-EP interface

Fig. 7 MAXI (right) on the Shuttle carrier (ELM-ES)

6. References

K.Kawasaki, M.Matsuoka, et al, 56th IAC, 2005, IAC-05-B5.2.06Y

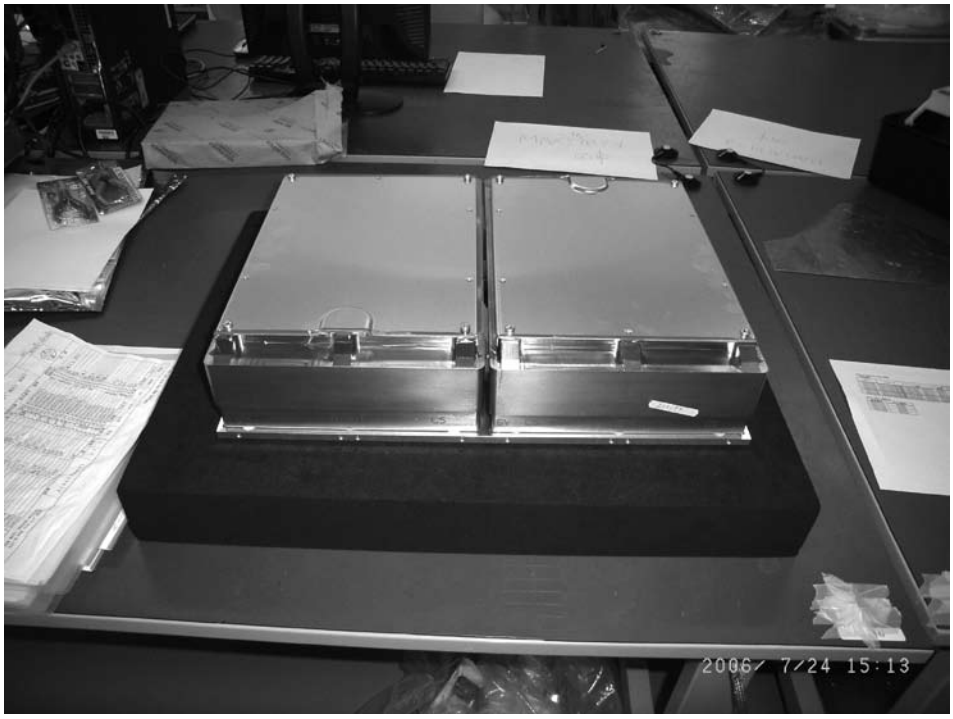

The MAXI Mission Overview and Schedule

Shiro Ueno,[1] Masaru Matsuoka,[1] Kazuyoshi Kawasaki,[1] Hiroshi Tomida,[1] Yasuki Adachi,[1] Mitsuhiro Kohama,[1] Motoko Suzuki,[1] Masaki Ishikawa,[1] Haruyoshi Katayama,[1] Tatehiro Mihara,[2] Mutsumi Sugizaki,[2] Naoki Isobe,[2] Hiroshi Tsunemi,[3] Emi Miyata,[3] Nobuyuki Kawai,[4] Jun Kataoka,[4] Atsumasa Yoshida,[5] Kazutaka Yamaoka,[5] Hitoshi Negoro,[6] Motoki Nakajima,[6] Mikio Morii,[7] Yoshihiro Ueda,[8] Satoshi Eguchi,[8] and MAXI team

[1] Japan Aerospace Exploration Agency, 2-1-1 Sengen, Tsukuba, 305-8505, Japan
[2] The Institute of Physical and Chemical Research, 2-1 Hirosawa, Wako, 351-0198, Japan
[3] Osaka University, 1-1 Machikaneyama, Toyonaka, 560-0043, Japan
[4] Tokyo Institute of Technology, 2-12-1 Ookayama, Meguro-ku, 152-8551, Japan
[5] Aoyama Gakuin University, 5-10-1 Fuchinobe, Sagamihara, 229-8558, Japan
[6] Nihon University, 1-8-14 Kanda-Surugadai, Chiyoda-ku, 101-8308, Japan
[7] Rikkyo University, 3-34-1 Nishi-ikebukuro, Toshima-ku, 171-8501, Japan
[8] Kyoto University, Kitashirakawa Oiwake-cho, Sakyo-ku, 606-8502, Japan
E-mail(SU): ueno.shiro@jaxa.jp

Abstract

Monitor of All-sky X-ray Image (MAXI) is an X-ray all-sky monitor, which will be delivered to the International Space Station (ISS) by a space shuttle crew in May 2009, to scan almost the entire sky once every 96 minutes for a mission life of two to five years. The detection sensitivity will be about 20 mCrab (5σ level) for one-orbit MAXI operation, 2–3 mCrab for one day, and 1 mCrab for one week, reaching a source confusion limit of 0.2 mCrab in half a year (Hiroi et al 2008). In this paper, brief descriptions are presented for the MAXI mission and payload , and three operation phases, 1) the launch-to-docking phase, 2) the initial in-orbit calibration phase, and 3) the routine operation phase. We also describes the MAXI data product and its release plan for public users.

Key words: X-ray Astronomy, All-sky X-ray Monitor, ISS, JEM, Kibo, MAXI

1. INTRODUCTION

The Exposed Facility of the Japanese Experiment Module (JEM) "Kibo" can be used as a site of space observations. Considering space sciences which can be performed under several limited conditions of the ISS, all-sky monitoring experiments are the best solution. Since the ISS always faces the bottom side to the Earth, the sky view from the ISS is rotating all the time. Moreover, there will be a small vibration in attitude. Thus the ISS is not a good site for precise pointing observations. Therefore the mission has become an all-sky monitor. The rotating sky enables us to scan almost the whole sky in every orbit without using any moving mechanism. The fields of view are free from the Earth occultation, which makes the observation efficient.

Many X-ray sources in the sky are highly variable in brightness and only observable above the Earth atmosphere. MAXI will perform the systematic survey of the X-ray variabilities to study the nature of active celestial objects. MAXI can detect X-ray transient phenomena and rapidly inform the world of its sky positions and X-ray brightness. The MAXI overview is presented in Ueno et al (2004) and Matsuoka et al (2007).

2. MAXI MISSION

Monitor of All-sky X-ray Image (MAXI) is an all-sky X-ray monitoring mission, which was proposed by the X-ray astronomy group of the Institute of Physical and Chemical Research (RIKEN) in 1996, and was selected in 1997 as a first-generation payload for the Exposed Facility of the Japanese Experiment Module "Kibo"(JEM "Kibo"), part of the International Space Station (ISS). In the development of the MAXI system (Fig. 1), we have completed the fabrication and the on-ground calibration of the MAXI flight hardware.

On the other hand, some components of the MAXI ground system are still under construction. In our current schedule, MAXI will be delivered to the ISS by a space shuttle crew in May 2009. The mission life will be two to five years, depending on the MAXI performance and resource availability on the JEM "Kibo".

3. Mission Objectives

MAXI will detect more than one thousand X-ray sources in the 0.5 to 30 keV band and monitor them with about ten times higher sensitivity than previous all-sky X-ray monitors. The 5σ detection sensitivity will be 2–3 mCrab for the one-day MAXI operation and 1 mCrab for one week (Hiroi et al. 2008). The mission objectives of MAXI are to:
1) make a time-resolved catalog of X-ray sources;
2) search for time variability of active galactic nuclei (AGN);
3) study the population of various types of AGN;
4) make complete light curves of X-ray novae (Negoro et al. 2008);
5) find and monitor transient objects;
6) make a spectral mapping of galactic hot gas with the X-ray CCD camera (Miyata et al. 2008);
7) detect Gamma-ray bursts and their afterglows;
8) monitor long-term variation of flaring stars.

Objectives 1) through 6) are solid goals with the MAXI sensitivity. Regarding Objective 7), the probability of Gamma-ray bursts (GRB) occurring in the MAXI fields of view is rather low (less than ten GRB a year), because MAXI views less than 2 % of the whole sky at any given moment. Suzuki et al (2008) estimates a detection probability of GRBs and afterglows in this proceedings. To achieve Objective 8) requires the precise calibrations of effective areas over the field of view, and the accurate determination or reproduction of instrumental background levels.

The MAXI ground system will transmit an alert through the Internet when it detects any significant X-ray transient phenomenon. Other observatories or satellites can turn their telescopes toward the source to make follow-up observations (Ishikawa et al. 2008; Negoro et al 2008).

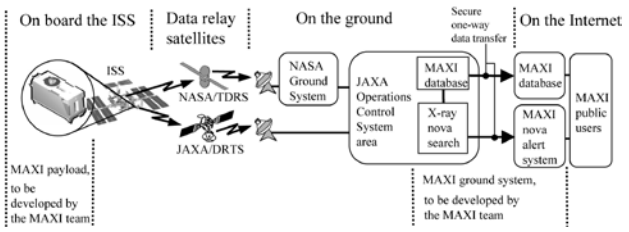

Fig. 1. The MAXI system. We have two downlink paths for the MAXI data. The MAXI team is responsible for the MAXI payload and its ground system. The MAXI mission, including the rapid distribution of observational results. The MAXI data will be transmitted to the Internet through a secure one-way path. Teaming up with public users is also an important task of the MAXI team for follow-up observations.

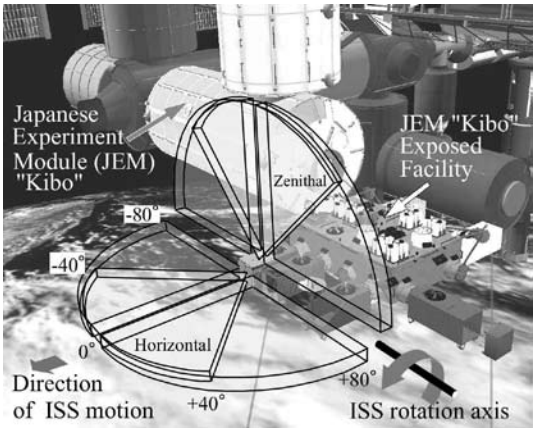

Fig. 2. The computer graphic picture of the Japanese Experiment Module(JEM) overlaid with visualized fields of view of the MAXI Gas Slit Camera (GSC). Position angles are shown along the fields of view. The rotation and the orbit motion of the International Space Station are synchronized at the same period of about 96 minutes. Not shown are the fields of view of the other type of camera, the MAXI Solid-state Slit Camera (SSC). The fields of view of SSC covers a smaller position-angle range from -45 deg to $+45$ deg.

4. MAXI PAYLOAD AND ITS X-RAY CAMERAS

4.1. The MAXI Payload

MAXI will be attached to one of the ten ports of the JEM "Kibo" Exposed facility (Fig. 2). The attachment port, called the Equipment Exchange Unit (EEU), has a mechanism to hold a payload, and provides various resources such as electricity, communication channels, and fluid through a single-phase heat pipe for heat reduction.

Figures 3 and 4 show the MAXI payload, which weighs 535 kg with dimensions of 185 cm (length) × 80 cm (width) × 77 cm (height). MAXI has simple X-ray eyes: eight combinations of a slit and orthogonally arranged collimator plates, which produce one-dimensional X-ray image along sky great circle on twelve position-sensitive proportional counters (Gas Slit Camera; GSC) in the 2–30 keV band (Mihara et al. 2008) and two X-ray CCD units (Solid-state Slit Camera; SSC) in the 0.5–12 keV band (Tomida et al. 2008).

4.2. X-ray Cameras

Table 1 presents the characteristics of GSC and SSC. The GSC has two fields of view toward two directions, 84 degrees apart from each other: a horizontal and a zenithal fields of view (see Fig. 2). The directions of the fan-shaped fields of view are fixed on the International Space Station (ISS). Since the ISS orbits with its bottom side always facing the Earth, MAXI automatically scans almost the whole sky every orbit with a period of about 96 minutes.

While MAXI flies through high background regions

Table 1. Specification of MAXI X-ray Cameras

Camera	GSC	SSC
Detector	Gas: Xe(99%)+CO2(1%)	CCD: Si
Energy range	2–30 keV	0.5–12 keV
Number of detector units	12	2
Detector geometrical area	5350 cm^2	200 cm^2
FOV per detector unit (FWHM)	1.5°×80°	1.5×90°
FOV per Horizon/Zenith units (FWHM)	1.5°×160°	1.5°×90°
Energy resolution	18%	< 150 eV at 5.9 keV
Timing resolution	≤200μs	—
Angular resolution (PSF FWHM)	∼ 0.5°	
Duty cycle for arbitrary sky position (typical)	∼ 100 sec / 90 min	
Exposure time per orbital period (typical)	∼ 160 cm·sec / 90 min	

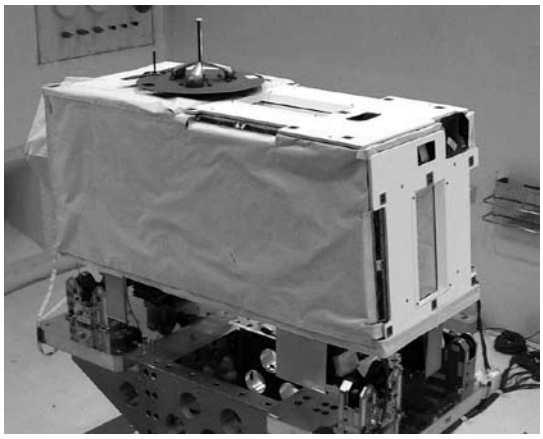

Fig. 3. The Monitor of All-sky X-ray Image (MAXI) flight model, which will be attached to the International Space Station in 2009.

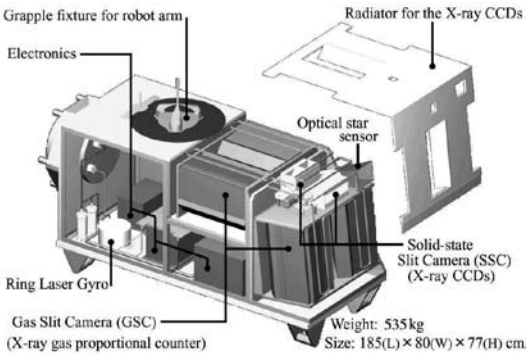

Fig. 4. The Monitor of All-sky X-ray Image (MAXI) payload.

such as the South Atlantic Anomaly, it cannot make useful observations. The sky region missed by either of the horizontal or the zenithal field of view due to such high background environments will be covered by the other field of view within one orbit time.

The CCD must be operated below −60°C to achieve the energy resolution of 143 eV FWHM at 5.9 keV. To cool CCD, a one-stage Peltier cooler is attached to the backside of each CCD chip to create a temperature gradient of $\Delta T = -40$°C between the chip and a SSC camera body. Each Peltier cooler consumes typically 1 W (in total 32 W for two SSC units). The heat from the Peltier coolers are transported by a Loop Heat Pipe (LHP) from the SSC units to two radiators on MAXI (this system is called Loop Heat Pipe and Radiator System, LHPRS). The rest parts of MAXI are cooled by the coolant circulated by the JEM.

The JEM "Kibo" provides an active thermal control system (ATCS), but its coolant temperature is 16 to 24°C, which is too warm to cool the SSC camera bodies. LHPRS has a thermal diode function, which is suitable in the ISS thermal environment where sky sink temperature for the MAXI radiators changes with a large amplitude and a short period (96 minutes).

The details of GSC and SSC are presented by Mihara et al. (2008) and Tomida et al. (2008), respectively.

5. The MAXI MISSION OPERATION PLAN

5.1. Analysis of the MAXI Mission Scenarios

From the launch of MAXI to the end of the mission, there are many ISS specific issues to be assessed for the MAXI mission success. Some of them are beyond the control of the MAXI team, and what we did is just assess and prepare for them. One example is the installation of the MAXI payload to the ISS with a robotic arm, during which the MAXI instruments have to survive at low temperatures with no electricity. We have assumed

such specific operation scenarios, and have verified by analysis that the MAXI mission withstands the worst cases.

5.2. Preparation for the Quick Start of the MAXI Data Analysis and Distribution after the Launch

Taking account of the mission life and the role as an all-sky monitor, it is essential to start the distribution of reliable and easily-utilized data to public users in the early stage of the MAXI mission.

The MAXI ground system for the scientific analysis and distribution is still under construction. We will complete the ground system, publish the detailed specification of the MAXI system, and start teaming up with potential MAXI users in advance to the MAXI launch currently scheduled for May 2009. For the quick start, the initial in-orbit calibration plan is also important (See Section 5.4 for in-orbit calibration).

5.3. Operations between the Launch and the Docking

Before MAXI is connected to the ISS through the Exposed Facility, no telecommand and telemetry to and from the MAXI data processor is available, and hence there is no ground operation planned by the MAXI mission team. Meanwhile, the JEM system operator will directly monitor the MAXI inside temperatures at two points bypassing the MAXI data processor, in order to confirm that the MAXI payload is within the expected temperature range during the transportation to the ISS.

After the shuttle docks with the ISS, the first space walk for MAXI will take place inside the shuttle payload bay to remove the MAXI contamination cover. The contamination cover prevents dust and particulate matter in the payload bay from falling into the MAXI X-ray camera slits and the MAXI star sensor baffle during launch.

Before MAXI is moved out from the shuttle payload bay, the "Kibo" Exposed Facility is transferred from the payload bay to the ISS. After the checkout of the exposed facility docked with the ISS, the exposed pallet carrying MAXI and two other payloads is transferred from the shuttle payload bay to the Exposed Facility. The exposed pallet is a pallet-shaped temporary storage space for exposed payloads, and is called Experiment Logistics Module Exposed Section (ELM-ES).

On the ELM-ES, the second space walk is schedule to remove MLI (Multi Layer thermal Insulator) from the payload interface unit (PIU) of MAXI. We need the MLI to keep PIU within its allowable temperature range during the MAXI transfer from the shuttle to the ISS. After removing the MLI from PIU, we raise the temperature of the MAXI payload using electrical heater. We need this preheating in advance to the MAXI transfer from ELM-ES to the "Kibo" exposed facility, because the grasped part of MAXI for the JEM robotic arm has no interface of power supply to the MAXI electrical heater.

Then MAXI is moved from the exposed pallet to the "Kibo" Exposed Facility, and is docked with Port 1. MAXI has two channels of power supply from the "Kibo" Exposed Facility: one is for experiment; the other for survival heater. MAXI is always supplied with either of the operation or the survival powers throughout the MAXI mission life.

5.4. Operations in the Initial In-orbit Calibration Phase

5.4.1. Performance evaluation using the MAXI simulation software

By Monte Calro simulation, Eguchi et al (2008), Sugizaki et al (2008), and Hiroi et al (2008) have evaluated the performance of the MAXI GSC observations in this proceedings.

In their simulations, all the MAXI structure were assumed to be in the positions as designed in drawings. In other words, the simulation has not predicted any systematic errors possibly caused by misalignment of parts, especially collimator plates and slit, and by limitations of our on-ground and in-orbit calibrations.

5.4.2. Position and flux determination accuracy estimated on the ground

The MAXI slit collimator is a source of systematic errors against position and flux determination accuracy. The 100-μm thin collimator sheets are supported in place using spring coils, which provides tension to keep the sheets flat. Even with the tension, the sheets bend by their own weight if the collimator is placed with the sheets parallel to the ground. Thus we have tested the engineering model, with the sheets vertical to the ground, in the laboratory using an X-ray beam line (Isobe et al. 2004).

Of the 64 collimator sheets over a GSC counter, every pair of adjacent sheets makes a triangular response of X-ray transmission with width of 1.5 degrees (FWHM at position angle of 0 deg). At every position angle examined in the field of view, the X-ray transmission directions of plate pairs are misaligned with a 3σ deviation of 0.12 degrees. The 3σ deviation of the field of view from a great circle is measured to be 0.03 degrees for the engineering model. With an estimated attitude determination accuracy of 0.05 deg (3σ) for the GSC and SSC units, the collimator quality is good enough to achieve position determination accuracy of 0.1 degrees in the scanning direction. On the other hand, the accuracy in the position angle direction depends on the quality of the slit and the X-ray counter. We also achieve the accuracy of 0.1 deg in this direction.

5.4.3. In-orbit calibration of the MAXI reference frame with the star sensor and the gyro

MAXI has the attitude determination system, which consists of Visual Star Camera (VSC), 3-axis Ring Laser Gyro (RLG), and onboard software (Horike et al. 2008).

In the MAXI initial operation phase, we calibrate the relative orientation of VSC and RLG, and also adjust some parameters of the onboard software.

5.4.4. In-orbit calibration of the orientation and the effective area of the MAXI X-ray cameras

For MAXI, the in-orbit calibration is crucial to achieve a position determination accuracy better than 0.1 degrees and a flux determination accuracy better than 10%. We cannot control the MAXI attitude, or the direction of the fields of view. What we plan to do with MAXI is:

1. Assume the directions of the X-ray fields of view, relative to the MAXI attitude reference frame defined with VSC and RLG;
2. Based on the assumed relative orientations and the measured MAXI attitude, reconstruct a 2-D X-ray image on the sky, and read the positions (RA and DEC) of known X-ray sources;
3. Adjust the assumed relative orientations of the X-ray fields of view so that the known source positions read from X-ray images become consistent with their cataloged positions.

The ISS goes around the Earth with the period of 96 minutes, the orbit inclination of 51.6 degrees, and the precession period of about two months. Thus every celestial source change its detected position in the MAXI field of view cyclically with a period of two months. Any given source is detected in a limited region of a field of view, depending on its declination angle in the equatorial coordinate system.

Figure 5 shows the coverage of field of view with a given celestial source. Fig. 6 shows the frequency of Crab Nebula's crossing the MAXI field of view at a given position angle (Panel a), and the same plot for Vela X-1 (Panel b). To cover the whole MAXI fields of view for calibration, we need more than one celestial source as flux and position calibrators.

5.5. Operations in the Routine Phase

5.5.1. MAXI ground system and its operation plan

The MAXI ground system consists of the following four components (see Fig. 1):

1. Database inside the JAXA Operations Control System (OCS) area, storing time-sorted event data for quick look and nova search;
2. Nova search system inside the JAXA OCS area, searching for significant X-ray transient events, such as X-ray novae;
3. Database on the Internet, providing images, spectra, and light curves in response to the public user access using web browsers;

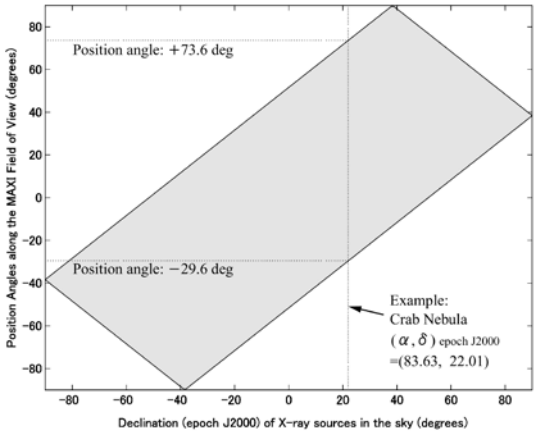

Fig. 5. The coverage of the field of view for a source with given declination angle. For example, Crab nebulae, a useful calibration source in X-ray astronomy, moves across the FOV at the position angles between -29.6 degrees and $+73.6$ degrees.

4. Nova alert system, issuing alerts on detecting significant transient events to registered users.

Components 1 and 2 are connected to the Operational Control System network, isolated from the Internet for security reasons. To transfer the MAXI data to Components 3 and 4 on the Internet efficiently, we construct secure one-way data paths using a two-port hard disk and a photo coupler.

Component 1 has five tasks: **1)** Data reception from the Operating Control System (OCS); **2)** First reduction of the raw data, and the storage in a database; **3)** Distribution of the first reduction data to other computers; **4)** Data backup; **5)** System diagnosis. Component 1 takes 0.2 – 0.3 seconds to process one-second MAXI data in the 20-kbps data stream.

5.5.2. Quick distribution of observation results

One of the MAXI main objectives is the quick distribution of observation results, including the transmission of X-ray nova alerts to the Internet.

On average, the 50–70% of the observational data will be downlinked in real time (with delay of a few to ten seconds). The duration of the real-time connection depends on the operation plans of the data relay satellites. During the ISS's real-time communication outage, data are stored in the onboard recorders. Then the data are replayed during next contact. The stored data takes 20 minutes to a few hours to arrive the MAXI ground system, depending the timing of source detection. The fastest way to distribute nova alerts is to perform nova search onboard the MAXI payload, and downlink the results with priority whenever a real-time connection is established. Instead, the MAXI team has chosen to per-

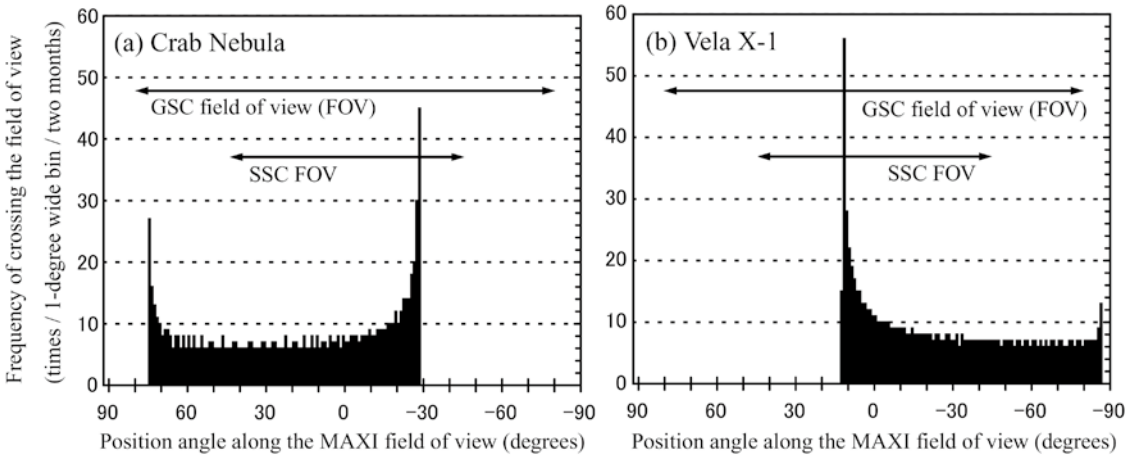

Fig. 6. Frequency of crossing the field of view, for Crab Nebula (Panel a) and Vela X-1 (Panel b).

form an X-ray nova search on the ground using more flexible hardware and software environments.

The details of the MAXI data transfer and process are presented by Ishikawa et al. (2008).

5.6. MAXI Data Product and Release Plan

The MAXI data distribution and archive system is described by Kohama et al. (2008) in this proceedings.

5.6.1. Nova alerts

The MAXI ground system will transmit an alert through the Internet on detecting any significant transient phenomenon, so that other observatories or satellites can turn their telescopes toward the source to make follow-up observations.

When the real time connection is established between MAXI and the MAXI ground system, the alert will be emitted a few seconds to one minutes from the source detection.

5.6.2. Processed data for known X-ray sources

For a pre-selected sample of known X-ray sources, you will be able to download **1)** light curves with background information; **2)** energy spectra with background information and detector responses; **3)** all-sky maps; with daily, weekly, and monthly updates.

5.6.3. Processed data for user-selected objects

Users will be able to specify any sky areas, energy bands, time windows, and data categories, using a web browser.

The MAXI team has no plan to release raw data to anonymous users, because the MAXI raw data (or X-ray event data) require the MAXI specific data reduction, quite different from the data reduction of pointed observation data. You can access the raw data through collaboration with the MAXI team.

6. Conclusion

MAXI will be delivered to the International Space Station in May 2009. We have finished the fabrication and on-ground test of the flight hardware, and are now constructing the MAXI ground system, including the science analysis software, the nova search system, and the data distribution system.

To start releasing useful and reliable data in the early phase of the MAXI mission, the MAXI team is planning a quick in-orbit calibration of the mission instruments.

At the MAXI portal Web page at RIKEN[1] , public users can access MAXI's latest information and processed data, such as X-ray light curves, spectra, and all-sky images. The registration desk for the MAXI nova alerts will be open at the same web page. Through collaboration with the MAXI team, you may access raw data for elaborate data reduction and data analysis.

References

Eguchi, S. et al. 2009, in this proceedings
Hiroi, K. et al. 2009, in this proceedings
Horike, N. et al. 2009, in this proceedings
Ishikawa, M. et al. 2009, in this proceedings
Isobe, N. et al. 2004, SPIE Proc., 5165, 354
Kohama, M. et al. 2009, in this proceedings
Matsuoka, M. et al. 2007, SPIE Proc., 6686, 111
Mihara, T. et al. 2009, in this proceedings
Miyata, E. et al. 2009, in this proceedings
Negoro, H. et al. 2009, in this proceedings
Sugizaki, M. et al. 2009, in this proceedings
Suzuki, M. et al. 2009, in this proceedings
Tomida, H. et al. 2009, in this proceedings
Ueno, S. et al. 2004, SPIE Proc., 5488, 197

*1 To access the MAXI information and data, please visit http://www.maxi.riken.jp/

The Gas Slit Camera, GSC, onboard MAXI

T. Mihara, M. Kohama, M. Sugizaki, N. Isobe, H. Chujo (RIKEN),
M. Matsuoka, M. Suzuki (JAXA), M. Nakajima (Nihon-u),
A. Yoshida (AGU), N. Kawai (Tokyo tech.)
and the MAXI team

Cosmic Radiation laboratory, RIKEN
Wako, Saitama, Japan
E-mail (TM): mihara@crab.riken.jp

ABSTRACT

The Gas Slit Camera (GSC) onboard MAXI consists of 12 slit cameras. Each camera utilizes slat collimator, a slit and a proportional counter (PC). The slat collimator limits the FOV into an arc of 1.5 × 80 degrees. The slit makes one-dimensional image on the PC within the FOV. The one-dimensional position-sensitive PC is filled with Xe gas. Thin carbon fibers (10 μm in diameter) are used as the resistive anodes, which enables position resolution of 1 mm. Six anode cells are surrounded by the veto layers, which achieve a low background rate by anti-coincidence. Six cameras are placed to cover an arc of 1.5 × 160 degrees of the forward direction, and other six cameras are to the zenith direction. The total area of the twelve PCs is 5350 cm^2. The energy range is 2-30 keV. The sensitivity of one scan is 7 mCrab (5σ), which reaches 1 mCrab in one week.

1. Slit Camera

In the Slit Camera, one point of the sky corresponds to one point on the detector (1:1). We can accumulate multiple scans, which lead to data with high statistics.

In case of the coded mask as RXTE/ASM it is 1 : many. A bright X-ray source in the FOV effects in all the points on the detector. The summation in years and spectral analysis of each source are practically impossible.

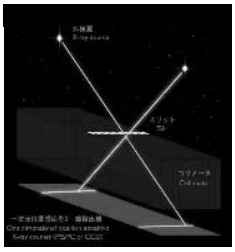

Fig.1. Schematic view of the slit camera .

2. Large Area

To achieve high sensitivity, we made the effective area of the PC as large as possible (5350cm^2 in 12 PCs) in the limiting size of the JEM-EF payload.

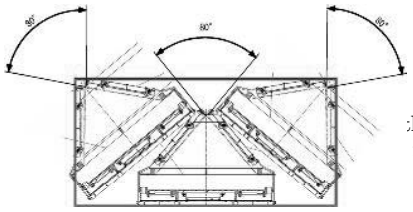

Fig.2. Packing three slit cameras in a rectanglar space.

3. Field of view (FOV)

Two FOVs are placed to forward and zenith directions, to compensate the unobservable sky (by SAA etc.) of one FOV with the other. The FOV of one camera is 80 degrees. Two cameras can cover 160 deg. The exposure time of a star near the scan poles is long as 1/cosθ. We placed the third camera in the equator of the scan to even the exposures.

The both edge of 10 deg. are omitted due to the shadow by the ISS structure. The forward FOV is tilted up by 6 deg. not to observe the Earth even when the ISS attitude changes. MAXI scans the all Sky with ISS rotation (90min). The two FOVs have no Earth occultation. The mechanics to move cameras are not needed. By limiting the observable time scale to be longer than 90 min., we can make the instrument simpler,

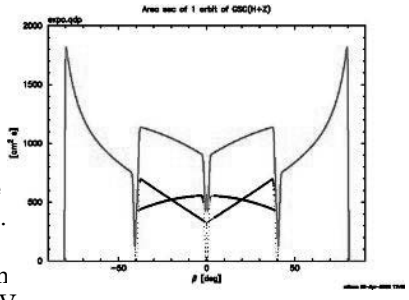

Fig.3. Effective exposure of GSC (Forward + Zenith cameras). Center (0 deg) is scan equator, ±90 deg. are scan poles.

and optimize it to search in the discovery space of the Long-term variability (> 1 hour) of AGNs etc.

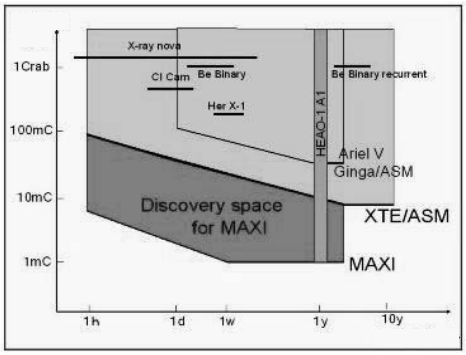

Fig.4. Discovery space of MAXI. Longer time scale than an hour to years in the low flux region.

4. GSC on MAXI

Fig. 5 is the MAXI flight model in the electric test. Radiators and side panels are removed and we can see the X-ray detectors. A slit camera of GSC consists of a slit and slat collimators. In Fig. 6 two cameras are shown.

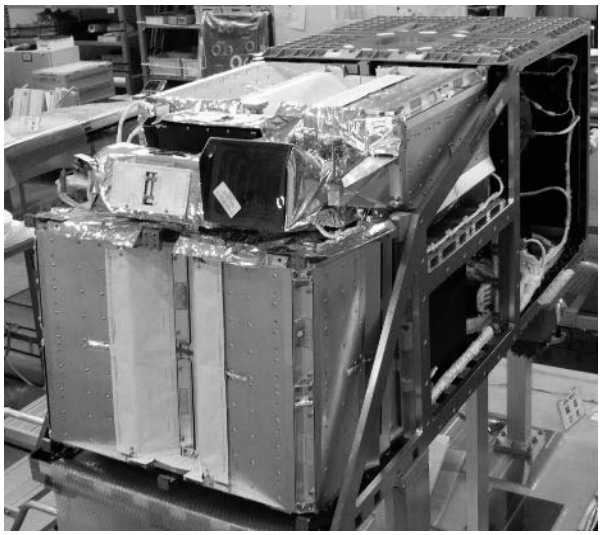

Fig.5. MAXI in the electric test. Six cameras in forward direction are facing us. The middle two cameras in the center are hidden. See also Fig.2.

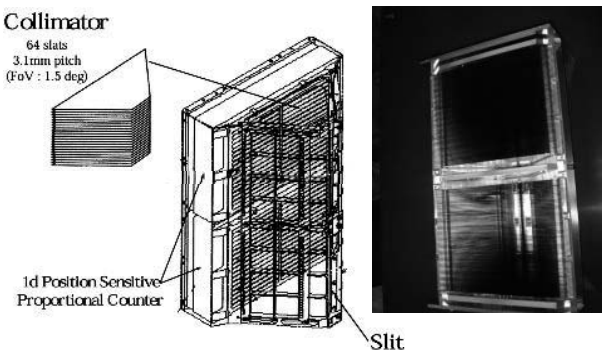

Fig.6. Two GSC cameras in one direction. The slit and slat collimators are shown. Right: collimators in bottom view.

5. Point spread function (PSF)

The PSF of GSC is designed as 1.5×1.5 deg FWHM at the center. The size depends on the incident angle. For example, it is smaller in the edges of the PC by $\cos\theta$, θ=0-40deg. To minimize the source confusion in the galactic center region, the PSF had better to be <1 deg. On the other hand, there is a difficulty in fabricating a finer collimator.

The size of the PSF within the long FOV is determined by the slit width and the position resolution of the PC.

PSF size=slit width+pos.res.of PC (1.1mm@8keV)

Narrowing the slit width for better pos. res. results in a low effective area and low sensitivity. By compromising, we chose 1.5 deg for PSF and 3.7mm for slit width. Also, the pos. res. of PC depends on the X-ray energy. The shape of PSF is rectangle convolved by the pos. res. of PC.

The size of the PSF in the scan direction is determined by the spacing between the slat collimators. The 1.5 deg FWHM of FOV gives 3.1mm spacing. The shape of PSF is triangular. The collimator was made of phosphor bronze. The thickness is 0.1mm to be thin compared to the spacing, and still, flat, and parallel. The surface was etched to have diffuse reflection for X-rays.

6. Proportional counter in GSC

The GSC PC was large-scaled the HETE/WXM PC. The GSC has twice longer wires and more cells. Both use the carbon fiber of 10μm in diameter for the resistive anode, which was developed in RIKEN.

The size of the Be window is 192×272mm, almost A4 paper size. To support the 740kgw pressure on the window, we made tall beams of 14mm height, in every 10mm, not to shadow the X-ray from the slit.

The PC body was made of Ti, which is strong and has a close heat-expansion rate as Be. The window is glued to the body with epoxy. The PC was fabricated by Metorex (Oxford inst.) in Finland.

Fig.7. Proportional counter used in GSC. The body size is 358 × 236 mm. The Be window is 100 μm thick and He-leak tight.

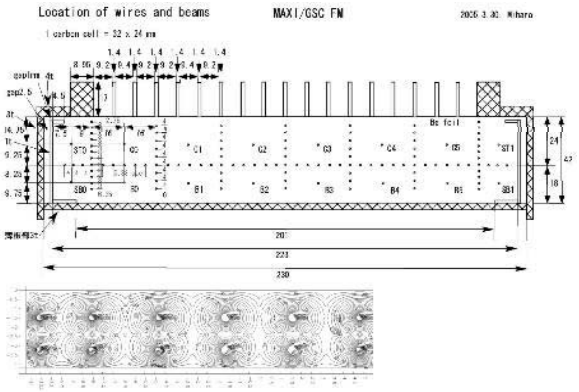

Fig.8. Cross section and sizes of a PC. Numbers are in the unit of mm. Bottom: The electric field calculation.

Compared to WXM PC, the shape of cells of the GSC PC was rectangular to decrease the number of signals from eight to six. The bottom and side vetos were placed. The position and spacing of the GND wires were optimized by the electric field calculation.

We tested several kinds of gas mixture and chose Xe+CO_2(1%) 1.4atm, which has low anomalous gas gain and still has quenching effect.

The position resolution and energy resolution are contradictory requirements. The position resolution is determined by the Johnson noise of the resistive wire. The low resistance of the carbon fiber has higher Johnson noise. Therefore we operate in rather high gas gain to obtain better position resolution. Then the anomalous gas gain appears and makes the energy resolution worse. The phenomena is that the gain depends on the X-ray stopped position in the cell (M curves). The operating gas gain of 5000 (HV=1650V) is determined to have enough position resolution and still have good energy resolution.

7. GSC Electronics (MDP)

The GSC PC has six position-sensitive anodes and 2 series of vetos, which results in14 analog signals in total. MAXI has 12 GSC PCs and the total signal number is 168 ch. Following method was used to process this much of signals .

Fig.9. Back side of the PC. Electrical circuits are mounted. Seven readouts are connected to the left and right preamp boards. The low-power high-voltage box is in the middle.

1. Preamps: Low-power hybrid IC Amptek A225 was used.
2. Gain amps: Hybrid IC (HIC) was developed for GSC. One HIC contains gain amp, shaping amp, lower-discriminator (LD) and peak hold in one package. The gain and LD are adjustable from outside to 512 and 4 levels, respectively.
3. HIC: Time constants of the shaping amp were adjusted to maximize the position resolution of GSC PC. Peak-hold capacitor is adjusted to sharpen LD. The radiationally weak MOS FET SD215 was replaced to a stronger type by Calogics company, and 2mm-thick Fe shield was added on the cover of the HIC in the outermost analog boards.
4. Analog board: One analog board was used for one PC. Cross talks between 14 channels were decreased by using coaxial jumper wires, not by the printed circuit.
5. Digital processing: The fuse-type FPGAs by ACTEL company were used for the Data Processing board. The digital errors were exterminated to a very low occurrence, such as once in a million.

References

Morii, M. et al. SPIE.6266. 62663 (2006)
"Development of the collimator response of gas slit camera of MAXI"

Tsuchiya, Y. et al. SPIE.5898.403 (2005)
"Detector response of GSC/MAXI and its expected performance in orbit"

Kataoka, J. et al. SPIE.5165.375 (2004)
"Ground-support electronics for testing the preflight performance of the MAXI-GSC"

Mihara, T. et al. SPIE.4497.173 (2002)
"Performance of the GSC engineering-counter for MAXI/ISS"

Mihara, T., Matsuoka, M., Kawai, N., Tsunemi, H. Proc. STAIF 2000, AIAA Conference on ISS Utilization 387 (2001)
"Monitor of all-sky X-ray image (MAXI) on JEM-EF"

Mihara, T. et al. Adv. Space Res. 25.897 (2000)
"MAXI (Monitor of All-sky X-ray Image) for JEM on the International Space Station"

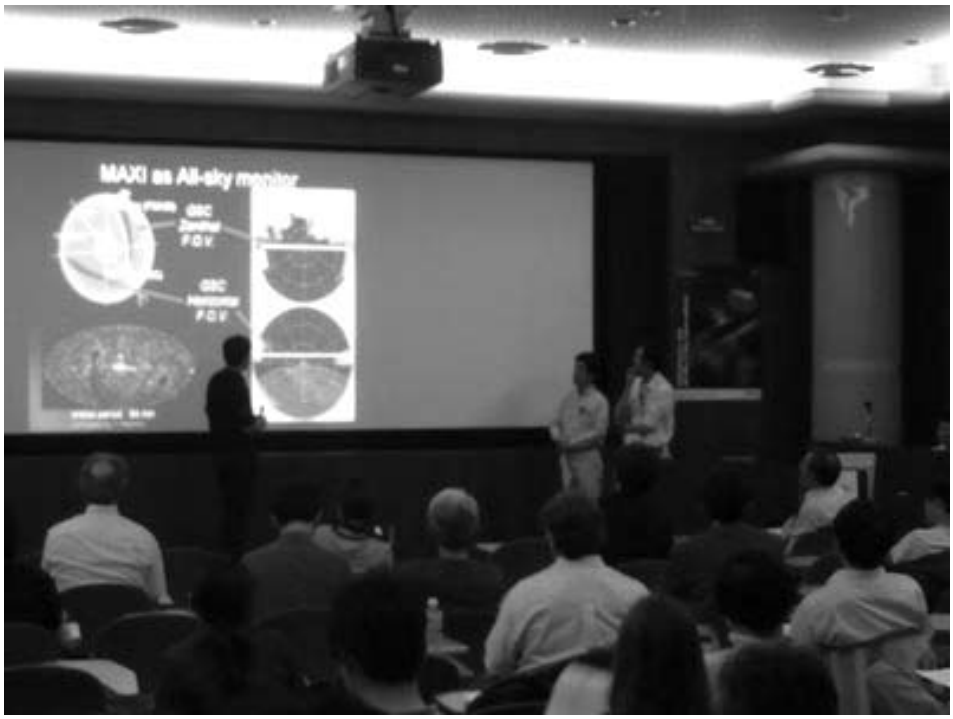

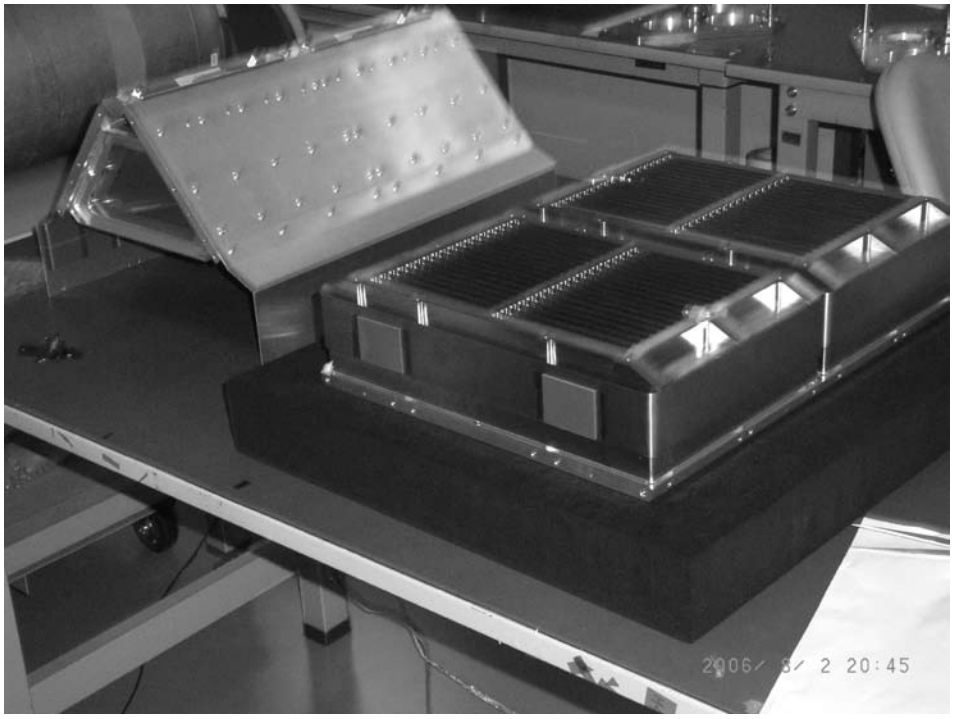

Solid-state slit camera (SSC) onboard MAXI

Hiroshi Tomida,[1] Masaru Matsuoka,[1] Kazuyoshi Kawasaki,[1] Shiro Ueno,[1]
Yasuki Adachi,[1] Mitsuhiro Kohama,[1,2] Motoko Suzuki,[1] Masaki Ishikawa,[1,9]
Haruyoshi Katayama,[1] Tatehiro Mihara,[2] Mutsumi Sugizaki,[2] Naoki Isobe,[2]
Hiroshi Tsunemi,[3] Emi Miyata,[3] Nobuyuki Kawai,[4] Jun Kataoka,[4]
Atsumasa Yoshida,[5] Kazutaka Yamaoka,[5] Hitoshi Negoro,[6] Motoki Nakajima,[6]
Yoshihiro Ueda,[7] Mikio Morii,[8] and MAXI team

[1] Japan Aerospace Exploration Agency (JAXA), Sengen 2-1-1, Tsukuba, Ibaraki, Japan
[2] The Institute of Physical and Chemical Research (RIKEN), Hirosawa 2-1, Wako, Saitama, Japan
[3] Osaka Unversity, Machikaneyama 1-1, Toyonaka, Osaka, Japan
[4] Tokyo Institute of Technology, Ookayama 2-12-1, Meguro, Tokyo, Japan
[5] Aoyama Gakuin University, Fuchinobe 5-10-15, Sagamihara, Kanagawa, Japan
[6] Nihon University, Kanda Surugadai 1-8-14, Chiyoda, Tokyo, Japan
[7] Kyoto University, Kita-Shirakawa Oiwakecho, Sakyo, Kyoto, Kyoto, Japan
[8] Rikkyo University, Nishi-Ikebukuro 3-34-1, Toshima, Tokyo, Japan
[9] Graduate Unversity for Advanced Study (Sokendai), Shonan Village, Hayama, Kanagawa, Japan
E-mail(HT): tomida.hiroshi@jaxa.jp

Abstract

SSC (Solid-state Slit Camera) is an X-ray camera onboard the MAXI mission. SSC consists of two SSC unit (SSCU) and SSC electronics (SSCE). SSCU includes 32 X-ray CCDs, slit and slat system, and so on. SSCE controls SSCU. SSC covers 0.5 – 12keV with energy resolution of <150eV at 5.9keV. CCDs are operated at –60°C utilizing thermo-electric cooler, loop heat pipe, and passive radiators.

Key words: All-Sky-Monitor, X-ray detector, CCD, soft X-ray

1. Introduction

CCD (charge-coupled device) has been nominal X-ray detector as photon counting device since the successful operation of SIS onboard the ASCA satellite (Burke *et al.* 1991). Its good position resolution and moderate energy resolution are suitable for X-ray astronomical observations. SSC (Solid-state Slit Camera), which is an X-ray camera of MAXI mission, also employs X-ray CCDs for X-ray detections. SSC has many characteristics different from GSC, another X-ray camera of MAXI (Mihara *et al.* (this proceedings)). The main objectives of SSC would be all-sky monitor in lower energy band, and the spectroscopy of largely extended celestial objects such as galactic ridge emission, Vela SNR, and so on. This paper describes the basic design and performances of the SSC system.

2. SSC System

The SSC system is composed of two SSC Units (SSCUs) and SSC Electronics (SSCE). Figure 1 shows the block diagram of SSC.

SSCU is a sensor part of SSC. One SSCU includes X-ray CCDs, preamplifiers, multiplexers, slit-collimator system, calibration sources, and so on. Figure 2 shows the schematic view and photograph of SSCUs. One of SSCUs monitors X-ray sky in the horizontal direction of MAXI, and another is for zenith direction. Hence, the former is called SSCU-H, and another is called SSCU-Z.

SSCE controls SSCUs. SSCE generates CCD drive signal according to commands from DP (data processor), and digitizes the video signal from SSCU. The Digitized data are transferred to DP. SSCE also controls CCD temperature using thermo-electric cooler (TEC) embedded in CCD chips.

Radiator and heat pipe are not a portion of SSC, however, they are very important to cool X-ray CCDs (section 5.). DP is also not a portion of SSC, although the data reduction in DP is essential to maximize the data quality of X-ray events (section 3.).

2.1. X-ray CCD

A photograph of an MAXI-CCD is shown in Figure 3. CCDs are FFTCCD-4673 fabricated by Hamamatsu Photonics K.K.[1] . The chip is front-illuminated and two-phase CCD operated in full frame transfer mode.

*1 http://www.hamamatsu.com/

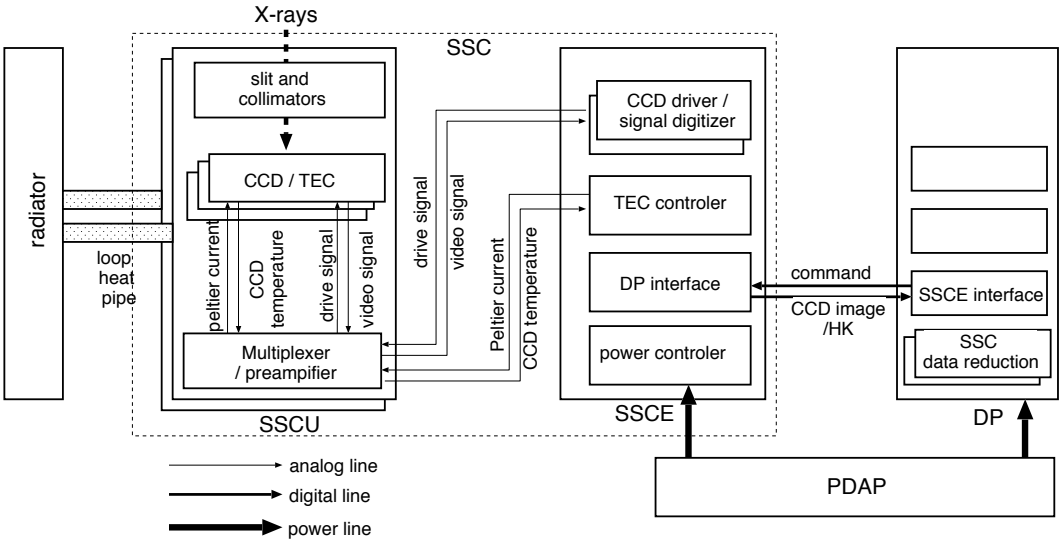

Fig. 1. Block diagram of the SSC system and signal flow between components.

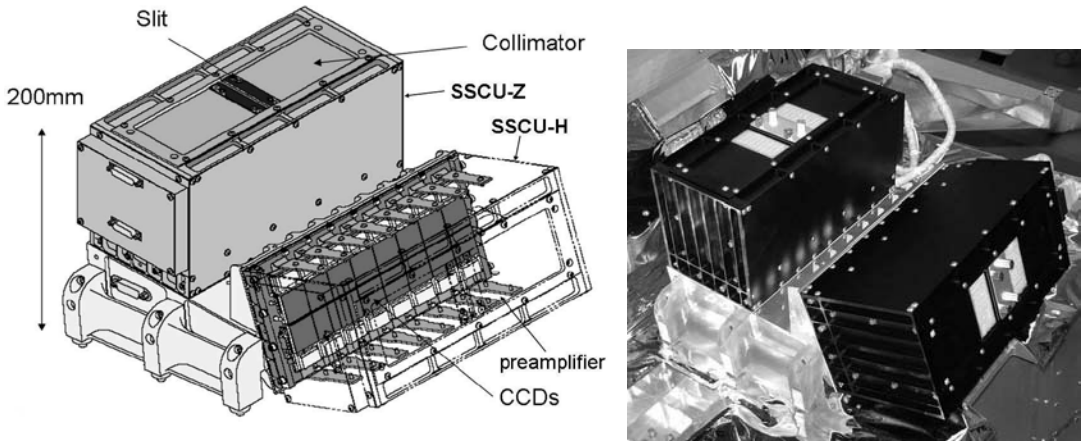

Fig. 2. Schematic view (left) and photograph (right) of SSCUs. In the photograph, protection covers are put on the slits.

The pixel number is 1024×1024, and the pixel size is 24 μm×24 μm, giving the CCD size of 25 mm × 25 mm for X-ray detection. In order to obtain the large X-ray collection area, each SSCU includes 16 CCDs, which are placed in 2×8 array as shown in Figure 2. The total X-ray detection area of 32 CCDs is $\sim$200cm^2. Charge injection (CI) is available to minimize the damage of particle radiation.

CCD has sensitivity for optical light, which degrade the sensitivity for low energy X-rays and the energy resolution. In order to block it, aluminum is coated on the CCD surface. No fragile filter is used, which makes the structure of SSCU quite simple.

SSC does not utilize X-ray mirror, hence the energy range is determined by mainly CCD. The quantum efficiency for soft X-ray is limited by the gate structure (dead layer) and aluminum on the front surface of CCD, and that of hard X-ray is by thickness of depletion layer. The gate structures is made of SiO_2 and Si whose designed thickness are 0.5 μm for both. The thickness of aluminum and depletion layer is 0.2 and 70μm, respectively. Then the energy range determined by CCD (quantum efficiency $>$ 10%) is 0.5–15keV for normally incident X-rays. The quantum efficiency for slant incident X-rays is larger for hard X-rays, and smaller for soft X-rays. Figure 4 shows the quantum efficiency of CCD as a function of X-ray energy. The detection efficiency of CCD extends to 15 keV, the energy range of SSC for hard X-ray is, however, limited by ADC. Then the energy range as X-ray camera including electronics is 0.5–12 keV.

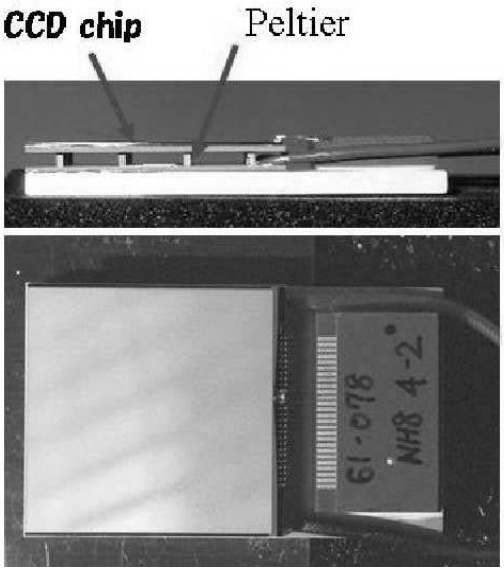

Fig. 3. A photograph of X-ray CCD equivalent to that in SSC.

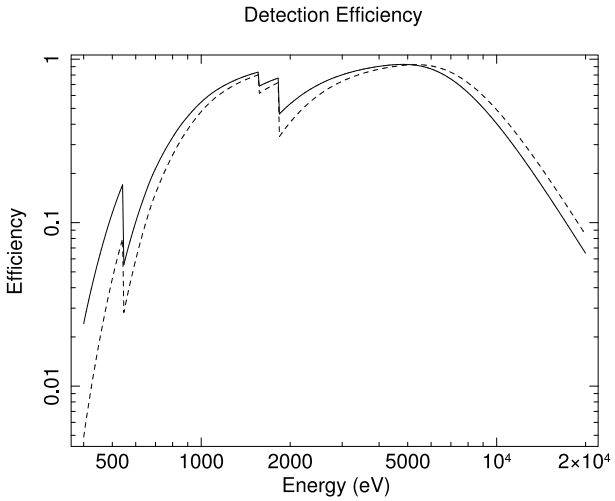

Fig. 4. The quantum efficiency of X-ray CCD as a function of incident energy calculated from the designed value of thickness of depletion layer and dead layers. The solid line represents incident angle = 0°, and the broken line is for incident angle = 40°.

2.2. Slit and Collimator

SSC has collimator and slit system but not X-ray mirrors. Collimators of SSC limit field of views (FOV) to be narrow and long shaped, and slit and CCDs determine the direction from which X-ray photons come in the narrow FOV. Figure 5 shows the design of slit and slat collimator system. This system is installed in each SSCU.

Slat collimators are made of thin sheets of phosphor bronze. The thickness is 0.1mm, and 24 sheets are placed above CCDs in the interval of 2.3 mm. The width of narrow FOV determined by slat collimators (θ_1 in Figure 5) is 1.5° in FWHM.

Slit of SSC consists of two sharp edges made of tungsten. The width between the two edges is 2.7mm. Since the position resolution of CCD is much better than the slit width, the angular resolution along the narrow FOV is determined by the slit width to be 1.5° (θ_2 in Figure 5). The angular length of the FOV (θ_3 in Figure 5) is 90°.

3. CCD Drive

CCD clocking signal is generated in SSCE. CCD is two dimension array, while SSC requires only 1-dimensional position information. Hence, multiple rows are summed in serial register at the bottom of imaging region, and the summed charges in serial register are transferred to read-out node. The number of summed rows in normal observation can be selected from 8, 16, 32 or 64 by commands. We call this number "binning" parameter. The binning of 64 is selected for the nominal observation. The larger binning gives the better timing resolution, and the better timing resolution provides better angular resolution in X-ray sky map. binning=1 is used for the diagnosis only. The clocking speed is 8μs/pixel, and a two-phase vertical transfer takes ~100 μs. The video signal from 16 CCDs in a SSCU are processed by one read-out electronics and one analog-to-digital converter (ADC). When a CCD is driven and read-out, other 15 CCDs are in exposure.

The charge injection (CI) is an effective method to restore the degraded performance of X-ray CCD (Tomida *et al.* (1997)). CI can be applied to SSC. The charge injection period is determined from the binning parameter, and the charge amount can be roughly controlled by commands through the clocking voltage. The charge-injected pixels (rows) are not summed in the serial register, and horizontally transferred without read-out. Then it takes longer time to read whole CCDs than that in non-CI operation. The operation mode with CI=ON and binning=64 reads 16 CCDs in 5.9s, which corresponds to the timing resolution in the nominal observation of SSC. The FOV of MAXI moves ~0.4° in 5.9s, which is smaller than the width of the narrow FOV (~1.5°).

Whether CI is applied or not can be controlled by command operation. CI is not required at the begining of the MAXI operation since the radiation damage would be small. However the application of CI after non-CI observation results in the significant change of the energy response. In that case, we have to construct new response functions, which is heavy and time-consuming work. Hence we decided that CI should be turned on from the beginning of the SSC operation.

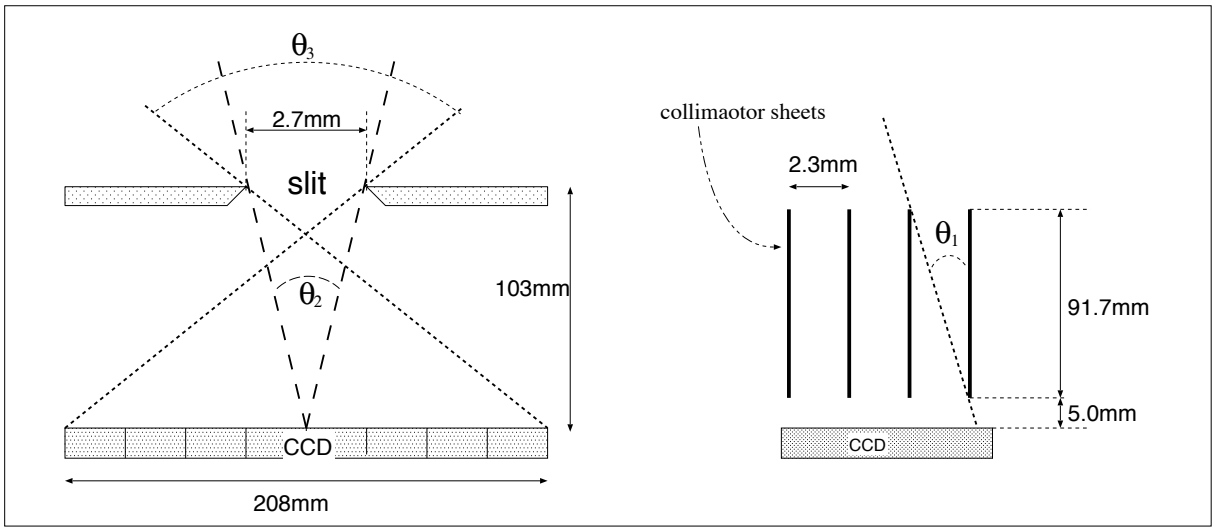

Fig. 5. Design of slit and slat collimators of SSC.

4. Data Reduction in Orbit

The CCD images digitized in SSCE are sent to DP (data processor). We designed the data reduction procedure in DP referring to that of timing mode of Suzaku/XIS (Koyama *et al.* 2007). The dark level, which is the time-averaged pixel data with no radiation of X-rays or charged particle, is determined for individual pixels and up-dated every frame.

DP searchs for the charge pattern characteristics of X-rays, which is called event. The event search is done for the pixel data after the dark-level subtraction, which we call pulse height (PH). An event is recognized when a pixel has PH between the lower and upper event threshold defined by command, and when the PH is a local maximum among adjacent 3 pixels in the row.

The MAXI telemetry data is transferred from MAXI-DP to the JEM/ISS through two physical networks in JEM/ISS. One network is MIL-1553B and another is Ethernet (Ishikawa *et al.* (this proceedings)). MIL-1553B is reliable and has much real-time connection, while the data transfer rate is limited to 50kbps at the maximum. Ethernet has data rate of 600kbps at maximum, while real-time connection is less available. It is not required that the event data in the two network should be identical. Then, we designed that Ethernet data is used for the detailed analysis (spectroscopy and diagnosis) and the MIL-1553B data is for the nova search and alert system (Negoro *et al.* (this proceedings)).

Each event data of Ethernet telemetry include CCDID, Y-address, X-address, and the PHs of adjacent 5 pixels (local maximum, trailing 2 pixels, and preceding 2 pixels). If the number of event is too large, the event data is compressed automatically or by commands. PHs of five pixels are summarized into a summed PH and the pixel pattern of the PH distribution in a row. There are 4 pixel patterns (grade 0 through grade 3), which is same as fast mode of ASCA/SIS. Grade 0 is a pixel pattern that all electrons excited by an incident X-ray is confined in one pixel.

DP compresses every X-ray event for the MIL-1553B telemetry. 14 bits are assigned for X-address and PH, and 2 bits for grade. The grade definition is same as that of Ethernet. The bit assignment for X-address and PH is determined by command. The nominal operation mode assigns 6 bits for X-address and 8 bits for PH, where 1 channel unit corresponds to 0.36 mm for position determination (X-address) and ~60eV for energy (PH). The maximum number of SSC event for MIL-1553B telemetry is limited 254 events/16 lines.

5. Control of CCD Temperature

A one-stage thermo electric cooler (TEC) is used to cool CCDs. TEC is included in MAXI-CCD of FFTCCD-4673 (Figure 3). CCD chip is mechanically supported by TEC only, therefore heat input to the CCD is mainly thermal radiation. The heat from TEC is transferred through loop heat pipe to radiator panels on the MAXI surface, and radiated away to the space. The loop heat pipe and radiator system is designed to cool the SSCU (camera body) around -20 °C . The cooling power is determined mainly by the size of radiator ($\sim 1 m^2$). The hot side of TEC are thermally connected to the SSCU body. TEC gives the temperature difference of >40 K between CCD chip and camera body. Hence, CCD will be operated below -60 °C .

6. Pre-Flight Performance

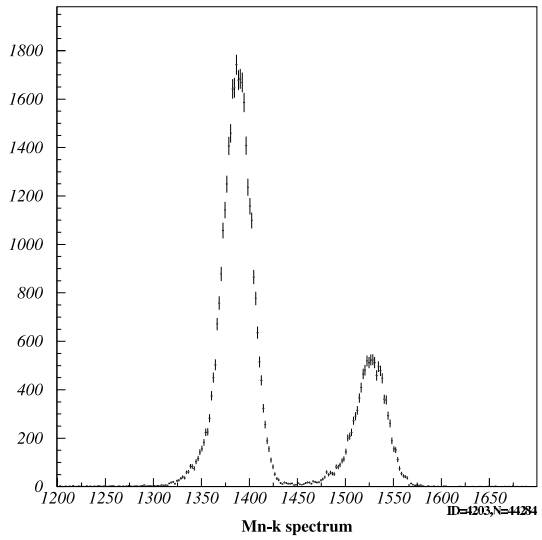

Fig. 6. Pulse height distribution of the SSC-Z/CCDID=3. X-rays from ^{55}Fe are irradiated.

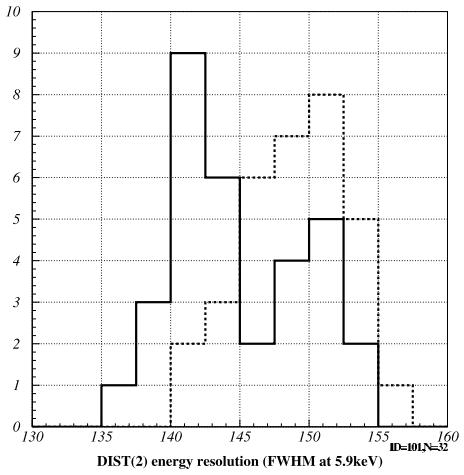

Fig. 7. The distribution of the energy resolution of 32 CCDs in SSC. The solid line is at the CCD temperature of −70°C , and the dotted line is at −60°C .

The camera level calibration of SSC was done using fluorescent X-rays from 9 materials and Mn-K X-rays from ^{55}Fe sources. The energy range is 0.52 (oxygen) to 12.5 keV (selenium).

Figure 6 shows the spectrum of ^{55}Fe sources with SSC-Z/CCDID=3. The CCD temperature is −70°C , X-rays from ^{55}Fe are irradiated, binning is 64, and the charge injection is applied (nominal operation). The spectrum is made of grades 0 events only. We can see Mn Kα and kβ lines are clearly resolved.

We fit the spectrum with two Gaussian model. One Gauusian constructs the main peak, and another Gaussian is small and resides at the lower energy side of the main peak. We defined the energy resolution as width of main Gaussian peak. The energy resolution of Figure 6 is 136 eV at 5.9 keV in FWHM, which is the best value of 32 CCDs in SSCUs. Figure 7 is the distribution of energy resolution for 32 CCDs at the CCD temperature of −60°C and −70°C . The average of energy resolution for 32 CCDs is 149eV for −60°C , and 145eV for −70°C .

The energy resolution of CCDs depends on the energy of incident X-ray. Figure 8 shows the energy resolution as a function of X-ray energy. The spectrum is made of grade 0-events only. The energy resolution is limited by mainly Fano-factor at the high energy region, and by mainly read-out noise at the low energy. The read-out noise of 32 CCDs ranges 5 to 10 electrons, which are determined from the fluctuation of PHs in horizontal over-clocked region. Charge transfer inefficiency is negligiblly small ($\sim 10^{-6}$).

Figure 9 shows the PH of SSC-Z/CCDID=3 as a function of incident X-ray energies, where PH is the channel at the center of main peak made of grade 0 events. CCD was operated in nominal parameters. We fitted the data with a linear function, and the solid line in the Figure 9 is the best fit line. We can see that the relation is well reproduced by a linear function.

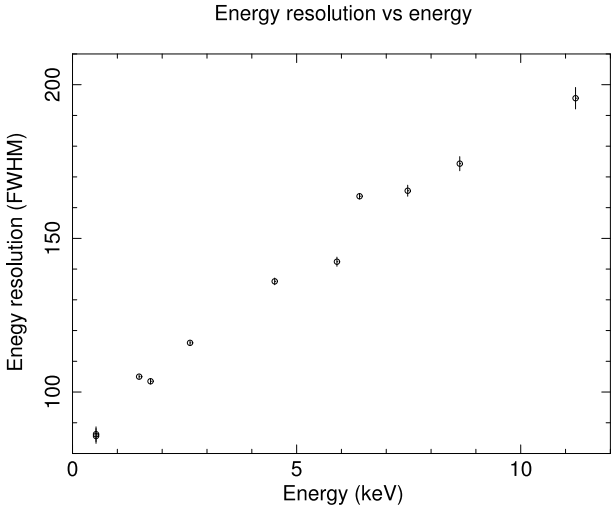

Fig. 8. The energy resolution of SSC-Z/CCDID=3 as a function of X-ray energy.

References

Burke *et al.* 1991, IEEE Trans. ED, 38, 1069
Koyama *et al.* 2007, PASJ, 59, 23
Tomida *et al.* 1997, PASJ, 49, 405
Ishikawa *et al.* This proceedings.
Mihara *et al.* This proceedings.
Negoro *et al.* This proceedings.

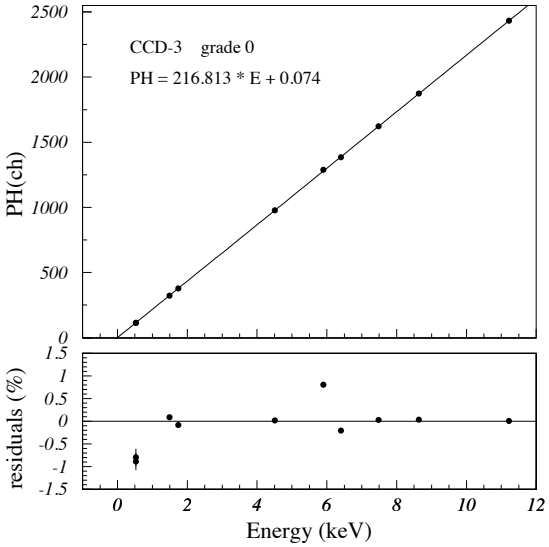

Fig. 9. Pulse height of SSC-Z/CCDID=3 as a function of X-ray energy. The lower panel shows the residuals between best fit model (linear function) and the data.

The on-board Attitude Determination System for MAXI

Naoko Horike*, Ken Maeda**, Shiro Ueno***
*NEC Aerospace Systems **NEC ***JAXA
E-mail: n-horike@pb.jp.ne.com

ABSTRACT

ADS（Attitude Determination System）is the on-board attitude determination system using a Star sensor (VSC) and Gyroscope (RLG).

The purpose of ADS is rapidly providing accurate attitude determination results to world investigators through the MAXI alert ground system. It is required that the accuracy of the occurrence of X-ray events must be less than 0.1 degree in direction in any situation of data downlink and VSC data acquisition.

KEY WORDS: MAXI, ADS, RLG, VSC

1. Introduction

It is commonly understanding that in the design phase of an Attitude Determination System, using sensor data quality is an important factor.

Taking this in consideration, the MAXI-ADS are designed to have the following functions

For the purpose of improving the VSC data noise characteristics, three logics are used to reject noise, generated by several causes, in VSC data. Especially the disturbance on orbit environment which interferes with VSC must be concerned.

RLG has a characteristic of the large readout noise. And the attitude disturbance around 8Hz will be expected due to ergometers used by astronauts. So RLG output data above 20Hz will be cut-off by a low-pass filter.

And the ADS algorithm is modified based on the on-board attitude determination systems, which is mainly used in Astronomy Missions of JAXA/ISAS.

In this paper, ADS function, operational condition, attitude determination algorithm and the test results will be introduced.

2. Introduction of MAXI ADS

The MAXI ADS is the embedded function in the MAXI on-board Application Software in the MAXI-DP master CPU, to avoid using ISS-JEM data interface directly.

MAXI ADS consists of one Star sensor and one Ring Leaser Gyro only. This is much simpler in comparison with common attitude determination sensor systems. Fig1 shows the outline view of VSC and RLG.

The ADS is the embedded function in MAXI on-board Application Software in the MAXI-DP master CPU which is the main CPU of MAXI-DP. Fig2 shows ADS System Configuration.

Fig3 shows VSC and RLG coordinate system definitions with regard to the MAXI coordinate system.

Fig1 MAXI ADS using sensors

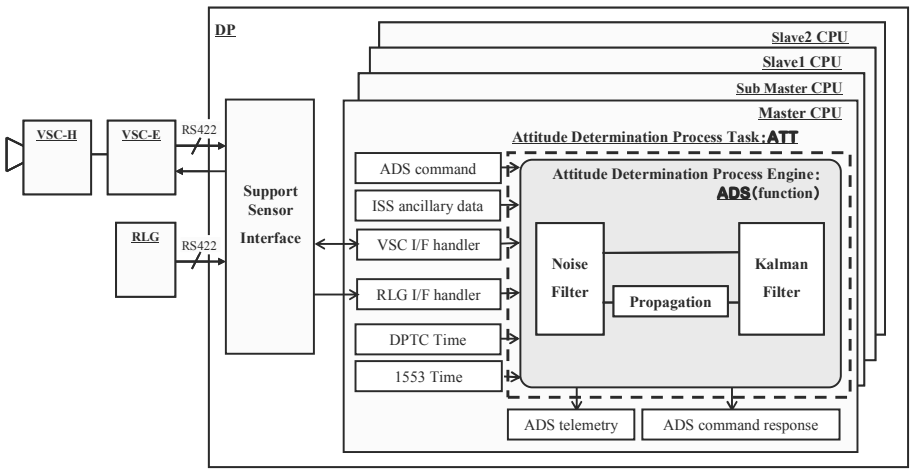

Fig2 ADS System Configuration

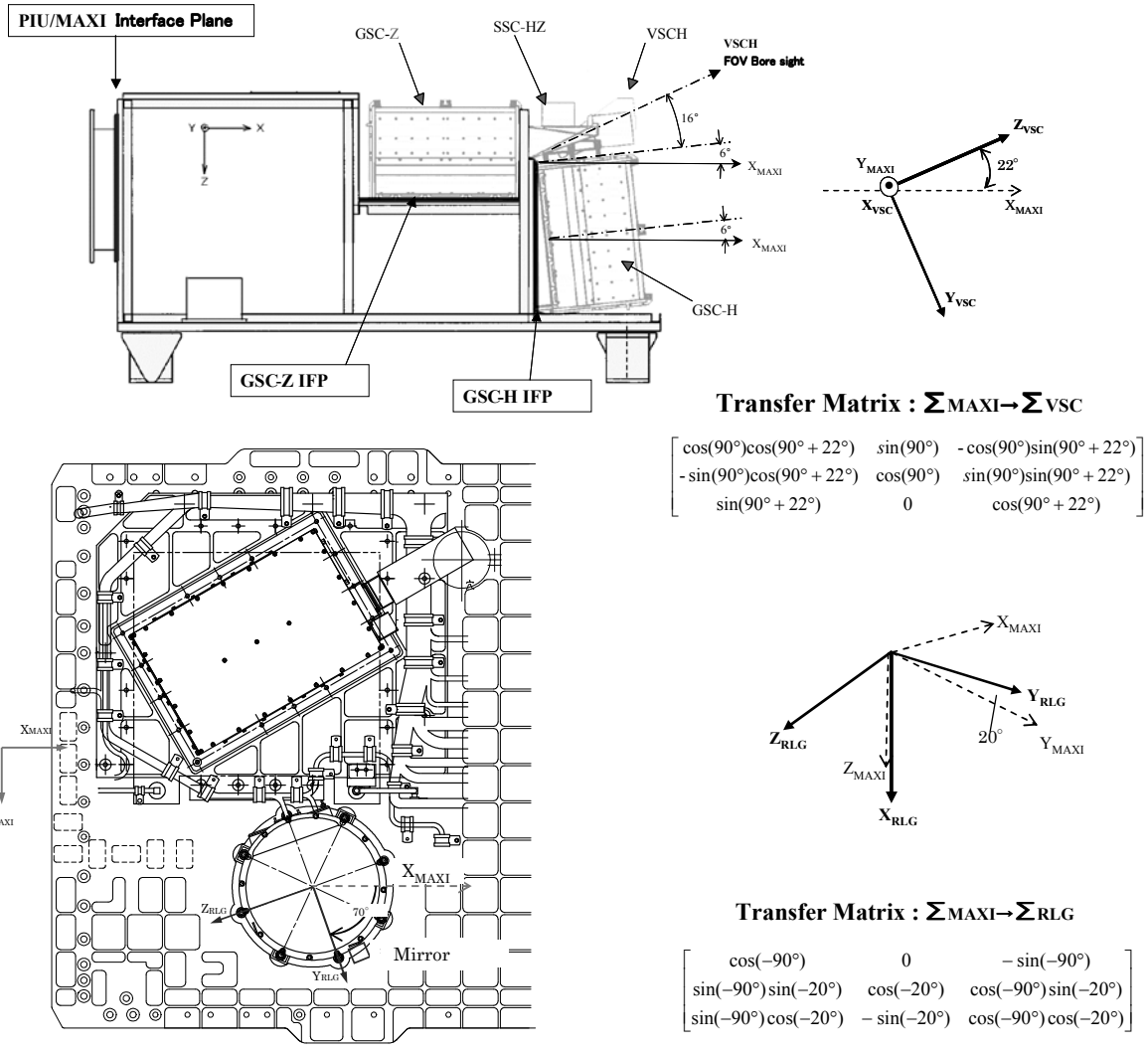

Fig3 VSC and RLG Coordinate system definition

3. MAXI ADS Function

The MAXI ADS functions are as follows:

- ADS rejects undesired VSC anomaly data caused by SAA, Sun and Day side of Earth Interference etc.
- ADS cuts high frequency RLG Readout noise off with Low Pass Filter.
- ADS propagates with filtered RLG data and updates the correction data with filtered VSC data.
- Kalman filter is used for estimating the residual attitude error.

4. MAXI ADS Operational Condition

4.1 VSC data operational Condition

VSC anomaly data on orbit environment must be rejected by ADS. The detailed explanations are described in the following.

- **VSC anomaly data rejection Logic**

  There are three logics for the VSC anomaly data rejection as follows.

  - **VSC Quality flag**

    Using the VSC telemetry item which VSC has decided the Quality result.
  - **On-board Autonomous calculation**

    Using the result of the Sun and the Day side of the Earth avoidance calculated by ADS with ISS ancillary data.
  - **External Command**

    Using ADS command operated from the ground station. Mainly this is prepared for SAA.

- **Definitions of Operational Condition**

  Fig4 shows VSC the concept of anomaly data rejection of ADS on orbit environment.

  External Commands are effective anytime

  Alternative Selection VSC Quality flag or On-board Autonomous calculation can be selected

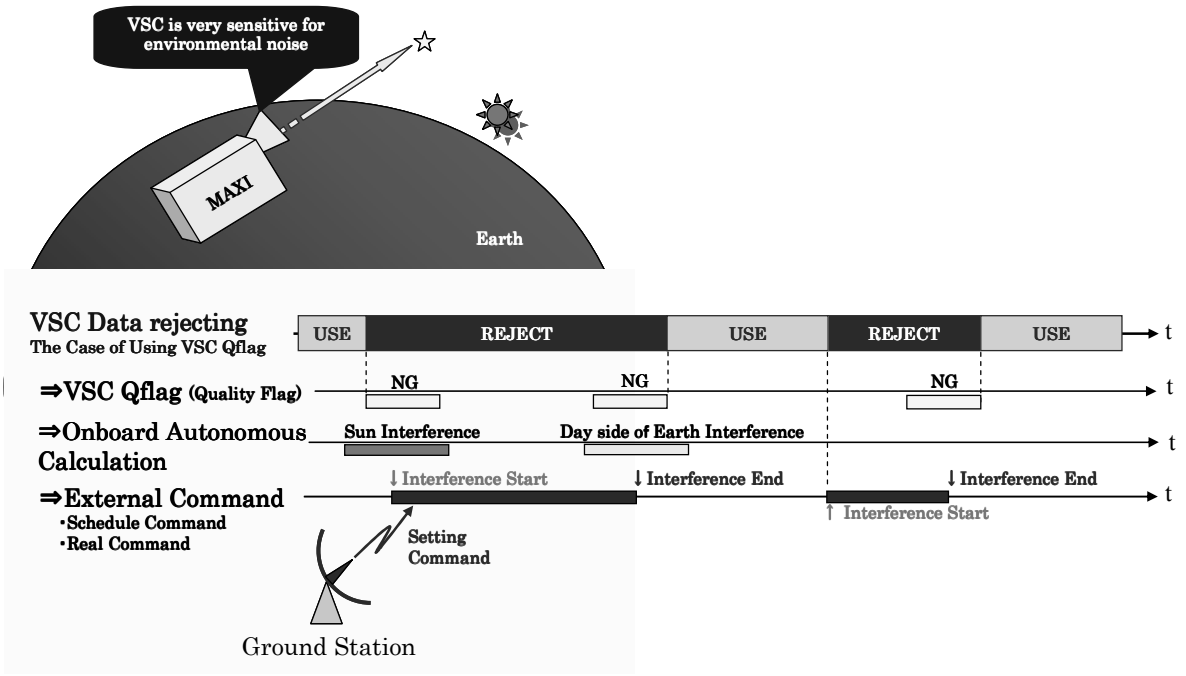

Fig4 VSC anomaly data rejection of ADS on orbit environment concept

4.2 RLG data filtering (Noise Filter)

RLG outputs 200Hz angular data with noise, generated by several causes. ADS gets about 200 data set every 1s. To improve the RLG data, noise characteristics on every RLG data is filtered because RLG data has a characteristic of large readout noise.

Also the attitude disturbance is monitored. Especially around 8Hz will be expected due to ergometers used by astronauts. And at least 90% of the amplitude must be kept after being filtered.

●Filter Design

The Error data above 20Hz between the RLG data and the values estimated by calculation angular rate for 50 ms, will be cut-off by the elliptic low-pass filter as follows. Fig5 shows the amplitude-frequency response.

- Design Method : IIR (Ellipse)
- Sample Frequency : 200Hz
- Cut-off Frequency : 20Hz
- Stopband Frequency : 25Hz
- Passband Attenuation : 0.4dB
- Stopband Attenuation : 30dB
- Filter Order : 5

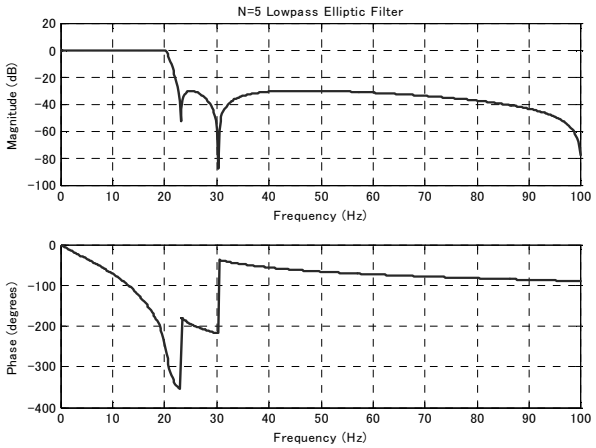

Fig5 Filter frequency response

4.3 ADS Timing Chart

Fig6 shows the ADS Timing Chart.

ADS determines the one previous cycle attitude with allowance for the 5 second VSC telemetry latency.

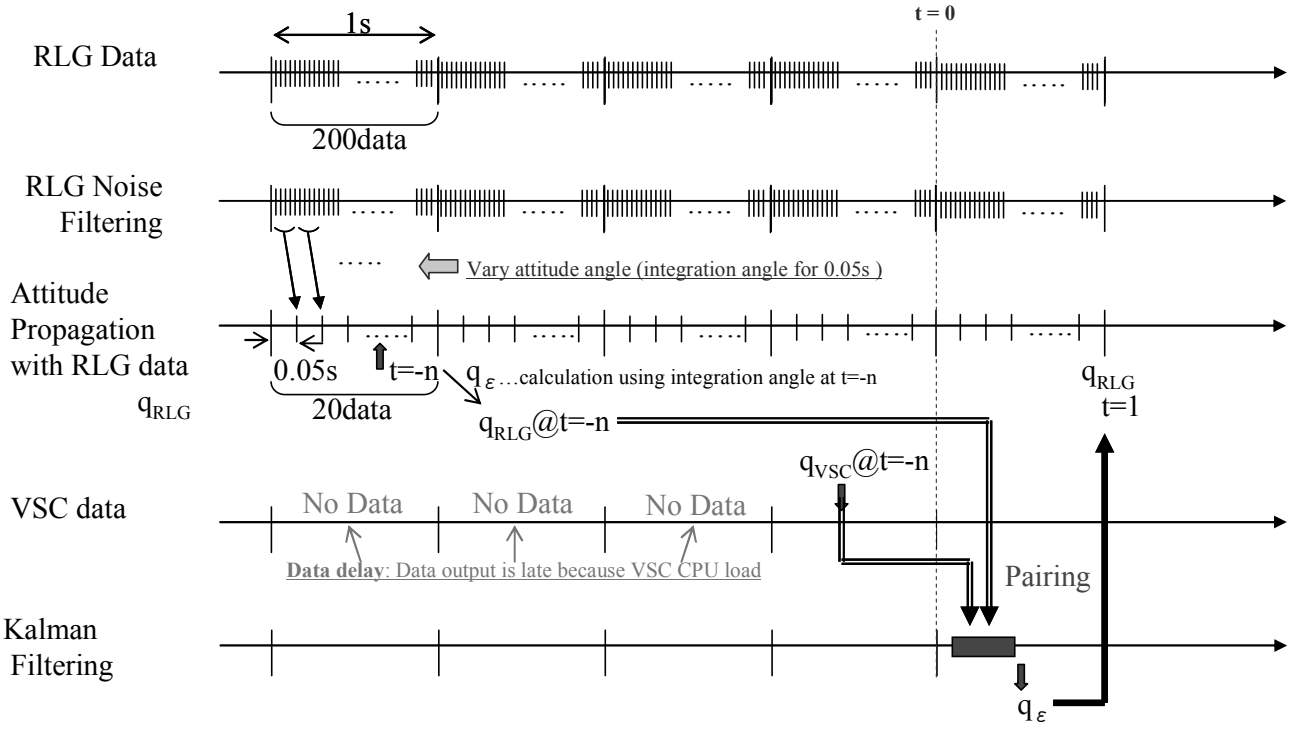

Fig6 ADS Timing Chart

5. MAXI ADS attitude determination algorithm

Fig7 shows the configuration of the Kalman Filter process.

,where $\mathbf{q}(t)$ is the actual attitude, $\bar{\mathbf{q}}_t$ is the estimated attitude and $\mathbf{K}_t$ is the Kalman Gain.

The algorithm of estimation uses for NOT actual attitude BUT propagated attitude error.

$\hat{\mathbf{q}}'_{\mathrm{v},t}$ $\hat{\mathbf{b}}'_t$ are propagated attitude error and bias error.

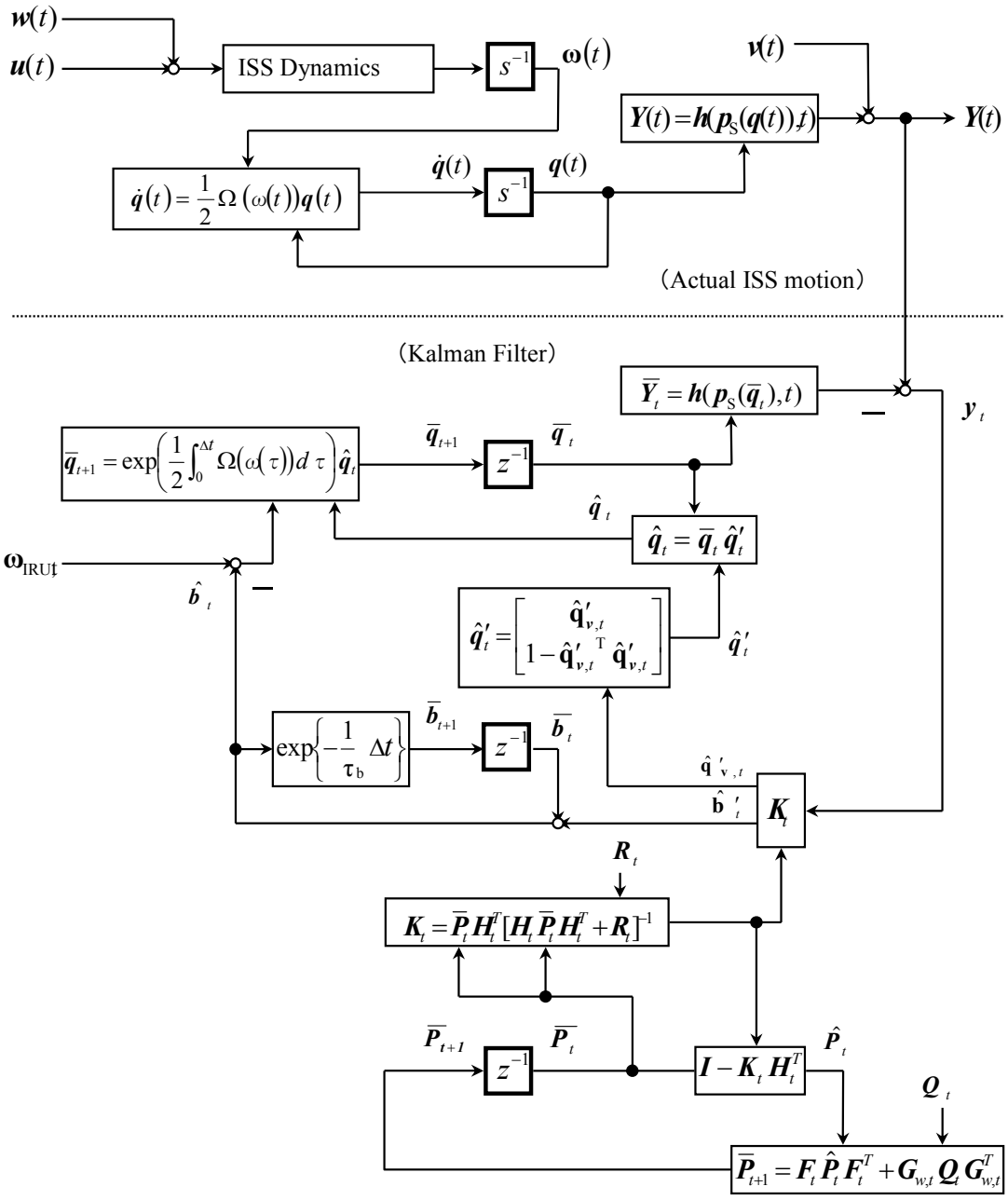

Fig7 The Kalman Filter process configuration

6. MAXI ADS the test results

An example of the ADS Kalman Filter Logic Evaluation result is shown in Fig8. This is based on a simulation during one ISS orbit with updated data of VSC.

The result shows that the ADS Kalman Filter logic realizes the accuracy within 0.002°of MAXI attitude on every axis. As the acceptable margin of error for the ADS Kalman Filter Logic is less than 0.016°at the design phase, this result satisfies the request.

7. Conclusion

MAXI ADS can realize rapidly providing accurate attitude determination results to world investigators through the MAXI alert ground system. And the attitude accuracy can be less than 0.1 degree in direction in any situation of data downlink and VSC data acquisition.

It is planned to calibrate RLG alignment and pulse weight after starting the MAXI operation.

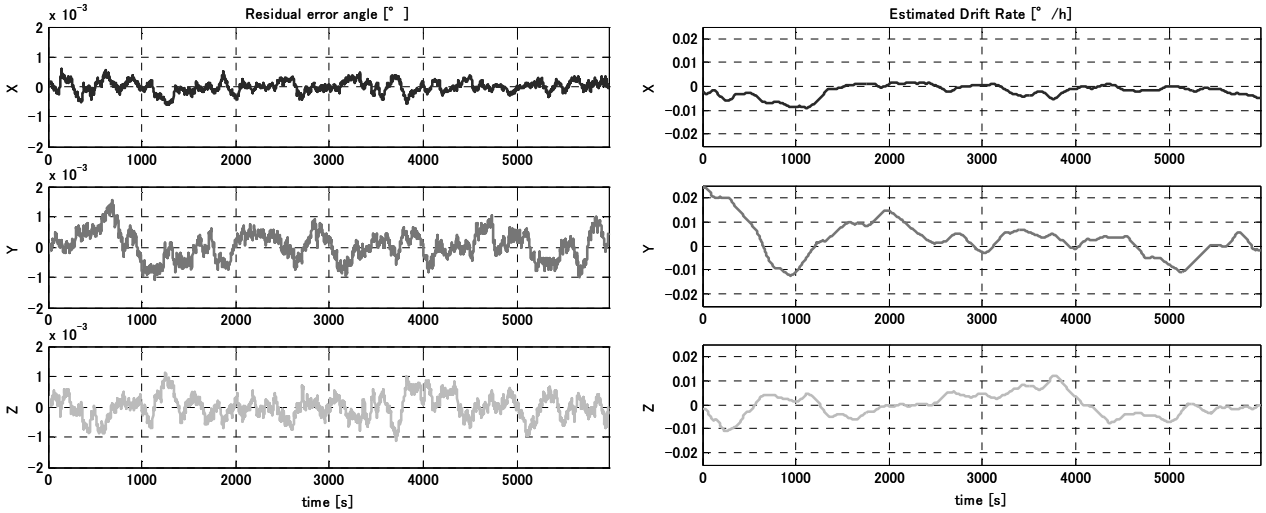

ADS Kalman Filter Logic Evaluation example

Fig8 ADS Kalman Filter Logic Evaluation result

8. References

[1] http://kibo.jaxa.jp/en/experiment/ef/maxi/

[2] http://maxi.riken.jp/astrows/

M.Matsuoka, K.Kawasaki, S.Ueno, H.Tomida, M.Kohama, M.Ishikawa, H.Katayama, M.Suzuki T.Miyakawa, T.Mihara, N.Isobe, H.Tsunemi, E.Miyata, H.Negoro, M.Nakajima, N.Kawai, J.Kataoka, A.Yoshida, K.Yamaoka and M.Morii

An Overview of MAXI onboard JEM-EF of the International Space Station

"UV, X-ray, and Gamma-ray Space Instrumentation for Astronomy XV", SPIE6686, pp/668611-1-9 (2007).

[3]Keiken NINOMIYA, Tatsuaki HASHIMOTO, Hiroshi IIDA, Masashi UO, Noboru MURANAKA,

Ken MAEDA, Naoto OGURA, Tetsu SAITOH, Koetsu FUJIWARA: “Kalman Filtering Used in The Attitude Determination System for Astronomy Missions of ISAS”. (ISAS REPORT #102 1999.2)

MAXI Data Downlink and Data Transfer on the Ground

Masaki Ishikawa,[1,8] Daiki Takahashi,[1] Masaru Matsuoka,[1] Shiro Ueno,[1] Hiroshi Tomida,[1]
Haruyoshi Katayama,[1] Kazuyoshi Kawasaki,[1] Mitsuhiro Kohama,[1] Motoko Suzuki,[1] Yasuki Adachi,[1] Tatehiro Mihara,[2]
Naoki Isobe,[2] Hiroshi Tsunemi,[3] Emi Miyata,[3] Atsumasa Yoshida,[4] Kazutaka Yamaoka,[4]
Nobuyuki Kawai[5], Jun Kataoka,[5] Motoki Nakajima,[6] Hiroshi Negoro,[6] Mikio Morii,[7] and MAXI Team

[1] Japan Aerospace Exploration Agency (JAXA)
[2] The Institute of Physical and Chemical Research (RIKEN)
[3] Department of Earth and Space Science , Osaka University
[4] Department of Physics and Mathematics, Aoyama Gakuin University
[5] Department of Physics, Tokyo Institute of Technology
[6] Department of Physics, Nihon University@
[7] Research Center for Measurement in Advanced Science, Rikkyo University
[8] Graduate University for Advanced Study (Sokendai)
E-mail(MI): ishikawa.masaki@jaxa.jp

Abstract

We describe the MAXI (Monitor of All sky X-ray Image) data downlink paths and the data transfer in the ground system. The MAXI telemetry data are downlinked using geostationary data-relay satellites, received at the ground system at Tsukuba Space Center, and forwarded to the RIKEN (the Institute of Physical and Chemical Research) ground system for advanced scientific analyses and data releases. A nova search system is placed at Tsukuba, which minimize its downtime due to network communication outages between Tsukuba and RIKEN.

Key words: High Energy Astrophysics, X-ray Astronomy, ISS, JEM, Kibo, MAXI, All-sky X-ray monitor

1. Introduction

MAXI is an all-sky X-ray monitor and one of its objectives is searching for X-ray transient events. At Tsukuba Space Center in Japan, All the MAXI telemetry data are routed to Tsukuba Space Center OCS (Operation Control System), and received by the MAXI ground system developed by the mission team. To minimize data transfer latency on one hand and to protect the space station's networks and the MAXI data on the other hand, we have developed dedicated ground systems. First we describe the MAXI data downlink paths, which are typical for payloads on the space station, and then briefly mention the data transfer inside the MAXI ground system.

2. Four Downlink Paths

The Japan Experiment Module (JEM)"Kibo" on the International Space Station (ISS) provides a user with up to three different types of data communication ports: MIL-1553B, Ethernet, and FDDI. Those ports are the start points of Low Rate Data Link (LRDL), Medium Rate Data Link (MRDL), and High Rate Data Link (HRDL), respectively.

The MAXI mission uses two of them: LRDL and MRDL. The LRDL, MRDL, and HRDL are not the names of "physical" networks, but they are "logical" networks. Actually, the MAXI telemetry data transmitted through the MIL-1553B interface (LRDL) and the data through the Ethernet interface (MRDL) both eventually come into the same physical networks on ISS (for example, FDDI). The LRDL and MRDL data are then multiplexed and downlinked as radio frequency (RF) signals.

The RF signals are downlinked through one or both of two data-relay systems utilizing geostationary satellites: one is JAXA's ICS (In-orbit Communication System) using only one satellite named "Kodama", and the other is NASA's system using TDRSS (the Tracking and Data Relay Satellite System).

Thus MAXI has four different downlink paths: 1) NASA LRDL, 2) ICS LRDL, 3) NASA MRDL, and 4) ICS MRDL. In the MAXI case, the LRDL and MRDL start at MAXI in orbit, and end at the MAXI data acquisition computers at Tsukuba Space Center in Japan.

If we take account of the visibility of data-relay satellites viewed from ISS's antennae only and omit the fact that we have to share downlink resources with other ISS users, the NASA link using more than one data-relay satellite provides higher availability than the ICS link.

For the MAXI team to use the NASA link resource, however, JAXA needs bilateral coordination with NASA. To use the ICS link, the MAXI team needs just JAXA-internal negotiations with other satellite teams.

During communication outages between ISS and the ground stations, the NASA link data are stored on NASA's HCOR (High Rate Communications Outage Recorder), and the ICS link data are stored on JAXA's HRDR (High Rate Data Recorder).

2.1. Low Rate Data Link (LRDL)

LRDL starts with a MIL-1553B bus on JEM "Kibo". The data throughput assigned to MAXI is not large (25 to 50 kbps). Since the MIL-1553B bus provides each user with fixed-sized data slots, data collisions do not occur. Health and status data and a level minimum set of experiment data of MAXI are downlinked through LRDL. MAXI's X-ray nova search is conducted for downlinked LRDL data, and confirmed using more detailed MRDL data. For LRDL data, technically, we can use both the NASA and the ICS links in parallel. To maximize the real-time downlink window, the MAXI team plans to use the NASA link.

Both the NASA and the ICS LRDL are used for command uplinks.

2.2. Medium Rate Data Link (MRDL)

MRDL starts with a 10Base-T Ethernet on JEM "Kibo". The data throughput assigned to MAXI is 200 to 600 kbps. This MRDL throughput allows us to use more data bits for experiment information (for example, measurements of time, positions, and energy) than the LRDL throughput. Some housekeeping telemetry data are downlinked by MRDL only, and are useful for us to obtain reliable results in calibrations and data analyses. Since the JEM Ethernet nodes are connected via a repeating hub, however, there is a possibility of data loss caused by multiple data frame collisions, depending on network traffic.

We have to prepare differently formatted MRDL data inside the MAXI data processor for the NASA link (MAXI data on CCSDS on IEEE802.3 frame) and for the ICS link (MAXI data on UDP on IP on Ethernet II frame). Thus we cannot use the two MRDL in parallel for downlinks. Our preference is using the NASA MRDL for its longer real-time connection.

Only the ICS MRDL is capable for command and file uplinks.

3. Data Transfer on the Ground

The MAXI ground system is located at two separate places, Tsukuba Space Center and RIKEN.

The Tsukuba ground system is for the MAXI operation, the first data reduction, and the X-ray nova search.

The RIKEN ground system receives all the MAXI data from the Tsukuba system. The RIKEN system is for advanced scientific data analyses, and the public release of the MAXI data and results.

3.1. Tsukuba Ground System

The Tsukuba ground system consists of the following two components:

1. Database inside the JAXA Operation Control System (OCS) area, acquiring telemetry data from the upper streams, storing time-sorted housekeeping and experiment data, conducting engineering units conversion, and distributing data for quick look, nova search, and the RIKEN ground system;

2. Nova search system inside the JAXA OCS area, searching for significant X-ray transient events, and issuing nova alerts to the Internet on detection of significant events;

3.1.1. Data Diode

To protect the JEM "Kibo" OCS from illegal network attacks, the MAXI data are transferred out from OCS through secure one-way data paths (Fig.1). We plan to use two types of one-way paths: two-ported hard disks and a photo coupler with an optical fiber between the emitter and the receiver.

3.1.2. MAXI-DB

Component 1 is a group of software modules, developed by JAXA and named "MAXI-DB" (Fig.1 and Fig.2). Each MAXI-DB consists of four main functional services of data receiving, data recording, data searching and supplying, and data processing for analysis. MAXI-DB also provides data backup service, system maintenance service, and GUI service. Using each individual service on several separate computers, we achieve the load balancing for quasi-real-times data processing.

3.1.3. Nova Search System

The Nova Search System searches for X-ray transient events. To avoid the downtime of the Nova Search System due to the network communication outage between Tsukuba and RIKEN, Tsukuba Space Center hosts the system, instead of RIKEN. This system sends nova alerts to registered users when significant events occur. The MAXI nova alert system is described by Negoro et al (2008).

3.2. RIKEN Ground System

The RIKEN ground system consists of the following two components:

1. Pipe-lined data analysis system running on a cluster of computers for advanced scientific data analyses

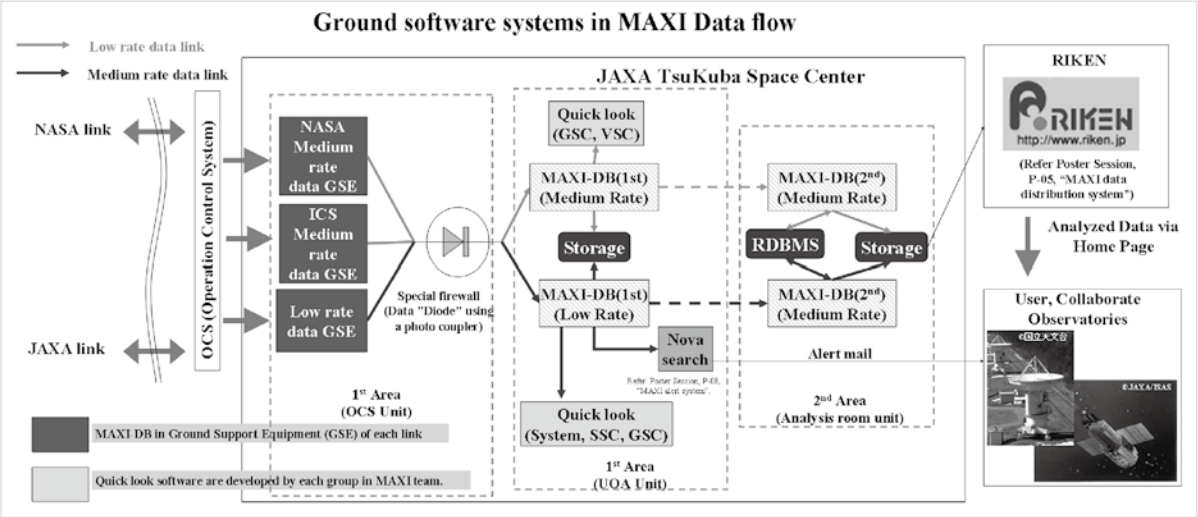

Fig. 1. MAXI Ground System and Data Flow

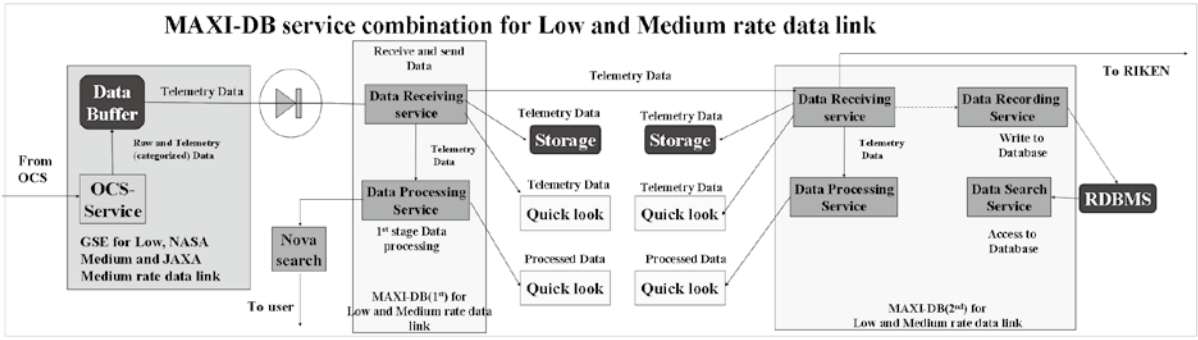

Fig. 2. MAXI-DB System at Tsukuba Space Center

2. Database on the Internet, providing images, spectra, and light curves in response to the public user access using web browsers;

The data analysis scheme is presented by Sugizaki et al (2008), and the data distribution system is presented by Kohama et al (2008).

4. Summary

We have four different downlink paths for the MAXI telemetry data. To obtain the real-time connection as much as possible, our preference is using the NASA link for both LRDL and MRDL data.

To protect the ISS operation network and the MAXI data, we use a secure hardware-level one-way data paths.

By distributing the services of MAXI-DB to several separate computers, we have succeeded in quasi-real-time pipe-line data processing.

References

Kohama, M. et al. 2009, in this proceedings
Negoro, H. et al. 2009, in this proceedings
Sugizaki, M. et al. 2009, in this proceedings

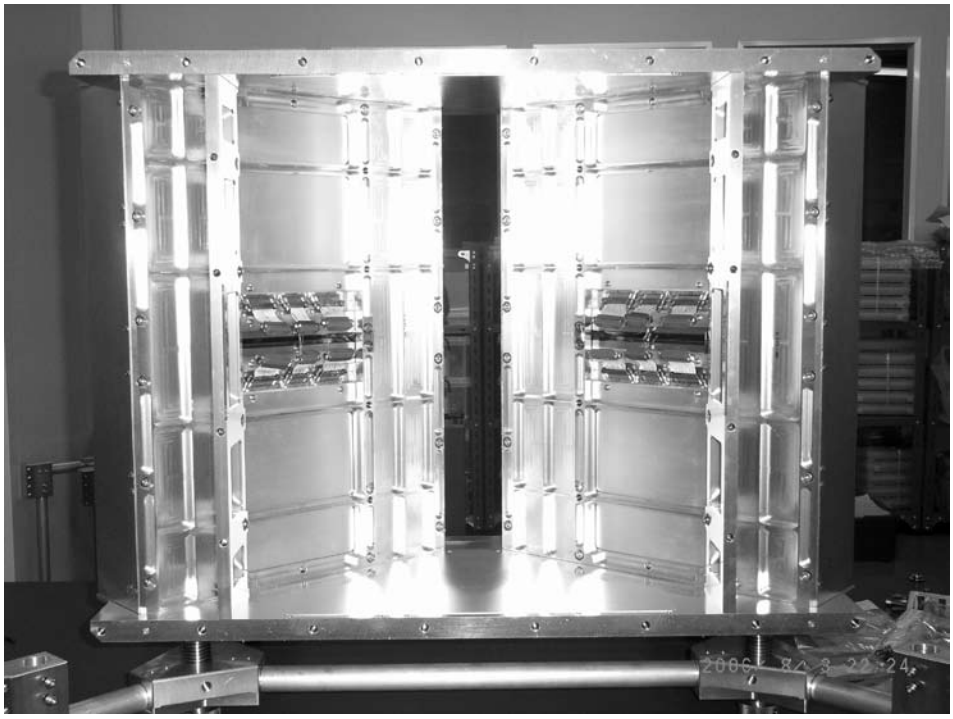

the Development of the MAXI Monitoring System

S. Mizobuchi,[1] M. Iida,[1] A. Ichibakase,[1] M. Nagase,[1]
H. Nakamoto,[1] M. Tomoda,[1] K. Hotta,[1] and T. Haru[1]

[1] Systems Engineering Consultants Co. LTD.
NES BLDG., 22-14, Sakuragaokacho, Shibuya-ku, Tokyo, 150-0031, Japan
E-mail(SM): mizobuchi@sec.co.jp

Abstract

Our company, SEC, is software company that is specialized for real-time system and involved in space exploration also. We provide control systems of rocket launch, on-board systems and grand-base systems of satellites, taking advantage of our skills in developing real-time systems. We have developed many satellite systems so far, starting from N-I rocket. In this paper, we present the development of the MAXI monitoring system.

We have to monitor and control MAXI through the telemetry data while observing for the stable MAXI operation. Therefore, the MAXI telemetry data include not only observation data for scientific purpose, but also the ancillary data as system status. Basically, the monitoring system is required to receive and to display telemetry data continuously in real-time without loss. We have developed the real-time monitoring system to satisfy these requirements. And also, our monitoring system has good look-and-feel and flexibility of the display design, display format and monitored telemetry data.

We will report the characteristic of the present monitoring system and the future plan.

Key words: System QL, Monitoring

1. Introduction

We offer various software in mainly five business fields (mobile network, wireless, internet, infrastructure system and advanced space technology system) based on real-time technology skill with a slogan of "For the social safety and evolution". For examples, we provide the transportation system such as spot control system of an airport, intelligent transport system (ITS) and those systems running for the social safety and evolution by making use of our own specialized field. In advanced space technology business field, we offer a wide-ranging system such as MAXI system QL, the astronomical application and embedded software for satellite-mounted detector. We have approximately thirty years of experience in this business field where high-quality products are required.

2. MAXI

MAXI that will be mounted on the JEM exposure part, communicates with a ground-based system by receiving commands and sending the Telemetry Data through the JEM as shown in a Fig1. The MAXI Flight system consists mainly of the Mission Data Processor (MDP), the Support Systems and the Data Processor (DP). The DP receives commands from a ground-based system and controls the MDP and the Support System.

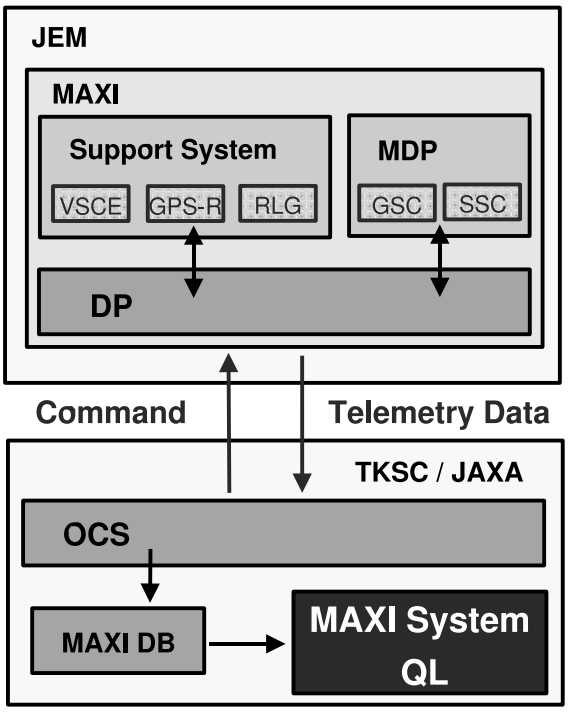

Fig. 1. The MAXI data flow

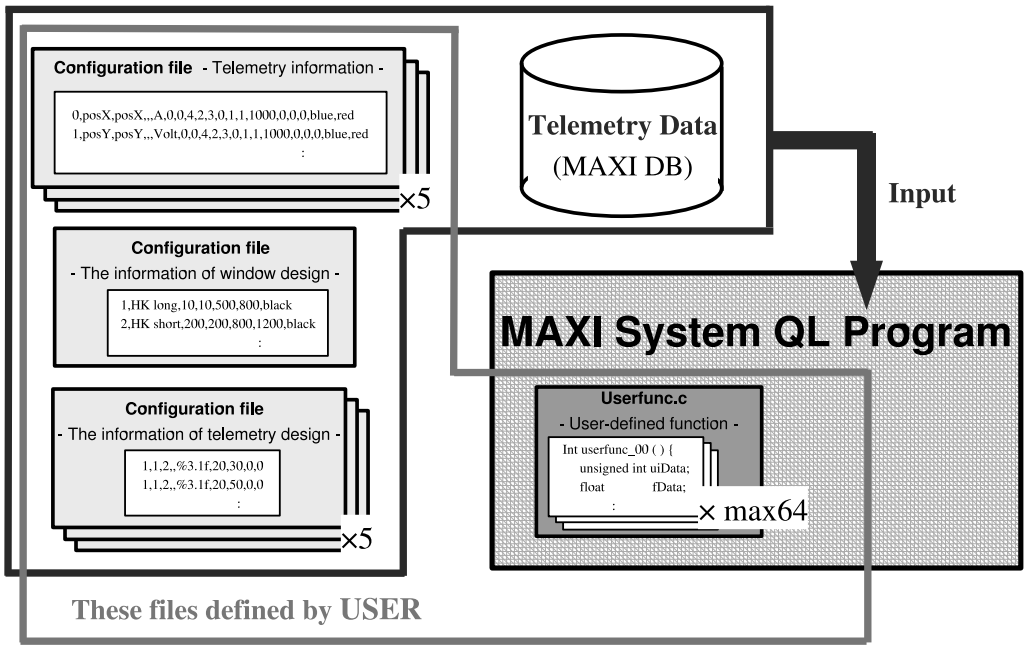

Fig. 2. The MAXI System QL configuration

At the same time, the DP controls many kinds of data taken from the MDP and the Support Systems, and sends them back to ground-based system as the telemetry. These data are stored in MAXI DB (Data Base) through the OCS (Operational Control System) and sent to the MAXI System QL (Quick Look) for monitoring the status of the MAXI flight system. The QL displays the status information in real time after receiving the telemetry data.

Our company supports to develop the MAXI DP, OCS, MAXI DB and MAXI system QL. Here, we especially focus the feature and the future plan of the system QL.

3. The MAXI system QL

3.1. The requirement

The telemetry data from the MAXI flight system include the H&S (Health and Status) data and HK (House Keeping) data of astronomical observational equipment, the unique data for the attitude control, the data of GPS time, the scientific data taken from the MDP and the data taken from the ISS (International Space Station).

For the steady observation, it is required to constantly monitor these data in real-time and to display the system status. If some of the equipments go into alert state, operators should be able to find the abnormal state and know more detailed information easily.

The persons who are responsible for the development of each equipment also monitor these information in real-time if needed. Therefore, it is required for the system QL to be flexible to change and customize the display design easily for each user.

3.2. The structure

As shown in a Fig2, the MAXI system QL program reads three kind of configuration files written in csv format by a user and displays the telemetry data on the screen by using these information. The designs of the display are completely defined by these configuration files. It is possible to handle following requirements easily simply by modifying these files.

- Customizing the displayed item of telemetry data for each user's requests
- Customizing the display design for each user's requests.
- Changing the number of display windows

The MAXI system QL is possible to display not only the raw telemetry data itself without any conversion but

The defined information	The detail
Configuration file	
Telemetry information	A text file of csv format, which defined the following information · For identifying the telemetry data · For extracting the displayed data from telemetry data set such as byte offset · For converting telemetry data from the raw value to the engineering value · For checking the status of the equipment · For displaying the telemetry data
The window design	A text file of csv format, which defined the window information of the MAXI system QL such as the position and size in the display.
The telemetry design	A text file of csv format, which defined the design of telemetry data displayed in one window. These file have the type, the ID, the display position, the width and the height of the displayed telemetry data.
Program file	
The user-defined function	The source programs with C-language, which define the function for converting telemetry data to engineering values. The MAXI system QL has six functions by the default and it is possible to add functions defined by a user.

Table 1. The detail of user-defined file

also converted data in engineering values from raw data. The QL has the six functions by the default for the conversing purpose. As shown in a Fig2, it is also possible to handle special conversion easily simply by programming a function and including it to the MAXI system QL program.

3.3. The user defined file

As previously mentioned in a section3.2., it is possible to modify four kind of file (three kind of configuration file and one kind of program file) in total. The configuration file is a text file of csv format, which define the telemetry information, the window design and the telemetry design, respectively. And the program file includes the user-defined function. The details of these files are put together in a Table1.

3.4. The QL display

The QL display samples of the raw telemetry data and the engineering value are shown in a Fig3 and a Fig4, respectively. The raw telemetry data itself are displayed mostly in hexadecimal form without any conversion. And the Engineering Value that is converted from raw data is displayed in the certain format. The display formats of both data type are also defined in configuration file, for example "%3d" and "%s".

The MAXI system QL has a status check feature for the specified telemetry data. These data are classified into three level of state (normal level, warning level and error level). The classified data are shown in the display with different colors, which are also defined in configuration file. The ongoing QL display designed are like shown in the Fig3 and the Fig4. Their background color is black and the font color of fixed text is white. The font color of the variable telemetry data that belongs in the normal level, the warning level and the error level is green, yellow and red, respectively. These telemetry data are updated every 0.5 seconds with the default setting. It is possible to fine-tune the update interval of the QL display depending on the receiving cycle of shown data.

The MAXI system QL has capabilities of printing and saving the display image. If user would like to use these functions, it is possible to do by just modifying the configuration file. The "Save" and "Print" buttons are show up in the QL display by adding one line written with the certain format. If user clicks these buttons, the display image is automatically saved with certain file name under certain directory, which are defined in the configuration file, or printed on the default printer.

4. The future plan

4.1. A tool for designing a display by GUI

The position information wrote in the configuration files are currently defined manually with a fine-tuning by user. It takes non-negligible time for making the configuration file and a user can make a mistake. Therefore, we are planning to develop a tool which can reflect a display design by using GUI into the definition file.

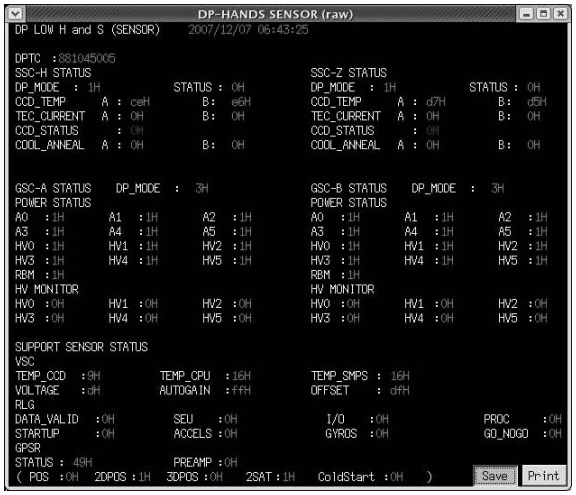

Fig. 3. The sample of QL display (Raw Value)

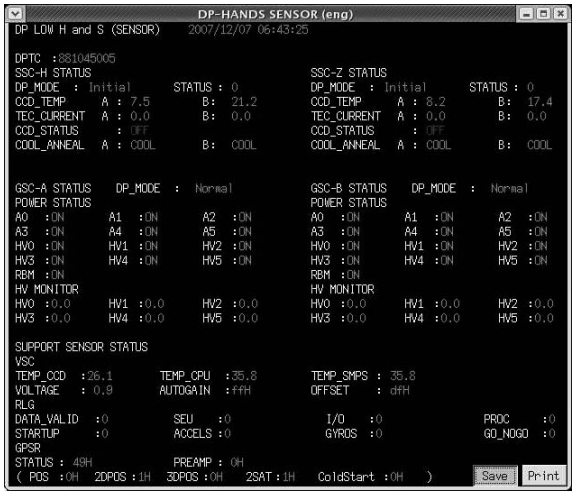

Fig. 4. The sample of QL display (Engineering Value)

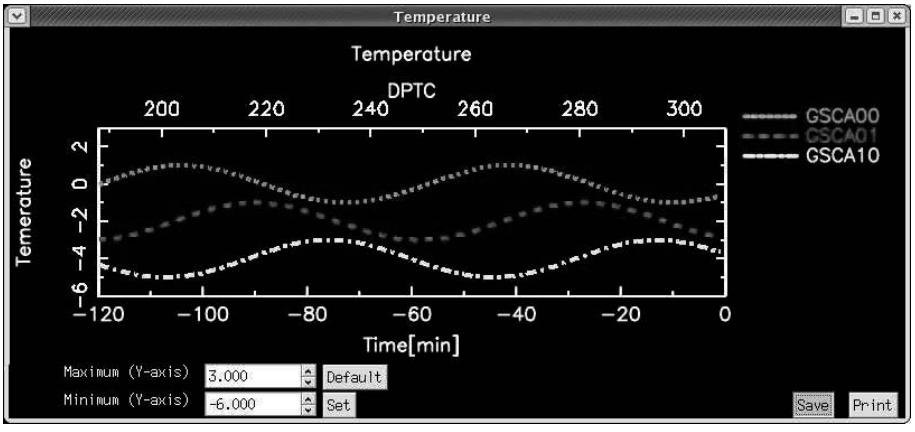

Fig. 5. The sample of graphs display

4.2. A tool for visualizing the telemetry data

The telemetry data are displayed on a screen as shown in the Fig3 and the Fig4 in real-time in the current system. We are planning to develop a tool, which can show the time variation and the distribution for each telemetry data simply by modifying the configuration file such as QL display. The sample of the graphs display is shown in a Fig5.

The each graph of telemetry data are distinguished by the combinations of the line type and the line color. This tool has the function for changing the scale of Y-axis. Two numerical input fields and two buttons are shown in the graph display. If user clicks the "set" button after inputting maximum and minimum value into the fields, these value are reflected in the scale of Y-axis. If user clicks the "Default" button, the scale of Y-axis come to default condition.

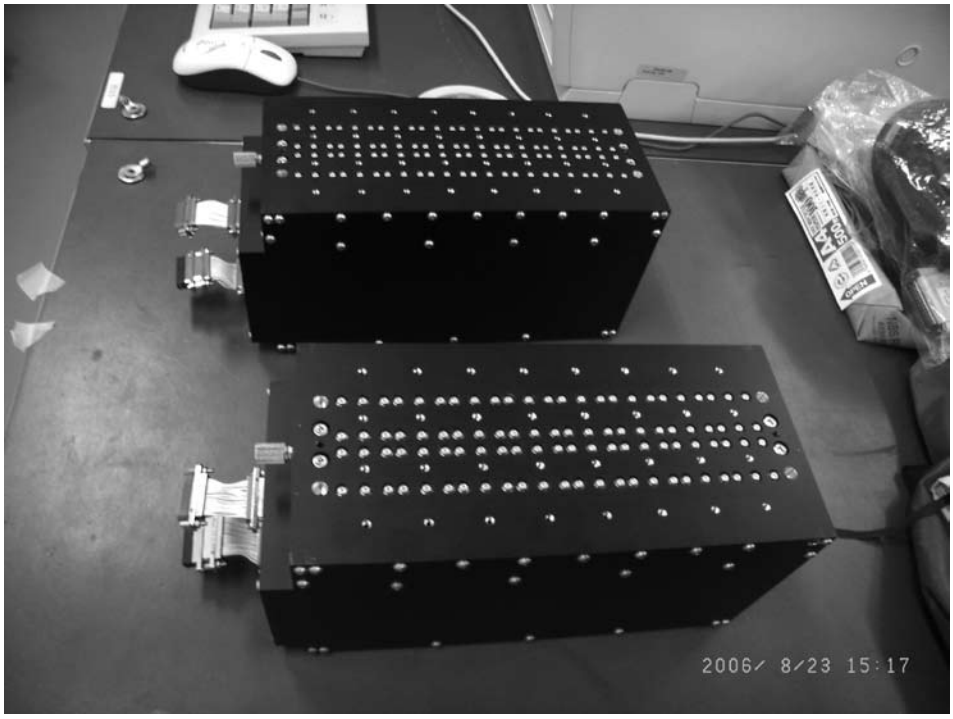

MAXI data distribution and the archive system

Kohama M.[1,2], Mihara T.[1], Sugizaki M.[1], Negoro H.[3],
Nakajima M.[3], Eguchi S.[4], Tomida H.[2], Ueno S.[2], Suzuki M.[2],
Kawasaki K.[2], Matsuoka M.[2], Ishikawa M.[2], Adachi Y.[2],
Kawai N.[5], Yoshida A.[6], Miyata E.[7], Tsunemi H.[7],
Ueda Y.[4], Morii M.[8] and MAXI team

[1] The Institute of Physical and Chemical Research, 2-1 Hirosawa, Wako, 351-0198, Japan
[2] 1Japan Aerospace Exploration Agency, 2-1-1 Sengen, Tsukuba, 305-8505, Japan
[3] Nihon University, 1-8-14 Kanda-Surugadai, Chiyoda-ku, 101-8308, Japan
[4] Kyoto University, Kitashirakawa Oiwake-cho, Sakyo-ku, 606-8502, Japan
[5] Tokyo Institute of Technology, 2-12-1 Ookayama, Meguro-ku, 152-8551, Japan
[6] Aoyama Gakuin University, 5-10-1 Fuchinobe, Sagamihara, 229-8558, Japan
[7] Osaka University, 1-1 Machikaneyama, Toyonaka, 560-0043, Japan
[8] Rikkyo University, 3-34-1 Nishi-ikebukuro, Toshima-ku, 171-8501, Japan
E-mail(MK): kohama@crab.riken.jp

Abstract

MAXI is designed for monitoring the all-sky in the X-ray band by scanning with slat collimators and slit aperture. The sensitivity of MAXI will reach about 5mCrab in 1 day, and 1 mCrab in 1 month. We plan to make most of the MAXI data products public in a timely manner. MAXI data will be distributed by the Web Interface (from RIKEN site, URL is http://www.maxi.riken.jp). MAXI will provide light curves, spectra, images of about 1000 cataloged objects. The data distribution will start in about 3 month after the MAXI activation. In this paper, we will describe about the data distribution system and explain the policy of the data distribution and the instruction of Web Interface.

Key words: MAXI data distribution

1. Introduction

Monitor of All-sky X-ray Image (MAXI) is an all-sky monitor with ability that can observe the all-sky with about 1.5 degree position resolution and high sensitivity (Ueno et al. 2008). MAXI employs two types of X-ray cameras, Gas Slit Camera (GSC: Mihara et al. 2008) and Solid-state Slit Camera (SSC: Tomida et al. 2008). Each consists of two perpendicular fan-beamed field of view that scans the sky with the revolution of the International Space Station. The observed data will be provided to world wide astronomers though the ground analytical system as soon as possible.

2. MAXI data distribution system

The MAXI data are down-linked through ISS teremetry. There are two types of telemetry, which are low-speed Mil-1553b interface and MEDIUM-speed Ethernet interface. The real-time coverage is about 30 to 70 percents. The data processing on the ground has two stages, which are Tsukuba Space Center (TKSC) and RIKEN. The health check of the detectors, the attitude determination and the data completeness check are done in TKSC. Then all the data are transfered to the RIKEN and distributed to the world from RIKEN server. At RIKEN, public archive data will be updated after the analytical process. The figure 1 shows overview of the MAXI data distribution system.

The MAXI public archive system has web interface for anonymous user. You can get analytical products from this site.

3. Policy of the data distribution

MAXI team discloses the astronomical products according to the following policy of the data distribution.

A) All the down-linked data will be used to the data distribution. The products for the distribution are new transients discovered with MAXI, All-sky map image, the light curves and the spectrum of the known sources, and archive data of any part of the sky.
B) The distribution products are in FITS format or TEXT format. We do not provide the MAXI specific software tools. MAXI data can be treated with the software, which are distributed from HEADAS etc.(Xspec or familiar software).

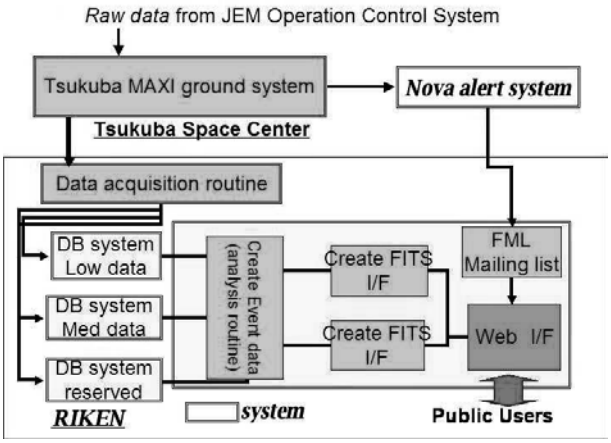

Fig. 1. Overview of the MAXI data distribution system

C) We do not provide the event data in early stage. Currently we do not have enough man power for the data distribution. If you want the event data, please contact and collaborate with the MAXI team.
D) A detail analysis will be done by collaborating with the MAXI team.

4. Distribution of products

We plan to start disribution of these products three month after the MAXI activation.

4.1. Novae alerts

The transient phenomena such as X-ray novae, GRB, and so on, discovered by the MAXI nova-alert system are immediately informed to users (Negoro et al. 2008). The MAXI team would like astronomers in any wavelength to use this information. The distribution method will be the mailing-list that the MAXI team sets up on the web site. Everyone who wants to use it can make his registration to the mailing-list. We will also utilize the existing astronomer mailing-list (ex. GCN circ. for GRBs).

4.2. All-Sky map

MAXI observes the whole sky 15 times a day, and can generate the all-sky images. After analyzed in the ground analysis system, the all-sky image of the day can be provided every day. We plan to provide the weekly image, and monthly image as well.

4.3. Regular updates of known sources

The flux and spectrum of about 1000 known sources will be updated regularly on the MAXI web site. We plan to list the light curves in two or more energy bands every day. The spectrum will be accumulated in one week to one month.

5. Archive system

We will issue the on-demand data products in about one year after the MAXI activation. Everyone who registered in the MAXI web site can request the MAXI data of any part of the sky. The selection criteria by users will be the position of the sky, the area (selection circle), the energy range, observation time-span and the detector (GSC and/or SSC).

6. User interface

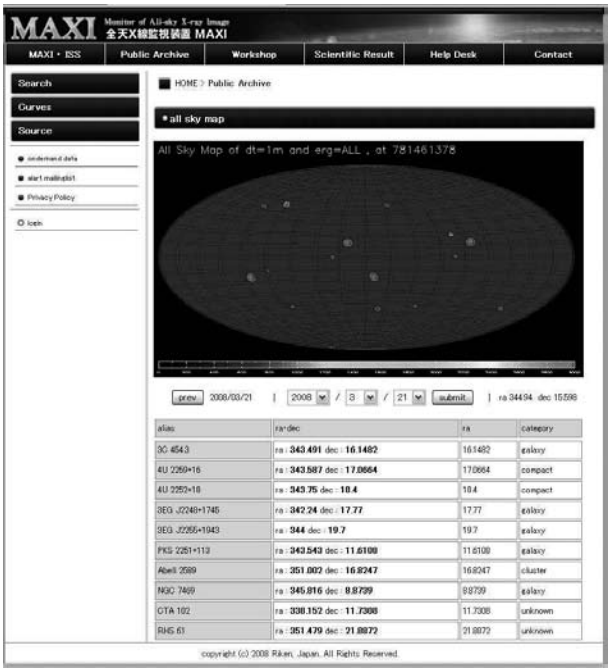

Fig. 2. Web interface of the MAXI data distribution system

The web site for data distribution will be set at RIKEN site.
http://www.maxi.riken.jp/

This site offers all the MAXI information for the astronomers. The all-sky image of the day will appear in the top page. Here, past images of one week span can be seen. Then, you choose in the menu and move to the data distribution page. The figure 2 shows the page of the data distribution page.

We plan to offer the regular data products of all the known sources which is selected by the MAXI team by two method. One is very easy way that users can get the MAXI products of any sources by clicking the point on the all-sky image. Another needs a little special technique such that user inputs directly the position or the name of the source. You will get the light curve and the spectrum in one page for each sources. Finally, we wish to help your astrophysical study by providing our MAXI data.

References

T. Mihara, et al. 2009, in this proceedings
H. Negoro, et al. 2009, in this proceedings
H. Tomida, et al. 2009, in this proceedings
S. Ueno et al. 2009, in this proceedings

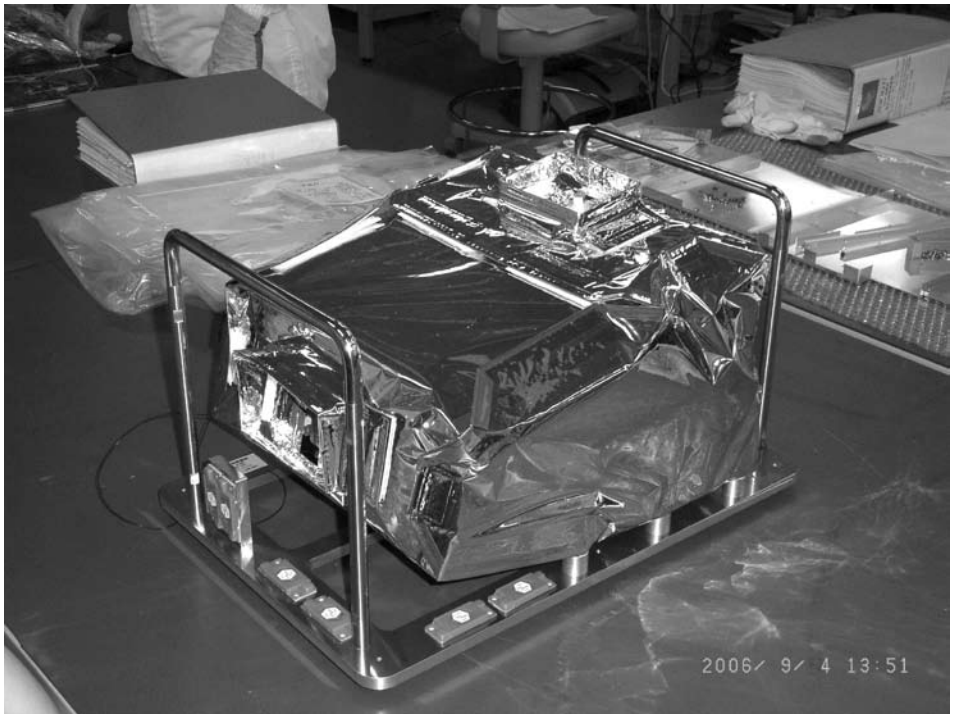

MAXI Simulator

Satoshi Eguchi,[1] Kazuo Hiroi,[1] Yoshihiro Ueda,[1] Mutsumi Sugizaki,[2]
Hiroshi Tomida,[3] Motoko Suzuki,[3] and the MAXI team

[1] Department of Astronomy, Kyoto University, Kyoto, 606-8502, Japan
[2] Riken, 2-1 Hirosawa, Wako, Saitama, 351-0198, Japan
[3] JAXA/TKSC, Sengen 2chome, Tsukuba, Ibaraki 305-8505, Japan
E-mail(SE): eguchi@kusastro.kyoto-u.ac.jp

Abstract

We are developing the MAXI simulator, a software that generates fully simulated data of the X-ray cameras of MAXI in space. The MAXI simulator is utilized for the development and tests of various software supporting the MAXI mission, including the "nova search" program (Negoro et al. 2008). To generate realistic data, the simulator is designed to take into account detailed conditions on the ISS, such as the occultation of the sky by the sun panel, background, and response functions of the instruments. We code the program in C++ by introducing "classes" that have hierarchical and expandable structure. With this design, it provides a framework for satellite simulators. In this paper, we present the design and current performance of the MAXI simulator, and discuss the possibility of its application to other space missions.

Key words: MAXI: software — sensitivity: simulations — simulator

1. Introduction

The MAXI simulator is a software that generates fully simulated data of the X-ray cameras of MAXI by Monte Carlo method (we have newly developed the code based on the original version written by Drs. B.C. Rubin and W. Yuan).

Figure 1 is a schematic view showing the data flow of MAXI. The data are downlinked via network of NASA and JAXA, pass through the operation control system (OCS), and finally enter the MAXI database (MAXI-DB; Ishikawa et al. 2008). The MAXI-DB compiles the telemetry data into scientific data. The quick look system, nova search program, and public release system are located in the downstream of the MAXI-DB.

The simulated data can be input to the MAXI-DB with a file-format converter by adding dummy housekeeping data. Once these data are registered in the MAXI-DB, all the downstream systems can operate to them in the same way as to the real data. Thus, the simulator is utilized for the development and tests of various software supporting the MAXI mission, including the MAXI-DB itself, nova search program (Negoro et al. 2008), and so on. In addition, we can study the realistic performance of MAXI, such as the sensitivity limit as a function of exposure (see Ueda et al. 2008 and Hiroi et al. 2008).

2. The structure of the MAXI simulator

The MAXI simulator is written in the C++ language, which introduces the concept of object oriented programming (OOP) into C. In OOP, software is composed of "classes." A class is a set of two or more variables and functions called "members." One can "derive" new classes from one by inheriting their original properties. Different from Java, another OOP language, C++ enables us to call libraries written not only in C but also in Fortran. With this feature, we can utilize various scientific libraries, such as spectral models in XSPEC[1] .

Figure 2 illustrates the structure of the MAXI simulator. It has a hierarchical structure. There is only one manager class on the top, below which sub-manager classes are placed. The role of the manager is to conduct the process of simulations; it takes "abstract" data from certain sub-manager, and passes the data to another sub-manager. Each sub-manager class owns abstract detector classes. "Concrete" detector classes, which have response functions and generate real data, are "derived" from these "abstract" detector classes.

The MAXI simulator can work as a framework for general satellite simulators. It is very important for the design of the MAXI simulator to separate the detector classes into abstract and concrete ones. The concrete detector classes are located in the lowest level in the simulator. We can thus easily develop simulators for other

*1 http://heasarc.nasa.gov/docs/xanadu/xspec/

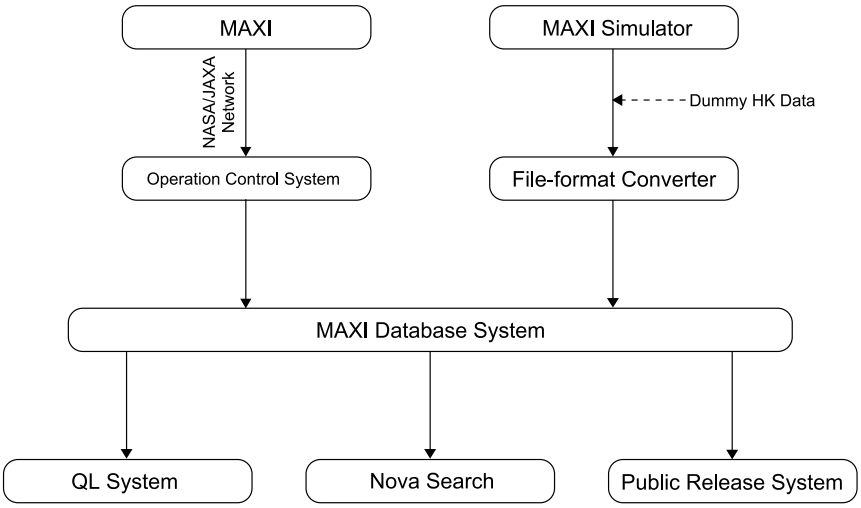

Fig. 1. The data flow of MAXI and the MAXI simulator.

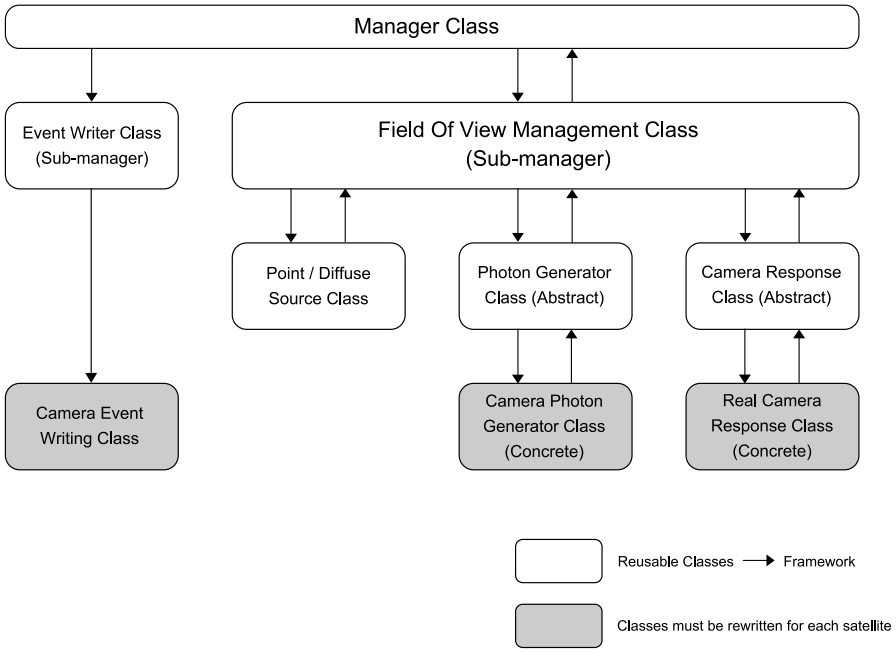

Fig. 2. The schematic structure of the MAXI simulator.

satellites just by replacing the concrete detector classes, keeping most classes of the MAXI simulator with the same structure.

3. The development status of the simulator and qualitative sensitivities of MAXI

The latest version of the MAXI simulator (Ver.6.3.103) can simulate both the Gas Slit Camera (GSC) and the Solid-state Slit Camera (SSC) events from not only point sources but also diffuse sources, although the detailed response function of the SSC is not fully taken into account. In the simulator, the image of diffuse sources (such as the cosmic X-ray background) are divided into meshes of equi solid-angle, with the HEALPix library[2] , and are treated in the same manner as for point sources. Although it is a general-purpose algorithm, this method requires much CPU time. To solve this problem, we introduce a multi-thread method based on OpenMP into the simulator. By using multi-core PCs, one can obtain the results 1.5–3 times faster than the case of a single-thread method.

Figure 3 is the result of all-sky simulations with GSCs, plotted in the Galactic coordinates. Here we input about 1700 point sources from the INTEGRAL General Reference Catalog (Ver.27)[3] . The non X-ray background are included. We excluded data when MAXI cannot perform observations due to the sun-angle constraint or in the South Atlantic Anomaly. Figure 3 shows the results with different exposures, 1-orbit (90 minutes), 1-day, 1-week, and 1-month, from the left top to the right bottom. It is clearly seen that the longer MAXI is exposed, the fainter sources MAXI can detect. A quantitative analysis of the sensitivity limits is reported by Hiroi et al. (2008).

4. Future work

The current version of the MAXI simulator does not consider the screening of the sky by objects on the ISS, such as solar paddles. We plan to implement this function in the near future to perform even more realistic simulations.

References

Brad C. Rubin et al., "All-Sky X-ray Observations in the Next Decade", p285, 1997
Hiroi, K., et al. 2009, in this proceedings
Ishikawa, M., et al. 2009, in this proceedings
Negoro, H., et al. 2009, in this proceedings
Ueda, Y., et al. 2009, in this proceedings
Weimin Yuan et al., "MAXI work shop on AGN variability", p13, 2001

*2 http://healpix.jpl.nasa.gov/
*3 http://isdc.unige.ch/index.cgi?Data+catalogs

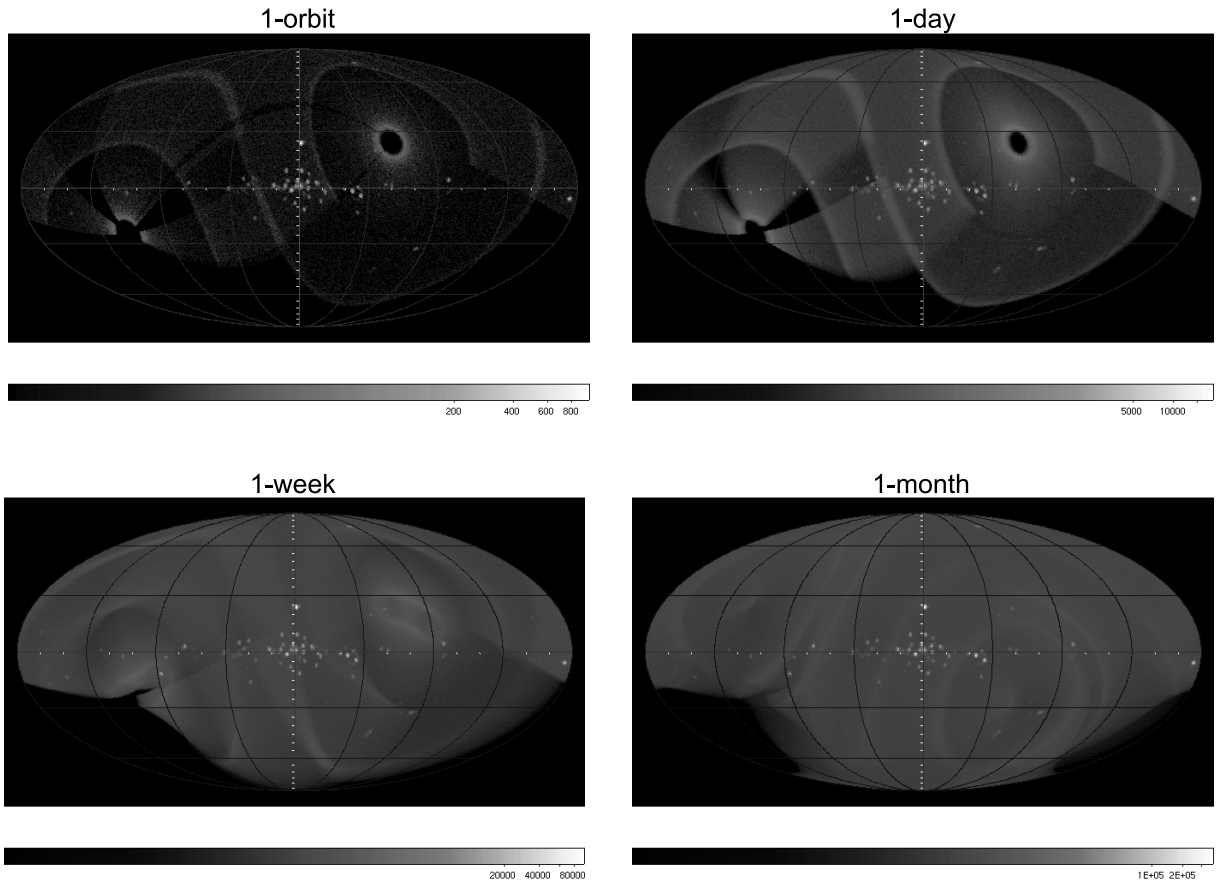

Fig. 3. The result of all-sky simulations with the MAXI simulator.

Response Builders of MAXI X-ray Slit Cameras and Simulator

Mutsumi Sugizaki on behalf of MAXI Software Team

RIKEN, 2-1 Hirosawa, Wako, Saitama, 351-0198, Japan
E-mail(MS): sugizaki@riken.jp

Abstract

MAXI, an all-sky X-ray monitor to be on-board on the ISS (International Space Station), carries two kinds of X-ray cameras: GSC (Gas Slit Camera) and SSC (Solid-state Slit Camera). Both X-ray cameras are scanning imagers combining position-sensitive detectors and collimators with one-dimensional FOV (field of view). They covers 90% of the whole sky every 90 minutes of the ISS orbital period. The response functions of these cameras for any X-ray sources on the sky depends on the ISS attitude, which always varies according to the orbital motion of the ISS. We are developing software to build response functions for any X-ray source on the sky from the source position coordinates, the instrument calibration data, and the ISS configuration parameters. We introduce the standard scheme of the MAXI data analysis and the response builders used in it. We then present the preliminary results of the response builders and the observation simulator which are currently being developed.

Key words: Methods: data analysis — ISS: All Sky Monitor — MAXI

1. Introduction

MAXI is a mission carried on the ISS to monitor all-sky X-ray image (ref. Ueno et al. 2004; Matsuoka et al. 2007; Ueno et al. in this proceedings). It onboards two kinds of X-ray cameras: GSC (Mihara et al. 2001; Mihara et al. in this proceedings) and SSC (Katayama et al. 2005; Tomida et al. in this proceedings). Both X-ray cameras are slit cameras with one-dimensional FOVs and scan the whole sky according to the rotation of the ISS synchronized with the orbital motion.

The response functions of the GSC and the SSC for any X-ray source depend on the ISS attitude, which is always changing according to the ISS orbital motion. The ISS activities, such as motions of the astronauts, rotations of the Solar-buttery paddles, docking with transfer vehicles, can also affect the ISS motion and sometimes interfere the FOVs of the X-ray cameras. These situations are quite different from those in the pointing X-ray telescopes onboard solitary astronomical satellite. The environmental issues specific to the ISS have to be cared in the MAXI data analysis.

We are developing software for the MAXI data analysis, which includes programs for telemetry-data reduction, response builders, and an observation simulator. In this paper, we briefly introduce the principle of the MAXI all-sky observation and describe the scheme of the standard data-analysis. We then present the preliminary results obtained using the response builders and the observation simulator which are now under development.

2. Principle of MAXI All-Sky Observation

Figure 1 illustrates the principle of the MAXI all-sky observation. Both X-ray cameras, GSC and SSC, are one-dimensional slit cameras. Each camera unit consists of a slat collimator with a narrow open window at the top and a position sensitive detector at the bottom. GSC employs position-sensitive gas proportional counters as the detector, whereas SSC employs CCD arrays. The one-dimensional FOVs of each camera scans the sky according to the rotation of the ISS. The cycle is synchronized with the orbital motion of about 90-minute period around the earth. Both GSC and SSC are segmented into the horizon units and the zenith units. The FOVs of the horizon units are towards the ISS moving direction along the earth horizon, and those of the zenith units are towards the anti-earth direction. Figure 2 shows the collimator effective-area profiles of one-dimensional FOVs of each GSC/SSC units. The combination of the two-segmental units scans the 90% of the whole sky twice per one orbital period of about 90 minutes.

3. Data Analysis Scheme

Figure 3 illustrate the schematic of the the MAXI data analysis from the telemetry data. The analysis flow is largely divided into two sections: the telemetry data reduction and the science analysis, whose processes are described in the following subsections. We employ relational-database system to store all the telemetry data in order to maximize the efficiency of the data reduction and analysis.

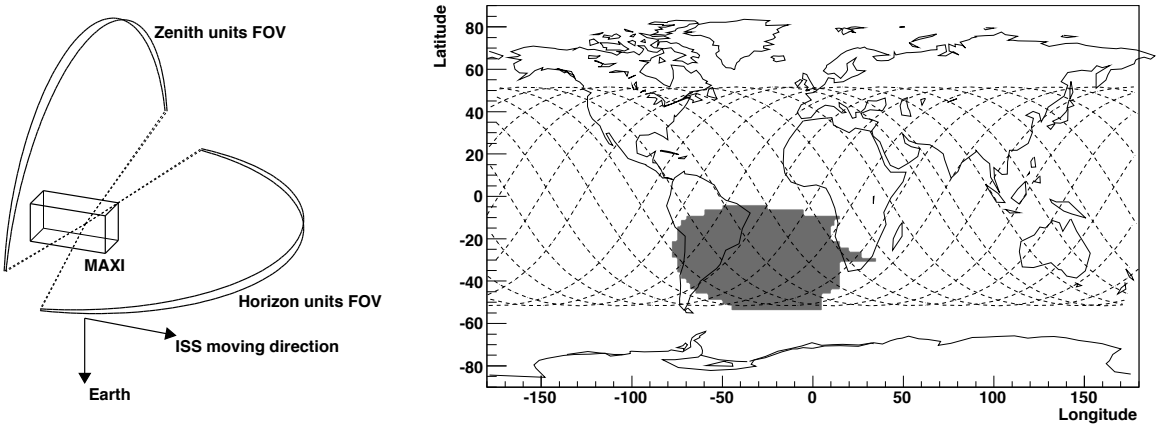

Fig. 1. Field of views of X-ray slit cameras on MAXI and direction of the ISS orbital motion (left). Trajectory of ISS orbital motion for one day (right). Grey area on the south Atlantic ocean represents the GSC SAA where the GSC counters are turned off.

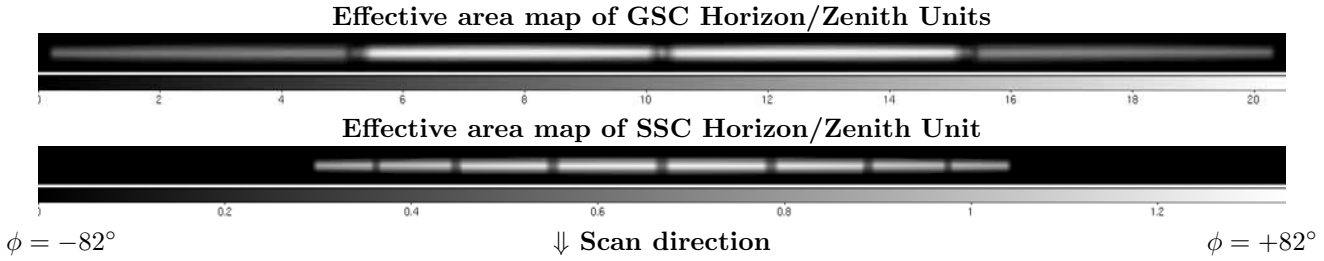

Fig. 2. Collimator effective-area map of GSC and SSC Horizon/Zenith units for incident angle. Units of grey scales are [cm^2]. Both images show the area of $-82^\circ < \phi < 82^\circ$ (along the direction parallel to the one-dimensional FOV) and $-2.5^\circ < \theta < 2.5^\circ$ (along the scan direction). The dips of the profiles corresponds to the detector insensitive areas, which are the shadows of the support structure of gas cells in GSC and the gaps between the CCD arrays in SSC.

3.1. Data Reduction

All the telemetry data are stored into database after the first reduction process. The database includes X-ray event data as well as auxiliary monitor data consisting of various housekeeping data and environmental information.

The event database stores all parameters relevant to each event such as the arrival time, the detector position, the incident angle, the expected sky position, and deposit energy. Some of these parameters are calculated during the reduction process using the instrument calibration data and the auxiliary monitor data.

The auxiliary monitor database collects information regarding the status of the ISS and the MAXI operation such as the ISS orbit and attitude parameters, configuration of the Solar-buttery paddles, temperatures of X-ray detectors and electronics, the mode of the data processor, data of radiation monitors, and so on.

The data-reduction process also requires the instrument calibration data. The calibration database are created from the ground calibration-test data and the in-orbit observation data. We employ the HEASARC CALDB system to be able to use the versatile management tool and provide the standard interface to software developers.

MAXI onboards two equipments to monitor the own attitude, VSC (Visual Star Camera) and RLG (Ring Laser Gyroscope), which work complimentarily. The attitude parameters are coarsely determined in orbit for the on-board realtime process, which are used in the quick nova-alert system. The parameters are then updated on the ground using the both VSC and RLG data after the downlink of all the relevant telemetry data is completed.

3.2. Science Analysis

The science analysis of MAXI data starts with the event selection for the target from the all-sky data. The event file for a target X-ray source is extracted from the event database, where the auxiliary monitor data is used to filter the events with various selection criteria. These database employ the relational database system in order to select the target events from the all-sky data efficiently and apply the flexible event-selection criteria.

Light curves, images, and energy spectra for the target X-ray source are then extracted from the event file. These products will be opened to public when the MAXI

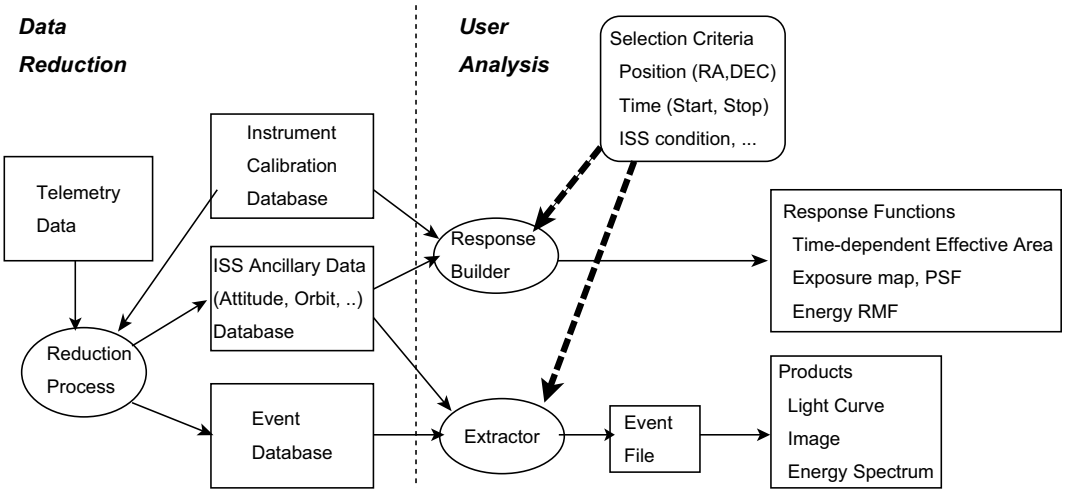

Fig. 3. Schematic of MAXI data analysis flow

mission is shifted into the normal operation phase (Kohama et al. in this proceedings).

The response builders calculate the response files for these light curves, energy spectra, and images from the instrument calibration data and the auxiliary monitor data. These details are described in the next section.

4. Response Builders

We here introduce the response builder of light curves, energy spectra, and images to be used in the standard analysis and show the preliminary results obtained using the programs under development. We used the instrument calibration data obtained from the ground experiments and assume the environmental parameters of ISS and MAXI expected from the current ISS configuration and orbits in 2007.

4.1. Light curve

The visibility and effective area of MAXI X-ray cameras for a given X-ray source are calculated from the source coordinates, the ISS position and configuration, transmission function of the slit collimators and the detector efficiency. The light-curve response builder calculates the effective area as a function of the time from these data.

Figure 4 shows the time variation of the GSC slit-collimator area for a point source at a given position (Crab nebula), obtained using the response builder. In the short time scale, the triangular response of the slat collimator with a duration of $\sim$45 seconds is clearly seen. The variation of the average exposure time per orbit (top panel of Figure 4) are caused by the variation of the source incident angle within the FOV due to the precession of the ISS orbit. The dips on the profile correspond to the down time for SAA and Sun area as well as the shadows of the support structures in detector areas.

4.2. Energy spectrum

The energy response function is represented by the effective area and the dispersion relation between the energy and the pulse height of the detector signal. The energy dispersion is owing to the X-ray detectors. GSC utilizes the gas proportional counters, whereas SSC utilizes CCD.

The effective area of the collimators and the detectors depends on the X-ray incident angle. Figure 5 shows the relation between the effective area and the X-ray energy for various incident angles in GSC. The peak effective area is determined by the collimator slit area, whereas the lower and the higher limits of the energy band are determined by the detector efficiency. The incident-angle dependence of the lower energy cutoff is due to the path length of the beryllium film at the front of the detector gas cell.

The dispersion relation between the X-ray energy and the pulse height of the readout signal depends on the absorbed position in the detector, which is also dependent on the photon incident angle. The energy response builder calculates the effective area and the energy redistribution matrix for each X-ray incident angle.

4.3. Point Spread Function and Exposure Map

The angular resolution of the GSC and the SSC are determined by the detector position resolution and the collimator windows size defined by their slit width and pitch of the slat panels.

The point spread function (PSF) and the exposure map of reconstructed image from GSC and SSC data depend on the instrument response as well as the instantaneous attitude. The response builder for the image analysis calculate the PSFs and the exposure map from the attitude data and the instrument calibration data.

In the case of SSC, the pixel size of the CCD (0.025

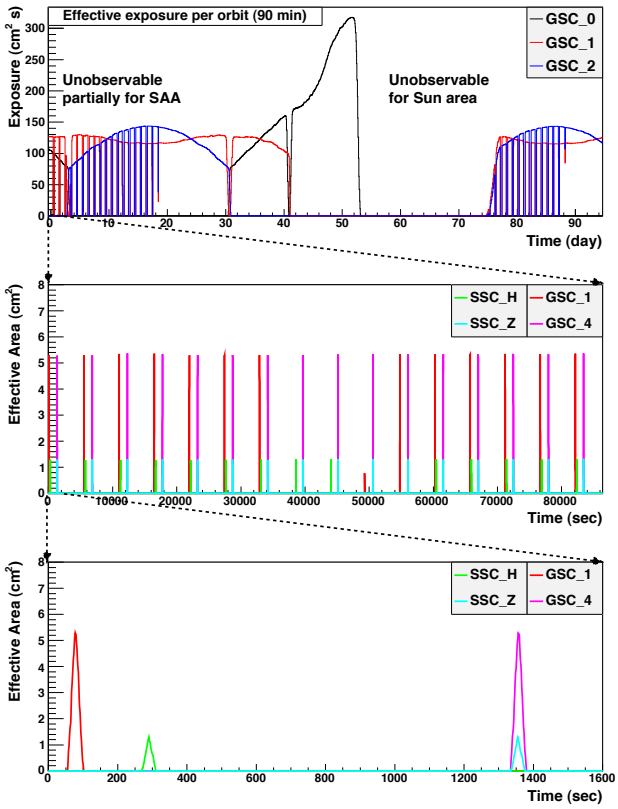

Fig. 4. Effective-are time variation for a given point source on the sky: Long-term variation of the average exposure time per orbit ($\approx$ 90 min) for each GSC counter unit (top). Effective-area variation within one day (middle). Effective-area variation in a scale of one scan (bottom).

mm) is much smaller than the slit width and the collimator pitch ($\simeq$ 2.3 mm). Thus, the profile of the collimator transmission function dominates the PSF.

In GSC, the position resolution of the gas counter depends on the X-ray energy, ranging from 1 to 4 mm within the energy band (Mihara et al. 2001). It is comparable to the slit width (3.7 mm) and the slat pitch (3.1 mm) of the GSC collimator. Thus, the detector resolution has to be taken into account. Figure 6 shows the expected PSFs for X-rays of 2 keV and 10 keV with incident angles of 2, 20, and 40 degree. The profile at 10 keV is obviously extended towards the incident angle. It is because the mean free path of these photons in the detector cannot be disregarded.

The exposure map is calculated from the effective-area map of the X-ray cameras, the ISS orbit and attitude data. Figure 7 shows the exposure maps of one GSC counter for one orbit and that of the entire 12 counters for one day. GSC covers 90% of the whole sky with an ISS-orbit cycle of $\sim$ 90 minutes.

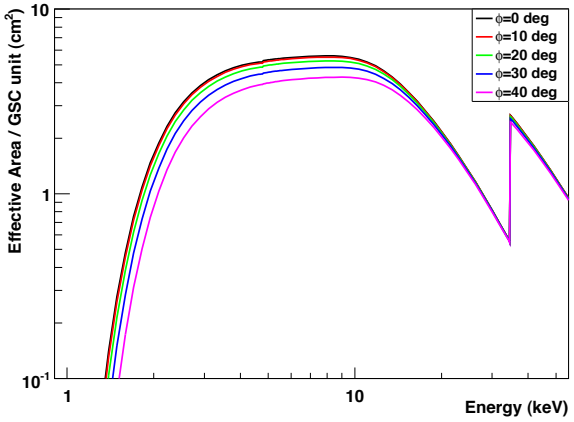

Fig. 5. Effective area of a GSC counter unit in the energy band of 1–50 keV for each X-ray incident angle of 0, 10, 20, 30, 40 degree.

5. Simulator

We are developing a MAXI observation simulator not only to study the scientific feasibility but also to examine the analysis software under development. The detail of the simulator is described in Eguchi et al. in this proceedings. Figure 8 and 9 show some results of all-sky image, light curves and energy spectra obtained from the simulated data of MAXI one-day observation.

6. Summary

We are building the standard analysis framework of MAXI data and developing the software which include programs for telemetry-data reduction, response builder, and observation simulator. The software will be used to process and analyze the archival products of MAXI data, which will be available after the MAXI mission is shifted to the normal operation phase. The status of the mission, information of the data archive and the latest software will be updated on the MAXI web site (http://maxi.riken.jp).

References

Eguchi, S., et al. in this proceedings (MAXI simulator)
Katayama, H., et al. 2005, Nucl. Instr. Meth. A541, 350-356
Kohama, M., et al. in this proceedings
Matsuoka, M., et al. 2007, Proc. SPIE 6686, 11-1-9
Mihara, T., et al. 2001, Proc. SPIE 4497, 173-186
Mihara, T., et al. in this proceedings (MAXI GSC)
Tomida, H., et al. in this proceedings (MAXI SSC)
Ueno, S., et al. 2004, Proc. SPIE 5488, 197-208
Ueno, S., et al. in this proceedings (MAXI mission overview)

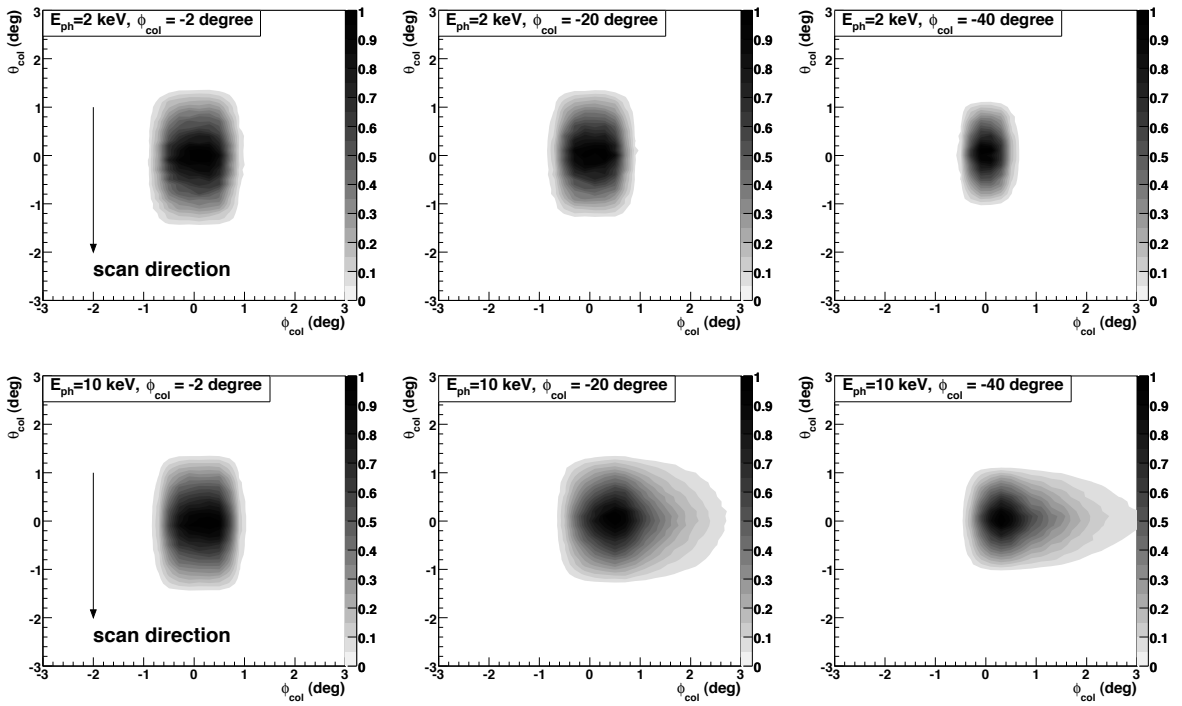

Fig. 6. Point Spread functions of a GSC camera for X-ray photons of 2-keV (top) and 10-keV (bottom) with an incident angle of 2° (left), 20° (center), and 40° (right).

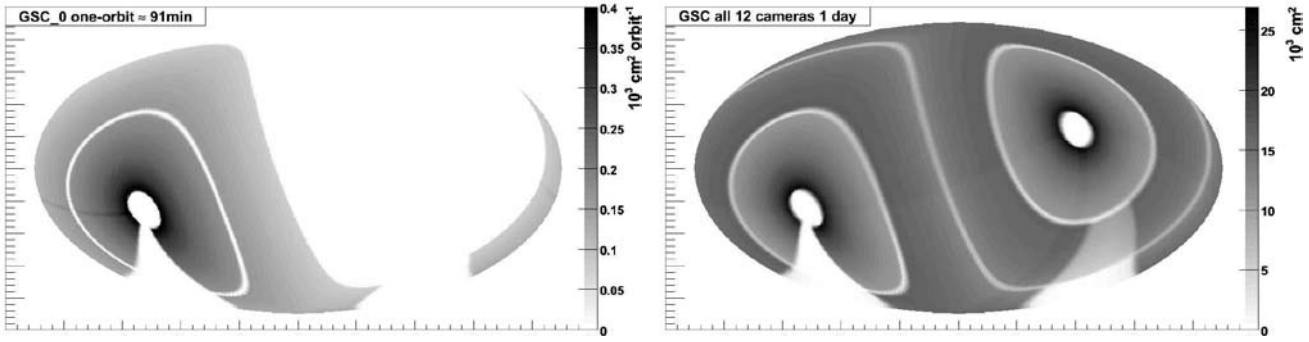

Fig. 7. All sky exposure map by one GSC-counter unit for one-orbit (left) and by entire 12 GSC-counter units for one-day (right). The uncovered area at the bottoms of the both figures corresponds to the Sun direction.

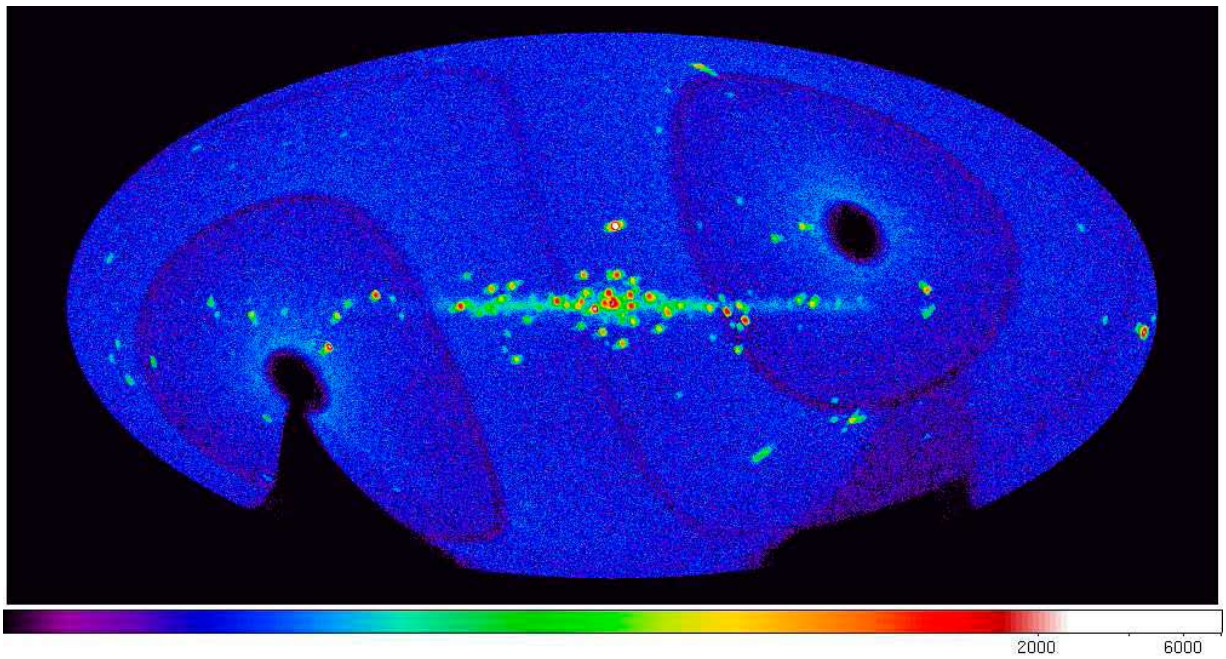

Fig. 8. Simulation of GSC observation of all-sky X-ray image for one day. Backgrounds by cosmic-ray particles are not included. The image of Figure 7 corresponds the exposure map for this data.

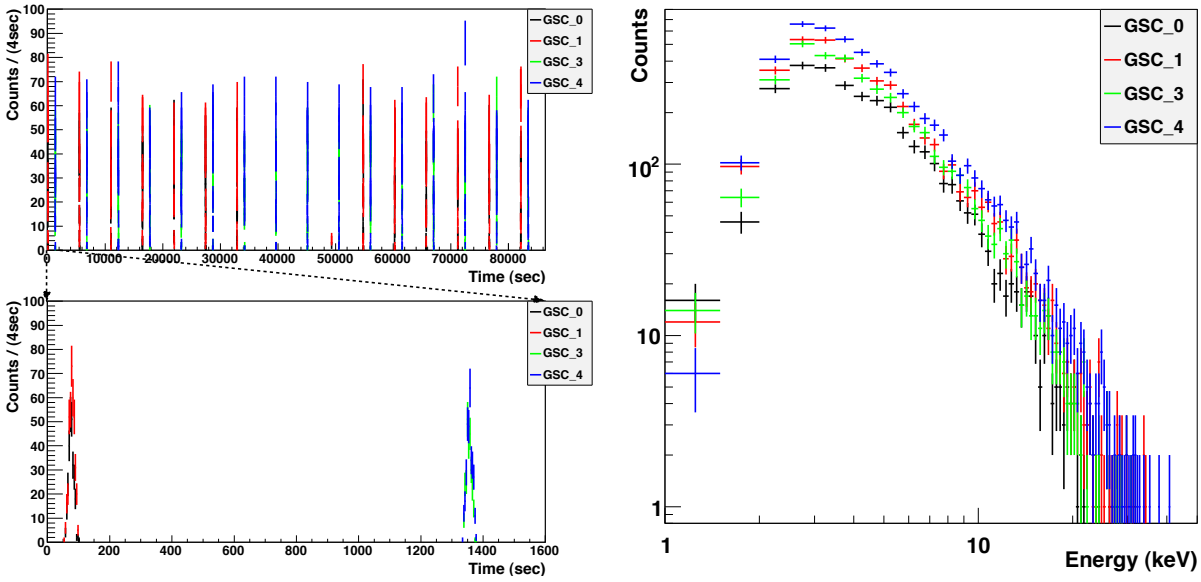

Fig. 9. Simulation of GSC observation of Crab nebula for one day. X-ray count rates by each GSC counter (left). Figure 4 corresponds to these response function. X-ray energy spectra by each GSC counter (right).

MAXI Catalog: Source Detection and Sensitivity

Kazuo Hiroi[1], Yoshihiro Ueda[1], Satoshi Eguchi[1], and the MAXI team

[1]Department of Astronomy, Kyoto University, Kyoto 606-8502, Japan
E-mail (K.H.): hiroi@kusastro.kyoto-u.ac.jp

Abstract

The MAXI source catalog will become a unique database of X-ray populations covering the 0.5–30 keV band in all sky. It will contain more than 1,300 AGNs (Ueda et al. 2009), including many new sources. We develop a software program of source detection of faint sources from MAXI/GSC data, where maximum likelihood fit is performed to a projected image by taking into account the image response and background. In this paper, we present our study to estimate the realistic sensitivities and the position accuracy of MAXI based on simulations.

Key words: catalogs — galaxies:active — X-rays:galaxies — X-rays:general

1. INTRODUCTION

One of the main goals of the MAXI mission is to provide a new X-ray catalog from the entire sky, including both transient and persistent sources. The Gas Slit Cameras (GSCs; Mihara et al. 2009) and the Solid-state Slit Cameras (SSCs; Tomida et al. 2009) cover the energy band of 2–30 keV and 0.5–12 keV, respectively, with unprecedented sensitivities as an all-sky mission. In particular, the large effective area of the GSCs at energies above 2 keV enables us to detect absorbed Active Galactic Nuclei (AGNs) that were missed in the ROSAT All Sky Survey, thus providing a unique database of extragalactic populations.

In this paper, we quantitatively evaluate the sensitivity and position accuracy of the MAXI GSCs, which are the most fundamental properties of the source catalog. Here we extensively utilize the MAXI simulator developed by Eguchi et al. (2009).

2. ANALYSIS METHOD

2.1. Simulation

We first produce simulated data of MAXI, to which our source detection method described in the next subsection is applied. In this paper, we only treat an extragalactic point-like source over the cosmic X-ray background, with three different operation times, 1 week, 1day, and 1 orbit (90 minutes) as representative cases. In the 1 week and 1 day simulation, we assume as real conditions as possible, by adopting realistic orbit and attitude information of MAXI and avoiding sky region around the Sun and the epoch of the South Atlantic Anomaly (SAA) passage. All the twelve GSCs are turned on, and their photons are summed in the image analysis. In the case of the 1 orbit simulation (i.e., only one exposure by a single camera for a given target), we assume three different directions of incident photons into the MAXI cameras as illustrated in Figure 1. The Sun and SAA are ignored. We only use data of the six GSCs with the zenithal field-of-view in the analysis to simulate the detection of very short-lived (< 20 minutes) transients. The simulation conditions are summarized below.

- Software
  – maxisim ver.7.0.1 (simulation)
  – dis45 ver.2.04 (image analysis)
- Source Spectrum
  – Crab-like (a power law of $\Gamma = 2.1$)
- Non X-ray Background Rate
  – 10 counts/s/counter
- Energy Band Used in the Analysis
  – 2–30 keV
- Exposure (Operation Time)
  – 1 week, 1 day, or 1 orbit

2.2. Image Fit

To extract the best sensitivities from the data, we have developed an analysis method by employing image fitting with the maximum likelihood algorithm. Firstly, we project the positions in RA and DEC of photon events around the target in the "sky coordinates", similar to image analysis of pointing satellites. To derive the flux, the position and their errors of the target, we perform 2-dimensional fitting to this simulated image by a model consisting of the point spread function (PSF) and background (the non X-ray background and the cosmic X-ray background).

One complexity in the analysis of MAXI data is that the PSF and background are position dependent, being determined by the orbit and attitude condition. To take this into account, we also utilize the MAXI simulator to construct the PSF and background models with a sufficiently larger number of photons to suppress the statistical fluctuation. An example of the PSF model integrated for the 1-week observation is shown in Figure 2.

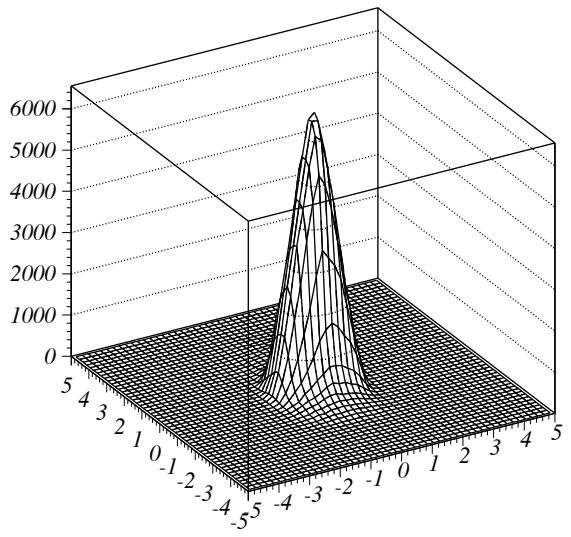

Fig. 2. An example of the PSF in the sky coordinate in units of degree, integrated for the 1-week observation. The z-axis is arbitrary.

To properly treat statistics with small numbers of photons in each bin, we adopt the Poisson maximum likelihood algorithm, utilizing the MINUIT package. The normalization of the PSF (i.e., flux) and background level are set to be free parameters. In the image fitting process, we consider two different situations, when the position of the source is (i) unknown and (ii) known. In the former case, we also make the position of the source free. Here we assume that the shape of the PSF does not largely differ in the region of interest, and ignore its position dependence for simplicity. In the latter case, the position is fixed at the input location.

We define the detection significance (σ_D) as

$$\sigma_D = \text{(best-fit flux) / (its } 1\sigma \text{ statistical error)}$$

and set $\sigma_D \geq 5$ as the criteria for secure detection (i.e., relative $\leq$20% error in the obtained flux). To evaluate the position accuracy, we make the error contour at 90% confidence level, or more simply, calculate the root sum square of the position errors in the two (x and y) directions.

Figure 3 shows the raw (left) and smoothed (right) images around the target, located in the center, for the 1-week simulation. Figure 4 shows its projection onto X-axis in a central region (with error bars), superposed with the best-fit model (dashed line: total, dotted line: only background). The left and right figures correspond to that of the 1-week simulation and of the 1-orbit simulation, respectively. By repeating such simulations with different input fluxes, we accurately estimate the 5 σ sensitivity (see Figure 5) and the position error for a given exposure.

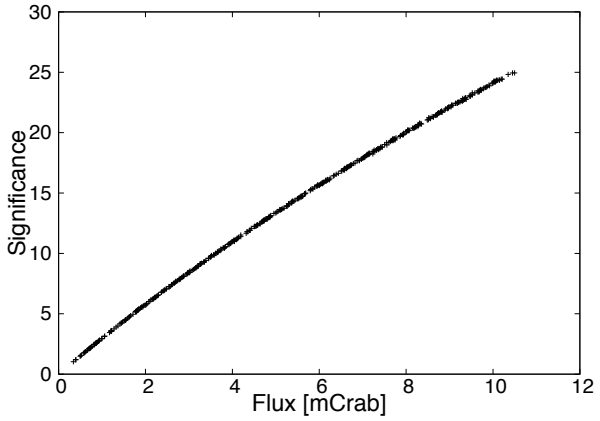

Fig. 5. The correlation between the detection significance and source flux for a 1-week simulation. The 5σ detection sensitivity is derived from this relation.

3. RESULTS

3.1. Sensitivity

The results are summarized in Table 1. In whichever case the position of the target is known or not, the 5σ sensitivity from the 1-week observation is found to be $\sim$2 mCrab, about 5 times better than that of the all sky monitor on RXTE. We confirm that the observing condition of this target in terms of effective exposure (i.e., exposure multiplied by the slit area) is close to the average over the entire sky. Hence, these results can be regarded as typical performance expected from MAXI. As for the result of 1-orbit simulation, we find the detection sensitivity becomes slightly ($< 10\%$) worse when the source position is unknown. It is also seen that the best sensitivity is obtained in pattern 3, where the photons from the target are collected by 2/3 of the six cameras at moderate incident angles.

3.2. Position Accuracy

Figure 6 shows examples of the error contour of the detected position at 90 % confidence level. We find that a typical error radius for targets with fluxes close to the 5σ sensitivity limit is $\approx$0.2–0.3 degree. The relation between the flux F and the error radius (combined from the two directions) is plotted in Figure 7. We find the positional error is roughly proportional to $F^{-0.89}$, steeper than a naive expectation of $F^{-0.5}$. We infer that this is due to

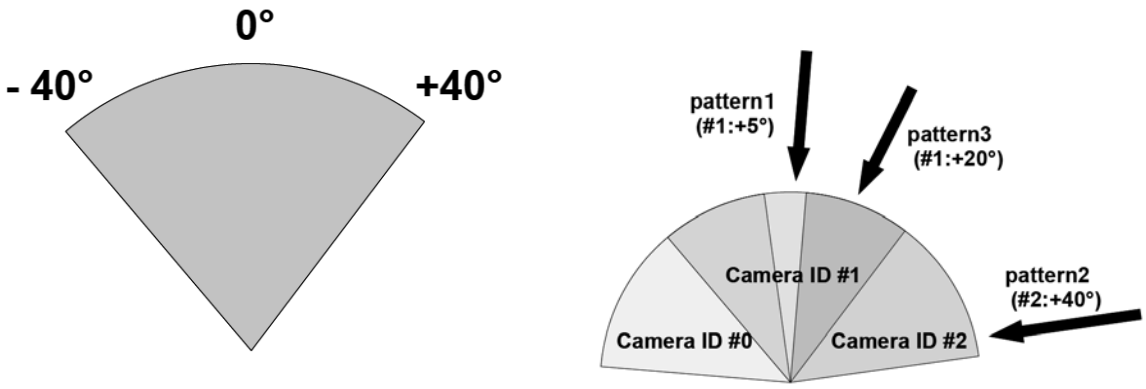

Fig. 1. The left figure shows the field of view covered by one GSC. In the simulation, we consider three patterns of incident direction of photons from a target, as illustrated in the right figure. For example, "pattern1(#1:+5°)" means that the target is located +5° away from the field-of-view center of Camera ID #1.

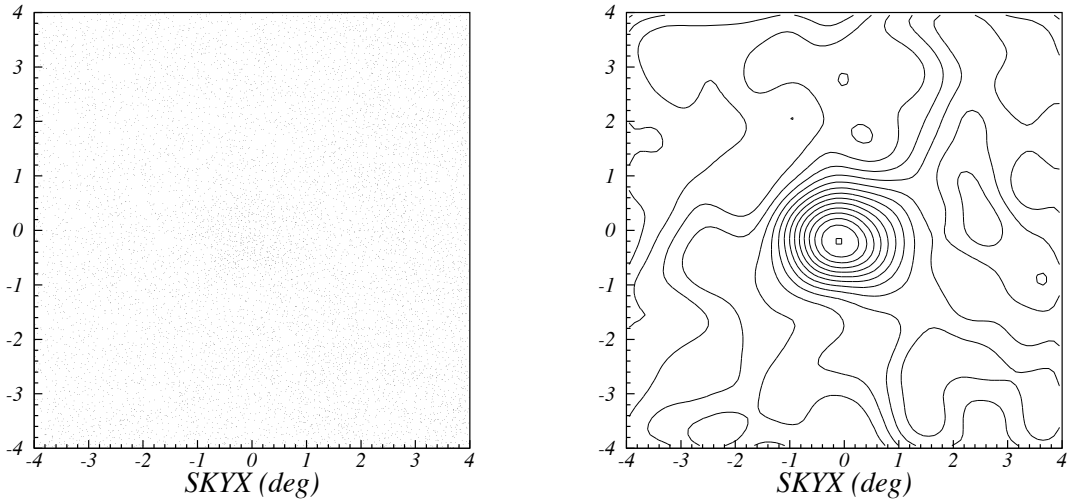

Fig. 3. An example of a simulated image around the target from a 1-week observation (left: raw, right: smoothed).The image size is 8 deg × 8 deg.

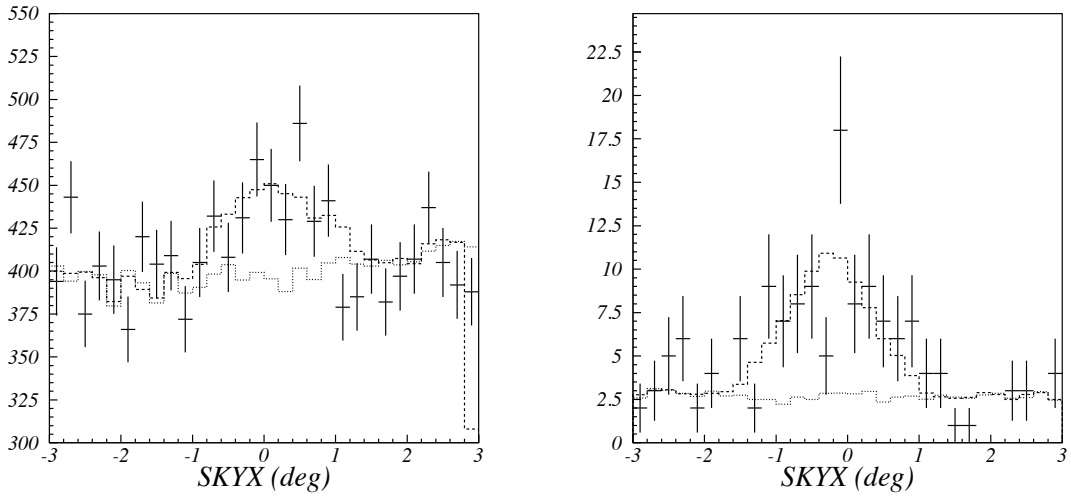

Fig. 4. The comparison of the (simulated) data and the best-fit model (left: 1 week, right: 1 orbit). The unit of vertical axis is counts per bin. We find that the background is dominant in 1-week simulation and that the source is dominant in 1-orbit one.

Table 1. The sensitivity of MAXI/GSCs. (unit mCrab)

	position	
exposure	known	unknown
1 week	1.7	1.7
1 day	4.4	4.5
1 orbit (pattern 1)	37	37
1 orbit (pattern 2)	40	40
1 orbit (pattern 3)	35	35

coupling between the position and flux determination in the fitting process.

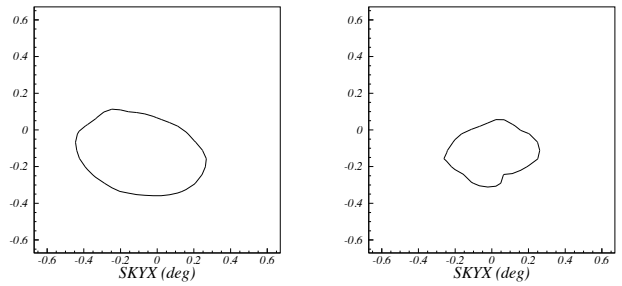

Fig. 6. Examples of the error contour of source position at 90% confidence level (left: 1 week, right: 1 orbit). The detection significance of both sources are about 5σ.

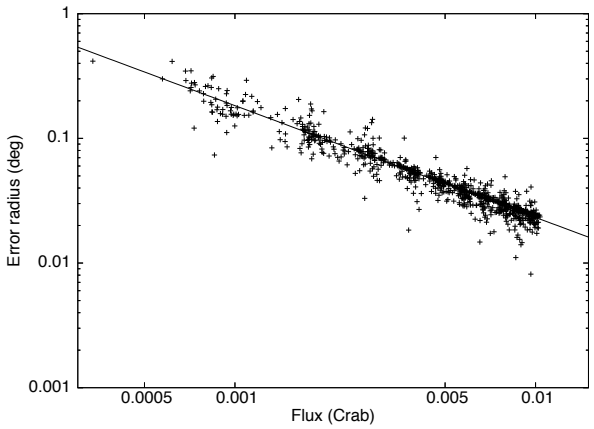

Fig. 7. The correlation between the flux and error radius (combined from the two directions). The curve shows the best-fit power law with a slope of –0.89.

4. SUMMARY

Our study shows that, by utilizing the image fitting method, we can achieve a sensitivity of about 2 mCrab for a point-like source from a 1-week operation of MAXI with typical observing conditions, assuming the non X-ray background rate of 10 c/s/counter. Based on our results, we plot a theoretical sensitivity curve as a function of operation time t in Figure 8. The sensitivity is roughly proportional to t^{-1} below $\sim 10^4$ sec (source-dominant case) but to $t^{-1/2}$ above it (background-dominant case).

This performance of MAXI is quite promising for scientific studies of not only Galactic but also extragalactic objects. We estimate that the sensitivity reaches the confusion limit (˜0.2 mCrab) from about 1.5 years operation of MAXI. At this flux level, about 1,300 AGNs are expected to be detected at Galactic latitudes larger than 15 degree. The MAXI catalog will contain many new transient and/or absorbed AGNs, and hence become a unique database of extragalactic populations complementary to other catalogs of all-sky missions, such as ROSAT, Swift/BAT, and INTEGRAL.

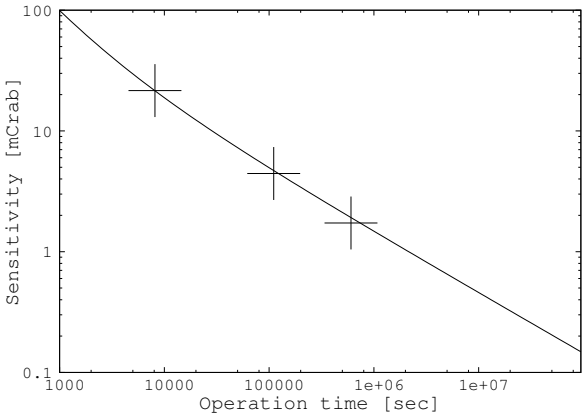

Fig. 8. Sensitivity curve as a function of integration time (actual operation time of MAXI with typical observing conditions) for a point-like source with a Crab-like spectrum. The three points correspond to the sensitivities of 1-orbit, 1-day, and 1-week observations, from left to right, obtained from our simulations.

References

Eguchi, S., et al. 2009, in this proceedings
Mihara, T., et al. 2009, in this proceedings
Tomida, H., et al. 2009, in this proceedings
Ueda, Y., et al. 2009, in this proceedings

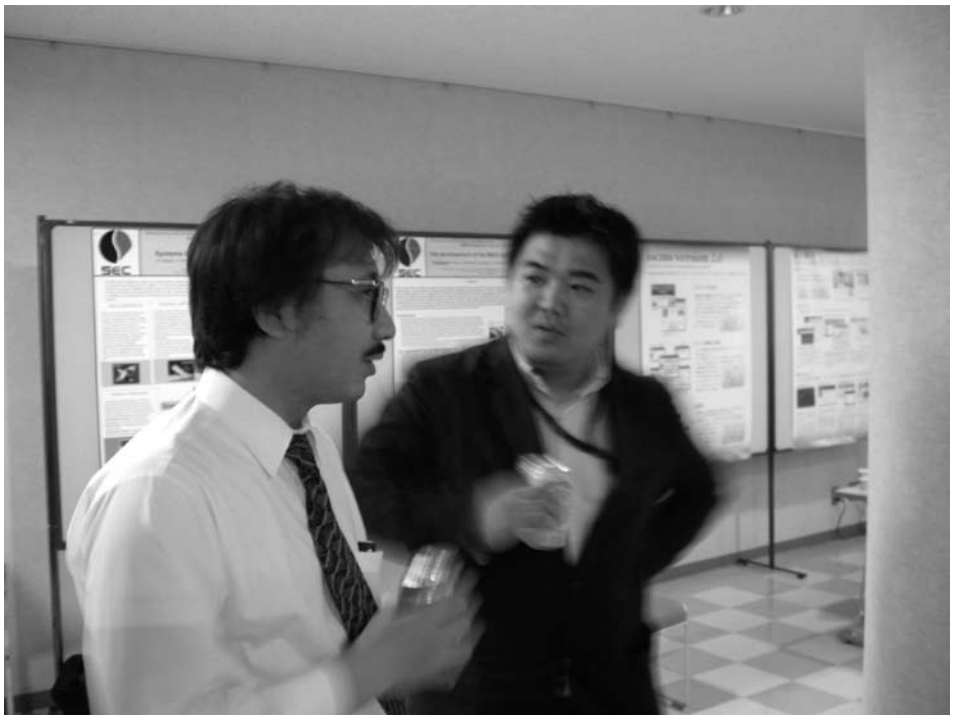

ACCRETING BINARIES AND NEUTRON STARS

Black Hole Transients and MAXI Nova Alert System

Hitoshi Negoro[1]

[1] Nihon University
1-8 Kanda Surugadai, Chiyoda, Tokyo, Japan 101-8308
E-mail(HN): negoro@phys.cst.nihon-u.ac.jp

Abstract

MAXI, Monitor of All-sky X-ray Image is one order of magnitude more sensitive than previous instruments, so that MAXI is the most advanced X-ray monitor to discover X-ray transient objects such as X-ray novae. MAXI's capability to discover black hole X-ray novae and scientific objectives are discussed through a historical and statistical analysis of newly compiled list of 45 black hole candidates. Finally, MAXI's nova finding and alert system is discussed.

Key words: X-ray transients: X-ray novae, black holes — MAXI, all sky monitor

1. Introduction

In the X-ray sky, new stars often appear and disappear. Such X-ray stars are referred to as X-ray transients. X-ray transients of which emission lasts relatively long, on timescales of days or months, are called *X-ray* novae (XNe), distinguishing them from flares, bursts, and flashes. X-ray novae are binary systems consisting of a main sequence star and a black hole (candidate) or a neutron star. Most black hole candidates, BHCs, are such X-ray novae (McClintock & Remilard 2007, hereafter MR07, and references therein). Inversely, X-ray novae sometimes stands for BH transients. Especially, so-called soft X-ray transients, SXTs, often indicate BH transients (Tanaka & Shibazaki 1996, TS96).

MAXI, Monitor of All-sky X-ray Image (Matsuoka et al. 1997), is undeniablely the best X-ray monitor to date to discover such X-ray transients. MAXI has the largest effective area to date, thereby providing a sensitivity that is one order of magnitude higher than that of previous instruments. Furthermore, by making the best use of the International Space Station, ISS, network, MAXI can send alert information to the world in as fast as $\sim$10 s!

In §2, the importance of the discovery of BH transients to the BH study is emphasized. In §3 and §4, a rate for the discovery of new BH transients with MAXI is estimated, and MAXI's scientific objectives are discussed. Finally, transient source finding/alert system of the MAXI ground software system, currently under development, is described.

2. Black Hole Study and Black Hole Transients

A number of efforts to find evidence for the existence of black holes has been made, and indications have been found (e.g., Narayan et al. 1997). However, so far we have only observed conditions *necessary* for the presence of black holes, and are still lacking any solid direct evidence, for instance, for the existence of the event horizon. Thus, the BHCs are still BH "candidates", though in this and other papers the term "black hole" is often used.

The number of BHCs that are persistent-emission sources is very small in our Galaxy. More than 90 % of BHCs are indeed X-ray transients (MR07). Thus, to study BHCs is to study BH transients. The BH transients also have provided us with new insights into the BH studies: powerful jets, various QPOs in addition to various states and the state transitions. Some of these properties are also good candidates for direct evidence for the black hole. In this sense, to discover BH transients is of great importance to the study of black holes.

3. X-ray Novae & MAXI

Currently, 20 mass-estimated BHCs and 25 second-class BHCs which show similar timing or spectral properties to those of the mass-estimated BHCs are known in our Galaxy (LMC X-1 and LMC X-3 are also included according to MR07). Shown in Table 1 & 2 is a newly compiled list of the BHCs, focusing especially on the first detections of the sources. After the publication of the paper by MR07, A 1742-289 was found to be a neutron star burster (Maeda et al. 1996). Casares et al. (2004) and Orosz et al. (2004) have upgraded X1354-64 and XTE J1650-500 to the mass-estimated BHCs, respectively, and 5 second-class BHCs have been added to the list.

3.1. Discovery Rate of Previous X-ray Novae

Figure 1 illustrates the history of the discoveries of the last 20 years, when *Ginga*/ASM and *RXTE*/ASM had

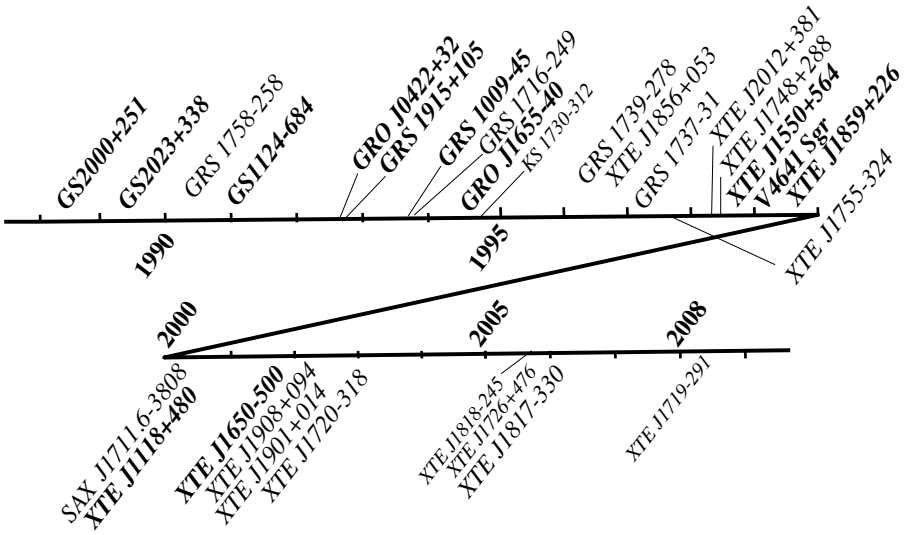

Fig. 1. XNe discovery history of the last 20 years. The sources written in bold font are mass-determined BHCs. The font size shows the grade of BHCs (see table 1–2).

and have been in use. Recurrent outbursts are omitted. In the last 20 years, 29 black hole transients have been found. The discovery rate is about 1.5 per year. Of course, each source was found with various instruments in various energy bands and with various detection limits. In fact, about 2/3 XNe were found with *Ginga*/ASM (GA) and *RXTE*/ASM (RA), and some others were found by pointing observations to the Galactic center region with *RXTE*/PCA (RP) and *Granat*/SIGMA (GS). Interestingly, however, the discovery rate is roughly constant.

This might be due to the large X-ray flux during the outburst. For instance, the flux at the first detection with *RXTE*/ASM, mainly reported to the IAUC and The Astronomer's Telegram, were 20 $\sim$ 200 mCrab above the detection limit of $\sim$ 20 mCrab.

3.2. Distribution of the BHCs on the Galactic Plane

Many BHCs are, however, located relatively close to the solar system. Figure 2 shows the geometric distribution of the 38 BHCs of which distances have been estimated on the Galactic plane. The distances to the sources in the direction of the Galactic center are unknown. Energy spectra of these sources are often heavily absorbed so that the sources are assumed to be near the Galactic center. Here, the sources less than 10 degrees apart from the center are adequately plotted near the center except for H 1705–250 and GRS 1716–249. V4641 is also likely to be such a Galactic center source though the source is plotted behind the center region.

It can be seen from the Fig. 2 that many BHCs are located near the Galactic center ($\sim$ 15 BHCs) and near the solar system ($\sim$ 11 BHCs within 4 kpc, and $\sim$ 15 within 6 kpc). Relatively long distance sources more than 6 kpc apart, except for the Galactic center ones and GRS 1915+105 and XTE J1859+226, are all bright, and/or persistent-emission sources found before 1987, the *Ginga* launch. About half of the Galactic center sources have been found by pointing observations, i.e., deeper observations. This implies that most XNe (BH transients) recently discovered are outbursts near the solar system and near the Galactic center, and that the discovery rate is limited mainly by the detection limit of the previous detectors.

3.3. Expected Discovery Rate of X-ray Novae with MAXI

MAXI with a much higher sensitivity will be able to observe a more extended region of our Galaxy and a deeper area near the Galactic center, compared with the previous all-sky monitors. The increase of sensitivity by one order of magnitude translates to a 3 times larger observable distance and to an about 10 times more extened scannable region (not volume). (Note that most BHCs are in the Galactic plane.)

If the observable distance has been limited to 3–5 kpc previously, then MAXI will be able to observe a 9–15 kpc distance, which corresponds to more than half the area of our Galaxy. MAXI/GSC having sensitivity up-to 30 keV will most certainly be helpful when looking for heavily absorbed, embedded sources near the Galactic center and in far distant region as *Granat*/SIGMA and *CGRO*/BASTE. Current simulation results also support this (Tomida, private comm.).

Taking into account the extension of observable region and the star distribution in our Galaxies, and also frequent scanning of the Galactic center region, an expected discovery rate of XNe with MAXI is optimistically 5–10 times higher than before: 1.5 BHCs/yr $\times$ 5–10 $\sim$ 7.5–15

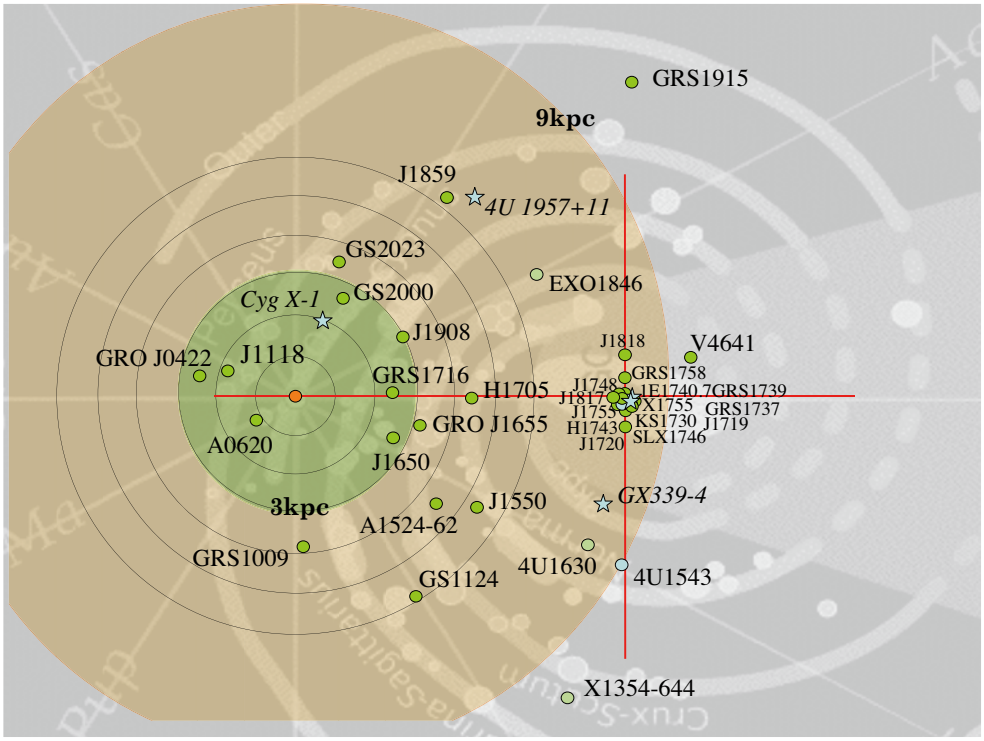

Fig. 2. The Galactic plane map of BHCs, of which distances have been measured. The background image is from wikipedia.org. The distances used are basically the latest estimates as shown in table 1–2. The sources near the Galactic center are projected onto the plane at the distance to the center. Source names starting with "J" should be read as "XTE J". The persistent emission sources are marked with (cyan) star symbols. The distance to the Galactic center is assumed to be 8 kpc.

BHCs/yr. This means that if MAXI works as expected, we could discover as many as one new BHC per month! Of course, recurrent outbursts of the known BHCs and other X-ray novae of neutron binaries are also expected to be observed frequently with MAXI.

4. MAXI Objectives

BHCs exhibit various timing and energy spectral features classified into several states: ultrasoft/slim-disk, very high, high/soft, intermediate, low/hard and quiescence/off states. MAXI has two different kinds of instruments, the GSC with the wide energy band sensitive at 2–30 keV and the SSC with good energy resolution, so that one can see detailed spectral evolution during an outburst just like that of GS 1124-684 observed with *Ginga* /ASM (Kitamoto et al. 1992) and LAC (Ebisawa et al. 1994). Of course, followup observations with other satellites or observatories like for instance *Suzaku* are essential for further detailed study.

Oda et al. (2007, also see Matsumoto in this volume) have found from their MHD simulations a new solution of the accretion disk model, a magnetically supported, optically thin cool disk, which is expected to appear during the transition between the hard and soft states. Observationally, it may be referred to the "high-to-low transition" state (Miyamoto et al. 1993) or the "intermediate" state (Mendez & van der Klis 1997). For such a study, MAXI will also be very helpful.

It has been difficult for pointing observatories to catch powerful, relativistic jets. Fender et al. (2004) have shown that the powerful jets tend to appear just before the transition to the soft state. From the continuous observations with MAXI it will be possible to predict the appearance of jets. It will therefore become easier than before to observe a jet source simultaneously in X-rays (MAXI) and other wavelengths, for instance with FOFAR (see Fender in this volume). The origin of these mysterious jets might be understood from upcoming MAXI and other wavelength data.

It is difficult for MAXI to detect high frequency QPOs, but their appearance is expected from that of low frequency QPOs detectable with MAXI (e.g., Remillard et al. 2002). Followup observations with *RXTE*, *Suzaku* and *ASTROSAT* are highly encouraged.

Finally, the beginning of an outburst, which has rarely been observed, is of great interest because we might finally be able to determine whether the event horizon really exists or not (c.f., Narayan et al. 1997).

Table 1. List of the Black Hole Candidates

Source Name[a]	Date[b]	Satellite[c]	Flux[d] [mCrab]	Recurrence[e]	Distance[f] [kpc]	References & Notes[g]
GRO J0422+32, v518 per	1992/08/05	CB	200		2.6 ± 0.7 $2.49 \pm 0.30^{\rm Hy}$	1
LMC X-3[1]	p	–	–	–	50 ± 2.3	
LMC X-1[1]	p	–	–	–	50 ± 2.3	
A0620-00, Mon X-1, V616 Mon	1975/08	AV		(1917)	1.16 ± 0.11	2, RJ
GRS 1009-45, MM Vel	1993/09/12	GW CB	600 ± 100@8-20keV 500 ± 100		5.0 ± 1.3, $5 \pm 1.5^{\rm Ha}$ $3.82 \pm 0.27^{\rm Hy}$	3
XTE J1118+480, KV Uma	2000/03/29	RA	39 ± 8		1.8 ± 0.5	4
GS1124-684, GRS1121-68, GU Mus	1991/01/08	GW GA	~ 2000 800		5 ± 1.3, $5.5 \pm 1.0^{\rm Ha}$ $5.89 \pm 0.26^{\rm Hy}$	5
X1354-64(4)[2], GS1354-645, BW Cir	1966/10?			71?,72?,87/02[GA300], 97/10-11[CB200,RA16]	$10?^{\rm Ch}$ ($> 27?^{\rm ref.10}$)	6–10
A1524-62[A], TrA X-1, KY TrA	1974/11	AV		90/08[GS]	$4.4^{\rm Ch}$	11,12
4U1543-47, IL Lupi	1971/08	Uhuru		83/08[Tenma],92/04[CB1080], 02/06[RA54]	$7.5 \pm 0.5, 4^{\rm Ch}$, $9.1 \pm 1^{\rm Ha}$	13–15
XTE J1550-564, V381 Nor	1998/09/07	RA	70	99/01[CB(300)],00/04[RA(60)], 01/01[RP],02/01[RP60], 03/03[II150]	5.3 ± 2.3	16–21, HFQPO, RJ
4U1630-472[A], Nor X-1, GX 337+00, A1630-742	1971/02	Uhuru		~ 1.8 yr interval	$8?^{\rm Ch}$	22, HFQPO
XTE J1650-500[3]	2001/09/05	RA	140 ± 20		$2.6^{\rm ref.24}$	23,24, HFQPO
GRO J1655-40, V1033 Sco	1994/07/27	CB		95/01[CB150],95/02[CB,MIR1700], 95/07[CB],96/04[RA71]	3.2 ± 0.2	25–30, HFQPO, RJ
GX339-4, V821Ara	p(1972 $\sim$?)	–	–	–	4, $6\text{-}15^{\rm ref.31}$	31
H1705-250, A1705-250, V2107 Oph	1977/08	AV/H1			8 ± 2, $4.3^{\rm Ch}$	32,33
SAX J1711.6-3808[B]	2001/02/08	BW	30 $\sim$ 80@2-9keV			34
GRS 1716-249[B], GRO 1719-24, Oph	1993/09/24 (09.25)	CB GS	70 ± 14@20-100keV 342 ± 45@35-75keV	94/09[GS,MIR]	$(2.4 \pm 0.4)^{\rm Hy}$	35,36
XTE J1719-291, SWIFT J171916.9-290410	2008/03/21	RP	5		(GC)	37
XTE J1720-318[C], Sco 2003	2003/01/09	RA	130 ± 20		$3\text{–}10^{\rm ref.37}$(GC)	38,39
XTE J1726-476, IGR J17269-4737	2005/10/04 (05/10/6-7)	RA II	32 ± 4 11@20-40keV			40 41
KS 1730-312[C], GRS1730-312	1994/09/23 (09.22–23)	MIR GS	70 ± 10@2-30keV 130@40-150keV		(GC)	42
GRS 1737-31[B]	1997/03/14	GS	90 ± 16@35-75keV 130 ± 20@75-150keV		(GC)	43

[a] Sources written in bold font are mass-determined BHCs (MR07 and recent papers cited). Upper scripts (^{A,B,C}) are BHC grades by MR07. Constellation names at the end are used, for instance "Nova Mus 1991".

[b] Date (or month) of the first discovery. p in this column indicates a "persistent" emission source, but a nova.

[c] AV="Ariel V", BW="BSAX/WFC", CB="CGRO/BASTE", GA="Ginga/ASM", GP="Granat/ART-P", GS="Granat/SIGMA", GW="Granat/WATCH", H1="HEAO1" II="INTEGRAL/IBIS(/ISGRI)", IJ="INTEGRAL/JEM-X", MIR="MIR-KVANT-TMM/SIGMA", RA="RXTE/ASM (2-12 keV)", RP="RXTE/PCA (typically 2–10 keV)", SX="Swift/XRT"

[d] Flux in the first detection in mCrab unit.

[e] Recurrence Dates, YY/MM, and [detected satellite[c] and flux[d]] are shown from MR07, TS96 and IAUC and ATel. Years or monthes in parenthesis are from optical plates.

[f] No mark: HR07, and references therein, Ch: Chen et al. 1997, Ha: Hameury et al. 2003, Hy: Hynes 2005. "(GC)" means that the source is assumed/likely to be near the Galactic center.

[g] References for the columns 2-4 (first detections), 5 (recurrences), and 6 (distance). HFQPO="high frequency QPO", RJ="relativistic jet", FXT="fast X-ray transient"

[1] LMCs are not Galactic sources; [2] $M > 7.8 M_\odot$, see Casares et al. 2004; [3] $M \sim 4 M_\odot$, see Orosz et al. 2004

Table 2. *continued.*

Source Name[a]	Date[b]	Satellite[c]	Flux[d] [mCrab]	Recurrence[e]	Distance[f] [kpc]	References & Notes[g]
GRS 1739-278[A]	1996/02/28 (96/03/18?)	MIR GS	200 ± 50@2-27keV 80 ± 28@40-75keV		(GC)	44 45
1E 1740.7-2942[A]	*p*	–	–	–	(GC)	46
H1743-322[A], IGR J1746-3213, XTE J17464-3213	1977/08	H1		77,03/05[II60,RP50], 04/07[RP16],05/08[RA21], 07/12[RA200],08/09[IJ10]	(GC)	47–52, HFQPO
SLX 1746-331[C]	1985/07-08	Spacelab-2		90,03/04[RP40], 07/10[RP8]	(GC)	53 54
XTE J1748-288[A]	1998/06/04	RA	90/300/470 @1.5-3/3-5/5-12keV		(GC)	55
XTE J1755-324[B]	1997/07/25	RA			(GC)	56
X1755-338[B], V4134 Sgr, 4U1755-33?	*p*	–	–	(GC)		57
GRS 1758-258[A]	*p*(90/03∼?)	GA (GS)	40 ± 8@10-20keV 90 ± 20@20-40keV		(GC)	58,44
XTE J1817-330	2006/01/26	RA	930 ± 30		(GC)	59
XTE J1818-245,	2005/08/12	RA	55 ± 5		(GC)	60
V4641 Sgr, SAXJ1819.3-2525, XTE J1819-254	1999/02/20 (99/02/18)	BW RA	 20	02/05[RP4.5], 03/08[RP20], 04/07[RP8.2],05/06[RP],07/07[SX]	7.4–12.3 (GC)	61–67, RJ, FXT
EXO 1846-031[C]	1985/04	EXOSAT	200	94/09	$7?^{\mathrm{Ch}}$	68
XTE J1856+053	1996/09/10	RP/RA[1]	66/35	07/02[RA23]		69,70
XTE J1859+226, V406 Vul	1999/10/09	RA	160 ± 15		11, $6.3 \pm 1.7^{\mathrm{Ha}}$ $(8 \pm 3)^{\mathrm{Hy}}$	71, HFQPO, RJ?
XTE J1901+014 (GRB020406)	2002/04/06	RA	900			72, FXT?
XTE J1908+094[B]	2002/02/17	RP			$> 3^{\mathrm{ref.74,75}}$	73-75
GRS1915+105, V1487 Aql	1992/08/15	GW	~ 300		11–12	76, HFQPO, RJ
Cyg X-1	*p*	–	–	–	2.0 ± 0.1	RJ
4U1957+11[C,77], 3U1956+11, V1408 Aql	*p*	–	–	–	7	77
GS2000+25(1), QZ Vul	1988/04/23	GA	$\sim 2,000 - 3,000$		2.7 ± 0.7	78
XTE J2012+381[B]	1998/05/24	RA	23			79
GS2023+338, V404 Cyg	1989/05/22	GA	$100 \sim 1,200$	(38/10,56/08)	2.2-3.7, $3.5 \pm 1^{\mathrm{Ha}}$	80

1. First detected with PCA on Sep. 17–18, and ASM data were retrospectively analyzed.

REFERENCES (#:IAU Circular, @: ATel.): 1. Paciesas et al. 1996 #5580; 2. Elvis et al. 1975 #2184; 3. Lapshov et al., Harmon et al. 1993 #5864; 4. Remillard et al. 2000 #7389; 5. Lund et al. (GW), Makino et al. (GA) 1991 #5161; 6. see Kitamoto et al. 1990; 7. Makino 1987 #4342; 8. Harmon & Robinson 1997 #6774; 9. Remilard et al. 1997 #6772; 10. Casares et al. 2004; 11. Kaluzienski 1975 STIN., 7528978; 12. Barret et al. 2002; 13. Tanaka et al. 1983 #3854; 14. Harmon et al.1992 #5504; 15. Miller et al. 2002 #7920; 16. Smith et al. 1998 #7008; 17. Harmon et al. 1999 #7098; 18. Smith et al. 2000 #7399; 19. Tomsick et al. 2001 #7575; 20. Swank et al. 2002 #7792; 21. Dubath et al. 2003 #8100; 22. e.g., Kalemci et al. 2008 ATel,. 1348; 23. Remillard 2001 #7707; 24. Homan et al. 2006; 25. Zhang et al. 1994 #6046; 26. Harmon et al. 1995 #6128; 27. Alexandorovich et al. 1995 #6143; 28. Harmon et al. 1995 #6147; 29. Harmon et al. 1995 #6196; 30. Remillard et al. 1996 #6393; 31. Hynes et al. 2004; 32. Kaluzienski & Holt 1977 #3104; 33. Griffiths et al. 1977 #3110; 34. in 't Zand et al. 2002 #7582; 35. Ballet et al. (CB), Harmon et al. (GS) 1993 #5781; 36. Churazov et al. (GS), Borozdin & Alexandrovich (MIR) 1994 # 6083; 37. Markwardt 2008 @1442; 38. Chaty & Bessolaz 2006; 39. Remillard et al. 2003 #8050, ATel113; 40. Levine et al. 2005 @623; 41. Turler et al. 2005 @624; 42. Borozdin et al. (MIR), Churazov et al. (GS) 1994 #6083; 43. Sunyaev et al. 1997 #6599; 44. Borozdin et al. 1996 #6350; 45. Paul et al. 1996 #6348; 46. Main et al. 1999; 47. Revnivtsev et al. 2003 @132; 48. Markwardt & Swank 2003 @133; 49. Swank et al. 2004 @301; 50. Swank et al. 2005 @576; 51. Kalemci et al. 2008 @1348; 52. Kuulkers et al. 2008 @1739; 53. Markwardt 2003 @143; 54. Markwardt 2007 @1235; 55. Smith et al. 1998 @25, # 6793; 56. Remillard et al. 1997 #6710; 57. (McClintock et al. 1978 #3251); 58. Mandau 1990 #5032; 59. Remillard et al. 2006 @ 714; 60. Levine et al. 2005 @578; 61. In'tZand 1999 #7119; 62. Warkwardt et al. 1999 #7120; 63. Markwardt & Swank 2002 #7906; 64. Bailyn et al. 2003 @171; 65. Swank 2004 @295; 66. Swank et al. 2005 @536; 67. Cackett & Miller 2007 @1135; 68. Parmer & White 1985 #4051; 69. Marshall et al. 1996 #6504; 70. Levine & Remilllard 2007 @1024; 71. Wood et al. 1999 #7274; 72. Remillard & Smith 2002 @88; 73. Wood et al. 2002 #7856; 74. in't Zand et al. 2002; 75. Chaty et al. 2006; 76. Castro-Tirado et al. 1992 #5590; 77. Wijnands R. et al. 2002; 78. Makino et al. 1988 #4587; 79. Remillard et al. 1998 #6920; 80. Makino et al. 1989 #4782;

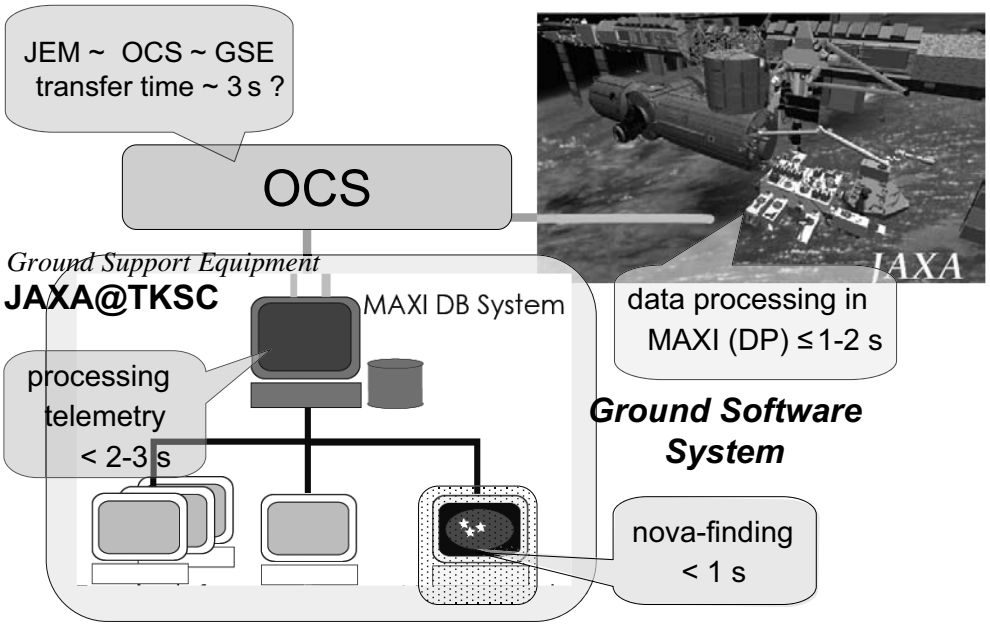

Fig. 3. Data flow and necessary time to generate/transfer data from MAXI onboard to a nova-finding system on the ground.

5. MAXI Nova Alert System

This section describes our nova (transient object) finding and alert system currently under development and how one can obtain information about a nova and other transient object discovered with MAXI.

Figure 3 illustrates the data flow from MAXI onboard the ISS to the ground data processing system. Telemetry data are generated every second and transfered to the ground using the ISS quasi-realtime network. However, the whole transfer takes about 10s to complete, even though our nova-finding system takes only less than 1s to obtain the first alert information (Negoro et al. 2008).

After the detection of a new source, we are planing to send alert information via the GCN (Gamma-ray burst Coordinates Network: http://gcn.gsfc.nasa.gov) circular for short transient events such as gamma-ray bursts on the timescale of seconds. For X-ray novae, which will be detectable on timescale of one scan (∼40 s) or hours, information will be sent via e-mail to the people who have registered at the MAXI web site (http://maxi.riken.jp; see Kohama et al. in this volume).

The author thanks David Röhrscheid for careful reading of the manuscript.

References

Barret D. 1992 ApJ., 392, L19
Casares J. 2004 ApJ., 613, L133
Chaty S. & Bessolaz N. 2006 A&A., 455, 639
Chaty S. et al. 2006 MNRAS., 365, 1387
Chen W. et al. 1997 ApJ., 491, 312
Ebisawa K. et al. 1994 ApJ., 46, 375
Esin A. et al. 1997 ApJ., 489, 865
Fender R. et al. 2004 MNRAS., 355, 1105
Hameury, J.-M. 2003 A&A., 339, 631
Homan J. et al. 2006 MNRAS., 366, 235
Hynes, R.I. 2004 ApJ., 609, 317
Hynes, R.I. 2005 ApJ., 623, 1026
in't Zand J.J. et al. 2002 A&A., 394, 553
Kitamoto S. et al. 1990 ApJ., 361, 590
Kitamoto S. et al. 1992 ApJ., 394, 609
Maeda Y. et al. 1996 PASJ., 48, 417
Main D.S. et al. 1999 ApJ., 525, 901
Matsuoka M. et al. 1997 SPIE., 3114, 414
Mendez M. and van der Klis M. 1997 ApJ., 479, 926
McClintock J.E. and Remillard R.A. 2007 (MR07) in *Compact Stellar X-ray Sources*, eds. W.H.G Lewin and M. van der Klis, Cambridge University Press. 39, Chap.4 (astro-ph/0306213v4)
Miyamoto S. et al. 1993 ApJ., 403, L39
Narayan R. et al. 1997 ApJ., 478, 79
Negoro H. et al. 2008 ASPC., 394, 597
Oda H. et al. 2007 PASJ., 59, 457
Orosz J.A. et al. 2004 ApJ., 616, 376
Remillard R.A. et al. 2002 ApJ., 580, 1030
Tanaka Y. and Shibazaki, N 1996 (TS96) ARAA., 34, 607
Wijnands R. et al. 2002 MNRAS., 331, 60

Suzaku Observations of Black-Hole Binaries and ULXs

Kazuo MAKISHIMA[1,2]

[1] Cosmic Radiation Laboratory, The Institute of Physical and Chemical Research (RIKEN)
[2] Department of Physics, The University of Tokyo
E-mail(KM): maxima@crab.riken.jp

Abstract

After a brief description of black hole investigations conducted in RIKEN, two highlights from the ongoing *Suzaku* mission are described. One is detailed understandings of the Low/Hard state of black hole binaries. The other is the reinforced interpretation of ULX objects as intermediate-mass black holes. A caution is cast upon the claimed detections of broad Fe-K lines from several Galactic X-ray sources. A mention is made also on the anticipated MAXI quest for the merger signals among active galactic nuclei.

Key words: black holes —Cyg X-1 — ULXs — Suzaku — MAXI

1. Introduction

As illustrated in Fig.1 by a pentagon, observational studies of black holes (BHs) comprises five distinct aspects of scientific importance. These are; to understand the physics of mass accretion onto BHs using their radiation as a probe; to search for general relativistic effects; to clarify how the gravitational energy release of accreting materials is partially extracted and converted into non-radiative energy outputs; to study the final stage of stellar evolution including the gravitational collapse and the BH formation; and to investigate how massive BHs at the galaxy nuclei have been formed possibly involving intermediate-mass BHs (IMBHs). These aspects are further combined to form composite research subjects, as indicated by shaded boxes in Fig.1.

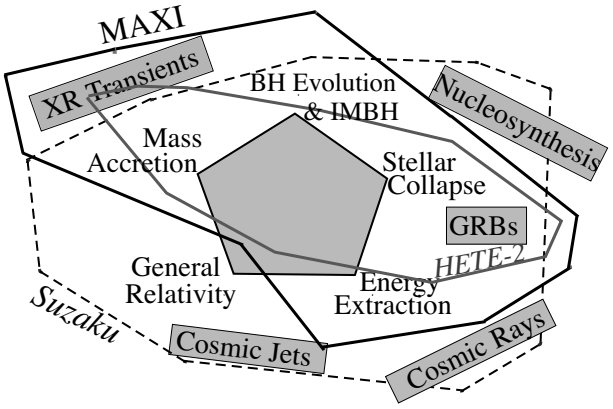

Fig. 1. A schematic overview of observational BH studies, and their coverage bythe three RIKEN-related missions; *HETE-2* (solid gray line), *Suzaku* (dashed line), and MAXI (solid black line).

2. Black Hole Researches in RIKEN

At the RIKEN Cosmic Radiation Laboratory, we have been carrying out extensive BH observations, mainly using the following three space missions. The scientifc ranges covered by them are also indicated in Fig.1.

- *HETE-2*: This is a small satellite launched in October 2000, under a collaboration among RIKEN, MIT, and a French group. It has revealed two origins of gamma-ray bursts; gravitational collapses of massive stars (for "long" events; Greiner et al. 2003), and mergers between two compact objects (for "short" ones: Villasenor et al. 2005).
- *Suzaku*: This is the 5th Japanese cosmic X-ray satellite, launched on 2005 July 10 (Mitsuda et al. 2007). We have participated in the development of the Hard X-ray Detector (HXD; Takahashi et al. 2007; Kokubun et al. 2007), in software developments, in-orbit calibrations, and verification of the timing accuracy. We also run "*Suzaku* Help Desk".
- MAXI: Since this is the central subject of the present workshop, we need only to remark that we are one of the core members of this mission, and are in particular responsible for releasing/archiving the MAXI data and leading the science using them.

Our activity as described above is collaborative with two other groups in RIKEN. One is the Nishina Center for Accelerator-Based Science, led by Dr. Y. Yano; we collaborate with them on the study of cosmic nucleosynthesis, as well as on hardware developments. The other is the Computational Astrophysics Laboratory led by Dr. T. Ebisuzaki, where they are conducting numerical studies of the formation of IMBH and super-massive BHs, and proposing for the ISS an ambitions EUSO mission to study the highest-energy cosmic rays.

3. *Suzaku* Highlights on Black Hole Binaries (BHBs)

3.1. Four spectral states of BHBs

It has been shown (e.g., Makishima 2007) that mass-accreting black-hole binaries (BHBs) take four typical spectral states, according to their accretion rates.

1. The Low/Hard State (LHS), corresponding to the normalized mass accretion rate η less than a few percent. The spectrum takes roughly a power-law shape, with a thermal cutoff at ~ 100 keV.
2. The Hight/Soft State (HSS), realized for η from a few to several tens percent. The spectrum consists of a soft component from a standard accretion disk, and an enigmatic power-law tail.
3. The Very High State (VHS), which appears at $\eta \sim 1$. Although the standard-disk is still present, its emission becomes strongly Comptonized, to form a power-law like continuum with a mild curvature.
4. The Slim Disk State (SDS) with even higher values of η (Kubota & Makishima 2004). Although the spectra resemble the HSS ones, the disk is much hotter, and its radial temperature profile is flatter than that of a standard disk.

3.2. Low/Hard state spectra

While the HSS spectra of BHBs (except for the enigmatic hard tail) have been understood well as originating from standard accretion disks, their LHS spectra have long remained ambiguous. Little is clear beyond what is rather certain, that the dominant hard X-ray continuum is a result of thermal Comptonization of some seed photons by a hot "corona" created near the BH. The seed photons could be provided either by a cool disk located somewhere in the system, or by the corona itself via thermal synchrotron process. The difficulty with the LHS lies mainly in the broad energy band in which the radiation emerges. Then, the research must be much promoted by *Suzaku*, which covers an extremely wide energy range of 0.2–600 keV with the HXD and the X-ray Imaging Spectrometer (XIS).

With the above motivation in mind, we have so far observed with *Suzaku* several BHBs, and detected two objects in a typical LHS; Cyg X-1 (Makishima et al. 2008) and GRO J1655−40 (Takahashi et al. 2008). By carefully investigating these data, we have successfully constructed a canonical model spectrum applicable to both objects over a typical energy range of 1–300 keV. As presented in Fig.2, the model consists of the following 5 components.

1. A thermal Compton continuum (`Compps_h` in Fig.2), with an electron temperature of $T_{\rm e} = 100 \sim 140$ keV and an optical depth of $\tau = 1.1 \sim 1.5$.
2. Another Compton continuum (`Compps_s`) with a comparable $T_{\rm e}$, and a lower optical depth of $\tau \sim 0.3$.
3. A direct disk emission (`diskbb`) at the softest end of the spectrum, with a temperature of ~ 0.2 keV.
4. The reflection components associated with the Compton continua.
5. A fluorescent Fe-K line, only slightly broadened.

The model in Fig.2 is for Cyg X-1, while that for GRO J1655−40 differs only in the weakness of the components 3 to 5. For example, the equivalent width (EW) of component 5 is ~ 300 eV and ~ 100 eV in Cyg X-1 and GRO J1566−40, respectively. This can be explained by their difference in the disk inclination, which is estimated as $i \sim 45^\circ$ for Cyg X-1 and $i \sim 70^\circ$ for the other. If these values of i are considered, the reflector in both objects are inferred to have a solid angle of $\Omega \sim 0.4 \times 2\pi$ as seen from the corona. In this way, the differences between the two objects can be explained consistently as inclination effects; this in turn supports a natural view that the disk is flat and the corona is rather spherical.

These results imply four important consequences. First, the disk-corona view is basically correct, and the seed photons are consistent with being fed by the disk. Second, the corona is highly inhomogeneous, because the Compton continua have at least the two optical depths, and the cool disk is partially visible without Comptonized. Third, the cool disk is truncated at a radius of $\sim 8R_{\rm S}$, where $R_{\rm S}$ is the Shcwarzshild radius. This inference is obtained by summing the area of the directly visible disk, and that of the Compton seed-photon source. Finally, the cool disk intrudes half way into the corona, because the reflector solid angle, $\Omega \sim 0.4 \times 2\pi$, is neither too large (in which case the disk would be mostly covered by the corona), nor too small (in which case the disk must be truncated outside the corona).

We have thus for the first time succeeded in constraining a realistic geometry of the corona-disk configuration.

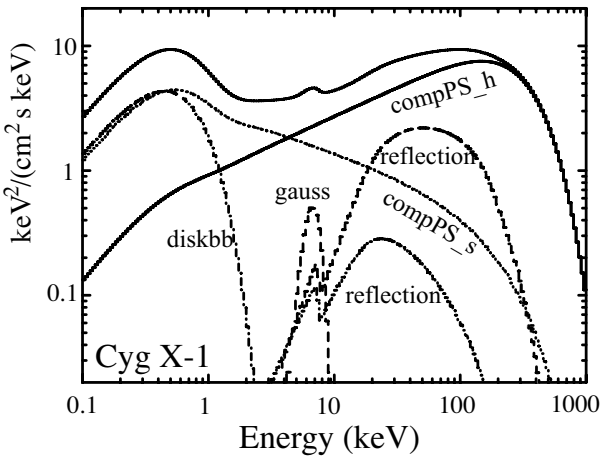

Fig. 2. A canonical $\nu F\nu$ spectrum of BHBs in the Low/Hard state, obtained by analyzing the *Suzaku* spectra of Cyg X-1 (Makishima et al. 2008) and GRO J1655-40 (Takahashi et al. 2008).

3.3. Rapid time vatiations

Another outstanding issue associated with the LHS of BHBs is their rapid flickering activity, known for more than 3 decades. Although a large number of studies have been conducted on this issue, it has remained difficult to interpret the phenomenon as a certain physical process taking place in the disk-corona system.

We analyzed the *Suzaku* data using a new method, namely judging instantaneous (on $\sim$ 1 sec time scales) source intensity using the XIS data which have higher statistics, and apply the judgement to the HXD data which have poorer statistics. We have thus obtained a pair of broad-band Cyg X-1 spectra, one covering brighter time intervals of the source, while the other fainter phases. By comparing them, we have arrived at the following inferences (Makishima et al. 2008).

1. The seed photon input to the corona increases in the brighter phase, enhancing the hard X-ray intensity.
2. Either $T_{\rm e}$ or τ (or both) of the corona decreases in the brighter phase, thus making the spectrum softer.
3. The cool disk does not vary either in its temperature or its emission area (the directly visible area plus that of the seed-photon source).
4. The relative fluxes between the two Compton continua are kept rather constant as the source varies.
5. The reflection and the Fe-K line both vary in proportion to the continuum intensity. Namely, both Ω and the Fe-K line EW remain constant.

As a possible picture that can explain all the above results, we may speculate that the corona is highly "porous" with a number of holes in it, and the source flares up in hard X-rays when the volume fraction of these holes decreases. Then, a larger number of Comptonized photons will come out even if the disk remains unchanged. The holes may correspond to regions threaded with strong magnetic fields, and the decrease of holes may be caused by their rapid reconnection.

4. The Nature of ULXs

ULXs, or Ultra-Luminous X-ray sources (Makishima et al. 2000), provide one of the most intriguing issues in the modern BH study. Since their luminosity reaches the Eddington limits of objects with 30 $\sim$ 1000 $M_\odot$, these objects could be IMBHs with such large masses (Mizuno et al. 2007; Makishima 2007). Alternatively, they could be ordinary stellar-mass BHs, radiating either at highly super-Eddington luminosities, or with a highly anisotropic angular pattern enhanced toward us.

The best way toward the elucidation of the nature of ULXs is to compare their behavior with that of BHBs, and draw appropriate analogy between the two classes. For this purpose, we studied 8 ULXs that have been observed repeatedly; M82 X-1, NGC 1313 X-1, NGC 1313 X-2, IC342 X-1, Holmberg IX X-1, Holmberg II X-1, M81 X-6, and NGC 5204 X-1. We analyzed their archival data from *Suzaku* (Mizuno et al. 2007) and *XMM-Newton*. Figure 3 show a color-color plot of these objects, using three typical energy bands; 1–2 keV, 2–4 keV, and 4–10 keV (Miyawaki 2008).

In Fig.3, the region indicated by a thick dashed circle was found to have a particular meaning; if an object falls within this circle, it exhibits the highest 1–10 keV luminosity L than in any other region of this plot. For each object, we hence employed the luminosity observed inside this circle as a fiducial luminosity $L_{\rm c}$, and normalized all its L measurements to $L_{\rm c}$. Then, all the 8 objects can be seen to behave in a very similar way in terms of $L/L_{\rm c}$. Although a few sources did not come inside the thick dashed circle, we were able to define their values of $L_{\rm c}$ in an appropriate way, so that their normalized behavior becomes parallel to that of the others.

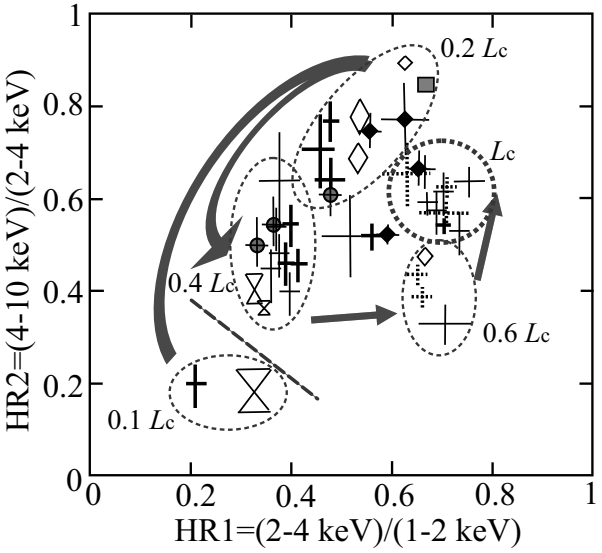

Fig. 3. A color-color plot for 8 ULXs, observed with *Suzaku* and *XMM-Newton*. Count rate ratios between the 4–10 keV to 2–4 keV bands are plotted against those between 2–4 keV to 1–2 keV (Miyawaki 2008). Thick gray arrows indicate a common luminosity evolution locus.

In Fig.3, the 8 sources form three typical branches. One of them appears at $L = (0.6 - 1.0)L_{\rm c}$, characterized by high values of HR1 and rather low HR2 values. This means that the spectrum has a strongly convex shape. Indeed, all the spectra in this branch are better fitted with a multi-color disk model than a single power-law. The second branch appears at $L = (0.2 - 0.4)L_{\rm c}$, with a relatively smaller HR1 values. Therefore, the spectra herein are suggested to be less convex. In fact, most of the spectra in this branch favor a single power-law modeling. The elongation of the branch implies that the spectral slope steepens as L increases. Finally, we find a

few data points with $L \sim 0.1 L_{\rm c}$, with very soft spectra.

Invoking our discussion in § 3.1., the highest luminosity branch seen in Fig.3 may be considered analogous to the SDS of BHBs. This was argued in detail by Tsunoda et al. (2006). The second branch in Fig.3 can be considered to correspond to the VHS of BHB, both characterized by slightly curved power-law-like spectra. Finally, the least luminous branch in Fig.3 may be regarded as the HSS. These results imply that the ULXs form a rather homogenous class, and the values of $L_{\rm c}$ are close to their Eddington limits. Therefore, these ULXs may be considered as IMBHs, having significantly higher masses than the Galactic BHBs and radiating at close to their Eddington limits. Furthermore, we obtained an indication of BH spin in one ULX (Isobe et al. 2008; not shown in Fig.3).

Among the 8 ULXs in Fig.3, one of the most interesting sources is M82 X-1 (gray square point). While this object was often regarded as a special one, the *Suzaku* XIS data place it (after carefully estimating source confusion; Miyawaki 2008) in a similar position as the other objects. Furthermore, we successfully detected this object up to ~ 20 keV using the *Suzaku* HXD, and showed its spectrum to become mildly convex in energies above ~ 7 keV (Miyawaki et al. 2009). We hence interpret it in a state corresponding to the VHS.

5. Broad Fe-K lines

An extremely important issue in the BH study is to search their behavior for general relativistic effects. In this sense, the extremely broad Fe-K emission lines provide one promising evidence. After the first report by *ASCA* (Tanaka et al. 1995), this feature has been suggested in the spectra of a number of Seyfert galaxies, including MCG−6-30-15 in particular. The case of this leading candidate has been apparently reinforced by *Suzaku* observations (Miniutti et al. 2007), although controversy continues.

Miller et al. (2008) claimed a detection of similar features from the Galactic BHB GX339-4, and argued that the BH is rapidly spinning: this is because the inferred disk inner radius is smaller than the last stable orbit around a non-rotating BH, namely $3R_{\rm S}$. Furthermore, Cackett et al. (2008) argued that similar broad Fe-K lines are also present in the *Suzaku* spectra of several low-mass binaries involving neutron stars.

In spite of these reports of the broad Fe-K line detections from Galactic objects, we need a particular caution as to the reality of such features. Indeed, our results on Cyg X-1 and GRO J1655−40 clearly argue against the presence of such extremely broadened Fe-K lines. Furthermore, through our quick-look analysis of the same *Suzaku* data of GX339-4 as used by Miller et al. (2008), we found no evidence of the reported feature. According to Takahashi (2005), the broad Fe-K lines in the neutron-star binaries are also likely to be an artifact, caused by ignorance of a new spectral component which appears over a 3–7 keV; this component is likely to be an optically-thick emission from radiation-pressure-driven outflows, rather than a broad Fe-K line.

We thus caution that the claimed relativistically broadened Fe-K line features in Galactic objects are highly dependent on the continuum models used to fit the data. As a result, there is currently no convincing evidence for such features in Galactic BHs or neutron stars.

6. Future Prospects with MAXI

As seen in § 4., we interpret ULXs as IMBHs. Furthermore, as argued by Ebisuzaki et al. (2001), these objects could serve as building blocks from which the super-massive black holes at galaxy nuclei are formed through repeated and hierarchical mergers. Then, we expect some active galactic nuclei to be in their final stage of mergers, wherein two semi-massive BHs are orbiting around each other in a gradually decaying binary orbit. In such objects, we may expect the X-ray intensity to be modulated by their orbital revolution, with a period of several weeks to a few months. Evidently, the MAXI mission provides the most ideal way to search for such signals.

The author would like to thank his colleagues at the RIKEN Cosmic Radiation Laboratory, at the Physics Department of the University of Tokyo, and the *Suzaku* HXD team.

References

Cackett, E. M. et al. 2008 ApJ 674, 416
Ebisuzaki, T. et al. 2001 ApJL 562, L19
Greiner, J. et al. 2003 Nature, 426, 157
Isobe, N. et al. 2008 PASJ 60, S241
Kokubun, M. et al. 2007 PASJ 59, S53
Kubota, A. & Makishima, K. 2004 ApJ 601, 428
Makishima, K. 2007 Prog. Theor. Phy. Suppl. 169, 214
Makishima, K. et al. 2000 ApJ 535, 632
Makishima, K. et al. 2008 PASJ 60, 585
Miller, J. M. et al. 2008 ApJL 679, L113
Miniutti, G. et al. 2007 PASJ, 59, S315
Mitsuda, K. et al. 2007 PASJ 59, S1
Miyawaki, R. et al. 2009 PASJ 62, in press
Miyawaki, R. 2008 PhD Thesis, University of Tokyo
Mizuno, T. et al. 2007 PASJ 59, S257
Takahashi, H. 2005 PhD Thesis, University of Tokyo
Takahashi, H. et al. 2008 PASJ 60, S69
Takahashi, T. et al. 2007 PASJ 59, S35
Tanaka, Y. et al. 1995 Nature 375, 659
Villasenor, J. S. et al. 2005 Nature, 437, 855

Orbital and superorbital variability and their coupling in X-ray binaries

Andrzej A. Zdziarski,[1] Juri Poutanen,[2] Askar Ibragimov,[2,3] Marek Gierliński,[4,5] and Linqing Wen[6,7,8]

[1]Centrum Astronomiczne im. M. Kopernika, Bartycka 18, 00-716 Warszawa, Poland
[2]Astronomy Division, Department of Physical Sciences, PO Box 3000, FIN-90014 University of Oulu, Finland
[3]Kazan State University, Astronomy Department, Kremlyovskaya 18, 420008 Kazan, Russia
[4]Department of Physics, University of Durham, Durham DH1 3LE, UK
[5]Obserwatorium Astronomiczne Uniwersytetu Jagiellońskiego, Orla 171, 30-244 Kraków, Poland
[6]Max-Planck-Institut für Gravitationsphysik, Albert-Einstein-Institut, Am Mühlenberg 1, D-14476 Golm, Germany
[7]Division of Physics, Mathematics and Astronomy, Caltech, Pasadena, CA 91125, USA
[8]School of Physics, University of Western Australia, Crawley, WA 6009, Australia
E-mail (AAZ): aaz@camk.edu.pl

Abstract

We review X-ray flux modulation from X-ray binaries on time scales corresponding to the orbital period and those at longer time scales (so called superorbital). Those modulations provide a powerful tool to constrain geometry of the accretion flow. The most common cause of the superorbital variability appears to be precession. We then discuss two specific examples of discoveries of a coupling between the two types of variability and their physical interpretation. One is Cyg X-1, a black-hole binary with a high-mass companion, in which case we find the presence of an accretion bulge formed by collision of the stellar wind with the outer edge of the precessing accretion disc. The other is 4U 1820–303, a neutron star accreting from a low-mass white dwarf, in which case we interpret the superorbital variability as accretion rate modulation induced by interactions in a triple stellar system. Then, the varying accretion rate leads to changes of the size of the accretion bulge in that system, obscuring the centrally-emitted X-rays.

Key words: accretion, accretion discs — stars: individual: (Cyg X-1, HDE 226868, 4U 1820–30) — X-rays: binaries — X-rays: stars

1. Introduction

A large number of X-ray binaries show X-ray flux periodicities at their orbital period. The current comprehensive list of such objects is given by Wen et al. (2006). Using strict criteria for the statistical significance of the presence of a modulation, they find 33 secure orbital periods in the *RXTE*/ASM data. Due to the limitation of the ASM sampling, they were unable to detect the 685-s X-ray binary period of the ultracompact low-mass X-ray binary (LMXB) 4U 1820–303, which, however, is clearly detected, e.g., in *RXTE*/PCA data (e.g., Zdziarski et al. 2007b, hereafter Z07, and references therein). Even faster X-ray modulations, at 569 s and 321 s, are found in *ROSAT* data for RX J1914.4+2456 (Cropper et al. 1998) and RX J0806.3+1527 (Israel et al. 1999), respectively. These two systems contain pairs of white dwarfs orbiting each other at the above respective period (Cropper et al. 1998; Israel et al. 2002; Ramsay et al. 2002).

In addition, a number of X-ray binaries show X-ray modulations at periods longer than their orbital periods, so-called superorbital periodicity. Sood et al. (2007) state that 35 such systems have been reported in literature. However, many of those claims remain uncertain, and Sood et al. (2007) selected 19 of them as secure. However, even some of those appear, in our opinion, uncertain. For example, they list the high-mass X-ray binary (HMXB) Cen X-3 as having a superorbital period of 140 d. On the other hand, the same object is presented by Raichur & Paul (2008) as a case of the *lack* of stable superorbital modulation. Another example is 4U 1916–053, which is listed as having a 199-d period in Sood et al. (2007) whereas Homer et al. (2001) (and later Wen et al. 2006) find no trace of such periodicity. Wen et al. (2006), using a uniform analysis method, find 6 objects as having coherent superorbital modulations in the *RXTE*/ASM data, and further 5 with quasi-periodicities. Using their method with no pre-selection of data, they did not find a superorbital periodicity in the black-hole HMXB Cyg X-1. However, its ∼150-d period manifests itself mostly in the hard spectral state, where its statistical significance is very high (e.g., Brocksopp et al. 1999a; Karitskaya et al. 2001; Özdemir & Demircan 2001; Lachowicz et al. 2006; Ibragimov et al. 2007; Poutanen et al. 2008, hereafter PZI08). Another black-hole binary in which

the superorbital modulation manifests itself only in the hard state appears to be the LMXB GX 339–4, in which it shows a ∼220-d periodicity, whereas that modulation is absent in the soft state (Zdziarski et al. 2004). (See, e.g., Zdziarski & Gierliński 2004; Done et al. 2007 for reviews and physical interpretation of the spectral states of black-hole binaries.)

The MAXI, an X-ray all-sky monitor mission on the Japanese Experiment Module of the *International Space Station*, is scheduled to be launched in 2009 March. Due to its unprecedented sensitivity of a few mCrab in a day covering most of the sky, the MAXI will monitor variability of a large number of X-ray sources at much lower flux levels than is now possible with the *RXTE*/ASM. It will thus be able to greatly enhance our knowledge of the variability of X-ray binaries, in particular of their orbital and superorbital periodicities.

2. Physical causes of orbital and superorbital flux periodicities

An orbital periodicity may be caused by a number of effects. Here, we review also some effects affecting other wavelengths than X-rays. First, a source associated with a compact object in a binary (usually a HMXB) may be eclipsed by its companion, see a list in Wen et al. (2006). Second, a flux modulation may be caused by an optically-thick disc rim (which is highest at the point of impact of the gas stream from the inner Lagrangian point in case of a donor filling its Roche lobe), obscuring the disc and/or its corona (e.g., White & Swank 1982; Hellier & Mason 1989; Heinz & Nowak 2001), usually in LMXBs. This obscuration may lead to strong partial eclipses in so-called X-ray dippers. More generally, the disc and any associated structures may depart from its axial symmetry due to the influence of the companion, which may cause an orbital modulation. Third, wind from a high-mass companion may absorb/scatter the emission from the vicinity of the compact object, and the degree of absorption will depend on the orbital phase. In the case of Cyg X-1, both X-ray and radio emission are modulated by this effect, which modulations were modeled by, e.g., Wen et al. (1999) and Szostek & Zdziarski (2007), respectively. Fourth, phase-dependent absorption (via photon-photon pair production) of high-energy γ-rays may occur in a photon field axially asymmetric with respect to the compact object, especially that of the stellar photons (e.g., Bednarek 1997; Dubus 2006). A fifth effect of the companion is reflection or reprocessing of the emission from around the compact object on the surface of the companion facing the compact object (Basko 1978). This effects appears to be responsible for, e.g., the UV flux modulation from the X-ray binary 4U 1820–303 (Arons & King 1993; Anderson et al. 1997). Finally, the optical/UV emission of the companion will be modulated if its shape departs from the spherical symmetry by partially or fully filling its Roche lobe, which effect is seen in Cyg X-1, e.g., Brocksopp et al. (1999b).

Then, there will be an intrinsic dependence of the emitted flux on the orbital phase if the orbit is elliptical. This leads, e.g., to periodic outbursts around the periastron of Cir X-1 (e.g., Parkinson et al. 2003) and Be/X-ray binaries (see, e.g., Coe 2000; Negueruela 2004 for reviews) in X-rays, and sometimes, at other wavelengths. Also, some orbital flux modulation may be due to the Doppler effect, which is in principle observable (Postnov & Shakura 1987), but has not yet been detected in a binary. (Obviously, the Doppler effect leads to widely observed shifts of spectral lines from binaries.)

The observed superorbital variability appears in most cases compatible with being caused by accretion disc and/or jet precession, which either results in variable obscuration of emitted X-rays as in Her X-1 (Katz 1973), or changes the viewing angle of the presumed anisotropic emitter, as in SS 433 (Katz 1980) or Cyg X-1 (e.g., Lachowicz et al. 2006; Ibragimov et al. 2007; PZI08), or both. The precession may be induced via tidal forces by the companion (Larwood 1998), with additional forces exerted by irradiation of the disc by the central X-ray source (e.g., Ogilvie & Dubus 2001). The only certainly known exception, in which the superorbital periodicity is clearly caused by modulation of the accretion rate, $\dot{M}$ (and thus not by a changing viewing angle of the source), appears to be 4U 1820–303 (Zdziarski et al. 2007a; Z07, and references therein). The $\dot{M}$ modulation can be achieved in a triple system via a secular modulation of the eccentricity of the inner system, proposed for this source by Chou & Grindlay (2001), and calculated in detail by Zdziarski et al. (2007a). Another system possibly of this type is the HMXB 2S 0114+650, where Farrell et al. (2008) have argued for changes of the $\dot{M}$ based on the spectral variability of the system.

3. Coupling between orbital and superorbital modulations

A number of binaries show both orbital and superorbital modulations. Those currently known are LMC X-4, 2S 0114+650, SMC X-1, Her X-1, SS 433, 4U 1820–303 and Cyg X-1. An interesting issue then is whether there is any dependence of the parameters of the orbital modulation on the superorbital phase (or, similarly, on an average of the flux level). The shape of the profile of the orbital modulation in Her X-1 was found to depend on its superorbital phase (Scott & Leahy 1999), which appears to be due to the shadowing effect of the precessing accretion disc and scattering in its wind in that system. Analogous dependencies of the shape of the orbital modulation on the average flux level have been found (Raichur & Paul 2008) in LMC X-4, SMC X-1, Her X-1, as well as in Cen X-3 (which object, however, shows a

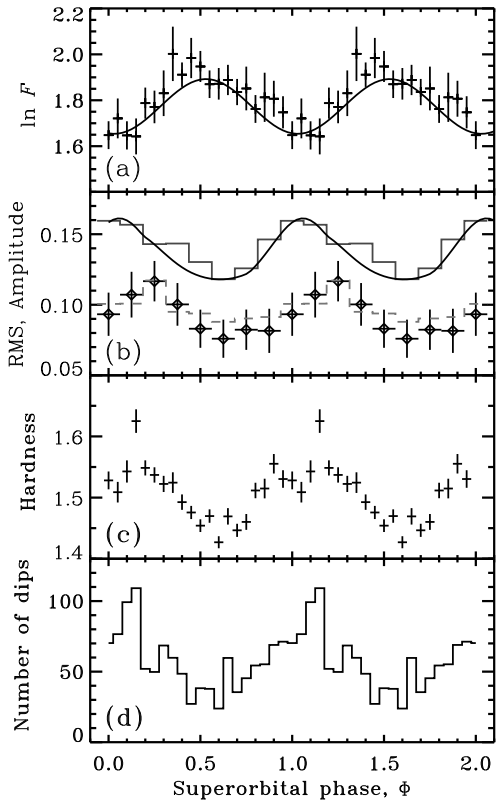

Fig. 1. (a) The superorbital phase diagram for the ASM 1.5–3 keV channel (the unit of F is count s^{-1}). (b) Comparison of the characterization of the 1.5–3 keV orbital modulation dependence on the superorbital phase using different methods. The crosses show the intrinsic fractional rms of the orbital modulation. The solid histogram gives the orbital variability amplitude fitted by sum of three harmonics. The dashed histogram gives the corresponding rms for the fitting function. The solid curves in (a–b) show the dependencies for a theoretical outflow model fitted to the data by PZI08. (c) The mean hardness ratio (5–12 keV/1.5–3 keV), and (d) the distribution of X-ray dips in the hard state. A visible offset of the ephemeris with respect to $\Phi = 0$ is due to the use of an ephemeris based also on older data (Lachowicz et al. 2006).

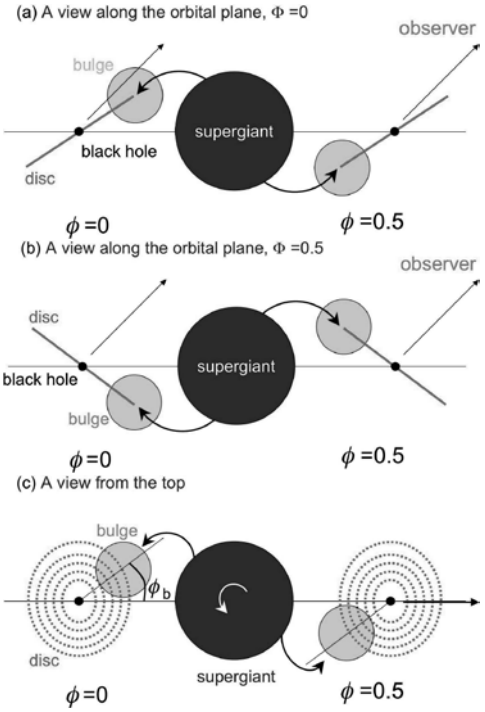

Fig. 2. A bulge at the outer edge of a precessing inclined disc. The material in the bulge absorbs some of the X-ray emission originating close to the disc center. The orbital modulation due to the bulge is seen to strongly depend on the superorbital phase. (Orbital modulation due to the stellar wind itself is not illustrated here for clarity.) A view along the orbital plane: (a) the superorbital phase $\Phi = 0$, when the disc is seen closest to edge-on and the effect of the bulge is strongest; (b) the opposite case of the superorbital phase $\Phi = 0.5$. (c) A view from the top.

chaotic superorbital behavior).

The Be/X-ray binary LS I +61°303 shows orbital variability in the radio, X-ray and TeV emission, and a superorbital variability of the peak radio flux during an orbit (Gregory et al. 1999; Gregory 2002). Gregory (2002) found a marked dependence of the phase of the peak of the orbital radio modulation on the superorbital phase. The presence of such a dependence may be due to interaction of the pulsar in that system with a variable circumstellar Be decretion disc (Gregory 2002; Zdziarski et al. 2008), but details remain unknown.

Then, strong coupling between the orbital and superorbital modulations is seen in the HMXB Cyg X-1 (PZI08) and in the LMXB 4U 1820–303 (Z07), which consists of a white dwarf accreting onto a weakly-magnetized neutron star. We review these two objects in detail below in Sections 4.–5.

4. The dependence of the orbital modulation on the superorbital phase in Cyg X-1

Such a dependence was searched for, studied, and interpreted theoretically by PZI08. They used the *RXTE*/ASM data, in which both orbital and superorbital modulations are clearly seen, see Section 1. The physical cause of the orbital X-ray modulation is bound-free absorption in the stellar wind, whereas the widely accepted underlying cause of the superorbital, ∼150-d, modulation is accretion disc precession, see Section 2. As found by Ibragimov et al. (2007), the resulting superorbital flux variability is most likely due to an anisotropy of the X-ray emission from the accretion flow (rather than due to absorption, obscuration or scattering).

PZI08 found the fractional amplitude of the orbital modulation strongly depends on the superorbital phase in the hard state, see Fig. 1a, b. Namely, the orbital modulation is strongest when the average flux level is lowest. The effect is visible in all of the three ASM channels, but it is strongest in the lowest-energy channel, 1.5–

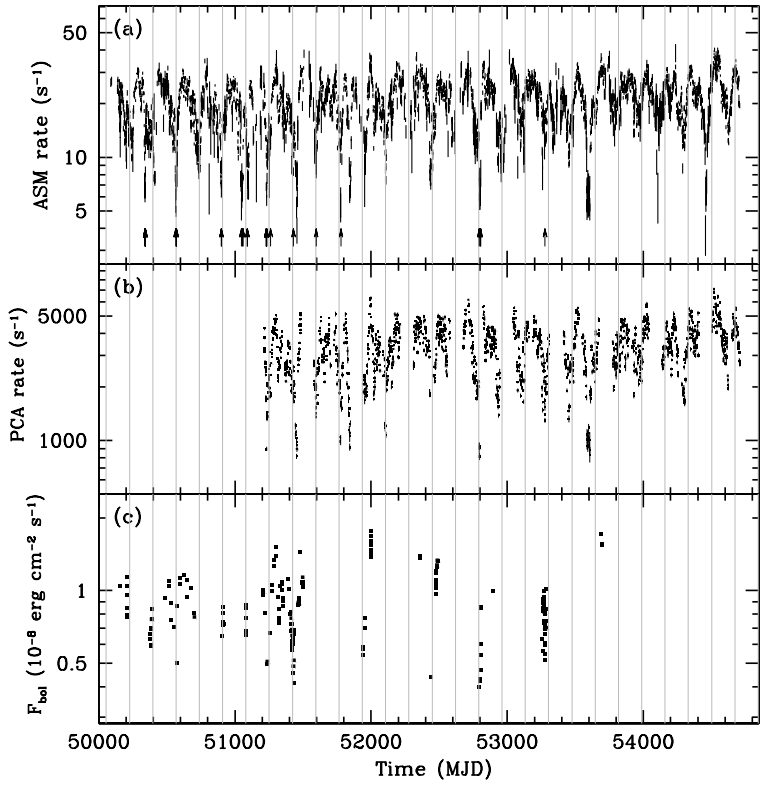

Fig. 3. (a) The *RXTE*/ASM light curve of 4U 1820–303. The short arrows shows the times of detected X-ray bursts. (b) The PCA light curve based on Galactic Bulge scans. (c) The light curve of the bolometric flux calculated from the PCA/HEXTE data. See Z07 for details. The ASM and PCA light curves have been extended up to MJD ∼54700. The vertical lines show the minima (the phase $\Phi = 0$) of the superorbital cycle according to the ephemeris of Chou & Grindlay (2001), which ephemeris is seen to become increasingly inaccurate in recent epochs.

3 keV, where the orbital modulation amplitude is highest (which reflects the energy dependence of the bound-free cross section averaged over the cosmic abundances).

A theoretical interpretation of this effect proposed by PZI08 is as follows. The cause of the part of the orbital modulation dependent on the superorbital phase is a structure at the outer edge of the accretion disc on the side of the companion. Such a structure is expected theoretically. Formation of the accretion disc in Cyg X-1 by a focused wind (Gies & Bolton 1986) leads, most likely, to a condensation of the wind matter near the disc outer edge on the side of the companion in the form of a bulge, similar to the disc bulge inferred to be present in low-mass X-ray binaries, e.g., White & Holt 1982; White & Swank 1982; Parmar & White 1988). On the other hand, the bulge can also be formed (see, e.g., Boroson et al. 2001) by a shock wave in the wind when it encounters the gravity of the companion, the disc, or a wind from the disc, which is also likely to be present. In any case, when the fast, > 1000 km s^{-1}, wind is stopped, the density increases dramatically.

Such a bulge is shown in Fig. 2. We see that at the minimum of the superorbital cycle (i.e., at the superorbital phase of $\Phi \simeq 0$), when the disc is most edge-on (Fig. 2a), the bulge crosses the line of sight to the X-ray source (which is close to the black hole) around the superior conjunction, i.e., at the orbital phase of $\phi \simeq 0$, and it is away from the line of sight at the inferior conjunction, i.e., at the orbital phase of $\phi \simeq 0.5$. On the other hand, at the maximum of the superorbital cycle ($\Phi \simeq 0.5$), the disc is most face-on (Fig. 2b), and the bulge is away from the line of sight at any orbital phase. Thus, the bulge introduces additional absorption only around $\Phi \simeq 0.5$, just as observed.

This model was put into the form of a set of equations and then fitted to the data by PZI08. They considered a number of models for the anisotropy of the X-ray emission, leading to the superorbital modulation, following Ibragimov et al. (2007). An exponential absorption profile of the bulge and either an isotropic or focused wind were assumed. In all models, the total optical depth of the bulge measured from its center was found to be $\simeq$1. The bulge center was found to be displaced from the line connecting the centers of the stars by $\simeq 25°$. The tilt of the precessing disc was found to be compatible with $\sim 10°$, at the assumed inclination of 40°. Prograde pre-

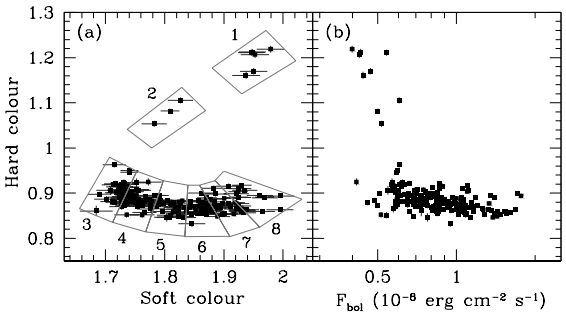

Fig. 4. (a) The intrinsic colour-colour diagram, as given by the ratio of the energy fluxes in the photon energy ranges of (9.7–16 keV)/(6.4–9.7 keV) and (4.0–6.4 keV)/(3.0–4.0 keV) for the hard colour and soft colour, respectively. The boxes show a division into 8 spectral substates. (b) The corresponding dependence of the hard colour on the bolometric flux. From Z07.

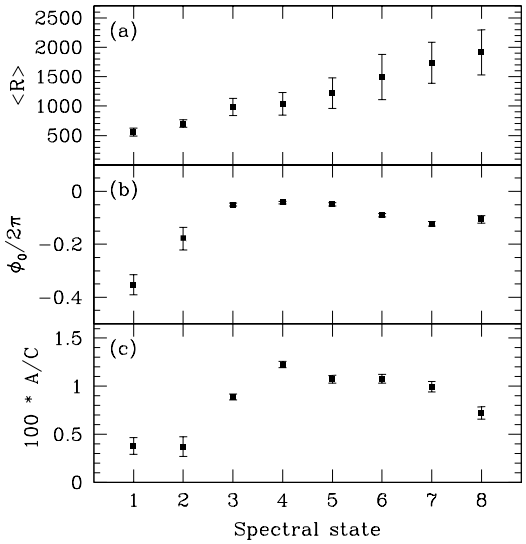

Fig. 5. The average PCA count rate ($\langle R \rangle$), the offset orbital phase (ϕ_0), and the fractional amplitude of the orbital modulation (denoted as A/C) vs. the spectral state, defined in Fig. 4. The error bars on $\langle R \rangle$ represent the standard deviation, not the errors of the average (which are negligibly small). From Z07.

cession was strongly favored by the fits.

PZI08 also have shown that both the X-ray spectral hardness and the frequency of X-ray dips (caused by absorption by wind blobs, Bałucińska-Church et al. 2000) increase towards the superorbital phase of 0, see Fig. 1c, d, which is also explained by the above model. Furthermore, the coupling of the orbital and superorbital modulations leads to appearance of asymmetric beat frequencies in the power spectrum, explaining the finding of such asymmetry by Lachowicz et al. (2006).

5. The dependence of the orbital modulation on the spectral state in 4U 1820–303

Such a dependence was searched for, studied, and interpreted theoretically by Z07. Long-term light curves of the system are shown in Fig. 3. We see a very pronounced superorbital variability, with the period of $\simeq$170 d. The strongest argument for the intrinsic, $\dot{M}$-driven, character of this variability is the occurrence of X-ray bursts (which generally take place at low accretion rates) only during the deep minima of the light curve, see Fig. 3a. As proposed by Chou & Grindlay (2001), the physical cause of the $\dot{M}$ modulation is quasi-periodically varying eccentricity, e, of the binary induced by a third star in the system, via the so-called Kozai effect (Kozai 1962). This was calculated in detail by Zdziarski et al. (2007a), who have modeled such e evolution and calculated the resulting $\dot{M}$ variability in a Roche-lobe overflow model.

The orbital modulation of the system was discovered in X-rays (Stella et al. 1987). Given the very short orbital period, it is not detectable in the ASM data, and therefore Z07 used PCA/HEXTE observations of 4U 1820–303. Their light curve is shown in Fig. 3c. We see their coverage of the superorbital variability is rather sparse, and it has proven difficult to study the orbital modulation directly as a function of the superorbital phase. On the other hand, the superorbital cycle is closely related to the spectral variability of the system, going between the so-called atoll (at low $\dot{M}$) and banana (at high $\dot{M}$) spectral states (Bloser et al. 2000). Therefore, Z07 have divided the pointed X-ray observations into 8 spectral substates, with the $\dot{M}$ increasing from the state 1 to 8, as shown in Fig. 4.

Then the orbital modulation was fitted within each substate by a sinusoidal dependence. Fig. 5 shows the results. We see that the PCA count rate increases with the state number (as expected). The fractional modulation amplitude very significantly increases from the atoll (1–2) to banana (3–8) states. Also, the offset phase increases. Z07 interpreted the results in terms of the size and location of the bulge at the disc rim (partially obscuring the central source) changing with the variable accretion rate. Z07 also found that the fractional modulation was independent of the photon energy. This argues for the part of the bulge obscuring the X-rays being almost completely ionized. More details and discussion of other options are given in Z07.

6. Discussion

We have reviewed orbital and superorbital modulation of X-ray binaries, concentrating on the X-ray spectral band. The physical causes of the orbital modulation are relatively well understood, see Section 2. The most common cause of the superorbital modulation appears be precession of accretion disc. However, details remain unclear, in particular what drives the precession, whether it is prograde or retrograde, and how a viscous disc can

coherently precess. On the other hand, some objects, especially 4U 1820–303, show very strong evidence of the superorbital variability being due to periodic changes of $\dot{M}$, and not due to precession. However, physical details also here remain unclear. One possibility is the effect of a third star in a hierarchical triple (Chou & Grindlay 2001; Zdziarski et al. 2007a).

Then, the properties of the orbital modulation may depend on the superorbital phase. We have discussed two specific examples. In Cyg X-1, the orbital modulation is strongest at the lowest observed flux, which appears to be due to the presence of an accretion bulge at the outer edge of the precessing disc. The bulge goes into the line of sight when the disc is most edge-on, which then corresponds to the lowest observed flux. An opposite effect is observed in 4U 1820–303. Here, the orbital modulation is weakest at the lowest observed flux. The reason for that appears that the size of the obscuring bulge increases with the increasing $\dot{M}$, periodically changing in that system (unlike Cyg X-1, where most likely there is no periodic $\dot{M}$ modulation).

AAZ has been supported by the Polish MNiSW grant NN203065933 (2007–2010) and the Polish Astroparticle Network 621/E-78/SN-0068/2007. This study has been partially supported by the Academy of Finland grants 110792 and 112986, and the International Space Science Institute (Bern). AI has been supported by the Finnish Graduate School in Astronomy and Space Physics, the Väisäla Foundation and the Russian President's program for support of leading science schools (grant NSH-4224.2008.2). LW has been supported by the Alexander von Humboldt Foundation's Sofja Kovalevskaja Programme funded by the German Federal Ministry of Education and Research.

References

Anderson S. F., Margon B., Deutsch E. W., Downes R. A., Allen R. G., 1997, ApJ, 482, L69
Arons J., King I. R., 1993, ApJ, 413, L121
Bałucińska-Church M., et al., 2000, MNRAS, 311, 861
Basko M. M., 1978, ApJ, 223, 268
Bednarek W., 1997, A&A, 322, 523
Bloser P. F., et al., 2000, ApJ, 542, 1000
Boroson B., Kallman T., Blondin J. M., Owen M. P., 2001, ApJ, 550, 919
Brocksopp C., et al., 1999a, MNRAS, 309, 1063
Brocksopp C., Tarasov A. E., Lyuty V. M., Roche O., 1999b, A&A, 343, 861
Chou Y., Grindlay J. E., 2001, ApJ, 563, 934
Coe M. J., 2000, ASPC, 214, 656
Cropper M., et al., 1998, MNRAS, 293, L57
Done C., Gierliński M., Kubota A., 2007, A&ARv, 15, 1
Dubus G., 2006, A&A, 451, 9
Farrell S. A., Sood R. K., O'Neill P. M., Dieters S., 2008, MNRAS, in press
Gies D. R., Bolton C. T., 1986, ApJ, 304, 389
Gregory P. C., 2002, ApJ, 575, 427
Gregory P. C., Peracaula M., Taylor A. R., 1999, ApJ, 520, 376
Heinz S., Nowak M. A., 2001, MNRAS, 320, 249
Hellier C., Mason K. O., 1989, MNRAS, 239, 715
Homer L., et al., 2001, MNRAS, 322, 827
Ibragimov A., Zdziarski A. A., Poutanen J., 2007, MNRAS, 381, 723
Israel G. L., et al., 1999, A&A, 349, L1
Israel G. L., et al., 2002, A&A, 386, L13
Karitskaya E. A., 2001, Astron. Rep., 45, 350
Katz J. I., 1973, Nat. Phys. Sci., 246, 87
Katz J. I., 1980, ApJ, 236, L127
Kozai Y., 1962, AJ, 67, 591
Lachowicz P., et al., 2006, MNRAS, 368, 1025
Larwood J., 1998, MNRAS, 299, L32
Negueruela I., 2004, preprint (astro-ph/0411335)
Ogilvie G. I., Dubus G., 2001, MNRAS, 320, 485
Özdemir S., Demircan O., 2001, Ap&SS, 278, 319
Parkinson P. M. S. et al., 2003, ApJ, 595, 333
Parmar A. N., White N. E., 1988, Mem. S. A. It., 59, 147
Postnov K. A., Shakura N. I., 1987, Sov. Astr. Lett., 13, 122 (PAZh, 13, 300)
Poutanen J., Zdziarski A. A., Ibragimov A., 2008, MNRAS, in press (PZI08)
Raichur H., Paul B., 2008, MNRAS, 387, 439
Ramsay G., Hakala P., Cropper M., 2002, MNRAS, 332, L7
Scott D. M., Leahy D. A., 1999, ApJ, 510, 974
Sood R., Farrell S., O'Neill P., Dieters S., 2007, AdSpR, 40, 1528
Stella L., Priedhorsky W., White N. E., 1987, ApJ, 312, L17
Szostek A., Zdziarski A. A., 2007, MNRAS, 375, 793
Wen L., Cui W., Levine A. M., Bradt H. V., 1999, ApJ, 525, 968
Wen L., Levine A. M., Corbet R. H. D., Bradt H. V., 2006, ApJS, 163, 372
White N. E., Holt S. S., 1982, ApJ, 257, 318
White N. E., Swank J. H., 1982, ApJ, 253, L61
Zdziarski A. A., Gierliński M., 2004, Progr. Theor. Phys. Suppl., 155, 99
Zdziarski A. A., et al., 2004, MNRAS, 351, 791
Zdziarski A. A., Wen L., Gierliński M., 2007a, MNRAS, 377, 1006
Zdziarski A. A., Gierliński M., Wen L., Kostrzewa, Z., 2007b, MNRAS, 377, 1017 (Z07)
Zdziarski A. A., Neronov A., Chernyakova M., 2008, preprint (arXiv:0802.1174)

MAXI, LOFAR and Microquasars

– All-sky monitoring of X-ray binaries in X-rays and radio –

Rob Fender[1,2]

[1] School of Physics & Astronomy, University of Southampton, UK
[2] Astronomical Institute 'Anton Pannekoek', University of Amsterdam, NL
E-mail: r.fender@soton.ac.uk

Abstract

In this paper I will discuss future synergies between the Japanese MAXI X-ray all-sky monitor, to be placed on the International Space Station in 2009, and the next-generation radio astronomy array LOFAR, currenlty under construction in The Netherlands. The wide fields of view and multiple beams of LOFAR will allow, in combination with MAXI, simultaneous all-sky monitoring of the sky in both the X-ray and radio bands. Focussing on microquasars, X-ray binary jet systems, I discuss how the combination of MAXI and LOFAR will help us to further understand the accretion–outflow coupling in such systems.

Key words: MAXI – LOFAR – Microquasars

1. Introduction

Wide-field and/or all-sky monitoring in X-ray/γ-rayss, in particular (but not exclusively) with CGRO BATSE and RXTE ASM, has produced a vast array of new, valuable, and in many cases unexpected, results. MAXI will carry forward this approach in X-ray astronomy, with all-sky monitoring in the soft X-ray band for at least three years from 2009.

Beyond the X-ray/γ-ray regime, all-sky monitoring has proved much harder to achieve, primarily due to the small fields of view achievable with focussing instruments at optical, infared and radio wavelengths. However, the new generation of radio telescopes will in large part be optimized for such wide-field surveying and monitoring, and will provide for the first time something close to all-sky monitoring at radio wavelengths (unfortunately the planet always blocks some of the sky to these earthbound facilities). In particular, the LOFAR *Radio Sky Monitor* is proposed to provide ∼daily monitoring of over 60% of the sky at the ∼mJy level.

Why do we care about complementary X-ray and radio observations ? Nearly all phenomena associated with flaring and transient X-ray behaviour are in fact associated with radio emission, and each wavelength regime offers a different but complementary diagnostic of the processes behind the transient outburst. In many cases, such as accreting systems, the transient X-ray behaviour is associated with an increase in the instantaneous accretion rate onto the central compact object, and the radio emission is synchrotron emission resulting from particle acceleration and outflow in a jet. Comparing the two allows us to make quantitative estimates of the accretion power being liberated in radiation, kinetic outflows or, in the case of black holes, possibly being advected across an event horizon (e.g. Körding, Fender & Migliari 2006). In addition to this incoherent synchrotron emission, coherent emission with shorter durations and much higher brightness temperatures is associated with e.g. pulsars and may have transient counterparts in other high-energy sources which have not yet been detected (for example the nature of the coherent extragalactic radio burst reported by Lorimer et al. [2007] remains unclear).

1.1. Microquasars

The term 'microquasar' has been profitably adopted for X-ray binary systems with jets since Mirabel et al. (1992). Since all classes of X-ray binary, with the exception of high-field X-ray pulsars, appear to show jets (e.g. Fender 2006) the terms 'microquasar' and 'X-ray binary' are almost synonymous. These systems are extreme examples of the accretion:outflow scenario discussed above, and often undergo outbursts in which a $\sim 10 M_{\odot}$ black hole brightens to close to its Eddington limit ($\sim 10^{39}$ erg s^{-1} whilst producing, during certain phases of the outburst, a sporadic but very powerful jet. As the name suggests, they may be compared quantitatively with supermassive black holes in active galactic nuclei (AGN), allowing us to understand the (rather straightforward) mass scaling relations in black hole accretion (Merloni, Heinz & di Matteo 2003; Körding, Falcke & Corbel 2006;

McHardy et al. 2007). In addition, understanding such scaling may allow us to use insights learned from the binaries to understand the cosmological evolution of black hole accretion and feedback.

In the past decade a rough phenomenological understanding of the relation between X-rays and radio emission in such systems has developed, summarized most recently in Fender, Belloni & Gallo (2004). Below about $\sim$ 1% of the Eddington luminosity, systems exist in a 'hard' X-ray state in which relatively steady radio emission indicates the presence of a long-lived, powerful outflow. Above this luminosity, systems often enter a hysteretic track involving a soft state with little core radio emission, and a powerful relativistic ejection event during the transition from hard to soft states (see e.g. Fig 1). Subsequently systems return to the 'hard' state track (in reality the picture is more complex and detailed than sketched out here, of course; see e.g. Homan & Belloni 2007 for more examples of such tracks).

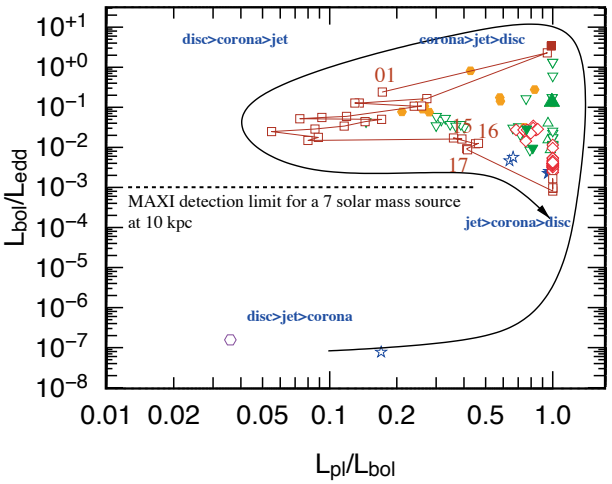

Fig. 1. A 'disc-fraction luminosity diagram' (DFLD; Körding Jester & Fender 2006) for a selection of X-ray binary systems (from Cabanac et al. 2008). A naive description of the division of accretion power between jet (kinetic), corona and accretion disc is indicated. Much of the most interesting behaviour occurs above $\sim 10^{-3}$ Eddington luminosity where the sources exhibit hysteresis and raapid switching of spectral and jet modes. MAXI will be able to detect a typical X-ray binary micoquasar source throughout the whole of this zone, with broad (0.5–30 keV) spectral coverage. Combination of this monitoring with radio observations will vastly improve our understanding of the disc-jet connection in microquasars. In addition, for more nearby sources MAXI will track the rise and decay to $\sim 10^{-4}$ Eddington, which is a very poorly sampled region of paramter space.

2. MAXI

As part of the proceedings of the MAXI workshop, the *Monitor of All-Sky X-ray Image* (e.g. Kawai et al. 1999; Matsuoka et al. 2007) requires little introduction. MAXI will attach to the *Kibo* exposed facility onboard the International Space Station (ISS) in 2009, scanning the entire sky once per ISS orbit and achieving milliCrab sensitivities on a timescale of a week. The monitoring will be made with both position sensitive gas-proportional counters for 2-30 keV X-rays and CCD cameras for 0.5-10 keV X-rays. Obvious targets include X-ray binaries, AGN and other outbursting high-energy objects such as soft gamma-ray repeaters, supernovae etc.

Much of the most interesting behaviour of X-ray binaries, and in particular the disc-jet coupling, occurs in the zone of hysteresis about $\sim 10^{-3}$ Eddington. MAXI will be able to track essentially all galactic transients throughout this zone and onto the hard state branch, providing a fantastic resource for our understanding of black hole accretion (see Fig 1). Combination of the MAXI results with those from radio monitoring programs, whether LOFAR or some other facility, should provide new insights into, and refinements of, our models for the accretion-outflow connection in relativistic objects.

3. LOFAR

LOFAR is a next-generation radio telescope under construction in The Netherlands with long-baseline stations under development in other European countries (currently Germany, The UK, France, Sweden). The array will operate in the 30–80 and 120–240 MHz bands (80–120 MHz being dominated by FM radio transmissions in northern Europe). The telescope is the flagship project

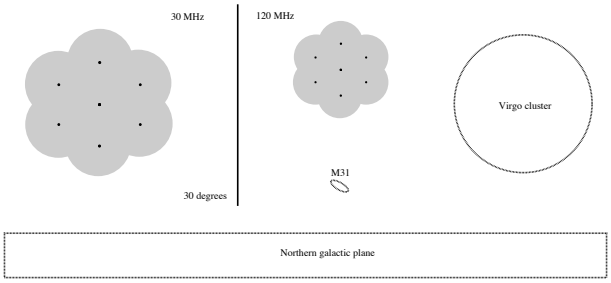

Fig. 2. The vast fields of view achievable with LOFAR due to its low frequency and multi-beam capability, compared to other astronomical facilities and astrophysical objects of interest in the local universe.

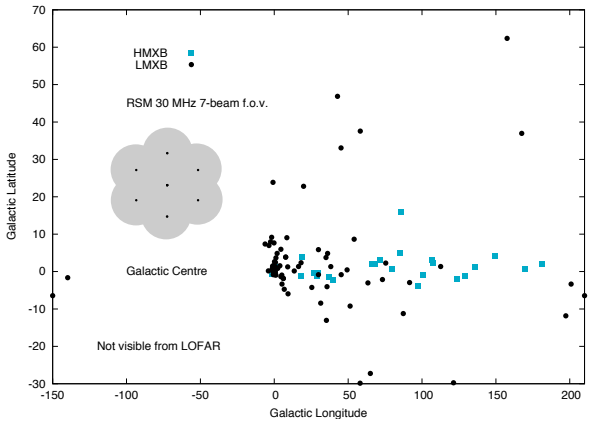

Fig. 3. A comparison of the galactic plane visible from LOFAR, the locations of known high-mass and low-mass X-ray binaries in the visible region, and the seven-beam 30 MHZ field of view. LOFAR pointings in the galactic plane will simultaneously measure many systems.

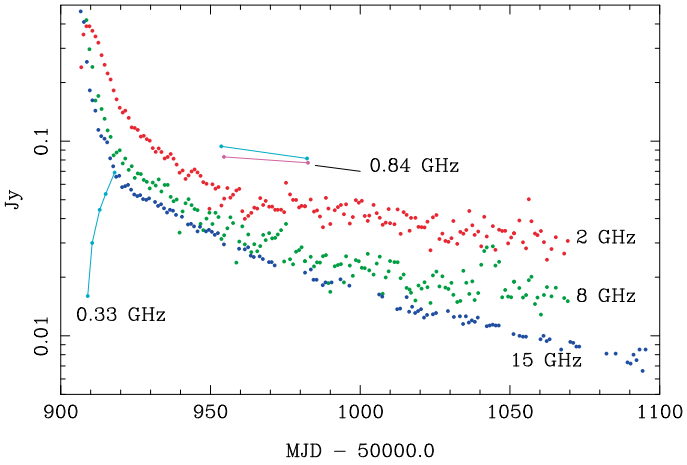

Fig. 4. Radio observations of the ouburst of the X-ray transient CI Cam, between 0.33 and 15 GHz. The lower frequencies, approaching the LOFAR frequency range, peak much later than the higher frequencies due to initial synchrotron self-absorption within the ejecta. This will result in a delay between the major outburst/ejection events and their detectability with LOFAR.

for ASTRON, and is the largest of the pathfinders for the lowest-frequency component of the Square Kilometere Array (SKA). Core Station One (CS1; see Gunst et al. 2006) is currently operating, and the next stage of deployment is about to begin, with 36 stations to be in the field by the end of 2009.

LOFAR has an enormous field of view compared to previous radio astronomy facilities (see Fig 2), allowing for the first time wide-field repetitive monitoring of the radio sky, in the *Radio Sky Monitor* mode (Fender et al. 2008).

For more information on the project, see:

http://www.lofar.org

4. Microquasars with MAXI and LOFAR

The sensivitiy of MAXI will be about one order of magnitude better than that of the RXTE ASM, and over a broader energy range, representing a significant improvement. Many X-ray transients will be detected and monitored by MAXI and, crucially, for nearby ($d \leq$ few kpc) sources MAXI will detect them while still below the $\sim 1\%$ luminosity limit above which the complex hysteretical behaviour occurs, thereby providing both early warning of outbursts and tracking of the decay phase of systems.

The population of X-ray binaries accessible to LOFAR is limited by its physical location in northern Europe, precluding observations of the galactic centre region which contains many bright X-ray binaries. Nevertheless, more than half of the galactic plane is visible from LOFAR, containing many known X-ray binary systems (see Fig 3).

While the low observing frequencies of LOFAR facilitate the extremely wide fields of view, they are not however optimum for observing X-ray binaries or other sources of synchrotron-emitting ejecta. The reason for this is that such ejecta are usually initially self-absorbed at such low frequencies, and may take some significant time to peak in the LOFAR band. In Fig 4 we present the light curve of an outburst from the binary system CI Cam (note: while the system itself is unusual, the outburst is fairly typical for a synchrotron 'bubble' event). The flux density at 330 MHz, just above the LOFAR high band, did not peak (corresponding to a transition from opticall thick to optically thin) until several tens of days after the initial outburst. Nevertheless, even the first observation at this frequency was above the detection limit of the LOFAR RSM.

If we use MAXI to trigger LOFAR on the rise of a new, nearby, transient, we should be able to track the flat-spectrum radio emission from the system over two to three orders of magnitude at the highest LOFAR frequencies (240 MHz; observations indicate the flat-spectrum emission from Cyg X-1 extends between 0.33–220 GHz so this is not too much of an extrapolation...). This will allow us to probe the luminosity range around which several anomalously radio-faint systems have been found (Gallo 2007) and so to further test and refine the 'universal' correlation in this state (Gallo, Fender & Pooley 2003). Note that post-outburst, this correlation may well be impossible to test as the emission in the LOFAR band may be dominated by emission from ejecta launched earlier during state transitions (see Fender, Belloni & Gallo 2004). Therefore, good coordination between MAXI and LOFAR is highly desirable in order to optimize their combined science in this area.

How many sources might we expect ? Grimm, Gil-

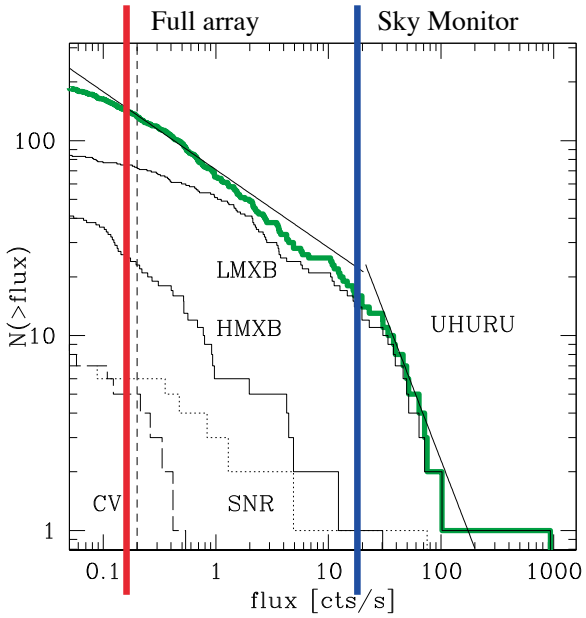

Fig. 5. The cumulative distribution function of X-ray sources detected by the RXTE ASM (Grimm, Gilfanov & Sunyaev 2002), dominated by LMXBs which are also likely to be jet (and therefore radio) sources in outburst. MAXI will be about ten times more sensitive than RXTE ASM, as a result of which more than 100 X-ray binaries should be detectable per orbit of the ISS. The vertical dashed line, originally placed to indicate the approximate completeness sample of the RXTE ASM data, also corresponds approximately to the one-second sensivity limit for MAXI. The red and blue vertical lines indicate an estimate of how far into the population LOFAR can observe, based upon empirical scalings between radio and X-ray luminosities in X-ray binaries. The RSM mode should be able to detect the brightest ~ 20 sources in each scan – this will include semi-persistent systems such as Cyg X-3, SS 433, as well the brightest binaries in outburst at that epoch. Deeper observations with the full array will allow detailed study of the entire binary population visible to MAXI, allowing tracking of radio behaviour over at least three orders of magnitude in luminosity for many sources.

fanov & Sunyaev (2002) derived the luminosity function for galactic X-ray binaries based upon RXTE ASM data. This is replotted in Fig 5 with approximate sensitivity limits for different LOFAR modes. Based on this it would be possible to monitor daily several hundred sources with a combination of MAXI and both *Radio Sky Monitor* mode and targetted observations of LOFAR. Even monitoring a few 10s of sources (*Radio Sky Monitor* mode alone) would be a very significant resource indeed.

Following the major jet ejection, associated with the hard to soft state transition (Fender, Belloni & Gallo 2004), has occurred, LOFAR is likely to be insensitive to the core once the ejecta have become optically thin and completely dominate at low frequencies. This will curtail attempts to track the core behaviour (for example, how much is the core emission really suppressed in the soft state, and when does it reactive in the soft to hard transition), which will be better done with higher-frequency facilities (e.g. EVLA, e-MERLIN, ATA over the MAXI lifetime). However, the emission at these frequencies is also very long-lived, and may be the best way to look at the large-scale jets which can develop over timescales of years and angular scales of arcminutes (e.g. Corbel et al. 2002). With international baselines of $\geq$ 1000km, at 240 MHz LOFAR will have an angular resolution of better than one arsec, plus very good sensitivity to low surface brightness emission, and so will be an excellent instrument to observe these jets as they decelerate and energise the ISM.

5. Summary

As a general tool for high-energy astrophysics, combined MAXI and LOFAR monitoring of the (northern) sky in the X-ray and radio bands will be etxremely valuable. Significant insights will be gained into the physics behind numerous phenomena not touched on here, such as soft gamma-ray repeaters, supernova, blazars etc.

In the field of microquasars, the combination of MAXI and LOFAR will probably be most apparent in two key areas:

1. **The radio:X-ray correlation in the hard state:** MAXI will detect a black hole X-ray transient at a distance of $\sim$ 10 kpc to an Eddington ratio X-ray luminosity of about 10^{-3}. During the rising phase of the outburst, assuming that the flat spectrum radio emission associated with the hard state extends to the LOFAR band ($\leq$ 240 MHz) then we will gain a valuable new sample of data for the radio:X-ray correlation in hard states. Once the radio spectrum becomes dominated by ejecta (as occurs following the brightest canonical hard state), LOFAR observations are likely to be less useful for this correlation as synchrotron-emitting ejecta will evolve slowly at

these frequencies, masking the level of core radio emission.

2. **Spatially resolving extended jets:** Once the major ejection during the hard → soft transition occurs, ejecta from black hole binaries typically separate from the core with proper motions of 10–30 mas d^{-1}. With international baselines, at the highest frequency (240 MHz), LOFAR has an angular resolution of ≤ 1 arsec, and so such eject should be resolvable after a couple of months. From this point onwards, with its sensitivity to optically thin radio emission and low surface brightness features, LOFAR may be the premium facility for emission the large-scale evolution of such ejecta as it interacts with the ISM (note that expanding radio emission on much large scales is still visible ten years after the 1998 outburst of XTE J1550-564: S. Corbel, private communication).

LOFAR is however much better suited to finding prompt *coherent* radio emission, such as that associated with pulsars, flare stars etc. and speculated to be associated with gamma-ray bursts, relativistic object mergers etc. Very naively, were such bursts to be associated with X-ray binary outbursts, we might expect them to occur around the most violently variable phase, i.e. the hard → soft state transition. Therefore we add another, much more speculative, point:

3. **Coherent bursts during state transitions:** there is a small chance that the violent processes associated with the state transitions, ejections, and reformation of the accretion flow, may be associated with coherent radio bursts.

These goals and speculations are summarized in Fig 6.

To end, within the LOFAR project, and the Transients Key Science Project (Fender et al. 2008) in particular, we look forward to a collaboration with MAXI which will be very profitable for the whole high-energy astrophysics community.

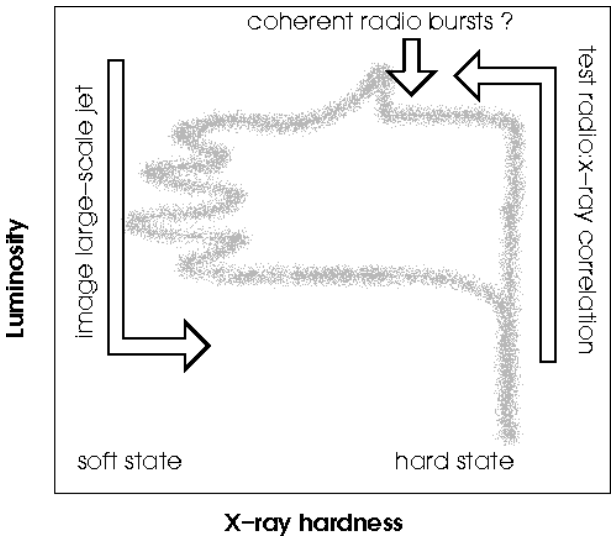

Fig. 6. Schematic illustrating two areas where MAXI and LOFAR will impact upon studies of microquasar systems. MAXI should detect many black hole transients in the rising phase of the outburst, above about $\sim 0.1\%$ Eddington. During this phase, until the transition to the soft state begins (left to right transition in the figure, typically between 1–30% Eddington; see also Fig 1), combined MAXI and LOFAR observations will be able to test the hard state radio:X-ray correlation. Once radio flaring occurs, during the hard to soft transition, the low-frequency LOFAR radio bands will be dominated for a long period of time by slowly evolving synchrotron emission and will not be useful for studying the correlation. However, after a couple of months any large-scale ejecta will be resolvable using the international LOFAR baselines, allowing us to trace the evolution of deceleration and in-situ particle acceleration as the jets interact with the ISM. Much more speculatively, during the explosive jet production phase there may be steep-spectrum coherent radio bursts which LOFAR would be well placed to observe.

References

Cabanac C., Fender R.P., Dunn R.J.H., Körding E., 2008, MNRAS submitted

Corbel S., Fender R.P., Tzioumis A.K., Tomsick J.A., Orosz J.A., Miller J.M., Wijnands R., Kaaret P., 2002, Science, 298, 196

Fender R., 2006, In: Compact stellar X-ray sources. Edited by Walter Lewin & Michiel van der Klis. Cambridge Astrophysics Series, No. 39. Cambridge, UK: Cambridge University Press, p. 381–419 **(astro-ph/0303339)**

Fender R., Belloni T., Gallo E., 2004, MNRAS, 355, 1105
Fender R., Wijers R., Stappers B., et al., 2008, In "Bursts, Pulses and Flickering: wide-field monitoring of the dynamic radio sky", Tzioumis, Lazio & Fender (Eds), Proceedings of Science **(arXiv:0805.4349)**
Gallo E., 2007, THE MULTICOLORED LANDSCAPE OF COMPACT OBJECTS AND THEIR EXPLOSIVE ORIGINS. AIP Conference Proceedings, Volume 924, pp. 715-722 (2007) **(astro-ph/0702126)**
Gallo E., Fender R., Pooley G.G., 2003, MNRAS, 344, 60
Grimm H.-J., Gilfanov M., Sunyaev R., 2002, MNRAS, 391, 923
Gunst A., van der Schaaf K., Bentum M.J., published in the Proceedings from SPS-DARTS 2006, The second annual IEEE BENELUX/DSP Valley Signal Processing Symposium, March 28-29 (2006), Antwerp, Belgium
Homan J., Belloni T., 2005, Ap&SS, 300, 107
Körding E., Falcke H., Corbel S., 2006, A&A, 456, 439
Körding E., Fender R., Migliari S., 2006, MNRAS, 369, 1451
Körding E., Jester S., Fender R., 2006, MNRAS, 371, 1366
Kawai N., et al., 1999, Astronomische Nachrichten, vol. 320, no. 4, p. 372
Lorimer D., Bailes M., McLaughlin M.A., Narkevic D.J., Crawford F., 2007, Science, 318, 777
McHardy I.M., Körding E., Knigge C., Uttley P., Fender R.P., 2006, Nature, 444, 730
Matsuoka M. et al., 2007, SPIE, 6686, 32
Merloni A., Heinz S., di Matteo T., 2003, MNRAS, 345, 1057
Mirabel I.F., Rodriguez L.F., Cordier B., Paul J., Lebrun F., 1992, Nature, 358, 215

Galactic Transient Sources with MAXI

Ken EBISAWA[1]

[1] JAXA/ISAS, Yoshinodai 3-1-1, Sagamihara, Kanagawa, 229-8510, Japan
E-mail(KE): ebisawa@isas.jaxa.jp

Abstract

Thanks to its superior sensitivity, energy resolution and wide energy coverage, MAXI is expected to open a new window in the study of Galactic X-ray transients. In this paper, I selected the following eight areas in which MAXI is expected to make significant contributions to our understanding of the Galactic transient sources: (1) Detailed study of bright transients, (2) Monitor spectral variations, (3) Accretion disk spectral variation, (4) Faint transients, (5) Transient search in crowded region, (6) Supergiant fast X-ray transients, (7) Ultra-soft transients, and (8) Extragalactic stellar transients. For each area, I explain what MAXI will be able to do, in contrast to previous observations by all sky monitors.

Key words: Galactic transients: black holes — neutron stars — white dwarfs

1. Introduction

The MAXI launch planned during the first half of 2009 may sound like a blessing for the study of Galactic transient sources, because operation of the RXTE ASM, MAXI's predecessor in a sense, is planned to be terminated in 2009. The RXTE ASM has been providing the "weather map" of the X-ray sky, such that light curves of several hundreds of X-ray sources in 2–10 keV are available for the last ∼12 years. MAXI will take over this important task, and will provide source light-curves of known X-ray sources or report discovery of new X-ray transients promptly to the world-wide community.

MAXI observations will be made contemporaneously with Chandra, XMM, Suzaku, INTEGRAL, Swift, and also *Fermi*. Furthermore, MAXI is much more sensitive than RXTE ASM at as low as 1 mCrab (GSC) or 3 mCrab (SSC) for one-week exposure, and its spectral resolution can go down to ∼2 % (SSC @ 6 keV). The much wider energy coverage than RXTE ASM, 0.5–30 keV, is also extremely useful to study spectral features of Galactic transient sources. Because of these characteristics, MAXI is expected to open a qualitatively new science in the study of Galactic transients. In this paper, I will introduce several topics, in my opinion, in which MAXI is expected to make significant contributions in the understanding of Galactic transient sources.

2. Detailed study of Bright Transients

MAXI will be able to study bright transient sources in much more detail than previous instruments. In particular, the following two topics are presumably intriguing in the study of bright transients.

2.1. Study of Very Initial-phase

It is extremely difficult to catch just the "onset" of X-ray novae, since we never know when and where the X-ray novae would appear on the sky. In a very rare and lucky situation, the GINGA ASM detected the onset of GS2000+25, because the source had been coincidentally in the ASM FOV before the nova was discovered (Tsunemi et al. 1989). After the source became brighter than ∼50mCrab (ASM sensitivity), up to the peak of 12 Crab, the X-ray light-curve and spectral evolution were closely monitored. It is well-known that X-ray novae often exhibit peculiar spectral evolution in the very beginning. One of such examples is GS2023+338, which is also discovered by GINGA ASM (Kitamoto et al. 1989). The source exhibited rather a soft spectrum in 1-10 keV (photon-index ∼ 2) during the initial week or so, while in just a few days the spectrum became extremely hard (photon-index ∼ 0). However, for both of GS2000+25 and GS2023+338, we never know the spectral evolution in the beginning before the source was dimmer than ∼50mCrab, which is crucial to know the outburst mechanism of X-ray novae.

Thanks to its sensitivity, wide sky coverage and frequent monitoring, MAX will not miss onsets of bright X-ray novae, and will be able to study their spectral evolutions from the very beginning when the source is just a few mCrab.

2.2. Spectral Transition

Many bright X-ray transients are known to exhibit spectral transitions, in most cases between the high-soft state and the low-hard state, at around a threshold luminosity of $\sim 10^{37}$ erg s^{-1} (2 – 10 keV). One notable example is GS1124–68 (Ebisawa et al. 1994), where the source was

in the high-soft state when observed at $\sim$ 100 days after the outburst by the Ginga main detector (LAC), while it was obviously in the low-hard state when observed at $\sim$ 160 days after the outburst. Meanwhile, the source seemed to be in the intermediate state at $\sim$130 days when the flux is about 0.1 Crab. Because the pointing observations by LAC were not continuous but patchy, we do not know the source behavior between these discrete observations.

We would like to know in which time-scale the state transition of X-ray novae takes place, and study detailed spectral evolution. If similar X-ray transients like GS1124–68 take place, MAXI will be able to carry out detailed study of spectral transition taking place at around $\sim$0.1 Crab.

3. Monitor Spectral Variation

Most X-ray binaries show spectral variations at various time-scales. Previous all sky monitors on-board Ginga, RXTE and other satellites did not have a sensitivity to detect these spectral variations taking place below $\sim$ 50 mCrab, thus such studies had to be made by pointing observations with main detectors, which were necessarily not continuous but rather patchy or sporadic.

Still, thanks to its great maneuverability, RXTE was able to carry out rather regular monitoring observations by the main detector (PCA) of Galactic X-ray binaries and AGNs. In one of such monitoring campaigns, spectral variation of a prime black hole binary LMC X-3 was studied, and the low-hard state of the source was discovered for the first time below $\sim$20 mCrab (Wilms et al. 2001).

Not only black holes, but also neutron binaries are known to have bimodal spectral states. For instance, the low-hard state of X1608-522 was studied with GINGA LAC at $\sim$40 mCrab, and its spectral and timing characteristics have been found to be very similar to those of black hole binaries (Yoshida et al. 1993). MAXI will be able to regularly study spectral variations of such rather dim black hole and neutron star binaries below $\sim$ 50 mCrab, increase the number of such samples significantly, and expect to reveal common properties of these these sources in the low state.

Bright neutron star binaries such as GX5-1 are known to show characteristic "Z-shape" spectral branches on the X-ray color-color diagram. For such bright sources (as bright as $\sim$ Crab), even GINGA ASM could study the spectral variations (van der Klis et al. 1991). Long-term monitoring of GX5-1 by GINGA ASM revealed that the Z-pattern is remarkably stable over the three years of observation. MAXI will be able to study such long-term spectral variations of practically all the bright low mass X-ray binaries brighter than 10 mCrab or so.

4. Accretion Disk Spectral Variation

The standard accretion disk model (Shakura and Sunyaev 1973) is established to explain the soft state X-ray energy spectrum of black hole binaries. In the soft state, if the standard accretion disk model is applied to explain the spectral variation, the inner disk radius is constant while the source luminosity and the disk temperature varies significantly (e.g. Ebisawa et al. 1993). The constant inner-radius corresponds to the inner-most stable circular orbit (ISCO) around the black holes, which is between three times the Schwarzschild radius and half the Schwarzschild radius, each corresponding to the non-rotating black holes and extremely fast-rotating black holes. Thus, from the X-ray measurements of ISCO, black hole mass and spin are expected to be constrained.

In the case of LMC X-3, such accretion disk variation was studied above $\sim$ 10 mCrab, which was so far only possible with pointing observations. Using MAXI, we can carry out such a study not only for bright X-ray binaries but also for rather dim black hole like LMC X-3. In this manner, MAXI may constrain the important black hole parameters, mass and spin, for many known black hole X-ray binaries.

When accretion rate becomes higher and the disk luminosity gets close to the Eddington limit, radial advection takes place, and the standard disk is considered to transform into the "slim disk" (e.g., Abramowicz et al. 1995). Slim disk and standard disk spectra are observationally distinguishable; disk temperature of the standard disk depends on the radius as $T \propto r^{-3/4}$, while in the case of slim disk the exponent becomes lower down to 0.5 (Watarai et al. 2000). Difference of the exponent is reflected in the X-ray energy spectra, and we may constrain the exponent p in $T \propto r^{-p}$ from model fitting for bright sources.

In fact, at the peak luminosity of the X-ray nova XTE J1550–56 ($\sim$2Crab), the standard disk model fit was not acceptable, but the slim disk model fits better with $p \sim 0.6$ (Kubota and Makishima 2004). This may be considered as an evidence of the slim disk in XTE J1550–56. From similar model fitting analysis, slim disk is considered to present in the Ultra-luminous X-ray sources too (ULXs; e.g. Okajima et al. 2006, Vierdayanti et al. 2006).

We do not have enough number of examples of the slim disk in X-ray binaries, since there are not many chances to observe the luminosity peaks of the accretion disk spectra. Since MAXI will continuously monitor bright transients and have sufficient spectral capability to constrain precise spectral models, we may obtain more examples of the slim disk in bright X-ray binaries.

5. Faint Transients

In 2–10 keV band, GINGA and RXTE all sky monitors had sensitivities of about ∼50 mCrab, while the LAC and PCA *scan* observations were very sensitive to detect sources a low as a few mCrab. Systematic scan observations with GINGA LAC and RXTE PCA were made on Galactic plane and center regions covering wide area, and many new transient sources have been discovered, almost always when new scans are made (e.g., Koyama et al. 1989). Even today, careful re-analysis of GINGA archives of the scan data lead to retrospective discovery of new X-ray transients (Yamauchi et al. 2005, 2007). Since MAXI's sensitivity is comparable to that of GINGA and PCA scan observations, new transient sources at a few mCrab are expected to be *regularly* discovered on the Galactic plane and center region.

Above ∼20 keV, coded mask is currently the only technology for imaging observation. INTEGRAL and Swift coded masks have sensitivities of ∼mCrab, and discovered many new hard X-ray sources. INTEGRAL discovered 225 new sources ("IGR" sources) in four years[1] , most of them heavily absorbed transients, while it does not cover the all sky regularly (the field of view is $30^\circ \times 30^\circ$). MAXI is sensitive up to 30 keV, has comparable sensitivity with INTEGRAL and Swift coded mask, and covers the entire sky regularly. Therefore, MAXI is expected to detect at least 50 transient sources per year which are as fain as a few mCrab above 20 keV.

6. Transients Search in Crowded Region

Galactic center/bulge region is known to nest many X-ray transient sources. While INTEGRAL and Swift may resolve individual sources above 20 keV, they may not detect sources which are bright only below 10 keV. Ginga and RXTE scan observations were powerful tools to detect such transient sources in the Galactic center/bulge region, but they are always suffer from source contamination, thus precise determination of the source position was often difficult (e.g., Yamauchi et al. 2007). MAXI is expected to precisely determine the positions of such soft transient sources below 10 keV in the Galactic center/bulge region which is crowded with many sources.

7. Supergiant Fast X-ray Transients

Super Fast X-ray Transients (SFXTs) are discovered with INTEGRAL serendipitously (e.g., Leyder et al. 2007). They have sharp rise (∼ tens of minutes), only a few hour durations, and complex time profiles. The peak luminosities are typically $\sim 10^{36}$ erg s^{-1}. Because of their short durations and low brightness, they are extremely hard to detect. In fact, existence of such sources had not been known before INTEGRAL, which could detect them because of the large field of view.

Characteristics of SFXTs below 10 keV are hardly known, since observations of SFXTs below 10 keV are scarce. MAXI is an ideal instrument to observe SFXTs both above and below 10 keV, since all the sky is covered in every 90 minutes – any SFXTs lasting for a few hours are hardly missed.

8. Ultra-soft Transients

Another strength of MAXI compared to previous all sky monitors is superior sensitivity below 2 keV. MAXI is practically the first all sky monitor which is sensitive in 0.5 – 2 keV energy range, where different kind of sources are dominant from those above 2 keV. One of the kinds of bright transients below ∼ 2 keV is novae, which is accreting or bursting white dwarfs. Novae have thin thermal spectra, which show prominent emission lines of below 2 keV, C, N, O and Si, which may be resolved with MAXI SSC.

Another kind of sources prominent below ∼ 2 keV is Super-Soft Sources (SSSs), which are nuclear burning white dwarfs. Many SSSs have been discovered in LMC, SMC and nearby Galaxies, but only a few Galactic SSSs have been known, because of the significant Galactic absorption. However, systematic monitoring of Galactic transient SSSs has hardly been made. It is possible that MAXI detect dozens of Galactic bright transient SSSs like GQ Muscae (Novae Muscae 1983; Ögelman et al. 1993), which was detected with EXOSAT and ROSAT.

9. Extragalactic Stellar Transients

Thanks to its superior sensitivity, MAXI may become the first X-ray monitor that may detect extragalactic stellar transients. LMC, SMC and M31 are known to be the nests of many transient sources. If we take an example of SMC, more than 24 transient pulsars have been detected after 1994 with ROSAT, ASCA, RXTE and BeppoSAX, while only SMC X-1 was the known pulsar previously. Obviously, there is a great discovery space of extragalactic stellar transients.

Another possible target of extragalactic compact sources is ULXs. Recently, M82 X-1 was detected for the first time above 10 keV with Suzaku PIN, which has a $30'' \times 30''$ FOV, though source contamination was not fully resolved (Miyawaki et al. 2008). In the case of MAXI observation of extragalactic stellar sources, source confusion becomes always a problem. However, if significant ULX outbursts take place, MAXI might be able to detect them. Some ULXs are known to have very soft spectrum (e.g., M101 X-1; Kong and Stefano 2005), so MAXI's superior sensitivity in low energy band is helpful.

*1 http://isdc.unige.ch/∼rodgigue/html/igrsources.html

10. Summary

MAXI will take over the important task of RXTE ASM since 2009, such that it continuously monitors the X-ray all sky, provides light curves of known sources and reports discovery of transient sources promptly. More over, thanks to its superior sensitivity, energy resolution and wide energy coverage, MAXI will be able to open a new window in the study of Galactic X-ray transients.

References

Abramowicz et al. 1995 ApJ, 438, L37
Ebisawa, et al. 1993 ApJ, 403, 684
Ebisawa, et al. 1989 PASJ, 46, 375
Kitamoto, S. et al. 1989 Nature, 342, 518
Kong, A. K. H. and Di Stefano, R. 2005 ApJ, 632, L107
Koyama, K. et al. 1989 PASJ, 41, 483
Kubota, A. and Makishima, K. 2004, 601, 428
Leyder J.-C. et al. 2007 A&A, 465, L35
Miyawaki, R. et al. 2008 PASJ, accepted
Ögelman et al. 1993 Nature, 361, 331
Okajima, T. et al. 2006 ApJ, 652, L105
Tsunemi, H. et al. 1989 ApJ., 337, L81
Shakura, N. I. and Sunyaev, R. A. 1973 A&A, 24, 337
van der Klis, M. et al. 1991 MNRAS, 248, 751
Vierdayanti, K. et al. 2006, PASJ, 58, 915
Watarai, K. et al. 2001 PASJ, 52, 133
Wilms, J. et al. 2001 MNRAS, 320, 327
Yamauchi et al. 2005 PASJ 57, 465
Yamauchi et al. 2007 PASJ 59, 1141
Yoshida, K. et al. 1993 MNRAS, 45, 605

Discovering and monitoring sub-luminous X-ray binaries using MAXI

Rudy Wijnands[1]

[1] Astronomical Institute 'Anton Pannekoek', University of Amsterdam,
Kruislaan 403, Amsterdam, The Netherlands
E-mail(RW): rudy@science.uva.nl

Abstract

Most studies of accreting neutron stars and black holes in X-ray binaries focus on those systems which are accreting at relatively high mass accretion rates and therefore have high associated X-ray luminosities ($> 10^{36}$ erg s^{-1}). Although the existence of very faint, sub-luminous systems is well known, the study of these systems is inhibited by the difficulties in finding them (both the persistent as well as the transient systems) in large numbers using currently available all-sky monitoring instruments. These systems are usually found serendipitously in pointed observations with small field-of-view instruments which have the needed sensitivity to detect them. I will briefly review our current knowledge and understanding about these enigmatically faint systems and how they can be used to probe the extreme physically processes associated with accreting neutron stars and black holes in ways which cannot be done for their brighter cousins. I will also discuss the problems in finding these systems and how MAXI will significantly improve on this situation. The 1 mCrab sensitivity of MAXI within a week (about 10^{35} erg s^{-1} at a distance of 8 kpc) will be extremely useful in finding and monitoring these sub-luminous X-ray binaries.

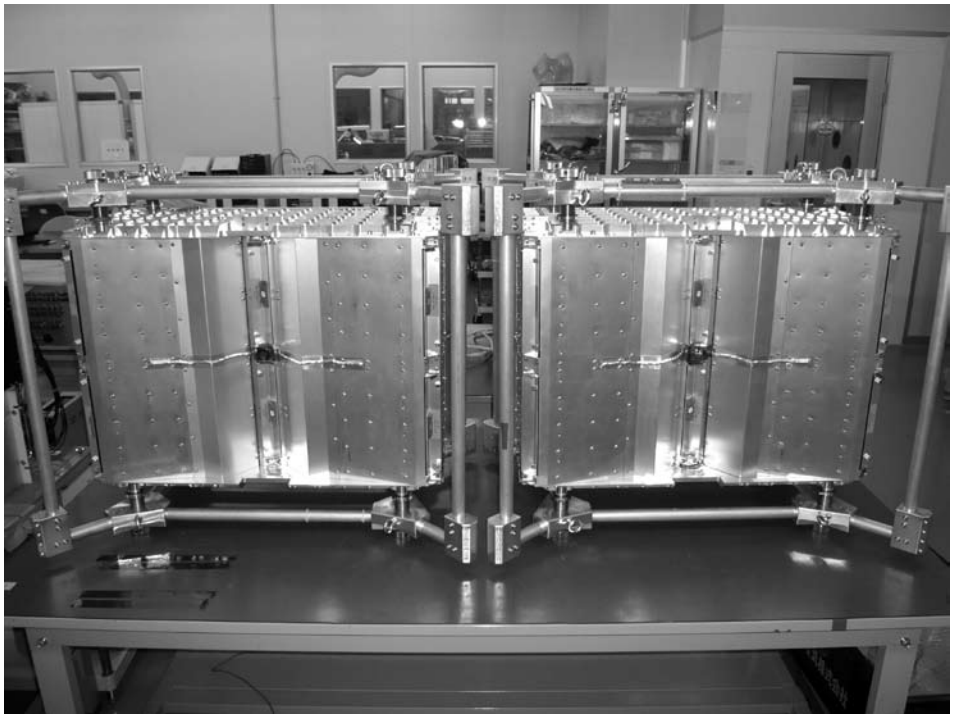

Active flaring states of GRS 1915+105 and Cyg X-3 in radio/X-ray monitoring

Sergei Trushkin and Nikolaj Nizhelskij[1], Taro Kotani[2],
Nabuyuki Kawai[3], Masato Tsuboi[4], Masaki Namiki [5]

[1] Special astrophysical Observatory RAS, Nizhnij Arkhyz, Russia
[2] Aoyama Gakuin University, 5-10-1 Fuchinobe, Sagamihara,Kanagawa, Japan
[3] Tokyo Institute of Technology, O-okayama, Tokyo, Japan
[4] ISAS/JAEA, Sagamihara, Kanagawa, Japan
[5] Osaka University, Toyonaka, Osaka, Japan
E-mail(ST): satr@sao.ru

Abstract

In multi-wavelength collaboration we studied the variability of the microquasars GRS1915+105 and Cyg X-3 during 2005 to May 2008 with the RATAN-600 radio telescope of SAO RAS. We detected clear correlation of the flaring radio fluxes and X-rays 'spikes' at 2-12 keV emission redundant in RXTE ASM from GRS1915+105 during eight relatively bright (200-600 mJy) radio flares in October 2005. Spectra of these flares at maximum are optically thick at frequencies lower than 2.3 GHz and optically thin at the higher frequencies. During the radio flares the spectra of the X-ray spikes become softer than those of the quiescent phase. Thus these data indicate the transitions from the very high/hard state to high/soft state during which massive ejections probably occur. These ejections are detected as radio flares. Such X-ray/radio events correlation detected later in 2006-2008. In December 2005 after of the 4-year quiescent radio state (100–200 mJy) Cyg X-3 entered the softer X-ray state with low level of hard (15-50 keV) X-ray and high (∼0.5 crab) in the soft band (1-10 keV). In the following 500 days we have detected more 10 bright (> 1Jy) flaring events correlated with rising phases of ASM-Swift-BAT intensity of Cyg X-3. A first 1 Jy-flare was detected on 3 February 2006 after 18 days of the quenched radio emission (< 20mJy). The spectrum of the flare at the maximum is flat from 1 to 100 GHz, obtained the quasi-simultaneous observations with RT45m telescope and millimeter array (NMA) of Nobeyama Radio Observatory.

Key words: microquasars: variability — X-ray emission: — radio radiation

1. Introduction

The most important feature of the relativistic accretion process in the radio band are the jets – collimated outflows from a cosmic system of stellar mass as Galactic X-ray binaries (XRB) or galactic mass, active galactic nuclei (AGN). The relativistic jets discovered in the first time in SS433 (Spencer, 1979, Hjellming & Johnston 1981), then were detected in Cyg X-3 (Geldzahler et al. 1983), 1E1740-2942 (Mirabel, Rodriguz et al. 1992), GRS 1915+105 (Mirabel & Rodriguz, 1994), GRO 1655-40 (Hjellming et al. 1995) and then some others XRB. These jet-producing XRB are now named *microquasars* for analogy with the jets from quasars and blasars, VLBI-mapped a lot of times before XRB. Superluminal Galactic X-ray sources apparently accelerate radio-emitting material to relativistic speeds like jet sources observed in AGNs or quasars. The blobs of synchrotron-emitting electrons relativistically and ballistically move from host objects, which we see as the phenomenon of jets.

2. Observations program

The long-time monitoring sets of microquasars has systematically service, produced with the RATAN-600 radio telescope for years. Almost daily monitoring observations were carried out from September 2005 to May 2006, in July 2006, from November 2006 to March 2007 and from December 2007 to February 2008 and from June to August 2008 at frequencies at 1, 2.3, 4.8 7.7, 11.2, and 30 GHz. The multi-frequency light curves of the microquasars Cyg X-3, GRS 1915+10, SS433 have been measured at time scale to 100-150 days. We can directly compare them with time series of the X-ray observatory RXTE (Levine et al. 1996) and hard X-ray data from Swift/BAT (15-50 keV) (Barthelmy et al. 2005). The observations have been made with the 'Northern sector' antenna of the RATAN-600 radio telescope in a transit

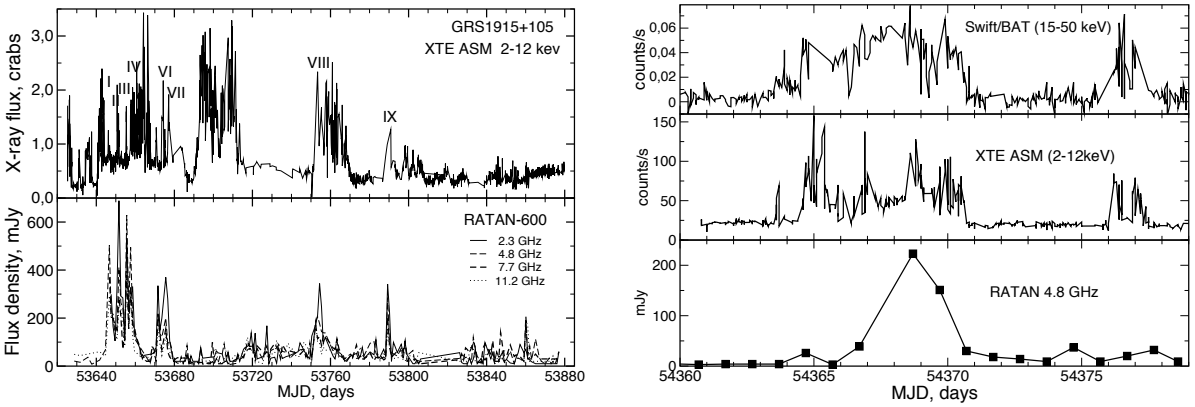

Fig. 1. Light curves of GRS1915+105 at radio frequencies and at 2-12 keV from September 2005 to March 2006 (*left*) and light curves of GRS1915+105 at radio frequencies and X-ray 2-12 keV and 15-50 keV fluxes in September 2007 (*right*)

mode. The errors of measured fluxes of the sources do not exceed 5-10 percent for sources with fluxes about and more 100 mJy. The details of the observations and the errors are given by Trushkin et al. (2006).

3. GRS 1915+105: X-ray – radio correlation

The bright and transient X-ray source, a low-mass binary, probably hosting a black hole $\sim 14M_\odot$, GRS 1915+105 was discovered by Castro-Tirado et al. (1992) with the WATCH instrument on board GRANAT. An apparent super-luminous motion of the jet components was detected by Mirabel & Rodriguez (1994). Foster et al. (1996) detected that 2.3/8.5 GHz emission from GRS1915+105 correlated with X-rays with episodes of hard X-ray emission, detected with BATSE.

A phenomenological classification of the radio emission indicates two distinct emission modes; plateau and flaring. Plateau radio emission is caracterized as optically thick, flat-topped light curve beginning with a rapid onset followed by a decrease of flux density. In the radio flaring state, radio light curves are clustered with large flares, which are characterised by a rapid increase of the flux by two orders of magnitude in less than 18 hours, followed by an optically thin exponential decay. These observed large radio flares are considered as a propagation of plasmoids emitting synchrotron radiation.

Fender et al. (2002) discussed the alert observations of two flares (July 2000), when for the first time detected the quasi-periodical oscillations with P = 30.87 minutes at two frequencies; 4.8 and 8.64 GHz. Linear polarization was measured at a level of 1-2 percent at both frequencies.

Vadawale et al. (2003) have analyzed the short-time radio flares from GRS 1915+105 detected with Green Bank Interferometer (GBI) and All sky Monitoring (ASM) RXTE data (Levine et al. 1996) and found many cases of the X-ray and radio correlations.

In Fig.1(*left)* the radio and X-ray light curves are shown for the total set of 2005-2006. The nine radio flares have the counterparts in X-rays. The radio spectrum was optically thin in the first two flares, and optically thick in the third one (details are given by Namiki et al. 2006). In Fig.1 (*right)* the radio and soft and hard X-ray light curves during September-October 2007. Again we see detectable correlation between the radio flare and a soft X-ray 'spike' in the high state.

Most of radio flares show power-law spectra with index of -0.6 at the higher frequencies with a low-frequency turnover at 1 GHz, which can be interpreted as absorbed synchrotron emission.

The profiles of the X-ray spikes during the radio flares are clearly distinguishable from other spikes because its shape shows a fast-rise and a exponential-decay. The X-ray spikes, which reflect random activity of the accretion disk, show an irregular pattern. During a bright radio flare, the spectra of the X-ray spikes become softer than those of the quiescent phase, by a fraction of $\sim$30% (Namiki et al. 2006). But such rule is not applicable to all radio flares.

Miller at al. (2006) have detected a one-side large-scale radio jet from GRS1915+105 with VLBA mapping during an X-ray and radio outburst on 23 February 2006 (MJD53789.258). Then the optically thin flare with fluxes 340, 340, 342, 285, 206, and 153 mJy was detected at frequencies 1, 2.3, 4.8, 7.7, 11.2 and 21.7 GHz, respectively.

4. Cyg X-3: 2006-2007 – a new long-term active period

For $\sim$100 days (September – December 2005) Cyg X-3 was in a quiescent state of $\sim$100 mJy (Fig.4). In December 2005 its X-ray flux began to increase and the radio flux at 2-11 GHz increased also. Then the flux density of the source at 4.8 GHz was found to drop from 103 mJy

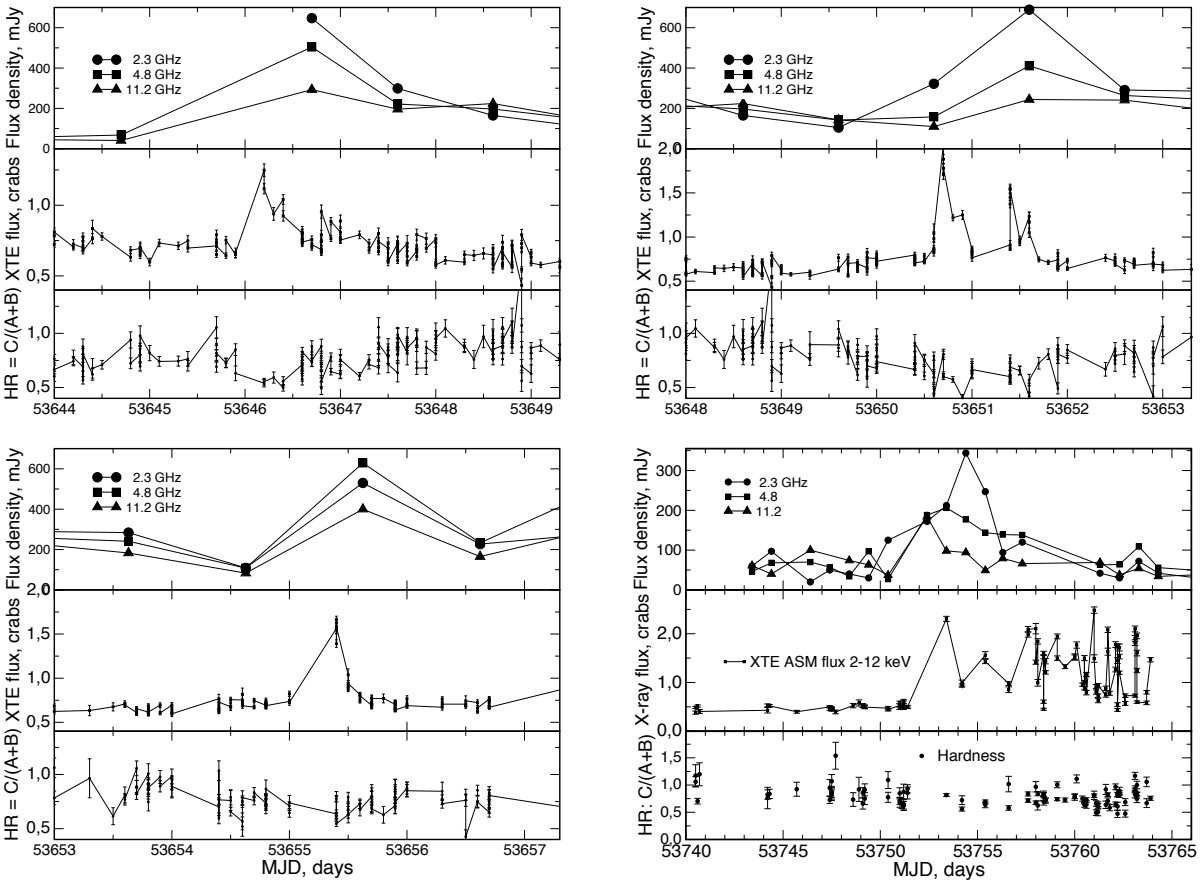

Fig. 2. The light curves of GRS 1915+105 around four most prominent X-ray 'spikes' (upper) and hard ratio C[12-5keV]/(A+B)[1.5-5keV] from XTE ASM data (bottom).

on 2006 Jan 14.4 (UT) to 43 mJy on Jan 15.4 (UT), and to 22 mJy on Jan 17.4 (UT). The source is known to exhibit radio flares typically with a few peaks exceeding 1-5 Jy following such a quenched state as Waltman et al. (1994) have showed in the intensive monitoring of Cyg X-3 with the Green Bank Interferometer at 2.25 and 8.3 GHz. The source has been monitored from 2006 Jan 25 (UT) with the Nobeyama Radio Observatory 45m Telescope (NRO45m Telescope), the Nobeyama Millimeter Array (NMA) and Japanese VLBI Network telescopes. On Feb 2.2 (UT), about 18 days after it entered the quenched state, the rise of a first peak is detected with the NRO45m Telescope and YRT32m. On Feb 3.2 (UT), the flux densities reached the first peak at all the sampling frequencies from 2.25 GHz to 110.10 GHz, (Tsuboi et al. 2006,2008). The spectrum at maximum (3 February) of the flare was flat as measured by RATAN, NRO RT45m and NMA from 2 to 110 GHz. The next peak of the active events on 10 February reached the level of near 1 Jy again with a similar flat spectrum. Then three short-time flares have happened during a week. The flare on 18 February had the inverted spectrum with the same spectral index α=+0.75 from 2.3 to 22 GHz. It is interesting that no jet structure has been detected with Japanese VLBI Network just after the first maximum of the flare. In other hand the following bright flares were jet ejections. For example the flare in 18 May 2006 have clear evidence of jet structure (Tudose et al. 2007)

In the active period (2006) there were two powerful flares, March 14 to 3-5 Jy and May 11 with flux densities of 12-16 Jy at 2-30 GHz. In the May flare fluxes have grown up by a factor ∼1000 within a day. The change of the spectrum during the flare on May 11-19 followed the model of a single ejection of the relativistic electrons, moving in thermal matter in the intensive WR-star wind. It stays in optically thin mode at higher frequencies, meanwhile at lower frequency 614 MHz Pal et al (2006) Cyg X-3 was in hard absorption. In the continuing active state of Cyg X-3 we detected a very fast-rise flare at 2.3 and 8.5 GHz with RT32 (IAA) on 5 June 2006 (MJD53891) (Trushkin et al. 2006). In three hours the fluxes changed from $\sim$ 1 Jy to 2 Jy and then decreased to 100-400 mJy during 15 hours. We detected the similar behaviour in the the Jan-Feb 2007, when maximum flux reached 14 Jy at 2.3 GHz (Fig:4).

In Fig.5 the light curves of the July flare are shown. The phase of the flux rising continued during 4-5 days. For the first time we could clearly see the evolution of the spectrum during the phase of the flare (Fig.5). And it was amazing that the low-frequency part of the spectra evolved from nearly flat optically thin (at 1 GHz) on the first day to optically thick after 3-4 days. In the standard model of the expansion of the compact sources (jets components) there is no any explanation for such behaviour.

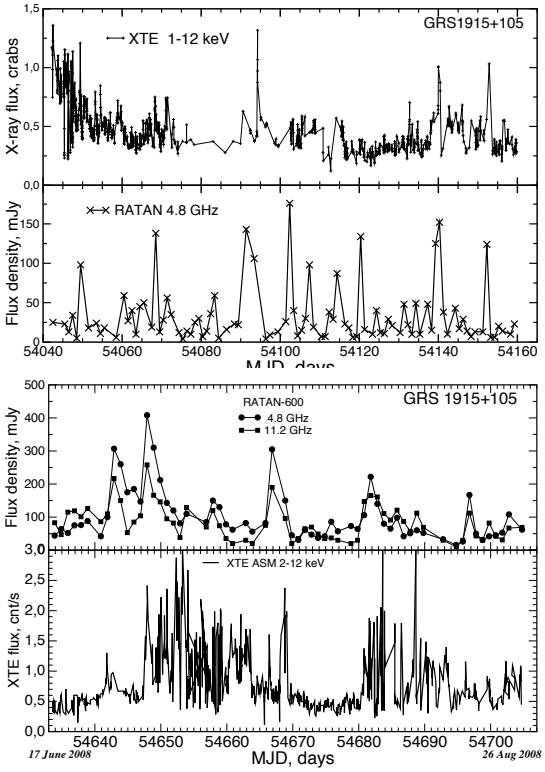

Fig. 3. Light curves of GRS1915+105 measured with RATAN-600 radio telescope and in ASM XTE in 2007 (*left*) and in 2008 (*right*)

We had to conclude that the thermal electron density, responsible for the low frequency absorption, grows up during grow-up of the relativistic electron density. The later stage of the spectral and temporal evolution could be fitted by the modified finite segments model by Marti et al. (1992) or Hjellming (1988) and Hjellming et al. (2000), which are modifications of the pioneer models by Shklovskij (1960) and van der Laan (1966).

Indeed in Fig.5 the radio spectra of the July flare evolved from the fourth day (MJD53942) as usual adiabatically expanding relativistic jets moving with $v_{jet} \sim 0.74c$, and thermal electron component has: $T_e = 10^4$ K, $n_{th} = 2\ 10^4 cm^{-3}$, magnetic field $B_0 = 0.07$ G, and energy index $\gamma = -1.85$. During the rising stage of the flare we should involve the intense internal shocks running through the jet (Vadawale et al. 2003).

5. SS433: new flaring events and their spectra

The first microquasar SS433, a bright variable emission star was identified with a rather bright compact radio source 1909+048 located in the center of a supernova remnant W50. In 1979 moving optical emission lines, Doppler-shifted due to precessing mass outflows with 78000 km/s, were discovered in the spectrum of SS433. At the same time in 1979 were discovered a unresolved compact core and 1 arcsec long aligned jets in the MER-

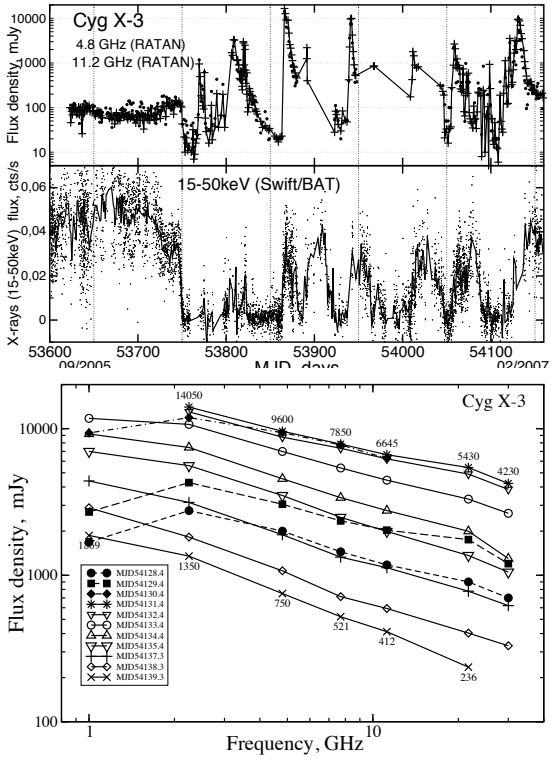

Fig. 4. (*top*) The RATAN and Swift/BAT light curves of Cyg X-3 from September 2005 to February 2007 and (*bottom*): The daily spectra of Cyg X-3 during the flare in Jan-Feb 2007.

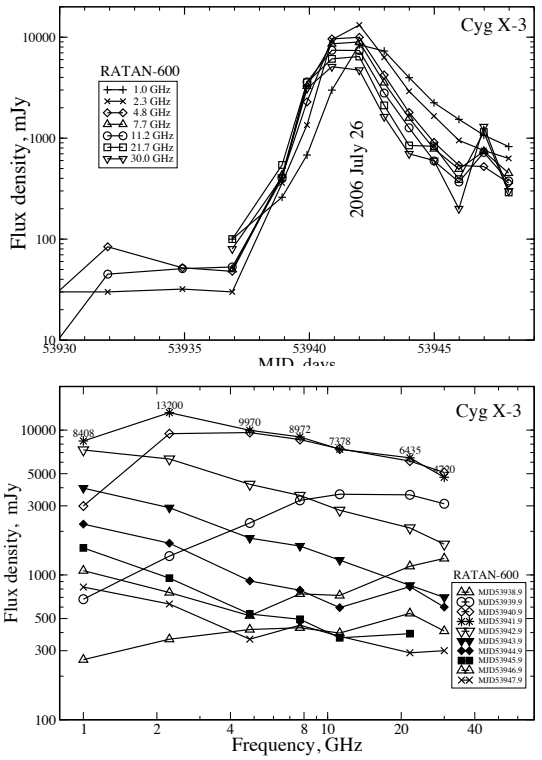

Fig. 5. The RATAN and RXTE ASM light curves of Cyg X-3 in July 2006 (*top*) and the daily spectra of Cyg X-3 during flare in July 2006 (*bottom*).

LIN radio image of SS433. Since 1979 many monitoring sets (e.g., with GBI (Waltman et al. 1994) , RATAN (Trushkin et al. 2006) were began. Different data do indicate a presence of a very narrow (about 1^o) collimated beam at least in X-ray and optical ranges. At present there is no doubt that SS433 is related to W50. A distance of near 5 kpc was later determined by different ways including the direct measurement of proper motions of the jets radio components.

Kotani et al. (2006) detected the fast variation in the X-ray emission of SS433 during the radio flares, and probably QPOs of 0.11 Hz. Massive ejections during this active period could be the reason of such behavior. The daily RATAN light curves are measured from September 2005 to May 2006. The activity of SS433 began during the second half of the monitoring set. Some flares happened just before and after the multi-band program of the studies of SS433 in April 2006 (Kotani et al. 2007).

In Fig.6(*top*) the light curves of SS433 during December 2007 - August 2008 are shown. The delay of the maximum flux of the bright flare in December 2007 at 1 GHz is about 2 days and 1 day at 2.3 GHz relative to the maxima at higher frequencies.

In Fig.6(*bottom*) the light curves during the bright flares in December 2007 - February 2008 are showed. The both flares decayed with exponential law ($S_\nu \propto exp(-t/t_0)$, where $t_0 = 25$ days for the second flare.

We detected the surprising coincident dates (6-7 Dec) of the bright flares in 2006 and 2007. Probably the 1-year periodicity of activity exit in radiation of SS433. Recently Nandi et al. (2005) discussed the periodicity of flaring events in ASM RXTE X-ray data, and found possible period about 368 days.

6. Conclusions

The long-time daily RATAN microquasar monitoring data give us fruitful material for comparison with the X-ray data from the ASM or ToO programs with RXTE, CHANDRA, Suzaku and INTEGRAL. We hope to continue such programs with MAXI in future.

The radio emission could be in two different optically thin and thick regimes at 1-2 and 10-20 GHz, and allows us to develop an adequate model of the flaring radio emission producing in the relativistic jets interacting with varying circumstellar medium or intense stellar wind.

We acknowledge the use of public data from the Swift data archive. These studies are supported by the Russian Foundation Base Research (RFBR) grant N 08-02-

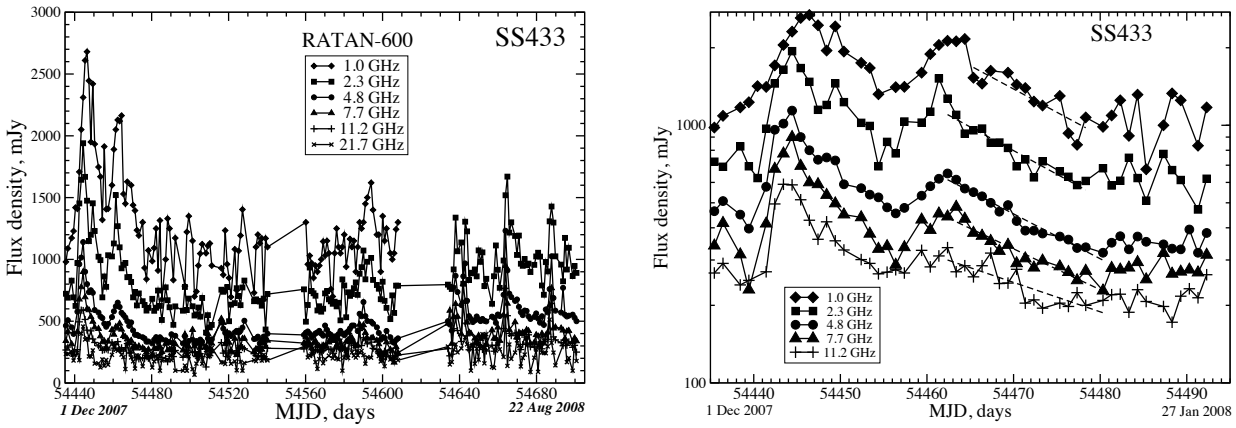

Fig. 6. The total light curves of SS433 in December 2007 - August 2008 (*left*) and during the powerful flaring events in December 2007 - January 2008 (*right*).

00504 and the mutual RFBR and Japan Society for the Promotion of Science (JSPS) grant N 05-02-19710. ST would like to thank the LOC of Third MAXI symposium for invitation to do this report.

References

Barthelmy S.D. et al. 2005 Space Science Reviews, 120, 143
Castro-Tirado A.J. et al. 1992 IAUC ,#5590
Fiedler R.L. et al. 1987 AJ, 94, 1244
Hjellming R.M., Johnston K.J. 1981, ApJ., 246, L141
Hjellming R.M. 1988 Galactic and extragalactic radio astronomy (2nd ed.) (A89-40409 17-90). Berlin and New York, Springer-Verlag, 381-438.
Hjellming R.M. et al. 2000 ApJ., 544, 977
Hjellming R.M., Rupen M.P. 1995 Nature, 375 464
Geldzahler B. et al. 1983 ApJ, 273, 65L
Kotani T. et al. 2006 ApJ, 637, 486
T. Kotani, et al. 2006 Proc. of the VI microquasars workshop: Microquasars and Beyond, 50
Levine A. et al. 1996 ApJ., 469, L33
Marscher A.P. & Gear W.K. 1985 ApJ., 298, 114
Marti J. et al. 1992 A&A, 258, 309
Miller-Jones J.C.A. et al. 2006 ATel., #758, 1
Mirabel I.F., & Rodriguez L.F. 1994, Nature, 371, 46
Namiki et al. 2006 Proceedings of the VI microquasars workshop: Microquasars and Beyond, 83
Nandi A. et al. 2005 MNRAS, 359, 629
Pal S. et al. 2006 ATel., #809, 1
Rees M.J. 1978 MNRAS, 184, 61P
Shklovskii I.S. 1960, AZh., 37, 256
Spencer R.E. 1979, Nature, 282, 483
Tsuboi M. et al. 2006 ATel., #727, 1
Tsuboi M. et al. 2008 PASJ, 60, 465
Trushkin S.A. et al. 2006 ATel., #828, 1
Trushkin S.A. et al. 2006, Proceedings of the VI microquasars workshop: Microquasars and Beyond, 15
Trushkin S.A. et al. 2003 Bull. SAO RAS, Izvestij SAO, 56, 57
Tudose et al. 2007 MNRAS 375, 11L
van der Laan H. 1966 Nature, 211, 1131
Vadawale S. et al. 2003 ApJ., 597, 1023
Waltman E.B. et al. 1994 A&A, 108, 179

Hard X-ray/soft γ-ray Characteristics of the Persistent Emission from Magnetars

– Results based on multi-year INTEGRAL, RXTE and XMM Newton observations –

L. Kuiper,[1] P.R. den Hartog[1] and W. Hermsen[1,2]

[1] SRON, Netherlands Instituut for Space Research, Sorbonnelaan 2, 3584 CA, Utrecht, The Netherlands
[2] Sterrenkundig Instituut "Anton Pannekoek", University of Amsterdam, Kruislaan 403, 1098 SJ, Amsterdam, The Netherlands
E-mail(LK): L.M.Kuiper@sron.nl

Abstract

In this paper the current status of high-energy research on the hard X-ray characteristics of the persistent emission from magnetars is reviewed. Focus is put on recent intriguing results for 1RXS J1708-40 from phase resolved spectral analysis over a 2 decades wide energy band ($\sim 3-300$ keV) combining contemporaneous RXTE, XMM and INTEGRAL data. For 1E 1841-045 and SGR 1806-10 we also present updated results. The perspective for future MAXI observations for this source class is also addressed.

Key words: Anomalous X-ray pulsars — Soft gamma-ray repeaters — hard X-rays — soft gamma-rays — persistent emission

1. Introduction

Anomalous X-ray pulsars (AXP) belong to a class of rare objects concentrated along the galactic plane and emitting pulsed X-rays with pulse periods in the range $\sim 2-12$ s, characteristic spin-down time scales of $\sim 10^3-10^5$ year and surface magnetic dipole field strengths well above the quantum critical value of $B_{QED} \simeq 4.4 \times 10^{13}$ Gauss. The fact that the observed X-ray luminosity is much larger than the spin-down power excludes an interpretation in which the (pulsed) X-ray emission originates from a spin-down powered pulsar (see e.g. Kaspi 2007 or Woods & Thompson 2006 for reviews on AXPs). On the other hand the lack of apparent bright optical counterparts and the absence of periodic modulation of the X-ray pulsations exclude an interpretation involving accreting compact sources.

Currently, models based on the decay of very strong magnetic fields ($10^{14}-10^{15}$ G) - so called "magnetar" models (e.g. Thompson, Lyutikov & Kulkarni 2002 and Thompson & Duncan 1996 and references therein) - explain the observed soft X-ray characteristics (0.5–10 keV) of AXPs at a satisfactory level. Bursting and (rotational) glitching behaviour have been observed from AXPs. These phenomena are common for Soft Gamma-ray Repeaters (SGRs) for which the magnetar model originally was developed. These shared properties provide strong evidence that both AXPs and SGRs are members of the same source class.

The X-ray spectra of AXPs in the 0.5–10 keV band are very soft and can be described empirically by a black body plus a power-law model. The softness of the spectra below ∼10 keV (power-law indices all >2) predicted non-detections for energies above ∼10 keV and thus explains the initial ignorance of studying the spectral properties of AXPs at energies above 10 keV.

It was, therefore, a big surprise that INTEGRAL IBIS-ISGRI (20-300 keV) measured hard X-rays from the direction of three AXPs.

Molkov et al. (2004) reported the discovery of an INTEGRAL source at the position of AXP 1E 1841-045 in SuperNova Remnant (SNR) Kes 73 for energies up to 120 keV. This was followed up by Kuiper et al. (2004), who analysed archival RXTE PCA and HEXTE data from monitoring observations, to prove that the hard X-ray emission comes from the AXP and not from the SNR. They discovered pulsed hard X-ray/soft γ-ray emission up to ∼150 keV.

Since then Revnivtsev et al. (2004) and den Hartog et al. (2006) published the INTEGRAL detections of AXP 1RXS J1708-40 and AXP 4U 0142+61, respectively. These works were again followed up by a search in archival RXTE PCA and HEXTE data (Kuiper et al. 2006) and pulsed hard X-ray emission was detected.

Currently ten AXPs (one should be considered as a candidate AXP) and five SGRs are known. For three persistently "bright" AXPs hard X-ray spectra (>20 keV) have been measured with INTEGRAL up to at least 150 keV. For the other seven AXPs no persistent

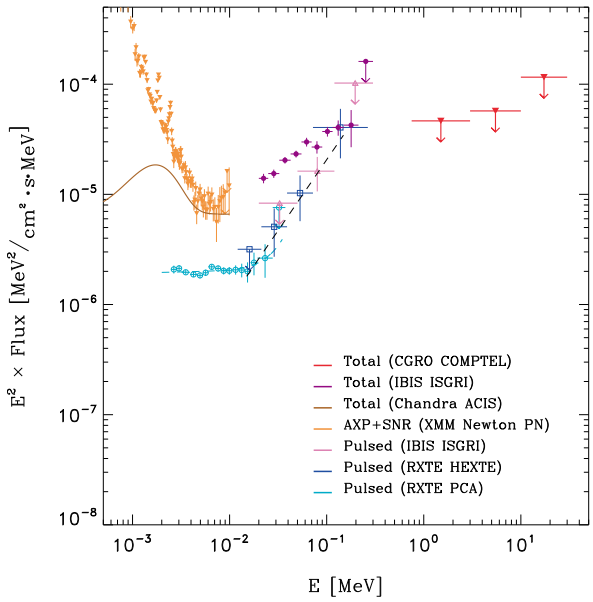

Fig. 1. High-energy total and pulsed spectra of 1E 1841-045 combining RXTE PCA, HEXTE and INTEGRAL ISGRI data for the $\sim 3-300$ keV pulsed spectrum; XMM Newton EPIC and INTEGRAL ISGRI for the total spectrum from 1E 1841-045 and Kes 73; and Chandra ACIS for the total (=pulsed plus DC) emission from 1E 1841-045. Also, CGRO COMPTEL 2σ upper-limits are shown. Note, the drastic upturn of the pulsed emission near 15 keV. The emission is 100% pulsed beyond ~ 100 keV.

hard X-ray detections can yet be claimed from the INTEGRAL data[1]. Also, from two SGRs, SGR 1806-10 (Mereghetti et al. (2005), Molkov et al. (2005)) and SGR 1900+14 (Götz et al. 2006), persistent hard X-ray emission has been detected. In the magnetar model persistent hard X-ray emission was initially ignored. Since the new findings described in this review, several theoretical attempts to explain the hard X-ray characteristics have been made (Heyl & Hernquist 2005(a,b), 2007; Thompson & Beloborodov 2005; Beloborodov & Thompson 2007; Baring & Harding 2007, 2008). However, so far theoretical consensus has not been reached and the observed phenomenology remains unexplained. In this paper the observational aspects are addressed and we summarize the hard X-ray/soft γ-ray emission characteristics above ~ 20 keV for the currently known sample of five magnetars emitting hard X-rays.

2. Persistent hard X-ray/soft γ-ray magnetars

2.1. 1E 1841-045 (in SNR Kes 73)

1E 1841-045 is located at the very center of SNR Kes 73. In the source catalogue published by Molkov et al. (2004), surveying the Sagittarius Arm tangent region, a hard X-ray (18-120 keV) source was reported from imaging studies positionally consistent with 1E 1841-045 and Kes 73. Subsequent work by Kuiper et al. (2004) showed that the emission above ~ 20 keV could be attributed, surprisingly, to the anomalous X-ray pulsar because the pulsed fingerprint was detectable up to ~ 150 keV using RXTE HEXTE (15-250 keV) data. The pulsed spectrum above ~ 10 keV appeared to be very hard with a photon index of 0.94 ± 0.16. The spectral picture for energies between 0.5 and 300 keV was updated by Kuiper et al. (2006) including now for the first time the total flux measurements from INTEGRAL IBIS ISGRI derived for seven logarithmically binned energy bands between 20 and 300 keV using INTEGRAL data collected between March 10, 2003 and Nov. 8, 2004. The RXTE HEXTE total flux values were abandoned in that work because it was realized that these were inaccurate due to the non-imaging nature of the instrument (on-off observation strategy with relatively large field of views). The total emission from 1E 1841-045 above 20 keV was consistent with a power-law model with a photon index of 1.32 ± 0.11. Comparison of the pulsed and total spectra above ~ 20 keV indicated that the emission is consistent with being 100% pulsed for energies beyond 100 keV. Assuming that the emission level above 20 keV is reasonably stable CGRO COMPTEL measurements performed earlier between 1991-2000 in the 0.75-30 MeV band demand a spectral break in the range 300 - 750 keV. Also, Kuiper et al. (2006) confirmed the presence of the pulsed signal in the > 20 keV INTEGRAL ISGRI data. In this work an updated INTEGRAL ISGRI total spectrum (20-300 keV) in ten logarithmically binned energy bands is presented using data from INTEGRAL observations performed between March 10, 2003 and May 26, 2006. Spectral analysis adopting a power-law model yields a photon index of 1.39 ± 0.05 and a 20-100 keV flux of $(5.9 \pm 0.2) \times 10^{-11}$ erg/cm^{2}s. The 20-300 keV spectral data do still not reveal a spectral break in this range. The current high-energy picture is shown in Fig.1.

2.2. 4U 0142+61

The detection of 4U 0142+61 at hard X-rays was announced by den Hartog et al. (2004) using INTEGRAL ISGRI data from survey observations of the Cassiopeia region performed in December 2003. More detailed information was provided by den Hartog et al. (2006), particularly, they measured a very hard, $\Gamma = 0.73 \pm 0.17$, power-law like spectrum for the total emission over the 20-150 keV range, and a luminosity in the 20-100 keV band of about 440 times the rotational energy loss. Moreover, they reported CGRO COMPTEL upper limits for the 0.75-30 MeV band demanding a spectral break between ~ 100 and 750 keV, assuming stable high-energy emission during the different CGRO and INTEGRAL observation epoches.

*[1] Pulsed high-energy emission up to ~ 24 keV has been detected from 1E 2259+586 in RXTE PCA data combining ~ 750 ks of exposure.

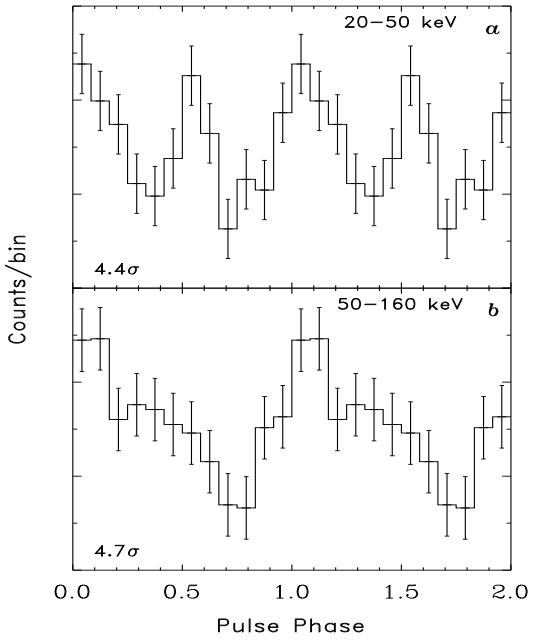

Fig. 2. The hard X-ray/soft γ-ray pulse profiles of 4U 0142+61 as measured by INTEGRAL IBIS ISGRI for the 20-50 (top) and 50-160 (bottom) keV bands. Significances of 4.4σ and 4.7σ are obtained for both bands, respectively.

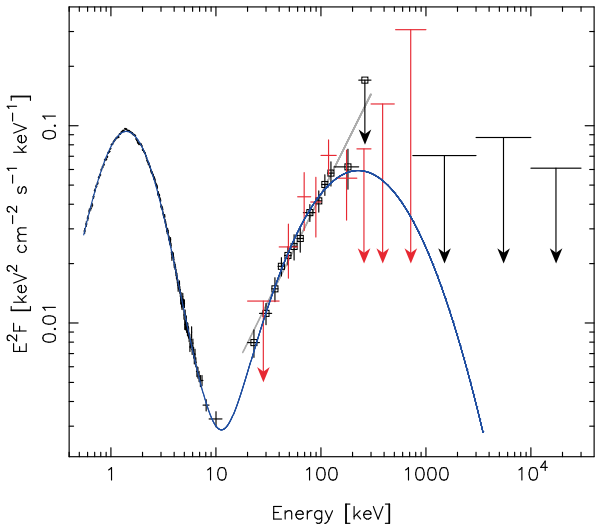

Fig. 3. The total high-energy spectrum of 4U 0142+61 from 0.5 keV up to 30,000 keV combining contemporaneous INTEGRAL ISGRI and SPI (red) data along with XMM Newton EPIC data. The best fit model (blue; a double log-parabola spectral model over the 0.5-1,000 keV band) has also been superposed together with CGRO COMPTEL upper limits (2σ). A spectral break is evident from these spectral measurements.

Revisiting archival RXTE data collected over the period March 28, 1996 - Sept. 18, 2003 Kuiper et al. (2006) found the pulsed signal of 4U 0142+61 up to ~ 50 keV in RXTE HEXTE data. The pulsed spectrum over the 2-32 keV range could be described adequately by a double power law model with a soft and hard index of $\Gamma_s = 4.09 \pm 0.04$ and $\Gamma_h = -0.8 \pm 0.10$, respectively. Such a drastic hardening, around 10 keV, had never been observed for any source.

den Hartog et al. (2008a) published the most detailed findings at high-energies for 4U 0142+61. By combining 4.5 Ms of screened INTEGRAL ISGRI data from observations performed between Dec. 12, 2003 and Aug. 13, 2006 they detected pulsed emission from 4U 0142+61 up to ~ 160 keV. The two profiles for the 20-50 keV (4.4σ) and 50-160 keV (4.7σ) bands are shown in Fig.2(a,b), respectively. The integral 20-160 keV pulsed signal reached a 6.5σ significance. The total high-energy signal ($>$ 20 keV) was studied for different epoches and no evidence was found for significant long-term time variability. Both the flux and photon index were stable within the 17% level (1σ). These authors also reported evidence for a spectral break in the total spectrum above 20 keV combining contemporaneous INTEGRAL ISGRI (20-300 keV) and SPI (20-1000 keV) data: the νF_ν spectrum peaks at 228^{+65}_{-41} keV. The total spectrum from 0.5 to 30,000 keV is shown in Fig. 3 displaying XMM Newton, INTEGRAL ISGRI and SPI and CGRO COMPTEL measured flux values and upper limits. The best fit model (blue; see for details den Hartog et al., 2008a) is superposed.

In den Hartog et al. (2008a) phase-resolved spectral analysis results were presented for three relatively broad phase intervals with boundaries dictated by the observed emission features in the underlying pulse-profiles over the 0.5 to 300 keV range. Data from RXTE PCA, INTEGRAL ISGRI, XMM Newton and (non-contemporaneous) ASCA GIS were combined for this purpose using consistent phase aligning. The ASCA GIS data showed different pulse morphologies and flux levels compared to data from the later performed XMM Newton and RXTE PCA observations. This might be related to a glitch happening near the ASCA observation. Clear trends are visible in the phase-resolved pulse-emission spectra (see for more details den Hartog et al., 2008a).

2.3. 1RXS J1708-40

High-energy emission ($>$ 20 keV) from 1RXS J1708-40 was reported by Revnitsev et al. (2004) and was confirmed by Kuiper et al. (2006) using more INTEGRAL data. Revisiting archival RXTE data (Jan. 12, 1998 - Oct. 26, 2003) and using INTEGRAL ISGRI data these authors detected pulsed emission even above 75 keV.

den Hartog et al. (2008b) presented new updates on the high-energy emission research using now all available (Jan. 29, 2003 – Oct. 5, 2006) INTEGRAL ISGRI data with 1RXS J1708-40 in the field of view. The total screened good time exposure was $\sim$ 12 Ms, which translated in an effective on-axis exposure of $\sim$ 5.2 Ms.

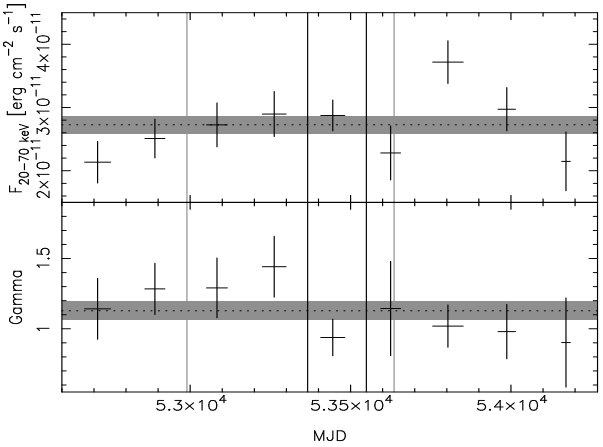

Fig. 4. Temporal behaviour of the hard X-ray flux in the 20-70 keV band (top) and photon index (bottom) of 1RXS J1708-40 as measured by INTEGRAL IBIS ISGRI. No significant flux variations have been detected. Epoches of glitches and possible glitches are indicated by black and grey vertical lines, respectively.

The long-term variability in the 20-300 keV band was studied by performing spectral analyses on a half-year and yearly base. No significant variability was found either in flux or in photon index (see Fig. 4) in contradiction with Götz et al. (2007), who claimed long-term hard X-ray variability in relation to glitch activity. Therefore, den Hartog et al. (2008b) considered the full ISGRI dataset and derived a time-averaged total spectrum (20-300 keV), described properly by a power-law model with photon index $\Gamma = 1.13 \pm 0.06$ and a 20-150 keV flux of $(6.61 \pm 0.23) \times 10^{-11}$ erg/cm^{2}s. No hint for a spectral break could be found below 300 keV. Assuming stable high-energy emission from 1991 up to 2006 the CGRO COMPTEL 2σ upper limits require a spectral break somewhere between 300 and 750 keV.

A timing analysis of the full ISGRI dataset yielded a considerably improved pulse profile, now, with a detection significance of 12.3σ for the 20-270 keV range. Pulsed emission is detected up to $\sim$ 270 keV. The morphology of the pulse profiles as a function of energy from 0.5 up to 270 keV is shown in Fig. 5. XMM-Newton EPIC PN data have been used for the part below 12 keV. Drastic morphology changes are visible in this collage. From these pulse profiles the total pulsed spectrum of 1RXS J1708-40 has be derived. Both the total and total pulsed spectrum (RXTE PCA and HEXTE data are also included) of 1RXS J1708-40 are shown in Fig. 6. The high-energy emission is consistent with being 100% pulsed beyond $\sim$ 150 keV.

The excellent statistics in the timing domain for INTEGRAL ISGRI (20-300 keV) and RXTE PCA (3-30 keV) allowed to explore the spectral characteristics as a function of phase over the 3-300 keV band. The phase-resolved spectra in ten 0.1 – wide phase bands over 2

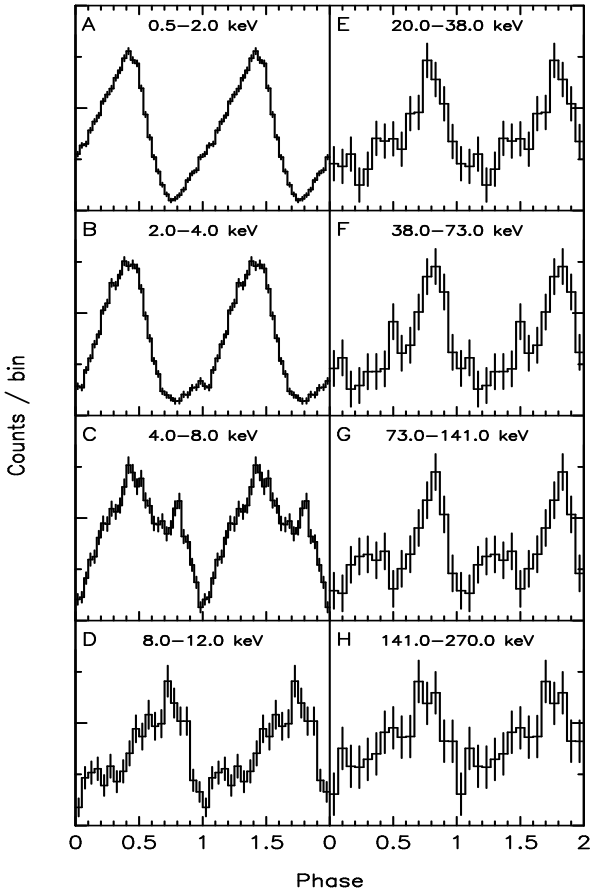

Fig. 5. Pulse profiles of 1RXS J1708-40 from soft to hard X-rays using XMM Newton EPIC PN data (0.5-12 keV) and INTEGRAL ISGRI data (20-270 keV). Note the stable morphology for energies beyond 20 keV.

decades in energy are shown as data points in Fig. 7. From these spectra three distinct spectral components with completely different shapes could be recognized: a) a soft PL with index 3.58 ± 0.34, b) a hard PL with index 0.99 ± 0.05 and c) a composite spectral model contributing over phases 0.7-0.9. These three spectral components have subsequently been used in spectral fit procedures fitting the data of each phase slice in terms of the sum of three model components, each with a free scale. The phase distributions of the normalizations of these three components, all evaluated at the pivot energy of 15.04 keV, are shown in Fig. 8 and represent three decoupled pulse profiles. The soft component peaks around phase 0.4 (c.f. Fig. 5), while the other two components peak around phase 0.8. The width of the curved component ($\sim$ 0.25 in phase) is about half the width of the hard component. These new results from phase resolved spectral analysis give important constraints showing that three dimensional modeling covering both the geometry of the emission regions and the different production processes is required to explain the findings.

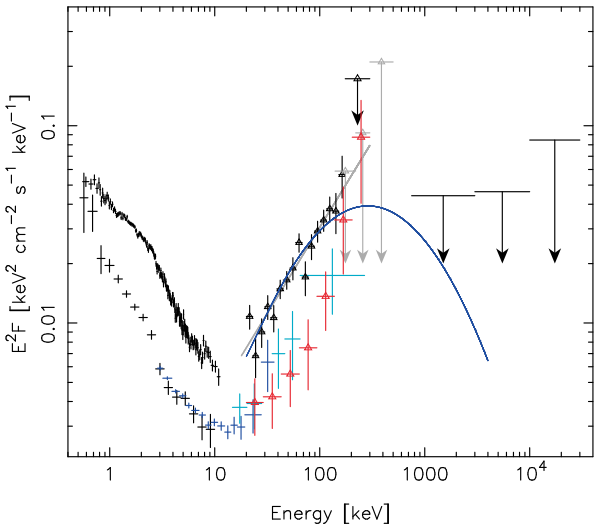

Fig. 6. The total and total pulsed high-energy (0.5-300 keV) spectrum of 1RXS J1708-40 as measured by XMM Newton (total, pulsed), RXTE PCA (pulsed), RXTE HEXTE (pulsed) and INTEGRAL IBIS ISGRI (total, pulsed). CGRO COMPTEL (0.75-30 MeV) 2σ upper limits are included for the total emission as well (see for more details den Hartog, 2008b).

2.4. SGR 1806-10

Persistent high-energy emission of SGR 1806-10 was detected by Mereghetti et al. (2005) and Molkov et al. (2005) using INTEGRAL ISGRI data from 2003-2004 observations, all taken before the giant flare of December 27, 2004. They found emission up to $\sim$ 200 keV with a power-law shape with photon index in the range 1.5 –1.9, significantly harder than the spectrum of a typical burst showing a thermal bremsstrahlung spectrum. A remarkable property exhibited by this source is that both the spectral hardness and intensity correlate with the burst rate or activity level, which culminated in the giant flare at the end of 2004. Pulsed emission, both pre- and post giant flare, is detected up to $\sim$ 30 keV using RXTE PCA data. It is *not* detected in either RXTE HEXTE or INTEGRAL ISGRI data (Kuiper et al. in prep.), indicating very low values for the pulsed fraction at energies beyond $\sim$ 20 keV contrary to what has been observed for the three AXPs showing hard spectral tails. The morphologies of the pulse profiles show drastic changes as a function of energy, from smooth single peaked (2-5 keV) to double peaked with one (very) sharp pulse in the 10-15 keV band.

2.5. SGR 1900+14

Götz et al. (2006) reported the detection of hard X-ray emission from SGR 1900+14 above 20 keV using INTEGRAL data collected during 2003-2004 observations. The total 20-100 keV emission spectrum could be described by a power-law model with a rather soft photon index of 3.1 ± 0.5. Triggered by this result Esposito et al.

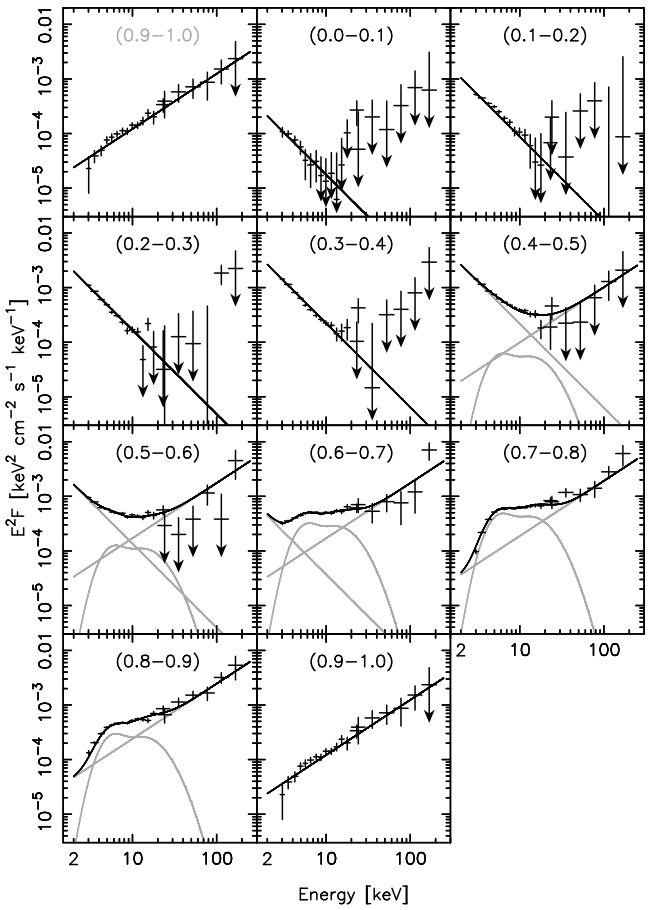

Fig. 7. Narrow-band ($\Delta\Phi = 0.1$) phase resolved spectra of 1RXS J1708-40. Phase intervals are indicated in the panels. Spectral fits using three components are superposed (black) as well as the component contribution separately (grey). Note the drastic change in shape moving from phase interval 0.9-1.0 to 0.0-0.1: the power-law index switched from very hard, $\Gamma = 0.99 \pm 0.05$, to very soft, $\Gamma = 3.58 \pm 0.34$.

(2007) revisited the BeppoSAX observations and found in the BeppoSAX observation performed before the August 27, 1998 giant flare indications for a hard spectral tail with a photon index 1.6 ± 0.3 at a $4\times$ larger flux level in the 20-100 keV band. This implies a drastic change in spectral behaviour before and after the 1998 giant flare.

3. Summary

From this review it is clear that detailed observations in the high-energy window are crucial for understanding the physical processes taking place under extreme conditions on the surface and in the magnetosphere of magnetars. A significant fraction of the magnetars currently known emit very luminous high-energy (> 20 keV) radiation. Hard spectral tails have been detected in the total emission from AXPs with power-law indices in the range 0.9–1.4, and somewhat softer tails for SGRs. Spectral breaks or bends in the total spectrum of AXPs occur

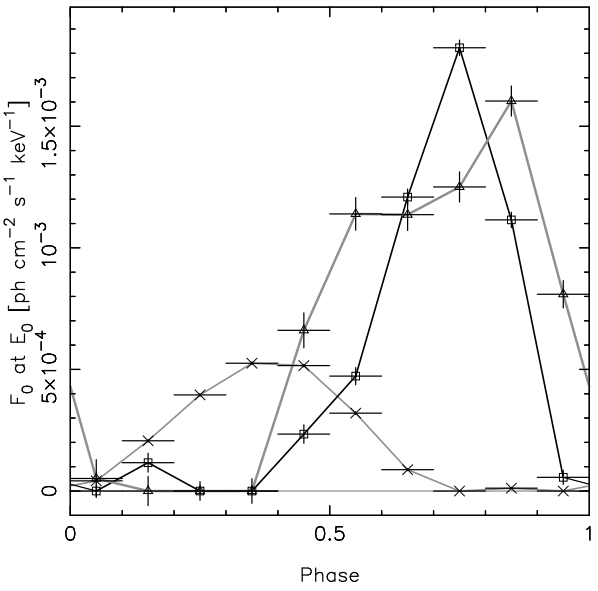

Fig. 8. Phase distributions of the normalizations, evaluated at 15.04 keV (the pivot energy), of the three spectral-model components. The soft PL component is indicated by crosses and a thin grey line, the hard PL by triangles and a thick grey line, and finally, the composite model by squares and a black line.

above $\sim$ 250 keV. The pulsed emission (AXPs) above 10 keV is even harder with indices between -1 and 1. For AXPs the pulsed fraction approaches 100% near 100-150 keV. So far, from SGRs no persistent pulsed emission has been detected above $\sim$ 30 keV. We have shown in phase-resolved spectral analyses that distinctly different components contribute to the total pulsed emission. These findings require theoretical models involving different production processes taking place at different sites in the magnetosphere.

4. MAXI perspective for magnetar research

With a 10 times larger sensitivity than the RXTE ASM (2-12 keV), observations with the Gas Slit Camera (GSC) of MAXI aboard the International Space Station (ISS) can be very useful for the research on AXPs and SGRs. This instrument sensitive to photons with energies in the range 2-30 keV has 12 cameras with proportional counters totaling a sensitive area of 5350 cm^2. Due to the scanning nature of the experiment a typical celestial source is twice per ISS orbit for 22 s in the field of view ($1\overset{\circ}{.}5 \times 160^\circ$) of one of the two camera arrays each consisting of six cameras. This strategy yields a 5σ sensitivity of $\sim$ 1 mCrab in a one-week accumulation. This is amply sufficient to determine the (total) emission state on a daily base for most of the AXPs which have total fluxes of about 5 mCrab between 2 and 10 keV. Above 10 keV the sensitivity of the MAXI GSC is too low to obtain meaningful results. Due to the sparse covering factor (0.8% duty cycle) of a source per ISS orbit of $\sim$ 90 minutes, there is little chance to catch a fast transient event lasting from seconds to minutes on the fly. Enhanced fluxes levels of AXPs and SGRs lasting from days to weeks can, however, easily be signalled provided that the flux level is sufficiently high. A point of concern is the rather crude angular response of $1\overset{\circ}{.}5$ (FWHM) which will give source confusion in crowded regions near the Galactic plane where the AXPs and SGRs are located. However, given the time resolution of 120μs of the GSC, for the bright AXPs, 4U 0142+61, 1RXS J1708-40 and 1E 1841-045, the sensitivity is high enough to extract the pulsed flux, typically 1 mCrab in the 2-10 keV band, from weekly accumulations. This allows also the construction of a pulsar ephemeris, the set of timing parameters determining the rotation behaviour of the pulsar as a function of time. This information is crucial for instruments like INTEGRAL IBIS ISGRI for which the extraction of the pulsed signal relies on pulse-phase folding techniques because of the weakness of the signal.

References

Baring M.G. & Harding A.K., 2007, Ap&SS 308, 109
Baring M.G. & Harding A.K., 2008, AIP Conf. Proc. 968, 93
Belobodorov A.M. & Thompson C., 2007, ApJ 657, 967
den Hartog P.R., et al., 2004, ATEL #293
den Hartog P.R., et al., 2006, A&A, 451, 587
den Hartog P.R., Kuiper L., Hermsen W, et al., 2008a, A&A, 489, 245
den Hartog P.R., Kuiper L., Hermsen W, 2008b, A&A, 489, 263
Esposito P., et al., 2007, A&A, 461, 605
Götz D., et al., 2006, A&A, 449, L31
Götz D., et al., 2007, A&A, 475, 317
Heyl J.S. & Hernquist L., 2005a, ApJ 616, 463
Heyl J.S. & Hernquist L., 2005b, MNRAS 362, 777
Heyl J.S., 2007, Ap&SS 308, 101
Kaspi V.M, 2007, Ap&SS 30, 1
Kuiper L., Hermsen W. & Mendez M. 2004, ApJ 613, 1173
Kuiper L., et al., 2006, ApJ, 645, 556
Mereghetti S., et al., 2005, A&A 433, L9
Molkov S.V., et al., 2004, Astronomy Letters 30, 534
Molkov S.V., et al., 2005, A&A 433, L13
Revnivtsev M.G., et al., 2004, Astronomy Letters 30, 382
Thompson C. & Duncan R.C., 1996, ApJ 473, 322
Thompson C., Lyutikov M., & Kulkarni S.R., 2002, ApJ 574, 332
Thompson C. & Belobodorov, 2005, ApJ 634, 565
Woods P. & Thompson C., 2006, In: Lewin, W., van der Klis, M. (eds) Compact Stellar X-ray Sources. Cambridge Astrophysics Series, vol. 39, 547

X-ray Study of Classical Novae : V458 Vul and V2491 Cyg

Dai Takei,[1] Masahiro Tsujimoto,[2,3*] Jeremy Drake,[3] Jan-Uwe Ness,[4†] Shunji Kitamoto[1] and Hiroshi Murakami[1]

[1] Department of Physics, Rikkyo University, 3-34-1 Nishi-Ikebukuro, Toshima, Tokyo 171-8501
[2] Department of Astronomy & Astrophysics, Pennsylvania State University,
525 Davey Laboratory, University Park, PA 16802, USA
[3] Japan Aerospace Exploration Agency, Institute of Space and Astronautical Science,
3-1-1 Yoshino-dai, Sagamihara, Kanagawa 229-8510
[4] School of Earth and Space Exploration, Arizona State University, Tempe, AZ 85287, USA
[5] Smithsonian Astrophysical Observatory, MS-3, 60 Garden Street, Cambridge, MA 02138, USA
E-mail(DT): takei@ast.rikkyo.ac.jp

Abstract

We conducted target of opportunity X-ray observations of the classical novae V458 Vulpeculae and V2491 Cygni using the Suzaku satellite. With a short exposure of ∼20 ks each, we obtained well-exposed spectra, enriching unique data sets of the shock X-ray emission from classical novae. V458 Vulpeculae shows lots of emission lines with a ∼1 keV plasma temperature, while V2491 Cygni shows an emission line from Fe with a ∼3 keV plasma temperature and a hard X-ray component. We report the results of these observations in this proceedings.

Key words: workshop: proceedings — stars: novae — X-rays: stars

1. Introduction

Classical novae are a class of cataclysmic variables. Sudden outburst occurs by nuclear fusion of hydrogen on the white dwarf surface. In a typical classical nova, the visual magnitude increases by ∼10 magnitudes within a few days. X-rays are emitted at various stages in the post-burst evolution via different mechanisms. Hard X-rays are emitted in an early phase, originating presumably from a shock in the expanding ejecta. Soft X-rays emerge in a later phase, arising from the photospheric emission of the white dwarf. The mass and chemical composition of the ejecta, the transition process, and the white dwarf mass can be estimated with X-ray spectroscopy, but almost all previous novae (except for a few bright enough for grating spectroscopy) were studied with insufficient statistics and spectral resolution. The X-ray Imaging Spectrometer (XIS) aboard the Suzaku satellite can obtain spectra of moderately bright novae with high signal-to-noise ratio and medium energy resolution in a reasonable telescope time. Here, we report the results of Suzaku observations of two recent novae — V458 Vulpeculae (Tsujimoto et al. 2008) and V2491 Cygni (Takei et al. 2008) — using the XIS, exposing for ∼20 ks each in the director's discretionary time.

** Chandra Fellow
*† Chandra Fellow

2. V458 Vulpeculae

V458 Vulpeculae was discovered on 2007 August 8 (Nakano et al. 2007; Samus 2007). Optical observations have been conducted since then. Swift failed to detect the initial X-rays, but reported its first detection on day 70 (Drake et al. 2007) and continued its monitoring. We conducted a ∼20 ks target of opportunity (ToO) observation with Suzaku on day 88. The background-subtracted spectrum was shown in figure 1. We identified emission lines from N, Ne, Mg, Si, S, and Ar. We fitted the spectrum using an isothermal optically-thin plasma model (APEC; Smith et al. 2001) with an interstellar extinction (wabs; Morrison & McCammon 1983). In addition, an absorbed power-law model (dotted lines in figure 1, $N_H = 8.9\times10^{21}$ cm^{-2}, $\Gamma = 2.2$) was added to account for the contribution by a nearby source. The best-fit parameters are shown in table 1.

3. V2491 Cygni

V2491 Cygni was discovered on 2008 April 10 (Nakano et al. 2008; Samus 2008). The optical light curve has an unusual behavior, showing a clear rebrightening followed by a sudden fading around day 15. Two ∼20 ks observations were performed with the Suzaku on days 9 and 29, just before and after the rebrightening. The second data are being processed now and not presented in this proceedings. In the first data, an emission line from Fe and a hard X-ray component was found in the spectrum

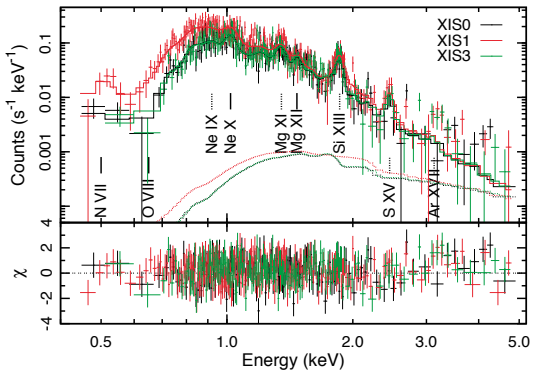

Fig. 1. XIS background-subtracted spectrum.

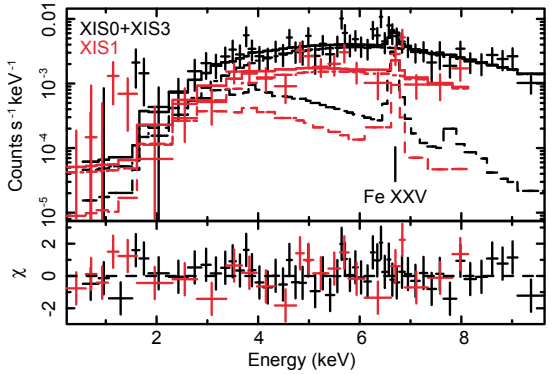

Fig. 2. XIS background-subtracted spectrum.

Table 1. Best-fits spectral parameters of V458 Vulpeculae.

Param.	Unit	Value
$N_{\rm H}^{*}$	($\rm cm^{-2}$)	3.1 (1.8–4.9)$\times10^{21}$
$k_{\rm B}T^{*}$	(keV)	0.64 (0.57–0.71)
$Z_{\rm N}^{*}$	(solar)	4.2 (0.0–)
$Z_{\rm O}^{*}$	(solar)	0.0 (0.0–2.3)
$Z_{\rm Ne}^{*}$	(solar)	0.6 (0.3–2.3)
$Z_{\rm Mg}^{*}$	(solar)	0.5 (0.2–0.7)
$Z_{\rm Si}^{*}$	(solar)	0.6 (0.3–1.8)
$Z_{\rm S}^{*}$	(solar)	0.8 (0.1–2.5)
$Z_{\rm Fe}^{*}$	(solar)	0.2 (0.1–0.5)
$Z_{\rm Ni}^{*}$	(solar)	0.2 (0.1–0.5)
$F_{\rm X}^{*\dagger}$	($\rm erg\ s^{-1}\ cm^{-2}$)	1.1 (0.4–1.7)$\times10^{-12}$
χ^2/d.o.f.	.....	394.3/440

* The uncertainties are indicated by the 90% confidence range. The upper limit for $Z_{\rm N}$ is unconstrained.
† The X-ray flux in the 0.45–5.0 keV band.

Table 2. Best-fits spectral parameters of V2491 Cygni.

Param.	Unit	Value
$N_{\rm H}^{*}$	($\rm cm^{-2}$)	8.1 (4.3–20.1)$\times10^{22}$
$k_{\rm B}T^{*}$	(keV)	3.1 (1.4–10.7)
Z^{*}	(solar)	3.0 (0.2–5.0)
$F_{\rm X}^{*\dagger}$(APEC)	($\rm erg\ s^{-1}\ cm^{-2}$)	1.0 (0.1–26.4)$\times10^{-13}$
Γ	.....	-0.4 (-1.7–$+0.1$)
$F_{\rm X}^{*\dagger}$(Power)	($\rm erg\ s^{-1}\ cm^{-2}$)	9.2 (0.5–18.9)$\times10^{-13}$
χ^2/d.o.f.	.....	64.5/72

* The uncertainties are indicated by the 90% confidence range.
† The X-ray flux in the 2.0–10.0 keV band.

(figure 2). We fitted the spectrum using an optically-thin plasma (APEC; Smith et al. 2001) and a power-law model with an interstellar extinction (wabs; Morrison & McCammon 1983). The best-fit parameters are shown in table 2.

4. Summary

We conducted Suzaku ToO observations of the classical novae V458 Vulpeculae and V2491 Cygni. With a short exposure of 20 ks each, we obtained well-exposed spectra, enriching unique data sets of the shock X-ray emission from classical novae. The two spectra are strikingly different. V458 Vulpeculae shows lots of emission lines with a ∼1 keV plasma temperature. The possible overabundance of N against other metals indicates that the plasma has an ejecta origin. V2491 Cygni is much harder. In addition to the ∼3 keV thermal component, a power-law component is necessary to explain the spectrum extending beyond 10 keV, which is indicative of a particle acceleration. In a quick-look data of the second V2491 Cygni observation, the spectrum is entirely different from the two presented here. These entirely different spectra and multiple spectral components may represent different stages of the shock evolution, but their relation is unclear. Obtaining well-exposed X-ray spectra of various novae at various epochs is vital for a better understanding. We demonstrated that Suzaku XIS data are capable of doing this. We will continue our Suzaku ToO studies in collaboration with Swift. We expect several sources per year can be a good target for Suzaku ToO. The MAXI is very useful for searching and monitoring of novae. We expect further progress of evolutionary studies of novae with Suzaku-MAXI collaboration.

References

Drake, J. J., et al. 2007, The Astronomer's Telegram, 1246, 1
Morrison, R., & McCammon, D. 1983, ApJ, 270, 119
Nakano, S., Kadota, K., Waagen, E., Swierczynski, S., Komorous, M., King, R., & Bortle, J. 2007, IAU Circ., 8861, 2
Nakano, S., et al. 2008, IAU Circ., 8934, 1
Samus, N. N. 2007, IAU Circ., 8863, 2
Samus, N. N. 2008, IAU Circ., 8934, 2
Smith, R. K., Brickhouse, N. S., Liedahl, D. A., & Raymond, J. C. 2001, ApJ, 556, L91
Takei, D., et al. 2008 in prep
Tsujimoto, M., et al. 2008, PASJ, submitted.

Long Term X-ray Intensity Variations of Cen X-3

B. Paul[1] and H. Raichur[1,2,3]

[1] Raman Research Institute, Sadashivanagar, C. V. Raman Avenue, Bangalore 560080, India
[2] Joint Astronomy Programme, Indian Institute of Science, Bangalore, 560080, India
[3] Present address: University of Florida, Astronomy Department, Gainesville, FL 32611, USA
E-mail(BP): bpaul@rri.res.in

ABSTRACT

We have carried out detailed investigations of the long term X-ray flux variations of the high mass X-ray binary pulsar Cen X-3 using archival X-ray data from the *Rossi X-ray timing Explorer (RXTE)*. In the lightcurves of several observations made with the Proportional Counter Array (PCA) and covering a wide range of X-ray intensity, we have detected Quasi Periodic Oscillation (QPO). We have observed a clustering of the QPO peak frequency at 40 and 90 mHz with no dependence of the QPO frequency and occurrence of QPOs on the X-ray intensity. If the observed X-ray intensity of Cen X-3 and its long term variations are related to the mass accretion rate, the lack of QPO frequency variation of Cen X-3 is in contrast with an inner disk origin of the QPOs. Using the same *RXTE*-PCA observations, we have also measured the pulsed flux of Cen X-3 in different flux states. We found that below a certain flux level, the X-ray lightcurve does not have any pulsations while above this level, the pulsed flux increases linearly with the peak flux. This is consistent with the X-ray emission of Cen X-3 having one unpulsed component and one varying component with a constant pulsed fraction. In the low state, the unpulsed component becomes dominant. The detected X-ray emission in the low state can be due to scattering of X-rays from the stellar wind of the companion star. We have also studied the orbital modulation of the Cen X-3 X-ray lightcurve using the long term X-ray lightcurve made with the All Sky Monitor on board the *RXTE*. We found an evolution of the orbital modulation of the X-ray lightcurve as a function of the flux state. In high state, the transitions are sharp indicating that most of the observed X-rays are produced in a small region. In the low state, the orbital modulation is smooth, indicating that most of the observed X-rays are produced in an extended region, probably by scattering of X-rays from a hidden central source. The QPO measurements, the pulsed flux measurements and the orbital modulation measurements indicate that the different flux states of Cen X-3 are produced by different degree of absorption. We propose that the absorption is caused by an aperiodically precessing accretion disk.

KEY WORDS: Stars: neutron – (Stars:) pulsars: individual: Cen X-3 – X-rays: stars – (Stars:) binaries: general – X-rays: individual: Cen X-3 – X-rays: binaries

1. Introduction

Several persistent X-ray binary sources exhibit large flux variations in their X-ray lightcurves on timescales significantly longer than their orbital periods (Wen et al. 2006). The long term flux variations can be highly periodic (Her X-1, LMC X-4, 2S 0114+650, SS433, 4U 1820–303, XTE J1716–389, Cyg X-1 etc.), quasi-periodic or with unstable period (SMC X-1, GRS 1747–312, Cyg X-2, LMC X-3, X1730–333 etc.). The periodic long term intensity variations, as seen in Her X-1, are understood to be due to obscuration of the central X-ray source by a warped precessing accretion disc.

Cen X-3 is a high mass X-ray binary pulsar with a spin period of ~ 4.8 s, orbital period of ~ 2.08 d, and strong long term flux variations. The long term lightcurve of this source obtained with the All Sky Monitor (ASM) of the *Rossi X-ray Timing Explorer (RXTE)* showed aperiodic flux variations by a factor of more than 40, along with two different accretion modes (Paul, Raichur & Mukherjee 2005). As the long term intensity variation of Cen X-3 does not remotely appear to have any periodic or quasi-periodic nature, it is often assumed that the X-ray flux variation is due to changing mass accretion rate. However, *GINGA* observations revealed that there is no correlation between the observed X-ray flux and pulse period derivative of Cen X-3 (Tsunemi, Kitamoto & Tamura 1996) indicating that the observed X-ray flux of Cen X-3 may not represent its mass accretion rate.

We show here results from several investigations of Cen X-3 in different X-ray flux states, carried out

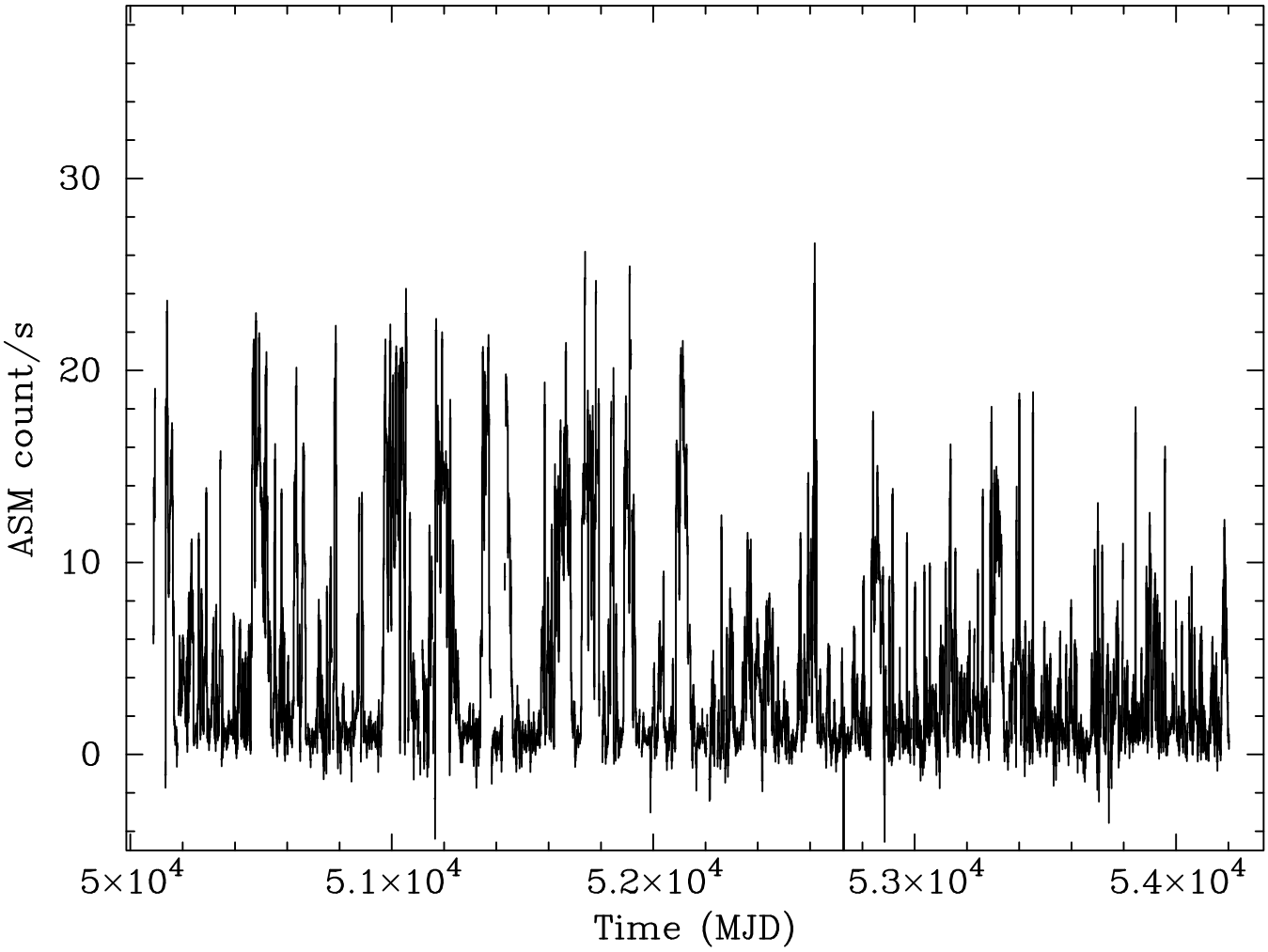

Fig. 1. The 1.5-12 keV *RXTE*-ASM lightcurve of Cen X-3 showing the aperiodic long term X-ray flux variations.

to understand the origin of its aperiodic long term flux variations. More details about these studies and comparison with Her X-1, LMC X-4 and SMC X-1 can be found in Raichur and Paul (2008a, 2008b).

2. Method

We have measured the Quasi Periodic Oscillation (QPO) feature in Cen X-3 in different flux levels using all the available *RXTE*-PCA data. In the accretion powered X-ray pulsars, the QPOs are produced due to inhomogenities in the inner accretion disk and the QPO frequency is expected to be related to the inner radius of the accretion disk. In several transient and persistent X-ray pulsars, the QPO frequency is found to be related to the X-ray flux or the inner radius (EXO 2030+375: Angelini, Stella & Parmar 1989, 3A 0535+262: Finger, Wilson & Harmon 1996, XTE J1858+034: Mukherjee et al. 2006, 4U 1626–67: Kaur et al. 2008). If the observed X-ray flux variation of Cen X-3 is due to changes in the mass accretion rate, a similar dependence of the QPO frequency and X-ray flux is expected.

We have measured the pulsed and peak X-ray emission of the source in its different flux states using the same *RXTE*-PCA observations. Evolution of the pulsed fraction with peak X-ray flux is useful to know the relative importance of scattered X-ray emission in different flux states.

We have also studied the orbital modulation of the Cen X-3 X-ray lightcurve as a function of its X-ray flux. The relative sizes of the observable X-ray source in different flux states can be known from the variations of the eclipse transition periods. The long term lightcurve obtained with the All Sky Monitor on board the *RXTE* has been used for this.

3. Results

We have analysed X-ray lightcurves from 81 observations of Cen X-3 made with the *RXTE*-PCA during 1996-

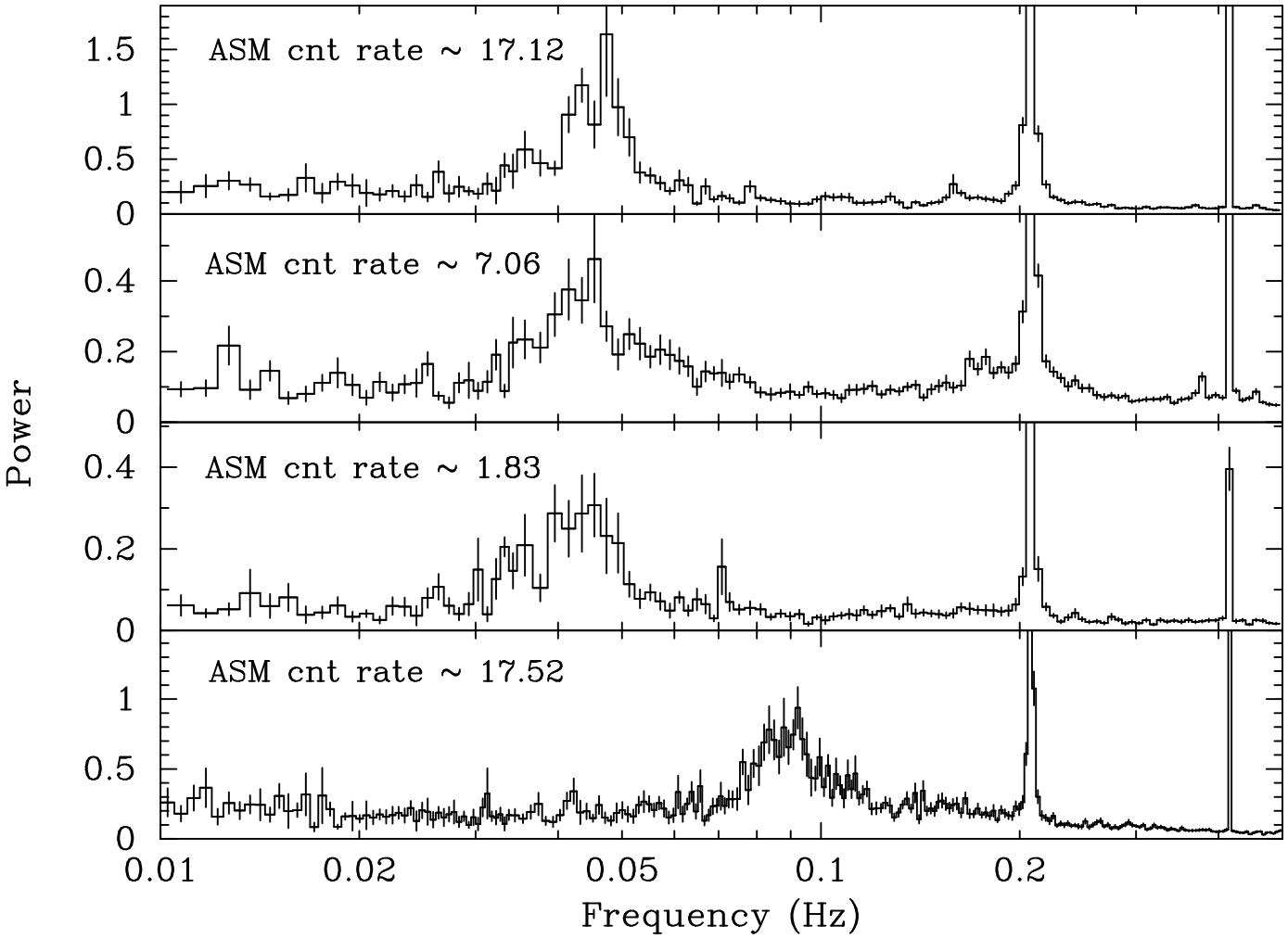

Fig. 2. The power spectra of Cen X-3 obtained from PCA lightcurves in different flux states are shown here. The top three panels show the 40 mHz QPO feature while the bottom panel shows the 90 mHz QPO feature detected only in 1996.

1998 and in 2000. The total useful exposure obtained from all these observations was 525 ks. Most of the observations were carried out outside the X-ray eclipse and data collected during the eclipses were excluded from our analysis. We have also used the 1.5-12 keV lightcurve of Cen X-3 obtained with the *RXTE*-ASM covering about 4100 days from January 1996 to study the orbital modulation in different flux states.

Power spectrum was created from each of the PCA lightcurves and we detected QPO features at 40 mHz in 9 observations and at 90 mHz in 2 observations. Four power spectra with QPO features detected in different flux states of Cen X-3 are shown in Figure 2. Inside each panel we have also shown the *RXTE*-ASM count rate of Cen X-3 during these observations indicating the flux level. We found that Cen X-3 shows intermittent QPOs in frequency ranges 40 mHz and 90 mHz. The QPO frequency and occurrence of the QPOs are not related to the flux state of the source.

Using a subset of the *RXTE*-PCA observations, we have also measured the pulsed flux of Cen X-3 as a function of the peak flux. We have selected 18 PCA observations representing a wide range of X-ray flux. The orbit averaged X-ray flux is measured simultaneously with the *RXTE*-ASM. No pulsations were detected when the orbit averaged ASM count rate of Cen X-3 was less than 0.8 count/sec which is equivalent to about 50 count/sec per proportional counter unit. In Figure 3 we have shown some of the pulse profiles obtained at different flux levels. In the top panel of Figure 3 we have shown a lightcurve folded in the low flux state when no pulses were detected. In Figure 3, apart from the changing pulsed fraction, the pulse shape is also different in different panel. We have independently verified that the pulse shape variation is not related to the X-ray flux.

In Figure 4 we have shown a plot of pulsed X-ray flux against the peak X-ray flux of Cen X-3. The pulse

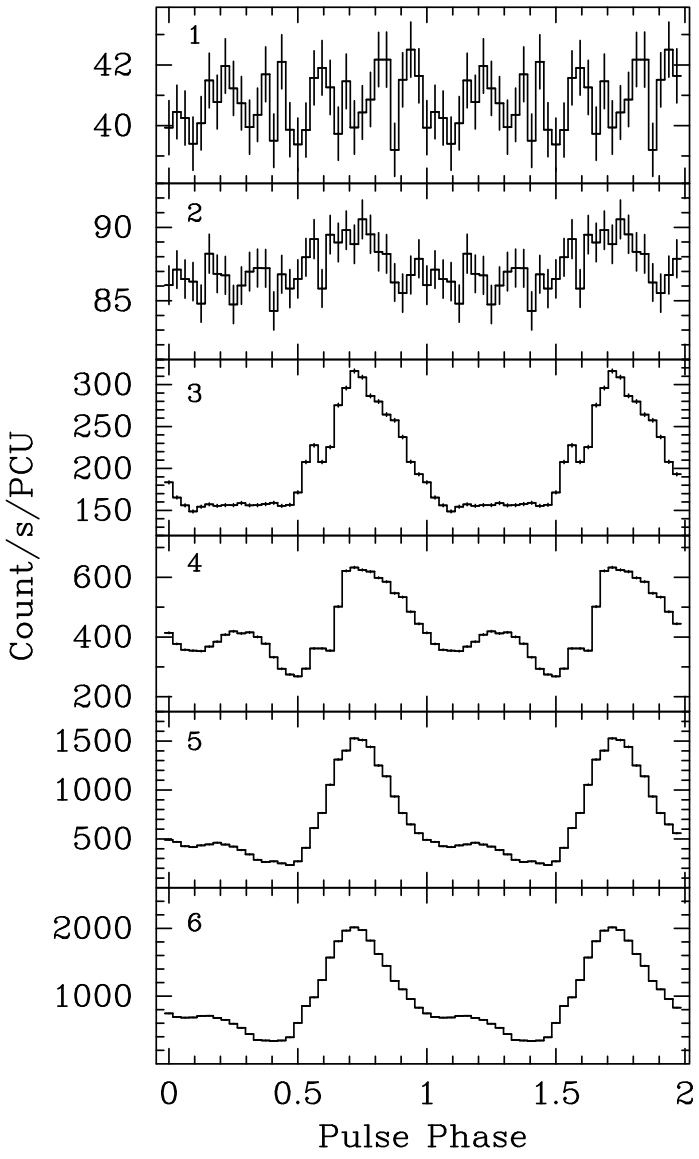

Fig. 3. Pulse profile of Cen X-3 is shown here in different flux states.

profiles shown in Figure 3 are shown in this plot with circles. We fitted the following two component function to the pulsed flux data.

$$F_{\max} - F_{\min} \simeq \begin{cases} 0, & F < F_0; \\ f(F_{\max} - F_0), & F \geq F_0; \end{cases} \quad (1)$$

We determined the value of the pulsed fraction of the pulsating component to be to be 90%, while the maximum value of the unpulsed component is a count rate of 175.5 per PCU. The pulsed X-ray flux in different flux states is consistent with the X-ray emission having two components, one with a large and constant pulsed fraction and a second unpulsed component that dominates in the low state.

From the *RXTE*-ASM data, we have made 3 separate lightcurves, one each for the high, intermediate and low flux states. First we excluded the data acquired during the X-ray eclipse and the remaining data was segregated into three sets depending on the average count rate per binary orbit of Cen X-3. These 3 lightcurves were then folded with the orbital period and intensity dependent orbital modulaton curves were obtained. The orbital modulation curves, shown in Figure 5 have been normalised with respect to the average count rate calculated over an orbital phase of 0.2 near the peak flux. The orbital modulation curves for the high and intermediate flux state are shown in the top panel while same for the low flux state is shown in the bottom panel of Figure 5. The high state data points are marked with circles. From Figure 5 we note thatn from a sharp eclipse

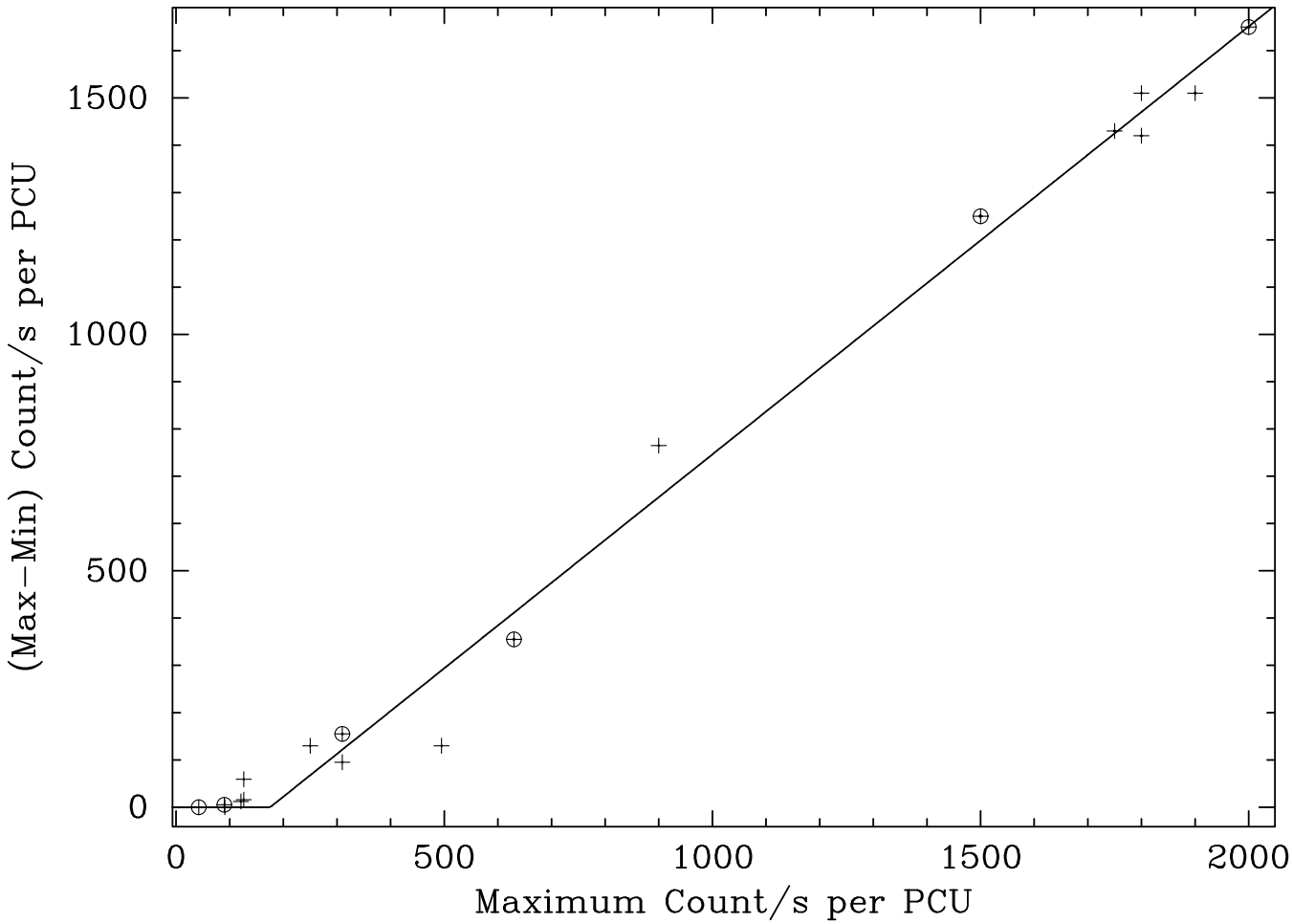

Fig. 4. Pulsed flux of Cen X-3 is plotted here against the peak flux. The points marked with circles correspond to the pulse profiles shown in Figure 3.

transition in the high flux state, the eclipse trnasitons become a gradual modulation in the low state. We have also measured that the the ratio of X-ray flux of Cen X-3 during eclipse and out-of-eclipse is larger in the low flux state by a factor of 7.0 ± 1.3 compared to the same in the high flux state. The flux state dependence of the orbital modulation pattern of Cen X-3 is very similar to that seen in the three accreting X-ray pulsars Her X-1, Cen X-3 and SMC X-1 (Naik & Paul 2003, Raichur & Paul 2008a, 2008b).

4. Discussions

The observed QPO properties of Cen X-3 is in agreement with a scenario in which the actual mass accretion rate and X-ray luminosity of the source does not change. The long term variation of the measured X-ray flux is due to change in obscuration by an aperiodically precessing warped accretion disk.

The measurement of pulsed X-ray flux as a function of the peak X-ray flux of Cen X-3 as shown in Figures 3 and 4, is consistent with a scenario in which the measured X-ray flux has two components. One component has a high pulsed fraction of 90% and is also highly variable, while the other componet is unpulsed. SMC X-1 also shows a similar characteristics over a wide range of its measured X-ray flux (Kaur, Paul, Raichur et al. 2007). The unpulsed component becomes dominant in the low state, leading to a non-detection of the pulses.

The flux dependent orbital modulations of Cen X-3 and its similarity with Her X-1, SMC X-1 and LMC X-4 indicate that in the low flux state, a large fraction of the observed X-rays are from an extended region which is comparable to the size of the companion star. A different visibility of the larger emission region in different orbital phases leads to the smooth orbital modulation in the low state.

Based on the three independent investigations briefly described above we have proposed (Raichur & Paul 2008a, 2008b) that the long term intensity variations in Cen X-3 are primarily due to obscuration of the compact

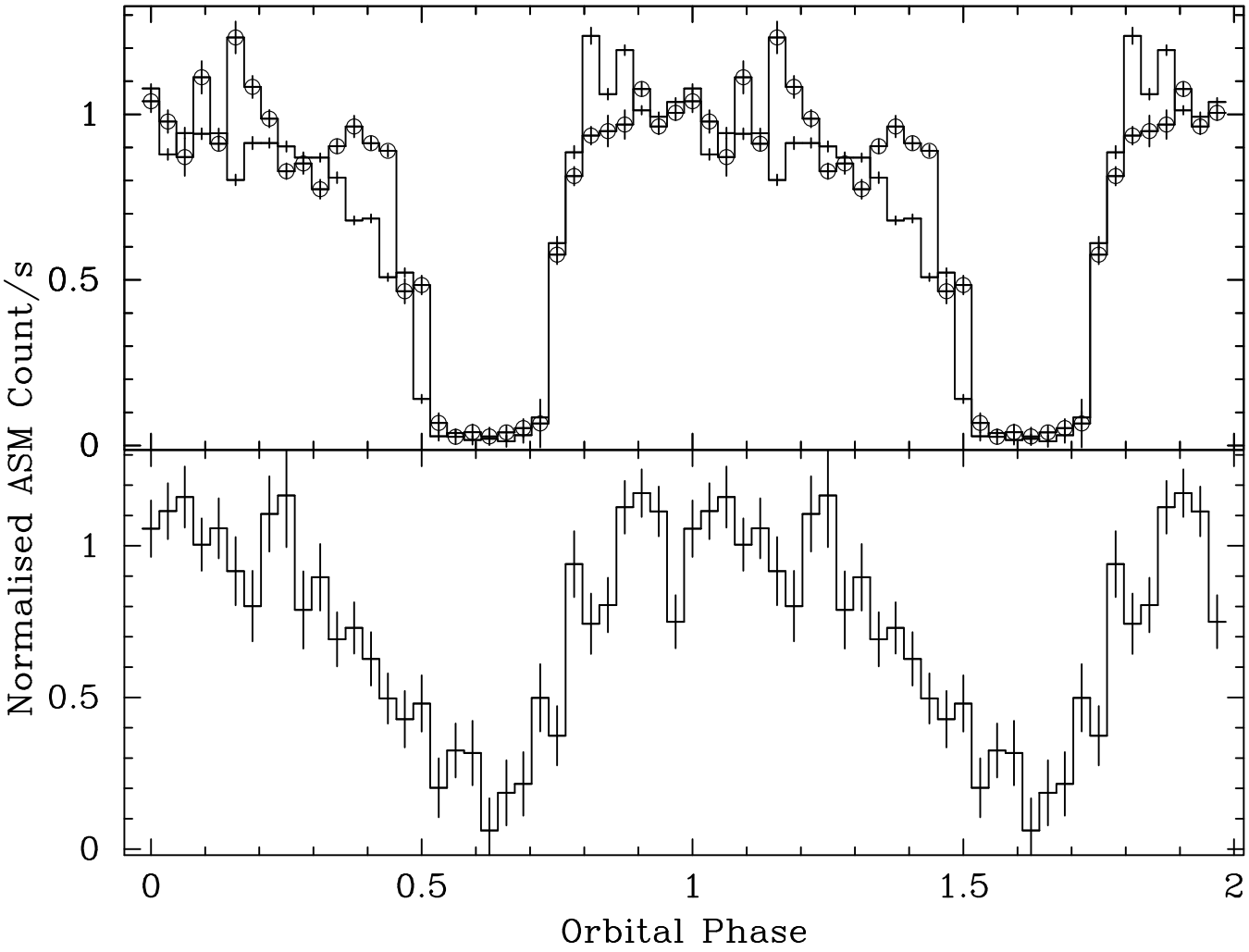

Fig. 5. Orbital X-ray modulation of Cen X-3 in high flux state (top panel, circles), medium flux state (top panel, crosses) and low flux state (bottom panel) are shown here.

X-ray source by the accretion disk. In the low flux state, the detected X-rays are unpulsed and originate from an extended region. The unpulsed X-ray emission from an extended region could be due to scattering of the X-rays from the central source by the stellar wind.

The MAXI mission will produce long term lightcurves of a large number X-ray sources with higher signal to noise ratio and over a larger energy band. The MAXI database will therefore be very useful for similar investigations in a large number X-ray binaries. For bright sources like Cen X-3, the MAXI datasets will be useful for more detailed investigations, including flux dependent spectral measurements.

References

Angelini, L., Stella, L., & Parmar, A. N., 1989, ApJ, 346, 906

Finger, M. H., Wilson, R. B., & Harmon, B. A., 1996, ApJ, 459, 288

Kaur, R., Paul, B., Kumar, B., & Sagar, R., 2008, ApJ, 676, 1184

Kaur, R., Paul, B., Raichur, H., Sagar, R., 2007, ApJ, 660, 1409

Mukherjee, U., Bapna, S., Raichur, H., Paul, B., & Jaaffrey, 2006, JApA, 27, 25

Naik, S., Paul, B., 2003, A&A, 401, 265

Paul, B., Raichur, H., & Mukherjee, U., 2005, A&A, 442, 15

Raichur, H., & Paul, B., 2008a, ApJ, 685, 1109

Raichur, H., & Paul, B., 2008a, MNRAS, 387, 439

Tsunemi, H., Kitamoto, S., Tamura, K., 1996, ApJ, 456, 316

Wen, L., Levine, A. M., Corbet, R. H. D., Bradt, H. V., 2006, ApJS, 163, 372

Multi-Wavelength Observations of the Microquasar SS433

Taro Kotani,[0,1] Sergei Fabrika,[2] Nobuyuki Kawai,[1] Kenzo Kinugasa,[3]
Kaori Kubota,[4] Sergei Trushkin,[2] and Masato Tsuboi[5,6]

[0] Aoyama Gakuin U., 5-10-1 Fuchinobe, Sagamihara, Kanagawa 229-8558, Japan
[1] Depertment of Physics, Tokyo Tech, 2-12-1 O-okayama Meguro, Tokyo 152-8551, Japan
[2] SAO RAS, Nizhnij Arkhyz, Karachaevo-Cherkassia 369167, Russia
[3] Gunma Astronomical Observatory, 6860-86 Nakayama, Takayama, Gunma 377-0702, Japan
[5] JAXA/ISAS, 3-1-1 Yoshinodai, Sagamihara, Kanagawa 229-8510, Japan
[6] Nobeyama Radio Observatory, Minamimaki, Minamisaku, Nagano 384-1305, Japan
E-mail(TK): kotani@phys.aoyama.ac.jp

Abstract

A radio-IR-optical-X-ray observation campaigns have been performed in 2006 April and 2006 December for SS433, the unique microquasar known for the very stable continuous jet emanating at a quarter of the speed of light. The participating observatories/telescopes include Suzaku, RXTE, BTA, 150-cm Telescope at Gunma, Nayuta at Nishi-Harima, Crimean Observatory, MITSuME, VSOLJ, 1.4-m Telescope at SAAO, RATAN-600, RT-32 at IAA RAS, and Nobeyama Millimeter Array. In the April campaign, five radio flares have been detected and the source seems to be in the active state. In the December campaign, a single radio flare has been detected, and we triggered a series of observations with RXTE.

Key words: X-ray binary: SS433 — transient — multi-wavelength

1. Introduction

SS433 is the unique microquasar known for the very stable continuous jet emanating at a quarter of the speed of light. Multi-wavelength observation campaigns are very important to understand the system, in which multi-wavelength emission mechanisms are working; synchrotron radio emission from the high-energy electrons in the jet, thermal optical emission from the super-critical accretion disk, and X-ray from the inner edge of the disk and the central engine.

We have performed multi-wavelength observation campaigns for several microquasars including SS433 (Trushkin et al. 2006; Kotani et al. 2006; Kubota et al. 2008), Cyg X-3 (Tosaki et al. 2006; Tsuboi et al. 2006, 2008), and GRS 1915+105. Two campaigns performed in 2006 are reviewed in the following.

2. Campaign in 2006 April

The source has been observed with the X-ray astronomical satellite Suzaku at MJD = 53830 and 53833. An optical-IR-radio observation campaign was performed to cover the periods of the Suzaku observations. Spectra have been taken with the 6-m Telescope (Afanasiev et al. 2001) at the Special Astrophysical Observatory, Russian Academy of Science (SAO RAS), the 122-cm Telescope at the Padova-Asiago Observatory (Iijima 2002), the 150-cm Telescope at the Gunma Astronomical Observatory obayashi04, and the Nayuta (Narusawa et al. 2006) Telescope at the Nishi-Harima Astronomical Observatory. Photometric data have been obtained with the KGB-38 Telescope at the Crimean Astrophysical Observatory (Pavlenko et al. 20000, a non-filter 40-cm Telescope at the Kyoto University equiped with an SR-7 CCD camera of SBIG, MITSuME Akeno 50 cm (Kotani et al. 2005; Shimokawabe et al. 2008) at the Akeno Observatory, MITSuME OAO 50 cm (Kotani et al. 2005; Shimokawabe et al. 2008) at the Okayama Astrophysical Observatory (OAO), the 51-cm Telescope at the Osaka Kyoiku University (Yokoo et al. 1994), and telescopes in VSNET kato04 and in the Variable Star Observers League in Japan (VSOLJ) (Kato et al. 2004). Infrared photometry data have been obtained with the IRSF 1.4-m Telescope (Kandori et al. 2006) at the South African Astronomical Observatory (SAAO). The radio activity from 1.0 GHz to 21.7 GHz has been monitored with the RATAN-600 korolkov79,trushkin07 at SAO in the period covering the campaign. Radio observations at 2.3 and 8.5 GHz have been carried out simulteneously with the 32-m radio telescope (RTF-32) at the Institute of Applied Astronomy RAS (IAA RAS). The Nobeyama Millimeter Array (NMA) (Morita 1994; Tsutsumi et al. 1997) at the Nobeyama Radio Observatory have also participated in the campaign. A comprehensive observation log is presented in Kotani et al. (2006), and the X-ray data are

analyzed in Kubota et al. (2008).

The radio light curves exhibit five radio flares, suggesting that the source has been in the active state successively ejecting massive jets.

3. Campaign in 2006 December

SS433 has been monitored with RATAN-600 (Korolkov & Pariiskii 1979; Trushkin et al. 2008) and the 60-cm Maksutov telescope at the Crimean Observatory (Pavlenko et al. 2000) from 2006 November. The observation log and light curves are shown in Table 1-4 and Fig. 1.

In December, a significant radio flare has been detected (Trushkin et al. 2006). The 1-22-GHz flux densities has increased from a quiet optically thin synchrotron spectrum,

$$S_\nu/\mathrm{Jy} = 1.05 \times (\nu/\mathrm{GHz})^{-0.54},$$

on 2006 December 6.48 (MJD=54075.48) to flaring one,

$$S_\nu/\mathrm{Jy} = 2.90 \times (\nu/\mathrm{GHz})^{-0.43}$$

on 2006 Dec 8.47 (MJD=54077.47). The optical magnitude has also been increased from V=13.94 mag and Rc=12.52 mag at MJD=54075.691 to B=15.61 mag, V=13.41 mag, and Rc=11.99 mag at MJD54076.633. The last visual magnitude is one of the maximum values during last years.

We have triggered a series of RXTE TOO observations. Spectroscopic and radio follow-up observations have been performed at Gunma Astronomical Observatory (Obayashi et al. 2004) and with the Nobeyama Millimeter Array (Morita 1994; Tsutsumi et al. 1997). The optical light curves again show a rise in the last bins of the data, but no flare is detected in other bands.

This research was partially supported by the Ministry of Education, Science, Sports and Culture, Grant-in-Aid for Scientific Research (B), 18340057. The studies are supported by the Russian Foundation Base Research (RFBR) grant N 05-02-17556 and the mutual RFBR and Japan Society for the Promotion of Science (JSPS) grant N 05-02-19710.

References

Afanasiev V. L., Dodonov S. N., Moiseev A.V. 2001, in Stellar dynamics: from classic to modern, eds. L. P. Osipkov, I.I. Nikiforov, Saint Petersburg, 103

Iijima, T. 2002, A&A 387, 1013

Jahoda, K., Swank, J. H., Giles, A. B., Stark, M. J., Strohmayer, T., Zhang, W., & Morgan, E. H. 1996, Proc. SPIE, 2808, 59

Kandori, R., Kusakabe, N., Tamura, M., Nakajima, Y., Nagayama, T., Nagashima, C., Hashimoto, J., Hough, J., et al. 2006, Proc. SPIE 6269, 159

Kato, T., Uemura, M., Ishioka, R., Nogami, D., Kunjaya, C., Baba, H., Yamaoka, H. 2004, PASJ 56, 1

Korolkov, D. V., & Pariiskii, I. N. 1979, Sky Telescope, 57, 324

Kotani, T., Kawai, N., Yanagisawa, K., Watanabe, J., Arimoto, M., Fukushima, H., Hattori, T., Inata, M., et al. 2005, in 4th Workshop on Gamma-Ray Bursts in the Afterglow Era, eds. L. Piro, L. Amati, S. Covino, and B. Gendre (Italian Physical Society, Bologna) 755

Kotani, T., Kubota, K., Namiki, M., Kawai, N., Ueda, Y., Trushkin, S., Fabrika, S., Afanasiev, V., et al. 2006, in Proceedings of VI Microquasar Workshop: Microquasars and Beyond, 050

Kubota, K., Ueda, Y., Kotani, T., Kawai, N., Namiki,, M., Kinugasa, K., Ozaki, S., Iijima, T., Fabrika, S. 2008, in proceedings of *VI Microquasar Workshop: Microquasars and Beyond*, in press

Morita, K.-I. 1994, in ASP Conference Series, 59, Astronomy with Millimeter and Submillimeter Wave Interferometry, eds. M. Ishiguro and J. Welch (Astronomical Society of the Pacific, San Francisco) 18

Narusawa, S.-Y., Ozaki, S., & Kambe, E. 2006, PASJ 58, 617

Obayashi, H., Hashimoto, O., Nishihara, E., Kinugasa, K. 2004, in Third Rome Workshop on Gamma-Ray Bursts in the Afterglow Era, eds. M. Feroci, F. Frontera, N. Masetti, and L. Piro (Astronomical Society of the Pacific, San Francisco) 540

Pavlenko, E. P., Shugarov, S. Yu., Katysheva, N. I. 2000, Astrofizika, 43, 419

Shimokawabe, T., Kawai, N., Kotani, T., Yatsu, Y., Ishimura, T., Vasquez, N., Mori, Y., Kudo, Y., et al. 2008, American Inst. Phys. Conference Ser. 1000, 543

Tosaki, T., et al. 2006, ATel 952

Trushkin, S., Goranskii, V., Kotani, T. 2006, ATel 960

Trushkin, S. A., Namiki, M., Kotani, T., Kawai, N., Fabrika, S. 2008, PASJ, in preparation

Tsuboi, et al. 2006, ATeL 727

Tsuboi, M., et al. 2008, PASJ 60, 465

Tsutsumi, T., Morita, K.-I., Umeyama, S. 1997, in ASP Conf. Ser. 125, Astronomical Data Analysis Software and Systems VI, eds. G. Hunt and H. E. Payne (Astronomical Society of the Pacific, San Francisco) 50

Yokoo, T., Arimoto, J., Matsumoto, K., Takahashi, A., Sadakane, K. 1994, PASJ 46, L191

Table 1. X-Ray observation log.

Start		End		Expos.	Remark
(MJD)		(MJD)		(ks)	
Observatory: RXTE (Jahoda et al. 1996). PI: T. Kotani.					
2006/12/16 22:37	(54085.9425)	2006/12/16 23:25	(54085.9758)	2.9	
2006/12/17 23:48	(54086.9918)	2006/12/18 00:15	(54087.0105)	1.6	
2006/12/18 23:21	(54087.9730)	2006/12/18 23:50	(54087.9932)	1.7	
2006/12/19 22:54	(54088.9543)	2006/12/19 23:24	(54088.9751)	1.8	
2006/12/20 21:51	(54089.9105)	2006/12/20 22:27	(54089.9355)	2.2	
2006/12/21 23:04	(54090.9612)	2006/12/21 23:40	(54090.9862)	2.2	
2006/12/22 22:36	(54091.9418)	2006/12/22 23:13	(54091.9675)	2.2	
2006/12/23 17:40	(54092.7362)	2006/12/23 18:13	(54092.7591)	2.0	
2006/12/24 20:08	(54093.8390)	2006/12/24 20:41	(54093.8619)	2.0	
2006/12/25 21:37	(54094.9008)	2006/12/25 22:27	(54094.9355)	3.0	
2006/12/26 21:44	(54095.9057)	2006/12/26 22:07	(54095.9216)	1.4	
2006/12/27 17:29	(54096.7286)	2006/12/27 18:18	(54096.7626)	2.9	

Table 2. Spectroscopy log.

Start		Exposure	Remark
(MJD)		(s)	
Telescope: 150 cm (Obayashi et al. 2004). Observatory: Gunma. PI: K. Kinugasa.			
2006/12/11 08:55	(54080.37)	1080	
2006/12/19 08:44	(54088.36)	1080	
2006/12/20 08:33	(54089.36)	900	
2006/12/23 08:41	(54092.36)	540	
2006/12/25 08:35	(54094.36)	720	

Table 3. Photometry log.

Start (MJD)	End (MJD)	Frames	Remark
Instrument: 60-cm reflector. Observatory: Crimean (Pavlenko et al. 2000). PI: V. Goranskij.			
54071.6747	54071.6873	V:5, B:0, Rc:0, I:0	50-cm Maksutov telescope
54072.6355	54072.6600	V:5, B:3, Rc:2, I:0	
54073.6347	54073.6480	V:2, B:3, Rc:1, I:1	
54074.6385	54074.6708	V:4, B:1, Rc:1, I:0	
54075.6877	54075.6907	V:2, B:2, Rc:1, I:1	
54076.6328	—	V:1, B:1, Rc:1, I:1	
54077.6282	54077.6936	V:19, B:19, Rc:18, I:18	
54078.6326	54078.7085	V:24, B:24, Rc:24, I:23	
54079.6289	54079.7103	V:24, B:23, Rc:24, I:19	
54084.6418	—	V:1, B:1, Rc:1, I:1	
54085.6216	54085.6914	V:26, B:26, Rc:26, I:20	
54086.6510	54086.6567	V:2, B:2, Rc:1, I:0	
54091.6376	54091.6838	V:21, B:21, Rc:18, I:11	
54095.6463	54095.6678	V:7, B:6, Rc:4, I:3	

Table 4. Radio observation log.

Start		End		Remark
	(MJD)		(MJD)	
Telescope: RATAN-600 (Korolkov & Pariiskii 1979; Trushkin et al. 2008). Observatory: SAO RAS. PI: S. Trushkin.				
2006/11/03	(54042)	2007/02/16	(54148)	1.0 GHz–21.7 GHz
Telescope: Nobeyama Millimeter Array (Morita 1994; Tsutsumi et al. 1997). Observatory: Nobeyama. PI: K. Nakanishi				
2006/12/11 05:01	(54080.2090)	2006/12/11 07:30	(54080.3125)	115.271204 GHz
2006/12/27 04:15	(54096.1771)	2006/12/27 07:41	(54096.3201)	115.360478 GHz
2006/12/28 04:08	(54097.1722)	2006/12/28 09:08	(54097.3806)	115.360478 GHz
2006/12/29 04:12	(54098.1750)	2006/12/29 09:14	(54098.3847)	115.360478 GHz
2007/01/19 03:02	(54119.1264)	2007/01/19 06:29	(54119.2701)	115.271204 GHz
2007/01/21 03:08	(54121.1306)	2007/01/21 06:28	(54121.2694)	146.969049 GHz
2007/02/16 02:36	(54147.1083)	2007/02/16 04:00	(54147.1667)	109.782182 GHz
2007/02/18 23:54	(54149.9958)	2007/02/19 01:30	(54150.0625)	109.782182 GHz

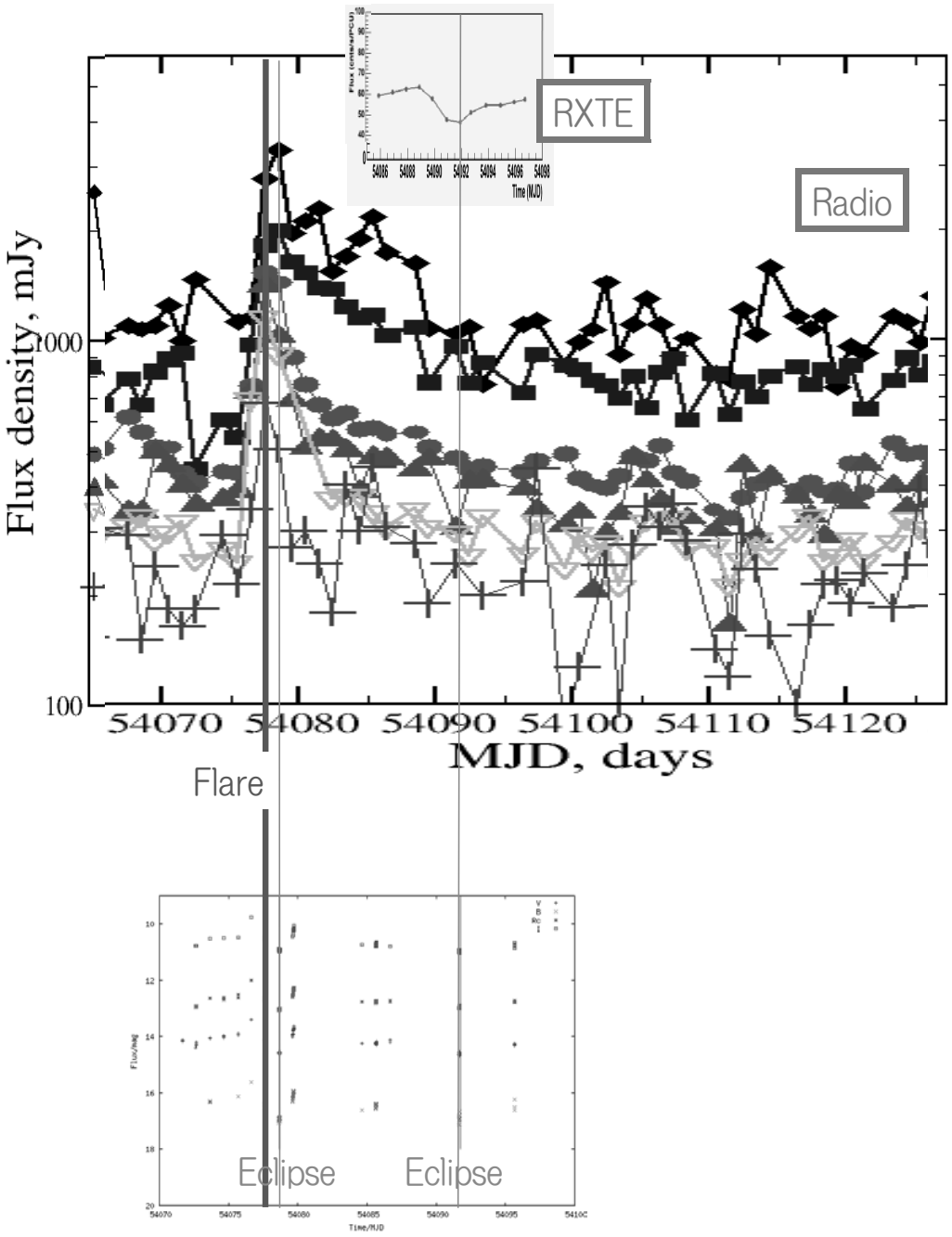

Fig. 1. Radio, optical, and X-ray light curves. A radio flare and two eclipses are indicated by vertical lines.

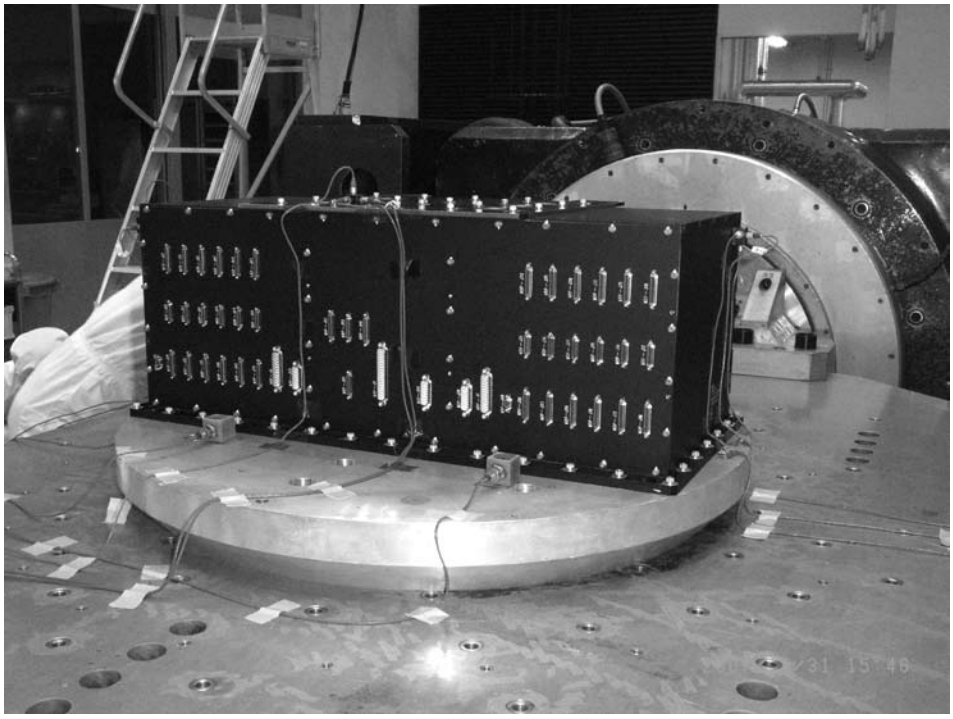

Suzaku observation of AXP 1E 1841-045 and the future observation in the MAXI era

Mikio Morii,[1]

[1] Rikkyo University
E-mail(MM): mmorii@rikkyo.ac.jp

Abstract

We report results of the Suzaku observation of the anomalous X-ray pulsar (AXP) 1E 1841−045. We obtained the spectrum from 0.4 keV to ∼70 keV simultaneously. The model consisting of a blackbody and two power-law functions could simulate the spectrum well. We also found that the power-law function at the higher energy can be replaced with a thermal bremsstrahlung. The fact that the hard X-ray emission can be interpreted as a thermal bremsstrahlung would support the theoretical emission model proposed by Thompson & Beloborodov (2005). Emission mechanism of the hard X-ray component can be understood by detecting the variability of the photon index and cutoff energy. In this reason, the MAXI monitoring for magnetars (AXPs and SGRs) are extremely important. The monitoring of the pulse frequency and pulse profiles of magnetars are also important as well as that of the flux. MAXI can detect transient phenomena and trigger the multi-wavelength observation. Especially, near-infrared monitoring observation and correlation study would be able to elucidate the mysterious infrared emission mechanism of magnetars. We estimated the detectability of the magnetars and their pulsation by MAXI using the MAXI simulator.

Key words: workshop: proceedings — LaTeX2.09: style file — instructions

1. Introduction

Anomalous X-ray pulsars (AXPs) and soft gamma repeaters (SGRs) are thought to be magnetars, which are strongly magnetized neutron stars with emission powered by the dissipation of magnetic energy (see Woods & Thompson (2006) for a recent review). So far, 10 AXPs (including 3 transient AXPs) and 6 SGRs have been found. They distribute along with the Galactic plane and the Large and Small Magellanic Clouds. Their characteristics are as follows: (1) Their spin periods concentrate in a narrow range (2 – 12 s). Spin periods and spin-down rates imply the strong dipole magnetic fields of 10^{14} – 10^{15} G. (2) Their X-ray luminosities ($L_{\rm X} \sim 10^{34}$–10^{36} ergs s^{-1}) exceeding the spin-down energy loss rate of neutron stars suggests that AXPs and SGRs are not rotation-powered pulsars. (3) They are radio quiet with exceptions of XTE J1810−197 (Camilo et al. 2006) and 1E 1547.0−5408 (Camilo et al. 2007). (4) They showed spiky short bursts with durations $\Delta t \sim 0.1$ s, and sometimes showed giant flare. (5) Their X-ray spectra are simulated by a compound of a blackbody and power-law function with rather steep photon index ($\Gamma \sim 2$ - 4) or two temperature blackbodies. Above ~ 10 keV, there is another hard X-ray component extending to ~ 150 keV. (6) They shows various time variability like flux variation, pulse profile change, timing noise of pulse period, and glitch of pulse period. (7) They have infrared/optical counterparts and these fluxes are variable. Owing to the last two characteristics, magnetars are thought to be good target of MAXI.

In this paper, we at first show the results of Suzaku observation of the AXP 1E 1841-045 (Morii et al. 2008), and secondly we show science of magnetars achieved by MAXI.

2. Suzaku observation of AXP 1E 1841-045

1E 1841−045 is one of prototypes of AXPs. It locates on the center of the supernova remnant (SNR) Kes 73 with a diameter of about 4′ (Morii et al. 2003). By using a Chandra data (0.6 – 7.0 keV) Morii et al. (2003) showed that the spectrum was simulated well with a model consisting of the blackbody ($kT = 0.44 \pm 0.02$ keV) and the power-law function ($\Gamma = 2.0 \pm 0.3$). Kuiper, Hermsen & Mendez (2004) discovered a very hard (photon index: 0.94 ± 0.16) pulsed hard X-ray emission up to ~ 150 keV, using the RXTE/PCA (1.8 – 23.8 keV) and the RXTE/HEXTE (15 – 250 keV). this hard X-ray component is thought to amount substantial fraction in the energy range below ~ 10 keV. Therefore, the Suzaku

wide band spectroscopy is important to determine the spectrum.

We observed AXP 1E 1841-045 by Suzaku (Mitsuda et al. 2007) on April 19-22, 2006 as a target of AO-1. We used XIS and HXD/PIN detectors to cover the energy range of 0.4 – 10 keV and 12 – about 70 keV, respectively. HXD/GSO was used for the upper limit at around 100 keV. The exposure of the observation was 100 ks. We followed the standard method to analyze the data (Morii et al. 2008). The pulse phase-averaged spectrum was well fitted by three component consisting of a blackbody, power-law function, and another power-law function. Interestingly, the photon index of the power-law of the higher energy part was ∼1.6. This value can also be explained by thermal bremsstrahlung. Here, the Gaunt factor and the exponential cut-off around 100 keV can change the photon index of bremsstrahlung of 1 (Rybicki & Lightman 1979) to ∼1.6 in the energy range of PIN (10 – 50 keV). Then we also fitted the phase-averaged spectrum by a compound of a blackbody, power-law function, and thermal bremsstrahlung (figure 1). This model also fitted the spectrum well, with a bremsstrahlung temperature of $kT = 51.7^{+14.1}_{-8.8}(\mathrm{stat})^{+68.0}_{-22.1}(\mathrm{syst})$ keV.

Interpretation for a hard X-ray by a thermal bremsstrahlung is interesting, because one of theoretical model of emission mechanism predicted the similar spectrum of a thermal bremsstrahlung (Beloborodov & Thompson 2007). Moreover, we checked a self-consistency for the thermal bremsstrahlung emission. For this emission to be valid, the emission region must be optically thin. Assuming that the Thomson cross-section, optical depth must be $l > 3.4 \times 10^9$ cm. It is too large value in comparison with the radius of neutron stars (∼ 10 km). Nevertheless, in the ultra strong magnetic field, the cross-section of the Thomson scattering is suppressed by $7.6 \times 10^{-5}(kT/10\mathrm{keV})^2(B/10B_{\mathrm{QED}})^{-2}$, where the $B_{\mathrm{QED}} = 4.4 \times 10^{13}$ G is the quantum critical magnetic field (Thompson & Duncan 1995). Then, $l > 2.9 \times 10^4$ cm for $B = 7.1 \times 10^{14}$ G and $kT = 100$ keV, where the B is the dipole magnetic field at the surface of this AXP estimated by $3.2 \times 10^{19}(P\dot{P})^{1/2}$ G. So, the l become a reasonable size. It can be said that optically thin emission like thermal bremsstrahlung itself is an expression of the ultra strong magnetic field of magnetars.

2.1. Comparison of spectra between Suzaku and Integral

By comparing the Suzaku and Integral spectra (figure 2), we found that the flux at around $20 - 70$ keV is consistent between them. However, the spectrum of Integral is slight harder than that of Suzaku. The photon indices of Suzaku and Integral are $+0.38 \pm 0.05(\mathrm{stat}) \pm 0.16(\mathrm{syst})$ and $+0.68 \pm 0.11$, respectively. The significance of the difference is 1.5 sigma level. There are the following possibilities: 1) just a systematic difference between the Suzaku and Integral. 2) time variation of the hard X-ray component. The spectrum of Integral was obtained by long span of 1.7 years, while that of Suzaku was obtained by only 3 days. and 3) An effect of a comptonized hump, which is expected in the spectrum come from the region with intermediate optical thickness. The detailed calculation was shown in Miyamoto (1978) and Sunyaev & Titarchuk (1980). If this possibility is true, the shape of the hump may be sensitive to the structure of the magnetosphere of magnetars. Therefore, the time variability of hard X-ray spectrum is interesting, and hence the detection of magnetar flare using MAXI is important.

3. Magnetar observation by MAXI

3.1. magnetar science by MAXI

Magnetars shows transient phenomena as shown in the introduction. Interestingly, new magnetars have been discovered as transient sources. Recent examples are XTE J1810-197 (Ibrahim et al. 2004), CXOU J164710.2-455216 (Naik et al. 2008), and SGR 0501+4516 (Barthelmy et al. 2008). MAXI will discover new magnetars. Even for the known magnetars, they shows flares in the time scales from days to months (Kaspi et al. 2003, Gotthelf & Halpern 2006). MAXI can detect such flares and broadcast this occurrence quickly. We can trigger the multi-wavelength observation. Especially, follow-up observations in hard X-ray, infrared/optical and radio bands are quite interesting, because their emission mechanisms are still open question. The multi-wavelength flux monitoring and correlation study is a key to elucidate the emission mechanism.

3.2. MAXI simulation for magnetars

To check the detectability of magnetars by MAXI, we simulated four bright magnetars, 4U 0142+61, 1E 2259+586, 1RXS J170849.0-400910, and XTE J1810-197 by using MAXI GSC simulator. The last XTE J1810-197 is a transient AXP, which once became bright on 2003 July (Ibrahim et al. 2004). We used peak flux for this AXP (Gotthelf & Halpern 2006). For sources other than last one, we used the spectra consisting of a blackbody and power-law function. The spectral parameters are obtained by the analysis of the Chandra archival data. For the last one, we used two temperature blackbodies (Gotthelf & Halpern 2006). The table 1 shows the parameters inputed for the MAXI GSC simulator. For GSC simulator, we set the status of all 12 counters working and backgrounds of CXB and NXB were taken into consideration. The detectability for these sources are shown in figure 3 and table 2. For all of them, the persistent flux monitoring can be possible within a time scale of a week. Such a frequent monitoring was not possible by RXTE/PCA pointing observation. For 1RXS J170849.0-400910, pulse period monitoring is possible. Interestingly, this source showed glitches (Kaspi & Gavriil 2003), which is a key

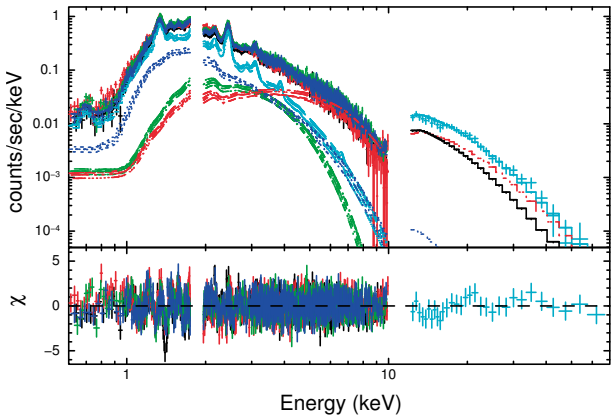

Fig. 1. Spectrum of AXP 1E 1841−045 obtained by Suzaku observation. It is fitted with a combination of the SNR Kes 73 and the AXP spectra. Here, the SNR spectrum was determined by the spectrum analysis for Chandra data. The AXP spectrum was three component model consisting of a blackbody(green), power-law(blue) and thermal bremsstrahlung(red). Black histogram in PIN region is the component of the cosmic X-ray background and Galactic ridge X-ray emission. This figure is extracted from Morii et al. (2008).

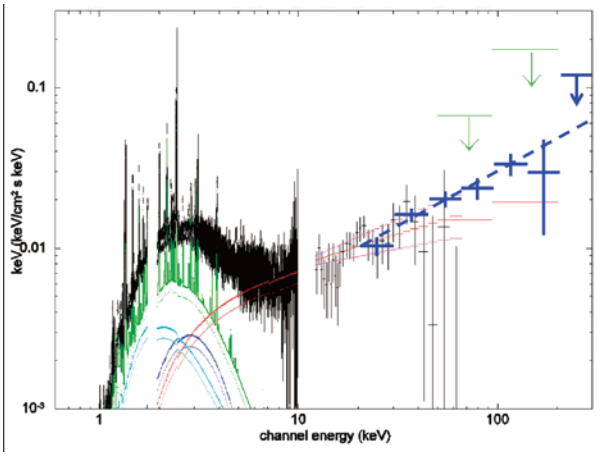

Fig. 2. νF_ν plot of AXP 1E 1841-045 obtained by Suzaku observation compared with Integral spectrum (Kuiper et al. 2006). Black data crosses below and above 10 keV shows Suzaku XIS and PIN data, respectively. The red histogram shows power-law component of the AXP. The Magenta histogram shows the systematic uncertainty range caused by the 3% uncertainty of the non X-ray background of PIN. Green upper limit shows GSO upper limit. Blue crosses shows Integral spectrum extracted from Kuiper et al. (2006).

to understand the internal structure of magnetars. Transient sources like XTE J1810-197 can be monitored very frequently. Pulse profile change and pulse period change (glitch) could be monitored, when the source was bright. Fortunately, XTE J1810-197 was bright for a few hundred days.

3.3. transient AXPs

A transient AXP XTE 1810-197 is a good example to simulate how MAXI will detect the flares of magnetars and monitor them. This object was serendipitously discovered within the field of view of the RXTE/PCA, when RXTE performed a pointing observation for nearby SGR 1806-20 (Ibrahim et al. 2004). In addition, this object could not be found by RXTE/ASM, then there are about 100 day blank of observation around the initial flare-up duration, as shown in Gotthelf & Halpern (2006). MAXI would detect this source only in 0.4 days in 5 sigma level, and pulsation can be detected in 3 days exposures. Therefore, MAXI would broadcast the appearance of this type of objects so quickly. MAXI can also monitor the declining light curve so frequently.

3.4. Monitoring in near-infrared band

Near-infrared (NIR) counterparts are found for about a half of magnetars (Woods & Thompson 2006). The emission mechanism is open question. Mainly two models are proposed: magnetospheric origin (Kern & Martin 2002, Eichler, Gedalin & Lyubarsky 2002, Lu & Zhang 2004) or dust disk around a magnetar (Wang, Chakrabarty & Kaplan 2006). If dust disk model is correct, the strong flux correlation between X-ray and NIR bands are expected as shown in figure 2 of Ertan, Göğüş & Alpar (2006). In this figure, light curves of 1E 2259+586

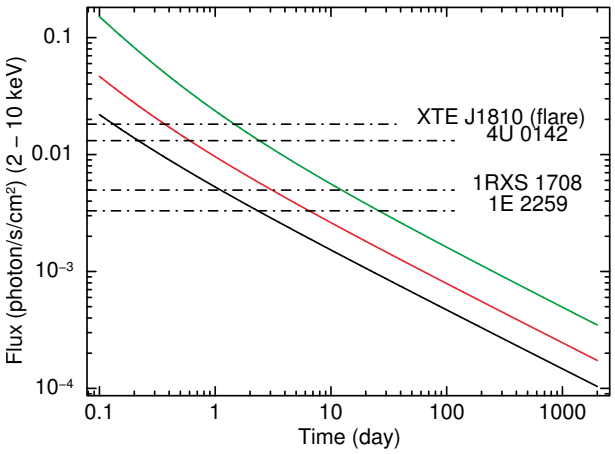

Fig. 3. Detectability for the four bright magnetars. The horizontal and vertical axes show exposure time (day) and flux (photon/s/cm^2) in 2 – 10 keV. The black, red and green curves show detection lines with 3, 5, and 10 sigma level.

in X-ray and near-infrared bands are shown, when 1E 2259+586 showed activities (spiky bursts, flare-up of the persistent emission) and the decay of the persistent flux in a time scale of a week. According to the disk model developed by Ertan, Göğüş & Alpar (2006), strong correlation was expected. Then, if this source flare again in MAXI era, we will be able to follow the X-ray light curve of 1E 2259+586 and also detect the flare and trigger ToO observations of infrared band. By this type of follow-up observation, mystery of the infrared emission mechanism of magnetars will be solved. Other type of observation like regular monitoring of the NIR flux can also be used to take a correlation between X-ray obtained by MAXI.

4. Summary

Scientific goals for magnetar observation by MAXI are as follows:

(1) MAXI will detect flares of known magnetars with time scales of day to month. MAXI will also discover new transient magnetars like XTE J1810-197, CXOU J164710.2-455216, and SGR 0501+4516.

(2) MAXI will monitor the pulse profile and pulse period change. Glitch detection is important to study for the internal structure of magnetars.

(3) MAXI will broadcast the appearance of magnetar activities, and trigger quick follow-up observations in multi-wavelength.

(4) Infrared emission mechanism of magnetars are controversial: Magnetospheric or dust disk around magnetars. Dust disk model predict strong flux correlation between X-ray and NIR. Then, MAXI and NIR collaboration is important. The NIR follow-up observation after magnetar-flare is decisive for the infrared emission mechanism.

References

Barthelmy, S. D. et al. 2008, GCN Circular 8113
Beloborodov, A. M. & Thompson, C. 2007, ApJ, 657, 967
Camilo, F., Ransom, S. M., Halpern, J. P., Reynolds, J., Helfand, D. J., Zimmerman, N., & Sarkissian, J. 2006, Nature, 442, 892
Camilo, F., Ransom, S. M., Halpern, J. P., & Reynolds, J. 2007, ApJ, 666, L93
Eichler, D., Gedalin, M. & Lyubarsky, Y. 2002, ApJ, 578, L121
Ertan, Ü, Göğüş, E. & Alpar, M. A. 2006, ApJ, 640, 435
Gotthelf, E. V. & Halpern, J. P. 2006, astro-ph/0608473
Ibrahim, A. I. et al. 2004, ApJ, 609, L21
Kaspi, V. M. & Gavriil, F. P. 2003, ApJ, 596, L71
Kaspi, V. M., Gavriil, F. P., Woods, P. M., Jensen, J. B., Roberts, M. S. E., Chakrabarty, D. 2003, ApJ, 588, L93
Kern, B. & Martin, C. 2002, Nature, 417, 527
Kuiper, L., Hermsen, W., & Mendez, M. 2004, ApJ, 613, 1173
Kuiper, L., Hermsen, W., den Hartog, P. R., & Collmar, W. 2006, ApJ, 645, 556
Lu, Y. & Zhang, S. N. 2004, MNRAS, 354, 1201
Mitsuda, K. et al. 2007, PASJ, 59, S1
Miyamoto, S. 1978, A&A, 63, 69
Morii, M., Sato, R., Kataoka, J., & Kawai, N. 2003, PASJ, 55, L45
Morii, M., Kitamoto, S., Shibazaki, N., Kawai, N., Arimoto, M., Ueno, M., Kohmura, T., Terada, Y., Yamauchi, S., Takahashi, H. 2008, PASJ, submitted
Naik, S. et al. 2008, 60, 237
Rybicki, G. B. & Lightman, A. P. 1979, "Radiative Processes in Astrophysics," John Wiley & Sons
Sunyaev, R. A. & Titarchuk, L. G. 1980, 86, 121
Thompson, C. & Duncan, R. C. 1995, MNRAS, 275, 255

Wang, Z. & Kaspi, V. M. 2008, ApJ, 675, 695
Woods, P. M., & Thompson, C., "Soft Gamma repeaters and anomalous X-ray pulsars: magnetar candidates," in Compact Stellar X-ray Sources, edited by Lewin, W. H. G. and van der Klis, M., Cambridge University Press, New York, 2006, pp. 547–586 (astro-ph/0406133).

Table 1. Parameters for the GSC simulator to simulate for bright magnetars.

Objects	absorbed flux erg/s/cm^2 (2 - 10 keV)	N_H cm^{-2}	photon index	temperature keV
4U 0142+61	6.4×10^{-11}	0.93×10^{22}	3.4	0.47
1E 2259+586	1.5×10^{-11}	0.97×10^{22}	3.6	0.41
1RXS J170849.0-400910	2.8×10^{-11}	1.5×10^{22}	2.4	0.43
XTE J1810-197 (flare peak)	9×10^{-11}	0.65×10^{22}	–	0.25 / 0.68

Table 2. Detectability of bright magnetars

Objects	absorbed flux erg/s/cm^2 (2 - 10 keV)	source detection 5 sigma level	pulse fraction (%)	pulse detection 3 sigma level
4U 0142+61	6.4×10^{-11}	0.6 day	4 %	1 year
1E 2259+586	1.5×10^{-11}	7 day	23 %	$>$ 1 year
1RXS J170849.0-400910	2.8×10^{-11}	3 day	21 %	40 day
XTE J1810-197 (flare peak)	9×10^{-11}	0.4 day	43 %	3 day

New Magnetar Frontiers with MAXI Survey

Nakagawa Yujin E.,[1] Yoshida Atsumasa,[2] Yamaoka Kazutaka[2]

[1] Institute of Physical and Chemical Research (RIKEN), 2-1 Hirosawa, Wako, Saitama 351-0198, Japan
[2] Graduate School of Science and Engineering, Aoyama Gakuin University, 5-10-1 Fuchinobe, Sagamihara, Kanagawa 229-8558, Japan
E-mail(YEN): yujin@crab.riken.jp

Abstract

Feasibility studies of searching new magnetar candidates by the GSC on-board MAXI are presented. The GSC/MAXI can marginally detect a faint $\sim$ 1 mCrab source with only 7 days time integrated observations. Furthermore, the faint $\sim$ 1 mCrab source is clearly detected by observations with a 30 days exposure time. A survey of the galactic plane ($|b| \leq 5$) by the GSC/MAXI may find numerous new magnetar candidates and may reveal new frontiers of magnetar studies.

Key words: workshop: proceedings — LaTeX2.09: style file — instructions

1. Introduction

There has been great discussion about magnetars which may be neutron stars with a super strong magnetic fields $\sim 10^{15}$ G (Duncan & Thompson 1992; Paczyński 1992; Thompson & Duncan 1995; Thompson & Duncan 1996). Several studies have found 12 X-ray magnetar candidates in the galactic plane as well as 2 candidates in the Large Magellanic Cloud or the Small Magnllanic Cloud (e.g., Woods & Thompson 2006; Barthelmy et al. 2008). There are two apparent types in the magnetar candidates that is soft gamma repeaters (SGRs) and anomalous X-ray pulsars (AXPs).

Over the past three decades, the candidates were observed by many satellites. However, some important issues such as a birth rate, a nature of a super strong magnetic field and an emission mechanism still remain unclear. What seems lacking is statistical spectral and temporal studies. Muno et al. (2008) reported that a birth rate of the X-ray candidates could range between 0.003 and 0.06 yr^{-1} based on the XMM-Newton and *Chandra* archive data for the galactic plane ($|b| \leq 5$). Let us look at an important fact, namely that their suvey region covers just $\sim$4% of the galactic plane. Thus a survey of entire region of the galactic plane should be the first prioritized issue.

The main objective of our study is to survey the new X-ray mangetar candidates and to give their accurate birst rate using the Gas Slit Camera (GSC) onboard Monitor of All-sky X-ray Image (MAXI) which has the best sensitivity in near future. Considering an unabsorbed flux of known candidates lies around $F \sim 10^{-11}\,\mathrm{erg\,cm^{-2}\,s^{-1}}$ (e.g., Nakagawa et al. 2009), the GSC/MAXI may survey the most sky with just 7 days observation. In this paper, we present simulation results of the GSC/MAXI for the X-ray magnetar candidates.

2. Feasibility Study with GSC/MAXI Simulation

2.1. Simulation Setup

The simulations of the GSC/MAXI were made using *maxisim* (6.3.103). In the simulations, cosmic X-ray background (CXB) and non X-ray background (NXB) should be considered. The spectrum of CXB was assumed to be $F(E) = 4.93 \times 10^{-3} E^{-1.29} e^{-E/40.0}$ (Boldt 1987), where E is a photon energy. The count rate of NXB was assumed to be 10 counts s^{-1}.

The simulations were performed with all 12 cameras of the GSC/MAXI for the time period from 54103 to 54433 (MJD). The field of view was assumed to be $(\phi, \theta) = (42.0^\circ, 1.6^\circ)$, where ϕ and θ are incident angles in a detector coordinate frame. To protect the GSC/MAXI from the solar heat, its incident angle was restricted to be $(\phi, \theta) > (70^\circ, 30^\circ)$.

To investigate feasibility of searching the new X-ray magnetar candidates with the GSC/MAXI, the simulations were performed for sources with two brightness $\sim$1 mCrab and $\sim$3 mCrab. A two blackbody function was used as the spectral model. The spectral parameteres of SGR 1806−20 ($\sim$1 mCrab) and AXP 4U 0142+614 ($\sim$3 mCrab) were used in the simulations. The spectral parameters are summarized in table 1 (Nakagawa et al. 2009). Here, the non-thermal hard component (> 20 keV) discovered by INTEGRAL (Molkov et al. 2005; Götz et al. 2006; Kuiper et al. 2006) was not considered in these simulations. The reductions of the simulated GSC/MAXI event data were made using HEAsoft 6.5 software. The foreground and background

Table 1. The spectral parameters for SGR 1806−20 and AXP 4U 0142+614 which were used in the simulations (Nakagawa et al. 2009).

Source	$N_{\rm H}^{\rm a}$ ($10^{22}\,{\rm cm}^{-2}$)	$kT_{\rm LT}^{\rm b}$ (keV)	$R_{\rm LT}^{\rm c}$ (km)	$kT_{\rm HT}^{\rm b}$ (keV)	$R_{\rm HT}^{\rm c}$ (km)	$F^{\rm d}$
SGR 1806−20	5.18	0.84	1.64	2.62	0.28	2.5
AXP 4U 0142+614	0.53	0.36	9.38	0.82	0.89	5.7

a. $N_{\rm H}$ denotes the column density.
b. $kT_{\rm LT}$ and $kT_{\rm HT}$ denote the blackbody temperatures.
c. $R_{\rm LT}$ and $R_{\rm HT}$ denote the emission radii.
d. F denotes a flux in the energy range 2-10 keV in units of $10^{-11}\,{\rm erg\,cm^{-2}\,s^{-1}}$.

regions were determined by eye. The foreground data was extracted around the sources with a circular shape of a 2° radius. The background data was extracted around the sources with an annulus shape where the inner and outer radii were 2° and 8°, respectively. The center of the foregound and backgroud regions was aligned to the center of the sources.

2.2. Simulation Results

To investigate source detectability of the GSC/MAXI, the images with 7, 30 and 330 days time integrations were created from the simulation data for SGR 1806−20 (the *top* panels in figure 1) and AXP 4U 0142+614 (the *bottom* panels figure 1). The sources were marginally detected with only 7 days time integration. In addition, the sources were clearly detected with the 30 and 330 days time integrations.

Figure 2 shows the simulated light curves with a 1 day time resolution during a period from 54103 to 54433 (MJD) for SGR 1806−20 (*top*) and AXP 4U 0142+614 (*bottom*). Although one can see the apparent temporal variations of a count rate, they are due to variations with time of effective area. Furthermore, the apparent high count rate of SGR 1806−20 relative to AXP 4U 0142+614 was due to a difference of incident angles to the GSC/MAXI.

The simulated spectra in 2-30 keV for SGR 1806−20 and AXP 4U 0142+614 are presented in figures 3 and 4, respectively.

3. Conclusions

The GSC/MAXI has a great sensitivity to detect new magnetar candidates in the unsurveyed galactic plane ($|b| \leq 5$). The $\sim$ 1 mCrab source was marginally detected with just 7 days time integration in the simulations. Considering that the survey region of the XMM-Newton and *Chandra* covers just $\sim$ 4% of the galactic plane ($|b| \leq 5$; Muno et al. 2008), a survey by the GSC/MAXI may find numerous new magnetar candidates and may reveal new frontiers of magnetar studies.

This work is supported in part by a special postdoctoral researchers program in RIKEN.

References

Barthelmy S.D. et al. 2008, GRB Coord. Netw. Circ., 8113
Boldt E. 1987 IAU Circ., 124, 611B
Duncan R.C., & Thompson C. 1992 ApJ., 392, L9
Götz D. et al. 2006, A&A, 449, L31
Kuiper L. et al. 2006, ApJ, 645, 556
Molkov S. et al. 2005, A&A, 433, L13
Muno M.P. et al. 2008 ApJ., 680, 639
Nakagawa Y.E. et al. 2009 PASJ in press, arXiv: astro-ph/0710.3816
Paczyński B. 1992, Acta Astron., 42, 145
Thompson C., & Duncan R. 1995, MNRAS, 275, 255
Thompson C., & Duncan R. 1996, ApJ, 473, 322
Woods P.M., & Thompson, C. 2006 in Compact Stellar X-Ray Sources, ed. W.H. Lewin & M. van der Klis (Cambridge: Cambridge University Press), ch. 14

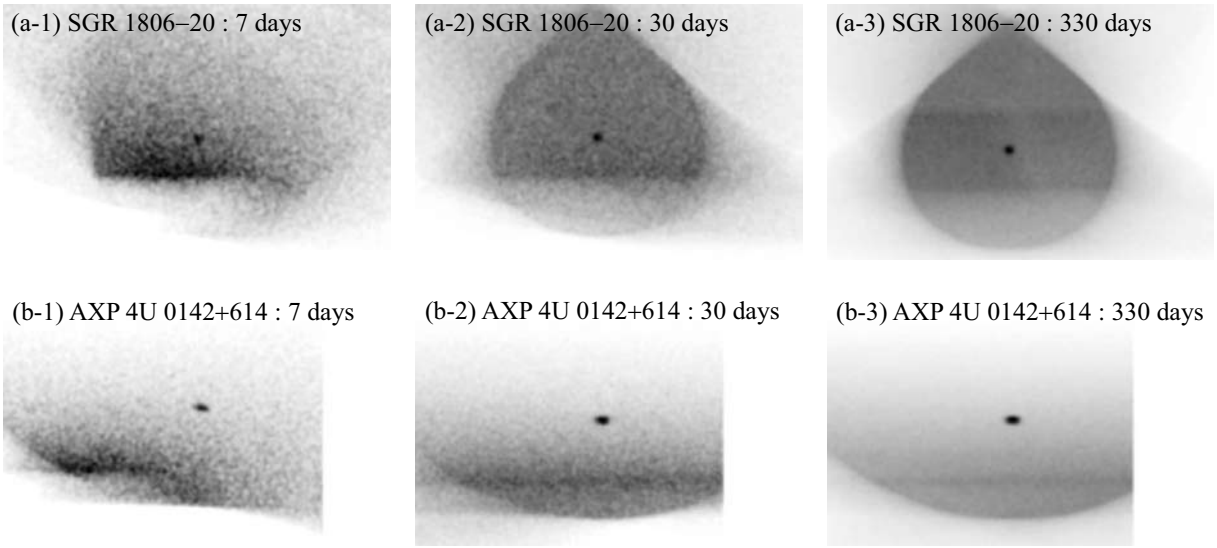

Fig. 1. The simulated images for three exposure times 7, 30 and 330 days for SGR 1806−20 (*top*) and AXP 4U 0142+614 (*bottom*).

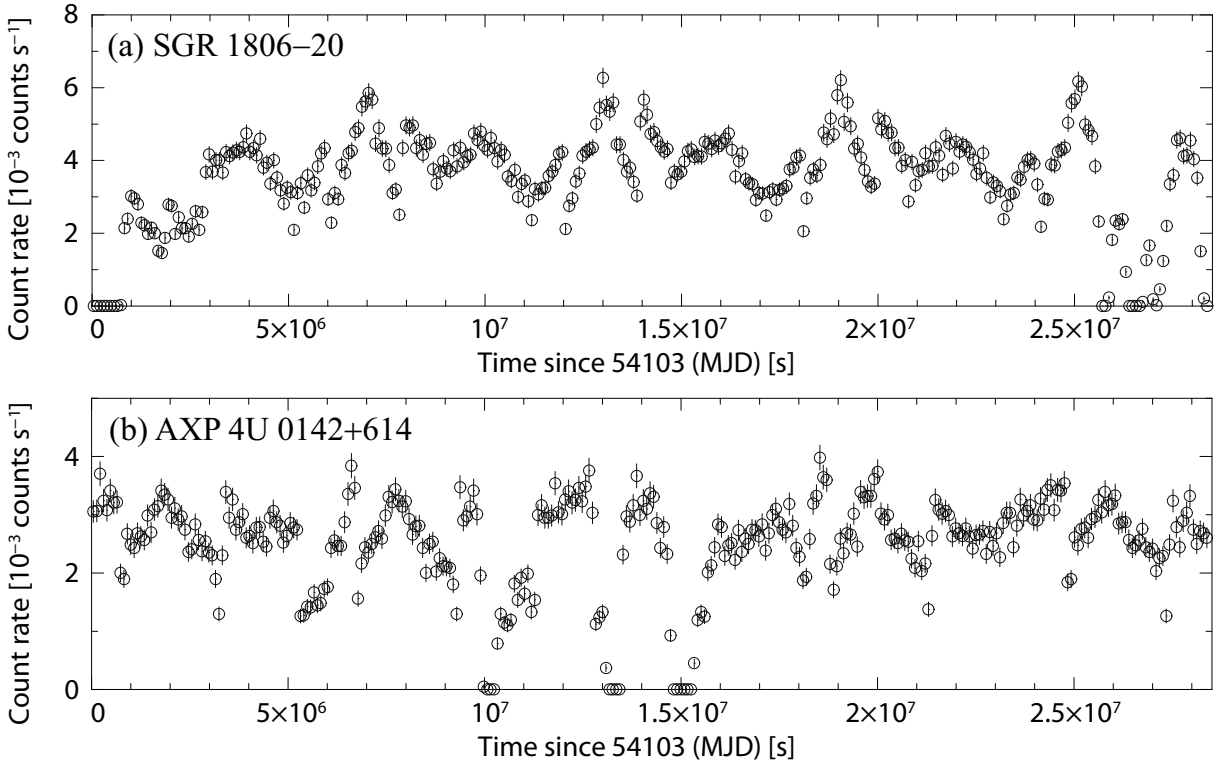

Fig. 2. The simulated 1 day light curves during a period from 54103 to 54433 (MJD) for SGR 1806−20 (a) and AXP 4U 0142+614 (b). The apparent temporal variations of a count rate are due to variations with time of effective area. In addition, the apparent high count rate of the SGR 1806−20 light curve relative to the AXP 4U 0142+614 light curve was due to a difference of incident angles to the GSC/MAXI. Note that the background was not subtracted from the count rate.

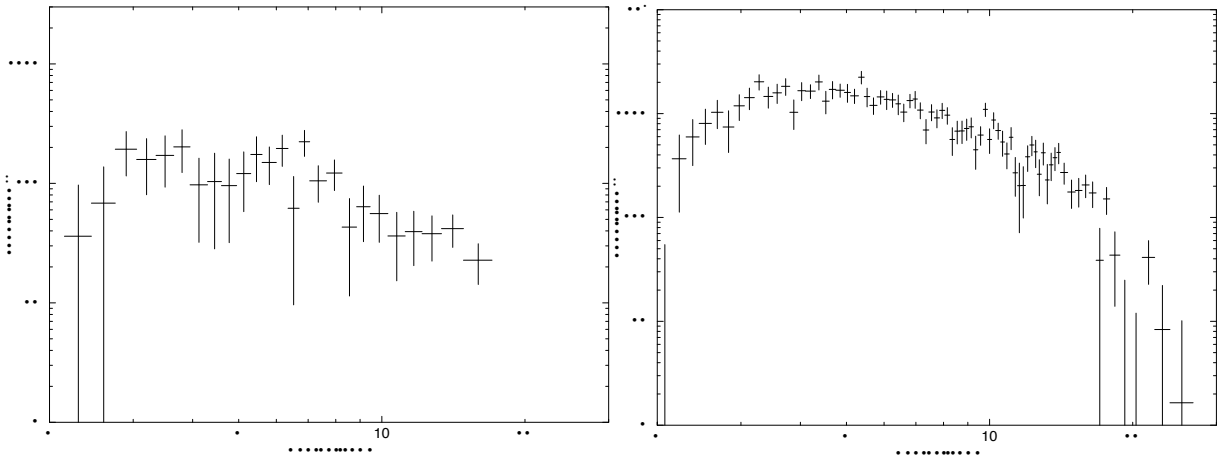

Fig. 3. The simulated spectra in 2-30 keV accumulated data over 30 (*left*) and 330 (*right*) days for SGR 1806−20.

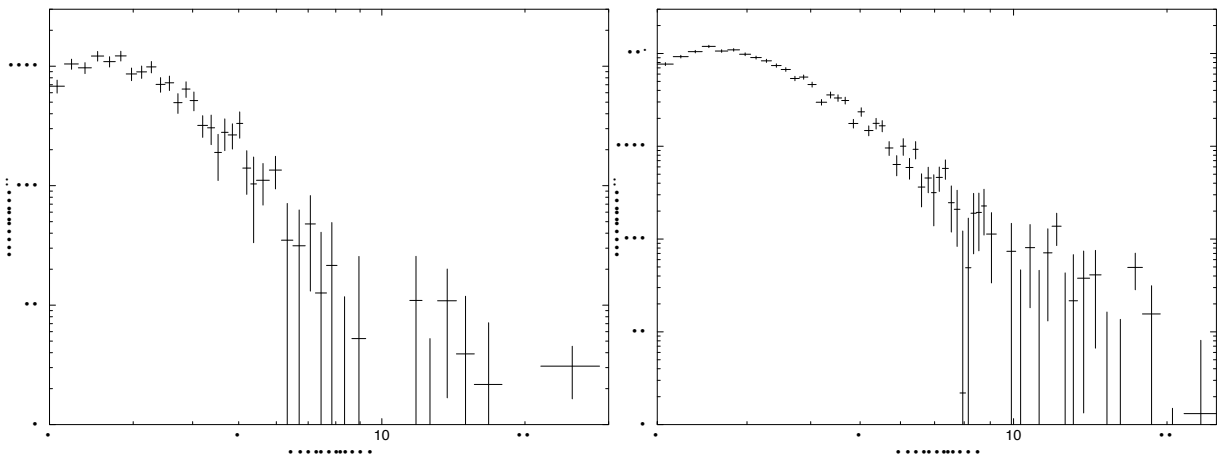

Fig. 4. The simulated spectra in 2-30 keV accumulated data over 30 (*left*) and 330 (*right*) days for AXP 4U 0142+614.

THEORY OF ACCRETION

Variability Science in Accretion Disk Theory

Ryoji Matsumoto,[1] Mami Machida,[2] and Hiroshi Oda[3]

[1] Department of Physics, Graduate School of Science, Chiba University
[2] National Astronomical Observatory
[3] Graduate School of Science and Technology, Chiba University
E-mail(RM): matumoto@astro.s.chiba-u.ac.jp

Abstract

Global three-dimensional magnetohydrodynamic simulations of black hole accretion disks enable us to study the time variabilities of black hole accretion disks without introducing the phenomenological α viscosity. Numerical simulations including optically thin radiative cooling revealed that when the disk luminosity exceeds $0.01L_{\rm Edd}$, where $L_{\rm Edd}$ is the Eddington luminosity, cooling instability taking place in the low/hard state disk creates a magnetically supported, optically thin luminous disk (high/hard state disk) whose X-ray luminosity exceeds $0.1L_{\rm Edd}$ when the accretion rate continues to increase. We found that when the outer region of the disk ($r > 20r_{\rm s}$, where $r_{\rm s}$ is the Schwarzschild radius) undergoes this transition, an inner torus is formed in $r < 10r_{\rm s}$. The inner torus produces low-frequency quasi-periodic oscillations (QPOs) and high-frequency QPOs whose frequency are $1-10$Hz, and ~ 100Hz, respectively for stellar mass black holes, and $10^{-6}-10^{-5}$Hz, and $\sim 10^{-4}$Hz, respectively for Seyfert galaxies with black hole mass $10^7M_\odot$. When the magnetic energy stored in the disk is released, the disk completes the transition to an optically thick, high/soft state. Monitoring observations by MAXI will detect these transitions in stellar mass black holes and QPOs in AGNs.

Key words: Accretion: Accretion Disk – Black Hole – Magnetohydrodynamics – QPO

1. Introduction

Black hole candidates (BHCs) show time variabilities whose time scale ranges from dynamical time scale to viscous time scale of accretion disks. The rotation period of the disk around a Schwarzschild black hole with mass M is $t_{\rm rot} = 2\pi/(GM/r_{\rm ms}^3)^{1/2} \sim 5\times10^{-4}M/M_\odot$sec at the last stable orbit $r_{\rm ms} = 3r_{\rm s}$ where $r_{\rm s}$ is the Schwarzschild radius. This period is about 5ms in galactic BHCs ($M \sim 10M_\odot$), 30min for our galactic center black hole ($M \sim 4\times10^6M_\odot$), and about 1 day for a supermassive black hole with mass $M \sim 2\times10^8M_\odot$. The rotation period can be shorter for Kerr black holes. When the innermost region of the black hole accretion disk has one-armed structure or a hot spot, the disk luminosity observed from the direction near the equatorial plane will change with this rotation time scale.

Quasi-periodic oscillations (QPOs) sometimes observed in galactic BHCs can also be produced by disk oscillations (e.g., Kato 2001). Typical angular frequency of the radial disk oscillation at radius r is the epicyclic frequency (frequency of the radial oscillation around a circular Keplerian orbit) $\kappa(r) = [(GM/r^3)(1-3r_{\rm s}/r)]^{1/2}$ in disks around a Schwarzschild black hole. This frequency has maximum $\kappa_{\rm max} = 0.0625(GM/r_{\rm s}^3)^{1/2} \sim 0.045(r_{\rm s}/c)$ at $r = 4r_{\rm s}$. The oscillation period $t_{\rm osc}$ corresponding to $\kappa_{\rm max}$ is $t_{\rm osc} \sim 1.4\times10^{-3}(M/M_\odot)$sec. The period of high frequency QPOs in galactic BHCs is the same order as $t_{\rm osc}$. It indicates that high frequency QPOs are excited in the innermost region of the disk. Since the frequency of high frequency QPOs strongly depends on the metric of space time, it gives us clues to measure the mass and spin of the black hole.

The power spectral density (PSD) of X-ray time variations in galactic BHCs in low/hard state show $1/f$ spectrum around 1Hz. The slope of the PSD becomes flatter in $f < 0.1$Hz and steeper in $f > 10$Hz. The low frequency time variations in Cyg X-1 are characterized by the X-ray shots which take place with interval of several seconds (Negoro et al. 2001). Machida and Matsumoto (2003) showed by global three-dimensional resistive magnetohydrodynamic (MHD) simulations that X-ray shots are produced by magnetic reconnection in the innermost plunging region of the disk. Smaller scale magnetic reconnections ubiquitously taking place in the disk create $1/f$ X-ray fluctuations (Kawaguchi et al. 2000).

Galactic BHCs sometimes show outbursts. During an outburst, the BHCs undergo transition from a low/hard state to a high/soft state. This transition typically takes days but Machida et al.(2006) showed by 3D MHD simulations that the transition from a low/hard state to an in-

termediate high/hard (luminous hard) state takes place in thermal time scale $t_{\rm th} \sim t_{\rm dyn}/\alpha$, where $t_{\rm dyn}$ is the dynamical time scale, and α is the viscosity parameter introduced in conventional theories of accretion disks. This time scale is less than 1 sec in galactic BHCs and days-month in AGNs. We will discuss the physical mechanism of the hard-to-soft transitions in section 3.

In galactic BHCs, high frequency QPOs are observed when the source luminosity exceeds $0.1L_{\rm Edd}$, where $L_{\rm Edd}$ is the Eddington luminosity. In AGNs with $M \sim 5 \times 10^7 M_\odot$, the period of the high frequency QPOs will be around 1 day. Long time scale observations by MAXI will be able to detect high frequency QPOs in such AGNs. Galactic BHCs also show low frequency QPOs whose frequency is several Hz and increases with the luminosity. In AGNs with $M \sim 5 \times 10^7 M_\odot$, the period of low frequency QPOs will be 10 days-1 month. We would like to discuss the excitation mechanisms of the low frequency QPOs in section 4 (see also Machida et al. 2008 and Machida's paper in this proceedings).

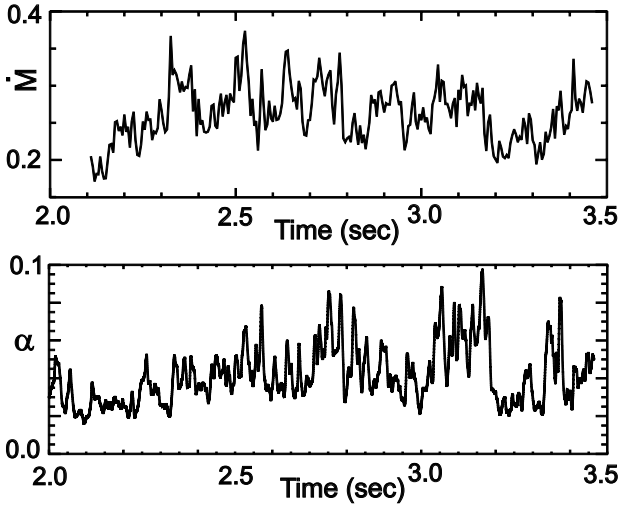

Fig. 2. Time variations of accretion rate measured at $r = 2.5r_{\rm s}$ and efficiency of angular momentum transport $\alpha =< -B_r B_\varphi/(4\pi) > /P$ obtained from global 3D MHD simulations of accretion disks (Machida and Matsumoto 2008). The time unit is 1 sec for $10M_\odot$ black hole.

2. Three-dimensional MHD Simulations of Radiatively Inefficient Black Hole Accretion Disks

Angular momentum of the rotating plasma should be transported outward or extracted from the disk to enable the accretion of the disk material. The thermal time scale and viscous time scale of an accretion disk depend on the efficiency of the angular momentum transport. In conventional theory of accretion disks, the angular momentum transport is incorporated by introducing the α parameter by assuming that the $r\varphi$- component of the stress tensor is proportional to pressure, $t_{r\varphi} = \alpha P$. By comparing the theory and observation of dwarf novae, α is estimated to be 0.01-0.1. However, 3D hydrodynamical simulations of black hole accretion disks revealed that the hydrodynamical turbulence excited in the disk is too weak (e.g., Hawley 1991). This puzzle was resolved by taking into account the magnetic fields and magnetic turbulence generated by the magneto-rotational instability (MRI; Balbus and Hawley 1991). Three-dimensional MHD simulations of a local part of the disk showed that magnetic fields are amplified

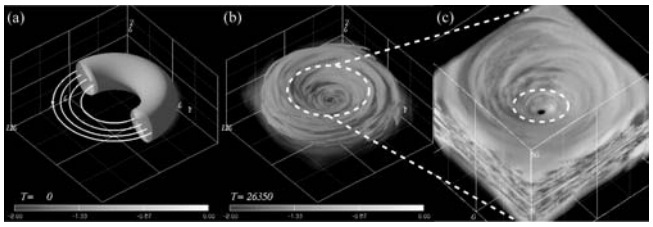

Fig. 1. Results of a 3D MHD simulation of formation of a black hole accretion disk. Grey scale shows density. (left) Initial state. White curves show magnetic field lines. (middle) Quasi-steady state. (right) Enlargement of the innermost region of the accretion disk.

until the magnetic pressure $p_{\rm mag}$ becomes about 10% of the gas pressure $p_{\rm gas}$ (i.e., $\beta = p_{\rm gas}/p_{\rm mag} \sim 10$), and that the Maxwell stress transports angular momentum with efficiency $\alpha =< -B_r B_\varphi/(4\pi) > /P \sim 0.01 - 0.1$. These results have been confirmed by global 3D MHD simulations (e.g., Matsumoto 1999; Hawley 2000; Machida et al. 2000).

Figure 1 shows a result of global 3D MHD simulations of a torus initially threaded by weak azimuthal magnetic fields (Machida and Matsumoto 2003). Assuming that the torus is optically thin and radiatively inefficient, we neglected the radiative cooling term in the energy equation. General relativistic effects are simulated by using the pseudo-Newtonian potential $\phi = -GM/(r - r_{\rm s})$. In figure 1, density distribution is depicted by grey-scale. White curves in the left panel show magnetic field lines. As the MRI grows, the initial torus is deformed into an accretion disk by efficiently transporting the angular momentum. The disk material spirally infalls toward the central black hole.

Figure 2 shows the time variation of the mass accretion rate measured at $r = 2.5r_{\rm s}$ (top panel) and the time variation of the efficiency of the angular momentum transport α in the quasi-steady state. The unit of time is 1 sec for $10M_\odot$ black hole. The time unit can be scaled arbitrary in proportion to the black hole mass. The accretion rate and α show large amplitude fluctuations similar to the X-ray light curves of black hole candidates. The range of α $(= 0.01 - 0.1)$ is consistent with the values conventionally assumed in disk models based on the α prescription of viscosity.

Figure 3 shows the PSD of time variabilities of mass

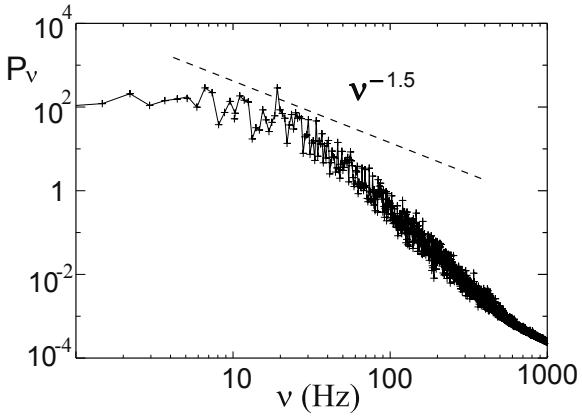

Fig. 3. Power spectral density of time variation of accretion rate obtained from a MHD simulation of radiatively inefficient, hot disk.

accretion rate obtained from global 3D MHD simulations of optically thin, hot disk (Machida and Matsumoto 2008). It reproduces the $1/f$ fluctuations around 10Hz observed in stellar mass black holes and steepening of the PSD in $\nu > 10$Hz.

3. Hard-to-Soft State Transition

During an outburst of galactic black hole candidates, they undergo hard-to-soft state transition. The top panel of figure 4 schematically shows the color-luminosity diagram of the evolution of an outburst. An outburst starts from the X-ray hard, low luminosity state (low/hard state). The X-ray luminosity of the source increases almost preserving the X-ray color (from the right bottom to the right top). When the luminosity attains $\sim 0.1 L_{\rm Edd}$, the source undergoes a transition to the high/soft state.

The bottom panel of figure 4 shows the theoretically obtained thermal equilibrium curves of accretion disks (Abramowicz et al. 1995). The left branch is an optically thin branch, and the right branch is an optically thick branch. The upper half of the optically thin branch corresponds to the low/hard state, in which the advective cooling balances with the heating. Such accretion flows are called advection dominated accretion flows (ADAF; e.g., Narayan & Yi 1994) or radiatively inefficient accretion flows (RIAF). Such disks are hot ($T \sim 10^{11}$K), optically thin, and emit hard X-rays. Since the radiative cooling rate increases with the accretion rate, optically thin thermal equilibrium disappears when the accretion rate exceeds the threshold. The disk will then undergo a transition to the optically thick, high/soft state. The critical luminosity for this transition is $\sim 0.01 L_{\rm Edd}$ when $\alpha = 0.01 - 0.1$. However, BHCs often stay in hard state even when their luminosity exceeds the theoretically expected threshold for the hard-to-soft transition.

Machida et al. (2006) carried out global 3D MHD

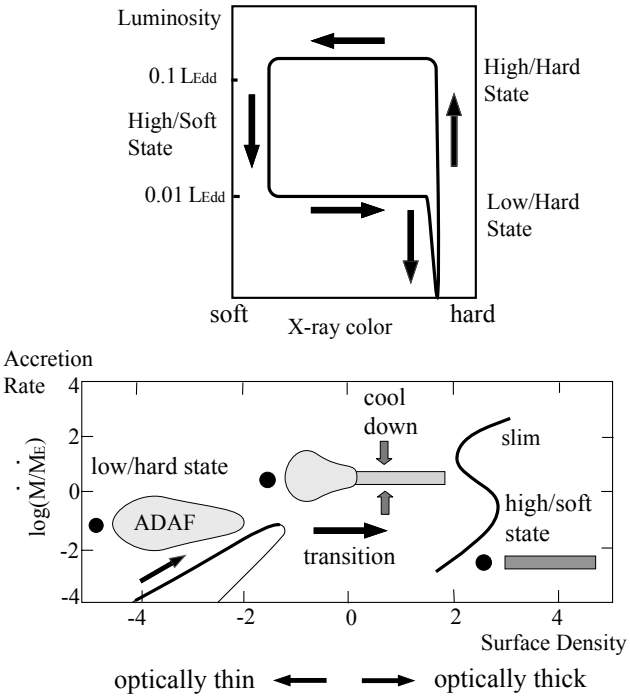

Fig. 4. (top) A schematic color-luminosity diagram of the time evolution of black hole outbursts. (bottom) Thermal equilibrium curves of black hole accretion disks (Abramowicz et al. 1995).

simulations of black hole accretion disks including optically thin radiative cooling. The top panel of figure 5 shows the result of the simulation without including the radiative cooling. Geometrically thick, hot disk is formed. The bottom panel of figure 5 shows the density (left) and temperature (right) of the disk obtained by a simulation including the radiative cooling. As the cooling instability grows, the disk shrinks in the vertical direction and forms a dense, cool disk in the equatorial region. Since the critical accretion rate for the cooling instability is higher in the inner region closer to the black hole, inner regions of the disk ($r < 10 r_{\rm s}$) still stays in the low density, hot state.

We found that since the disk shrinks in the vertical direction almost conserving the mean azimuthal magnetic flux, magnetic field is amplified in the disk and that the disk is supported by magnetic pressure. Figure 6 shows the evolution of the density, temperature, and plasma β in the equatorial region. As the cooling instability grows, magnetic pressure dominant (low β), cool disk is formed. Once a low-β disk is formed, buoyant escape of the magnetic flux will be suppressed because the Parker instability is stabilized by the magnetic tension (Shibata et al. 1990). Since the cooling balances with the heating in such disks, the low-β disk stays in a quasi-steady state. Such disks are optically thin because the disk cannot shrink in the vertical direction due to the

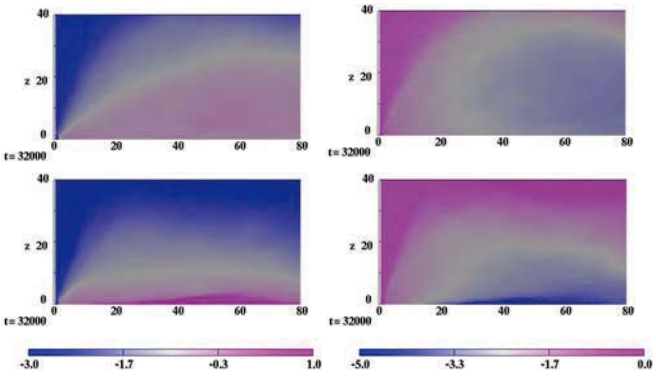

Fig. 5. Results of global 3D MHD simulations of black hole accretion disks. Left panels show the density, and the right panels show the temperature. (top) Without cooling. (bottom) A result of simulation including optically thin radiative cooling. Dense, cool disk is formed in the equatorial region.

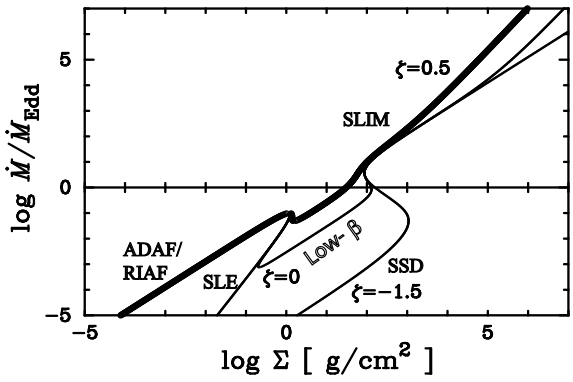

Fig. 7. Thermal equilibrium curves of black hole accretion disks including azimuthal magnetic field (Oda et al. 2008). Magnetic pressure supported equilibrium state (low-β branch) connects the optically thin ADAF/RIAF branch and the optically thick SSD (Shakura Sunyaev Disk) and SLIM disk branch.

enhanced magnetic pressure. The low-β disk explains why black hole candidates stay in X-ray hard state even when their luminosity exceeds the threshold for the onset of the cooling instability.

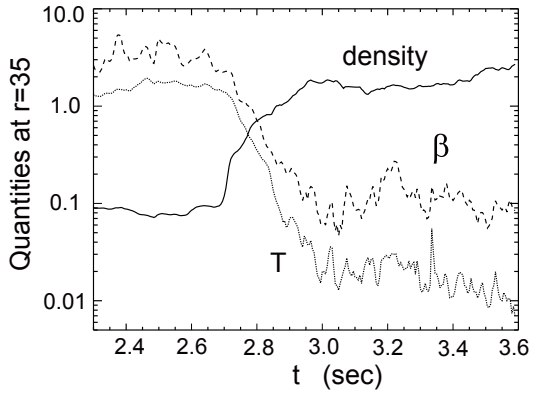

Fig. 6. Time evolution of density, temperature, and plasma β at the equatorial plane during the cooling instability for $10M_\odot$ black hole.

We obtained thermal equilibrium curves of black hole accretion disks taking into account the mean azimuthal magnetic fields (Oda et al. 2007, 2008). Figure 7 shows a result using the cooling function applicable both to optically thin and thick region. The parameter ζ denotes the radial advection rate of azimuthal magnetic flux. We assumed that the $r\varphi$-component of stress tensor is proportional to the total pressure including the gas pressure, magnetic pressure, and the radiation pressure. We found that when the azimuthal magnetic flux is large enough ($\zeta > -1$), low-β branch connects the optically thin branch and the optically thick branch. During the hard-to-soft transition, the black hole candidate will evolve quasi-steadily along this equilibrium curve until their X-ray luminosity approaches $L_{\rm Edd}$. We can explain the existence of the high/hard (or bright hard) state by this low-β branch. When the mass accretion rate is close to the Eddington mass accretion rate $\dot{M}_{\rm Edd} = L_{\rm Edd}/(\eta c^2)$, where η is the energy conversion efficiency which we take $\eta = 0.1$, limit-cycle oscillation is expected between the low-β branch and the slim disk branch. A galactic microquasar GRS1915+105 may stay in this state.

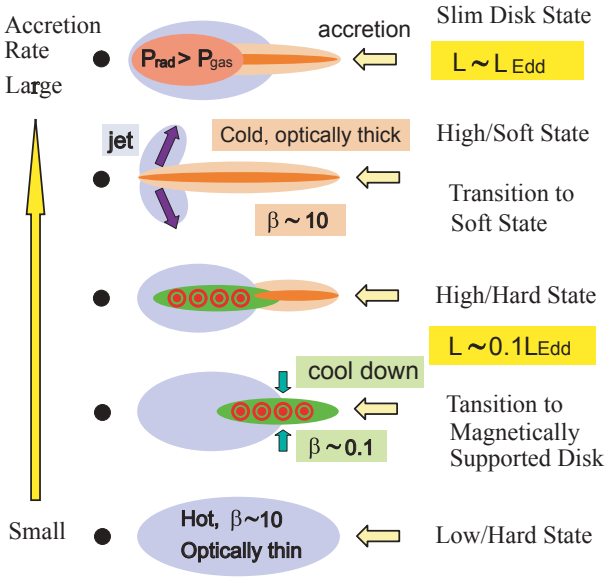

Fig. 8. A schematic picture of the evolution of magnetized black hole accretion disks.

Figure 8 schematically shows the evolution of a black hole candidate during an outburst. When the accretion rate increases and the X-ray luminosity exceeds $0.01L_{\rm Edd}$, cooling instability takes place in the outer region of the disk. When $L \sim 0.1L_{\rm Edd}$, the cooling instability takes place in the innermost region close to the black hole. When the magnetic energy stored in the low-

β disk is released by magnetic reconnection or buoyant rise of the magnetic flux, relativistic jets will be launched from the innermost region of the disk. When the accretion rate increases further, radiation pressure supported slim disk will be formed. Narrow line Seyfert galaxies whose luminosity is close to $L_{\rm Edd}$ may stay in this state.

4. Quasi Periodic Oscillations of Black Hole Accretion Disks

In galactic black hole candidates, quasi periodic oscillations are observed when their luminosity is high ($L > 0.1L_{\rm Edd}$). It indicates that QPOs appear when the cooling instability takes place in the disk. We carried out global 3D MHD simulations starting from a cool, outer torus at $r = 50r_{\rm s}$ (Matsumoto et al. 2007, Machida et al. 2008). We found that when cool gas accretes to the black hole, an inner torus is formed in $r < 10r_{\rm s}$ because angular momentum transport rate decreases. When the magnetic field is weak, the inner torus subjects to the non-axisymmetric instability known as the Papaloizou Pringle instability (Papaloizou & Pringle 1984) and deforms itself into a crescent shape (figure 9). Magnetic fields are strongly amplified in the deformed torus. Figure 10 shows the time variation of the magnetic energy and Joule heating rate. Quasi-periodic sawtooth like oscillation is excited. This oscillation is driven by the magnetic field amplification and subsequent release of magnetic energy due to magnetic reconnection. As the magnetic energy is amplified and β approaches unity, magnetic reconnection taking place in the disk releases the magnetic energy stored in the disk and restores the disk into a weakly magnetized state. Subsequently, non-axisymmetric instability grows and magnetic energy is amplified again. The period of the sawtooth-like oscillation is about 10 rotation period of the inner torus, which corresponds to 1-10Hz in stellar mass black holes. This

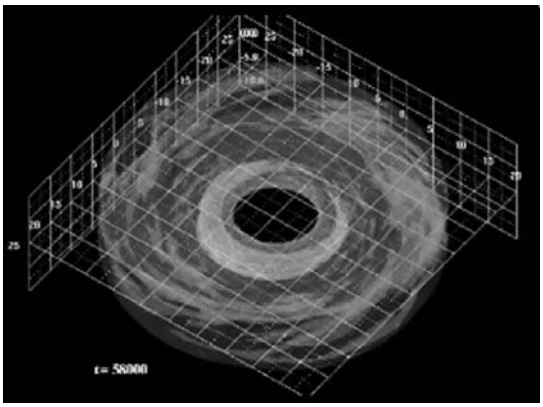

Fig. 9. Formation of an inner torus and growth of non-axisymmetric structure in the inner torus. Grey scale shows density.

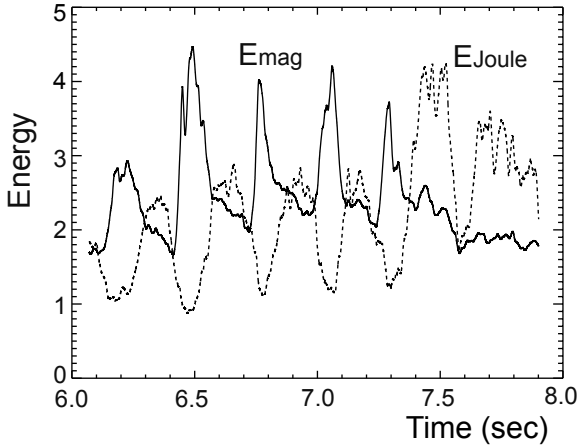

Fig. 10. Sawtooth-like oscillation in the inner torus around a $10M_\odot$ black hole obtained from global 3D MHD simulation of cool accretion flows (Matsumoto et al. 2007).

frequency coincides with the low frequency QPOs (LFQPOs) observed in galactic black hole candidates.

Figure 11 shows the power spectral density of the time variation of mass accretion rate when the sawtooth-like oscillation is excited in the inner torus. Twin peak high frequency oscillations (HFQPOs) with frequency ratio 2:3 are also excited (Matsumoto et al. 2007).

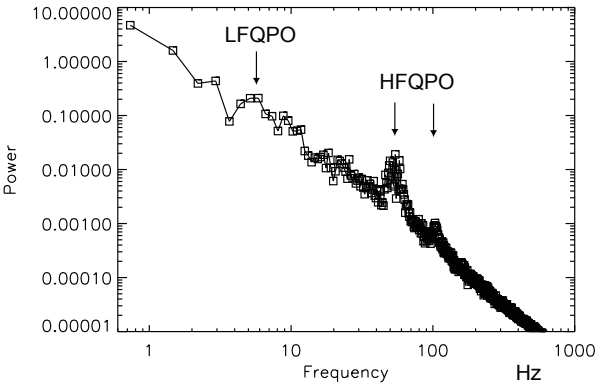

Fig. 11. Power spectral density of time variation of accretion rate at $r = 2.5r_{\rm s}$ obtained from the global 3D MHD simulation of a cool accretion flow around a $10M_\odot$ black hole.

5. Summary and Discussion

Global 3D MHD simulations of black hole accretion disks reproduced $1/f$ fluctuations of low/hard state disks, and low frequency QPOs and high frequency QPOs observed in luminous disks. Global simulations including radiative cooling showed that a magnetically supported (low-β) disk is formed during the hard-to-soft transition. The low-β disk is geometrically slim, optically thin and spectrally hard until their luminosity approaches the Eddington luminosity. These results explain why black hole

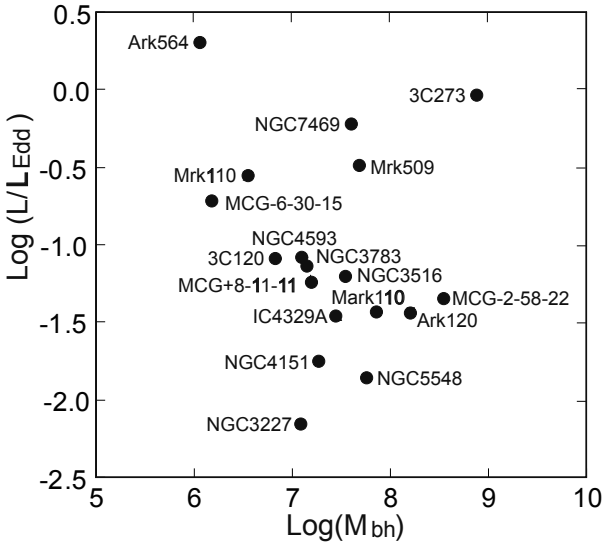

Fig. 12. Black hole mass and the ratio of their luminosity to the Eddington luminosity for nearby Seyfert galaxies and quasars whose X-ray flux exceeds 10mCrab.

candidates stay in high/hard state even when their luminosity exceeds the upper limit for the existence of radiatively inefficient, optically thin disk (ADAF/RIAF)

The transition from ADAF/RIAF to low-β disk proceeds from the outer region of the disk. When the outer disk is cooled by this transition, the cool accreting gas forms an inner torus in $r < 10r_{\rm s}$. We showed that low frequency QPOs are excited in the inner torus and that the inner torus is deformed into a crescent shape. When the disk is observed from the direction close to the equatorial plane, periodic time variabilities with time scale of the rotation period of the inner torus will be observed. Numerical simulations also indicate that the low frequency QPOs accompany high frequency QPOs.

The period of the low frequency QPOs is about 10 rotation period of the inner torus ($0.01 - 0.1M/M_{\odot}$ sec). The period will be $10^5 - 10^6$ sec in Seyfert galaxies whose black hole mass is $10^7 M_{\odot}$. Figure 12 plots the black hole mass and X-ray luminosity normalized by the Eddington luminosity for nearby Seyfert galaxies and quasars whose X-ray luminosity exceeds 10mCrab. We adopted the black hole mass and X-ray luminosity reported by Turner et al. (1999) and Bian & Zhao (2003). More than 10 galaxies exist in the luminosity range we expect low frequency QPOs ($0.01L_{\rm Edd} - 1L_{\rm Edd}$). MAXI will be able to detect low frequency QPOs from these AGNs. Higher time-resolution observations by Suzaku or XMM will be able to detect high frequency QPOs.

Another interesting time variability of BHCs is the relaxation oscillation between the gas pressure (or magnetic pressure) dominant disk and radiation pressure dominant slim disk (Honma et al. 1991). The quasi periodic bursts observed in GRS1915+105 can be explained by this mechanism. The period of the relaxation oscillation is $\sim 10M/M_{\odot}$ sec. We expect similar relaxation oscillations with period $\sim 10^7$sec in narrow line Seyfert galaxies such as Ark564 whose X-ray luminosity is $\sim L_{\rm Edd}$ and black hole mass $M \sim 10^6 M_{\odot}$.

We thank T. Kawaguchi for summarizing the black hole mass and X-ray luminosity of nearby AGNs shown in figure 12. Numerical simulations were carried out by using VPP5000 at National Astronomical Observatory, Japan. This work is supported by the Grants-in-Aid for Scientific Research of Ministry of Education, Culture, Sports, Science, and Technology (RM: 17030003, 20340040).

References

Abramowicz, M.A. et al. 1995, ApJ, 438, L37
Balbus, S.A., & Hawley, J.F. 1991, ApJ, 376, 214
Bian W., & Zhao, Y. 2000, ApJ, 591, 733
Hawley, J.F. 1991, ApJ, 381, 496
Hawley, J.F. 2000, ApJ, 528, 462
Honma, F., Matsumoto, R., & Kato, S. 1991, PASJ, 43, 147
Kato, S. 2001, PASJ, 53, 1
Kawaguchi et al. 2000, PASJ, 52, L1
Machida, M., Hayashi, M.R., & Matsumoto, R. 2000, ApJ, 532, L67
Machida, M., & Matsumoto, R. 2003, ApJ, 585, 429
Machida, M., Nakamura, K.E., & Matsumoto, R. 2006, PASJ, 58, 193
Machida, M., & Matsumoto, R. 2008, PASJ, 60, 613
Matsumoto, R. 1999, Proceedings of the International Conference on Numerical Astrophysics 1998, Ed. S. Miyama et al., Kluwer Academic (Astrophysics and Space Science Library v240), p.195
Matsumoto, R., & Machida, M. 2007, Proceedings of IAU Symposium 238, Black Holes from Stars to Galaxies - Across the Range of Masses, Ed. V. Karas, G. Matt, Cambridge University Press, p.37
Narayan, R., & Yi, I. 1994, ApJ, 428, L13
Negoro, H., Kitamoto, H., & Mineshige, S. 2001, ApJ, 554, 528
Oda, H., Machida, M., Nakamura, K.E., & Matsumoto, R. 2007, PASJ, 59, 457
Oda, H., Machida, M., Nakamura, K.E., & Matsumoto, R. 2008, Astrophysics of Compact Objects, AIP Conference Proceedings, 968, p.408
Papaloizou, J.C.B., & Pringle, J.E. 1984, MNRAS, 208, 721
Shibata, K., Tajima, T., & Matsumoto, R. 1990, ApJ, 350, 295
Turner, T.J., George, I.M., Nandra, K. , & Turcan, D. 1999, ApJ, 524, 667

Quasi-Periodic Osicllations and Variable Emissions in Magnetohydrodynamic Accretion Flows

Yoshiaki Kato

Institute of Space and Astronautical Science, Japan Aerospace Exploration Agency (ISAS/JAXA)
3-1-1 Yoshinodai, Sagamihara, Kanagawa 229-8510, Japan
E-mail(YK): kato.yoshiaki@isas.jaxa.jp

Abstract

We present our study of oscillations and emissions in three-dimensional (3-D) magnetohydrodynamic (MHD) accretion flows around black holes. It is found that a pair of persistent quasi-periodic oscillations (twin QPOs) is excited at the resonant radius, where the ratio of Keplerian frequency to epicyclic frequency is close to 2:1. The power spectrum density (PSD) shows that the lower peak frequency corresponds to the Keplerian frequency, while the upper peak frequency corresponds to the sum of Keplerian frequency and epicyclic frequency. The results provide the first direct evidence for the excitation of resonant disk oscillation in MHD accretion flows. It is also found that the emergent spectra from radio to gamma-ray of the MHD accretion flows fluctuates in the wide range of frequency and does not always vary coherently.

Key words: accretion, accretion disks — magnetohydrodynamics: MHD — quasi-periodic oscillations — radiation: radiative transfer

1. Introduction

Quasi-Periodic X-ray brightness oscillations ranging from 1 mHz to 1 kHz have been observed in some low-mass X-ray binaries. After the discovery of high frequency QPOs (HF-QPOs) whose frequnecy is comparable to the oribital frequency at the innermost stable circular orbit (ISCO), the HF-QPOs are believed to be a footprint of the metric of compact objects such as neutron stars and black holes. Recently, Remillard et al. (2005) pointed out that more than one type of accretion disk can play QPOs and optically thin plasma could be a plausible source of modulated emissions of HF-QPOs. Several models have been proposed by different groups, however, the modualation mechanism of HF-QPOs has been not been settled yet.

Disk oscillations are the most promising mechanism of the HF-QPOs. This is because the disk oscillation model can explain two simultaneous QPOs having a constant ratio of peak frequencies. Recently, magnetohydrodynamic (MHD) simulations have been widely accepted as a standard framework for studying the dynamics of accretion flows, however, the properties of disk oscillations in MHD accretion flows are poorly understood. This is why we motivated to study oscillations and waves in MHD accretion flows. In this proceedings, we introduce our study of the disk oscillations in MHD accretion flows (Kato 2004) and briefly report on the emission properties of the disk oscillations.

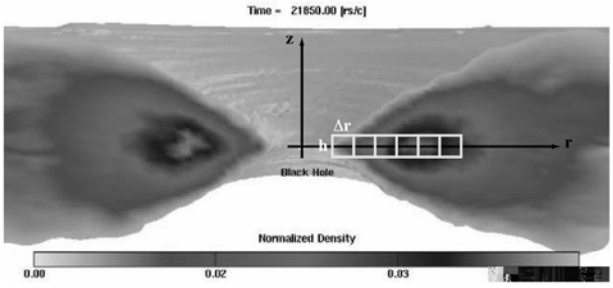

Fig. 1. A perspective view of 3-D MHD accretion flows. Gray-scale indicates the normalized density. A black hole is located at the origin.

2. MHD studies on HF-QPOs

The figure 1 shows a snapshot of quasi-steady MHD accretion flows plunging into black holes. We sampled time variation of mass fluxes both in radial and vertical direction at each cells in the equatorial plane ($|z| < h/2 = 5r_{\rm s}$ where $r_{\rm s}$ is the Schwartzchild radius). In this study, we assume that emissivity of each cells is proportional to the gravitational energy loss in terms of mass fluxes (see Kato 2004 in detail).

2.1. Oscillations and Waves

In the figure 2, radial and vertical oscillations are displayed. The horizontal axis indicates the radius and the vertical axis indicates the time. For a 10 solar mass black hole, sampling is started at 1 sec from the beginning of

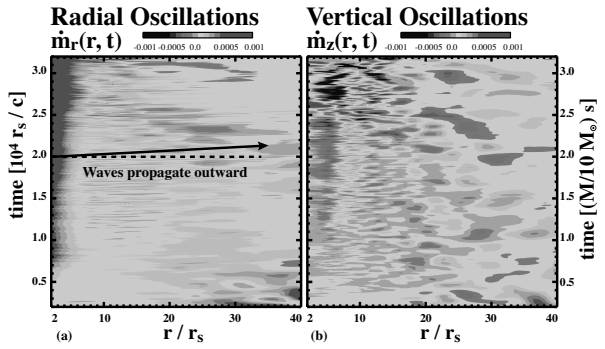

Fig. 2. Radial and vertical oscillations in spact-time diagram. The horizontal axis is the radius and the vertical axis is the time. Gray-scale indicates the mass fluxes at each cells.

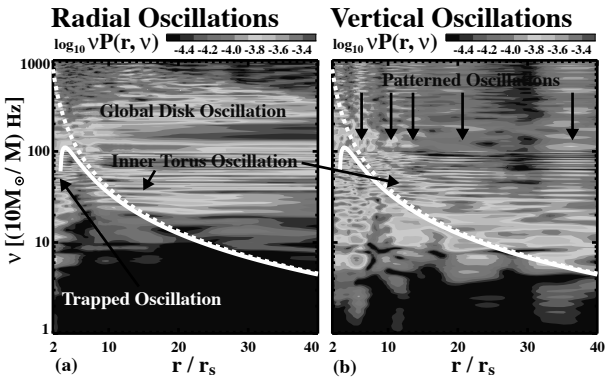

Fig. 3. Power Spectrum Density (PSD) of the radial and the vertical oscillations. The horizontal axis is the radius and the vertical axis is the time. Gray-scale indicates the mass fluxes at each cells.

the simulation and is ended 3 sec and the sampling duration is 2 sec in total. The first 1 sec is called as the early phase and the last 1 sec is called as the late phase in this study. The mass fluxes are displayed in gray-scale.

2.2. Global disk oscillations

The figure 3 shows PSDs of the radial and the vertical oscillations as a function of radius. The power of oscillations is shown by gray-scale. A dashed line and a solid line indicate Keplerian frequency and epicyclic frequency as a function of radius, respectively. In radial oscillations, we found some global oscillations. In vertical oscillations, we found several patterned oscillations. One of them is located at $6r_{\rm s}$. In addition, we found weak trapped oscillations inside the radius where the epicyclic frequency become maximum and also weak oscillations of inner torus located around $10r_{\rm s}$.

2.3. Twin HF-QPOs

Integrated PSD over the radius is shown in figure 4. We found two twin QPOs. One is transient twin QPOs only in early phase and theother is persistent twin QPOs in both early and late phase of MHD accretion flows.

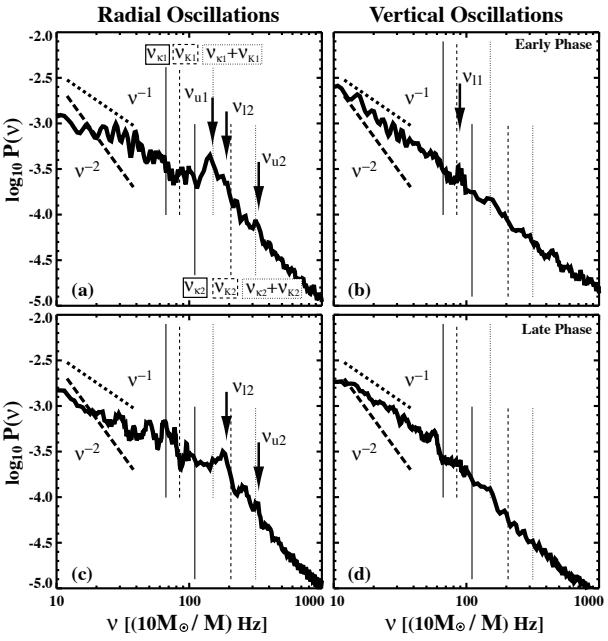

Fig. 4. Integrated PSD of the radial and the vertical oscillation.

In twin QPOs in radial oscillations, the lower peak frequency corresponds to the Kepler frequency and the higher peak frequency corresponds to the sum of Keper frequency and epicyclic frequency at the resonant radius where the ratio of Kepler and epicyclic frequency is close to 2 in the Schwartzchild black hole. Radial oscillation is excited at the resonant radius and it propagate the accretion disk globally. We have discovered for the first time resonant global disk oscillations in magnetized accretion disks.

2.4. Short Summary

We have found twin QPOs in the integrated PSD of variabilities in the magnetized accretion flows. Frequencies of QPOs corresponds to the resonant frequencies at the resonant radius. These QPOs are likely to be excited at the resonant radius where the ratio of the Kepler frequency and the epicyclic frequency is 2:1. This may be caused by the wave-warp resonance (see S. Kato 2004 in detail; see also Abramowicz 2003, Rebusco 2004). The ratio of resultant upper and lower frequencies of QPOs is close to 3:2 which is consistent with the observed ratio (Remillard et al. 2002).

3. Radiation Transfer Calculations

We compute radiation properties of our 3-D MHD simulation data and compare our result with the spectral energy distribution (SED) of the Galactic center source, Sgr A*. For a radiative transfer calculation, there are three parameters, normalization density, black hole mass, and electron temperature. The normalization den-

sity is leave as a free parameter in order to fit the observed SED and the electron temperature is estimated by the gas temperature in the MHD simulation. The black hole mass is fixed as $3.6 \times 10^6 M_\odot$ (Eckert et al. 2005). For radiative process, Synchrotron emision/absorption, inverse-Compton scattering, and Bremsstrahlung emission/absorption by thermal electrons (e.g., Narayan & Yi 1995; Manmoto 2000) are taken into consideration in this study.

3.1. Emergent SED

In figure 5, we plot SEDs of MHD accretion flows. The emergent SED is consistent with the observed SED of Sgr A* from radio to gamma-ray in quiescent state. Radio band consist of self-absorbed synchrotron emission. From submillimeter to optical band consist of synchrotron self-compton emission. Above X-ray band consist of Bremsstrahlung emission.

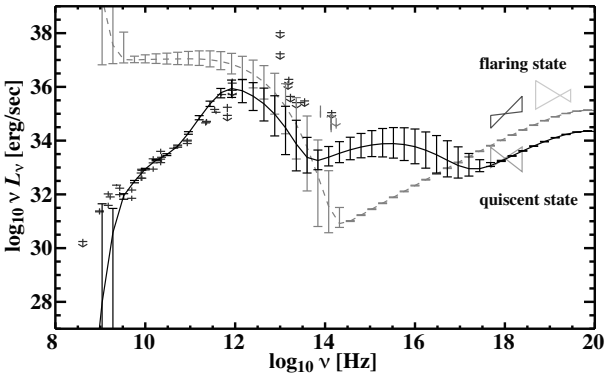

Fig. 5. Spectral Energy Distribution (SED) of MHD accretion flows ranging from radio to gamma-ray. Solid and dashed lines indicate the emergent spectra and the emitted spectra, respectively. Bars indicate the time variation. Cross points and "bow ties" indicate the observed spectra in the Galactic center (Narayan et al. 1998; Eckart et al. 2006; Baganoff 2001; Belandger et al. 2005)

3.2. Synthesis Images

We created images of centimeter, submillimeter, and infrared bands by using the ray-tracing calculation displayed in figure 6. We found that the size of a core emission region in the centimeter and the submillimeter bands is about 30 $r_{\rm s}$ around a black hole. In the infrared band, we found that a disk like emission region extends more than 100 $r_{\rm s}$. Direction of magnetic vectors in centimeter and submillimeter bands is similar but that of infrared band is different from the others.

4. Future Prospects

Radiation transfer studies of MHD data will be a keystone between theory and observation. Intensive timing analysis both on variable emissions in MHD accretion

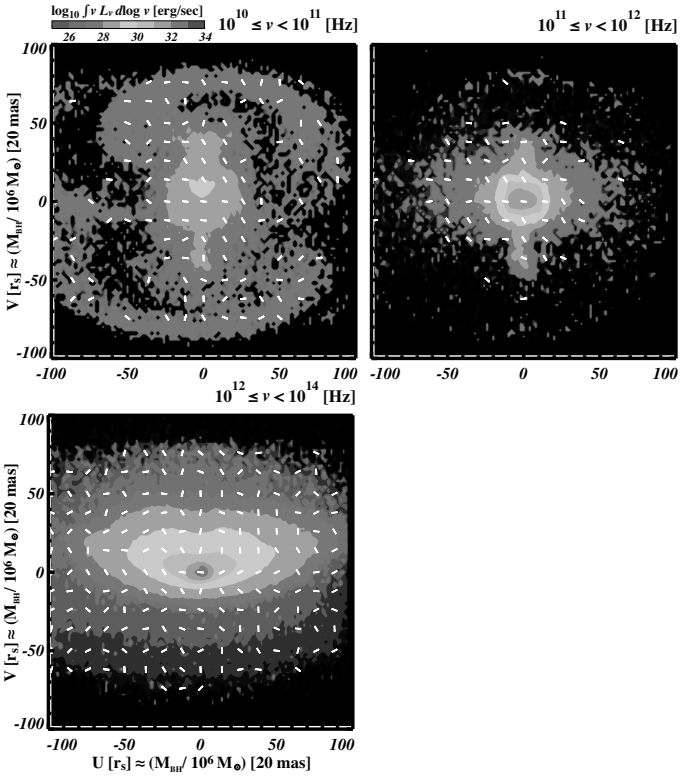

Fig. 6. Synthesis images in centimeter, submillimeter, and infrared bands. White arrows indicate the magnetic vector which is perpendicular to the polarization vector.

flows and on X-ray brightness oscillations in X-ray binaries will provide a crucial information on the origin of QPOs.

References

Abramowicz, M. A. et al. 2003 PASJ, 55, 467
Baganoff, F. K., et al. 2001 Nature, 413, 45
Baganoff, F. K., et al. 2003 ApJ, 591, 891
Bélanger, G., et al. 2006 ApJ, 636, 275
Eckart, A. et al. 2005 The Evolution of Starbursts, 783, 17
Eckart, A., et al. 2006, A&A, 450, 535
Kato, S. 2004 PASJ, 56, 905
Kato, Y. 2004 PASJ, 56, 931
Manmoto, T. 2000 ApJ, 534, 734
Narayan, R., & Yi, I. 1995 ApJ, 452, 710
Narayan, R. et al. 1998 ApJ, 492, 554
Rebusco, P. 2004 PASJ, 56, 553
Remillard, R. A. et al. 2002 ApJ, 580, 1030
Remillard, R. A. 2005 Astronomische Nachrichten, 326, 804

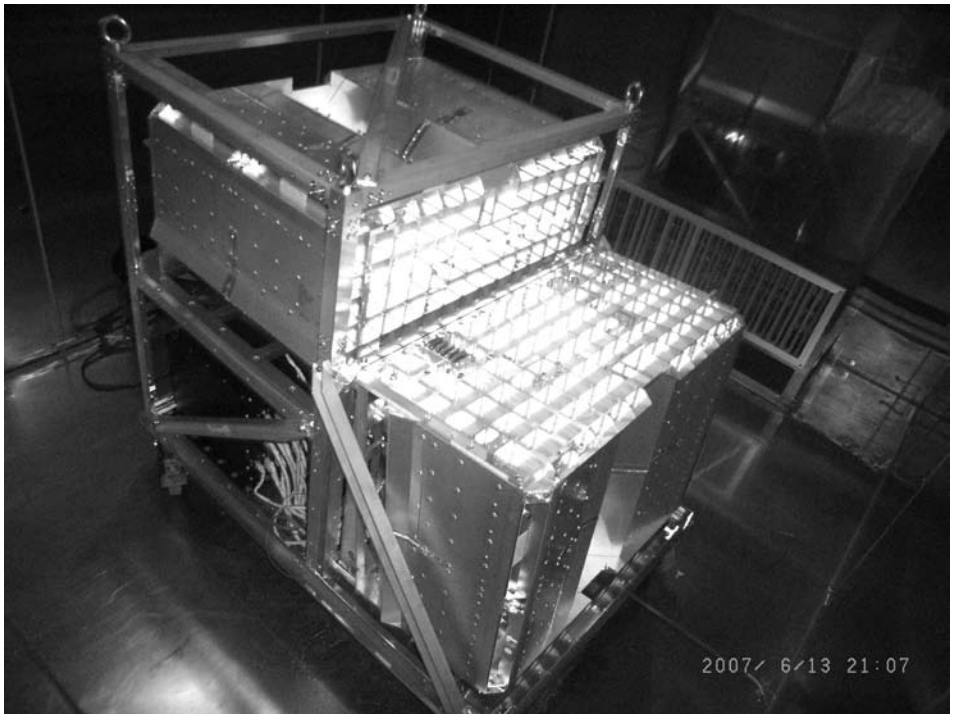

X-ray Emissions from Three-dimensional Magnetohydrodynamic Coronal Accretion Flows

Norita Kawanaka,[1] Yoshiaki Kato,[2] and Shin Mineshige[3]

[1] Research Center for the Early Universe, Graduate School of Science,
The University of Tokyo, 7-3-1, Hongo, Bunkyo-ku, Tokyo, 113-0033, Japan
[2] Institute of Space and Astronautical Science, JAXA, 3-1-1, Yoshinodai, Sagamihara, Kanagawa, 229-8510, Japan
[3] Department of Astronomy, Kyoto University, Oiwake-cho, Kitashirakawa, Sakyo-ku, Kyoto, 606-8502, Japan
E-mail(NK): norita@resceu.s.u-tokyo.ac.jp

Abstract

In explaining the spectral properties of active galactic nuclei (AGNs) and X-ray binaries, it is often assumed that they consists of a geometrically thin, optically thick disk and hot, optically thin corona surrounding the thin disk. As for a model of a corona, we adopt the simulation data of three-dimensional, non-radiative MHD accretion flows calculated by Kato and coworkers, while for a thin disk we assume a standard type disk. We perform Monte Carlo radiative transfer simulations in the corona, taking into account the Compton scattering of the soft photons from the thin disk by hot thermal electrons and coronal irradiation heating of the thin disk, which emits blacbody radiation. By adjusting the density parameter of the MHD coronal flow, we can produce the emergent spectra which are consistent with those of typical Seyfert galaxies. Moreover, we find rapid time variability in X-ray emission spectra, originating from the density fluctuation produced by the magnetorotational instability in the MHD corona.

Key words: accretion, accretion disk – black hole physics – radiative transfer – X-rays: general

1. Introduction

Accreting black holes, such as active galactic nuclei (AGNs) and black hole binaries (BHBs) during their very-high spectral state [state with luminosities around a few tenths of the Eddington limit ($L_{\rm Edd}$)], show the radiation spectra dominated by two components; the thermal bump in UV/soft X-ray band and the power-law emission with a spectral index of $\alpha \sim 1$ in the X-ray band (possibly with a high energy cutoff around MeV). In addition, iron fluorescent line emission feature ($\sim 6-7$keV) and reflection hump (a few tens-100keV) are often observed. These components are often explained by the disk-corona model (Liang & Price 1977; Bisnovatyi-Kogan & Blinnikov 1977; Haardt & Maraschi 1991, 1993). In this model, the accretion flow consists of geometrically thin, optically thick accretion disk whose structure is studied by Shakura & Sunyaev (1973), and hot, optically thin corona surrounding the disk. The thermal bump is believed as the thermal emission from the optically thick disk, and the power-law component is interpreted to be formed by photons which are emitted from the disk and Compton up-scattered by hot electrons in the corona. So far, however, most of theoretical corona models assume that the coronal structure is steady in time and then the spectral energy distribution is also steady. Such feature cannot explain the highly time-variable spectral behavior of accreting black holes.

On the other hand, in understanding the structure and dynamics of accretion flows, the magnetohydrodynamic (MHD) approach is indispensable, since Balbus & Hawley (1991) rediscovered the magnetorotational instability (MRI) as the fundamental mechanism of angular momentum transfer in accretion disks. Detailed dynamical features of MHD accretion flows have been investigated via global three-dimensional numerical simulations by many authors (Matsumoto 1999; Stone & Pringle 2001; Machida et al. 2001; Hawley & Krolik 2001, 2002; Machida & Matsumoto 2003; Armitage & Reynolds 2003; De Villiers et al. 2003; Gammie et al. 2003; Igumenshchev et al. 2003). In those accretion flows simulated in their studies, the dissipated energy would not be radiated away efficiently, because of their low density, and be advected inward to the central black hole (Ichimaru 1977; Narayan & Yi 1994; Abramowicz et al. 1995; Kato et al. 1998). Such accretion flows are referred to as "radiative inefficient accretion flows" (RIAFs). The RIAF model is believed to fit the emergent spectrum of Sagittarius A*, some authors have calculated the time dependent radiation spectra predicted from simulated MHD accretion flows with the aim to reproduce the observed behavior of Sgr A* (Hawley &

Balbus 2002; Goldstone et al. 2005; Ohsuga et al. 2005; Moscibrodzka et al. 2007).

In this study, we adopted the three-dimensional simulation data of RIAFs by Kato et al. (2004, hereafter KMS04) as a model of time-dependent, hot and optically thin corona, and calculate for the first time the emergent spectra of disk-corona accretion flow systems. We assume that the optically thick, geometrically thin disk is embedded in the corona, and that this disk is emitting soft photons with thermal spectrum. The interactions other than radiative processes, such as mass evaporation/condensation or heat conduction, are neglected, for simplicity. We perform three-dimensional Monte Carlo radiative transfer simulations to properly calculate the radiation processes and the emergent spectra predicted from this disk corona model (for the detail see Kawanaka et al. 2008).

2. Model and Calculation Method

2.1. Overview of the Adopted MHD Corona Model

KMS04 investigated the evolution of a torus threaded by weak localized poloidal magnetic fields by performing the three-dimensional MHD simulation. They solved the basic equations of the resistive MHD in the cylindrical coordinates, $(r,\ \phi,\ z)$. The calculation was started with a rotating torus in hydrostatic balance located around $r = r_0 = 40r_{\rm S}$. The entire computational box size is $0 \leq r \leq 200r_{\rm S}$, $0 \leq \phi \leq 2\pi$, and $-50r_{\rm S} \leq z \leq 50r_{\rm S}$, and they simulated a full 360° domain (see KMS04 and Kato 2004 for more detail).

The simulated MHD flow has almost steady structure, but is slightly oscillating because of the turbulence driven by MRI, and geometrically thick density distribution is produced. In this quasi-steady accretion flow, the density profile is $\rho \propto r$ in the inner part ($r < 20r_{\rm S}$), while $\rho \propto r^{-1}$ in the outer part ($r > 20r_{\rm S}$) (see Fig. 4 in KMS04). We use this quasi-steady density distribution as well as the ion temperature distribution in modeling the corona in which hot thermal electrons up-scatter the soft photons emerging from the cold disk virtually located in the equatorial plane. The dataof physical properties are given at each point in the simulation box associated with Cartesian coordinates $(x,\ y,\ z)$, in which the black hole is located at the origin of the coordinate axes, the z-axis is set to be the rotation axis of the accretion flow, and the x-y plane corresponds to the equatorial plane. We employ Cartesian grids with numbers $(N_x,\ N_y,\ N_z) = (101,\ 101,\ 101)$ of cells. The size of the calculating box is $2X \times 2Y \times 2Z$, where we set $(X,\ Y,\ Z) = (99.9r_{\rm S},\ 99.9r_{\rm S},\ 99.9r_{\rm S})$.

In the MHD simulations with no radiative loss the density is given as non-dimensional number $\tilde{\rho}$ with the normalization factor ρ_0, which is treated a free parameter in our calculation. Basically the coronal density is determined by evaporation of the disk gas, but here we determine ρ_0 so that the spectral features predicted from the corona with such density agree with the observations.

As for the electron temperature, we should note that it is not the same as the proton temperature, which is directly derived from the simulation. Actually the electrons in a corona are cooled via inverse Compton scattering, and so should have a lower temperature in the realistic situation. We can evaluate the electron temperature, T_e, through the energy balance of the electrons between Coulomb collisions with ions and radiative cooling,

$$\int_{-Z}^{Z}\int_{r_{\rm in}}^{r_{\rm out}} \lambda_{ie} 2\pi r dr dz = \int L_C(\nu;\ r_{\rm in} \leq r \leq r_{\rm out}) d\nu. \quad (1)$$

Here λ_{ie} is the energy transfer rate from ions to electrons (Stepney & Guilbert 1983) and $L_C(\nu)$ is the coronal luminosity at frequency ν. In the present study, we divide the corona into three regions ($0 \leq r \leq 10r_{\rm S}$, $10r_{\rm S} < r \leq 30r_{\rm S}$, and $30r_{\rm S} < r$; $(r_{\rm in},\ r_{\rm out}) = (0, 10r_{\rm S})$, $(10r_{\rm S}, 30r_{\rm S})$ and $(30r_{\rm S}, \infty)$) for simplicity, and suppose that the electrons in the accretion flow in each region have the temperature which is independent of the radius r and the altitude z. The coronal luminosity, L_C, is obtained by Monte Carlo simulations (see next subsection) for a guess value of T_e. Since this T_e does not always satisfy Eq. (1), we should do some iterations to calculate the appropriate electron temperature and the emergent spectrum.

2.2. Radiative Transfer Simulations

In our calculation, as noted above, a cold and geometrically thin disk that produces blackbody radiation is assumed artificially. When irradiation flux, $F_{\rm irr}$, by the corona is strong enough to heat the disk surface at a certain radius, the radiation temperature there should be enhanced from the intrinsic temperature derived from the standard disk model. In the following calculation we set $r_{\rm in} = 3r_{\rm S}$, $\dot{M}_{\rm disk} = 10^{-3}\dot{M}_{\rm Edd}$ (with $\dot{M}_{\rm Edd} = 10L_{\rm Edd}/c^2$) and the mass of a central black hole to be $M = 10^8 M_\odot$, which is believed to be the typical value for AGNs. Thus, the normalized time corresponds to $\tilde{t} \cong r_{\rm S}/c = 10^3$sec.

The method of the Monte Carlo simulation is based on Pozdnyakov et al. (1977). In order to efficiently calculate the emergent spectra, we introduce a photon weight w. When emerged from the disk we set that each photon has the weight of $w_0 = 1$, and then we calculate the escape probability, P_0. The escape probability of a photon after i-th scattering (for $i \geq 1$), P_i, is evaluated as

$$P_i = \exp\left(-\int \left[\frac{\rho(x_i,\ y_i,\ z_i)}{m_p}\right] \sigma_{\rm KN}(x_i,\ y_i,\ z_i) dl\right), \quad (2)$$

where $(x,\ y,\ z) = (x_0,\ y_0,\ 0)$ corresponds to the point on the equatorial plane (i.e. the disk plane), in which the thermal soft photons are generated, $(x_i\ , y_i,\ z_i)$ is the

point where a photon is subject to the i-th scattering, m_p is the proton mass, $\sigma_{\rm KN}$ is the Klein-Nishina cross section (Rybicki & Lightman 1979), and the integral of dl should be done along the photon direction there from the point $(x_i,\ y_i,\ z_i)$ to the boundary of the calculating box. The quantity of w_0P_0 represents the transmitted portion of photons and is recorded to calculate the penetrated spectrum if the path of the photon does not cross with the equatorial plane, and will no longer continue to be counted and will be regarded to be absorbed by the disk. As for the remaining portion of a photon, its weight becomes $w_1 = w_0(1 - P_0)$. The transmitted portion of photons after i-th scattering, w_iP_i is recorded to calculate the emergent spectrum, and the remaining portion, $w_i(1 - P_i)$, undergoes the $(i + 1)$-th scattering. This calculation is continued until the weight w_i becomes sufficiently small ($w_i \ll 1$) or the path of the remaining photon crosses the equatorial plane, regarding to be absorbed by the disk.

3. Results

First, we show the emergent spectra from the accretion disk with MHD coronal flow with various density parameters for the corona in Fig. 1. The adopted density parameters ρ_0 for the corona are $\rho_0 = 5.1 \times 10^{-15},\ 1.6 \times 10^{-14}$, and 5.1×10^{-14}g cm^{-3}. These values correspond to the number density of $\sim 10^9$cm^{-3}. Such density is consistent with some corona models (see Liu et al. 2002, 2003). Due to the inverse Compton scattering in the corona, the power-law component with the spectral index of $\alpha \sim 1-2$ ($F_\nu \propto \nu^{-\alpha}$) appears in the higher energy band. In the calculated spectra, we cannot find a bump-like structure clearly in the UV/soft X-ray band which is usually seen in typical spectra of AGNs. As ρ_0 increases, the total luminosities increases, while the power-law index decreases. The corona with higher density (especially with higher scattering optical depth) would irradiate the underlying disk with higher energy flux because larger number of photons originated from the disk would gain the energy and be backscattered. The the disk is heatened by the corona and so the energy flux of the seed photon field would increase. This is why the total luminosity rises with the coronal density.

In Table 1 we summarize the scattering optical depths τ (evaluated by integrating the scattering opacity over the z-direction from the equatorial plane), the Compton y parameters of the corona (averaged in each region), and the spectral indices of the power law component estimated from the calculation results for 3 density parameters. The MHD simulation of coronal flow was started from the initial condition of a magnetized torus located around at $r \sim 40r_S$. The radius of maximum gas density (and of maximum τ) decreases inward with time and stays around $r \sim 20r_S$. According to the theory of unsaturated inverse Compton scattering, the power-law index of the Comptonized emission component depends on the plasma density and temperature through this equation:

$$\alpha = -\frac{3}{2} + \sqrt{\frac{9}{4} + \frac{4}{y}}. \quad (3)$$

Here $y \equiv (4k_BT/m_ec^2)\tau$ is the Compton y-parameter (Rybicki & Lightman 1973), where T and τ are the temperature and Thompson optical depth of the corona, respectively. The spectral indices derived from this equation using y-parameters in Table 1 do not always agree with those estimated from the spectra. This is because τ and $T_{\rm cor}$ have spatial distributions and we cannot evaluate y-parameter of the corona uniquely.

In our calculation, ρ_0 is determined so as to reproduce the observation. By tuning the coronal density parameter, we can reproduce the luminosity of the power-law component which is as intense as that of the thermal component originated from the optically thick disk. Such feature is typical in Seyfert galaxies. However, the coronal temperature cannot be chosen freely but should be determined by imposing the energy balance of the electrons between Coulomb collisions and the cooling via inverse Compton scattering, as we have done. Nevertheless the resulting coronal temperature is substantially reduced from the plasma temperature derived by the simulation ($\sim 10^{13}$ K) to $\sim 10^9$K, which makes the high energy cutoff of computed spectra consistent with observations.

The spectral variation caused by the time variation of MHD coronal flow structure is shown in Fig. 2. In the highest energy range ($\geq 10^{18}$Hz) the spectra show fluctuations because of poor photon statistics. As for the soft X-ray band (with $\log\nu \simeq 17 - 18$) where the spectra show a smooth power-law shape, the spectral index slightly changes with time, and then the X-ray flux fluctuates a little (see also Fig. 3). According to the MHD simulation on which our radiative transfer calculations are based, the three-dimensional structure of the coronal accretion flow is fluctuating everywhere in each timestep. On the other hand, the spectral index depends on the distribution of y-parameter of the corona, as we note in the last subsection. So we can conclude that the fluctuations of the spectral indices of the computed spectra in Fig. 2 reflect the fluctuation of y, which comes from the density fluctuations (which is supposed to be due to MRI) in the coronal flow.

Fig. 3. shows the X-ray lightcurve derived from our simulations. From this plot we can see that the X-ray luminosity from our disk-corona system can change by factors of a few tens of percent on timescales of the orbital period at the last stable orbit ($r = 3r_{\rm S}$), i.e. about $10^3(M/10^8)M_\odot$ sec. In the whole calculation we do not vary the properties of the soft photon source (i.e. the un-

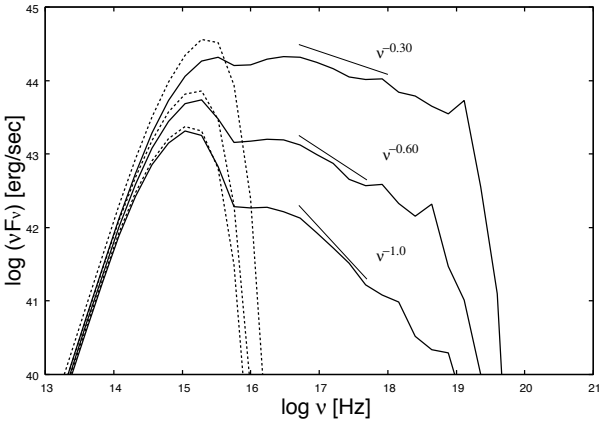

Fig. 1. Broadband spectra from a disk at the accretion rate of $10^{-3}\dot{M}_{\rm Edd}$ and a MHD coronal flow around a black hole of $10^8 M_\odot$ with the density normalization parameters 5.1×10^{-15}, 1.6×10^{-14} and 5.1×10^{-14} g cm^{-3} *solid lines*. The spectra of the seed photons (including those from the cold disk and the reflection component; *dashed lines*) are also shown for the comparison. The short solid lines near the spectra show the power-law fit of νF_ν.

Table 1. Coronal properties

ρ_0 (g cm^{-3})	region	$T_{\rm cor}$ [K]	τ	y	α
5.1×10^{-14}	$0<r<10r_{\rm S}$	$\sim 5.2\times10^9$	~ 0.2	~ 0.5	~ 1.30
	$10r_{\rm S}<r<30r_{\rm S}$	$\sim 3.4\times10^9$	~ 0.9	~ 3	
	$30r_{\rm S}<r$	$\sim 7.6\times10^8$	~ 0.7	~ 0.5	
1.6×10^{-14}	$0<r<10r_{\rm S}$	$\sim 5.2\times10^9$	~ 0.05	~ 0.2	~ 1.60
	$10r_{\rm S}<r<30r_{\rm S}$	$\sim 3.4\times10^9$	~ 0.25	~ 0.55	
	$30r_{\rm S}<r$	$\sim 7.5\times10^8$	~ 0.2	~ 0.1	
5.1×10^{-15}	$0<r<10r_{\rm S}$	$\sim 5.2\times10^9$	~ 0.02	~ 0.05	~ 2.00
	$10r_{\rm S}<r<30r_{\rm S}$	$\sim 3.4\times10^9$	~ 0.09	~ 0.15	
	$30r_{\rm S}<r$	$\sim 7.6\times10^8$	~ 0.07	~ 0.03	

derlying cold disk). This variation which we obtained is due to the density fluctuation (and accompanying temperature fluctuation) of the coronal flow.

4. Discussion and Conclusion

We have calculated the emergent spectra and their time variabilities predicted based on the disk-corona model, in which a cold standard disk at the equatorial plane is sandwiched by a hot coronal flow. As for the structure and dynamics of the corona we use the three-dimensional MHD simulation data by Kato (2004). The power-law indices and the cutoff energy scales of the calculated spectra are roughly in agreement with those of Seyfert galaxies. Moreover, we find significant variability of the power-law X-ray emission. The power-law X-ray emission flux predicted from our model changes by a few tens of percent on timescales of the orbital period near the last stable orbit, which is about $10^3(M/10^8M_\odot)$ sec. This variability comes purely from the fluctuation of the coronal flow around $r\sim 20r_S$, where the scattering optical depth of the coronal flow attains its largest value in its structure. This fluctuation is driven by the turbulence as a result of MRI.

we should mention the interaction between the corona and the underlying disk. In the transition zone between the hot corona and the cold disk where density and temperature abruptly change, the heat conduction and the mass evaporation would be important as the mass and energy exchanging processes (Meyer & Meyer-Hofmeister 1994; Liu et al. 2002). Evaporation of photospheric material was actually shown to be essential in the context of solar flares (see e.g. Yokoyama & Shibata 1994). By including these effects in the simulation we will be able to obtain a more realistic model of the coronal structure and dynamics. To what extent the disk-corona structure can extend to the inner region is important when we consider the relativistic skewing of the iron line emission profile because most of the observations of iron line profiles imply that the iron fluorescence line photons are emitted from around/inside the last stable orbit. The detailed analysis of such disk-corona interactions and their observational implications are left as a future work.

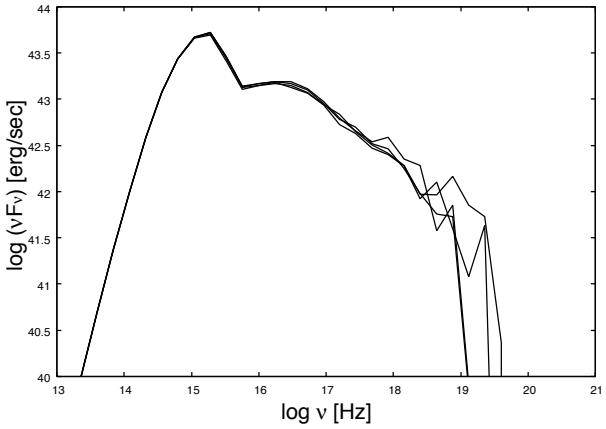

Fig. 2. Spectral variation of the Comptonized emission predicted from the standard disk with a MHD coronal flow around a black hole of $10^8 M_\odot$. Here we set the density parameter as 1.6×10^{-14}g cm^{-3}.

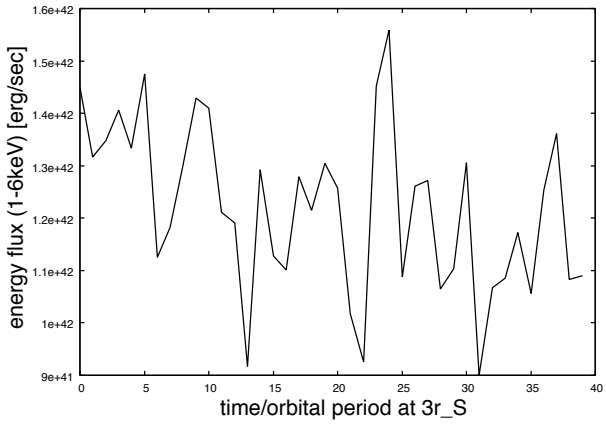

Fig. 3. Time variation of the X-ray luminosity (1-6keV). Here we set the density parameter as 1.6×10^{-14}g cm^{-3}.

Finally, we mention about the application of our corona model for black hole binaries in their low/hard state (LHS), which appears under relatively low accretion rates. In such situations, a geometrically thick and optically thin accretion flow will appear in the innermost regions of the disk near the central black hole, while the geometrically thin and optically thick disk (i.e. standard disk) is truncated at a larger radius. This accretion flow is called as ADAF and the structure and spectral behavior of such accretion flow has been continuously investigated (Ichimaru 1977; Narayan & Yi 1994). In those theoretical models, hard power-law X-ray emissions are considered to be generated via inverse Compton scattering in the innermost hot accretion flow, and the seed photons of Comptonization are thought to be supplied by synchrotron emission from electrons in the inner region. Recently, however, Suzaku revealed the broadband X-ray spectra of black hole binaries such as GRO J1655-40 (Takahashi et al. 2008) and Cyg X-1 (Makishima et al. 2008) and it has been realized that they can be fitted by "double compton" model. In that model hard X-ray emission is produced in hot Comptonizing corona which has two characteristic optical depths, and the seed photons are provided by a geometrically thin and optically thick disk. This radiative process is different from that considered in the original ADAF model. Moreover, the fact that two coronal components which have different optical depths implies that the corona has a spatial distribution in the optical depth. These features are well reproduced in our corona model. As for the spectral variability, the observed spectrum becomes softer in the high flux phase, which implies the lower coronal temperature, and the underlying disk is supposed to remain unchanged. The coronal temperature should be lowered if Compton upscatterings occur efficiently and vice versa, so this observation can be interpreted as follows: X-ray luminosity varies solely because of the oscillation in the Comptonizing coronal flow while the underlying disk which emits seed photons into the corona does not need to vary. This interpretation is fully consistent with our corona model. In the forthcoming paper (Kawanaka et al. in prep), we explain the X-ray spectrum and its

variability and interpret the observational data theoretically with our MHD corona model.

References

Abramowicz, M. A., Chen, X., Kato, S., Lasota, J.-P & Regev, O. 1995, ApJ, 438, L37

Armitage, P. J. & Reynolds, C. S. 2003, MNRAS, 341, 1041

Balbus, S. A. & Hawley, J. F. 1991, ApJ, 376, 214

Bisnovatyi-Kogan, G. S. & Blinnikov, S. I. 1977, A&A, 59, 111

De Villers, J. -P., Hawley, J. F. & Krolik, J. H. 2003, ApJ, 599, 1238

Gammie, C. F., McKinney, J. C. & Toth, G. 2003, ApJ, 589, 444

Haardt, F. & Maraschi, L. 1991, ApJ, 380, L51

Haardt, F. & Maraschi, L. 1993, ApJ, 413, 507

Hawley, J. F. & Krolik, J. H. 2001, ApJ, 548, 348

Hawley, J. F. & Krolik, J. H. 2002, ApJ, 566, 164

Ichimaru, S. 1977, ApJ, 214, 840

Igumenshchev, I. V., Narayan, R. & Abramowicz, M. A. 2003, ApJ, 592, 1042

Kato, S., Fukue, J. & Mineshige, S. 1998, Black-Hole Accretion Disks (Kyoto: Kyoto Univ. Press)

Kato, Y. 2004, PASJ, 56, 931

Kato, Y., Mineshige, S. & Shibata, K. 2004, ApJ, 605, 307 (KMS04)

Kawanaka, N., Mineshige, S. & Iwasawa, K. 2005, ApJ, 635, 167

Kawanaka, N., Kato, Y. & Mineshige, S. 2008. PASJ, 60, 399

Liang, E. P. T & Price, R. H. 1977, ApJL, 218, 247

Liu, B. F., Mineshige, S., Meyer, F., Meyer-Hofmeister. E. & Kawaguchi, T. 2002, ApJ, 575, 117

Machida, M. & Matsumoto, R. 2003, ApJ, 585, 429

Machida, M., Matsumoto, R. & Mineshige, S. 2001, PASJ, 53, L1

Makishima, K., Takahashi, H., Yamada, S., Done, C., Kubota, A., Dotani, T., Ebisawa, K., Itoh, T., Kitamoto, S., Negoro, H., Ueda, Y. & Yamaoka, K. 2008, PASJ, 60, 585

Matsumoto, R. 1999, in Numerical Astrophysics, ed. S. M. Miyama, K. Tomisaka & T. Hanawa (Boston: Kluwer), 195

Meyer, F. & Meyer-Hofmeister, E. 1994, A&A, 288, 175

Moscibrodzka, M., Proga, D., Czerny, B. & Siemiginowska, A. 2008, ApJ, 679, 626

Narayan, R. & Yi, I. 1994, ApJ, 428, L13

Ohsuga, K., Kato, Y. & Mineshige, S. 2005, ApJ, 627, 782

Pozdnyakov, L. A., Sobol, I. M. & Sunyaev, R.A. 1977, Soviet Astron., 21, 708

Rybicki, G. B., & Lightman, A. P. 1979, Radiative Processes in Astrophysics (New York: Wiley)

Shakura, N. I. & Sunyaev, R. A. 1973, A&A, 24, 337

Stone, J. M. & Pringle, J. E. 2001, MNRAS, 322, 461

Takahashi, H. et al., 2008, PASJ, 60, 69

Yokoyama T. & Shibata, K. 1994, ApJ, 436, L197

Magneto-hydrodynamic Simulations of Excitation of Low-Frequency QPOs in Black Hole Candidates

MACHIDA Mami[1], and MATSUMOTO Ryoji[2]

[1] Division of Theoretical Astronomy, National Astronomical Observatory of Japan, Osawa, Mitaka, Tokyo 181-8588, Japan
[2] Faculty of Science, Chiba University, 1-33, Yayoi-cho, Inage-ku, Chiba, 263-8588, Japan
E-mail(MM): mami@th.nao.ac.jp

Abstract

We present the results of global three-dimensional magneto-hydrodynamic simulations of black hole accretion flows. We focus on the excitation mechanism of low frequency quasi-periodic oscillations observed during the state transition of black hole candidates. When a cool gas is supplied, a constant angular momentum inner torus is formed around $4 - 8r_{\rm s}$ where $r_{\rm s}$ is the Schwartzchild radius. This inner torus deforms itself from circle to crescent quasi-periodically. The origin of the torus defomation from circle to crescent is the Papaloizou & Pringle instability. The magnetic energy release by the magnetic reconnection is the reason why the trous deformed to the crescent shape returns to the circle shape. The time interval of these deformation is about 1 day when we assumed a $10^7 M_\odot$ black hole. In this presentation, we show the dependence of numerical results on the gas temperature supplied from the outer region.

Key words: MHD simulations : state transitions — : accretion disks

1. Introduction

Black hole X-ray binaries are suitable for studing accretion disks because they do not have the radiation from the central object. Black hole candidates (BHCs) show transitions between a low/hard state (LHS) and a high/soft state (HSS). LHS is dominated by a hard power-law component and HSS is characterized by the soft black body component. During the transition, BHCs stay in a hard intermediate state. The light curves during LHS show rapid X-ray fluctuations and sometimes show quasi-periodic oscillations (QPOs) in the Fourier Power Spectral Density (PSD). Steady outflows emerge during the LHS. In this state, mass accretes to the black hole as an optically thin, advection dominated accretion flow. The energy spectrum of the hard intermediate state is softer than that in the LHS, but total luminosity is larger than that in the LHS. Low frequency ($1 - 10$HZ) QPOs are observed in the luminous hard state and in the hard intermediate state. High frequency QPOs (~ 100Hz) are sometimes observed in these states.

These observations indicate that QPOs are associated with the cooling of the disk. By carring out global 3D magneto-hydrodynamic (MHD) simulations including radiative cooling, *Machida et al. (2006)* showed that when the accretion rate exceeds the limit for the onset of the cooling instability, the radiatively inefficient, optically thin disk shows a transition to a magnetically supported, cool, intermediate state. *Oda et al. (2007)* denoted a steady model of the magnetically supported disks and showed that their luminosity can exceed $0.1L_{\rm Edd}$, where $L_{\rm Edd}$ is the Eddington luminosity. When the transition to the cool disk takes place from the outre region, cool gas will be supplied to the inner region.

In this paper, we report the results of global 3D MHD simulatios which produce low-frequency QPOs and discuss their excitation mechanisms.

2. Numerical Method

We solved the resistive MHD equations in a cylindrical coordinate system (ϖ, φ, z) by using a modified Lax–Wendroff scheme with an artificial viscosity. In this calculation, we included the Joule heating term but neglected the radiative cooling term in the energy equation. We assume the anomalous resistivity adopted by solar flare simulations. General relativistic effects are simulated by using the pseudo-Newtonian potential(*Paczynski and Witta 1980*).

The units of length and velocity are the Schwarzschild radius $r_{\rm s}$ and the light speed c, respectively. The unit time is $t_0 = r_{\rm s}c^{-1} = 10^{-4}M/M_\odot$ sec. The unit temperature is given by $T_0 = m_{\rm p}c^2 k_{\rm B} = 1.1 \times 10^{13}$ K, where $m_{\rm p}$ is the proton mass and $k_{\rm B}$ is the Boltzmann constant.

The number of grids is $(N_\varpi, N_\varphi, z) = (250, 64, 384)$. The outer boundaries at $\varpi = 132$ and at $|z| = 70$ are free boundaries where waves can be transmitted. We

included the full circle ($0 \leq \varpi \leq 2\pi$) in the simulation region, and applied periodic boundary conditions in the azimuthal direction. An absorbing boundary condition is imposed at $r = r_{\rm in} = 2$.

The initial model is a torus threaded by weak azimuthal magnetic fields. The initial plasma β ($\beta \equiv P_{\rm gas}/P_{\rm mag}$) is 100 at $\varpi = \varpi_{\rm b}$. Here, $\varpi_{\rm b}$ is the radius of the pressure maximum of the initial torus and we assumed $\varpi_{\rm b} = 35$. The initial torus has an angular momentum $L \propto \varpi^a$, where $a = 0.46$. The maximum sound speed of the initial torus is $c_{\rm b} = 0.01$. This sound speed corresponds to the cooler gas than the optically thin advection dominated accretin flows. We adopted $\gamma = 5/3$ where γ is the specific heat ratio.

3. Results

Figure 1 shows the snap shot of the density distribution in $\varpi - z$ plane averaged in the azimuthal direction. Mass accretion takes place due to the magnetic turbulence produced by the magneto-rotational instability, then the initial torus deforms to the disk like shape. The averaged angular momentum transport rate is less than $\alpha < 0.01$ and averaged plasma β is about $\beta \sim 10$.

Figure 2 shows the snap shots of the equatorial density distribution averaged in $|z| < 1$. In this cooler disk model, an inner torus is formed around $\varpi \sim 4 - 8r_{\rm s}$. The inner torus is formed because the angular momentum transport rate decreases when the disk cools down. The inner torus deforms itself to a crescent shape due to the growth of the Papaloizou-Pringle instability.

The top pannel of figure 3 plots the time evolution of the ratio of the Joule heating rate to the magnetic energy averaged in $4 < \varpi < 10$, $|z| < 1$, and $0 \leq \varphi \leq 2\pi$. The ratio increases when magnetic energy is released. Bottom pannel of figure 3 shows the time evolution of the amplitude of the non-axisymmetric $m = 1$ mode of the density where m is the mode number in the azimuthal direction. The amplitude of the azimuthal mode is computed by Fourier decomposing the density contrast. The amplitude of $m = 1$ mode anti-correlates with $\eta J^2/\langle B^2/8\pi \rangle$. It indicates that the magnetic energy is released when the $m = 1$ mode disappears. The amplitude of the $m = 1$ mode also correlates with the magnetic pressure and the angular momentum transport rate.

Figure 4 shows the spatial distribution of time variabilities in mass accretion rate νP_ν in $55000 < t < 61000$. Here P_ν is the Fourier power of the time variation of mass accretion rate. Low frequency QPOs around $4-8$Hz appear in $5 < \varpi < 10$, where the inner torus is formed.

Figure 5 shows the Powe Spectral Density (PSD) of time variation of the mass accretion rate averaged in $2.5 < \varpi < 10$ and $|z| < 1$. Black and gray curves show PSD for cooler case and hotter case ($c_{\rm b} = 0.03$), respectively. The PSD for the latter model is similar to the results of *Machdia and Matsumoto (2003)*. The PSD for cooler model has a broad low frequency peak around $4 - 8$Hz. This low frequency peak corresponds to the oscillation involving amplification and release of magnetic energy in the inner torus. The PSD in the cooler model has a slope steeper than that in hotter model in $10 < \nu < 30$Hz.

4. Discussion

In this paper, we studied the structure and time variation of the black hole accretion flows when the cooler gas supplied from the outer region. In such models, an inner torus is formed around $\varpi \sim 4 - 8r_{\rm s}$. Such a torus is formed when the angular momentum transport rate is small enough. Since Maxwell stress decreases due to the decrease of magnetic energy, a nearly constant angular momentum torus is formed in the accretion flow. We found that the inner torus deforms itself into a crescent shape due to the growth of the Papoloizou and Pringle instability. Such non-axisymmetric structures enhance the growth of the MRI. As magnetic energy increases, angular momentum transport rate increases and accretion rate also increases. When the magnetic energy accumulated in the disk is released, the disk returns to circular shape. As the magnetic energy released, it accumulattes again. The frequency of this cycle is about $1000t_0$. It creates a low frequency peak around $4-8$Hz in the PSD of the mass accretion rate.

Homan et al. (2005) pointed out that during the transition from the LHS to HSS, GX339−4 shows a subtransition from a hard intermediate state dominated by power-law X-ray radiation to soft intermediated state dominated by radiation from optically thick disk. They also showed that the low frequency QPOs appear when the X-ray spectrum stays in the hard intermediate state and soft intermediate state and sometimes in LHS.

Homan (2008) also pointed out that the root mean square of the PSD of hard intermediate state when the QPO appears in its PSD is smaller than that of LHS. The rms. of the PSD obtained from numerical simulations also shows the same tendancy in figure 5. In the LHS when the QPO does not appear PSD is wider than the cooler case. Therefore, our model can explain that rms. becomes smaller when the low frequency QPO appears.

References

Homan J. et al. 2005, ApJ, 624, 295
Homan J 2008, MAXI proceedings
Machida M. and Matsumoto R. 2003, ApJ, 585, 429
Machida M., Nakamura K.E., and Matsumoto R. 2006, PASJ, 58, 193
Machida M. and Matsumoto R. 2008, PASJ, 60, 613
Oda et al. 2007, PASJ, 59, 457

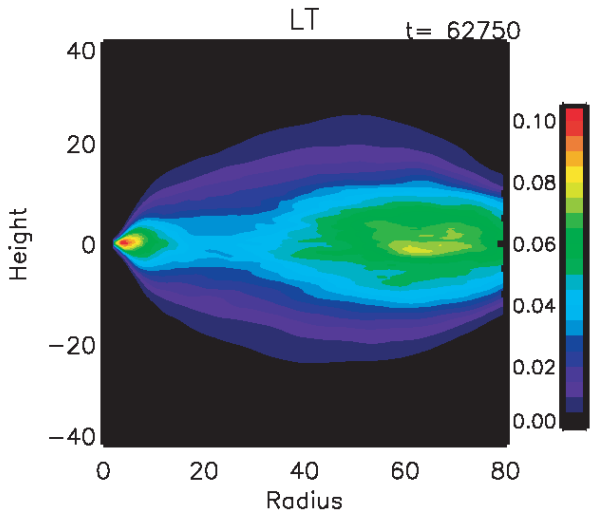

Fig. 1. The snap shot of the density distribution averaged in the azimuthal direction.

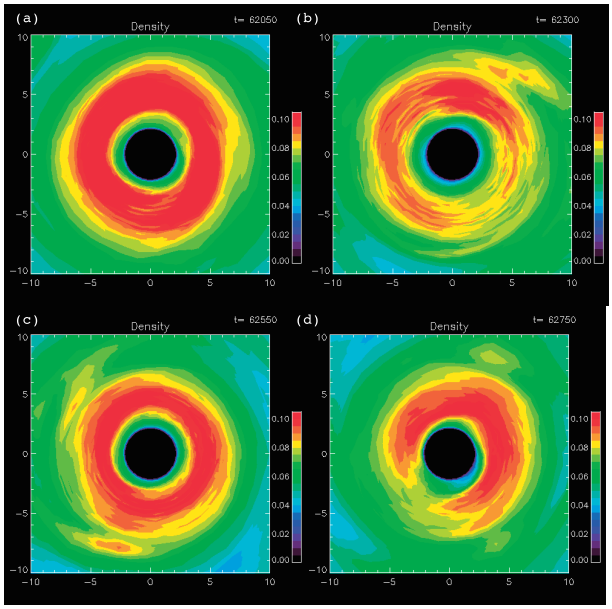

Fig. 2. Snap shots of the density distribution in $\varpi - \varphi$ plane. The time evolution is a,b,c and d.

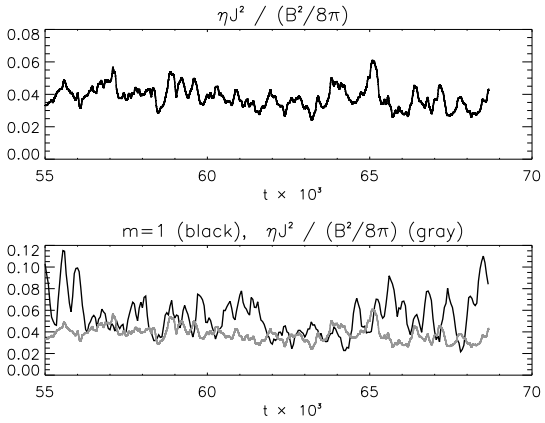

Fig. 3. (top) Time evolution of the ratio of the Joule heating rate to magnetic energy. (bottom) Time evolution of the Fourier amplitude of the non-axisymmetric mode with the azimuthal mode number $m = 1$ computed from the density distribution. Gray curve depicts the same curve as that in the top pannel.

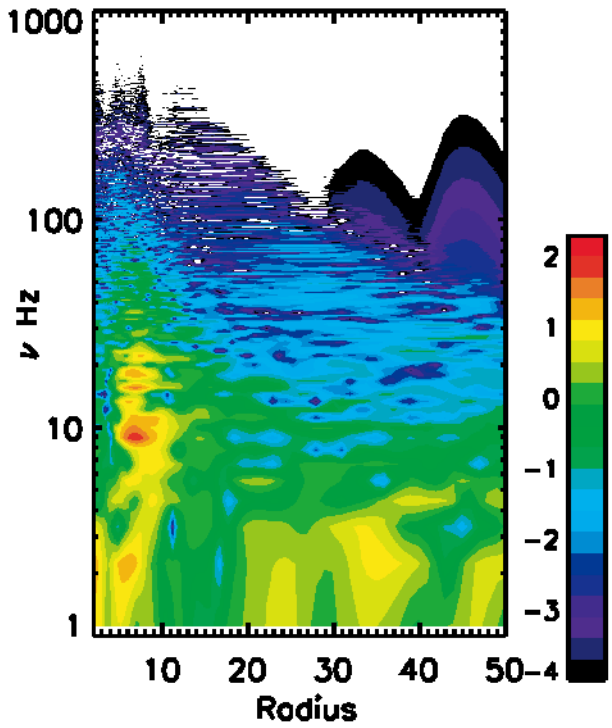

Fig. 4. Radial distribution of the PSD of the time variation of mass accretion rate measured in $55000 < t < 61000$.

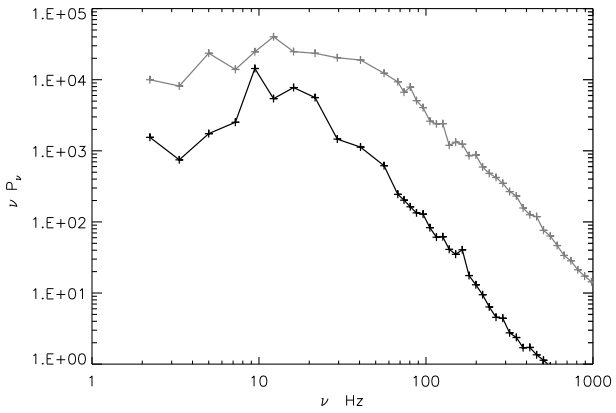

Fig. 5. Power spectrum νP_ν averaged in $2.5 < \varpi < 29$ and $|z| < 1$. Black curve shows the cooler case and gray one shows the hot accretion flow.

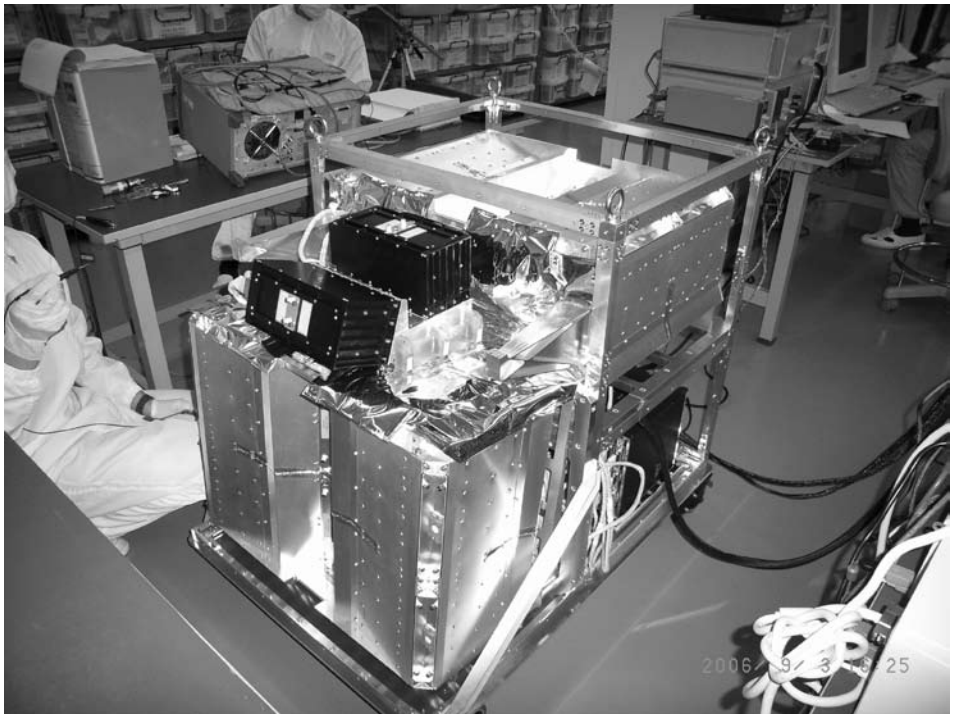

Radiation Hydrodynamic / Radiation Magnetohydrodynamic Simulations of Accretion Flows and Outflows around Black Holes

Ken OHSUGA

Institute of Physical and Chemical Research (RIKEN), 2-1, Hirosawa, Wako, Staitama 351-0198, Japan
E-mail(KO): ohsuga@crab.riken.jp

Abstract

We perform global two-dimensional radiation hydrodynamic (RHD) and radiation magnetohydrodynamic (RMHD) simulations of accretion flows around black holes. Our RHD simulations reveal that the steady, supercritical accretion is feasible. The disk luminosity is several times larger than the Eddington luminosity. The disk is geometrically and optically thick. It is supported by the radiation pressure. The strong radiation pressure force drives the outflow above the disk. Our RMHD simulations demonstrate three distinct modes of accretion. When the density is large, a thick, very luminous disk forms. When the density is moderate, the accreting gas can effectively cool, thus generating a thin disk. When the density is too low for radiative cooling to be important, a disk becomes hot, thick, and faint. Strong outflows emerge, which are driven either by radiation pressure force for the dense disk or magnetic pressure force for the less dense disks.

Key words: black holes — accretion disks — numerical simulations

1. Introduction

It is widely believed that accretion flows onto black holes drives major activities of astrophysical black holes, such as active galactic nuclei, black hole binaries, and gamma-ray bursts. The basic accretion processes and radiation properties in moderate luminosity state can well be described by the standard-disk model by Shakura & Sunyaev (1973). This model was followed by the radiatively inefficient accretion flow (RIAF) model and the slim disk model for understanding accretion flow in low and very high luminosity states (Ichimaru 1977, Abramowicz et al. 1988, Narayan & Yi 1994).

These models can successfully account for many properties of accreting objects. However, they are (radially) one-dimensional models so that they cannot treat multi-dimensional motion, such as outflow and internal circulation. Such multi-dimensional motion would affect the dynamics and the structure of the accretion flows through the transportation of the mass, the momentum/angular momentum, and the energy. Thus, we need multi-dimensional approach to study accretion flows and outflows.

The conventional one-dimensional models do not solve the radiation fields and the magnetic fields. Therefore, they can not investigate the radiative and magnetic effects, such as the radiation pressure driven outflows as well as magnetic wind. In addition, the phenomenological viscosity model (so-called α model) is assumed, although the disk viscosity is thought to be of magnetic origin (Balbus & Hawley 1991).

Here, we take two independent, but complementary approaches to study the accretion flows. In section 2, we present our results of two-dimensional radiation hydrodynamic (RHD) simulations. The simulations are the first to clarify the structure of supercritical accretion flow in quasi-steady regimes. We, next, in section 3, present the results of global two-dimensional radiation-magnetohydrodynamic (RMHD) simulations. Our RMHD simulations demonstrate three distinct modes of accretion (corresponding to the standard disk model, RIAF model, and slim disk model) with the same code by varying mass density normalisations.

2. Radiation Hydrodynamic (RHD) Simulations

Two-dimensional RHD simulations of supercritical accretion disks were initiated by Eggum, Coroniti, & Katz (1988), who assumed the equilibrium between gas and radiation. The improved simulations, in which the energy of gas and radiation are separately treated, were performed by Okuda (2002). However, those simulations were computational-time limited and could not follow quasi-steady state of accretion.

We start simulations with an initially empty place and continuously add mass with angular momentum, which is 0.45 times Keplerian angular momentum, through the outer disk boundary at $r = 500r_S$, where r_S is the Schwarzschild radius. The mass input rate is set to be

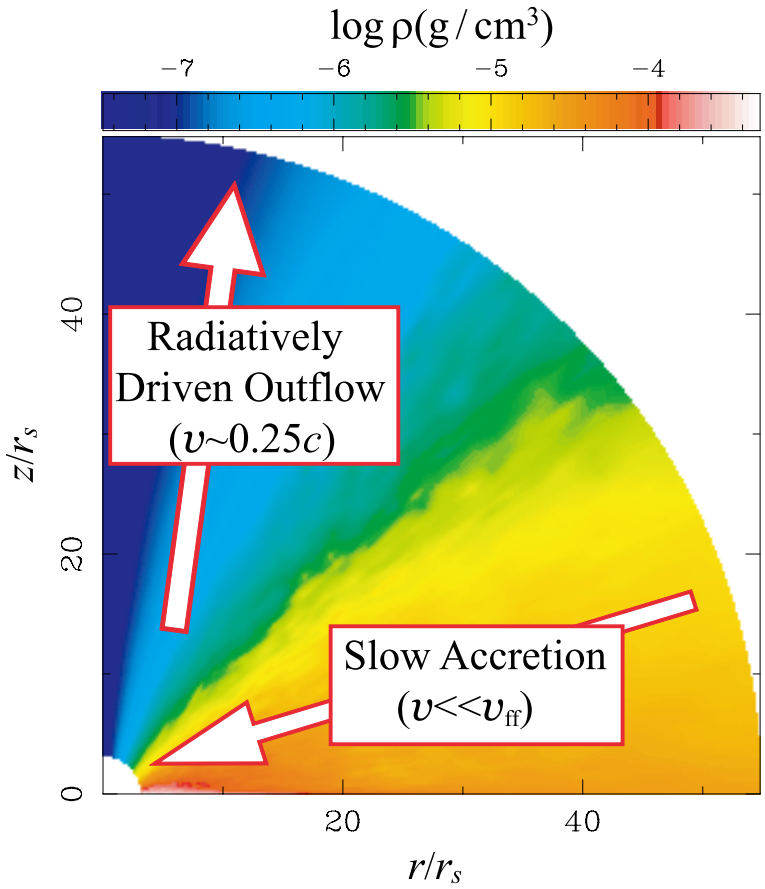

Fig. 1. the cross-sectional view of the density distributions in the quasi-steady state. The matter slowly accretes onto the black hole within the disk, while the high-velocity outflow appear around the rotation axis via the strong radiation force. The disk luminosity exceeds the Eddington luminosity. Our simulations, for the first time, reveals that the steady, supercritical accretion is feasible.

$10^3 L_{\rm E}/c^2$, where $L_{\rm E}$ is the Eddington luminosity and c is the speed of light. The black hole mass is assumed to be $10M_\odot$. To simplify the radiation processes and to save computational time, we adopt the flux-limited diffusion approximation. We employ the α viscosity model ($\alpha = 0.1$), since the magnetic fields are not solved in the RHD simulations (see Ohsuga et al. 2005, Ohsuga 2006 for more detail).

Overall evolution is divided into two distinct phases: the accumulation phase and the quasi-steady phase. The injected matter falls inward because of the gravity. Since angular momentum of the injected matter is set to be equal to the Keplerian angular momentum at $r = 100r_S$, it is natural that the gas tends to accumulate around the regions with the radius of $100r_S$ by degrees. This is the accumulation phase. Eventually, the viscosity starts to work so that the angular momentum of the gas can be transported outward, which drives inflow gas motion in a quasi-steady fashion. This is the quasi-steady phase. Then, the outflow driven by radiation pressure is generated around the rotation axis.

Figure 1 displays the cross-sectional view of the density distributions in the quasi-steady state. We understand with this figure that the flow structure is roughly divided into two regions: the disk region around the equatorial plane (characterised by orange color) and the outflow region above the inflow region (characterised by blue color).

The disk luminosity is several times larger than the Eddington luminosity. Our simulations, for the fist time, demonstrate that the steady, supercritical accretion is feasible. In addition, the emission of the supercritical accretion flows is moderately collimated, so that the apparent luminosity could become more than $10L_{\rm E}$ in the face-on view. It implies that the huge X-ray flux of the ultra-luminous X-ray sources is understood by the supercritical accretion onto the stellar mass black holes.

Here, we note that the energy conversion efficiency of the supercritical flows is smaller than the prediction of the standard disk model, 0.1. This is due to the photon-trapping. The huge amount of photons generated deep inside the disk is swallowed by the black hole with accreting matter, since the photon diffusion timescale exceeds the accretion timescale.

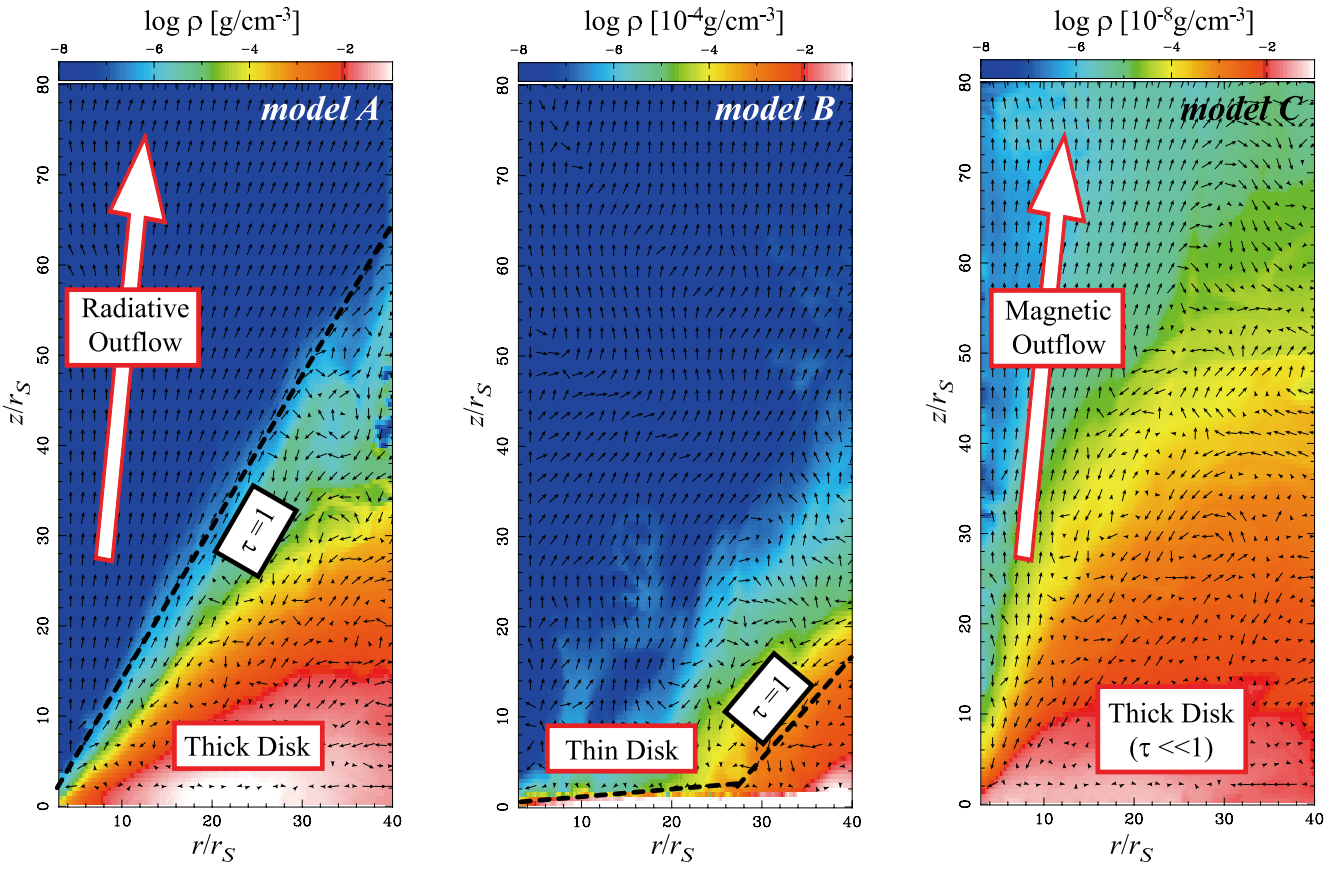

Fig. 2. Density distributions (color) overlaid with velocity vectors around the black holes. The dotted line indicates the photosphere, at which the optical thickness measured from the upper boundary is unity. The geometrically and optically thick disk forms in model A. The disk in model B is optically thick but geometrically thin. We find the geometrically thick but optically thin disk in model C. The radiation pressure force drives the outflow above the disk in model A, while the powerful outflow is generated via the magnetic pressure force in model C. The magnetic pressure also drives the outflow in model B, though it is not powerful.

We find that the strong radiation pressure force drives high-velocity outflow, whose typical velocity is around $0.25c$. Therefore, the supercritical accretion objects have the blueshifted absorption lines by the highly ionized ions. Such blueshifted absorption lines was observed in the UV and X-ray spectra of quasars (Becker et al. 2000 Pounds et al. 2003, Reeves, O'Brien, & Ward 2003). On the other hand, the inflow velocity is much smaller than the free-fall velocity, since the sum of the radiation and centrifugal forces is nearly balanced with the gravitational force (Ohsuga & Mineshige 2007).

3. Radiation Magnetohydrodynamic (RMHD) Simulations

One big issue associated with our global RHD simulations is that the alpha model is employed (see previous section), since the magnetic fields are not solved. The disk viscosity should be calculated in a self-consistent fashion based on magnetohydrodynamics. Hence, the RMHD simulations are needed.

Three-dimensional RMHD simulations have been performed with using the shearing-box approximation (Turner et al. 2003). However, global multi-dimensional RMHD simulations, which are essential to establish a realistic picture of accretion disks, have not been attempted so far. Thus, we perform global two-dimensional RMHD simulations.

We start calculations with a rotating torus at $40r_S$ embedded in non-rotating isothermal corona. We assign the density parameter, the density at the center of the torus in the initial state, as $1\mathrm{g/cm^3}$ (model A), $10^{-4}\mathrm{g/cm^3}$ (model B), and $10^{-8}\mathrm{g/cm^3}$ (model C).

Figure 2 represent the density distributions (color) and velocity fields (vector) of three models, models A, B, and C from the left to the right, respectively.

In model A, the mass accretion rate exceeds the critical rate. The luminosity is comparable to or slightly exceeds the Eddington luminosity. The disk is optically and geometrically thick. It is supported by radiation pressure, which is predominant over the gas and magnetic pressures. The magnetic energy density is two times as large as the gas energy density. We find that the quasi-steady

outflow launches from the disk surface via the strong radiation pressure force. The outflow velocity exceeds the escape velocity. The magnetic field lines stretch out within the outflow region, thus being almost parallel to the rotation axis, while the toroidal component of the magnetic fields is dominant over other components of that in the disk region. Recent radio observations revealed that the magnetic field lines are along the jet axis (Giroletti et al. 2008).

The disk in model B is also optically thick. However, it is geometrical thin, since the radiative cooling is efficient, and since the radiation pressure does not support the disk. The mass accretion rate is about 1% of the critical rate and the disk luminosity is about $10^{-3}L_{\rm E}$. Magnetic energy is about 30% of the gas energy in the disk region. The disk wind, associated with helical magnetic fields, sometimes emerges via the magnetic pressure force. This result would resolve the problem, by which the black hole binaries exhibit the absorption lines, implying the wind outflow from the disc in moderate luminosity state (Miller et al. 2006, Kubota et al. 2007).

In model C, the density is too low for radiative cooling and radiation pressure to be important. Thus, the disk consists of hot rarefied plasma. It is geometrically thick but optically thin. Our simulations reveal that the magnetic energy is around 20% of the gas energy, and the radiation energy is negligible. The mass accretion rate is smaller than 0.01% of the critical rate. We find that the vertical component of the magnetic fields is dominant over the radial component near the rotation axis, which is surrounded by the regions with strong toroidal magnetic fields. It is so-called magnetic tower jet (see also Kato, Mineshige & Shibata 2004). In contrast with models A and B, the kinetic energy output rate via the outflows exceeds the disk luminosity.

4. Conclusions

We have performed long-term two-dimensional radiation hydrodynamic (RHD) simulations of supercritical accretion flow. They for the first time reveal that the steady supercritical accretion is feasible in the case of disk geometry. The emission is mildly collimated so that the apparent luminosity can exceed the Eddington luminosity by a factor of ~ 10 in the face-on view. The strong radiation pressure force drives high-velocity ($\sim 0.25c$) outflow above the disk.

By performing two-dimensional radiation magnetohydrodynamic (RMHD) simulations, we can basically reproduce three distinct regimes of accretion flow (supercritical, standard, and radiatively inefficient flow) with one code but with different density normalization. The outflows are generated via the radiation pressure for the dense disk and via the magnetic pressure for the less dense disk.

References

Abramowicz, M. A., Czerny, B., Lasota, J. P., & Szuszkiewicz, E. 1988, ApJ, 332, 646

Balbus, S. A. & Hawley, J. F. A. 1991, ApJ, 376, 214

Becker, R. H., White, R. L., Gregg, M. D., Brotherton, M. S., Laurent-Muehleisen, S. A., & Arav, N. 2000, ApJ, 538, 72

Eggum, G. E., Coroniti, F. V., & Katz, J. I. 1988, ApJ, 330, 142

Giroletti, M. et al. in press (2008), astro-ph/arXiv: 0807.1786

Ichimaru, S. 1977, ApJ, 214, 840

Kato, Y., Mineshige, S., & Shibata, K. 2004, ApJ, 605, 307

Kubota, A. et al. 2007, PASJ, 59, 185

Miller, J. M. et al. 2006, Nature, 441, 953

Narayan, R. & Yi, I. 1994, ApJL, 428, 13

Okuda, T. 2002, PASJ, 54, 253

Ohsuga, K. 2006, ApJ, 640, 923

Ohsuga, K. & Mineshige, S. 2007, ApJ, 670, 1283

Ohsuga, K., Mori, M., Nakamoto, T., & Mineshige, S. 2005, ApJ, 628, 368

Pounds, K. A., Reeves, J. N., King, A. R., Page, K. L., O'Brien, P. T., & Turner, M. J. L. 2003, MNRAS, 345, 705

Reeves, J. N., O'Brien, P. T., & Ward, M. J. 2003, ApJ, 593, 65

Shakura, N. I. & Sunyaev, R. A. 1973, A&A, 24, 337

Turner, N. J., Stone, J. M., Krolik, J. H., & Sano, T. 2003, ApJ, 593, 992

Soft X-ray Emission and Lithium Production in Cen X-4 during Quiescence

Shin-ichiro Fujimoto,[1] Ryuichi Matsuba,[2] and Kenzo Arai,[3]

[1] Department of Electronic Control, Kumamoto National College of Technology, 2659-2 Suya, Koshi, Kumamoto 861-1102, Japan
[2] Institute for e-Learning Development, Kumamoto University, Kumamoto 860-8555, Japan
[3] Department of Physics, Kumamoto University, Kumamoto 860-8555, Japan
E-mail(SF): fujimoto@ec.knct.ac.jp

Abstract

We investigate emission mechanism of soft X-ray radiation from a neutron star soft X-ray transient (NSSXT), Cen X-4 and unusually high abundances of Li on a low-mass secondary in Cen X-4 during a quiescent state. An accretion flow in NSSXTs in quiescence is though to be an advection-dominated one and truncated by magneto-centrifugal forces due to the magnetic field of a neutron star. The advection dominated accretion flow (ADAF) is very hot ($> 1\,\mathrm{MeV}$) enough to synthesize abundant neutrons through the spallation of ^{4}He via protons in the flow. Although almost all charged nuclei in the ADAF are outflowed by the magneto-centrifugal forces, the neutrons accrete onto the neutron star because of no influence of the magnetic field on the neutrons. Consequently, the accretion flow is composed of neutrons near the neutron star. The accretion energy of the neutrons liberated on the surface of the star is a possible energy budget for soft X-ray radiation in a NSSXT in quiescence. Moreover, Li is abundantly synthesized in the ADAF through $\alpha-\alpha$ reactions and is transfered to the surface of the secondary by the magneto-centrifugal forces. We find that for reasonable values of the mass accretion rate and the magnetic field of the neutron star, the estimated soft X-ray luminosity and abundance of Li on the secondary are comparable to those observed in Cen X-4.

Key words: Accretion, accretion disks — neutron stars — nuclear reactions, nucleosynthesis, abundances — stars: abundances

1. Introduction

X-ray emission from neutron star soft X-ray transients (NSSXTs) in quiescence is phenomenologically fitted with two components, a blackbody-like soft component and power-law hard component. Although the origin of the hard component is still unclear, there are two scenarios for the soft X-ray component. The energy source for the blackbody-like, soft X-ray is interpreted as deep crustal heating (Brown et al., 1998; Rutledge et al., 2001a,b). However, the quiescent state of Cen X-4 is variable on timescales (at a factor of ~ 0.4, ~ 3, and ~ 0.45 in 5 yr (Rutledge et al., 2001a), a few days (Campana et al., 1997), and down to $\sim 100\,\mathrm{s}$ (Campana et al., 2004), respectively). This could rule out the scenario of the energy source due to the deep crustal heating.

The other energy budget for the soft X-ray radiation is residual polar accretion onto a neutron star from a quasi spherical advection dominated accretion flow (ADAF) (Zhang et al., 1998; Menou et al., 1999), which possibly exists around the neutron star during quiescence (Narayan et al., 1996, 1997). Due to magnetic fields and fast rotation of the neutron star, accreting material is expelled through propeller effects, which cause winds driven via magneto-centrifugal forces when a mass accretion rate is sufficiently low. Even when the propeller effects operate, accretion through the polar region of the star is possible because of weak centrifugal forces in the region. The fraction of the mass accretion rate that reached the neutron star surface has been estimated to be $\sim 10^{-3}$ for reasonable values of the mass accretion rate and magnetic field of the star (Menou et al., 1999). However, the fraction could be much lower if the accretion flow has a toroidal morphology with empty funnels along the rotational axis (Menou et al., 1999). We note that the MHD simulation of an ADAF show that the flow has funnels with densities lower than that at the equatorial plane (Machida et al., 2004).

ADAF has very low density, so that ions interact inefficiently with electrons. As a result of the inefficient interaction between the ions and the electrons, which are main coolant in ADAF, the ions have high temperatures due to viscous heating and attain to ~ 30 MeV near an

inner edge of ADAF (Narayan & Yi, 1994, 1995a,b). Due to such high temperatures, helium breaks via the spallation with protons to produce neutrons in ADAF. Due to magneto-centrifugal forces, almost all charged particles are ejected from an inner region of the ADAF. However, neutrons continues to accrete onto the neutron star, since neutrons are not affected by the magnetic field of the neutron star. As the neutrons liberate almost all its gravitational binding energy onto the surface of the neutron star, the liberated energy is a possible energy budget for the blackbody-like, soft X-ray radiation.

Moreover, Li produced in ADAFs by α-α reactions transports to a secondary star through the propeller effects (Yi & Narayan, 1997). The transportation enhances the Li abundance on the low-mass secondary, and causes a high abundance of Li observed on the low-mass secondary in a NSSXT, Cen X-4 (Martin et al., 1994). We note that Li is destroyed in the deep convective envelope of usual late-type stars, and that high abundances of Li have been detected in late-type secondaries of black hole soft X-ray transients (BHSXTs) in quiescence (Wallerstein, 1992; Martin et al., 1992, 1994, 1996), and have been examined by Fujimoto et al. (2008) (hereafter FMA08). As we can see later, the estimated soft X-ray luminosity and abundance of Li on the secondary are comparable to those observed in Cen X-4, for reasonable values of the mass accretion rate and magnetic field of the neutron star.

In the present study, we propose a new mechanism to produce a soft X-ray radiation from NSSXTs, that is the liberation of the gravitational energy of neutrons on the surface of the star accreting through a neutron-ADAF. We also examine production of Li through the transportation of Li from the ADAF to the secondary.

The paper is organized as follows: in §2, we examine an abundance distribution in an accretion flow around a neutron star. We estimate the soft X-ray luminosity, which is interpreted as the energy liberation of neutrons accreted through a neutron accretion flow in §3. In §4, we examine Li production on a secondary in NSSXTs. Finally we summarize our results in §5.

2. Abundance distribution in an advection dominated accretion flow

We assume that an accretion flow around a neutron star is an ADAF in quiescence in the present study. The temperature of ions in ADAFs is comparable to virial temperature, and is given at radius r by (Narayan & Yi, 1994, 1995a,b);

$$T = 3.7 \times 10^{12} \frac{r_{\rm in}}{r}\,{\rm K} = 31.9 \frac{r_{\rm in}}{r}\,{\rm MeV}. \qquad (1)$$

Here $r_{\rm in}$ is the radius at the inner edge of the ADAF, and is set to be $3r_g$, where r_g is the Schwarzschild radius for a neutron star with mass $M = 1.4 M_\odot$. We note that $r_{\rm in}$ becomes much greater during the operation of the propeller effects, which will be discussed later. The number density is given by

$$n = 1.7 \times 10^{18} \alpha^{-1} m^{-1} \dot{m} \left(\frac{r}{r_{\rm in}}\right)^{-3/2} {\rm cm}^{-3}, \qquad (2)$$

where α is the viscous parameter, $m = M/M_\odot$, and $\dot{m}$ is the mass accretion rate in units of the Eddington accretion rate $\dot{M}_{\rm Edd} = 1.4 \times 10^{17}\, m\ {\rm g\,s^{-1}} = 2.1 \times 10^{-9} m\, M_\odot\,{\rm yr}^{-1}$.

Once the temperatures, densities and drift timescales are specified, we can follow the abundance evolution in an ADAF from the outer boundary $r_{\rm out}$ to $r_{\rm in}$, using a nuclear reaction network. We set $r_{\rm out}$ to be $100\,r_g$. It is likely that $r_{\rm out}$ becomes much larger during the quiescent state (Narayan et al., 1997), but the abundance distribution in the ADAF is independent from the choice of larger $r_{\rm out}$ because of low temperatures (< 1 MeV) in the outer region (Guessoum & Kazanas, 1999). We have developed a nuclear reaction network, in which four $\alpha - \alpha$ reactions to synthesize ^{6}He,^{6}Li,^{7}Li, and ^{7}Be are taken into account, based on a network in FMA08. Our network contains 21 species of nuclei; n, p, D, T, ^{3}He, ^{4}He, ^{6}He, ^{6}Li, ^{7}Li, ^{7}Be, ^{9}B, ^{11}C, ^{12}C, ^{13}N, ^{14}N, ^{15}O, ^{16}O, ^{17}F, ^{20}Ne, ^{21}Na, and ^{24}Mg, and 18 reactions, whose rates are taken from Table 1 in (Guessoum & Gould, 1989) or thermally averaged with experimental cross sections (Read & Viola, 1984) for $\alpha - \alpha$ reactions. It should be emphasized that photodisintegration reactions are not important for abundance evolution inside ADAFs, since the ADAF is optically thin and photons have no chance to interact with nuclei due to low gas densities (Eq. (2)). Initial abundance at $r_{\rm out}$ is set to be the solar composition (Anders & Grevesse, 1989) without Li.

Figure 1 shows the abundance distribution of neutrons, ^{4}He, ^{6}Li, ^{7}Li, and ^{7}Be inside ADAFs for $\alpha = 0.3$, $m = 1.4$, and $\dot{m} = 0.01$ and 0.1. Neutrons are produced significantly via the breakup of ^{4}He at an inner region ($r < 20 r_g$). The distribution of neutrons is similar to that in Figure 1 of (Jean & Guessoum, 2001). Lithium is appreciably synthesized at the inner region of the ADAF. ^{7}Be is comparable to and slightly lower than ^{7}Li, while ^{6}He is much lower than ^{6}Li. We note that the number fraction of neutrons $Y_{\rm n}$ and Li abundances depends not on m solely, but on the combination $\dot{m}/\alpha^2$. Hereafter we fix $\alpha = 0.3$ in the present paper (Narayan et al., 1997).

3. New interpretation of soft X-ray emission in terms of neutron-ADAF

The very low mass accretion rates on to a neutron star ($\leq 10^{-5}$ in units of $\dot{M}_{\rm Edd}$ (Asai et al., 1996)) have been suggested the termination of mass accretion via the propeller effects, which can explain a sudden spectral

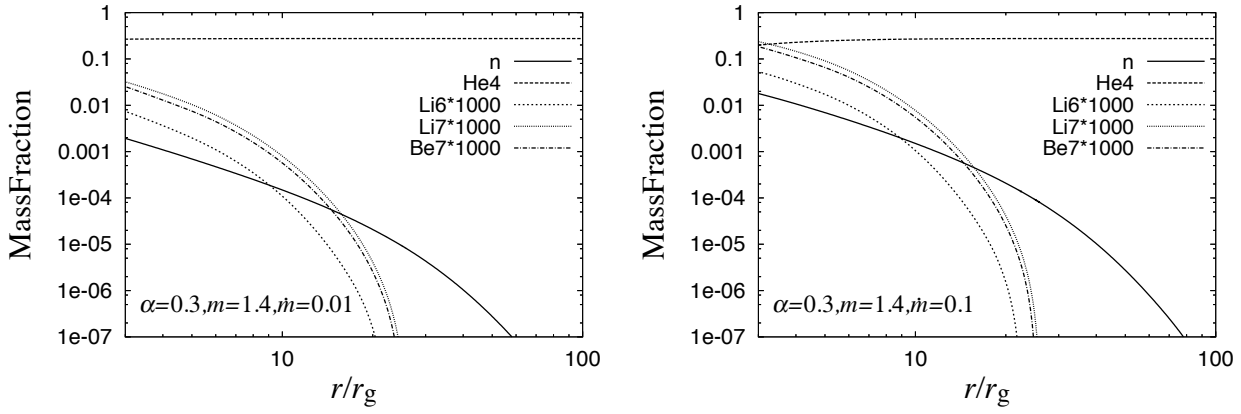

Fig. 1. Abundance distribution in ADAFs for $\alpha = 0.3$, $m = 1.4$, and $\dot{m} = 0.01$ (left panel) and 0.1 (right panel). The solid, dashed, short-dashed, dotted, and dash-dotted lines indicate the mass fractions of n, ^{4}He, ^{6}Li, ^{7}Li, and ^{7}Be, respectively.

state transition observed in X-ray from three NSSXTs, Aql X-1 (Campana et al., 1998; Zhang et al., 1998), SAX J1808.4-3658 (Gilfanov et al., 1998), and 4U 1608-52 (Chen et al., 2006). Through the propeller effects, the material is ejected from ADAF around the ejection radius $r_{\rm ej}$, which is given by the Alfvén radius,

$$r_{\rm ej} = 9.74 \left(\frac{B_{\rm NS}}{10^8{\rm G}}\right)^{4/7} \left(\frac{m}{1.4}\right)^{-2/7} \left(\frac{\dot{m}}{0.01}\right)^{-2/7} r_g, \quad (3)$$

if $r_{\rm ej}$ is larger than the corotation radius (Yi & Narayan, 1997),

$$r_c = 9.4 \left(\frac{m}{1.4}\right)^{1/3} \left(\frac{P_{\rm NS}}{1\,{\rm msec}}\right)^{2/3} {\rm km}, \quad (4)$$

otherwise the propeller effects do not work. Here, $B_{\rm NS}$ and $P_{\rm NS}$ are the magnetic field and the rotational period of the neutron star, respectively. Figure 2 shows $r_{\rm ej}$ for $B_{\rm NS} = 10^8$G (dashed line) and 10^9G (dotted line) as a function of $\dot{m}$. We also show the radius where the mass fraction of ^{7}Li equals to 10^{-7} in the ADAF (solid line).

The propeller effects operating in NSSXTs during quiescence have important meaning to an accretion flow around the neutron star. As shown in Figure 1, appreciable fractions of neutrons are produced in the ADAF at $r_{\rm ej}$, which is smaller than 20 r_g for a reasonable set of parameters (Figure 2). Although almost all charged particles are ejected due to magneto-centrifugal forces near $r_{\rm ej}$, neutrons are not affected by the magnetic field of the neutron star because of the charge-less of neutrons. Consequently, even after the operation of the propeller effects, accretion of neutrons continues to take place onto the neutron star, and a *neutron-ADAF* is formed around the neutron star.

As the neutron-ADAF emits little radiation during accretion, the neutrons accreting onto the neutron star liberate almost all its gravitational binding energy onto the surface of the neutron star. The liberated energy is a possible candidate for a energy budget of the blackbody-like, soft X-ray radiation. If we interpret the soft X-ray radiation of $\sim 10^{32}\,{\rm erg\,s^{-1}}$ as the energy liberation onto the neutron star through the neutron-ADAF, a mass accretion rate of neutrons through the neutron-ADAF $\dot{m}_n \sim 10^{-6}$ is required in units of the Eddington accretion rate. We note that the quiescent soft X-ray luminosity in Cen X-4 is $2 - 3 \times 10^{32}\,{\rm erg\,s^{-1}}$ (Asai et al., 1998).

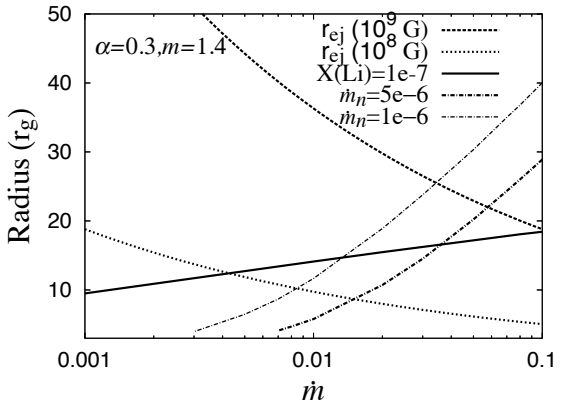

Fig. 2. Radius where the mass fraction of ^{7}Li equals to 10^{-7} in the ADAF, r(Li), and ejection (Alfvén) radius $r_{\rm ej}$ vs mass accretion rates. Solid, dashed, and dotted lines indicate r(Li), $r_{\rm ej}$ for the magnetic field of the neutron star $B_{\rm NS} = 10^8$G, and $r_{\rm ej}$ for $B_{\rm NS} = 10^9$G, respectively, in units of r_g. We also present radii where a mass accretion rate of neutrons $\dot{m}_n$ equals to 1×10^{-6} (thin dash-dotted line) or 5×10^{-6} (dash-dotted line).

We have evaluated $\dot{m}_n = \dot{m} X_{\rm n,ADAF}$, assuming $r_{\rm ej} > r_c$, where $X_{\rm n,ADAF}$ is the mass fraction of neutrons at $r_{\rm ej}$. For a given $\dot{m}$, higher $B_{\rm NS}$ means larger $r_{\rm ej}$ and thus smaller $\dot{m}_n$ because of smaller $X_{\rm n,ADAF}$. The blackbody-

like, soft X-ray emission with an order of $10^{32}\,\mathrm{erg\,s^{-1}}$ requires $\dot{m} \geq 7 \times 10^{-3}$ for a neutron star with $B_{\rm NS} \geq 10^8\,\mathrm{G}$. Radii where $\dot{m}_n$ equals to 1×10^{-6} (thin dash-dotted line) or 5×10^{-6} (dash-dotted line) are shown in Figure 2.

4. Transportation of Li to the secondary through the propeller effect

The material in an ADAF is outflowed via the propeller effects, so that a fraction of Li produced in the ADAF can be transfered to the secondary and enhance Li abundances on the secondary. A fraction of the Li on the secondary is returned to the ADAF through mass accretion. We can estimate an equilibrium abundances of Li. For isotropic ejection of Li from the ADAF, the production rate of Li on the secondary is given by

$$\dot{M}^{+}_{\rm Li} = \dot{M} X_{\rm Li,ADAF} \left(\frac{R_*}{a}\right)^2, \tag{5}$$

where $X_{\rm Li,ADAF}$, R_* and a are the mass fraction of Li (^{6}Li and ^{7}Li) at an ejection radius of the ADAF, $r_{\rm ej}$, the radius of the secondary, and the binary separation, respectively. While the mass transfer rate of Li from the surface to the ADAF is expressed as $\dot{M}^{-}_{\rm Li} = \dot{M} X_{\rm Li}$, where $X_{\rm Li}$ is the mass fraction of Li on the secondary. For equilibrium between the production and loss rates $\dot{M}^{+}_{\rm Li} = \dot{M}^{-}_{\rm Li}$, one can obtain an equilibrium Li abundance

$$Y_{\rm Li,\,eq} = \frac{1}{7}\left(\frac{R_*}{a}\right)^2 X_{\rm Li,ADAF}, \tag{6}$$

where an averaged mass number of Li, $\bar{A}_{\rm Li}$, is set to be 7, because of larger fractions of ^{7}Li compared with ^{6}Li, as shown in Figure 1.

We find that $Y_{\rm Li,\,eq}$ is comparable to the observed Li abundances in Cen X-4 ($6.67 \times 10^{-10}(Y_p/0.9)$ (Casares et al., 2007)) for $X_{\rm Li,ADAF} = 0.817 \times 10^{-7}$, which is realized at $\sim 14 r_g$ and $\sim 18 r_g$ in the ADAF for $\dot{m} = 0.01$ and 0.1, respectively (Figure 1). We note that Li isotopic ratios ^{6}Li/^{7}Li in the ADAF at the above radii are 0.19, which is comparable to the observed ratio in Cen X-4 ($0.12^{+0.08}_{-0.05}$) (Casares et al., 2007). Moreover, we find that for $\dot{m} \sim 0.01-0.02$ and $B_{\rm NS} = 2-3\times10^8$ G, the estimated values for the Li abundance as well as the soft X-ray luminosity are comparable to the observed values.

We note that the estimate for Li abundance is largely different from that in (Yi & Narayan, 1997), because they have only considered the decrease in Li due to nuclear burning and have ignored the decrease in Li via mass accretion, which is much larger than that through Li burning, in a short time scale of years. It should be emphasized that $Y_{\rm Li,\,eq}$ depends on α and $\dot{m}$ as the combination of $\dot{m}/\alpha^2$, as well as $r_{\rm ej}$, through $X_{\rm Li,ADAF}$.

It should be emphasized that the accretion rates, $\dot{m} \sim 0.01 - 0.02$, are comparable to 1/3 of the mass transfer rate predicted by binary evolution models (King et al., 1996; Menou et al., 1999) for a secondary mass of $0.23 M_\odot$ and the orbital period of 0.629 day (Casares et al., 2007) and is consistent with an averaged rate estimated by Heinke et al. (2007) based on an outburst luminosity and a quiescent duration. We note that the magnetic field of the neutron star has been estimated as $\sim 2 \times 10^9$ G by Zhang et al. (1998), although in their evaluation they adopted a state change luminosity and a spin period of the star, which are uncertain.

5. Summary

We have proposed the emission mechanism of soft X-ray radiation from NSSXTs and have examined unusually high abundances of Li on a low-mass secondary in Cen X-4 during a quiescent state. Inside the hot ($> 1\,\mathrm{MeV}$) ADAF around a neutron star, neutrons are abundantly synthesized through the spallation of ^{4}He via protons in the flow. We find that the neutron-ADAF is formed around the neutron star after the operation of the propeller effects. The accretion energy of the neutrons liberated on the surface of the star is a possible energy budget for soft X-ray radiation in a NSSXT in quiescence. Moreover, Li is abundantly synthesized in the ADAF through $\alpha - \alpha$ reactions and is transfered to the surface of the secondary by the magneto-centrifugal forces. We find that the estimated soft X-ray luminosity and abundance of Li on the secondary are comparable to observed values in Cen X-4 for reasonable values of the mass accretion rate and the magnetic field of the neutron star, or $2-4\times10^{-11} M_\odot\,\mathrm{yr}^{-1}$ and $1-2\times10^8$ G, respectively. We also find that the isotopic ratio of lithium ^{6}Li/ ^{7}Li is found to be comparable to an observed ratio in Cen X-4.

References

Anders, E., & Grevesse, N. 1989, Geochim. Cosmochim. Acta 53, 197

Asai, K., et al. 1996, PASJ, 48, 257

Asai, K., Dotani, T., Hoshi, R., Tanaka, Y., Robinson, C. R., & Terada, K. 1998, PASJ, 50, 611

Brown, E. F., Bildsten, L., & Rutledge, R. E. 1998, ApJ, 504, 95

Campana, S., Mereghetti, S., Stella, L., & Colpi, M. 1997, A&A, 324, 941

Campana, S., et al. 1998, ApJ, 499, L65

Campana, S., Israel, G. L., Stella, L., Gastaldello, F., & Mereghetti, S. 2004, ApJ, 601, 474

Casares, J., Bonifacio, P., González Hernández, J. I., Molaro, P., & Zoccali, M. 2007, A&A, 470, 1033

Chen, X., Zhang, S. N., & Ding, G. Q. 2006, ApJ, 650, 299

Fujimoto, S., Matsuba, R., & Arai, K. 2008, ApJ, 673, 51 (FMA08)

Garcia, M. R., McClintock, J. E., Narayan, R., Callanan, P., Barret, D., & Murray, S. S. 2001, ApJ, 553, L47

Gilfanov, M., Revnivtsev, M., Sunyaev, R., & Churazov, E. 1998, A&A, 338, L83

Guessoum, N., & Gould, R. J. 1989, ApJ, 345, 356

Guessoum, N., & Kazanas, D. 1999, ApJ, 512, 332

Heinke, C. O., Jonker, P. G., Wijnands, R., & Taam, R. E. 2007, ApJ, 660, 1424

Jean, P., & Guessoum, N. 2001, A&A, 378, 509

King, A. R., Kolb, U., & Burderi, L. 1996, ApJ, 464, L127

Machida, M., Nakamura, K., & Matsumoto, R. 2004, PASJ, 56, 671

Martin, E. L., Rebolo, R., Casares, J., & Charles, P. A. 1992, Nature, 358, 129

Martin, E. L., Rebolo, R., Casares, J., & Charles, P. A. 1994, ApJ, 435, 791

Martin, E. L., Casares, J., Charles, P. A., & Rebolo, R. 1995, A&A, 303, 785

Martin, E. L., Casares, J., Molaro, P., Rebolo, R., & Charles, P. 1996, New Astron. 1, 197

Menou, K., Esin, A. A., Narayan, R., Garcia, M. R., Lasota, J.-P., & McClintock, J. E. 1999, ApJ, 520, 276

Narayan, R., & Yi, I. 1994, ApJ, 428, L13

Narayan, R., & Yi, I. 1995a, ApJ, 444, 231

Narayan, R., & Yi, I. 1995b, ApJ, 452, 710

Narayan, R., McClintock, J. E., & Yi, I. 1996, ApJ, 457, 821

Narayan, R., Barret, D., & McClintock, J. E. 1997, ApJ, 482, 448

Read, S. M., & Viola, V. E., Jr. 1984, Atomic Data and Nuclear Data Tables, 31, 359

Rutledge, R. E., Bildsten, L., Brown, E. F., Pavlov, G. G., & Zavlin, V. E. 2001, ApJ, 551, 921

Rutledge, R. E., Bildsten, L., Brown, E. F., Pavlov, G. G., & Zavlin, V. E. 2001, ApJ, 559, 1054

Wallerstein, G. 1992, Nature, 356, 569

Yi, I., & Narayan, R. 1997, ApJ, 486, 363

Zhang, S. N., Yu, W., & Zhang, W. 1998, ApJ, 494, L71

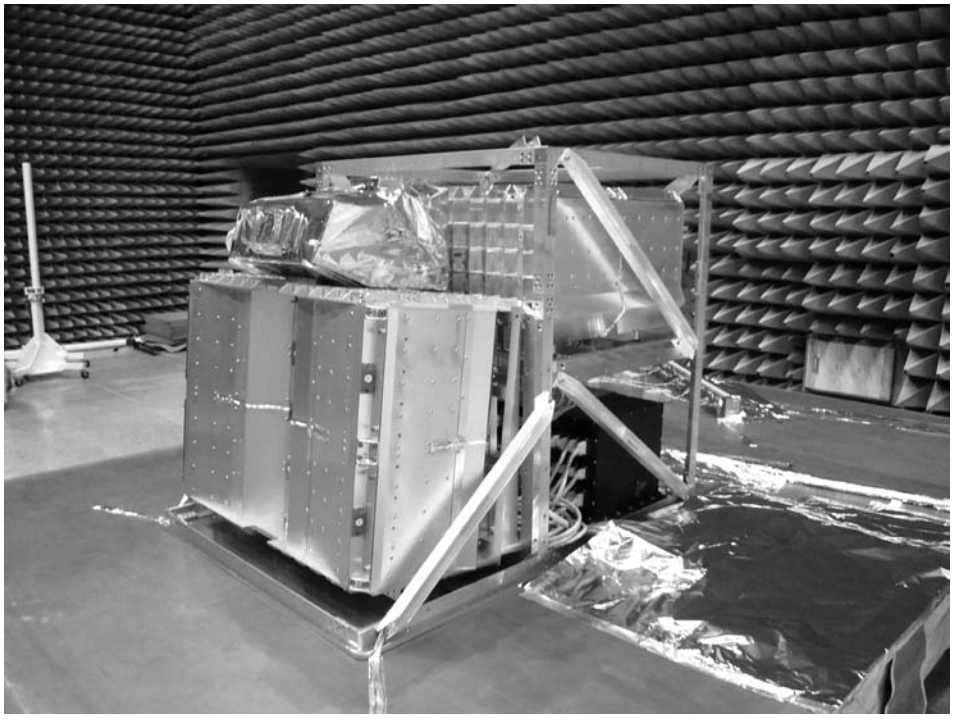

Eclipsing light curves for accretion flows around a rotating black hole and atmospheric effects of the companion star

Rohta Takahashi[1]

[1] Cosmic Radiation Laboratory, the Institute of Physical and Chemical Research (RIKEN)
2-1 Hirosawa, Wako, Saitama 351-0198, Japan
E-mail: rohta@riken.jp

Abstract

We calculate eclipsing light curves for accretion flows around a rotating black hole taking into account the atmospheric effects of the companion star such as the atmospheric absorption and scattering effects. By using the solar-type atmospheric model, we have taken into account the atmospheric effects of the companion star, such as the photoionization by HI and HeI. We found that the eclipsing light curves observed at 1 keV possibly contain the information of the black hole spin. However, in our atmospheric model, the effects of the atmosphere are much larger than the effects of the black hole spin. Therefore, even in the case that the light curves contain the information of the black hole spin, it may be difficult to extract the information of the black hole spin if we do not have the realistic atmospheric profiles, such as the temperature, and the number densities for several elements. If the light curves of the occultation events of the black hole binaries are detected by MAXI, the light curves contain the information of the atmosphere of the companion star and, possibly, a black hole's spin. Takahashi & Watarai (2007) also contains other details of the present study.

Key words: workshop: proceedings — LaTeX2.09: style file — instructions

1. Introduction

In order to obtain physical information of the strong gravity region in the vicinity of black holes, direct imaging of a black hole is an extremely promising method. The emission from the vicinity of the event horizon contains information about the physical parameters of a black hole. Since the apparent shapes of the black hole shadows and the appearances of the circular orbit around the black hole are deformed by the effects of the black hole's rotation and charge (e.g. Cunningham & Bardeen 1972, Bardeen 1973, Takahashi 2004, 2005), the size and the position of the most luminous parts generally existing in the vicinity of the shadow depend on the physical parameters of black holes.

In general, methods for probing strong-field gravity near supermassive black holes or stellar-mass black holes are quite limited. Although the past VLBI observations give the images of the galactic centers with the spatial resolution within 100 Schwarzschild radii (e.g., for Sgr A*, Shen et al. 2005, for M87, Junor, Biretta & Livio 1999), the direct mapping of the shadows of both supermassive and stellar-mass black holes has not been performed so far. Several future interferometers have plans to image the shadows around massive black holes: e.g. VSOP-2 for radio (Hirabayashi et al. 2005). While these planned interferometers will image the massive black hole, direct imaging of the stellar-mass black holes are difficult because the apparent size of the black hole shadow is extremely small. Even with the future planned radio or X-ray interferometer, the direct mapping of the shadow of the stellar-mass black hole is practically impossible. However, if the stellar-mass black hole in the binary system is occulted by its companion star, the eclipsing light curves give the direct information for the spatial distribution of the brightness patterns of the accretion flows around the black hole. This is the primary motivation of the present study.

In the present study, we study the method to investigate the physical information included in the strong-gravity region around the black hole by light-curve analysis for an accretion disc around a black hole occulted by its companion star. The basic idea for the eclipsing light curve analysis was first proposed by Fukue (1987). Watarai, Takahashi & Fukue (2005) investigated the eclipsing light curves for the supercritical accretion flows which may be suggested as the accretion flow model for some X-ray black-hole binaries. In principle, light curves obtained at the time of eclipsing have information about the black hole if the region around the black hole is optically thin. However, the real observational data of the eclipsing light curves may contain the addi-

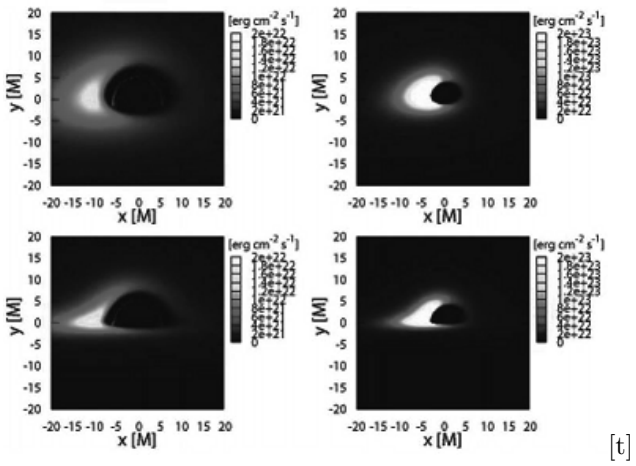

Fig. 1. Bolometric flux distribution (erg cm^{-2} s^{-1}) for black-hole spins of $a/M = 0$ (*left panels*) and 1 (*right panels*), and inclination angles of $i = 60°$ (*top panels*) and $80°$ (*bottom panels*). The relativistic standard discs are adopted. The inner edge of the accretion disc is assumed to be the marginally stable circular orbit. For non-rotating black holes, indirect images can be seen in the region within the inner stable circular orbit. The flux distributions are asymmetric due to the disc rotation and the frame-dragging effects. The shapes of the shadows casted by the black holes are asymmetric due to frame-dragging effects around the rotating black holes.

tional effects which are not sometimes simple. One of such effects is the atmospheric effects of the companion star. Recently, Pietsch et al. (2006) give the observational data of the eclipsing light curves for the X-ray binary M33 X-7 detected by *Chandra*. In soft X-ray, the atmospheric effects in the companion star may vanish the relativistic effects in the eclipsing light curves. In other words, the eclipsing light curves also contain the information of the atmosphere of the companion star. Thus, the eclipsing light curve analysis will be used for the investigation of the atmosphere of the companion star. In the present study, we also investigate the companion star's atmospheric effects in the eclipsing light curves of the black-hole binaries, and compare these effects with the effects of the black hole's rotation.

2. Eclipsing Light Curves without Atmospheric Effects

In order to calculate a light curve during an eclipse, some assumptions were required. In the present study, we assume the relativistic standard disc (Novikov & Thorne 1973, Page & Thorne 1974) at equatorial plane. Based on this model, the radial profile of the effective temperature of the accretion flow can be calculated. Then, at each radius, we assume the black body spectrum with the effective temperature calculated from the relativistic standard accretion disc model.

The calculation method for the observed spectrum of the emission in the Kerr metric is established (e.g. Cunningham & Bardeen 1973). At each light ray, the observed specific intensity, $I_{\nu_{\rm obs}}$ [erg s^{-1} cm^{-2} str^{-1} Hz^{-1}], of the accretion disc observed at the photon frequency $\nu_{\rm obs}$ is calculated as $I_{\nu_{\rm obs}} = g^3 I_{\nu_{\rm rest}}$, where $\nu_{\rm rest}$ is the photon frequency measured in the local rest frame of the accretion flow, $T_{\rm eff}$ is the temperature of the relativistic standard accretion disc at the radius where the light ray intersects, $I_{\nu_{\rm rest}}$ is the specific intensity measured at the local rest frame of the accretion disc, and g is the frequency ratio defined $g = \nu_{\rm obs}/\nu_{\rm rest}$. The frequency ratio g is calculated same as Cunningham & Bardeen (1973). In this study, we assume $I_{\nu_{\rm rest}}$ is the black body spectrum with the effective temperature at the radius where the light ray intersects, i.e. $I_{\nu_{\rm rest}} = B_{\nu_{\rm rest}}(T)$, where T is the temperature of the accretion disc. By using the relation $d\nu_{\rm obs} = g d\nu_{\rm rest}$ and the assumption of the isotropic radiation at the local rest frame of the accretion disc, the observed flux $F_{\rm obs}$ [erg s^{-1} cm^{-2}] is calculated as $F_{\rm obs} = (1/d^2)\int g I_{\nu_{\rm obs}} d\nu_{\rm obs} = (1/d^2)\int g^4 I_{\nu_{\rm rest}} d\nu_{\rm rest}$ where d is the distance to the accretion disc. By integrating the observed flux in x-y plane, we can calculate the observed bolometric lumi-

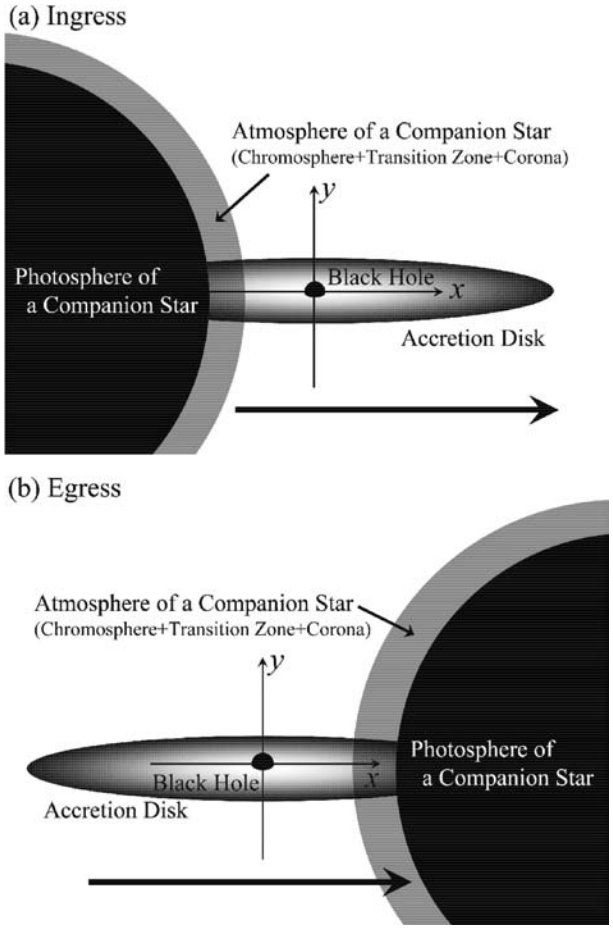

Fig. 2. Schematic diagrams for the eclipsing black-hole binaries when the ingress (*top panel*) and the egress (*bottom panel*).

nosity $L_{\rm bol}$ [erg s^{-1}]. On the other hand, the observed flux at the observed photon frequency $\nu_{\rm obs}$, $F^{\rm obs}_{\nu_{\rm obs}}$ [erg s^{-1} cm^{-2} Hz^{-1}], is calculated by using the delta-function as $F_{\nu_{\rm obs}} = (1/d^2)\int g^4 I_{\nu_{\rm rest}} \delta(\nu_{\rm obs} - g\nu_{\rm rest}) d\nu_{\rm rest}$. By integrating the flux in x-y plane, the luminosity at the observed frequency $\nu_{\rm obs}$, $L_{\nu_{\rm obs}}$ [erg s^{-1} Hz^{-1}] is calculated. The luminosity are calculated by the ray-tracing method, which is commonly used in the past studies (e.g. Fukue & Yokoyama 1988, Takahashi 2004).

For all calculations in the present study, we assume a black hole mass of $10M_\odot$ and mass accretion rate of $1\dot{M}_{\rm Edd}$, and the disc thickness is neglected. Here $\dot{M}_{\rm Edd}$ is the Eddington mass accretion rate defined as $\dot{M}_{\rm Edd} \equiv L_{\rm Edd}/c^2 = 1.4 \times 10^{17}(M/M_\odot)$ [g/s] where $L_{\rm Edd}$ is the Eddington luminosity (e.g. Kato, Fukue & Mineshige 1998). Also, we implicitly assume that the binary system has a relatively high inclination angle, $i > 60^\circ$. In figure 1, we show examples of the spatial distribution of the observed flux of the accretion flows in the vicinity of the black holes. For all panels of figure 1, the mass center of the black hole is at the center of the image. The width and the height of the images in figure 1 are both 20 M where M is the gravitational radius and 1 M corresponds to 0.5 Schwarzschild radius. We define x-axis and y-axis as the horizontal line and the vertical line crossing at the center of the each image of figure 1. In figure 1, the position of the mass center of the black hole is at $(x,\ y) = (0,\ 0)$, and the displayed region is -10 $[M]< x < 10$ $[M]$ and -10 $[M]< y < 10$ $[M]$. Based on the calculations of the observed luminosity described above, we calculate the eclipsing light curves.

In figure 2, we show the schematic diagrams for the eclipsing black-hole binaries when the ingress (*top panel*) and the egress (*bottom panel*). We also plot x-axis and y-axis in panels of figure 2. When the ingress and the egress phases described in figure 2, the companion star is crossing the line of sight between the observer and the black hole binary along the direction of x-axis. Since the size of the companion star is generally much larger than the emission region around the black hole, we assume the carve of the stellar surface as the straight line in our calculations. Although in our calculations the brightness profiles of the accretion disc are calculated within $r < 200$ $[M]$, the light curves are calculated in the range of -60 $[M]< x < 60$ $[M]$. That is, in terms of the range in y-axis direction, we use the brightness profile of the disc in the range of -200 $[M]< y < 200$ $[M]$, but the brightness profiles of the accretion disc are given within $r < 200$ $[M]$.

3. Atmospheric Model of Companion Star and Eclipsing Light Curves with Atmospheric Effects

In the present study, we use the atmospheric model calculated for the solar atmosphere (Daw et al. 1995, Fontenla et al. 1993, Gabriel 1976). In the top panel of figure 3, we plot HI number density $N_{\rm HI}$ [cm^{-3}] (*solid line*) and temperature T [K] (*dashed line*) of the adopted atmosphere model. Here, H [km] denote the height above the photosphere. Temperature of the atmosphere suddenly increase and the number density decrease in the transition zone between the lower chromosphere ($\sim 10^{3-4}$ [K]) and the upper corona ($\sim 10^6$ [K]). The two separate temperatures of HI correspond to two stable regions of the cooling function of HI (e.g. chapter 6 in Spitzer 1978).

Table 1. Cross sections [cm^2] for photoionization absorption due to HI, HeI, HeII and Compton scattering in X-ray of 0.1 keV, 1 keV and 10 keV.

	0.1 keV	1 keV	10 keV
$\sigma_{\rm HI}$	1.9×10^{-20}	1.1×10^{-23}	4.5×10^{-27}
$\sigma_{\rm HeI}$	3.9×10^{-19}	3.4×10^{-22}	1.4×10^{-25}
$\sigma_{\rm HeII}$	3.0×10^{-19}	2.7×10^{-22}	1.3×10^{-25}
$\sigma_{\rm Comp}$	1.4×10^{-25}	1.3×10^{-25}	6.4×10^{-25}

In figure 4, we show the schematic diagrams for the observer, the eclipsing black-hole binaries, the companion star with its atmosphere and the light ray penetrating the atmosphere. Here, the light ray penetrates the atmosphere with the length of $2\ell_{\rm max}$. $H_{\rm max}$ is the length from the center of the companion star to the maximum height of the atmosphere, and H is the length between the center of the companion star and the point where the light ray penetrate the atmosphere. The optical depth, $\tau(\nu)$, in the atmosphere can be calculated as

$$\tau(\nu) = \int d\ell\ (\sigma_{\rm abs} N_{\rm abs} + \sigma_{\rm sca} N_{\rm sca}), \qquad (1)$$

where $\sigma_{\rm abs}$ and $\sigma_{\rm sca}$ are cross sections of the absorption and scattering, respectively, and $N_{\rm abs}$ and $N_{\rm sca}$ are the number densities of the absorber and the scattering medium, respectively. The integrations are performed along the atmosphere of the companion star in the line of sight.

In soft X-ray band, the photoionization absorption by hydrogen and helium contribute to opacity. The photoionization absorption cross sections of HI, HeI and HeII in soft X-ray are summarized in table 1. We also calculate the Compton scattering cross section in the same table. Since for 0.1 keV and 1 keV the scattering cross section is significantly lower than the absorption cross sections, we can neglect the effects of the Compton scatterings. On the other hand, for 10 keV the scattering effects are dominated. In this case, we only take into account the out-going photons as the scattering effects for simplicity. We see that the photoionization absorption cross sections of HI, HeI and HeII are comparable in soft X-ray. Calculations by Fontenla et al (1993) shows that the number density of HeII, $N_{\rm HeII}$, is significantly lower,

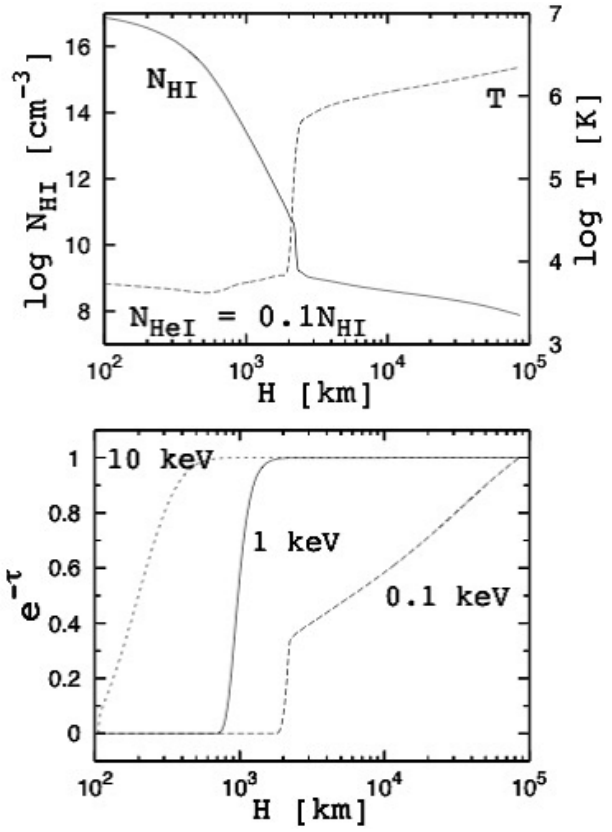

Fig. 3. HI number density $N_{\rm HI}$ [cm^{-3}] (*solid line*) and temperature T [K] (*dashed line*) of the adopted atmosphere model (*top panel*). The atmosphere model has been constructed for the solar atmosphere (Daw et al. 1995). The number density of HeI, $N_{\rm HeI}$, is assumed to be $N_{\rm HeI} = 0.1 N_{\rm HI}$. The corresponding transparency ratio, $e^{-\tau}$, of the modeled atmosphere (*bottom panel*) for X-ray: 0.1 keV (*long dashed line*), 1 keV (*solid line*), 10 keV (*short dashed line*). Here, τ is the optical depth of the photoionization absorption by HI and HeII.

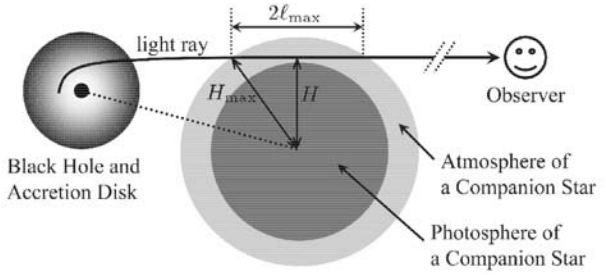

Fig. 4. Schematic diagrams for the observer, the eclipsing black-hole binaries, the companion star with its atmosphere and the light ray penetrating the atmosphere. Here, the light ray penetrate the atmosphere with the distance $2\ell_{\rm max}$. $H_{\rm max}$ is the distance from the center of the companion star to the maximum height of the atmosphere, and H is the distance between the center of the companion star and the point where the light ray penetrate the atmosphere.

e.g. by order 4, than that of HI, $N_{\rm HI}$, in the solar atmosphere, i.e. $N_{\rm HeII} \ll N_{\rm HI}$, and the number density of HeI is lower by about order 1 than that of HI through the atmosphere, i.e. $N_{\rm HeI} \sim N_{\rm HI}$. Therefore, in the present study, we neglect the scattering effects in the atmosphere for 0.1 keV and the absorption by HeII for 0.1 keV, 1 keV and 10 keV. Then, we calculate the optical depth in the atmosphere as

$$\tau(\nu) = 2\int_0^{\ell_{\rm max}} d\ell\, (\sigma_{\rm HI} N_{\rm HI} + \sigma_{\rm HeI} N_{\rm HeI} + \sigma_{\rm Comp} N_e), \quad (2)$$

where $\ell_{\rm max} = (H_{\rm max}^2 - H^2)^{1/2}$, $H_{\rm max}$ is set to 10^5 [km], the number density of electrons N_e is calculated only in the photosphere based on numerical table given by Fontenla et al. (1993). However, according to Fontenla et al. (1993) the number density of electrons in the atmosphere is lower than that of HI by factor 3-4 in the almost region of photosphere, then the scattering effects are negligible in the photosphere. Near the transition zone, the number density of the electron is lower than that of HI within factor 1, and for cases of 10 keV the scattering effects contribute to the optical depth. By using the optical depth calculated above, we solve the radiative transfer equation along the atmosphere in the line of sight. The brightness decreases along the light rays in the atmosphere by the exponential of the optical depth.

By using the optical depth τ calculated above, the observed luminosity with the atmospheric effects is calculated by multiplying the factor $e^{-\tau(\nu_{\rm obs})}$ to the observed luminosity without the effects of the atmospheric effects. The observed luminosity without the atmospheric effects corresponds to the case of $\tau = 0$. Since the distance between the accretion disc and the atmosphere of the companion star is very large, here we evaluate the optical depth τ at the observed photon frequency $\nu_{\rm obs}$. In the bottom panel of figure 3, we show the corresponding transparency ratio, $e^{-\tau}$, of the modeled atmosphere for X-ray: 0.1 keV (*long dashed line*), 1 keV (*solid line*), 10 keV (*short dashed line*). In the cases of 1 keV and 10 keV, while the lines in the corona are optically thin, the photoionization absorption is effective in the photosphere. By using the optical depths calculated as figure 3, we calculate the eclipsing light curves with the atmospheric effects of the companion star in later section.

4. Black Hole Shadows with the Atmospheric Effects

We first calculate the images of the black hole shadows with absorption effects in the atmosphere of the companion star. In figure 5, we show images of black hole shadows when ingress at the observed frequency of 1 keV for cases with no absorption effects (*top panels*) and atmospheric photoionization absorptions (*bottom panels*). We assume the mass of the companion star to be 1 $M_\odot$. The size of each image is same as figure 1, i.e. -20 $[M] < x <$20

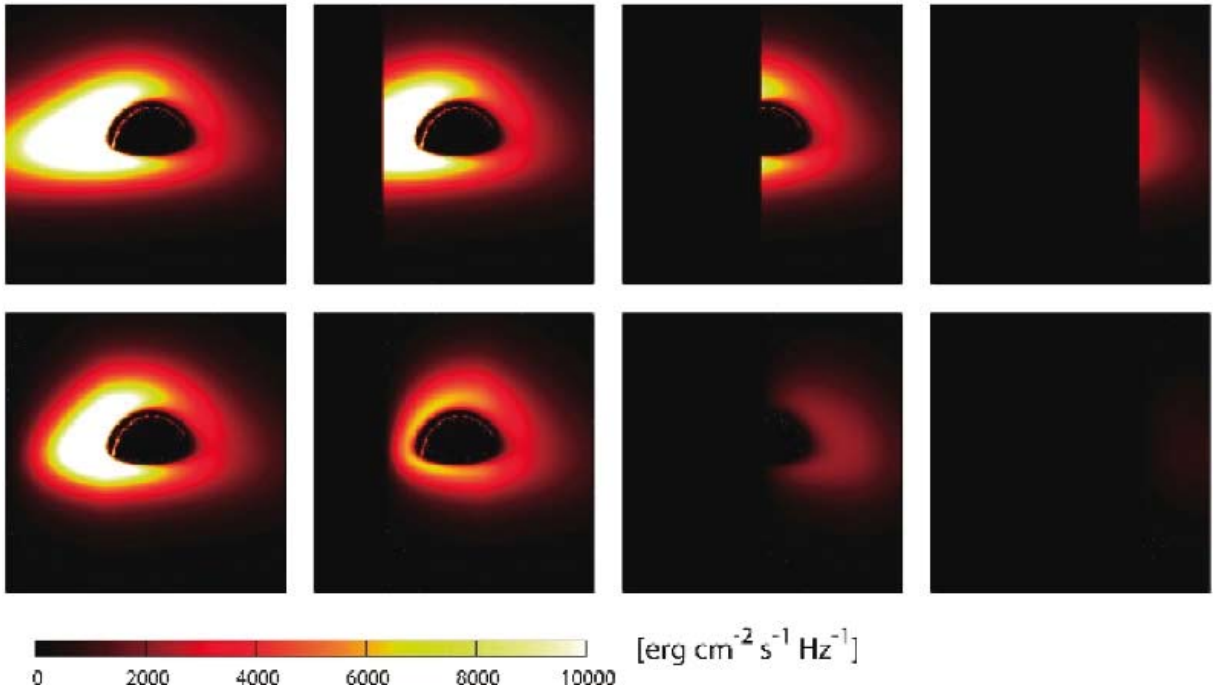

Fig. 5. Images of black hole shadows with $a/M = 0.5$ when ingress at the observed frequency of 1 keV for cases with no absorption effects (*top panels*) and atmospheric absorptions (*bottom panels*). The size of each image is same as figure 1, i.e. $-20 < x/M < 20$ and $-20 < y/M < 20$. For no absorption case for top panels, the edges of the companion star are located at -20, -10, 0 and 10 in units of M (*left to right*). For the absorption case for bottom panels, we define these edges as positions with $\tau(\nu) = 7$.

$[M]$ and -20 $[M] < y < 20$ $[M]$. For no absorption case for top panels, the edges of the companion star are located at -20, -10, 0 and 10 in units of M (*left to right*). For the cases with the atmospheric effects (*bottom panels*), we define these edges as positions with $\tau(\nu) = 7$. We can see that the brightness around the black hole shadow are decreased by the photoionization absorption in the atmosphere. In addition to the decrease of the absolute values of the brightness, the clear edges of the companion star which can be seen for no absorption cases are smeared out by the absorption effects. This is because the effective region with absorption effects is comparable to the size of X-ray emitting regions. We next calculate the eclipsing light curves with effects of the photoionization absorption. In figure 6, we show normalized light curves with (*thick lines*) and without (*thin lines*) the atmospheric effects of the companion star. The observed energy is set to be 1 keV in figure 6. The black hole spins are $a/M = 0$ (*solid lines*) and 1 (*dotted lines*), and the observed inclination angles with respect to the rotation axis of the accretion disc are $i = 60°$ (*top panels*) and 80° (*bottom panels*). While the normalization light curves with no absorption effects largely change in a short time when the most luminous parts of the accretion disc are occulted or unocculted by the sharp edge of the companion star, the normalization light curves with absorption effects gradually decrease or increase compared to the cases with no absorption effects. This is because the atmosphere of the companion star absorb some fraction of X-ray photons gradually before the most luminous part of the accretion disc is completely occulted or unocculted. In other words, the width of the absorption region which causes the gradual changes of the X-ray brightness of the accretion disc is comparable to size of the luminous parts of the accretion disc as denoted above.

Since the size of the most luminous parts of the accretion disc depends on the black hole spin, the crossing timescale of the companion star along the most luminous parts of the accretion disc can be one of the key physical quantities which distinguish the cases of rapidly rotating black holes and the cases of no rotating black hole. But these effects are generally smeared out by the atmospheric effects of the companion star at some fraction. In our calculations assuming the solar atmosphere, the atmospheric absorption can not completely smeared out the difference between the cases of rapidly rotating black holes and the cases of no rotating black hole. Then, the observed eclipsing light curves at 1 keV with the atmospheric effects of the companion star possibly contain the information of the black hole spin. However, since the effects of the atmosphere is larger than the effects of the spin, only when we have the reliable atmospheric model, we can determine the black hole spin from the

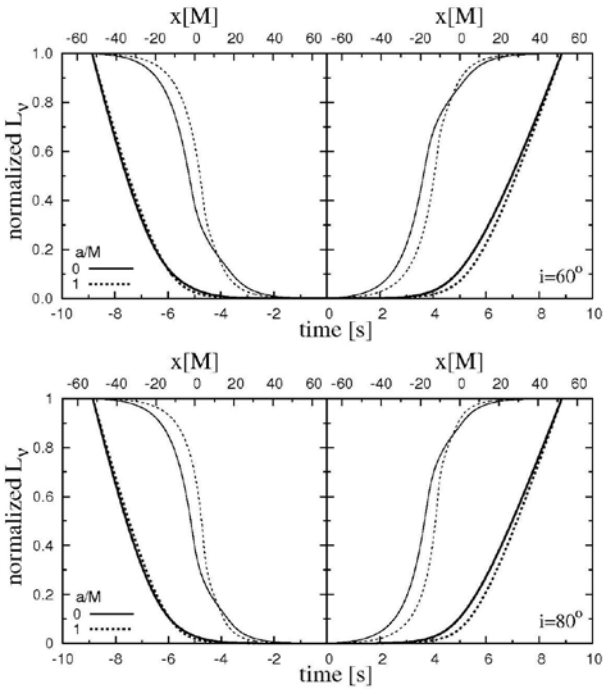

Fig. 6. Normalized light curves with (*thick lines*) and without (*thin lines*) the atmospheric effects of the companion star at observed energy of 1 keV for black hole spins $a/M = 0$ (*solid lines*) and 1 (*dotted lines*), and the observed inclination angles with respect to the rotation axis of the accretion disc $i = 60°$ (*top panels*) and $80°$ (*bottom panels*).

eclipsing light curves observed by the wavelength where the atmospheric absorption is effective.

5. Concluding Remarks

In this paper, we propose an eclipsing light-curve diagnosis for accretion flows around rotating black holes. When emission from an inner part of the accretion disc around black hole is occulted by a companion star, the light curves at ingress and egress show the asymmetric features due to the relativistic effects such as Doppler boosting originally pointed out by Fukue (1987). We show that the eclipsing light curves without the atmospheric effects clearly reflect the effects of the black hole's rotation. We also investigate the eclipsing light curves with the atmospheric effects of the companion star. Based on the adopted atmospheric model, after evaluating the absorption and scattering effects in X-ray, we calculate the images of the black hole shadows, the normalized light curves. Since the size of the most luminous parts of the accretion disc depends on the black hole spin, the crossing timescale of the companion star along the most luminous parts of the accretion disc can be one of the key physical quantities which distinguish the cases of rapidly rotating black holes and the cases of no rotating black hole.

In our calculations assuming the solar atmosphere, while the effects of black hole spins are negligible when the observed photon energy of 0.1 keV for both cases with no atmospheric effects and with atmospheric effects, for the observed photon energies of 1 keV and 10 keV the atmospheric absorption can not completely smeared out the difference between the cases of rapidly rotating black holes and the cases of no rotating black hole. However, these effects are smeared out by the atmospheric effects of the companion star at some fraction, and in our atmospheric model, the effects of the atmosphere are much larger than the effects of the black-hole spin. Therefore, even in the case that the light-curves contain the information of the black hole spin, it may be difficult to extract the information of the black hole spin if we do not have the realistic atmospheric profiles, such as, the temperature, the number densities for several elements. Even in such cases, based on our calculations, the light curve asymmetries due to the rotation of the accretion disc exist. Only when we have the reliable atmospheric model, in principle, the black hole spin can be determined from the eclipsing light curves observed around 1 keV. Takahashi & Watarai (2007) gives more information about these topics.

References

Bardeen, J.M., 1973, in Black Holes, ed. C. DeWitt and B. DeWitt (Gordon and Breach, New York)
Bardeen, J.M., Press, W.H., Teukolsky, S.A., 1972, ApJ, 178, 347
Cunningham, C. T., Bardeen, J. M., 1972, ApJ, 173, 137
Daw, A., DeLuca, E. E., Gould, L., 1995, ApJ, 453, 929
Fukue, J., 1987, Nature, 327, 600
Fukue, J., & Yokoyama, T., 1988, PASJ, 40, 15
Hirabayashi, H., et al., 2005, in Proc. 7th Symp. European VLBI Network on New Developments in VLBI Science and Technology, ed. R. Bachiller, F. Colomer, J.-F. Desmars, & P. de Vicente (Obs. Astron. Nac. Spain), 285 (astro-ph/0501020)
Junor, W., Biretta, J. A., Livio, M., 1999, Nature, 401, 891
Kato, S., Fukue, J., Mineshige, S., 1998, Black-Hole Accretion discs, Kyoto University Press
Shen, Z.-Q., Lo, K. Y., Liang, M.-C., Ho, P. T. P., Zhao, J.-H., 2005, Nature, 438, 62
Spitzer, L. Jr., 1978, Physical Processes in the Interstellar Medium, John Wiley & Sons, Inc.
Takahashi, R., 2004, ApJ, 611, 996
Takahashi, R., 2005, PASJ, 57, 273
Takahashi R., Watarai K. 2007 MNRAS, 374, 1515
Watarai, K., Takahashi, R., Fukue, J., 2005, PASJ, 57, 827
Watarai, K., Ohsuga, K., Takahashi, R., & Fukue, J., 2005, PASJ, 57, 513

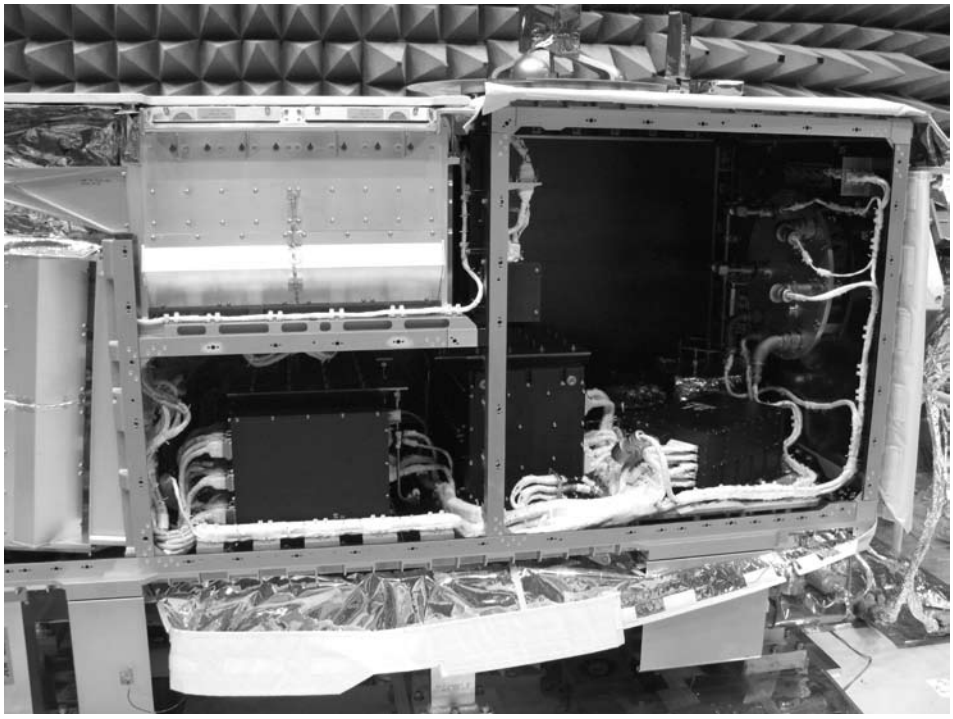

ACTIVE GALACTIC NUCLEI

Extragalactic Survey with MAXI

Yoshihiro Ueda[1], Kazuo Hiroi[1], Satoshi Eguchi[1], and the MAXI team

[1] Department of Astronomy, Kyoto University, Kyoto 606-8502, Japan
E-mail(YU): ueda@kusastro.kyoto-u.ac.jp

Abstract

We summarize the prospects for extragalactic survey with the MAXI mission. By integrating all the data taken for ~ 1.5 years, we estimate that about 1,300 Active Galactic Nuclei (AGNs) will be detected in the 3–20 keV band with the Gas Slit Cameras from extragalactic sky at Galactic latitudes higher than 15°. The MAXI survey will achieve the best sensitivity for populations of moderately absorbed AGNs among any all sky X-ray missions, and is complementary to *ROSAT* all sky survey and hard X-ray (>10 keV) surveys by the *Swift* and *INTEGRAL* satellites. Many "transient" AGNs could be newly detected with MAXI. In this paper, we discuss the scientific significance of the MAXI survey.

Key words: catalogs — galaxies: active — X-rays: galaxies — X-rays: general

1. Introduction

X-ray surveys at high Galactic latitude are powerful approach for studying the nature of extragalactic populations, mainly Active Galactic Nuclei (AGNs). While the X-ray background below 10 keV has been mostly resolved into discrete sources in ultra deep surveys with *Chandra*, surveys with a much larger area that cover a brighter flux range are indispensable for the global understanding of the cosmological evolution of AGNs. In particular, all sky surveys above 2 keV with sensitivities of $\sim 10^{-12}$ erg cm^{-2} s^{-1} (2–10 keV) bridging the *HEAO1* all-sky survey (Piccinotti et al. 1982) and *ASCA* / *XMM-Newton* serendipitous surveys (Ueda et al. 2005, Watson et al. 2009) are still missing, which are important to trace AGN evolution in the low to intermediate redshift universe.

With its unprecedented sensitivity from the whole sky in the hard band above 2 keV, MAXI will provide a new X-ray source catalog that becomes the basis of all scientific studies of the mission. In this paper, we summarize the prospects for the extragalactic survey performed with the Gas Slit Cameras. Details on source detection method and estimates of the sensitivity are given in Hiroi et al. (2009, this conference).

2. Sensitivity of MAXI

The ultimate sensitivity of MAXI is determined by the source confusion limit, constrained by the angular resolution of the imager. By assuming a beam size of $1.5^\circ \times 1.5^\circ$, the cumulative number density of one source per 10 beams is calulated to be $N(>S) = 0.044$ deg^{-2}. Figure 1 shows an expected log N - log S relation of AGNs in the 3–20 keV band, based on the population synthesis model by Ueda et al. (2003). It can be seen that the confusion limit of MAXI corresponds to $\approx 5 \times 10^{-12}$ erg cm^{-2} s^{-1} (3–20 keV), i.e., 0.2 mCrab, as an optimistic estimate.

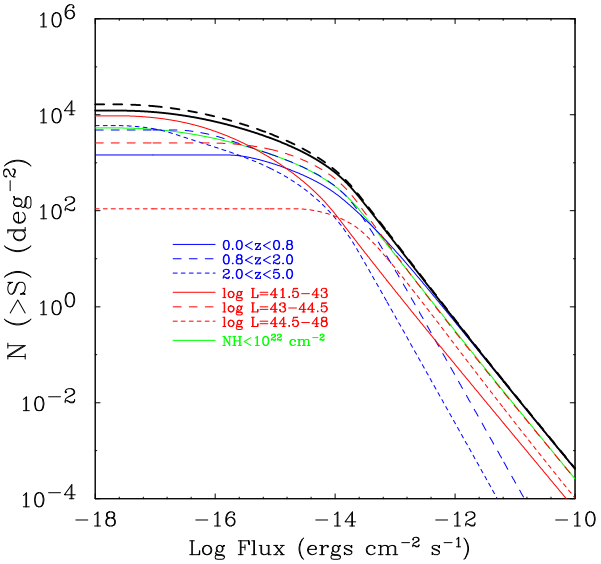

Fig. 1. Expected log N - log S relation of AGNs in the 3–20 keV band from the population synthesis model by Ueda et al. (2003).

To achieve the best sensitivity from the MAXI survey, we develop an analysis method utilizing maximum likelihood fit to a projected image (Hiroi et al. 2009). Using the MAXI simulator developed by Eguchi et al. (2009, this conference), we estimate a realistic sensitivity of ~ 2 mCrab from 1 week operation for a point source with 5σ

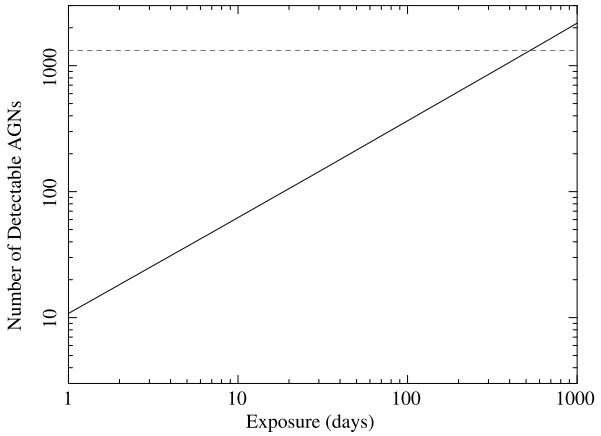

Fig. 2. Total number of AGNs from the MAXI extragalactic survey as a function of exposure (operation time). The horizontal line is the maximum number corresponding to the confusion limit.

detection, and hence ~ 0.2 mCrab (confusion limit) from 1.5 years operation. Figure 2 shows the expected number of detectable AGNs from an area of 30,000 deg^2 at $|b| > 15°$, based on the Ueda et al. (2003) model. We expect about 50, 140, and 1000 sources from an exposure of 1 week, 1 month, and 1 year, respectively.

3. Content of the MAXI Catalog

The MAXI AGN catalog will contain many heavily obscured AGNs with absorption column densities of $N_{\rm H} \sim 10^{23-24}$ cm^{-2} thanks to the large effective area above 5 keV. At the confusion limit, we estimate the number ratio between unabsorbed AGNs ($\log N_{\rm H} < 22$) and absorbed ones ($\log N_{\rm H} > 22$) to be about 800 : 500. The fraction of Compton-thick AGNs with $\log N_{\rm H} > 24$ is expected to be a few percents in the total. This estimate is quite uncertain, however, depending on the $N_{\rm H}$ distribution of AGNs and its evolution.

The variability of AGNs can have significant impacts on the content of the catalog produced every 1.5 years, in particular at fluxes near the sensitivity limit. Also, we may detect many "transient" AGNs that are observable only during their flare phase. For instance, the timescale of "shots" seen in Galactic black holes in the low/hard state (Negoro et al. 1994) will become $\sim 10^6$ sec for a black hole mass of 10^8 M$_\odot$.

4. Summary

We have shown from simulation studies that the fluxes of about 50 AGNs can be determined every week with an accuracy of 20% from the MAXI mission. We will have a new extragalactic catalog of about 1300 AGNs every 1.5 years, which is the largest one as an all-sky survey that covers energies above 2 keV. This catalog will be deeper than the *ROSAT* all sky survey for objects with absorptions of $\log N_{\rm H} \gtrsim 21.5$, and deeper than the *Swift*/BAT survey for $\log N_{\rm H} \lesssim 23.5$. In addition, the catalog will include many transient AGNs. These properties of the catalog will make the scientific outputs of MAXI unique among any other missions.

References

Eguchi, S. et al. 2009, this volume
Hiroi, K., Ueda, Y., Eguchi, S. 2009, this volume
Negoro, H., Miyamoto, S., Kitamoto, S. 1994, ApJ, 423, L127
Piccinotti, G., et al. 1982, ApJ, 253, 485
Ueda, Y., Akiyama, M., Ohta, K., Miyaji, T. 2003, ApJ, 598, 886
Ueda, Y. et al. 2005, ApJS, 161, 185
Watson, M.G. et al. 2009, A&A, 493, 339

MAXI and AGN X-ray Variability

Ian M^{c}Hardy[1]

[1] School of Physics and Astronomy, University of Southampton, University Road, Southampton SO17 1BJ, UK
E-mail(IM): imh@astro.soton.ac.uk

Abstract

The X-ray emission from AGN comes from very close to the central black hole and observations of the way in which that emission varies provide the best diagnostic of the origin of the variations, the structure of the emission region and how it scales with mass and accretion rate. Spectral variations also enable us to study the structure of the gas surrounding the central X-ray source and, by comparing X-ray variations with those seen in other wavebands, eg optical, we can deduce the origin of those other-band variations. In this paper I will briefly highlight some recent relevant observations, mainly from the Rossi X-ray Timing Explorer (RXTE), which are relevant to the above topics and will indicate the areas in which future observations with MAXI will improve our understanding.

Key words: AGN - X-ray variability - MAXI

1. The important questions in AGN X-ray Variability

Ever since the realisation that Active Galactic Nuclei (AGN) were powered by accretion onto supermassive black holes, astronomers have wondered how the emission from those black holes might compare with, or differ from, the emission from the much smaller black holes in Galactic black hole X-ray binary systems (GBHs). GBHs occur in a number of spectral-timing states, particularly the low-flux, hard-spectrum 'hard' state and the high-flux, soft-spectrum 'soft' state. Before we can compare GBHs with AGN, we therefore need to be sure that we are comparing the same thing and so the first question which I will discuss below (Section 2) is whether AGN are found in the same 'states' as GBHs. As one might reasonably assume that variability timescales might scale with the size of the system, ie with black hole mass, the search for characteristic timescales which might occur in both GBHs and AGN has been a major aim (eg M^{c}Hardy 1988,1989). In Section 3 I will therefore review current progress in GBH/AGN timescale comparisons.

Once we have achieved a reasonable measurement and classification of X-ray variability, we are then in a position to try and build physical models to explain the variability. In Section 4 I will review our current understanding of such models. Most of the X-ray observations of AGN have been of relatively radio quiet Seyfert galaxies, whose X-ray emission is not relativistically beamed. However AGN whose emission comes predominantly from a relativistic beam oriented close to the line of sight, ie blazars, are bright X-ray sources which will also be detectable by MAXI. Are the variability patterns of blazars the same as those of non-beamed AGN or does relativistic beaming shorten the observed characteristic timescales? In Section 5 I will review how blazar X-ray variability is related to that of Seyferts and GBHs. In Section 6 I will review our present improved understanding of the relationship between X-ray and optical variability in AGN and in Section 7 I will discuss how observations of X-ray spectral changes can tell us about the gas surrounding the AGN.

2. AGN X-ray States

The PSDs of the GBH Cyg X-1 in both its high/soft and low/hard states are shown in Fig 1. In the soft state the low frequency PSD is described by a powerlaw of slope -1 (ie $P(\nu) \propto \nu^{-\alpha}$ where $\alpha \sim 1$) which steepens above a bend frequency, ν_B (or timescale T_B) to a steeper slope of $\alpha > 2$. In the hard state there is a second bend at low frequencies below which the PSD flattens to $\alpha = 0$. If the S/N is high enough, hard state PSDs can also usually be described as the sum of a number of Lorentzian shaped components, giving a somewhat bumpy appearance, as can be seen in the hard state PSD of Cyg X-1 in Fig 1.

The energy spectra of AGN are more comparable to those of GBHs in the hard than the soft state, which initially led observers to presume that AGN would also be in the hard state. In order to determine AGN PSDs over a sufficiently large frequency range that their state may be determined it is, however, necessary to monitor them for many years. Although attempts were made to

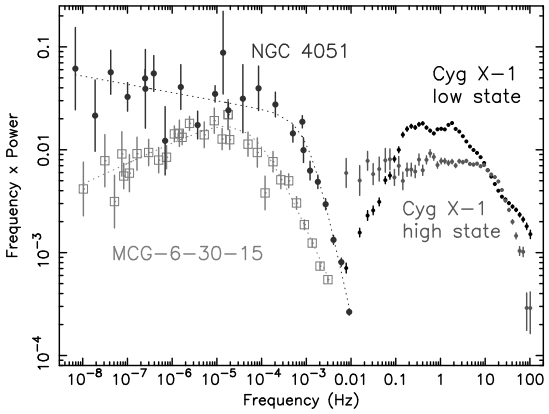

Fig. 1. PSDs of NGC4051 (filled circles) and MCG-6-30-15 (open squares), unfolded from the distortions introduced by the irregular sampling, compared with the PSDs of the GBH Cyg X-1 in both the high/soft and low/hard states. The low frequency part of the PSDs of both NGC4051 and MCG-6-30-15 are determined from observations by *RXTE* and the high frequency parts come from observations by XMM-Newton.

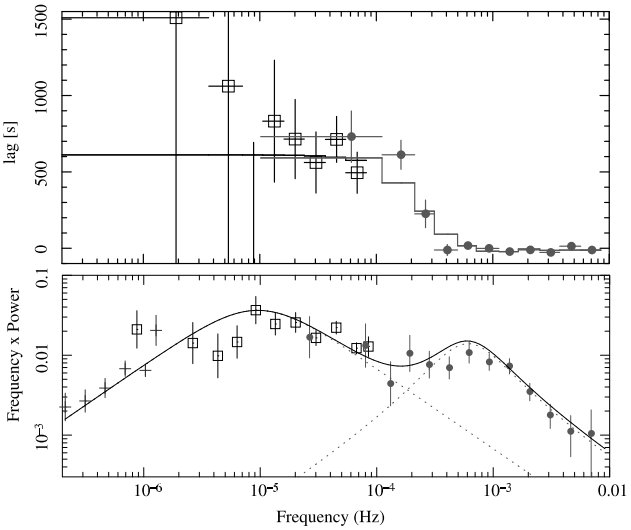

Fig. 2. Top panel: Lag between the hard (2-10 keV) and soft (0.5-2 keV) X-ray bands as a function of Fourier frequency, for Akn564. A positive lag means that the hard band lags the soft. Bottom panel: PSD of Akn564 showing a fit to the two-Lorentzian model (M^{c}Hardy et al 2007). Note how the cross-over frequency between the two Lorentzians corresponds to the frequency at which the lags rapidly change.

determine the long timescale variability of AGN using archival data from a variety of satellites (eg M^{c}Hardy 1988; Papadakis and M^{c}Hardy 1995), and PSD bends were detected, it was not until *RXTE* was launched in 1995 that it was possible to measure PSD shapes with sufficient accuracy to determine AGN states. A number of long timescale AGN monitoring programmes have been carried out with *RXTE* and in Fig 1 I show the PSDs resulting from two of the longest running monitoring campaigns (M^{c}Hardy et al 2004 and 2005). Although the PSDs of NGC4051 and MCG-6-30-15 both extend almost 4 decades below the high frequency bend, and the low frequency bend in Cyg X-1 lies only about 1.5 to 2 decades below the high frequency bend, in neither case is a second bend seen. It is therefore almost certain that both AGN are in the soft state.

We note that the bend MCG-6-30-15 is at a longer timescale than that in NGC4051. As the black hole mass is larger in MCG-6-30-15, these observations are consistent with scaling of bend timescale with black hole mass (discussed in more detail in Section 3). In some other AGN of larger black hole mass there is not sufficient coverage of the PSD below the bend to determine with any confidence whether the AGN is in a soft or hard state. However in only one case, Akn564, is there any detection of a second bend at low frequencies and all other cases are consistent with a soft-state interpretation.

2.1. Akn564: A very high state AGN?

In Fig 2, lower panel, I show the PSD of the very high accretion rate narrow line Seyfert 1 galaxy (NLS1), Akn564 (M^{c}Hardy et al 2007). We can see that the PSD can be described well by the sum of two Lorentzian shaped components. Although this shape describes the PSD of GBHs in the hard state, it actually also describes the PSDs in most cases apart from in the soft state. Thus when the energy spectrum is very soft and the flux is very high (the very high state, or VHS, when the accretion rate is very high), the PSDs of GBHs have a similar form, the only difference being that the peak Lorentzian frequencies are at higher frequencies in the VHS. As Akn564 has an accretion rate which is at approximately at the Eddington limit, we interpret its PSD as being that of a VHS object.

If we Fourier analyse lightcurves into components of different frequencies, we can measure the lag spectrum, ie the lag between different energy bands as a function of Fourier frequency. In the upper panel of Fig 2 we plot the lag spectrum between the hard (2-10 keV) and soft (0.5-2 keV) energy bands for Akn564 from a combination of *ASCA* and *XMM-Newton* observations. We note that the lags are relatively constant (and large) at low frequencies and also constant (but very short) at high frequencies, with a rapid change in lag at about the frequency where we change from one Lorentzian component to another in the PSD (bottom panel). Similar behaviour is seen in GBHs. We interpret the combined lag and PSD spectra as showing that there are two separate regions where the variations are mainly generated. Although *XMM-Newton* can measure lags on timescales shorter than a day, it is hard to measure lags on months or years timescales as the energy range of *RXTE* does not extend below 2 keV. With its extended energy range, MAXI can potentially give us the very valuable long timescale lags.

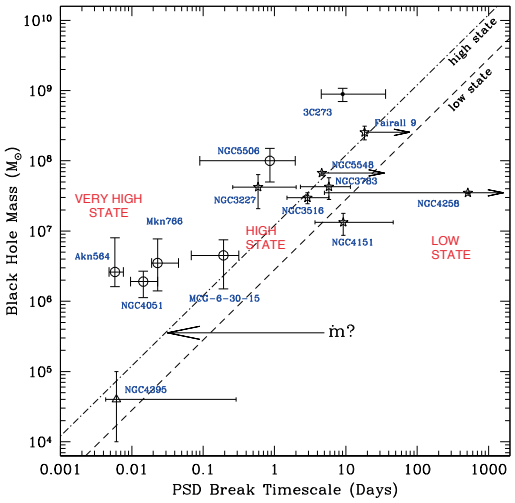

Fig. 3. PSD bend timescales as a function of black hole mass (M^{c}Hardy et al 2004 and 2005). The lines marked 'high state' and 'low state' are just linear extrapolations from typical bend timescales of Cyg X-1 in the high-soft and low-hard states.

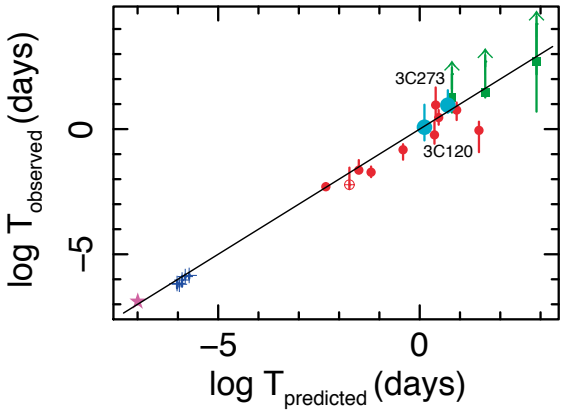

Fig. 4. Log of the observed vs. the predicted PSD bend timescales (in units of days). The star is GRS1915+105 and the crosses are Cyg X-1. The red circles are the AGN which were included in the fit and the three green squares, whose upper bend timescales are unbounded, are AGN which were not included in the fit. We also plot the blazar 3C273 (M^{c}Hardy et al, in preparation, and Section 5 here) and the radio galaxy 3C120.

3. Scaling of Characteristic AGN and Binary Timescales

Scaling of PSD timescales between AGN and GBHs has been carried out in two main areas: scaling of the timescale of the high frequency bend, and scaling of the amplitude of the high frequency part of the PSD at frequencies above the bend. M^{c}Hardy (1988) defined the Normalised Variability Amplitude (NVA) which is the square root of the power in the PSD (in rms units) at a fixed frequency (10^{-4}Hz which is above the Poisson noise level and also above the bend frequency). As black hole mass measurements were very rare at that time, NVA could only be scaled with luminosity as a proxy and it was found to decrease as luminosity increased. Green et al (1993) found a similar result. A refined analysis by Hayashida et al (1998), now with more black hole masses available, found an inverse scaling of high frequency AGN PSD amplitude with black hole mass. Recently Gierlinski et al (2008) have demonstrated a similar correlation in hard state GBHs with possible similarity for AGN. In none of these analyses is any dependence on accretion rate indicated although, in these AGN samples, the range of accretion rates available was not large. Gierlinksi et al suggest that the high frequency part of the PSD in hard state GBHs is limited by the innermost stable orbit, which should depend only on mass. Further work is necessary to determine how the mainly soft-state AGN fit into this pattern. Scaling of the bend timescale, T_B, is more relevant to MAXI as measurement of T_B requires long timescale monitoring, hence we will concentrate on it here. MAXI does not have sufficient sensitivity to define PSD slopes on short timescales (∼day) above the bend.

Early archival observations (M^{c}Hardy 1988; Papadakis and M^{c}Hardy 1995) indicated a probable scaling of black hole mass with T_B but it was not until monitoring began with *RXTE* in 1996 that the long timescale lightcurves necessary to measure T_B became available (eg Edelson and Nandra 1999; Uttley et al 2002; Markowitz et al 2003). A rough scaling of T_B with mass was noted but there was a great deal of scatter. In Fig 3 I show an updated version of the plot originally shown in M^{c}Hardy et al 2004 and 2005. It was noticed that, for a given black hole mass, the highly accreting NLS1s had shorter bend timescales than AGN with lower accretion rates, indicating that T_B scaled approximately inversely with accretion rate. A proper 3D analysis of T_B as a function of black hole mass and accretion rate (in Eddington units), covering both AGN and soft-state GBHs showed that $T_B \propto M/\dot{m}_E$ (M^{c}Hardy et al 2006). A comparison of the observed bend timescales with those predicted by this relationship is shown in Fig 4. We can see that the relationship applies over 10 decades of timescale. Subsequent work by Koerding et al (2007) shows that, with a slight offset, the hard state GBHs and neutron stars also follow the same mass/accretion rate scaling. Thus as far as we can tell, almost all accreting objects behave in the same way.

We have simulated MAXI lightcurves (Fig 5) of typical AGN (5 mCrab) of 3 year duration (with thanks for assistance from Jan Kataoka). If the input PSD model has a slope of -1 at low frequencies and -2 at high frequencies, and a bend at a timescale of 10 days, MAXI has difficulty finding the bend. A single powerlaw PSD of slope -1.3 fits (Fig 6) the simulated PSD as well as one with a bend. However if we force the slope below

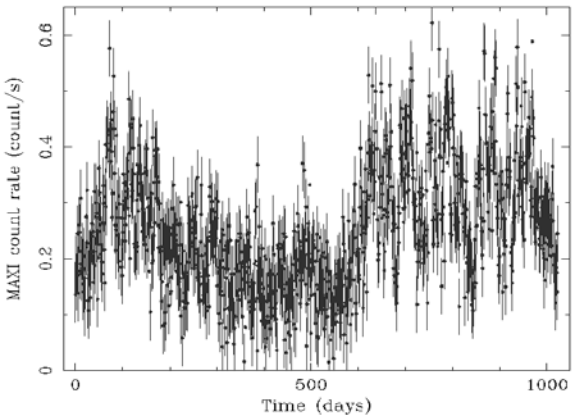

Fig. 5. Simulated MAXI lightcurve for a 5 mCrab source with a PSD of low frequency slope -1, high frequency slope -2 and bend timescale 10 days.

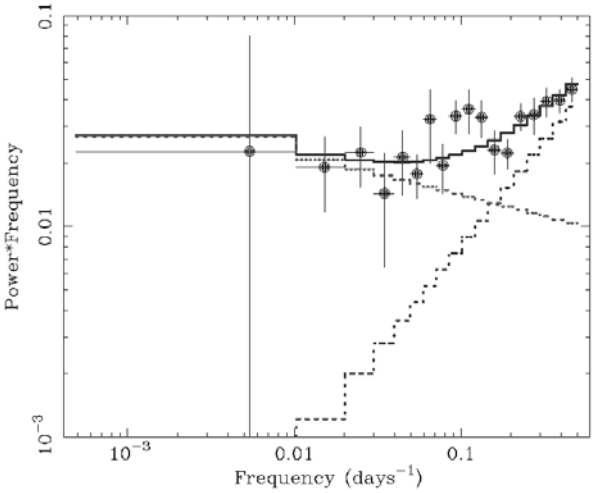

Fig. 6. PSD derived from the lightcurve shown in Fig 5. The best fit single powerlaw, including the Poissonian noise, is shown as a continuous solid line. The dot-dash line shows the PSD with noise removed and the dotted line shows the Poisson noise.

the bend to be -1, which applies in almost all AGN, then MAXI is able to find the bend timescale quite accurately. Also, if we can add in high frequency data from SUZAKU or *XMM-Newton* as we typically do with *RXTE* data, then with MAXI data we can find the bend timescale quite well. However we stress that, to be really useful, the observations must continue for at least 5 years, and probably 10.

4. Origin of the Variations

We have previously found that the rms variability scales linearly with flux in both GBHs (Uttley and M^{c}Hardy 2001) and AGN (eg see Fig 7). Thus variations on short timescales (which determine the rms variability) must be responding to variations on long timescales (which determine the average flux level). A model which produces just this type of variability was proposed by Lyubarskii (1997). He proposed that accretion rate variations are produced in the outer parts of the accretion disc and propagate inwards where they modulate the intrinsic variations being produced by more inner radii. As higher frequency variations will tend to be damped by viscosity, and as the characteristic damping timescale will tend to decrease as we move in towards hotter parts of the accretion disc, the net affect is that the outermost parts of the disc are responsible mostly for the low frequency variations and the inner parts for the higher frequencies. The fact that the variations from the outer parts modulate the variations from the inner parts automatically produces the rms-flux relationship.

Note that the Lyubarskii model produces accretion rate variations, but these variations are not the same as X-ray variations. This basic model has therefore been incorporated into a more general emission model by Churazov et al (2001) and Kotov et al (2001) which has subsequently been quantified by Arevalo and Uttley (2006). In this model the variations propagate inwards and eventually modulate the X-ray emission region. Thus the source of variations and the source of X-ray emission are separated. If the X-ray emission region has a radial temperature, or energy, gradient, with higher energy photons being emitted, preferentially, at smaller radii, then we can explain many of the spectral-timing observations of AGN, such as the lag spectra (eg M^{c}Hardy et al 2007). The lags then represent the time it takes for the variations to propagate from the centroid of the low energy emission to the centroid of the higher energy emission. If the low frequency variations are all produced at larger radii than any of the X-ray emission region then all Fourier frequencies will produce the same lag. But if some of the higher frequency variations are produced within the X-ray emission region, then the location of the effective centroid of the low energy emission region, as seen by the high frequency variation, will move inwards, thus reducing the lag.

5. X-ray Variability of Blazars

The X-ray emission from blazars is almost certainly inverse Compton emission from a relativistic jet oriented towards the observer (eg M^{c}Hardy et al 2007b). Thus the emission mechanism is probably different to that in Seyfert galaxies where thermal Compton scattering from an un-beamed emission region is probably responsible. One might therefore naively expect that any blazar timescales would be subject to relativistic time dilation and hence observed timescales would be shorter than the intrinsic source timescales. We have monitored the X-ray emission from a number of blazars and have begun to derive bend timescales. In Figs 3 and 4 we plot the blazar

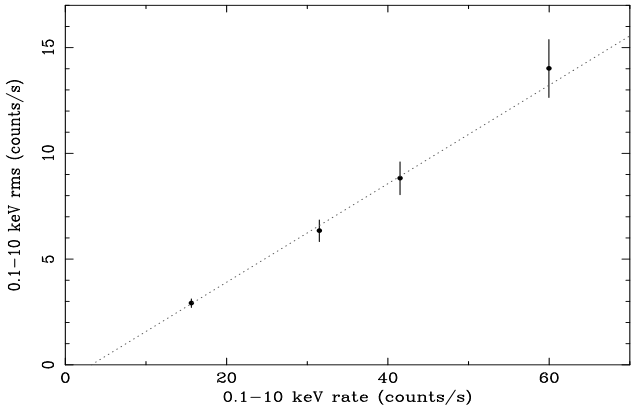

Fig. 7. Rms-flux relationship for the Seyfert galaxy NGC4051 (M^{c}Hardy et al 2004).

3C273 and note that it fits very well with the moderate accretion rate (ie probably soft state) non-beamed Seyfert galaxies, without the need to invoke time dilation. We therefore conclude that the source of the variations (ie not the source of the X-rays) lies outside the jet and simply modulates the jet emission in some non-linear way. If we tap on the jet from outside (ie in the 'laboratory', or observers frame, ignoring the small redshift correction for 3C273) then any observer in the laboratory frame will see modulations at the same tapping frequency. Only if the source of the variations is within the jet will the observed frequency be affected by the relativistic motion of the emitting region.

We have also calculated the rms-flux relation for 3C273 and 3C279. Both blazars display a linear relationship exactly the same as for Seyfert galaxies. This observation provides additional support to the suggestion that the origin of the variations is just the same as in Seyfert galaxies and GBHs, ie accretion rate variations propogating in thro the disc and corona and eventually modulating the jet.

6. Relationship between X-ray and Optical Variability

The origin of optical variations in Seyfert galaxies has, for many years, been at best a mystery and, at worst, a complete muddle. It has often been suggested that optical variability arises from reprocessing of X-ray variation but most early X-ray/optical studies found either weak (Peterson et al 2000) or non-existent (Done et al 1990) X-ray/optical correlations. Only in the case of NGC5548 (Uttley et al 2003) was a strong X-ray/optical correlation found. We therefore began a programme of optical monitoring observations with the Liverpool robotic telescope on La Palma (LT), and with the SMARTS telescopes in Chile (eg Arevalo et al 2008) to parallel our *RXTE* X-ray monitoring, supplemented published observations (eg Sergeev et al 2005) and data from other robotic telescopes (eg MAGNUM - in collaborations with Minezaki and colleagues).

A pattern is now slowly emerging. On short timescales (weeks), we see quite a strong correlation with close to zero lag but on longer timescales (months/years) we often see variations in the optical which have no parallel in the X-rays. An example is shown in Fig 8 from Breedt et al (2008). The short-timescale correlation is almost certainly due to reprocessing of X-ray emission by the accretion disc. Given the likely light-travel time to the reprocessing region, a lag close to zero days is expected and is entirely consistent with the observations. The additional variability seen in the optical band is not yet well constrained by observations but there are two main possibilities - geometry changes or accretion rate changes. The geometry of the X-ray source could be changing slowly, eg the X-ray emitting corona could be expanding or contracting, altering the solid angle subtended at the X-ray source by the reprocessing region. Alternatively, accretion rate changes in the disc could either move radially the reprocessing region, again altering its solid angle at the X-ray source, or accretion rate changes could alter the intrinsic thermal emission from the disc. At present (Breedt et al 2008) all of these possibilities are consistent with the observations. We would expect the long timescale variations in intrinsic emission from the disc to be more important in high accretion rate sources where the disc is more luminous. There are hints that that might be the case but further observations are required for confirmation.

As can be seen from Fig 8, in order to study X-ray/optical variability it is not necessary to monitor on a hourly timescale. Observations every few days are quite sufficient to follow the optical variations. Thus MAXI is very well suited to this programme. However again I note that a two-year period of observations would not be enough to detect any pattern above the random fluctuations which are also seen in the optical and X-ray lightcurves. It is necessary to observe for typically 5, or more, years.

7. X-ray Spectral Variability and Absorption

Monitoring of X-ray spectra can enable us to study the absorbing gas surrounding the AGN. In Fig 9 we see both the X-ray flux and the X-ray photon index of NGC3227 over a 4 year period (from Lamer et al 2003). The photon index was derived assuming a constant Galactic absorbing column. We note that at about MJD-50000 of 1900 there is an extreme apparent hardening of the spectrum with little change of X-ray flux. As the spectrum becomes almost unphysically hard (photon index of zero), a more likely explanation is that it is the absorbing column that is changing. If we fix the photon index and allow the column to change, then we find that the col-

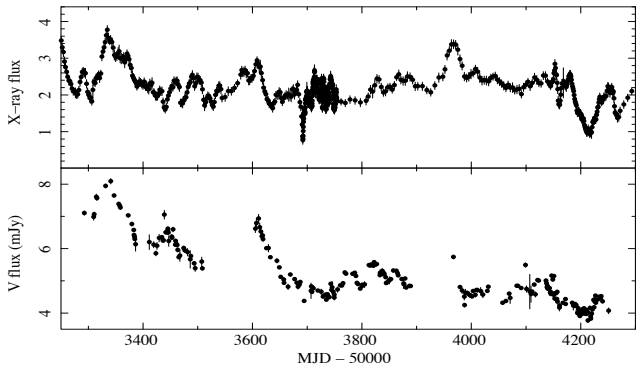

Fig. 8. Top panel: 2-10 keV X-ray flux from *RXTE* for Mkn79. Bottom panel: V-band flux from the Liverpool robotic telescope, MAGNUM and the Crimean observatory (Breedt et al 2008).

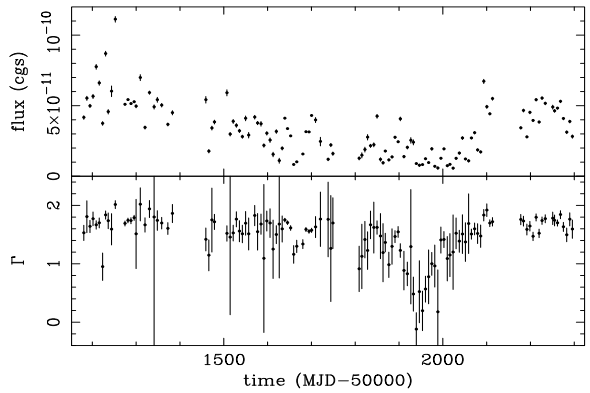

Fig. 9. 2-10 keV X-ray flux (top panel) and X-ray photon index (bottom panel) from *RXTE* for NGC3227, assuming a constant absorbing column (Lamer et al 2003).

umn varies from a very low value up to $\sim 10^{23}$ cm^{-2}, and back again over a period of 100 days, which we interpret as an absorbing cloud passing over the source. As there was also an XMM-Newton observation at the same time which enabled us to determine the ionisation parameter of the absorbing gas and hence determine the distance of the gas cloud from the central X-ray source. We found that it lay at a distance of about 14 light days, at about the inner edge of the broad line region.

With the extended soft spectral range of MAXI compared to *RXTE* it will be possible to detect other large, long timescale, spectral events in many AGN, and to measure the frequency of such events, thereby providing a broad overview of the large scale structure of the gas surrounding the central X-ray source in AGN.

8. Conclusions

Over the last two decades, and particularly since the launch of *RXTE* in 1995, observations of the X-ray variability of AGN have improved our understanding of the inner workings of AGN much more than all of the measurements of single, or few-epoch, multi-band spectral energy distributions have ever done, no matter how many bands they covered. We now know, at least to first order, how emission regions scale with black hole mass and accretion rate over a huge dynamic range. We have a reasonable model for the way in which the variations are produced. We are beginning to understand how optical variations in AGN are produced and we are able to study the gas surrounding the AGN, and its movement, by monitoring its affect on the X-ray spectrum. With MAXI we are going to be able to improve our understanding of most of the above topics, particularly those which require long-timescale observations, ie scaling of PSD bend timescales, relationship between variations in other bands such as the optical and spectral variations caused by movement of surrounding gas across the source. However to be really useful it is important that MAXI continues for a good deal longer than the nominal 2 year lifetime. Most previous advances have required lightcurves of 5 years or more and so I strongly urge that MAXI remains in operation for at least 5 years, and preferably 10.

9. References

Arevalo, P. and Uttley, P., 2006, MNRAS, 367, 801
Arevalo, P. et al, 2008, MNRAS, 388, 211
Breedt, E. et al, 2008, MNRAS (in press)
Churazov, E. et al, 2001, 321, 759
Done, C. et al 1990, MNRAS, 243, 713
Edelson, R. and Nandra, K, 1996, ApJ, 514, 682
Gierlinski, M. et al 2008, MNRAS, 383, 741
Green, A. et al 1993, MNRAS, 265, 664
Hayashida, K., et al, 1998, ApJ, 500, 642
Koerding, E. et al 2007, MNRAS, 380, 301
Kotov, O. et a, 2001, MNRAS, 327, 799
Lamer, G. et al 2003, MNRAS, 342, L41
Lyubarskii, Y., et al 1997, MNRAS, 292, 679
Markowitz, A. et al 2003, ApJ, 593, 96
M^{c}Hardy I.M., 1988, Mem. del Soc. Ast. Ital, 59, 239.
M^{c}Hardy I.M., 1989, ESA-SP, 296, 1111
M^{c}Hardy I.M., et al, 2004, MNRAS, 348, 783
M^{c}Hardy I.M., et al, 2005, MNRAS, 359, 1469
M^{c}Hardy I.M., et al, 2006, Nature, 444, 730
M^{c}Hardy I.M., et al, 2007, MNRAS, 382, 985
M^{c}Hardy I.M., et al, 2007b, MNRAS, 375, 1521
Papadakis, I. & M^{c}Hardy I.M., 1995, MNRAS, 273, 923
Peterson, B. et al 2000, ApJ, 542, 161
Sergeev, S., et al, 2005, ApJ, 622, 129
Uttley, P. and M^{c}Hardy I.M., 2001, MNRAS,
Uttley, P. et al, 2002, MNRAS, 332, 231
Uttley, P. et al, 2003, ApJL, 584, L53

Relation between X-ray Black Hole Mass and X-ray Variability

– Expectation for MAXI –

Kiyoshi Hayashida[1]

[1] Department of Earth and Space Science, Osaka University, 1-1 Machikaneyama, Toyonaka, Osaka 560-0043, Japan
E-mail(KH): hayasida@ess.sci.osaka-u.ac.jp

ABSTRACT

X-ray variability of AGNs has been employed to constrain the size of the emission region as well as the mechanism of the emission. We propose an empirical method to estimate the black hole (BH) masses in AGNs from their X-ray variability and apply the method to various classes of AGNs, broad line Seyfert 1 galaxies (BLS1s), narrow line Seyfert 1 galaxies (NLS1s), and low luminosity AGNs (LLAGN). Stability of the power spectrum density is examined, and alternative definitions of the variability time scales are compared. Comparison with independent BH mass estimation indicates X-ray variability provides order of magnitude estimation for the BH mass scale, though deviation is evident in some cases. Further studies with various AGNs at various flux states reveal how the X-ray variability is affected by other parameters than BH mass, e.g., accretion rate or class of AGNs. We expect for long term observations with MAXI to provide clue to such an issue.

KEY WORDS: active—galaxies: nuclei—X-rays: galaxies: variability: black hole

1. Black Hole Mass Estimation from X-ray Variability

Variability of radiation from AGNs has been used to estimate the size of their emission region. The size estimated in such a way, together with a huge amount of the radiation, is considered to be one of the observational proof of the existence of super-massive black holes (SMBHs) in AGNs. X-ray variability is especially important and efficient to estimate the size of the BHs, because it usually has a shorter time scale than that in the longer wavelength. In fact, Barr and Mushotzky (1986) indicated that the time scale of the X-ray variability of AGNs, for which they employed the shortest doubling time, has a positive correlation with their X-ray luminosities. The upper limits of BH masses were provided by Wandel and Mushotzky (1986) from the same data.

We have proposed a new and empirical method to estimate the black hole masses in AGNs from their X-ray variability (Hayashida et al. 1998). Key assumptions of the method are 1) X-ray variability of BHs, from stellar BHs to AGN, are similar each other, 2) the variability time scales are linearly proportional to the central BH masses, and 3) Cyg X-1 BH mass is 10 $M_{\odot}$. We employ the normalized power spectrum density (NPSD) of X-ray light curve to define a variability time scale, where the NPSD is the power spectrum density normalized by the average intensity squared. If the X-ray variability is similar for different size of BHs, their NPSDs should align along the 1/frequency line, as we shown in Hayashida et al. (1998) by a simple arithmetic. In other word, if we make NPSD $\times$ frequency of those sources, they should stand side by side in the diagram. Their positions in the NPSD $\times$ f diagram reflect the relative system size of those BHs. These procedures are illustrated in Fig. 1.

We first applied the method to several Seyferts observed with the Ginga satellite (Hayashida et al. 1998). We have expanded the work to various classes of AGNs observed with the ASCA satellite, and we compared the estimated BH masses with those by other methods. We introduce those works in this paper. In addition, we also propose possible targets of future all sky X-ray monitor experiments, such as MAXI. Note that some of the plots are cited from Hayashida et al. (2003).

2. Black Hole Mass and X-ray Variability for Various Classes of AGNs

2.1. Narrow Line Seyfert 1 and Broad Line Seyfert 1

Narrow Line Seyfert 1 (NLS1) galaxies are known to show a rapid and large amplitude X-ray variability. We quantified the X-ray variabilities of NLS1s by their NPSDs and estimated their BH masses. Fig. 2 cited from Hayashida (2000) illustrate systematic trends that the NLS1s have lower mass black hole than BLS1s; the BH masses in NLS1s range from $10^5 - 10^7$ $M_{\odot}$, while those in BLS1s $10^7 - 10^8$ $M_{\odot}$ according to our estimations. We think this is the most important factor which distinguish these two classes of Seyfert.

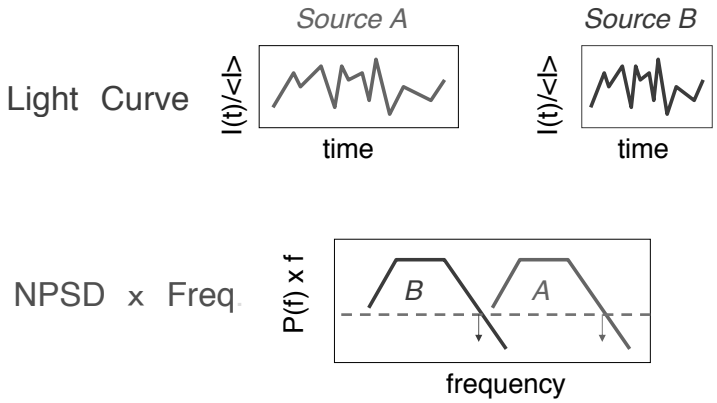

Fig. 1. Schematic Diagram of Scaling Relation of Variability. We consider there are two sources of which sizes are different by some factor. The assumption we made is that their X-ray light curves normalized by their average intensity is self similar expect for the scale of the time axis (top panels), and the time scale is linearly proportional to the BH size or mass. The corresponding NPSDs align in the NPSD×Frequency diagram side by side. The position of the two NPSD are differ by the ratio of their system size (BH mass). We measure the position from the corssing point of the NPSD and the horizontal bar (in our case we set fP(f)=1/1000). See Hayashida et al. (1998, 2003)on detailed description.

Another remarkable point of the NLS1s is their enhanced soft X-ray component, usually approximated with a blackbody of temperature of 0.1-0.2keV. If we regards the component as a thermal emission from an accretion disk, it constrains the BH mass and accretion rate of the source. Such discussions are found in, e.g., Hayashida (2000) and Mineshige et al (1999).

2.2. Low Luminosity AGNs and Seyfert 2

It is known that there is a class of AGNs of which luminosities are significantly lower than typical Seyferts or quasars. We investigated the X-ray variabilities of such low luminosity AGNs (LLAGN), including LINERs, observed with ASCA (Awaki et al., 2001). Although they usually show a small amplitude X-ray variability, we obtained at least the lower limit of the BH mass from them. The results indicate those LLAGNs contain BHs 10^6 or larger, and they emit at extremely low efficiency, less than 1% of the Eddington luminosity (see Fig.3, which is cited from Awaki et al. (2001)). Long term X-ray variability of the LLAGN, M81, were investigated by Ishisaki et al. (1996) and Iyomoto et al. (2001) . Iyomoto et al. (2001) employed a structure function in order to quantify the X-ray variability from highly gaped data.

On the other hands, we found a contrasting case in NGC4395, which is known as the least luminous Seyfert. Regardless of its low luminosity (Lx$\sim$ 10^{39} erg/s) the optical-UV spectrum of NGC4395 is similar to that in a Seyfert type. We found rapid X-ray variability in the source, leading to the mass estimation of the BH of $10^4 - 10^5$ $M_\odot$ (Iwasawa et al., 2000).

Examination of the unification model of the type 1 and 2 AGNs is one of the most important issues in AGN study. If the unification scheme holds, the distributions of the BH masses should be identical for the two types of AGNs. Awaki et al. (2006) examined that issue in terms of RMS fractional variability.

2.3. Blazars

X-ray variabilities of blazars were systematically studied by Kataoka et al. (2001). It is found that the shape of the power spectrum densities of blazars is systematically different from that of Seyferts. Power law index of the PSD for blazars ranges from 2 to 3, while that for Seyferts 1 to 2. It may reflect their difference in the emission mechanism from radio quiet AGNs. Application of the scaling relation between stellar black hole candidates and Seyferts, which we assumed, may not be appropriate for the blazars. Instead, physical interpretation of the knee frequency of the power spectrum and size estimation from it are presented in Kataoka et al. (2001).

3. Calibration of BH mass estimation from X-ray Variability

3.1. Stability and canonicality of the normalized power spectrum density

Stability of the NPSD (at high frequency part) of stellar mass BHs was one of the motivation of our using it as a BH scale measure. We now have some data to check the stability of the NPSD of AGNs. We confirm that the NPSD was stable within factor of two for MCG-6-30-15 observed several times with Ginga and ASCA. In the case of 1H0707-495, the NPSD was unchanged regardless of a flux drop of factor of 6 from 1995 to 1998 (see Fig.4). On the contrary, we found inconsistency of nearly one order of magnitude in the NPSD of NGC5548, which might be due to a short data length compared with the variability time scale.

3.2. Various Definitions of the Variability Time Scales

X-ray variability of the AGN can be characterized by various measures. Break frequency of the X-ray power spectrum density (PSD) is one of them, which has been

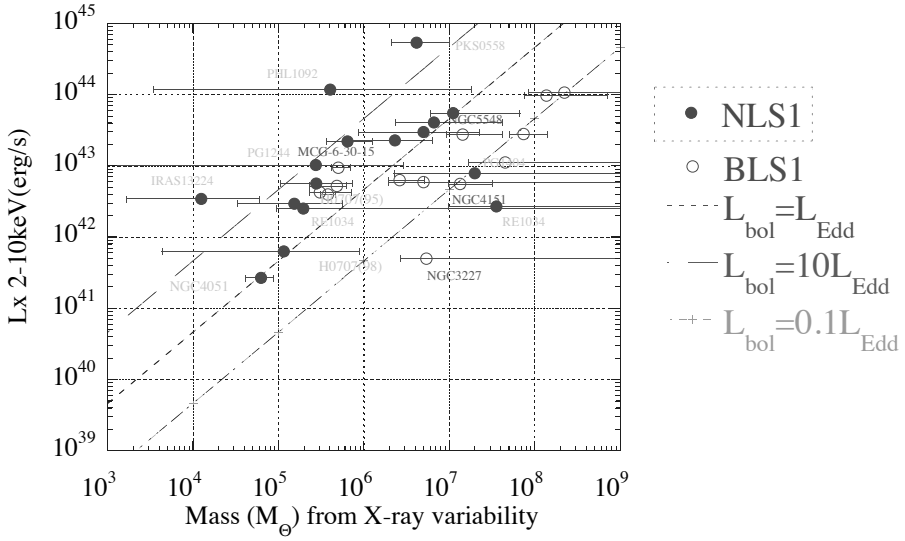

Fig. 2. BH masses Estimated from X-ray Variability. The figure is cited from Hayashida (2000). Closed circles indicate NLS1s, while open circles do BLS1s. Dotted, dashed, dotted-dashed lines indicate 1,10, 0.1 times of the Eddington luminosity, respectively, where bolometric correction of 27.2 is assumed. Cited from Hayashida et al. (2003).

employed by authors. One of the reason why we used the time scale $fP(f) = 1e-3$ (Fig.1) not the break frequency was that the break frequency had been obtained only for a few AGNs. Nevertheless, extensive long term observations of AGNs with RXTE have been providing the PSD break frequencies for more than 10 sources (e.g., Markowitz et al. 2003, Uttley & McHardy 2005). Note that there are two breaks in the PSD of stellar BHs in their hard state, one from f^0 to f^{-1} and the other from f^{-1} to f^{-2}. The break frequency employed in the X-ray variability studies of AGNs corresponds to the latter one.

If the X-ray variability scales to the BH mass, as we assumed, the time scale corresponding to the break frequency should be proportional to that of $fP(f) = 1e-3$. We compare the two scales in Fig.5, showing rough proportionality among them McHardy et al. (2006) indicated that the break frequency gives physical scale (or BH masses) more accurately by considering the accretion rate (or luminosity) as the second parameter. Deviation from the proportionality shown in Fig.5 might be resolved by considering such dependence. Examination of the accretion rate dependence may be one of the important task for the MAXI mission.

On the other hand, fractional rms variability is simply an integration of the NPSD, and can be used as a conventional measure of the X-ray variability. When we establish the NPSD scaling relation, we can reduce it to the scaling relation in the rms variability. In this case, one have to be care about the time bin size to calculate the rms variability.

3.3. Various ways to estimate BH Masses

BH masses in AGNs has been dynamically evaluated from the line width from the broad line region (BLR) either by applying the photo-ionization model or by performing the reverberation mapping. The latter is considered to be more reliable. In Fig. 6, we compare the BH masses from the BLR reverberation mapping summarized in Wandel, Peterson, and Malkan (1999) with those from the X-ray variability for the AGNs both estimates are presented. It is found that the both methods agree within about one order of magnitude. Since Wandel et al. (1999) estimated the systematic error of their BH mass estimation is a factor of a few, the systematic error of our method is at most one order of magnitude.

Recent studies emplying the PSD break frequency with accretion rate (luminosity) dependence taken into account (McHardy et al. 2006) gives tighter relation. This assures that the X-ray variability gives BH mass scales, and implies that the BH accretion physics is very similar for various scales of BHs.

Dynamical masses of BHs in galactic, not only active but also normal, nuclei are estimated by observing the stellar kinematics or gas motion. One of the most accurate estimation was given for NGC4258 as 3.6×10^7 $M_\odot$

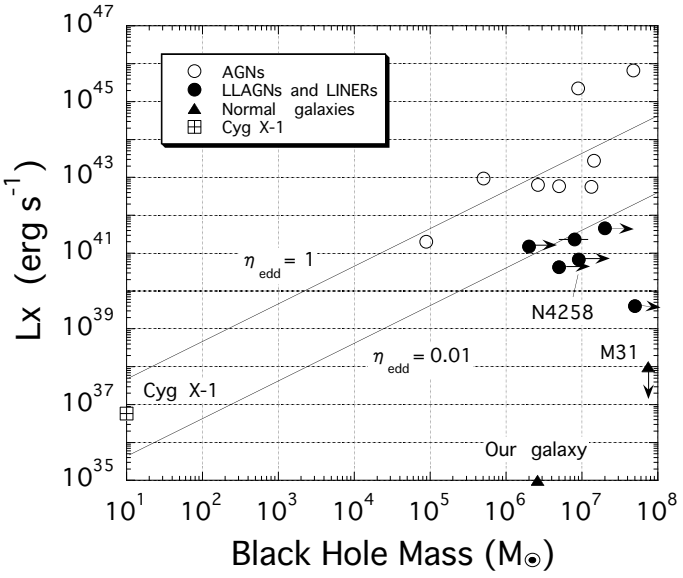

Fig. 3. The Lower limit of the BH Masses in LLAGNs Estimated from X-ray Variability. The lower limit of the BH masses are larger than 10^6 $M_\odot$, indicating those LLAGNs have super massive black hole as large as Seyferts and quasars but emit much lower power than those typical AGNs. The figure is cited from Awaki et al. (2001).

through maser line mapping (Miyoshi et al., 1995), which is now considered to be the most striking evidence for the existence of a SMBH. Observations of stellar kinematics through optical imaging spectroscopy also provide the BH masses in nearby galaxies. The number of such observations have rapidly increased these years, revealing most of them have SMBH at their nuclei. Large number of BH masses also lead to the finding of a interesting correlation between the BH mass and the velocity dispersion of galactic bulge (e.g., Gebhardt et al., 2000, Ferrarese et al., 2000). The correlation is so tight that it will be used to estimate the BH masses from the velocity dispersion of bulge.

There are many ways to estimate the masses of SMBHs in galactic nuclei. Each method has merits and demerits, and its application range is different. It is now important to compare the results each other in order to check their validity. In the future, when the number of SMBHs of which dynamical mass are accurately measured is large enough, empirical methods (BH mass estimation from the X-ray variability or that from bulge velocity dispersion) will be less important. Nevertheless, the study on the X-ray variability or those on BH mass bulge velocity dispersion will still be important to examine the BH accretion physics or the formation of SMBHs in galaxies in turn.

4. Targets of MAXI mission

One of the distinctive features of the MAXI mission is its high sensitivity or low detection limit. It will enable us to obtain daily X-ray fluxes for tens of AGNs. If we adopt the scaling hypothesis on the X-ray variability of AGNs such as we made, the longer time scale variability will extend out work to larger mass AGNs, namely, quasars. X-ray variability data for quasars with time scales longer than days is also important in the sense that there is a possibility to observe a possible break in their power spectrum. For a 10^6 $M_\odot$ BH, the light crossing time for 10 Schwarzshild radius (Rs) is 100s, while that for 10^9 $M_\odot$ BH is 10^5 s, longer than 1 day. The X-ray light curves of quasars obtained with the MAXI mission will first enable us to examine significant reduction of the power corresponding to such a scale.

We also need to check the deviation from simple scaling relation on the BH mass and X-ray variability. As shown by McHardy et al. (2006), the deviation might be explained by accretion rate as the second parameter. If that is the case, examination of the X-ray variability of a single object at different flux state will be a clue to that issue.

We assumed the X-ray variability of AGNs is aperiodic. In fact, there have been only a few reports on the possible detection of the periodicity in AGNs; IRAS18325-5926 (Iwasawa et al., 1998), and Mrk766 (Boller et al., 2001). Nevertheless, the observation span might have been too short for the periodicity to be detected. Whatever the origin of the periodicity is, the time scale must directly tell us the size of some physical processes in the AGNs. We will expect systematic search for the periodicity in X-rays from AGNs with the MAXI

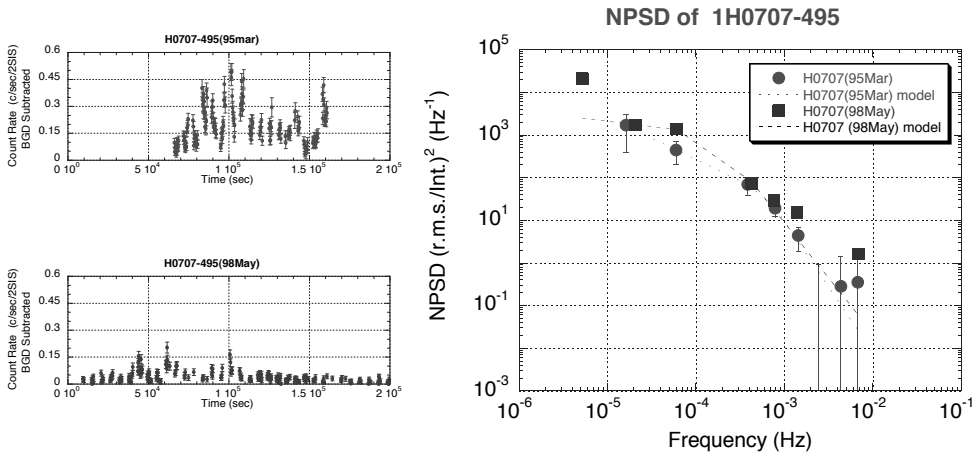

Fig. 4. X-ray Light Curves and NPSDs of 1H0707-495 Observed with ASCA both in 1995 and 1998. The X-ray flux decreased by factor of 6, while the NPSD was almost unchanged. Cited from Hayashida et al. (2003).

mission.

Finally, we would point out another point of long term unbiased X-ray monitoring of AGNs. Most of the AGNs currently observed with X-ray missions are selected from the sample observed in the previous missions or all sky surveys. As mentioned in Horikawa et al. (2003), some of the AGNs, in particular NLS1s, show X-ray variability over one order of magnitude. The number of AGNs of which X-ray flux was observed to decrease by more than one order of magnitude is larger than that of the increasing case. We might have missed to catch AGNs of which X-ray flux increased suddenly, namely bursting phase of the AGN phenomena.

References

Awaki, H., Sakano, M., Terashima, Y. and Hayashida, K. 2001, PASJ, 53, 647

Awaki, H., Murakami, H., Ogawa, Y., Leighly, K., 2006, ApJ, 645, 928

Barr, P., Mushotzky, R.F., 1986, Nature, 320, 421

Boller, Th., Keil, R., Trumper, J., O'Brien, P. T., Reeves, J., Page, M., 2001, A&A, 365, L146

Ferrarese, L., Merritt, D., 2000, ApJ, 539, L9

Gebhardt, K., Bender, R. Bower, G., Dressler, A., Faber, S., Filippenko, A., Green, R., Grillmar, C., Ho, L., Kormendy, J., Iauer, R., Magorrian, J., Pinkney, J., Richston, D., Tremain, S., ApJ, 2000, 539, L13

Hayashida, K., Miyamoto, S., Kitamoto, S., Negoro, H., Inoue, H. 1998, ApJ, 500, 642

Hayashida, K. 2000, New Astron. Reviews, 44, 419

Hayashida, K., Horikawa, T., R. Fujita, H. Awaki, 2003, MAXI Workshop on AGN Variability, 153

Horikawa, T., Hayashida, K., Katayama, H., 2003, MAXI Workshop on AGN Variability, 143

Ishisaki, Y., Makishima, K., Iyomoto, K., Hayashida, K., Inoue, H., Mitsuda, K., Tanaka, Y., Uno, S., Kohmura, Y., Mushotzky, R.F., Petre, R., Selemitsos, P.J., Terashima, Y., 1996, MNRAS, 48, 237

McHardy, I.M., Koerding, E., Knigge, C., Uttley, P., Fender, R.P., Nature, 2006, 444, 730

Mineshige, S., Kawaguchi, T., Takeuchi, M., Hayashida, K., 2000, PASJ, 52, 499

Miyoshi, M., Moran, J., Herrnstein, J., Greenhill, L., Nakai, N., Diamond, P., Inoue, M., 1995, Nature, 373, 127

Iwasawa, K., Fabian, A. C., Brandt, W. N., Kunieda, H., Misaki, K., Terashima, Y., Reynolds, C. S., 1998, MNRAS, 295, L20

Iwasawa, K., Fabian, A. C., Almaini, O., Lira, P., Lawrence, A., Hayashida, K., Inoue, H., 2000, MNRAS, 318, 879

Iyomoto, N., Makishima, K., 2001, MNRAS, 321, 767

Kataoka, J., Takahashi, T., Wagner, S.J., Iyomoto, N., Edwards, P.G., Hayashida, K., Inoue, S., Madejski, G.M., Takahara, F., Tanihata, C., Kawai, N., 2001, ApJ, 560, 659

Sunyaev, R. and Revnivtsev, M. 2000, A&A, 358, 617

Uttley, P. and McHardy, I.M., 2005, MNRAS, 363, 586

Vaughan, S., Iwasawa, K., Fabian, A. C., Hayashida, K., 2005, MNRAS, 356, 524

Wandel, A., Mushotzky, R.F., 1986, ApJ, 306, L61

Wandel, A., Peterson, B., and Malkan, M.A., 1999, ApJ, 526, 57

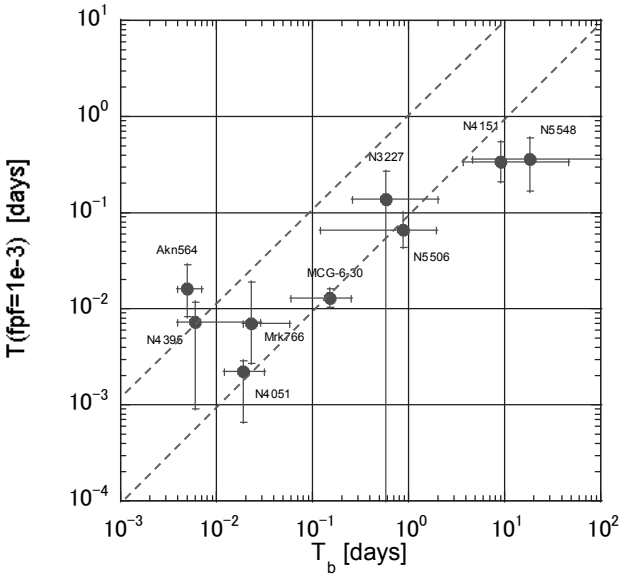

Fig. 5. Comparison of two variability time scales for 9 AGNs. The horizontala axis show the PSD break time scale taken from the compilation by Uttley & McHardy 2005, whereas the vertical axis show our variability time scale based on the $fP(f) = 1e-3$ condition (Hayashida et al. 1998, 2000). The two time scale show rough proportionality, though deviation within one order of magnitude is visible.

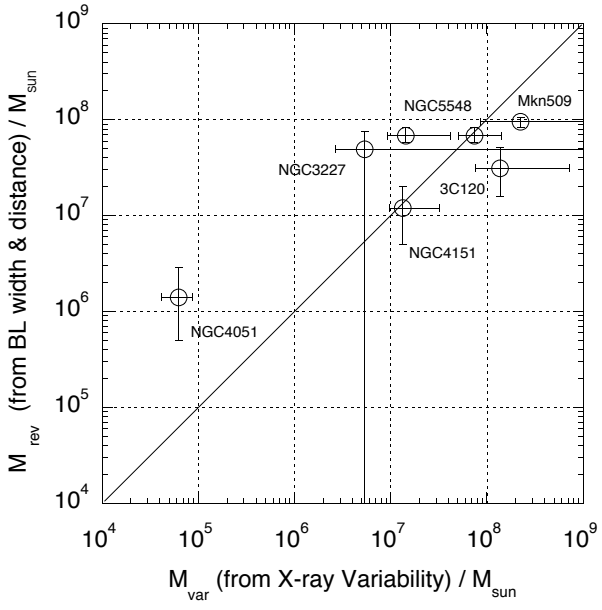

Fig. 6. BH Masses from Reverberation Mapping vs those from X-ray Variability. The masses are in the solar mass unit. The data of reverberation mapping are from Wandel et al. (1999). Agreement within about one order of magnitude indicates the systematic error of BH mass estimation from X-ray variability. Cited from Hayashida et al. (2003)

MAXI and GLAST studies of Jets in Active Galaxies

Greg Madejski[1], Jun Kataoka[2], and Marek Sikora[3]

[1] KIPAC and SLAC, Stanford University, Stanford, CA 94305
[2] Tokyo Institute of Technology, 2-12-1, Ohokayama, Tokyo, Japan
[3] Copernicus Astronomical Center, Warsaw, Poland
E-mail(GM): madejski@slac.stanford.edu

Abstract

The recent launch of GLAST - coinciding with the MAXI workshop - opens a new era for studies of jet-dominated active galaxies, known as blazars. While the emission processes operating in various spectral bands in blazars are reasonably well understood, the knowledge of the details of the structure of the jet, location of the dissipation region with respect to the accreting black hole, and coupling of the jet to the accretion process are known only at a rudimentary level. Blazars are variable, and this provides an opportunity to use the variability in various bands - and in particular, the relationship of respective time series to each other - to explore the relative location of regions responsible for emission in the respective bands. Observationally, this requires well-sampled time series in as many spectral bands as possible. To this end, with its all-sky, sensitive monitoring capability, the recently launched GLAST, and MAXI, to be deployed in 2009, are the most promising instruments bound to provide good sampling in respectively the energetic gamma-ray, and the soft X-ray band. This paper highlights the inferences regarding blazar jets that can be gleaned from such joint observations.

Key words: galaxies: active – X-rays: galaxies – galaxies: quasars

1. Introduction: MAXI and active galaxies

The MAXI All-sky monitor, planned to be deployed on the International Space Station in 2009, will be the pre-eminent facility to monitor the entire sky in the soft X-ray band. The most important extragalactic targets for MAXI will be active galactic nuclei, often strongly variable in the X-ray band. There, the well-sampled time series for many objects - and the resulting Power Density Spectra - are bound to significantly advance our understanding of the central engines of AGN. In particular, those are likely to provide an independent estimate of the masses and mass function of the central black holes, which can be otherwise difficult to obtain via other means, especially for objects at a considerable redshift.

Besides measuring the properties of the time series themselves, the MAXI data will be tremendously useful for cross-correlation of the well-sampled time series against those measured in other bands. One class of AGN where such measurements will be particularly valuable are those active galaxies where the dominant portion of the observed radiation is produced in a relativistic jet pointing close to our line of sight. Such objects are known as blazars, and those are the objects where the MAXI - GLAST[1] synergy will be most apparent. They generally are characterized by broad-band spectra often extending to the highest observable regimes such as the GeV or even TeV band, coupled with large amplitude, chaotic variability seen in all bands; strong polarization in the radio, optical, and IR; and the presence of strong radio emission arising from extremely compact ($\sim$ milliarcsec) and often physically variable structures imaged with the Very Long Baseline Interferometry (VLBI), often associated with the so-called apparent superluminal expansion. It is in fact the flux measured in the GeV or TeV band that often dominates the overall energetics. Clearly, time-resolved gamma-ray observations, combined with monitoring in other bands, are important for detailed studies of blazars, with the goal of understanding the emission mechanisms, leading in turn to determination of the content of radiating particles, then the structure of the jet (the energy dissipation mechanism) and ultimately its connection to the central engine, presumably powering the blazar phenomenon via accretion onto the supermassive black hole.

*[1] At the time of preparation of this manuscript, GLAST - or Gamma-ray Large Area Telescope - was renamed to be the Fermi Gamma-ray Space Telescope. Since the conference took place prior to renaming, for consistency, this paper will use the name "GLAST" throughout.

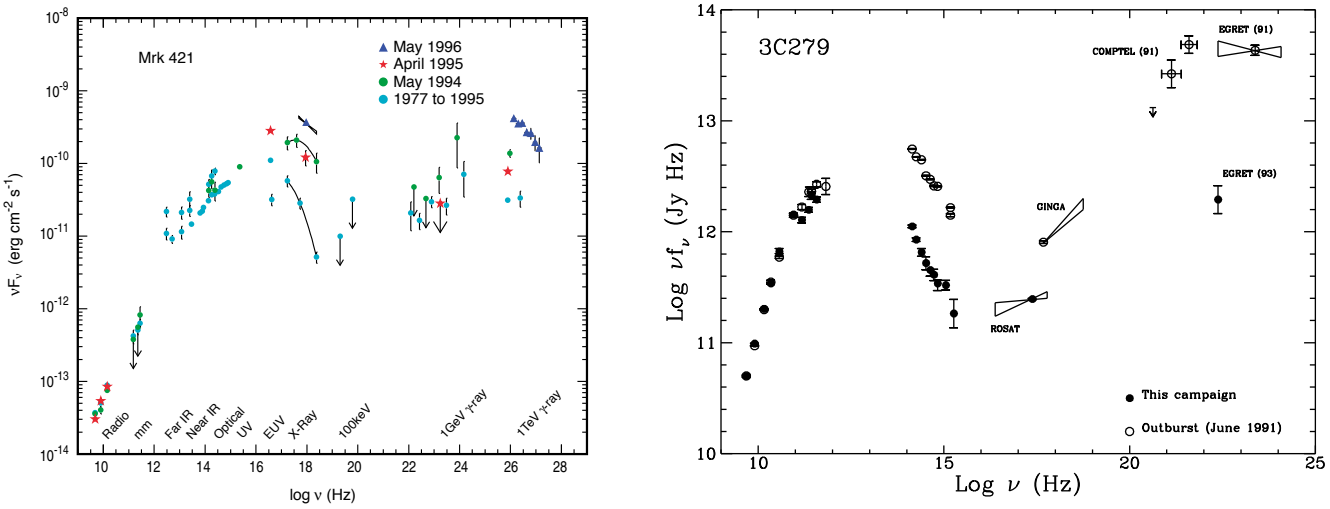

Fig. 1. Examples of broad-band spectra of two blazars. Left panel illustrates the broad band spectrum and variability range in various bands of Mkn 421, the first blazar detected unambiguously in the TeV band (Macomb et al. 1995). Right panel illustrates broad-band spectrum of 3C279, a blazar associated with quasar at $z = 0.524$, detected as a bright gamma-ray source with EGRET (Kniffen et al. 1993). The data are from separate multi-band campaigns, reported in Maraschi et al. (1994) and Wehrle et al. (1998)

2. Gamma-ray Large Area Telescope and MAXI as the key tools for studies of blazars

GLAST's main instrument, the Large Area Telescope, or LAT, relies on the conversion of gamma-rays into electron-positron pairs; tracking of those pairs allows the determination of the direction of the incident gamma-ray. Such a design results in a wide solid angle of the sky, ~ 2 steradians, simultaneously available to the detector. During the normal operation, GLAST points away from the Earth, and slight rocking of the axis of the spacecraft allows monitoring of the entire sky on time scales shorter than a day-long or even shorter, since the whole sky is surveyed in ~ 3 hours. GLAST's bandpass covers ~ 20 MeV to ~ 300 GeV, featuring a peak effective area (at ~ 1 GeV) of $\sim 10,000$ cm^2. The point spread function of the instrument (corresponding to 68% containment) is about 0.5° at 1 GeV, and the energy resolution is about 10% (the details of the instrument are given in Atwood et al. 2008). Those parameters are significantly better than the LAT's predecessor, the EGRET instrument onboard of the Compton Gamma-ray Observatory, allowing studies for many more blazars at shorter time scales than previously possible.

3. Diversity of blazar emission processes in the X-ray band

Why is then the X-ray band important for understanding of blazars? Bulk of the emission arises in the Doppler-boosted relativistic jet; in a sub-class of blazars showing quasar-like properties, a (generally) small fraction of the optical and UV light is also detected to be emitted nearly isotropically, in the accretion disk, and often reprocessed in the broad emission line region. The Lorentz factors of the jets $\Gamma_{\rm jet}$ are measured via superluminal expansion, and are roughly ~ 10 (Jorstad et al. 2001). The broad-band spectra (plotted in the log $(E \times F(E))$ vs. $\log(E)$ form) of two representative objects studied extensively, 3C279, and Mkn 421, are shown in Figure 1. Very broadly, the emission consists of two peaks, one with a maximum between the far IR and soft X-ray band, and another in the gamma-ray band. Since the low energy peak often shows considerable polarization (measured so far in the radio, IR and optical bands), it is generally agreed upon that the dominant emission mechanism responsible for radiation in the low-energy peak is the synchrotron process of ultra-relativistic electrons accelerated in magnetic field. Most modeling suggests that the Lorentz factors of electrons $\gamma_{\rm el}$ radiating near the peak are around $10^3 - 10^4$ for the (generally higher luminosity) blazars associated with quasars (such as 3C279 in Fig. 1), and $10^5 - 10^6$ for line-devoid, generally lower luminosity objects (such as Mkn 421 in Fig. 1), which are often sources of TeV gamma-ray emission. The high energy peak, on the other hand, is generally attributed to Compton scattering by the same population of electrons that produce the low energy peak, with target photons being the ambient, external, diffuse (quasi-isotropic) radiation field in the former class, and the synchrotron radiation internal to the jet in the latter class. Probably the most compelling reason for the difference between the two classes is the mass accretion rate (in Eddington units). In the latter class, the accretion corresponding to a low $L/L_{\rm Edd}$ forms a "hot" flow, where the density of the accreting material is never sufficiently high to allow

efficient cooling and formation of a "standard, " "cold" - and thus luminous accretion disk, and therefore the energy is advected to the black hole with the falling matter. In the former class, $L/L_{\rm Edd}$ might be higher, allowing for a "cold" (roughly $10,000 - 30,000$ Kelvin), luminous disk to form - and thus we detect the quasi-isotropic signatures of accretion such as the emission lines, and sometimes even the "blue bump."

As is apparent from Figure 1, the minimum between the two peaks is located in the X-ray band. In the former sub-class (as in 3C279), the optical / UV spectrum, being generally quite steep (soft), is presumably the "tail" of the synchrotron component, while the X-ray emission - generally showing relatively hard spectra, with energy indices $\alpha_{\rm X} < 1$ - suggests an association with the onset of the Compton component. There, at least in the context of the models considered above, the X-ray emission is due to the *low energy end* of the electron energy distribution. Since the observed X-ray spectra are not measured to be harder than $\alpha_{\rm X} < 0$ - this suggests that the X-ray band probes the "most populous" part of the electron population, where the electron number density is the greatest. With this, in the blazars associated with quasars, the *X-ray spectral measurements are crucial in determining the total content of the radiating particles in the jet*. As an aside, in principle, such a measurement could be performed in the low-frequency radio regime, since the low-frequency radio and X-ray bands both mirror the low energy electron population. There, however, the synchrotron self-absorption makes the lowest energy portion of the jet inaccessible, and since the inner jet is thus optically thick, the radio observations can penetrate only down to a "photosphere" and thus probe considerably more extended spatial region.

The situation in the latter class of blazars - such as Mkn 421 - is the opposite. There, the low-energy (synchrotron) component peaks in the optical/UV or even the soft X-ray regime; the X-ray spectra are generally much softer (with $\alpha_{\rm X} \sim 1$ or softer) than in blazars associated with quasars and represent the high energy portions/tails of the synchrotron spectral component. Here, the X-ray band probes the highest energy "tail" of the electron distribution. Detailed studies in this band are indispensable in determining the extent of the energy distribution of the most energetic radiating electrons, which in turn is needed to provide the strongest constraints on the particle acceleration mechanisms.

4. Two facets of time variability

High energy emission from essentially all active galaxies is variable, which provides a difficulty but also an opportunity. On one hand, a reliable measurement of the broad-band spectrum must be obtained simultaneously, but on the other hand, the time variability in any single band - but also, a relationship of such variability amongst various bands - provides an opportunity to explore causal relationships between the respective emission processes and/or emission regions. With this, there are clearly two separate aspects - and associated challenges - of time variability studies of any astronomical sources. One is the sensitive measurement of properties of the time series in any single band, while the other is cross-band correlations.

4.1. Intra-band variability

The "standard" approach for the former aspect is to measure the Power Density Spectrum, which is essentially a Fourier transform of the time series. Another is the Structure Function; both were covered in detail in presentations at the Workshop, including those by McHardy, Hayashida, and past presentations by Kataoka, Edelson, Markowitz and others: in reference to blazars, see, in particular, a review by Kataoka (2008). Over a narrow range, PDSs or SFs of such time series are generally well-described by a power law, but the index of the power law changes with the variability frequency, at some "break" frequency $f_{\rm break}$. In accreting black holes - where the emission is presumably mainly due to nearly-isotropic radiation from the accretion disk - this break frequency has been demonstrated to correlate well with the mass of the accreting object (see, e.g., the relevant figure in McHardy, these proceedings, an extension of earlier work by Hayashida et al. 1998). Remarkably, this relation seems to hold down to masses of stellar size black holes.

Studies of jet-dominated blazars are quite sparse, with the first robust report for a sample of X-ray bright BL Lac objects by Kataoka et al. (2001), suggesting a break on day-long time scales, but with no clear correlation with the black hole mass (which, in turn, is difficult to determine in blazars). So far, reports for a clear PDS break are limited to one object, 3C273 possessing at least some blazar-like characteristics, but also showing substantial contribution from the emission from the accretion disk (McHardy, these proceedings; see also I. McHardy's presentation at the Blazar Variability Workshop in Paris, April 2008). There, the break frequency seems to follow that expected from the BH mass. Clearly, more detailed studies of blazars are needed, to determine their PDSs, compare those to the results for non-jet AGN, and determine whether there is any clear correlation with the black hole mass. Such studies are challenging, since they require well-sampled monitoring over a long span of time, corresponding to many years. MAXI is ideally positioned for this task.

4.2. Inter-band variability

The inter-band variability studies are equally difficult, again, because of the severe effect of sampling on the

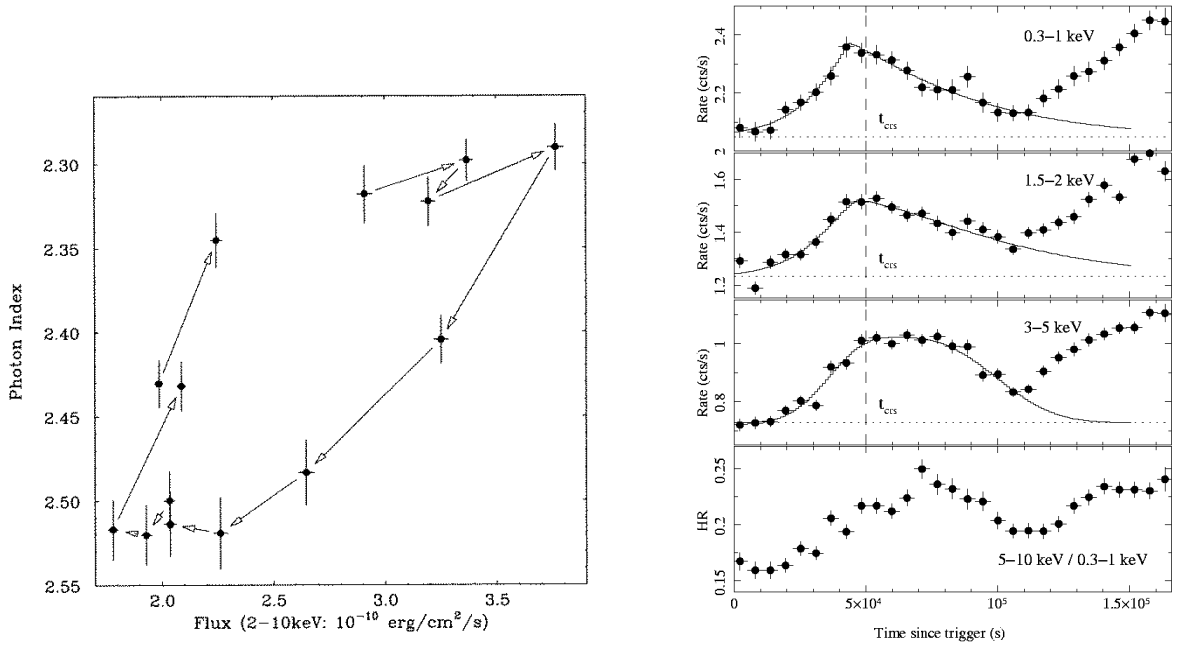

Fig. 2. Results of time-resolved X-ray spectroscopy of blazars. Left panel shows the evolution of the spectrum of blazar Mkn 421 observed in 1994 with the ASCA satellite, with the X-ray spectrum becoming harder when the source increased in intensity; the total length of the observation was about 1 day (from Takahashi et al. 1996). Right panel shows the Suzaku observation of another TeV-emitting blazar, 1ES1218+304. There, the spectral variability had an opposite sense: the source become brighter in soft X-rays, while the hard X-ray flare peaked ~ 20 ks later (from Sato et al. 2008).

robustness of determination of any lags or leads. With this, since many instruments provide data for a single source at a time, planning, scheduling, and coordination of various facilities is quite complex and challenging. Nonetheless, there are some recent successes resulting from well-planned campaigns: one notable example using a large suite of telescopes ranging from radio to X-ray bands, and including optical polarimetry, is the variability study of BL Lacertae (Marscher et al. 2008). There, the data indicate that there are multiple dissipation regions in the jet, and at least some of the X-ray flux arises at a distance $\sim$ thousands of $R_{\rm S}$ from the black hole. This observational result has many implications on the structure and the content of the jet, and similar observations need to be conducted using other objects.

Another important observational result concerns monitoring the TeV-emitting blazars, such as Mkn 421 mentined in Sec. 3. There, at least in the context of widely accepted leptonic models, the X-ray band and the TeV band both should reflect the high-energy end of the radiating electron population, so variability patterns should be correlated. While this is generally the case, the amplitudes of flares detected in the respective X-ray and TeV bands do not necessarily follow the trend expected in the simplest scenarios (for a recent discussion, see, e.g., Fossati et al. 2008). Clearly, more detailed understanding of those objects will require good temporal coverage in the X-ray band.

Meeting those goals requires overcoming rather severe observational challenges. The determination of the PDSs and inter-band correlations alike is difficult because of strong detrimental effect of the sampling pattern on the resulting PDS and cross-correlation function, as discussed in the last Section below. Data are sparse, because most X-ray facilities observe one object at a time (or, at most one field with a bright blazar at a time). With this, MAXI, monitoring all sky simultaneously, provides much better sampled X-ray data for a number of objects. Still, it is important to note that MAXI is sufficiently sensitive only for a limited number of blazars, since blazars often can be relatively faint in the X-ray band (see above). Still, given the need for good sampling, a temporal coverage of MAXI is indispensable.

4.3. Recent intra-band spectral variability studies of blazars: Suzaku observation of 1ES 1218+304

The cross-band variability studies show great promise as a tool to study the details of structure of blazar jets emitting over a broad range of spectral bands as above. But even studies of spectrally-resolved variability in a single band (such as, e.g., wide-band X-ray observations) can be very fruitful. Among the most important results regarding the nature of the radiating particle distribution in blazars was the Asca observation of the X-ray spectral variability in the TeV-emitting blazar Mkn 421, with the broad-band spectrum shown in Fig. 1. There, the

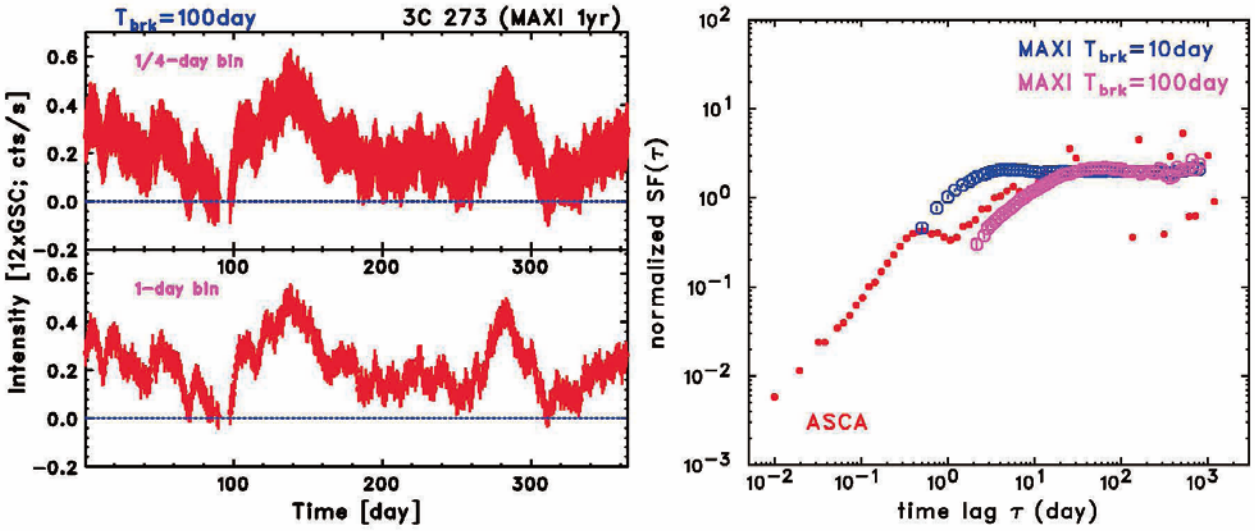

Fig. 3. Right panel: Simulated X-ray light curve of 3C273 as observed with MAXI. Data are binned at 1/4 day (upper plot) and 1 day (lower plot) intervals. Right panel: Structure Function for the blazar Mkn 421 calculated from the simulated light curves obtained with MAXI; the assumed mean flux is 10 milliCrab. For comparison, the plot also includes SF derived from combining the Asca and RXTE ASM data. (Figure from Kataoka 2008)

X-ray spectrum corresponds to the most energetic tail of the electron distribution, and the Asca data revealed that the X-ray spectrum became harder as the object became brighter, with hardening of the spectrum occurring more rapidly than the increase of brightness. More importantly, in the decay phase, the spectrum became softer more rapidly than the flux decrease (Takahashi et al. 1996; see Fig. 2, left panel). At least regarding the flux decay phase, this is precisely the kind of spectral variability expected in the synchrotron or Compton process, where the energy loss is energy dependent. The knowledge of the characteristic synchrotron cooling time $\tau_{\rm cool}(E)$ - going as $\tau_{\rm cool} \propto E^{-1/2}$ (derived from the cooling time scale for electrons $\tau_{\rm cool}(\gamma_{\rm el}) \propto \gamma_{\rm el}^{-1}$) - allowed an independent constraint on the Lorentz factors of the radiating electrons $\gamma_{\rm el}$, and, in fact, yielded values of $\gamma_{\rm el}$ similar to those inferred from broad-band spectral fitting.

Of course the implicit assumption in the analysis above is that the acceleration process is very rapid, significantly more rapid than the electron energy loss time scale even at the highest observable energy (note that the acceleration time scales for more energetic electrons are longer, with the dependence of the acceleration time scale on the photon energy going as $\tau_{\rm acc}(E) \propto E^{1/2}$, derived from $\tau_{\rm acc}(\gamma_{\rm el}) \propto \gamma_{\rm el}$). This, in turn, might depend on a particular blazar, or even on a particular event. In fact, an opposite behavior to that described above for Mkn 421 was detected recently with Suzaku in another TeV-emitting blazar 1ES1218+304, via observations reported by Sato et al. (2008). There, the $\sim$ 2 day long observation revealed a well-resolved X-ray flare with a rise time of $\sim$ 50 ks. The spectrally resolved Suzaku light curve (see Fig. 2, right panel) indicated that the hard X-ray (5 - 10 keV) flux in the flare clearly lagged that in the soft X-rays (0.3 - 1 keV) by about 20 ks. This was associated with the profile of the flare, which became more symmetric at higher energies. This lag can now be interpreted as an energy-dependent signature of the electron *acceleration* process. Those two features of the energy-resolved time series now suggest that the acceleration and cooling time scales in this object are roughly comparable for electrons radiating at $\sim$ 2 keV - and this puts further constraints on the electron acceleration process, and in particular, on the level of turbulence in magnetic field (see Sato et al. 2008).

5. Future facilities to study blazars in the X-ray band

The launch of GLAST is taking place when several X-ray sensitive observatories are operational and delivering high quality data, but also with several additional ones under construction. Most notably, the Chandra satellite, featuring the bandpass of $\sim 0.5 - 10$ keV, is providing probably the most sensitive measurements on many sources. Important discovery with Chandra - mainly owing to the superb quality, sub-arc sec imaging - was the detection and mapping of the kpc size X-ray emitting jets in a number of blazars, including those that are bright gamma-ray emitters detected with EGRET. XMM-Newton observatory has capabilities in many ways

similar to Chandra's, with somewhat worse point spread function of its three mirrors, but with substantially better effective area, allowing sensitive measurements of flux variability of active galaxies on even shorter time scales than Chandra. Just as is the case for Chandra, XMM-Newton is also in a deep (several day-long) orbit, allowing uninterrupted data streams and unambiguous variability studies on time scales of a $\sim$ day down to the Poisson limit, generally corresponding to a few hundred seconds. Suzaku has possibly the best effective area for its low-energy (XIS) detectors, and also features an additional, hard X-ray detector - extending the bandpass (for most AGN) to at least 50 keV; however, the low-Earth orbit and Sun angle constraints place some limitations on the sampling pattern and the resulting measurements of the intra- and cross-band variability properties. Swift satellite features nearly all-sky pointing capability, and is bound to be an important tool for rapidly responding to, and following exceptional flares of blazars. In the near future, NuSTAR, sensitive in the hard X-ray ($\sim 10-80$ keV) band, slated to be launched in 2011 or 2012, will be monitoring the hard X-ray flux for at least a few blazars for $\sim$ weeks, but both Swift and NuSTAR, with their low-Earth orbits, will be subjects to periodic source occultations. All those facilities, however, can observe only *one target at a time*. With the Rossi X-ray Time Explorer - with its All-Sky Monitor - nearing the end of its operational life, a working all-sky monitor is essential, and that capability will be provided by MAXI. This will be important for GLAST, but equally, or even more so, for the current and future TeV-sensitive Cerenkov telescopes. MAXI will provide a trigger and monitoring capability for observations of the TeV-emitting blazars regardless whether they are or are not subjects on ongoing multi-band campaigns.

What are MAXI's capabilities to measure variability of blazars? Bright objects such as 3C273 ($\simeq$ 5 milliCrab) and Mkn 421 ($\simeq$ 10 milliCrab) can be detected with more than 5 σ level every day, allowing for the first time non-bias monitoring of the sources from daily to more than yearly time scales. Figure 3 (left panel) shows the simulated long-term (1 year) light curve for 3C273, assuming a PSD slope of 2.0 with a break time of $1/f_{\rm break} \simeq 100$ day. The resultant structure function (calculated as in Kataoka 2008) is illustrated in the right panel of Figure 3: it clearly reveals variability nature of blazars on long time scales, significantly longer than the characteristic break. Detailed measurements of such features in the PDS and SF are bound to probe whether the variability properties are mainly governed by the changes in the accretion flow, or by the properties of the energy dissipation process and attendant instabilities in the relativistic jet.

Acknowledgements: The lead author is grateful to the conference organizers for their hospitality and support, and acknowledges valuable comments from Drs. Benoit Lott and Luigi Costamante, as well as support via the Department of Energy Contract DE-AC02-76SF00515 to the Stanford Linear Accelerator Center.

References

Atwood, W., et al. 2008, submitted to ApJ
Fossati, G., et al. 2008, ApJ, 677, 906
Hayashida, K., et al. 1998, ApJ, 500, 642
Jorstad, S., et al. 2001, ApJS 134, 181
Kataoka, J. et al. 2001, ApJ, 560, 659
Kataoka, J. 2008, in Proceedings of Science, Proc. of Workshop on Blazar Variability Across the Electromagnetic Spectrum, Ed. B. Giebels, arXiv:0806.4243
Kniffen, D. et al. 1993, ApJ 411, 133
Macomb, D., et al. 1995, ApJ, 459, L111
Maraschi, L., et al. 1994, ApJ, 435, L91
Marscher, A. P., et al. 2008, Nature, 453, 966
Sato, R., et al. 2008, ApJ, 680, 9L
Wehrle, A., et al. 1998, ApJ, 497, 178

Multiwavelength observations of Blazars

Stefan J. Wagner [1]

[1] Landessternwarte Heidelberg
E-mail(SW): s.wagner@lsw.uni-heidelberg.de

Abstract

Blazars exhibit very broad spectral energy distributions, extending over up to 20 orders of magnitude in photon energy. Blazars also very on a wide range of time scales with power density spectra that have been measured over as many as 9 orders of magnitude in time for the best studied objects. Given these characteristics, coordinated multiwavelength observations are required to understand the physical processes in Blazars. Apart from detailed studies of a very small number of prominent targets, statistical investigations of homogenous observations are important, but difficult to assemble due to technical constraints. The current status of multiwavelength investigations will be reviewed with a special emphasis on future opportunities.

Multiwavelength observations of Blazars

Stefan J. Wagner
Landessternwarte
Heidelberg
Germany

acknowledgements D. Emmanoulopoulos, E. Ferrero, G. Pedaletti,
O. Kurtanidze (Abastumani), G. Bicknell (ANU Canberra)
HESS collaboration

Multiwavelength observations

Broadband studies of Blazars are monitoring studies: 3 reasons
Scale-free spatial and temporal structures
Localizing emitting regions
Clues on Lorentz factors, Uncertainties in Doppler corrections

Special emphasis:
"Astrophysics with All-Sky X-Ray Observations"

All-Sky >> many sources >> populations (parameter studies)
>> alerts for pointed studies
>> long-term studies >> flux/sensitivity is 'only' bias
(window function well understood)
>> avoid coincidences

From examples to samples: avoiding biases, enabling parameter studies

SED studies and timing: 1st reason

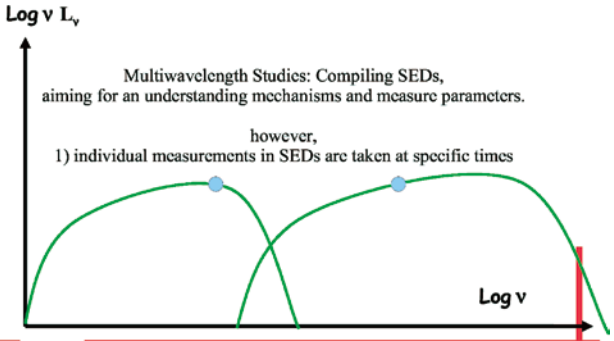

SED studies and timing: 1st reason

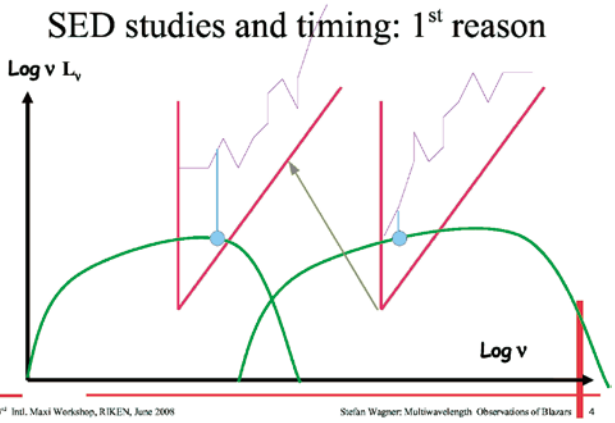

SED studies and timing: 2nd reason

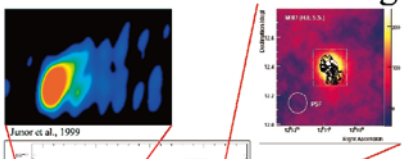

Aharonian et al.,
HESS collaboration, 2006

M87

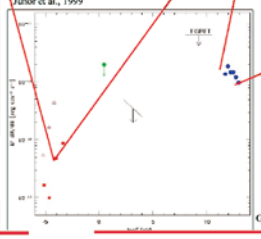

individual measurements in SEDs
are integrated over
very different spatial scales

SED studies and timing: 2nd reason

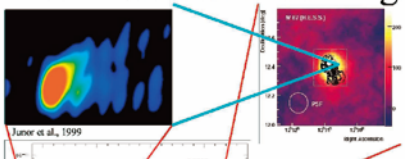

M87

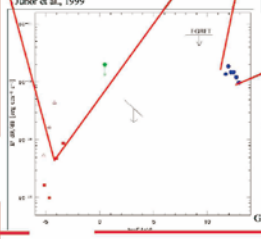

7 orders of magnitude (linear)
21 orders of magnitude (volume)

scaling/decomposition/cross-identification
(only) possible through variability

SED studies and timing: 3rd reason

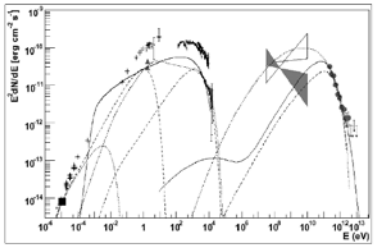

Aharonian et al. (HESS collaboration, 2006)

simultaneous (single epoch) SEDs do not provide a unique constraint for models of acceleration and radiative processes.
(It has not been demonstrated, but there is hope that time-resolved multifrequency studies will provide unique constraints.)

General motivation

Seaking correlations to identify sources
(when known coincidences are insufficient)

1960s finding radio sources: "3C273B = ... "
1970s finding X-ray sources: "Ariel ... = PKS 2155-304"
1990 finding Gamma-ray sources: 3C66A, PKS 1406-076
2000s finding TeV sources (see Elina Lindfors)

Finding sources in the sky;
localizing subvolumes in the sources (in space and time);
localizing subvolumes in parameter space (B, n, γ);
identify and understand processes (qualitative relations between bands)

Review:

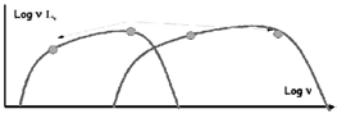

Within synchrotron band: Radio-Optical Correlations
Lunar Occultations (e.g. Dent)
Flares (e.g. van der Laan)
Outburst and VLBI components (Babadzhanyants)
Polarisation characteristics (Kikuchi)
but: IDV (SW and Quirrenbach)
relation to X-ray bands (e.g. Urry; Brinkmann; Courvoisier; Edelson)

Within HE bump: 3C279 (Wehrle)

Synchrotron – HE bump: several in 1980s (without mentioning)
involving gamma-rays (1406-076; Mkn 421: Takahashi & SW)

but several counter-examples ("orphan" events); poor coverage in energy

Parameter Space

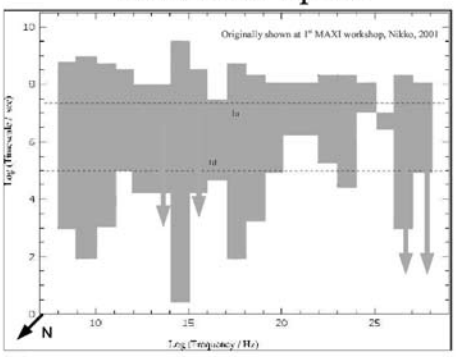

Long, continuous light-curves

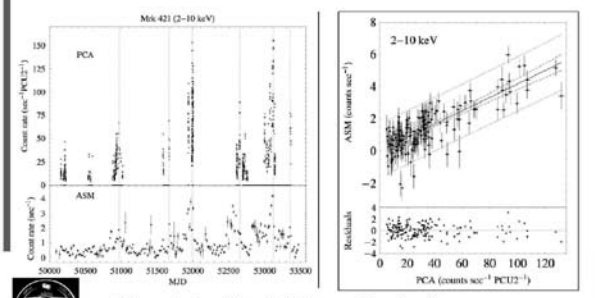

uninterrupted, unbiased, but coarse binning, few sources

D. Emmanoulopoulos & SW (2008)

Self-similar structures?

Mrk 421, XTE (2-10 keV)

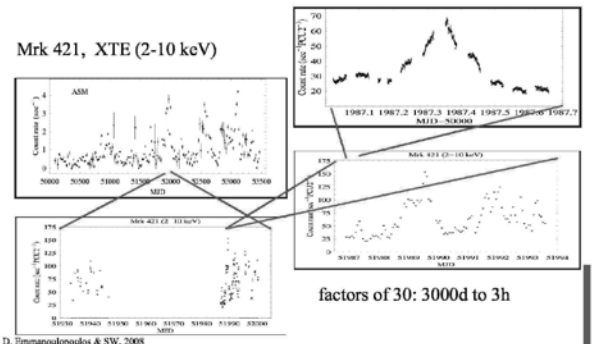

factors of 30: 3000d to 3h

D. Emmanoulopoulos & SW, 2008

Spatial and temporal scales

Temporal scales:
Mrk 421, X-rays: 100 s - 10 Msec
3C345, optical: 300 s - 1 Gsec

Spatial scales:
M87, radio (GHz): 10 mpc - 100 kpc

self-similar structures

self-similar flares
(power-law PDS)

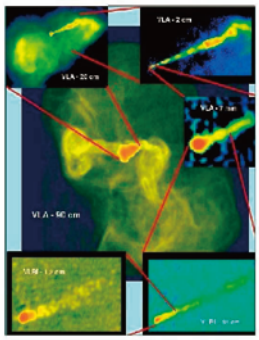

Small scales

Variability as a tool to small spatial scales
Fast flares extend resolution to very
comapct regions.
Strongly structured jets
(Single blobs in VLBI resulting from
limited dynamic range).

Mrk 501 shows many small clouds.

If the self-similarity extends
to smaller spatial scales,
small clouds might refer to fast flares.

Extreme examples from IDV and VHE.

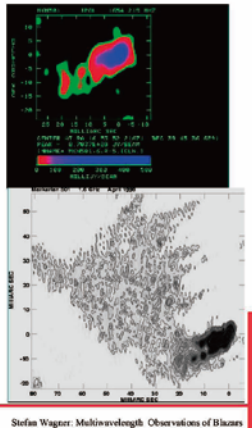

Giovannini et al., 2000

Small scales: Intraday Variability

Intraday variability (IDV)
S5 0716+714 (z~0.3)
Radio (5, 8.4 GHz) and optical (650 nm)
variations on timescales ~ 100 ksec

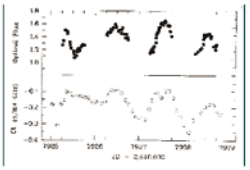

Wagner et al., 1994

implied linear dimensions:
500 times smaller than (resolved) vlbi knots,
100 times smaller than unresolved vlbi core
(assumed to be self-absorbed).
Variable subvolume one million times smaller
than any resolved structures
(radiation density 100 000 times larger)

Krichbaum et al., 2001

Just how small can they be?

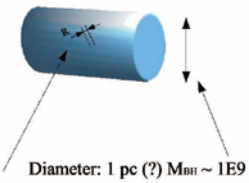

Diameter: 1 pc (?) $M_{BH} \sim 1E9$

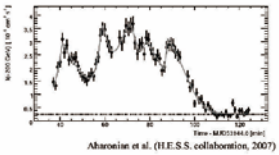

Aharonian et al. (H.E.S.S. collaboration, 2007)

PKS 2155-304 (flare in 2006)
time-scale 60 sec ... 300 sec
linear scale from causality

Emitting volume: $R\mathcal{D} < 4.6E12$ cm
Cross-section of emitting volume: $\mathcal{D}^2$ E-11 A (A= cross-section of jet)

[Inferences in both cases: $\mathcal{D}$ might be as high as 100]

Filling factors and duty cycles

Subvolumes producing 0.1 to 10 times the quiescent flux
with individual filling factors E-10...E-15 should result in large
numbers of such subvolumes blending the integrated light curves.

The contrast to observations implies one of three possibilities:

1) Duty cycle is very low
2) Zone of variations extends over small radial range only
3) Distribution function in some crucial parameter very steep
(highly nonliner system)

(1) is essential a special case of (3)

consider (2): Where do Blazars produce their emission?

Emission site in M 87

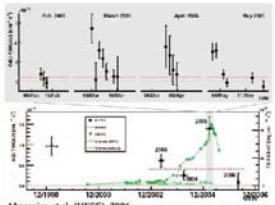

Aharonian et al. (HESS), 2006

Albert et al. (MAGIC), 2008, astro-ph/0806.0988

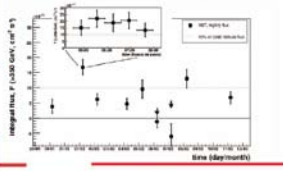

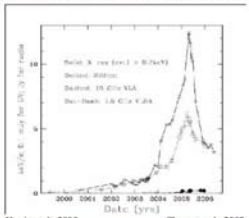

Harris et al., 2005 Cheung et al., 2007

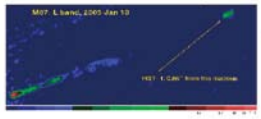

Locating site of PKS 2155-304

Evidence from spectral monitoring: Non-detection of spectral changes during bright VHE flare (Costamante et al., 2008) implies minimum distance > 100 Rg

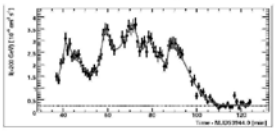

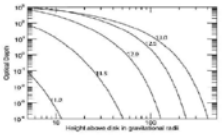

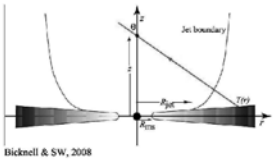

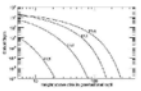

Bicknell & SW, 2008

simple worries γ_{min}, γ_{max}, Γ

Almost all SED "fits" of Blazars invoke high γ min.
There are other observations/problems that suggest that this is required.
(e.g. Blundell et al., 2004, Tsang & Kirk, 2007, SW, 1997)
There are very few (no?) acceleration mechanisms achieving this.

Optical and Xray observations can derive those:

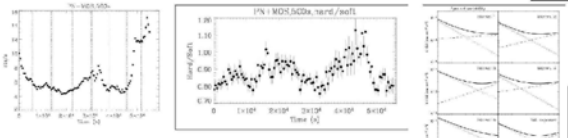

Optical/XMM studies og 0716+714 (Ferrero et al., 2006)

simple worries γ_{min}, γ_{max}, Γ

MeV Blazars (Bloemen et al., 1995), GeV Blazars, TeV Blazars
E(max) in Synchrotron/IC changes by <3/>7 orders of magnitude

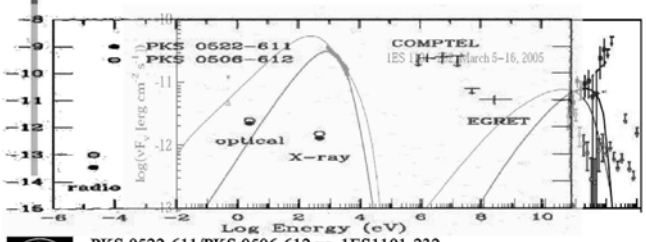

PKS 0522-611/PKS 0506-612 vs. 1ES1101-232 (Aharonian et al., HESS, 2007)

simple worries γ_{min}, γ_{max}, Γ

observed SED needs to be corrected for
various excesses (host galaxies, extended emission),
various absorptions (SSA, E, n_H, pair absorption),
redshift, and ... Doppler factor(s).

Notoriously difficult: VLBI vs. variability (IDV, VHE) $\mathcal{D}$~1...100
large values possible in exceptional sources (IDV of various kinds)
but difficult for large classes (TeV Blazars). [Remember M87]
... if TeV Blazars they are: PKS 2155-304 200 GeV – ($\mathcal{D}$~ 100) > 2 GeV

Radial or lateral stratification, divergent trajectories?
Different parts of the jets (different subvolumes, flares, wavelengths)
may be subject to different Doppler corrections.

Summary

Simultaneous multifrequency monitoring required to compare oranges (or the right season) to oranges and (hopefully) break the degeneracy of different acceleration/radiation mechanisms.

Variability across the EM spectrum occurs on a wide range of timescales. Individual components/flares relate to regions of very different sizes (but they are not very different otherwise).

Very small filling factors of emissivity. Stratified media. Single-zone models ought to be self-consistent

Multifrequency observations may also provide localisations

Range of Lorentz factors may be constrained with Maxi observations.

Doppler factors might be diverse and provide the biggest challenge.

The End

Thank you for your attention

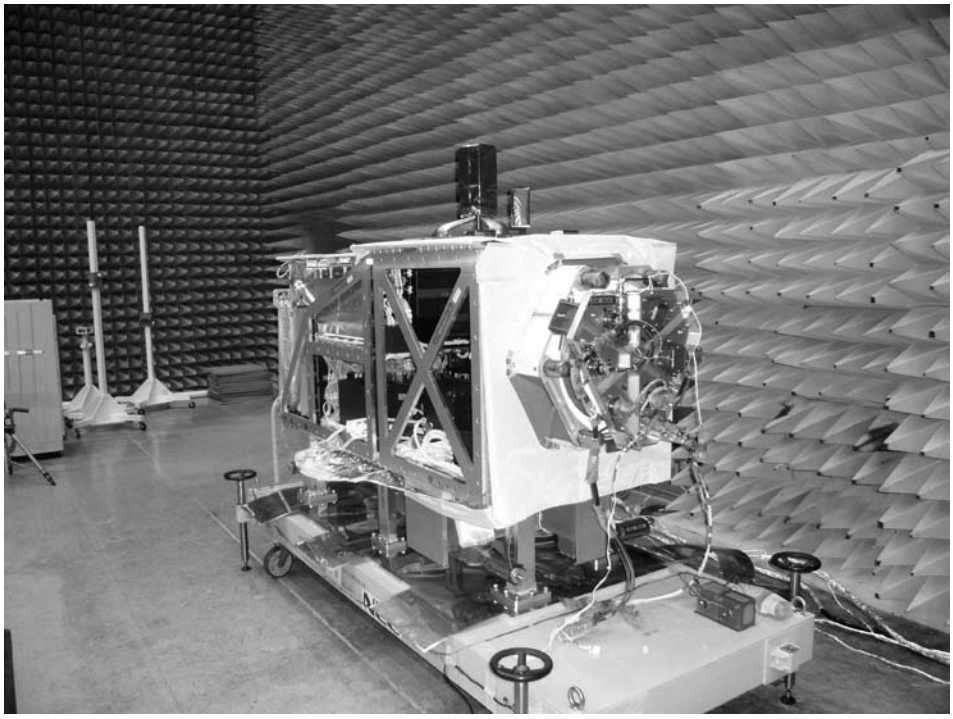

A search for large amplitude X-ray variables with the XMM-Newton Serendipitous Survey

Weimin Yuan [1]

[1] Yunnan Astronomical Observatory, Chinese Academy of Sciences, PO Box 110, Kunming, Yunnan, 650011 China
E-mail: wmy@ynao.ac.cn

Abstract

I report on our ongoing programme to search for X-ray sources with long-term, large amplitude X-ray variability. The method is to compare the fluxes of X-ray sources from the XMM-Newton Serendipitous Survey with those from previous ROSAT pointed observations and the ROSAT All-sky Survey. Here I decribe the method and present some of the preliminary results, part of which has been presented in Yuan et al. (2004, 2006).

Key words: X-ray sources, X-ray flares, variability

1. Introduction

The X-ray sky is an active one. The X-ray emission produced from celestial objects is often variable, some with large amplitudes. There is a rich variety of highly variable X-ray sources, from accreting black hole binaries to active galactic nuclei (AGN). Apart from studying the details of the physical processes in the known types of X-ray variables, monitoring the X-ray sky may also lead to discoveries of new phenomena of X-ray variability. For example, Of particular interest is a new type of non-recurrent X-ray flares from non-active galaxies, which showed variability by a factor of hundreds, or even up to thousands (e.g. Komossa et al. 2004). These events were interpreted in terms of tidal disruptions of stars by the central massive black holes in galaxies (e.g. Rees 1988). In fact, all kinds of high-amplitude variability are of interest in astrophysics, as they are often traces of extremely violent physical conditions or processes, such as, cataclysmic processes of evolution, extreme accretion events, and violent acceleration of high-energy particles.

Generally, observations of the variability of X-ray sources are pursued mainly in two approaches. One is sky monitoring/scanning with dedicated wide-angle/all-sky monitors. It has the advantage of large sky coverage but is usually of low sensitivity and spatial resolution, and can thus observe only relatively bright objects. On the other hand, long observations pointed at pre-selected targets with conventional X-ray observatories can pick up weak sources, but the observational efficiency is low. What is virtually left unexplored lies in between these two regimes—the long-term temporal properties of the bulk of X-ray sources, most of which are extragalactic and faint. To fill this gap, systematic surveys for X-ray variability are needed in large sky regions with high sensitivities and good spatial resolution. The XMM-Newton X-ray Observatory presents such an opportunity, with its a large field of view (FOV), good imaging capability, and high throughput. These virtues enable it to detect significant numbers of X-ray sources in the XMM-Newton Serendipitous Survey (Watson et al. 2001). For the typical exposure time of 20 ksec, its EPIC (European Photon Imaging Cameras) will detect about 50–100 sources over the whole FOV of ~ 0.2 sq. deg. Each year XMM-Newton observations cover $\sim$100 sq. deg. of the sky (detecting $\sim$ 50,000 sources); a considerable fraction among them was previously observed with ROSAT pointings (PSPC or HRI). These observations thus form an ideal database with which to study the long-term variability of X-ray sources.

Here I describe and report the progress of our on-going programme to search for the long-term variability of X-ray sources along this line. The method is to make use of the data obtained in the fast-growing sky regions covered by both the XMM-Newton Serendipitous Survey and the previous ROSAT pointed observations, and to compare the fluxes of sources measured by the two instruments.

2. Search for X-ray variable sources with XMM-Newton

Our aim is to detect long-term X-ray variability for sources falling within the field of views of both the XMM-Newton and previous ROSAT observations, by comparing the source fluxes at the two epochs. The search was designed to be carried out automatically on a field-by-field basis. The ROSAT catalogues used in the cross-correlation include the 2nd ROSAT PSPC catalogue

(ROSAT team 2000b) the HRI catalogue (ROSAT team 2000a), and the ROSAT All-sky Survey (RASS) (Voges et al. 1999). Though the RASS data are not deep, they are still useful in detecting those which were bright during the RASS but dim during XMM observations. For the matching of XMM and ROSAT sources, we use the results of the catalogue cross-correlation products provided by the XMM-Newton data processing pipeline ('XMM pipeline' hereafter) generated by the XMMSSC. To enable comparisons of the fluxes the restricted energy band in the overlapping 0.2–2.4keV is used. We used the following procedure in the search:

- Retrieve information of all XMM observations and select those with acceptable data quality.
- For a given XMM observation, it is determined whether the field has ever been observed by previous ROSAT (PSPC or HRI) pointed observations.
- The information on the XMM sources are extracted from files generated by the XMM pipeline and the 0.2-2.4keV fluxes are calculated. Their ROSAT counterparts (including the RASS sources) are searched from the cross-correlation catalogues of the XMM pipeline. For sources detected by both XMM and ROSAT, the variability factors are calculated as flux ratios.
- For sources detected in only one of the two missions, the lower limits on the variability factors are obtained by from the flux limits. For ROSAT, the flux limits are estimated from the X-ray images, exposure maps, and background maps at the source positions. For XMM, the sensitivity maps provided by the XMM pipeline are used.
- The X-ray images of the sources are created.
- Select candidates of variable sources for given thresholds.
- Visually inspect each candidate to screen out spurious sources or variables.

Due to various imperfectness of EPIC observations and the X-ray CCDs, the results thus produced contain a large number of spurious cases, which are mainly caused by the detection of spurious sources (mainly from XMM). Thus visual inspection of the X-ray images is carried out to screen out spurious candidates. This problem is expected to become largely resolved with the improvement of the source detection algorithm in the XMM-Newton processing pipeline. The final results are lists of screened candidates of variable sources with estimated variability factors and the X-ray images. As demonstration we show in Fig. 1 the X-ray images of the same piece of sky region as observed by ROSAT (left panel) and XMM (right panel), in which a variable X-ray source was detected with this programme.

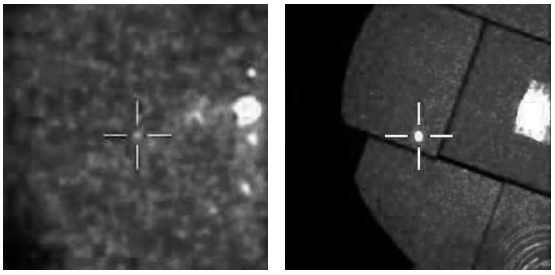

Fig. 1. Example images (10'×10') of the same piece of sky region as observed by ROSAT PSPC (left panel) and XMM-Newton EPIC MOS (right panel), respectively. It can be seen that a serendipitous source (marked by crosses) brightened dramatically from one observation to the other (comparing the source brightness with the background fluctuations). (From Yuan et al. 2006).

3. Preliminary results

The search can be done in a mostly automatic manner. So far we have performed the search over the adequate fields observed by XMM-Newton in its first-year operation. Among the ∼ 470 XMM pointings, 386 (∼66 sqr.deg.) were overlapped (or at least partially) with ROSAT pointed observations. As the first step, we are concerned only with objects showing large variability amplitude (e.g. by factors >10). So far, only objects brighter in XMM observations than in ROSAT observations were considered. There are ten candidates were found to have the XMM-to-ROSAT flux ratios larger than 10, and up to ∼30.

Among the ten candidates of highly variable X-ray sources found, two are previously known objects; they are the cataclysmic variable OY Car and the micro-quasars GRS 1758-258, which both were observed as targets. The micro-quasars GRS 1758-258 was caught in outburst states during the XMM observations, which has been presented in detail in Ramsay et al. (2001). There are two sources found to be bright, nearby stars (V=8.6mag and 4mag, respectively), which underwent X-ray flares. Interestingly, there are two sources appearing to be associated with faint stars (∼14mag), one with very red colour. There is one source whose counterpart is not clear because of its relatively large distance to the closest optical object (12arcsec)—probably a star in the Galactic halo; alternatively, it may originate from a background galaxy (Fig. 2). There are two sources with no optical counterparts found down to the DSS limit. One is close to the Galactic centre region (Fig. 3) and may also be associated with a radio source. It is possibly an X-ray binary. Follow-up identification and study of these sources are underway.

The only extragalactic source identified so far, which

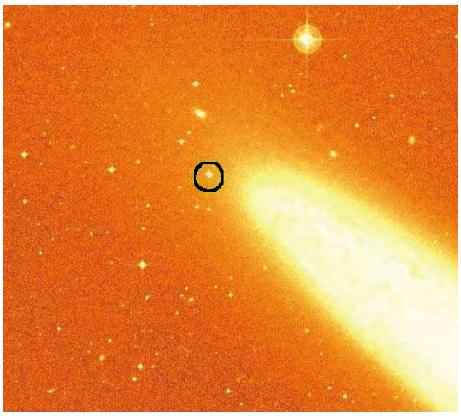

Fig. 2. Example of one variable X-ray source (the centre of the circle), which may be associated with a faint halo star (12″ away) or from a source in the background galaxy (from Yuan et al. 2006).

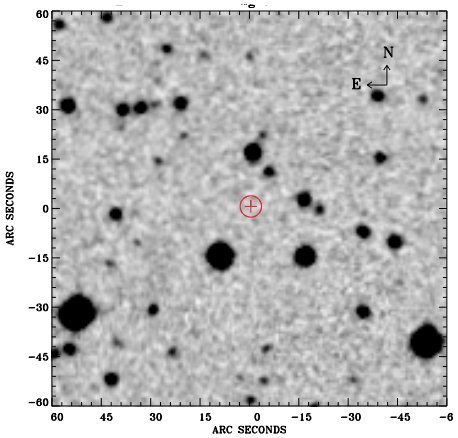

Fig. 3. Another example variable X-ray source, which is located in a region close to the Galactic centre. It has no optical counterpart down to the DSS plate limit (from Yuan et al. 2006).

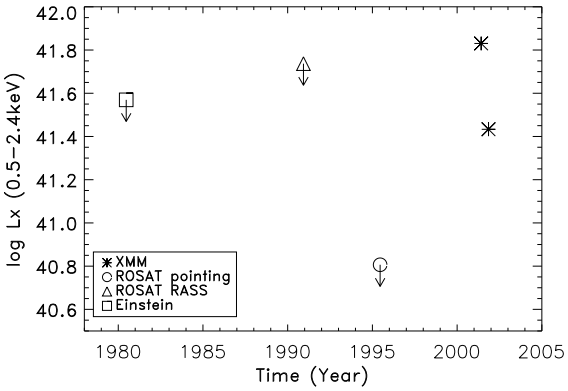

Fig. 4. Long-term light curve of 0.5–2.4 keV X-ray luminosity of the galaxy NGC7589. The arrows denote upper limits (from Yuan et al. 2004).

varied by a factor of more than 10, is from the nucleus of the galaxy NGC7589. Fig. 4 shows the X-ray light curve of NGC7589 in 0.5–2.4 keV, which is in the overlapping energy band of various X-ray missions. Its X-ray luminosity shows a dramatic increase by a factor of >10, occurring sometime between the ROSAT pointing and the XMM observation in orbit 272, on a timescale less than $\sim$5 years. Given the poor sampling, the flux seen by XMM may not represent the flux at the 'highest state', which means that the peak luminosity could be even higher. Therefore the actual variability amplitude must be >10. The flux decreased by a factor of 2.5 between the two XMM observations over a period of 5 months, whereas the overall 0.4–10 keV spectral shape appeared to remain unchanged. The 0.4–10 keV XMM spectrum can be approximated by a power-law with photon index of 1.7–1.8, though it seems to flatten above 5 keV, suggesting a possible complex model, such as partial covering or disc reflection. At its low light state, NGC7589 is typical of low luminosity AGN (Yuan et al. 2004).

NGC7589 is a giant, low-surface brightness galaxy (Fig. 5). The galaxy was spectroscopically observed in the Sloan Digital Sky Survey (SDSS; York et al. 2000) on Sep. 29th, 2000, about 8 months prior to the high state caught by XMM. The contribution of stellar light from the host galaxy was subtracted from the observed spectrum by modeling stellar absorption lines employing a range of galaxy spectral template. A broad Hα line (see Fig. 6), which is blueshifted, is evident and had a width of FWHM$\approx$3428 km s^{-1}, compared to the narrow lines of FWHM $\approx$228 km s^{-1}. This broad emission line indicates the presence of an AGN in this galaxy. No broad Hβ line can be detected.

We performed spectral classification for NGC7589 using the emission-line ratios. On the diagnostic diagrams

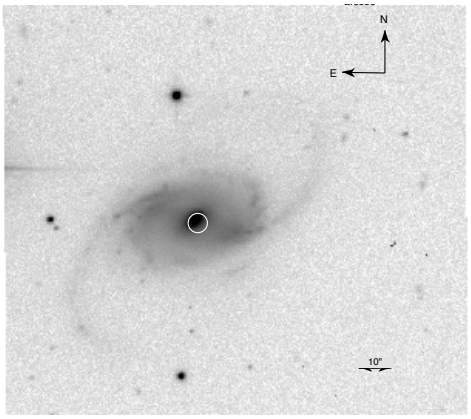

Fig. 5. Optical counterpart, NGC7589, of one of the highly variable sources discovered. A circle represents the position and its 3σ error of the X-ray source. A 10 arcsec angular distance corresponds to 5.65 kpc (from Yuan et al. 2004).

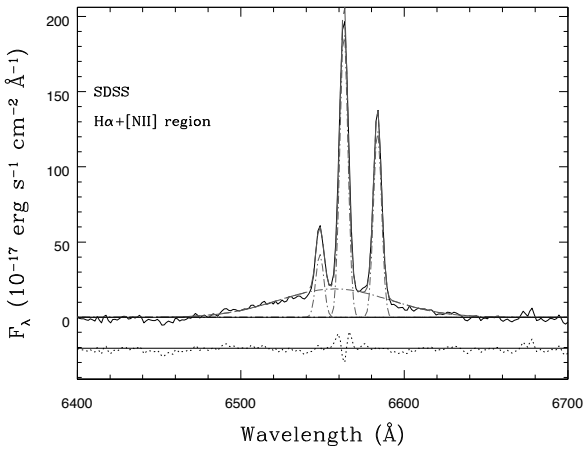

Fig. 6. The Hα+[NII] line region of the SDSS spectrum of NGC7589 after subtracting the host galaxy starlight. A broad Hα line component is evident, which is blueshifted with respect to the narrow lines.

of Veilleux & Osterbrock (1987), the line ratios locate the object in the Seyfert locus but very close to the borderline with the LINERs. This also holds if we use the classical definition of LINERs (Heckman et al. 1980) which only makes use of Oxygen emission-line ratios. Therefore, NGC7589 can be regarded as one of the type of the Seyfert-LINER transition galaxy, either Seyfert 1.9 or LINER I. This property makes the large amplitude X-ray variability, which is rare in LINERs, somewhat intriguing. Part of this work has been published in Yuan et al. (2004).

So far, no object was found to show variability as large as those candidate systems of tidal disruption of stars by black holes, which are expected to vary by a factor of hundreds or more.

4. Summary

We have initiated a programme of systematic search for long-term highly variable X-ray sources in the sky regions covered by the serendipitous surveys of both XMM-Newton and ROSAT, as well as the RASS. So far, we have searched over data from the first-year XMM observations (470 fields, 386 overlapping with previous ROSAT pointings) and obtained some preliminary results. Ten X-ray sources have been found which have varied by a factor of more than 10 on timescales of years. Identification of the previously unknown ones among them is underway. No object was found to show variability by a factor above a hundred; such amount of amplitude is required to be considered as candidates of flares from inactive galactic nuclei as discovered recently (Komossa 2002).

We are now working toward enlarging the highly variable source sample by extending the search to more XMM observations. Identification of the other candidates found in the optical and other wavebands is also underway. and to identify the obtained candidates.

I thanks the organizers for invitation to the interesting workshop.

References

Heckman T., 1980, A&A 87, 152

Komossa S., 2002, 'Ludwig Biermann Award lecture: X-ray evidence for supermassive black holes at the centers of nearby, non-active galaxies', Rev. Mod. Astron., 15, 27

Komossa S., Halpern J., Schartel N., et al. 2004, ApJL, 603, 17

Ramsay G., Cropper M., Córdova F., et al. 2001, A&A, 365, L288

Rees M.J., 1988, Nat 333, 523

ROSAT team 2000a, 'The ROSAT Source Catalog of Pointed Observations with the High Resolution Imager (1RXH) (3rd Release)', ROSAT News 71

ROSAT team 2000b, 'The Second ROSAT Source Catalog of Pointed Observations', ROSAT News 72

Veilleux S., Osterbrock D.E., 1987, ApJS 63, 195

Voges W., Aschenbach B., Boller Th., Broeninger H., Briel U., 1999, A&A, 349, 389

Watson M.G., Augures J.-L., Ballet J., et al., 2001, A&A 365, L51

York D.G., et al., 2000, AJ 120, 1579

Yuan W., Komossa St., Xu D., Osborne J.P., Watson M.G., McMahon R.G., 2004, MNRAS, 353, L29

Yuan W., Osborne J.P., Watson M.G., Komossa St., 2006, AdSpR, 38, 1421

The 2XMM catalogue and variability of X-ray sources

M. Sakano[1], G. Denkinson[1], D. Fyfe[1], G. Lamer[2], S. Mateos[1], J. P. Osborne[1], C. G. Page[1], J. Pye[1], S. Rosen[1], A. C. Schröder[1], I. M. Stewart[1,3], A-M. Stobbart[1], J. Tedds[1], M. G. Watson[1],

[1] Department of Physics & Astronomy, University of Leicester, Leicester, LE1 7RH. UK
[2] Astrophysikalisches Institut Potsdam (AIP), An der Sternwarte 16, 14482 Potsdam, Germany
[3] Jodrell Bank Centre for Astrophysics, University of Manchester, Oxford Road, Manchester M13 9PL, UK
E-mail(MS): mas@star.le.ac.uk

Abstract

We released the 2XMM catalogue, the largest ever X-ray source catalogue, on 22 August 2007. It contains 246,897 detections drawn from 3491 public XMM-*Newton* observations, which relate to 191,870 unique sources. The time variability, as well as spectrum, has been studied for the sources that have reasonable statistics, numbering 38,320 detections. Here we present the highlight of the 2XMM catalogue, in particular the time variability of the point sources, and discuss the potential future study with the X-ray monitoring instrument, MAXI.

Key words: X-ray: catalogue — source: variability — XMM-Newton

1. Introduction

Surveys are always important in astronomy in any wavelength. However it is neither easy nor often practical to perform deep and wide-field surveys, as the instruments with good spatial resolution and accordingly high sensitivity generally have a small field of view, whereas those with a wide field of view have only a poor sensitivity. In the light of this serendipitous surveys play an important role, which offers good sensitivity, as well as moderately wide and reasonably unbiased coverage.

In the X-ray band ROSAT All-Sky Survey (RASS) provides the best sample in terms of coverage (i.e., all-sky) and reasonable depth for sensitivity (Voges et al. 1999, 2000). However the energy band is limited to below ~2 keV. In the harder energy band above 2 keV, HEAO-1 all-sky survey is still the best in terms of coverage, although the sensitivity is poor. Various results have been published to compensate this lack of sensitivity in the hard X-ray band with serendipitous surveys, of which ASCA-AMSS (Ueda et al. 2005) is probably the most notable to date.

The XMM-Newton observatory is equipped with CCD cameras (EPIC), which has the large field of view, combined with the good sensitivity, good spatial resolution and large effective area of its mirrors. Hence it provides an ideal opportunity for the serendipitous survey. Even though most of the target fields were selected in a naturally biased way to observe their primary targets, the areas surrounding the targets are expected to give a reasonably unbiased dataset for the survey.

We have performed the serendipitous survey using all[1] the public data of XMM-Newton prior to 1 May 2007 as the key project of the XMM-Newton Survey Science Centre (SSC), and released the result as the 2XMM catalogue on 22 August 2007. It contains 246,897 detections, and among those 191,870 sources are regarded as unique. This is the largest ever X-ray source catalogue.

The full detail of the catalogue is found in Watson et al. (2008). In this paper we describe the highlights of the catalogue result, as well as some time variability characteristics of the catalogued sources, and further discuss its use in the future all-sky X-ray monitoring programme, particularly the MAXI.

2. The 2XMM catalogue – overview

2.1. The observed area and sensitivity

The EPIC onboard XMM-Newton has a good and direct imaging capability with the size of the point-spread function of ~10 arcsec, with the field of view (of the combined three EPIC instruments) of ~30 arcmin in diameter, with the large effective area of 2000 cm^2 at 1 keV for the sensitive energy band of 0.2–12 keV. The 3491 observed fields observed in 7 years, as is shown in Fig. 1, in total covers ~370 deg^2, i.e., ~1 per cent of the sky.

Fig. 2 shows a couple of examples of field of views of EPIC, which were used to compile the 2XMM catalogue. Even though not all the fields are in the ideal state, we

*[1] Some fields with bad quality or observed in an unsuitable mode for the serendipitous survey study were excluded (see Watson et al. 2008 for detail).

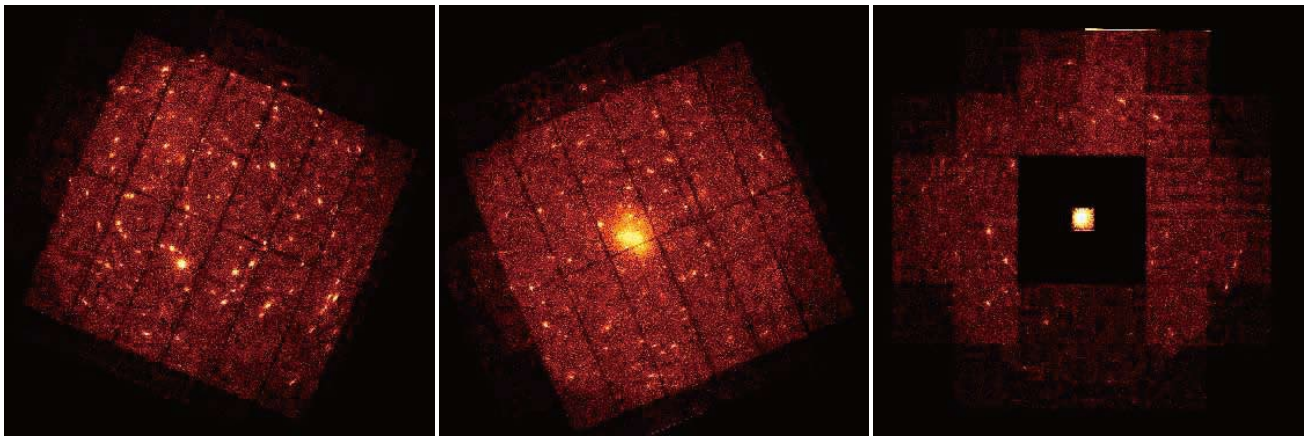

Fig. 2. Example field of views used in the 2XMM catalogue. *Left panel*: a deep observation in a high-galactic-latitude field, *Middle panel*: a distant cluster of galaxy, *Right panel*: an observation with a different mode from the most standard one — we did not use the central CCD chip in this case, whereas we did process and use the peripheral CCD chips.

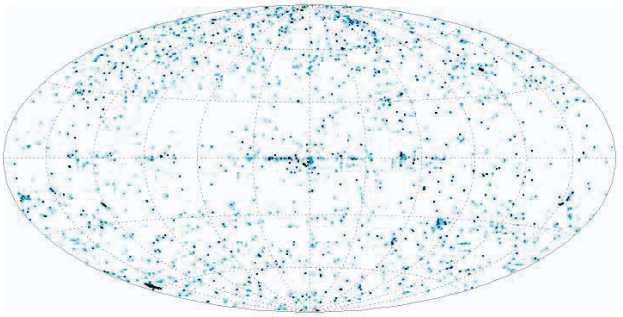

Fig. 1. Hammer-Aitoff equal area projection in the galactic coordinates of the fields used in the 2XMM catalogue.

have achieved reasonably clean data set by selecting the area used for the source detection, as well as further manual screening (Watson et al. 2008).

The sensitivity varies by more than an order of magnitude, depending on the exposure and coverage of the three EPIC instruments of each area of interest, from observation to observation. The limiting flux for the pn camera, which is the most sensitive one among all three EPIC instruments, are $[1, 9, 25] \times 10^{-14}\,\mathrm{erg\,cm^{-2}\,s^{-1}}$ for >90 per cent sky coverage in the soft (0.5–2 keV), hard (2–12 keV) and hardest (4.5–12 keV) bands, respectively.

2.2. The catalogued sources

The 2XMM catalogue contains 246,897 detections, of which 191,870 sources are regarded as unique. Of these, 27,522 sources were observed more than once. Of these unique sources, ~ 1400 sources are plausibly associated with the intended target. This means that $< 1\%$ of 2XMM sources are the target of the observation. We should note however that the number of sources *associated* with the target can be much larger in a few observations, such as nearby galaxies.

The catalogue contains various parameters, such as hardness ratio, including the source matching with the external databases (Watson et al. 2008). We have also extracted and released the plots of time-series and spectra for the sources that have enough statistics.

The 2XMM catalogue contains the entry of the spatial extent of each source, and indicates that 20,837 detections out of 246,897 are suggested to be extended. However due to much more degree of freedom in the case of extended sources in comparison with point-like sources, this figure should not be taken straightforwardly. Indeed the *flag* entry in the catalogue shows that roughly a half of these detections of extended sources are suspicious. Nevertheless a further close look revealed that the rate of spurious detections of extended sources seems to be reasonably low (< 5 per cent), if the clean detections (as stated in flagging) with reasonably high detection significance are chosen (Watson et al. 2008).

The 2XMM catalogue contains detections down to an EPIC detection likelihood L of 6. Around 90% of the detections have $L > 8$ and $\sim 82\%$ have $L > 10$. We have performed the Monte-Carlo simulation to investigate the false detection rate (Fig. 3). We found that the rates of the false detection for point sources in quiet high-galactic-latitude fields are roughly $\sim [2, 1, 0.5]$ per cent for the chosen minimum likelihood of $L_{\mathrm{min}} \geq [6, 8, 10]$, respectively, and that these rates are approximately constant over the range of exposures of each observation. The further detail is discussed in Watson et al. (2008).

The 2XMM catalogue lists the statistical positional error for each detection and each unique source. In addition we estimated the systematic positional error to be $\sigma_{\mathrm{sys}} = 0.35$ arcsec, based on the study of our data compared with the Sloan Digital Sky Survey (SDSS) DR5 Quasar Catalog (Schneider et al. 2007). The typical value for the statistical error is ~ 0.6 arcsec. Therefore

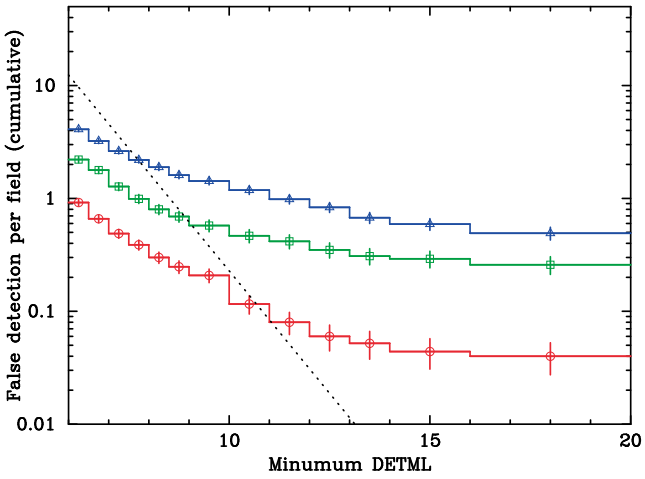

Fig. 3. The number of false detections per field estimated via simulations for typical high Galactic latitude fields as a function of the minimum likelihood $L_{\rm min}$ for various exposure times. The red circles show the results for exposures of $\sim 70\%$ of the median values, whereas the green squares and blue triangles show those with the exposures of 3 and 10 times higher than that (red ones), respectively. The dotted line represents the theoretical false detection number. This figure is adopted from Fig. 10 in Watson et al. (2008).

the total positional uncertainty is ~ 0.7 arcsec. Although there is a significant tail for the higher end in the statistical error, the majority of the sources have the total positional uncertainty of $\lesssim 2$ arcsec.

2.3. Flux distribution and Log$N$-Log$S$

Fig. 4 demonstrates the flux distribution of point sources in the 2XMM catalogue, where the sources with suspicious detection are excluded. The majority of the sources have the 2–12 keV flux of the order of 10^{-14} erg cm^{-2} s^{-1}, whereas there are a significant number of sources with the flux above 10^{-12} erg cm^{-2} s^{-1}.

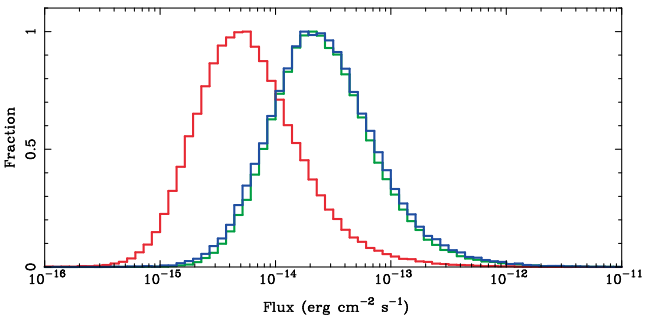

Fig. 4. The flux distribution of point sources in the 2XMM catalogue for the soft (0.5–2 keV; red), hard (2–12 keV; blue) and total (0.5–12 keV; green) bands. The sources with any suspected flag or detection likelihood of less than 10, or that are the targets of each observation, are excluded from this plot. This figure is adopted from Watson et al. (2008).

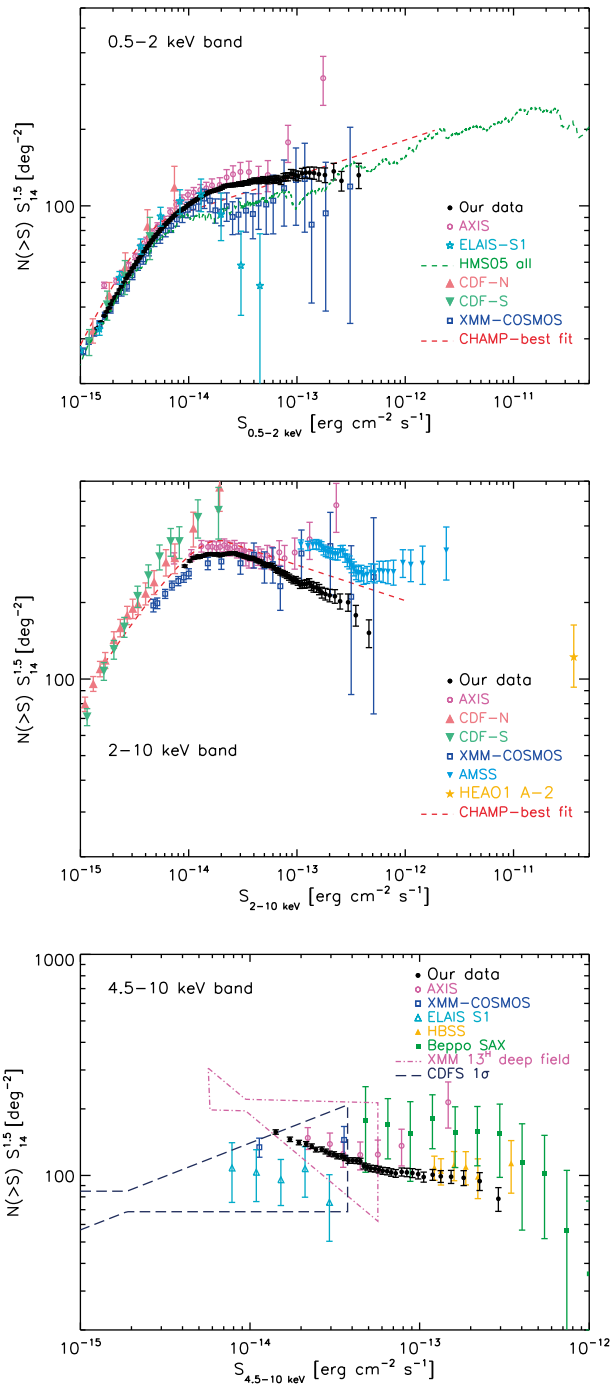

Fig. 5. The Log$N$-Log$S$ relation of the 2XMM sources (black) from the 1129 selected observations of high-latitude quiet fields, together with the results from other X-ray surveys (other colours). They are normalised to the standard Euclidean space for the energy band of 0.5–2, 2–10 keV and 4.5–10 keV for *Top*, *Middle* and *Bottom* panels, respectively. The error bars correspond to 1σ confidence. These figures are adopted from Mateos et al. (2008).

Fig. 4 includes the sources from both low and high galactic latitudes. As a result some of them should have significant galactic absorption in the line of sight, which adds an undesirable complication for scientific study. Thus we have selected the high-galactic-latitude ($|b_{\rm II}| > 20°$) and quiet field of views, which covers the sky area of 132.3 deg^2, and constructed Log$N$-Log$S$ relation plot for the sources in those fields (Fig. 5).

The selected field of views span the entire galactic longitude reasonably evenly in both galactic northern and southern hemispheres. Therefore the dataset should be least affected with the possible cosmic variance. On the other hand the sensitivity is obviously not as good as other modern deep X-ray surveys for fainter sources.

In the soft energy band of below 2 keV, our result confirms the previous ones in other X-ray surveys with better statistics for the medium flux range (10^{-15} – 10^{-12} erg cm^{-2} s^{-1}). In the hard energy band above 2 keV, our result basically confirms the previous ones in better statistics, except for some difference in the flux range of 10^{-13} – 10^{-12} erg cm^{-2} s^{-1}. In the hardest energy band of 4.5–10 keV, where XMM-Newton has the most distinctively higher sensitivity in comparison with other X-ray satellites, our result gives by far the tightest constraints to the Log$N$-Log$S$ relation in the flux range of 10^{-14} – 3×10^{-12} erg cm^{-2} s^{-1}. Comparison with the popular synthesis models suggests that the models may overpredict the number of faint absorbed AGNs (see Mateos et al. 2008 for detailed discussion).

2.4. Availability

The full 2XMM catalogue contains 297 columns (Watson et al. 2008) for each detection. The primary site for it is our XMM-SSC webpage:
http://xmmssc-www.star.le.ac.uk/Catalogue/ . It provides the full documentation and the hyper-links to the other hosting sites, such as XCAT and GSFC.

Associated with the catalogue table, an extensive range of data products such as the EPIC images from each observation and the spectra and time-series data when available, namely when a detection has enough statistics, are provided from the following websites:

ESA/XSA
http://xmm.esac.esa.int/xsa/

LEDAS
http://www.ledas.ac.uk/xmm/2xmmlink.html

The latter also supplies a single HTML summary page for each detection, which gives the key parameters including those for the corresponding unique source, as well as the hyper-links to the external databases.

2.5. Ongoing works of the XMM catalogues

We, the SSC, are processing further available public observations since the release of the 2XMM catalogue. It is expected that roughly ∼35,000 sources per year will be detected in XMM-Newton observations.

We are in the final stage of compiling the incremental 2XMM catalogue (2XMMi) that contains the detections from roughly one-year worth new observations in addition to all the detections in the 2XMM catalogue. The 2XMMi catalogue includes 289,083 detections, namely the increase by ∼42,000 detections since the 2XMM catalogue. It will be released in the end of August 2008.

We are also developing the publicly available facility to estimate the upper limit of the XMM-Newton X-ray flux for any given celestial position, when the source was not detected in the observations included in the 2XMM catalogue. The gateway will be set up in the SSC website (see Sec. 2.4.) soon.

3. Time variability of the 2XMM sources

In each observation, we have produced the time-series of each detected source when they have enough count statistics, subtracted the suitable background, and the performed the χ^2-test against the null hypothesis of constancy. We found that ∼10 and ∼5 per cent of the sources among tested for the respective fluxes of $\geq 10^{-11}$ and $\geq 10^{-12}$ erg cm^{-2} s^{-1} are variable during its observation, of which the typical exposure time is 4 hours. This difference in the rate of variable sources is likely to be due to the statistics of the sources, rather than the nature of the sources itself. There is no indication for any significant trend between the source variability, (spectral) hardness and source position in the galactic latitude.

The identification of these variable sources with the Simbad database reveals that ∼40 per cent of those are identified as non-degenerate stars, ∼13 per cent as either X-ray binaries (including cataclysmic variables) or AGNs, and ∼45 per cent as unidentified in the Simbad database. The completeness of the Simbad database for different object types is known to be highly non-uniform. Hence this can not be the definitive study. However it implies that even non-degenerate stars can be substantially variable.

Among the point-like 2XMM sources with the flux of $> 5 \times 10^{-14}$erg cm^{-2} s^{-1} with good enough statistics and clean detection flag, ∼4700 sources have been observed and detected in more than one occasion. We found that 42 per cent of those ∼4700 sources shows the significant variability between observations. In particular 99 per cent of the sources that show the short-term (within a single observation) variability are found to show the long-term (spanning multi-observations) variability as well.

4. Use of the 2XMM catalogue with the MAXI

The MAXI will monitor almost the entire sky every 90 minutes with the unprecedented sensitivity as the all-

sky X-ray monitor (e.g., Matsuoka in this proceeding). Therefore it is expected to see a number of sources, particularly transient sources, that have never been detected before.

However due to its poor spatial resolution of the MAXI, it will be sometimes not a trivial task to resolve sources in congested fields, such as the Galactic plane. If the region has ever been observed with XMM-Newton, the 2XMM catalogue will be a useful template to estimate the contribution from weak sources with the MAXI field of view, the flux of each of which may be below the detection threshold of the MAXI scan.

In case of the detection of new transient sources, the study of the X-ray counterpart (with much greater precision for the position), its nature in quiescence and its possible past recurrent activity are possible with the use of the 2XMM catalogue, providing the source is in the field of views included in the 2XMM catalogue. The 2XMM catalogue also provides the information of the possible counterpart in other wavelengths.

Another definite possibility is the statistical study of the characteristics of the X-ray sources. The MAXI will provide the statistical nature of the X-ray sources, such as the flux and time-scale of the variability in the brighter side, whereas the 2XMM catalogue, being the largest X-ray source catalogue, offers that in the fainter side, as a good complementary work with the MAXI.

5. Summary

We have constructed and released the 2XMM catalogue, the largest ever X-ray source catalogue. It contains 246,897 detections with XMM-Newton, of which 191,870 sources are unique. The sources in the 2XMM catalogue were in principle serendipitously detected. Although the list of 191,870 unique sources include the targets of each observation, the fraction is less than 1 per cent.

$\gtrsim$90 per cent of these sources are point-like. The false detection rate for the point-like sources in a quiet high-galactic-latitude field is $\sim$2 per cent, while users of the 2XMM catalogue can easily apply more strict condition to filter suspicious detections based on the detection likelihood of each source provided in the catalogue.

The 2XMM catalogue gives much tighter constraints to the Log$N$-Log$S$ relation of the X-ray source distribution, which implies the need of some change or modification in the population synthesis models. It is not inconsistent with the previous observational results.

We have found time variability of all sorts of point sources spread across the entire sky. This confirms that the time variability is a very common nature for most, if not all, of the X-ray point sources.

The incremental XMM catalogue, the 2XMMi catalogue, will have been released by the time this paper is published.

We are grateful for the contributions to this project made by our colleagues at the XMM-Newton Science Operations Centre at ESA's European Space Astronomy Centre (ESAC) in Spain. We would appreciate the cooperations by other members of the SSC and XMM-Newton scientists, including J. Ballet, X. Barcons, D. Barret, T. Boller, H. Brunner, M. Brusa, A. Caccianiga, F. J. Carrera, M. Ceballos, R. Della Ceca, M. Denby, S. Dupuy, S. Farrell, F. Fraschetti, M. J. Freyberg, P. Guillout, V. Hambaryan, T. Maccacaro, B. Mathiesen, R. McMahon, L. Michel, C. Motch, M. Page, M.W. Pakull, W. Pietsch, R. Saxton, A. Schwope, S. Sembay, P. Severgnini, M. Simpson, G. Sironi, G. Stewart, R. Warwick, N. Webb, R. West, D. Worrall and W. Yuan.

References

Mateos S. et al. 2008 A&A., submitted
Matsuoka M. 2008, in this proceeding
Schneider D.P. et al. 2007 AJ., 134, 102
Ueda Y. et al. 2005, ApJS., 161, 185
Voges W. et al. 1999, A&A., 349, 389
Voges W. et al. 2000, IAU Circ., 7432, 1
Watson M.G. et al. 2008 A&A., submitted (arXiv:0807.1067)

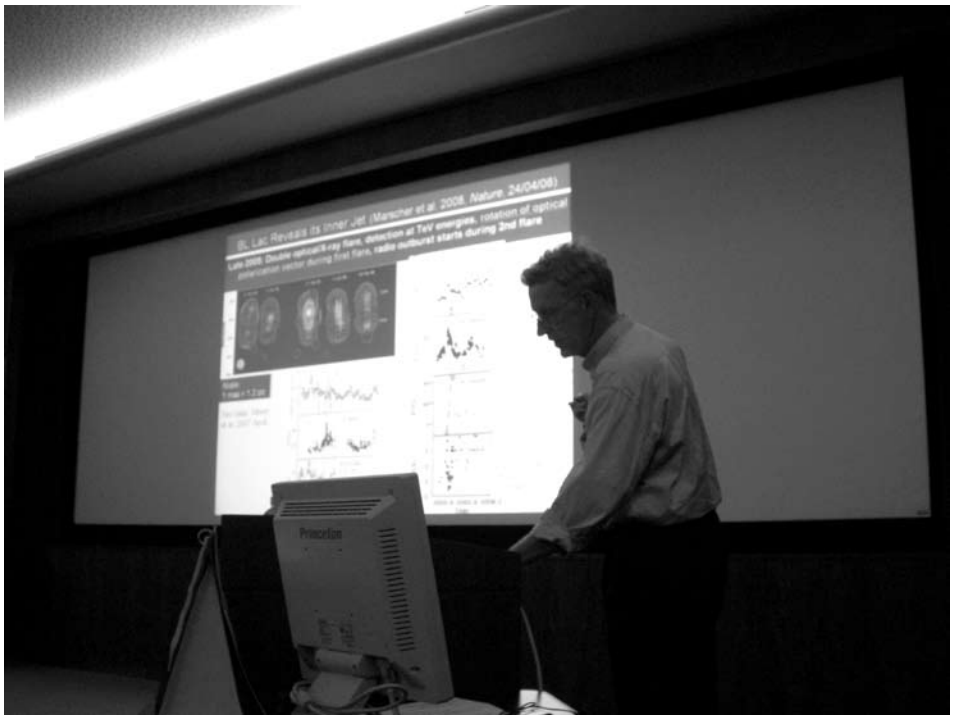

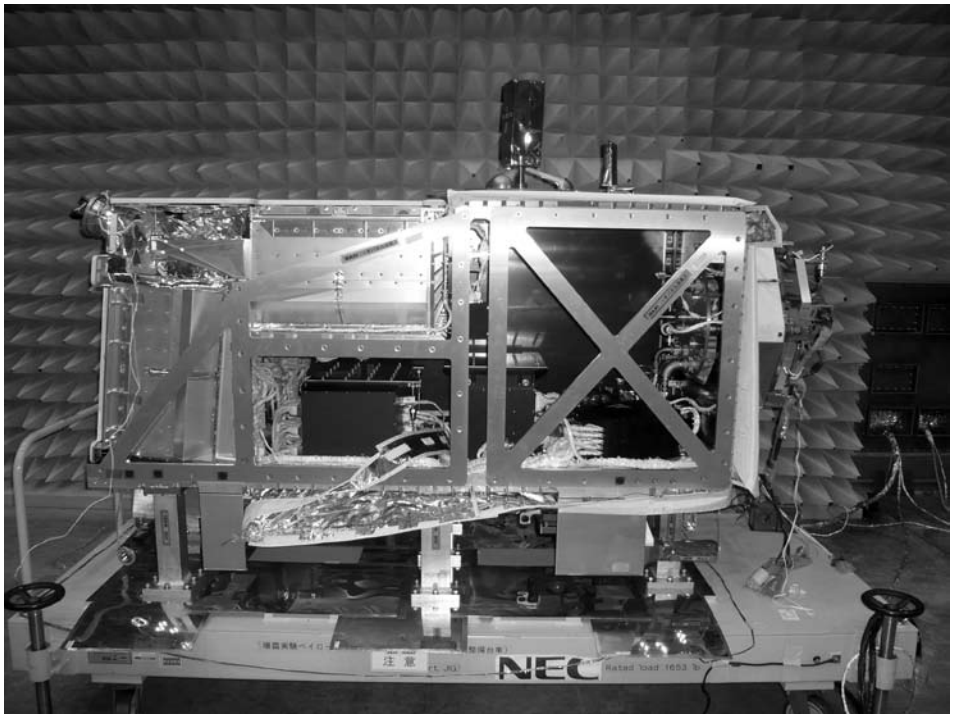

Probing a Supermassive Binary Black Hole with MAXI

Hayasaki Kimitake[1], Isobe Naoki[2], Sudou Hiroshi[3], Seta Hiromi[2] and Mineshige Shin[4]

[1]Yukawa Institute for Theoretical Physics, Kyoto University,
Oiwake-cho, Kitashirakawa, Sakyo-ku, Kyoto 606-8502, Japan
[2]RIKEN, 2-1 Hirosawa, Wako, Saitama 351-0198, Japan
[3]Faculty of Engineering, Gifu University, 1-1 Yanagido, Gifu 501-1193, Japan
[4]Department of Astronomy, Kyoto University,
Oiwake-cho, Kitashirakawa, Sakyo-ku, Kyoto 606-8502, Japan
E-mail(HK): kimitake@yukawa.kyoto-u.ac.jp

Abstract

Supermassive black holes are considered to have been coevolved with their host galaxies. This strongly suggests that black hole growth is mainly caused by black hole mergers and subsequent accretion of gas in the course of the galaxy merger. If so, a supermassive binary black hole with a sub-parsec scale separation are inevitably formed before the black holes merge by emitting gravitational radiation. However, there is yet no definitive observational evidence for the supermassive binary black hole in spite of some claims (e.g. quasi-periodic light variations from OJ287). In this paper, we study the smoothed particle hydrodynamics simulations of accretion flows around the sub-parsec scale binary black hole with a moderate orbital eccentricity. In the simulations we consider a triple-disk system composing of two accretion disks around black holes and one circumbinary disk surrounding the two. Here, the circumbinary disk works as a mass reservoir. We confirm that X-ray luminosity from accretion disks significantly depends on the orbital phase because of the eccentric orbit of the binary black hole. Note also that the X-ray luminosity exhibits the double peaks every binary orbit in the case of binary black hole with low mass ratios. Such properties could not only explain a basic feature of light variations from OJ287 but also provide a potentially important observational signature of the sub-parsec binary black hole in active galactic nuclei with MAXI.

Key words: black hole physics – accretion, accretion disks – binaries:general – galaxies:nuclei

1. Introduction

Most galaxies are thought to have supermassive black holes at their centers (Kormendy & Richstone 1995). Supermassive black holes play an important role not only in the activities of active galactic nuclei and quasars but also in the formation and global evolution of galaxies (Margorrian et al. 1998; Ferrarese & Merritt 2000; Grblack holeardt et al. 2000). Since galaxies are well-known to evolve through frequent mergers, this strongly suggests that black hole growth is mainly caused by black hole mergers and subsequent accretion of gas (Yu & Tremaine 2002). If so, a supermassive binary black hole with a sub-parsec scale separation are inevitably formed before two black holes merge by emitting gravitational radiation (Begelman et al. 1980; Milosavljević & Merritt 2001; Mayer et al. 2007).

Despite the general expectation that the binary black hole should form naturally during the course of galaxy formation and evolution, the currently available observational evidence for binary black holes have been largely circumstantial and indirect. These include the detection of X-shaped structures in radio galaxies (Merritt & Ekers 2002), double compact cores with a flat radio spectrum (Rodriguez et al. 2006), and close pairs of active galactic nuclei such as that seen in NGC 6240 (Komossa et al. 2003). As these systems evolve, we expect that their black holes would eventually form a strongly gravitationally bound binary on sub-parsec scales. Such small-scale binaries have been inferred to be present from the quasi-periodic outbursts detected in OJ 287 (Sillanpää 1988; Valtonen et al. 2008) and the proper motions seen toward the compact radio core in 3C 66B (Sudou et al. 2003), but the interpretation of neither case is unambiguous. Quite recently, Bogdanović et al. (2008) and Dotti et al. (2008) proposed the hypothesis that SDSSJO92712.65+294344.0 is a massive binary black hole, by interpreting the observed emission line features as those arising from the mass-transfer stream from the circumbinary disk.

In theoretical view, Hayasaki et al. (2007), using a smoothed particle hydrodynamics (SPH) code (Benz 1990a,b; Bate et al. 1995), studied the accretion flow

from a circumbinary disk onto the supermassive binary black hole with a semi-major axis $a = 0.1$ pc. They found that mass transfer occurs from the circumbinary disk to the supermassive binary black hole in two steps. First, the initially circularized circumbinary disk becomes elongated due to the azimuthal $m = 2$ component of the binary potential. The gas density then grows at the two points closest from the black holes. Next, when the gas reaches beyond the potential barrier of the binary, inflow is initiated so that the gas freely inspirals onto each of the black holes. The viscosity of the circumbinary disk is ineffective for the mass transfer process because the viscous timescale is much longer than the orbital period. For binary black hole systems on sub-parsec scales, the viscous timescale of the circumbinary disk can be written as

$$\frac{\tau_{\rm vis}}{P_{\rm orb}} \sim 7.31 \times 10^5 \left(\frac{0.1}{\alpha_{\rm SS}}\right)\left(\frac{10^3\ {\rm K}}{T}\right)\left(\frac{M_{\rm bh}}{10^8\ M_\odot}\right)\left(\frac{0.1\ {\rm pc}}{a}\right), \quad (1)$$

where $\alpha_{\rm SS} = 0.1$ is the Shakura-Sunyaev viscosity parameter (Shakura & Sunyaev 1973), $M_{\rm bh}$ is the total black hole mass, and a is the semi-major axis, respectively. The inner edge of the circumbinary disk is assumed to be at the $1:3$ resonance ($\sim 2.08a$), where the viscous force is balanced with the tidal/resonant force of the binary (Artymowiciz & Lubow 1994). The circumbinary disk is assumed to follow an isothermal equation of state.

The mass transfer rate significantly depends on the binary orbital phase in eccentric binaries, whereas it shows little variation with orbital phase in circular binaries. In both cases the mass transfer from the circumbinary disk to the central binary inevitably leads to the formation of an accretion disk around each of the black holes. Hayasaki et al. (2008) have, furthermore, performed a new set of simulations at higher resolution with an energy equation based on the blackbody assumption, adopting the same set of binary orbital parameters we had previously used (Hayasaki et al. 2007) ($a = 0.1$ pc, eccentricity $e = 0.5$, and mass ratio $q = 1.0$). By this two-stage simulation, it is possible to investigate the behavior of accretion disks around black holes.

2. Periodic light variations from two accretion disks

We describe the detail of the first-stage simulation as in Hayasaki et al. (2008). In order to reduce computational time and to significantly improve the resolution, we confine the simulations only to the accretion flow around the supermassive binary black hole by supplying mass periodically from the outer boundary condition, which is constructed from the SPH particles captured by the black holes (Hayasaki et al. 2007). The capture radii correspond to the effective gravitational radii $0.8r_{\rm L}$, where $r_{\rm L}$ is the innermost common gravitational radius of the binary potential for a circular binary. The number of SPH particles is $37,200$ at the end of the simulation. To reduce the fluctuation noise, the data are folded on the orbital period over $0 \le t \le 100$, where the unit of time is $P_{\rm orb} \simeq 296$ yr. The orbital phase dependence of the mass transfer rate obtained by this procedure is shown by the solid line in Figure 1.

In the second-stage simulation, we model the mass transfer process from the circumbinary disk to the supermassive binary black hole by injecting gas particles at a given phase-dependent rate We assume that the gravitational energy of the particles is converted to heat by the standard SPH viscosity (Monaghan & Gingold 1983). and is locally radiated away as a blackbody. The two black holes have an accretion radius $5 \times 10^{-3}a$, which is the radius of the inner boundary of the simulation that corresponds to $r_{\rm in} \simeq 104r_{\rm bh}$, where $r_{\rm bh}$ is the Schwarzschild radius of a black hole with mass $5.0 \times 10^7\ M_\odot$. The mass accretion rate at this radius is shown by the dotted line in Figure 1. It is noted that from the figure that the mass accretion rate shows a single peak every orbital period. The X-ray luminosity corresponding to the mass accretion rate is significantly sub-Eddington.

Supermassive binary black holes are generally considered to have unequal black hole masses. For example, a binary black hole system in OJ287 is indicated to have an extreme mass ratio $q \le 0.1$ (Valtonen et al. 2008). We have, therefore, performed the two-stage simulations with the shorter semi-major axis, $a = 0.01$ pc, the orbital eccentricity $e = 0.5$, and the mass ratio $q = 0.1$ (Hayasaki & Mineshige 2008). In the first-stage simulation, we calculate the mass transfer rate from the circumbinary disk to the effective gravitational radius of each black hole as the averaged values over $40 \le t \le 100$, where the unit of time is $P_{\rm orb} \simeq 9.4$ yr. The orbital phase dependence of the mass transfer rate of the primary black hole (hereafter, the primary transfer rate), and of the mass transfer rate of the secondary black hole (hereafter, the secondary transfer rate) are shown by the dashed line and the solid line in Figure 2*a*, respectively.

Next, we have performed the second-stage simulation with both the primary transfer rate and the secondary transfer rate. Here, each black hole has an accretion radius $5 \times 10^{-3}a$. The mass accretion rates at this radius are also shown in Figure 2*a*, where the dotted line shows the mass accretion rate on to the primary black hole (hereafter, the primary accretion rate), and the dash-dotted line shows the mass-accretion rate on to the secondary black hole (hereafter, the secondary accretion rate). Figure 2*b* shows the snapshot of the accretion flow around the supermassive binary black hole at the periastron of the 10th binary orbit. The white cross and

the white asterisk on the density map indicate the mass supply points from the circumbinary disk to the primary black hole and from the circumbinary disk to the secondary black hole, respectively.

From the figures, we confirm the formation of each accretion disk around black hole. These disks are significantly non-axisymmetric. The accretion disk around the primary black hole is much larger than the accretion disk around the secondary black hole. While the averaged secondary transfer rate during one orbital period is about 4.8 times higher than that of the primary transfer rate, the averaged secondary accretion rate are about 2.7 times higher than that of the primary accretion rate. These indicate that the system does not reach the quasi-steady state yet. Since the secondary accretion rate shows double peaks during one orbital period and is larger than the primary accretion rate with a single peak, the X-ray light variation would exhibit double peaks every orbit.

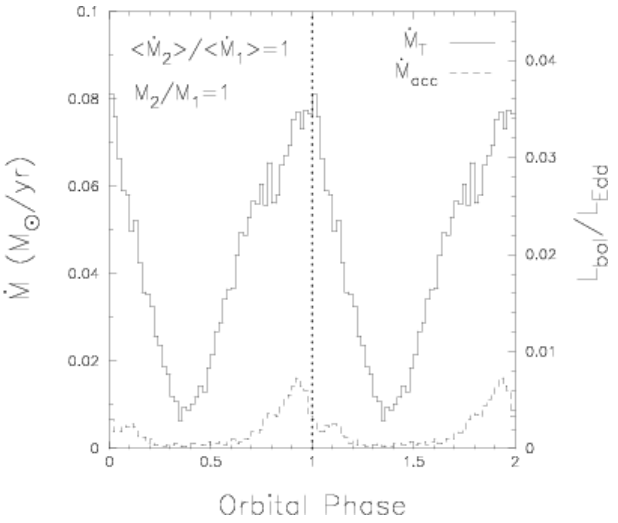

Fig. 1. Orbital phase dependence of the mass transfer rate $\dot{M}_{\rm T}$ from the circumbinary disks to the effective common gravitational radius of the black holes, and of the mass accretion rate $\dot{M}_{\rm acc}$ at the inner simulation boundary $r_{\rm in} = 5.0 \times 10^{-3} a$, of the primary black hole. The right axis shows the bolometric luminosity $L_{\rm bol}$ corresponding to the mass transfer and mass accretion rate with the energy conversion $\eta = 0.1$, normalized by the Eddington luminosity $L_{\rm Edd}$ for a total black hole mass $M_{\rm bh} = 1.0 \times 10^8\ M_\odot$, where η is defined by $L_{\rm bol} = \eta \dot{M}_{\rm bh} c^2$.

3. Summary and Discussion

We have studied the mass transfer process and/or mass accretion process around the supermassive binary black hole in the equal mass binary and unequal mass binary with the low mass ratio. In the equal mass binary, the X-ray lightcurve has a single peak during one orbital period, whereas the X-ray lightcurve shows double peaks in the binary black hole with low mass ratio $q = 0.1$. Each X-ray luminosity is significantly sub-Eddington in the early stage of the evolution of the accretion disks.

The orbital periods of the fiducial cases simulated here are prohibitively long for the lifetime of the MAXI $\sim 5\,$yr, even the case with $a = 0.01\,$pc. However, the generic features of the triple-disk BBH system discussed would remain unchanged for other orbital periods, which, from Kepler's third law, can be made shorter by reducing the binary separation and/or increasing the masses of the black holes. In addition, Hayasaki (2008) recently showed that the binary has enough a short period to coalesce within a Hubble time due to the emission of gravitational radiation by disk-binary interaction in the triple disk system. This study suggest that a supermassive binary black hole with an orbital period $\sim P_{\rm orb} = 1\,$yr exists in an active galactic nuclei. We expect that such the very short binary black hole will be detected by MAXI.

The authors thank YITP in Kyoto University, where this work was extensively discussed during the YITP-W-05-11 on September 20–21, 2005, the YITP-W-06-20 on February 13–15, 2007, and the YITP-W-07-19 on January 8-11, 2008. The simulations reported here were performed using the facility at the Centre for Astrophysics & Supercomputing at Swinburne University of Technology, Australia and at YITP in Kyoto University. This work has been supported in part by the Grants-in-Aid of the Ministry of Education, Science, Culture, and Sport and Technology (MEXT; 30374218 K.H., 14079205 K.H. & S.M.), and by the Grant-in-Aid for the 21st Century COE Scientific Research Programs on "Topological Science and Technology" and by the Grant-in-Aid for the Global COE Program "The Next Generation of Physics, Spun from Universality and Emergence" from the Ministry of Education, Culture, Sports, Science and Technology (MEXT) of Japan.

References

Artymowicz, P., & Lubow, S. H. 1994 ApJ., 421, 651

Bate, M. R., Bonnel, I. A., & Price, N. M. 1995 MNRAS., 277, 362

Begelman, M. C., Blandford, R. D., & Rees, M. J. 1980, Nature, 287, 307

Benz, W. 1990, in Numerical Modeling of Nonlinear Stellar Pulsations: Problems and Prospects, ed. R. J. Buchler (Dordrecht: Kluwer), 269

Benz, W., Bowers, R. L., Cameron, A. G. W., & Press, W. H. 1990 ApJ., 348, 647

Bogdanović, T., Eracleous, M., & Sigurdsson, S, 2008 (arXive:0809.3262)

Dotti, M., Montuori, C., Decarli, R., Volonteri, M., Colpi, M., & F. Haardt, 2008 (arXive:0809.3446)

Ferrarese, L., & Merritt, D. 2000 ApJ., 539, L9

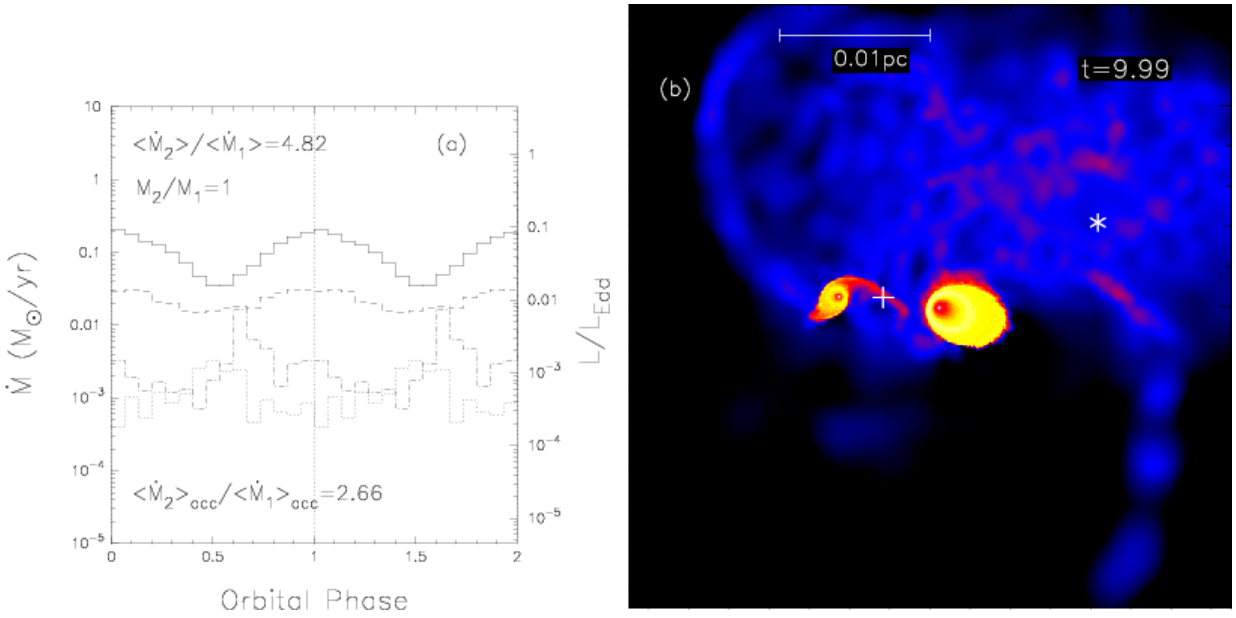

Fig. 2. *(a)* Orbital phase dependence of the mass transfer rate from the circumbinary disk to the effective common gravitational radius of each black hole, and of the mass accretion rate at the inner simulation boundary $r_{\rm in} = 5.0 \times 10^{-3} a$, of the black holes. The solid-line and dashed line show the mass transfer rate to the secondary black hole and the mass transfer rate to the primary black hole, respectively. The dotted line and the dash-dotted line show the mass accretion rate to the secondary black hole and the mass accretion rate to the primary black hole, respectively. In the right side of the panel, $< \dot{M}_2 > / < \dot{M}_1 >$, M_2/M_1, and $< \dot{M}_2 >_{\rm acc} / < \dot{M}_1 >_{\rm acc}$ show the ratio of the mass transfer rates, the mass ratio, and the ratio of the mass accretion rates. *(b)* Density maps of the two accretion disks around the supermassive binary black hole rotating with $P_{\rm orb} \sim 9.4\,{\rm yr}$, $e = 0.5$, and $q = 0.1$ at the periastron. Panel shows on a logarithmic scale the surface density contours over a range of 5 orders of magnitude. The white cross and the white asterisk indicate the positions of the mass input by the boundary condition. The supermassive binary black hole is rotating in a counterclockwise direction. The time and a length scale are shown in the top-right of the panel and the top-left of the panel, respectively. The total number of SPH particles is $112,297$ in the end of the simulation.

Hayasaki, K., Mineshige, S., & Sudou, H. 2007 PASJ., 59, 427

Hayasaki, K., Mineshige, S. & Ho, C.L. 2008 ApJ., 682, 1134

Hayasaki, K & Mineshige, S. 2008 Origin of matter and evolution of galaxies: The 10th International Symposium on Origin of Matter and Evolution of Galaxies: From the Dawn of Universe to the Formation of Solar System. (AIP Conference Proceedings), 1016, 406

Hayasaki, K. 2008 PASJ., in press (arXive0805.3408)

Komossa, S., Burwitz, V., Hasinger, G., Predehl, P., Kaastra, J. S., & Ikebe, Y. 2003 ApJ., 582, L15

Kormendy, J. & Richstone, D. 1995 ARA&A, 33, 581

Magorrian, J., et al. 1998 AJ., 115, 2285

Mayer, L., Kazantzidis, S., Madau, P., Colpi, M., Quinn, T., & Wadsley, J. 2007, Science, 316, 1874

Merritt, D., & Ekers, R. D. 2002, Science, 297, 1310

Milosavljević, M., & Merritt, D. 2001 ApJ., 563, 34

Monaghan J. J., & Gingold, R. A. 1983, J. Comput. Phys., 52, 374

Rodriguez, C., Taylor, G. B., Zavala, R. T., Peck, A. B., Pollack, L. K., & Romani, R. W. 2006 ApJ., 646, 49

Roos, N. 1981 A&A., 104, 218

Shakura, N. I., & Sunyaev, R. A. 1973 A&A., 24, 337

Sillanpää, A., Haarala, S., Valtonen, M., Sundelius, B., & Byrd, G. G. 1988 ApJ., 325, 628

Sudou, H., Iguchi, S., Muratai, Y., & Taniguchi, T. 2003, Science, 300, 1263

Valtonen, M. J., Lehto, H. J., Nilsson, K., Heidt, J., Takalo, L. O., Sillanpää, A., Villforth, C., Kidger, M., Poyner, G., Pursimo, T., Zola, S., Wu, J.-H., Zhou, X., Sadakane, K., Drozdz, M., Koziel, D., Marchev, D., Ogloza, W., Porowski, C., Siwak, M., Stachowski, G.; Winiarski, M., Hentunen, V.-P., Nissinen, M., Liakos, A., Dogru, S. 2008 Nature., 452, 851

Yu, Q., & Tremaine, S. 2002 MNRAS., 335, 965

The Blazar Sequence and the Cosmic Gamma-Ray Background Radiation

Yoshiyuki Inoue[1], Tomonori Totani[1] and Takuro Narumoto[1]

[1] Department of Astronomy, Kyoto University, Kitashirakawa, Sakyo-ku, Kyoto 606-8502, Japan
E-mail(YI): yinoue@kusastro.kyoto-u.ac.jp

Abstract

We present a new model of the blazar gamma-ray luminosity function (GLF) based on the EGRET blazar data, and study the contribution to extragalactic gamma-ray background (EGRB) radiation, taking into account the unified sequence of blazar spectral energy distribution (SED). This enables us to predict the EGRB spectrum in more realistic way than previous studies. We construct a model spectrum of EGRB by summing up the blazar EGRB component and another non-blazar AGN component, which is dominant in the cosmic X-ray background radiation. The non-blazar component has a nonthermal steep tail in EGRB spectrum, and it is dominant against the blazar component up to ~ 100 MeV. The model EGRB flux and spectrum are in nice agreement with the observed data from X-ray to 1 GeV band. These results indicate that AGNs including blazars are the major contributor to the high energy background radiation from X-ray to gamma-ray bands. Quantitative predictions for GLAST are also made.

Key words: workshop: proceedings — LaTeX2.09: style file — instructions

1. introduction

The origin of the extragalactic diffuse gamma-ray background (EGRB) has been argued in astrophysics for a long time. The EGRB spectrum was first discovered by the *SAS 2* satellite (Fichtel, Simpson, & Thompson 1978; Thompson & Fichtel 1982). Subsequently, the EGRB spectrum was confirmed up to an energy ~ 50 GeV by EGRET on board the Compton Gamma Ray Observatory. The EGRB flux is about 1×10^{-5} photons cm^{-2} s^{-1} sr^{-1} above 100 MeV and the spectrum is approximately a power law with a photon index of -2 in a wide range of $\sim$30 MeV – 100 GeV (Sreekumar et al. 1998; Strong, Moskalenko, & Reimer 2004a). It should be noted that, however, the EGRB measurement is strongly dependent on the modeling of foreground emission, which is dominated by the diffuse Galactic emission from cosmic-ray interactions in the Galactic disk region and must carefully be subtracted from the total background flux (Keshet, Waxman, & Loeb 2004; Strong, Moskalenko, & Reimer 2004b; Kamae, Abe, & Koi 2005).

Although several sources of gamma-rays (e.g., clusters of galaxies or dark matter annihilation) have been proposed as a significant contributor to EGRB [see, e.g., Narumoto & Totani (2006) and references therein], active galactic nuclei (AGNs) of the blazar class have been thought as the primary candidate for the origin of EGRB, since almost all of the extragalactic gamma-ray sources detected by EGRET are blazars. The blazar contribution to EGRB have been estimated by a number of papers (Padovani et al. 1993; Stecker, Salamon, & Malkan 1993; Salamon & Stecker 1994; Chiang et al. 1995; Stecker & Salamon 1996; Chiang & Mukherjee 1998; Mücke & Pohl 2000; Narumoto & Totani 2006; Giommi et al. 2006; Dermer 2007; Kneiske & Mannheim 2008).

Stecker & Salamon (1996) estimated that 100% of the EGRB radiation can be explained by blazars. However, their model was constructed based on the blazar luminosity function in radio bands, without comparison with the gamma-ray flux and redshift distributions of the EGRET blazars. Therefore it was not certain whether their model was statistically consistent with the EGRET blazar data. Chiang & Mukherjee (1998) found that only 20–40% of EGRB can be accounted for by blazars, taking into account the EGRET blazar data and assuming pure luminosity evolution for blazar LF. Narumoto & Totani (2006, hereafter NT06) extended this kind of analysis by introducing a luminosity-dependent density evolution (LDDE) of blazar GLF, which is motivated from the evolution of X-ray luminosity function (XLF) of AGNs. NT06 found that the LDDE model fits to the EGRET blazar data better than PLE models, and also confirmed that only 25–50% of EGRB can be explained by blazars. In most of these studies, however, it was assumed that the spectral energy distribution (SED) of blazars is a simple power-law, or a broken power-law with no dependence on the blazar luminosity.

Blazar SED has been theoretically and observationally studied in detail(Ghisellini & Tavecchio 2008, and

references therein). Blazar emission is widely believed to be the sum of the synchrotron and inverse Compton emission components produced by the same nonthermal electron population accelerated in relativistic jets. Multi-wavelength observational studies from radio to γ-ray bands have indicated an interesting feature in blazar SEDs; the synchrotron and Compton peak photon energies decrease as the bolometric luminosity increases (Fossati et al. 1997, 1998; Donato et al. 2001, Ghisellini & Tavecchio 2008; but see also Padovani et al. 2007). This is often called as the blazar SED sequence.

Here we predict the EGRB flux and spectrum from blazars, by constructing a blazar GLF model that is consistent with the flux and redshift distributions of the EGRET blazars, based on the LDDE model and the blazar SED sequence. By introducing the blazar SED sequence, we can make a reasonable prediction of the EGRB spectrum for the first time. Recently, Inoue, Totani, & Ueda (2008) has showed that the EGRB in the MeV band can naturally be explained by normal (i.e., non-blazar) AGNs that are the origin of the cosmic X-ray background. This MeV background component extends to ~ 100 MeV by the Comptonization photons produced by nonthermal electrons in hot coronae. Therefore, it should also contribute to the EGRB at ≤ 1 GeV. We will also make quantitative predictions for the Gamma-Ray Large Area Space Telescope (GLAST) that has successfully been launched on June 11th, 2008. Throughout this paper, we adopt the standard cosmological parameters of $(h, \Omega_M, \Omega_\Lambda)$=(0.7,0.3,0.7).

2. The Blazar SED Sequence

Fossati et al. (1997, 1998) and Donato et al. (2001, hereafter D01) constructed empirical blazar SED models based on fittings to observed SEDs from radio to γ-ray bands. These models are composed of the two components (synchrotron and Inverse Compton), and each of the two is described by a linear curve at low photon energies and a parabolic curve at high energies.

Here we construct our own SED sequence model mainly based on the SED model of D01, because there is a mathmatical discontinuity in the original D01 model. In this model the two different mathematical fitting formulae are used below and above the luminosity $\nu L_\nu = 10^{43}$ erg s^{-1} at 5GHz, and the luminosity of the inverse-Compton component suddenly changes with a jump at this critical luminosity. Once the blazar luminosity is specified at a reference frequency, this empirical model gives the full blazar SED from radio to gamma-ray bands. In Fig.1 we show this empirical blazar SED sequence model in comparison with averaged observed SED data (Fossati et al. 1998; D01). We will calculate EGRB with this model of the blazar SED sequence.

3. The Model of Gamma-ray Luminosity Function of Blazars

3.1. Relating Jet Power and X-ray Luminosity of AGNs

The cosmological evolution of X-ray luminosity function of AGNs has been investigated intensively (Ueda et al. 2003 (hereafter U03); Hasinger, Miyaji, & Schmidt 2005 (hereafter H05); Gilli, Comastri, & Hasinger 2007). These studies revealed that AGN XLF is well described with the LDDE model, in which peak redshift of density evolution increases with AGN luminosity. Here we construct two models of blazar GLF based on the two XLFs derived by U03 (in hard X-ray band) and H05 (in soft X-ray band). It is natural to expect that power of blazar jet is correlated with the mass accretion rate to the central super massive black hole, which is also correlated with the X-ray luminosity from accretion disk. Therefore we simply assume that the bolometric luminosity of radiation from jet, P, is proportional to disk X-ray luminosity, L_X. It should be noted that L_X is *not* the observed X-ray luminosity of a blazar having a jet luminosity P. This treatment is observationally supported from the EGRET blazar data, because NT06 found a better agreement between the LDDE model and the data than PLE models, adopting this treatment.

3.2. Model Formulations

In this paper we describe the blazar GLF in terms of νL_ν luminosity at rest frame reference energy $\epsilon_{\rm ref,res} \equiv$ 100 MeV. According to the assumption justified in the previous section, we simply relate the bolometric blazar luminosity P and X-ray luminosity by the parameter q, as $P = 10^q L_X$. Here, we define the disk luminosity L_X to be that in the rest frame 2–10 and 0.5–2 keV bands for the hard XLF (U03) and the soft XLF (H05), respectively. Thus, L_γ and L_X have been related through P.

The blazar GLF is then obtained from the AGN XLF,

$$\rho_\gamma(L_\gamma, z) = \kappa \frac{dL_X}{dL_\gamma} \rho_X(L_X, z), \quad (1)$$

where ρ_X and ρ_γ are the XLF and GLF, i.e., the comoving number densities of AGNs and blazars per unit X-ray and gamma-ray luminosity, respectively. The parameter κ is a normalization factor, representing the fraction of AGNs showing blazar activity. In our GLF model, we adopt the same form in U03 and H05 for ρ_X, as $\rho_X(L_X, z) = \rho_X(L_X, 0) f(L_X, z)$, where $\rho_X(L_X, 0)$ is the AGN XLF at present, which is characterized by the faint-end slope index γ_1, the bright-end slope index γ_2, and the break luminosity L_X^*, given as

$$\rho_X(L_X, 0) = \frac{A_X}{\ln(10) L_X} \left[\left(\frac{L_X}{L_X^*} \right)^{\gamma_1} + \left(\frac{L_X}{L_X^*} \right)^{\gamma_2} \right]^{-1} \quad (2)$$

and $f(L_X, z)$ is the density evolution function.

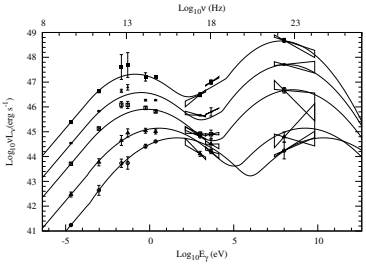

Fig. 1. The average SED of the blazars studied by Fossati et al. (1998), and D01. The each thin solid line represent the modified blazar spectra in this paper.

We set the minimum of the gamma-ray luminosity $L_{\gamma,\rm min}$=10^{43} erg s^{-1}, which is roughly corresponding to the lowest disk X-ray luminosity $L_X = 10^{41.5}$ erg s^{-1} set in U03 and H05, with typical values of the q parameter found in the likelihood analysis below.

4. Gamma-Ray Luminosity Function Determined by the EGRET Blazar Data

We use the maximum likelihood method to search for the best-fit model parameters of the blazar GLF to the distributions of the observed quantities of the EGRET blazars (gamma-ray flux and redshift). The analysis method and the data used are essentially the same as those in NT06.

In the first analysis, we take q as the only one free parameter for the U03 hard XLF and H05 soft XLF, with the XLF model parameters fixed at the values of U03 and H05. These are hereafter called as U03(q) and H05(q) fits, respectively. In the second analysis, we also take the faint-end slope index of XLF, γ_1, as another free parameter in addition to q. These are hereafter called as U03(q, γ_1) and H05(q, γ_1) fits, respectively. The best-fit values for these four fits are shown in Table.1. Figure 2 and Figure 3 show the redshift and luminosity distributions for the best-fit parameters with binned EGRET data. Quantitatively, the chance probabilities of getting the observed deviation estimated from the KS test are also shown in Table 1 and Table 2. Since the best KS test value is in the H05(q, γ_1) GLF model and H05 is the more recent XLF model, we basically discuss with H05(q, γ_1) GLF model below.

Table 1. Best-fit parameters for blazar GLF

	U03(q)	U03(q,γ_1)	H05(q)	H05(q,γ_1)
q	4.90	4.93	5.20	5.29
γ_1	0.86	1.06	0.87	1.26
κ	1.0×10^{-5}	7.6×10^{-6}	3.5×10^{-6}	1.5×10^{-6}

Table 2. KS test probability

	U03(q)	U03(q,γ_1)	H05(q)	H05(q,γ_1)
z	33.5%	25.4%	0.01%	29.3%
L_γ	47.6%	71.8%	1.3%	66.9%

5. The Gamma-Ray Background Spectrum

5.1. the EGRB Spectrum Calculation

We calculate the EGRB spectrum by integrating our blazar SED sequence model in the redshift and luminosity space, using the blazar GLF derived in §3. High energy photons ($>$ 20 GeV) from high redshift are absorbed by the interaction with the cosmic infrared background (CIB) radiation (Salamon & Stecker 1998; Totani & Takeuchi 2002; Kneiske et al. 2004), and $\tau_{\gamma\gamma}(z, \epsilon_\gamma)$ is the optical depth of the universe against this reaction, for a gamma-ray emitted from a source redshift z and received by an observer at $z = 0$ with a photon energy of ϵ_γ. In this paper, we adopted std model in Totani & Takeuchi 2002 for CIB model. Since these interaction creates e^+e^- pair, the created electrons would scatter cosmic microwave background (CMB) radiation (cascading emission) (Aharonian et al. 1994). We calculated the cascading emission as in Kneiske & Mannheim (2008).

5.2. The EGRB Spectrum by Blazars

Figure 4 shows the νF_ν EGRB spectrum predicted by the best-fit GLF model parameters obtained above. Here, we show the total EGRB flux as well as the contributions from different L_γ ranges. This EGRB spectrum is the primary spectrum directly from blazars, because in this calculation the effect of CIB absorption is included but the reprocessed emission by secondary electrons/positrons produced in IGM is not included. The data of *SMM* (Watanabe et al. 1999), COMPTEL (Kappadath et al. 1996) and EGRET (Strong et al. 2004a) are also shown. An important implication here is that the contribution from the so-called MeV blazars, which have their SED peaks at around MeV, is negligible for

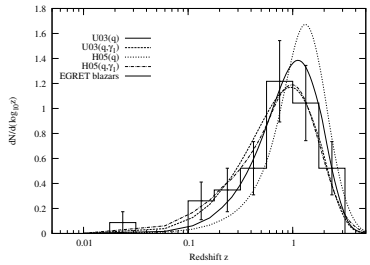

Fig. 2. Redshift distribution of the EGRET blazars. The histogram is the binned EGRET data. The solid, dashed, dotted, and dotted-dashed curves are the best-fit models for the U03(q), H05(q), U(q, γ_1), H05(q, γ_1) GLF model, respectively. The error bars are 1 σ Poisson error.

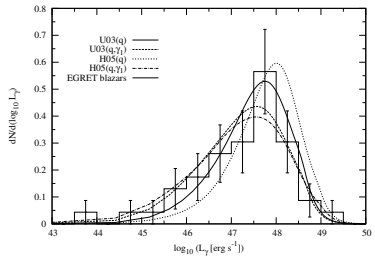

Fig. 3. Same as Fig.2, but for luminosity distribution of blazars of the EGRET blazars.

the MeV gamma-ray background, although such MeV blazars have been suspected as a possible origin of the MeV background. This is because MeV blazars have a large luminosity according to the blazar SED sequence, and the number density of such blazars is small in GLF.

5.3. EGRB from All AGNs and the Origin of EGRB

The total EGRB spectrum from blazars as well as non-blazar AGNs (gamma-rays from accretion disks) is shown in Figure 5. Here, the non-blazar component is the model constructed by Inoue et al. (2008), in which the EGRB in MeV range is explained by nonthermal electrons that is assumed to exist ubiquitously in hot coronae around AGN accretion disks. There is some discrepancy between the MeV EGRB data of *SMM* and COMPTEL, and the origin of this is not clear. Here we use two model parameter sets of $(\Gamma, \gamma_{\rm tr}) = (3.5, 4.4)$ and $(3.8, 4.4)$ in the Inoue et al.'s model, where Γ is the power-law index of nonthermal electron energy distribution and the $\gamma_{\rm tr}$ is the transition electron Lorentz factor above which the nonthermal component becomes dominant. These two parameter sets are chosen so that each of the two fits well to either of the SMM or COMPTEL data.

There is an excess of the EGRB data around GeV, compared with our model prediction. An interesting possibility is that such an excess is due to another component that is completely different from blazars, such as, dark matter annihilation (e.g., Oda, Totani, & Nagashima 2005). However, such GeV excess is also seen in the Galactic gamma-ray background spectrum (Pohl & Esposito 1998; Strong et al. 2004b; de Boer et al. 2005; Kamae, Abe, & Koi 2005), and Stecker, Hunter, & Kniffen (2008) have recently shown that these anomalies around GeV are likely caused by the systematic uncertainty in the calibration of the EGRET detector. They proposed the re-normalization factors for the EGRET data at the energy range from 30 MeV to 10 GeV, to make the EGRET data fit to the theoretically predicted galactic background spectrum. The cosmic X-ray and gamma-ray background spectrum with the EGRET data corrected by these factors is shown in Figure 5. Now the cosmic X-ray and gamma-ray background radiation are nicely explained by the emission from blazars and non-blazar AGNs in the entire range from X-ray to 10 GeV. Based on these results, we conclude that most of the EGRB flux can be explained by blazars and non-blazar AGNs, by GLFs that are consistent with the EGRET blazar data and AGN LF in X-ray band. Our prediction will soon be tested in much more detail by the GLAST data.

6. Predictions for the GLAST mission

Figure 6 shows the cumulative distribution of > 100 MeV photon flux of blazars. The four GLF models of U03(q), U03(q, γ_1), H05(q), and H05(q, γ_1), predict that about 480, 1040, 370, and 1560 blazars should be detected by GLAST, respectively, where we assumed the GLAST sensitivity to be $F_{\rm lim} = 2 \times 10^{-9}$ photons cm^{-2} s^{-1}. We find that the predicted fraction of resolved EGRB flux is $\sim 95\%$ against the total EGRB flux from all blazars

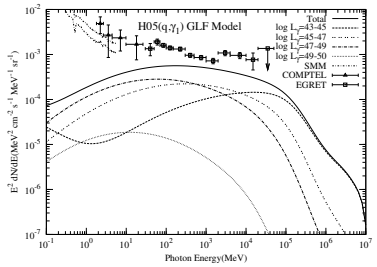

Fig. 4. Predicted spectrum of the cosmic background radiation in gamma-ray bands with H05(q, γ_1) GLF model. The data points of *SMM*(Watanabe et al. 1999), COMPTEL (Kappadath et al. 1996), EGRET (Strong et al. 2004a) experiments are also shown. The solid curves corresponds to the best-fit total background spectrum from blazars and non-blazars.

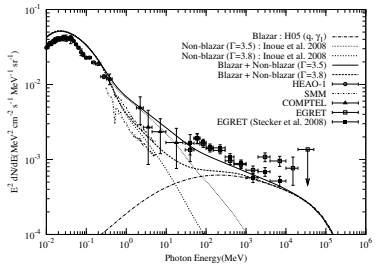

Fig. 5. Predicted spectrum of the cosmic background radiation in X-ray and gamma-ray bands based on our GLF model with H05(q, γ_1) GLF model. The data points of *HEAO-1* (Gruber et al. 1999), *SMM*, COMPTEL, EGRET experiments are also shown. The filled square data shows the correlated EGRET data using the Stecker et al. (2008) method. The solid curves corresponds to the background flux from blazar emission without the absorption effect. The dashed curves corresponds to that with the absorption effect. The dotted curves is the intergalactic cascading emission. The dotted-dashed lines is the total flux.

in the GLF model. Therefore, the EGRB from blazars should practically be resolved by GLAST. However, as seen in Fig. 5, there is a considerable contribution from non-blazar AGNs to the EGRB flux at 100 MeV, and this issue will be discussed below. Furthermore, resolvable fraction of total EGRB flux and of the hole blazar EGRB flux by blazars expected to be detected by GLAST is (37 %, 95 %) for the H05(q,γ_1) GLF model.

7. Conclusions

In this paper, we constructed a new model of the blazar gamma-ray luminosity function (GLF), taking into account the blazar SED sequence and the LDDE luminosity function evolution inferred from X-ray observations of AGNs. An implicit assumption here is that the jet activity of AGNs is associated with the accretion activity, and hence the blazar luminosity function has a similar evolution to that of X-ray AGNs. The GLF model parameters are constrained by fitting to the observed flux and redshift distribution of the EGRET blazars. By this model, for the first time, we can predict the spectrum of the extragalactic gamma-ray background (EGRB), rather than assuming a single power-law spectrum. The contribution from non-blazar AGNs to low energy EGRB is also considered, by using the model of Inoue et al. (2008) for the nonthermal emission from AGN accretion disks extending from MeV to higher energy band with a steep power-law.

The predicted EGRB flux and spectrum by the sum of blazars and non-blazar AGNs is in good agreement with the high energy background radiation data from X-ray to ~ 1 GeV, indicating that the EGRB below 1 GeV can mostly be explained by a combination of blazars and non-blazar AGNs. It should be noted that the contributions from blazars and non-blazar AGNs are comparable at 100 MeV. The previous studies about blazar GLF and EGRB concluded that at most 50% of EGRB can be explained when one constructs a GLF model that is consistent with the EGRET blazar data, and these studies considered the EGRB flux beyond the standard photon energy of EGRET catalog, i.e., 100 MeV. Therefore, previous studies and this work is nicely consistent with each other. At the photon energy range of > 1 GeV, the non-blazar component becomes negligible in the EGRB flux, and hence we predict that most of the EGRB flux should be accounted for by blazars. The EGRB data by Strong et al. (2004a) beyond 2 GeV are significantly higher than our model EGRB spectrum, and this may indicate the existence of another component. However, as argued by Stecker et al. (2008), there may be systematic error in the calibration of EGRET detector around GeV. If we correct the EGRET EGRB data by the factors proposed by Stecker et al. (2008), all the EGRB data are

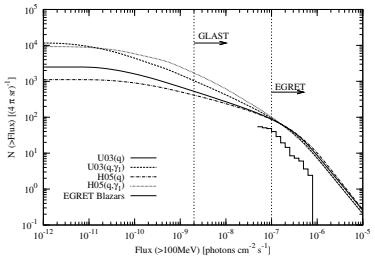

Fig. 6. log N - log F distribution of blazars. Each curve corresponds to U03(q), H05(q), U(q, γ_1), H05(q, γ_1) GLF model. The thin solid line shows the observed distribution of EGRET blazars. The detection limits of EGRET and GLAST are also shown.

in nice agreement with our model predictions. Therefore we conclude that most of the observed high-energy background radiation from X-ray to 10 GeV spanning 7 orders of magnitude in photon energy can be accounted for by AGNs including blazars, and for the moment we do not have to seriously consider another exotic component of EGRB.

We predicted the flux distribution of blazars by our model, and we found that 400–1500 blazars should be detected by GLAST, assuming a sensitivity of $F_{\rm lim} = 2 \times 10^{-9}$ photons cm^{-2} s^{-1} above 100 MeV. We found that GLAST should resolve almost all of the EGRB flux from blazars, with percentages of $\sim 95\%$ depending on the GLF models. Therefore, we have a clear prediction: if blazars and non-blazar AGNs are the dominant sources of EGRB, the GLAST will resolve almost all EGRB flux into discrete sources at photon energies > 1 GeV, while significant unresolved fraction would remain in the low energy band of < 100 MeV.

References

Aharonian, F. A., Coppi, P. S., & Voelk, H. J. 1994, ApJ, 423, L5

Chiang, J., Fichtel, C. E., von Montigny, C., Nolan, P. L., & Petrosian, V. 1995, ApJ, 452, 156

Chiang, J. & Mukherjee, R. 1998, ApJ, 496, 752

de Boer, W., Sander, C., Zhukov, V., Gladyshev, A. V., & Kazakov, D. I. 2005, A&A, 444, 51

Dermer, C. D. 2007, ApJ, 659, 958

Donato, D., Ghisellini, G., Tagliaferri, G., & Fossati, G. 2001, A&A, 375, 739

Fichtel, C. E., Simpson, G. A., & Thompson, D. J. 1978, ApJ, 222, 833

Fossati, G., Celotti, A., Ghisellini, G., & Maraschi, L. 1997, MNRAS, 289, 136

Fossati, G., Maraschi, L., Celotti, A., Comastri, A., & Ghisellini, G. 1998, MNRAS, 299, 433

Ghisellini, G. & Tavecchio, F. 2008, ArXiv e-prints, 802 Gilli, R., Comastri, A., & Hasinger, G. 2007, A&A, 463, 79

Giommi, P., Colafrancesco, S., Cavazzuti, E., Perri, M., & Pittori, C. 2006, A&A, 445, 843

Gruber, D. E., Matteson, J. L., Peterson, L. E., & Jung, G. V. 1999, ApJ, 520, 124

Hasinger, G., Miya ji, T., & Schmidt, M. 2005, A&A, 441, 417

Inoue, Y., Totani, T., & Ueda, Y. 2008, ApJ, 672, L5

Kamae, T., Abe, T., & Koi, T. 2005, ApJ, 620, 244

Kappadath, S. C., et al. 1996, A&AS, 120, C619+

Keshet, U., Waxman, E., & Loeb, A. 2004, Journal of Cosmology and Astro-Particle Physics, 4, 6

Kneiske, T. M., Bretz, T., Mannheim, K., & Hartmann, D. H. 2004, A&A, 413, 807

Kneiske, T. M. & Mannheim, K. 2008, A&A, 479, 41

Mücke, A. & Pohl, M. 2000, MNRAS, 312, 177

Narumoto, T. & Totani, T. 2006, ApJ, 643, 81

Oda, T., Totani, T., & Nagashima, M. 2005, ApJ, 633, L65

Padovani, P., Ghisellini, G., Fabian, A. C., & Celotti, A. 1993, MNRAS, 260, L21

Padovani, P., Giommi, P., Landt, H., & Perlman, E. S. 2007, ApJ, 662, 182

Pavlidou, V. & Venters, T. M. 2008, ApJ, 673, 114

Pohl, M. & Esposito, J. A. 1998, ApJ, 507, 327

Salamon, M. H. & Stecker, F. W. 1994, ApJ, 430, L21

—. 1998, ApJ, 493, 547

Sazonov, S., Revnivtsev, M., Krivonos, R., Churazov, E., & Sunyaev, R. 2007, A&A, 462, 57

Sreekumar, P., et al. 1998, ApJ, 494, 523

Stecker, F. W., Hunter, S. D., & Kni?en, D. A. 2008, Astroparticle Physics, 29, 25

Stecker, F. W. & Salamon, M. H. 1996, ApJ, 464, 600 Stecker, F. W., Salamon, M. H., & Malkan, M. A. 1993, ApJ, 410, L71

Strong, A. W., Moskalenko, I. V., & Reimer, O. 2004a, ApJ, 613, 956

—. 2004b, ApJ, 613, 962

Thompson, D. J. & Fichtel, C. E. 1982, A&A, 109, 352

Totani, T. & Takeuchi, T. T. 2002, ApJ, 570, 470

Ueda, Y., Akiyama, M., Ohta, K., & Miya ji, T. 2003, ApJ, 598, 886

Watanabe, K., Hartmann, D. H., Leising, M. D., & The, L.-S. 1999, ApJ, 516, 285

Multiwavelengh simultaneous observation of Blazar 3C454.3 at the gamma rays flare in November 2007

Y.A.Mori[1], J.Kataoka[1], N.Kawai[1], MITSuME/Suzaku/AGILE team

[1] Tokyo Institute of Technology, Meguro, Tokyo, Japan
E-mail(YAM): ymori@hp.phys.titech.ac.jp

ABSTRACT

The spectrum of blazars span over 20 decades from radio to gamma rays. To clarify a variety of physical phenomena of the blazar jets, a blazar must be monitored *in multiwavelengths* and *simultaneously*.

We succeeded in simultaneous multiwavelength observation of a blazar 3C 454.3, a QHB (quasar-hosted blazar) at z=0.859. It also belongs to the brightest quasar class, with its luminosity reaching 10^{48} erg/s. A huge gamma-ray flare of 3C 454.3 was reported by the AGILE satellite on November 2nd through December 1st, 2007. We proposed a ToO observation with the Suzaku satellite, which was approved and performed on Dec 5, 6. At the same time, we were monitoring its optical magnitudes in three colors (g', Rc, Ic) using the MITSuME Telescope at the ICRR Akeno Observatory, Yamanashi, Japan. Its R band magnitude increased from R=16 up to R=13.4 on December 1. We present the spectral energy distribution based on this multiwavelength observation, and discuss the emission models.

KEY WORDS: quasars:individual:3C 454.3 — X rays: Suzaku — optical: MITSuME

1. Introduction

1.1. Active Galactic Nuclei

Active galactic nucleus (AGN) is a compact luminous region at the center of a galaxy. The outstanding properties of AGNs are: high luminosity $> 10^{44}$ erg/s, sometimes reaches to 10^{49} erg/s, nonthermal emission in the radio, infrared, optical, ultra-violet, X-ray and gamma ray wavebands, rapid variability as short as hours. About 10 % of AGN has significant outflows named 'jet' from the supermassive black hole at the center of the host galaxy.

1.2. Blazar

Blazar is a class of AGN, which direction from observer $\theta \sim 1/\Gamma_{BLK} \sim 5$ degree. This narrow θ is occurred relativistic beaming effect. Its Spectral Energy Distribution (SED) has double-humped shape by Synchrotron Radiation in low energy side and Inverse Compton scattering in high energy side.

Blazar has a characteristic called Blazar Sequence, which negative relation of peak energy of hump and frequency of peak energy (see Fig.1). Blazar is divided into three classes by Blazar Sequence. From High frequency of peak energy these are named 'High-frequency peak BL Lac (HBL)', 'Low-frequency peak BL Lac (LBL)', 'Quasar Hosted Blazar (QHB)'. SED of QHB shows the peak energy of Inverse Compton scattering is larger than one of Synchrotron Radiation hump, so QHB needs External Compton scattering.

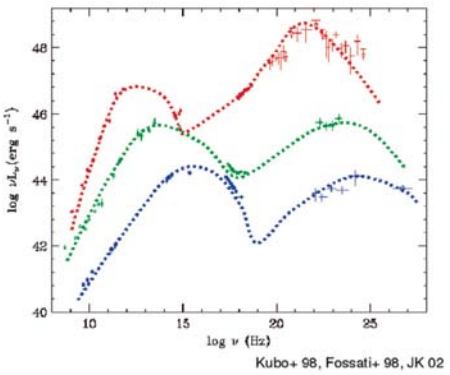

Fig. 1. SED of three classes of Blazar Sequence : The blue line shows High-frequency peak BL Lac (HBL), the green line shows Low-frequency peak BL Lac (LBL), the red line shows Quasar Hosted Blazar (QHB). The peak energy of hump has negative relation to the frequency of peak energy.

1.3. 3C 454.3

Among the Quasar Hosted Blazar (QHB) class of blazars, 3C454.3 (z = 0.859, R.A. = 22:53:57.7, Dec. = +16:08:54) is one of the brightest sources. QHB shows all the typical hallmarks of the class of blazar: large intensity variations at all frequencies, high radio and opti-

cal polarization, superluminal motion and a SED showing two broad peaks attributed to Synchrotron Radiation and Inverse Compton scattering. The Synchrotron power peaks in the Infra-red band while Inverse Compton scattering starts at soft X-ray frequencies and peaks at MeV energies (Giommi et al. 2002: Blom et al.1995)

In November-December 2007, 3C454.3 exploded and reach at optical 13.4 mag. This event triggered observations at gamma-ray energies with AGILE satellite. The Suzaku satellite pointed 3C454.3 as a Target of Opportunity (ToO) in X-ray band on Dec 5,6. The optical observations performed with the ground-based MITSuME telescope.

2. MITSuME telescope Instrument

Multicolor Imaging Telescopes for Survey and Monstrous Explosions (MITSuME) are a robotic telescope located at ICRR Akeno Observatory, Yamanasi, Japan and OAO, Okayama, Japan. The each MITSuME telescope has a Tricolor Camera, which allows us to take simultaneous images in g', Rc and Ic bands. This Camera have a 28 x 28 arcmin field of view.

These telescopes are built to perform for optical afterglow of Gamma-Ray Bursts (GRB), and respond to GRB Coordinate Network (GCN) alerts and start taking tricolor images automatically.

When there is no GRB that cat be observed, MITSuME Akeno telescope observe about 10 AGNs everyday, and create light curve to monitor activity of the flare.

Fig. 2. MITSuME Akeno 50cm

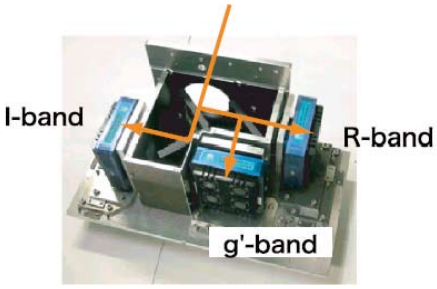

Fig. 3. Tricolor Camera

3. Observation of 3C 454.3

3.1. MITSuME observation

MITSuME Akeno Telescope observed 3C 454.3 several times in November and December, we analyzed data about two weeks, its include the data when simultaneous with Suzaku, i.e.that performed on December 5.

All raw g',R,I frames obtained by MITSuME were corrected for dark, bias and flat field with IRAF v 2.12. Instrumental magnitudes were obtained via aperture photometry using DAOPHOT (Stetson 1998) and Sextractor (Bertin & Arnouts 1996). Calibration of the optical source magnitude was obtained by differential photometry with respect to the comparison stars sequence reported by Raiteri et al. (1998) and Gonzalez-Perez et al. (2001). The fluxes are corrected for the Galactic extinction corresponding to a reddening of E{B-V} = 0.108 mag (Schlegel et al.1998).

At the same time, the Rapid Eye Mount (REM, Zerbi et al. 2004) telescope also observed 3C 454.3 on November and December, and data were analyzed by REM team.

The light curve in the R band of MITSuME and REM are shown in Fig.4.

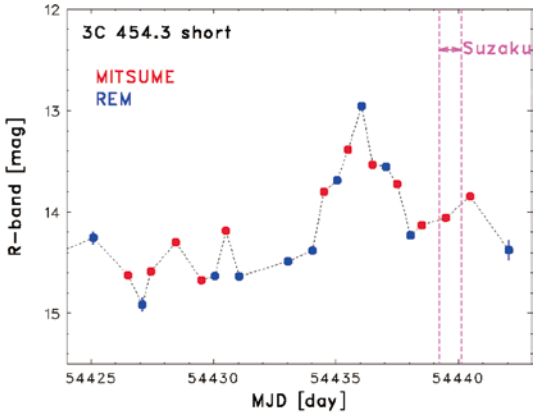

Fig. 4. MITSuME and REM light curve of 3C 454.3 in the R band from November 20 to December 8 : The red points and blue points show MITSuME and REM data (Tosti et al. in prep) respectively. The dates of Suzaku pointed observations of Dec 5, 6 are indicated by the dashed vertical lines.

3.2. Suzaku observation

3C 454.3 was observed by Suzaku between December 5-6. The total exposure time is 40 ksec. Event files from version 2.1.6.16 of the Suzaku pipeline processing were used and spectrum were extracted using XSELECT.

For each XIS, source spectra were extracted from circular regions of 4.3 arcmin radius centered on the source.

Fig. 5 shows the 0.4 - 2 keV, 2 - 10 keV XIS light curve and the hardness ratio from the Suzaku observation of 3C 454.3. The light curve of Suzaku data has about 10 %

time variance, and the hardness ratio is almost constant. So the spectrum were made from total accumulated data.

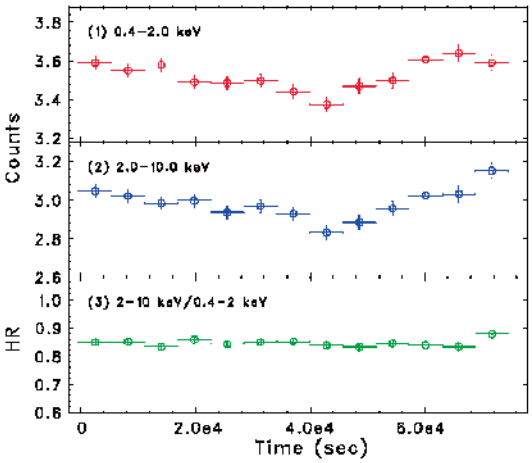

Fig. 5. Suzaku light curve of 3C 454.3 on December 5-6 : Panels from top to bottom show the 0.4 - 2 keV, 2 - 10 keV light curve, the hardness ratio (0.4 - 2 keV / 2 - 10 keV) respectively. The time variance is about 10 %, and the hardness ratio is constant.

All spectral fits were performed using XSPEC version 11.3.2ag. Errors on model parameters are quoted at the 90 percent confidence level. We applied a simple power law with Galactic absorption model according to $N_H = 0.724 \times 10^{21}$ cm^{-2} (Kalberla et al 2005). We obtained the photon index is $\Gamma = 1.51 \pm 0.003$.

The spectrum fitted with the above model are displayed in the top panels of Fig.6. The bottom panel shows the ratio between the data and the folded model. We note large deviation between the data and the model at low energy.

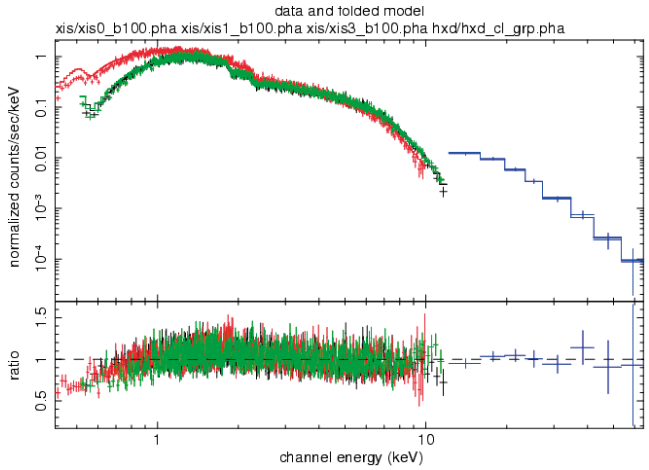

Fig. 6. Suzaku spectrum of 3C 454.3 on December 5-6 : High-precision X-ray spectrum from 0.4 to 60 keV. black points, red points, green points, blue points represent XIS0, XIS1, XIS3, HXD data, respectively. The bottom panel shows the ratio between the data and the folded model, a power law with Galactic absorption.

4. Broad-band spectral energy distribution

We combined our MITSuME, Suzaku measurements with non-simultaneous multifrequency data from NED to build the SED shown in Fig.7 and Fig.8. The general shape of the SED clearly follows the usual two-bump Synchrotron / Inverse Compton scenario.

First, we tried to fit the SED data with one-zone Synchrotron + Synchrotron self-Compton (SSC) models from a power law distribution of relativistic electrons with Lorentz factor of $\gamma_{min} = 1$, $\gamma_p = 200$ and $\gamma_{max} = 6000$ (see Fig.8). We found that this model can not explain the high energy at high frequency ($> 10^{22}$ Hz) . Moreover, this model does not fit to cut-off around 1 keV. (see Fig.7)

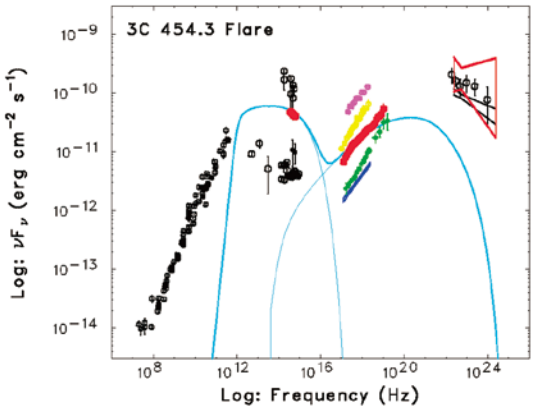

Fig. 7. SED of 3C454.3 : The sky blue line is Synchrotron + Synchrotron Self Compton model. The red points represent MITSuME, Suzaku, AGILE data (preliminary; Vercellone et al. in prep) on December 5-6. The black points represent from NED. The pink, yellow, green, blue represent previous observation by X-ray satellites

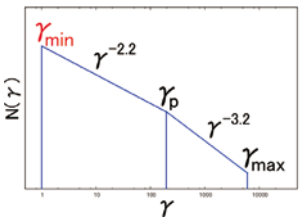

Fig. 8. electron distribution : the γ_{min} is lower limit of electron distribution. the γ_{max} is higher limit of one.

Next, we tried to fit the SED data with Synchrotron + External Compton (ERC) models from a power law distribution of relativistic electrons with Lorentz factor of $\gamma_{min} = 1$, $\gamma_p = 200$ and $\gamma_{max} = 6000$ (see Fig.8). We obtained reasonably good representations of the data for both the high energy at high frequency, and cut-off around 1 keV assuming parameters in Table.1. (see Fig.9)

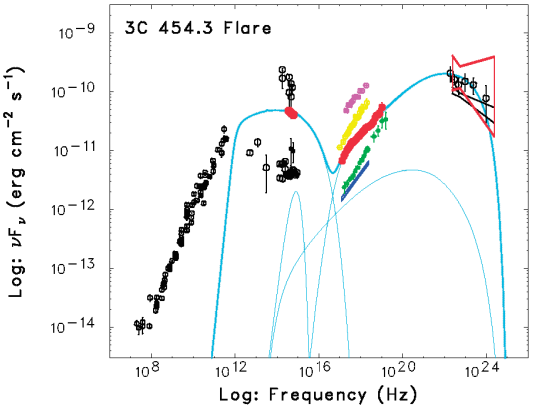

Fig. 9. SED of 3C454.3 : blue line is Synchrotron + External Compton scattering model. red points represent MITSuME, Suzaku, AGILE data on December 5-6. The black points represent from NED. The pink, yellow, green, blue represent previous observation by X-ray satellites

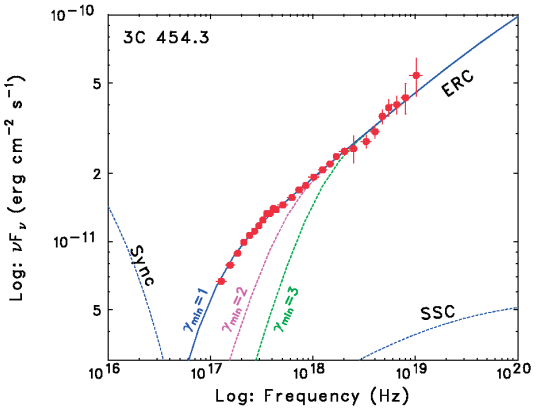

Fig. 10. An enlargement SED at around 1 keV : blue line, pink line, green line is Synchrotron + ERC model when $\gamma_{min} = 1$, 2, 3 respectively.

Table 1. parameters of Synchrotron + ERC model

electron distribution	
γ_{min}	1
γ_p	200
γ_{max}	6000
power1	2.2 ($\gamma_{min} < \gamma < \gamma_p$)
power2	3.2 ($\gamma_p < \gamma < \gamma_{max}$)

jet	
Γ	10
Θ	0.1 rad
B	10 Gauss
T_{disk}	1.0e4 K
L_{BLR}	1.35e43 erg/s
L_{sync}	1.30e43 erg/s
L_{SSC}	1.60e47 erg/s
L_{ERC}	5.8e48 erg/s
L_{elec}	1.1e45 erg/s
U_e/U_B	1/30

We tried to fit the SED data with ERC models case of $\gamma_{min} = 2$, and $\gamma_{min} = 3$. (see Fig.10) The result of fitting indicates that only $\gamma_{min} = 1$ is accepted to reproduce the data.

5. Conclusion

We succeeded in simultaneous multi-wavelength observations of a blazar 3C 454.3 at the “gamma-ray flare” for the first time. There is a remarkable cut-off at X ray spectrum. Its precise measurement of the low-energy limit of accelerated electrons $\gamma_{min} = 1$.

Multiwavelength spectrum is well fitted by ERC model. The γ rays are due to the Compton scattering of seed photons if T $\sim 10^{4-5}$ K.

6. Multiwavelength observation with Fermi Gamma-Ray Space Telescope / MAXI

We plan multi-wavelength observation of 8 AGNs after Fermi Gamma-Ray Space Telescope launched (see Table.2). We expect to conduct non-bias blazar survey even when the source is in a low state (see Fig.11).

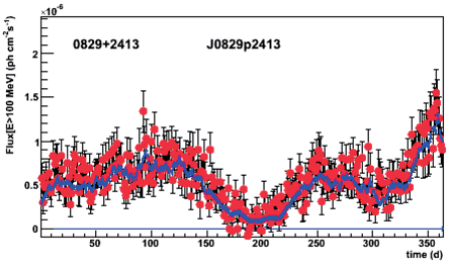

Fig. 11. Simulation of Fermi Gamma-Ray Space Telescope : Simulated Fermi Gamma-Ray Space Telescope light curve of Q0827+243 for 1 day binning of data.

acknowledgments. We would appreciate all member of MITSuME, Suzaku, AGILE team.

References

Blom et al.1995, A&A, 295, 330
Fossati, G. et al. 1998 MNRAS., 299, 433F
Ghisellini, G. et al. 2007 MNRAS., 382L, 82G
Giommi, P. et al. 2002 babs.conf, 63G
Gonzalez-Perez et al. 2001 AJ, 122, 2055G
Kubo, H. et al. 1998 ApJ., 504, 693K
Raiteri, C. M. et al. 2007 A&A., 473, 819R
Raiteri, C. M. et al. 1998 A&AS., 130, 495R
Schlegel, D.J. et al.1998 ApJ., 500, 525
Zerbi, F. et al. 2004 SPIE, 5492, 1590

Table 2. Source list of multiwavelength observation with Fermi Gamma-Ray Space Telescope

Source Name	z	class	Flux (2-10 keV) [10^{-12} erg/cm^2/s]	Flux ($>$ 100 MeV) [10^{-5} ph/cm^2/s]
PKS 0208-512	1	HPQ	9.5	85.5 $\pm$ 4.5
Q0827+243	0.94	LPQ	4.8	24.9 $\pm$ 3.9
PKS 1127-145	1.184	LPQ	11	38.3 $\pm$ 8.0
PKS 1510-089	0.36	LPQ	10	18.0 $\pm$ 3.8
3C 454.3	0.86	HPQ	11	53.7 $\pm$ 4.0
3C 279	0.536	HPQ	13	89 $\pm$ 3.2
PKS 0528+134	2.06	LPQ	30	60 $\pm$ 3.0
PKS 2126-15	3.3	LPQ	12	

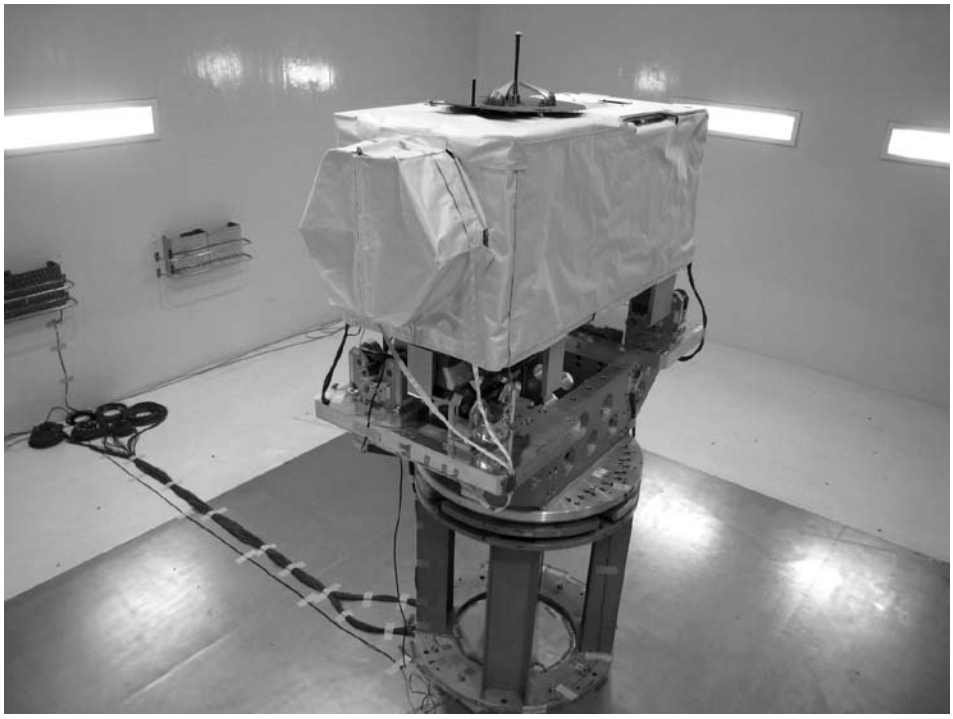

Near-Infrared Intraday Variations in AGNs

Takeo Minezaki,[1] Yuzuru Yoshii,[1,2] Yukiyasu Kobayashi,[3]
Keigo Enya[4], Masahiro Suganuma[3], Hiroyuki Tomita[1], Shintaro Koshida[5],
Masahiro Yamauchi[5], Yu Sakata[5], Shota Sugawara[5], and Tsutomu Aoki[6]

[1] Institute of Astronomy, School of Science, University of Tokyo
[2] Research Center for the Early Universe, School of Science, University of Tokyo
[3] National Astronomical Observatory, Japan
[4] Institite of Space and Astronautical Science, Japan Aerospace Exploration Agency
[5] Department of Astronomy, School of Science, University of Tokyo
[6] Kiso Observatory, Institute of Astronomy, School of Science, University of Tokyo
E-mail(TM): minezaki@ioa.s.u-tokyo.ac.jp

Abstract

We carried out a one-night optical V and near-infrared JHK monitoring observation of the least luminous Seyfert 1 galaxy, NGC 4395, on 2004 May 1, and detected intraday flux variations in the V, J, and H bands. The near-infrared flux variations are almost synchronized with the flux variation in the V band. This indicates that the intraday-variable component of near-infrared continuum emission of the NGC 4395 nucleus is an extension of UV-optical power-law continuum emission and originates in an outer region of the central accretion disk. In addition, a possible time lag of ~ 7 minutes between the V-band and infrared flux variations was found by cross-correlation analysis. These results can be explained by the X-ray reprocessing model, in which X-ray flux variation propagates with light velocity and drives the flux variations in optical and near-infrared wavelengths.

We also carried out the most intense monitoring observations in the optical and near-infrared wavebands for a Seyfert 1 galaxy, NGC 5548, and examined the correlation between the X-ray and optical flux variations. The X-ray light curve was taken from Uttley et al. (2003) as observed by the Rossi X-ray Timing Explorer (RXTE). The V-band flux variation shows a clear lag of $1-2$ days behind the X-ray flux variation, which supports the X-ray reprocessing model for the optical flux variation at short timescales.

Key words: AGN: time variation — AGN : multiwavelength (X-ray, optical, and near-infrared)

1. Introduction

It is generally accepted that the continuum emission of type 1 active galactic nuclei (AGNs) in UV and optical wavebands originates in the optically thick accretion disk, and the X-ray emission originates in the optically thin hot corona in the central part of the accretion disk, respectively. Studying the relationship between flux variations in UV/optical and X-ray wavebands can provide important clues about the connection between the disk and coronal emission and the mechanisms of flux variations in those wavebands. For example, it has been proposed that the UV/optical flux variation originates in the thermal reprocessing of X-ray variability by the accretion disk (Krolik et al. 1991). In this scheme, the UV/optical flux variation should lag behind the X-ray flux variation, which explains why the UV-optical continuum emissions are highly correlated and vary almost simultaneously in different wavelengths. In more detail, light travel time arguments for a standard accretion disk predict a small time lag between the UV-optical continuum emissions that increases with wavelength (Collier et al. 1999). Alternatively, if the UV/optical emission provides the "seed" photons for the X-ray Comptonization process, the UV/optical flux variation should be followed by the X-ray flux variation.

Previous studies have presented diverse and somewhat confusing results on the relationship between the X-ray and UV/optical flux variations of AGNs (e.g., Uttley 2006; McHardy this proceeding). For some sources, good correlation between the X-ray and UV/optical flux variations was found; a time lag of the optical flux variation behind that of X-rays was reported for NGC 4051 (Mason et al. 2002) and Ark 564 (Shemmer et al. 2001). In contrast, the time lag of the X-ray flux variation behind that of the UV/optical was reported for NGC 4051 (Shemmer et al. 2003), MCG-6-30-15 (Arevalo et al. 2005), and Mrk 509 (Marshall et al. 2008). However, no apparent correlation between the X-ray and UV/optical

flux variations was found for NGC 3516 (Maoz et al. 2002), or the correlation between X-ray spectral variation and UV/optical flux variations was found for NGC 7469 (Nandra et al. 2000).

In this study, we present recent results obtained by the Multicolor Active Galactic NUclei Monitoring (MAGNUM) project (Yoshii 2002), which supports the X-ray reprocessing model for the optical and near-infrared flux variations on short timescales, and then discuss the extent of the accretion disk based on the light travel time arguments. These results regarding NGC 4395 and NGC 5548 were presented in Minezaki et al. (2006) and Suganuma et al. (2006), respectively.

2. Near-Infrared Intraday Variations in NGC 4395

2.1. The least luminous Seyfert 1 galaxy, NGC 4395

NGC 4395 is a unique object known as the least luminous Seyfert 1 galaxy (Filippenko & Sargent 1989), having a bolometric luminosity of only $L_{\rm bol} \sim 10^{40-41}$ ergs $\rm s^{-1}$ with broad emission lines in the UV and optical spectra (Filippenko & Sargent 1989; Filippenko et al. 1993; Kraemer et al. 1999). Its spectral energy distribution from X-ray to radio wavelengths resembles those of normal type 1 AGNs rather than those of low-ionization nuclear emission-line regions (LINERs; Moran et al. 1999). Although a compact radio source has been detected, it is a radio-quiet AGN (Ho & Ulvestad 2001; Wrobel et al. 2001; Ho & Peng 2001). The mass of the central black hole measured by a reverberation-mapping observation of the CIV emission line is as small as $M_{\rm BH} = (3.6 \pm 1.1) \times 10^5\ M_\odot$ (Peterson et al. 2005).

Moreover, the NGC 4395 nucleus shows extreme variability at many wavelengths, probably because of its low luminosity and small black hole mass. Rapid large-amplitude variations were observed in X-rays (Lira et al. 1999; Iwasawa et al. 2000; Shih et al. 2003; Vaughan et al. 2005; Moran et al. 2005; O'Neil et al. 2006), and intraday variations were observed in UV and optical (Peterson et al. 2005; Skelton et al. 2005; Desroches et al. 2006).

In near-infrared, we carried out the first intensive monitoring observation and found intraday flux variations (Minezaki et al. 2006). We also carried out a long-term (more than a year) monitoring observation in optical and near-infrared wavebands; however, here we focus on the short timescale flux variations from the intensive monitoring observation.

2.2. Observations

A one-night monitoring observation was carried out on 2004 May 1 (UTC), using the multicolor imaging photometer (MIP) mounted on the 2-m telescope of the MAGNUM project at the Haleakala Observatories in Hawaii (Kobayashi et al. 1998a, 1998b). The observation started at 06:31 and ended at 12:35 on 2004 May 1 (UTC). Using the MIP's simultaneous optical and near-infrared imaging capability, a sequence of $(V,\ K)$, (V, H), and $(V,\ J)$ -bands imagings was repeated cyclically during the observation, and 59 data points for the V band and 20 data points each for the J, H, and K bands were obtained. The average monitoring interval was 6 minutes for the V band and 18 minutes for the J, H, and K bands.

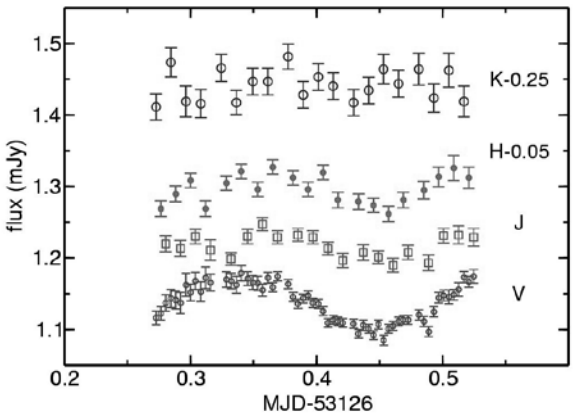

Fig. 1. Optical and near-infrared light curves of NGC 4395 on 2004 May 1 (UTC): V band (small open circles), J band (open squares), H band (small filled circles), and K band (open circles). For clarity, an offset of -0.05 mJy is applied to the H-band data points, and -0.25 mJy to the K-band data points.

2.3. Results

Figure 1 shows the optical and near-infrared light curves of NGC 4395 on 2004 May 1 (UTC). Galactic extinction was corrected for according to Schlegel et al. (1998). Clear flux variations in the V, J, and H bands were found during the six-hour monitoring period; this is the first detection of the intraday variation in the near-infrared for normal Seyfert 1 galaxies. The amplitude of the variations was $0.05-0.09$ mag; however, the real amplitude must be larger because nonvariable fluxes, such as the host galaxy flux and narrow-line flux, were not subtracted from the data. On the other hand, intraday variation was not clearly seen in the K band.

Apparently, the intraday variations in the V, J, and H bands are almost synchronized. In order to estimate the possible lag between the optical and near-infrared intraday variations, we applied a cross-correlation analysis. First, to increase the number of data points, the J-band and H-band light curves were combined according to the linear regressions of the J- and H-band fluxes to the V-band flux obtained simultaneously during the one-night monitoring observation. Then a cross-correlation function (CCF) was computed based on the linear interpolation method (Gaskell & Peterson 1987; White &

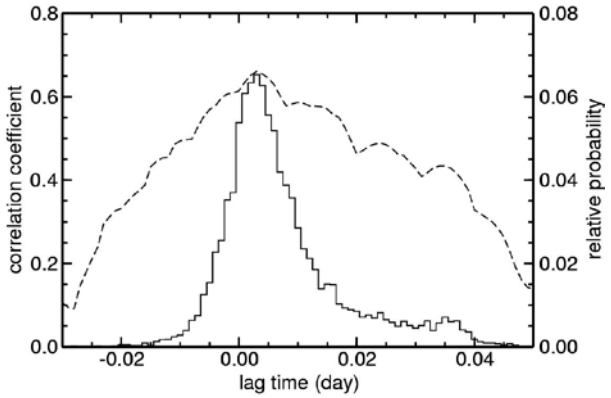

Fig. 2. CCF (dashed line) and CCCD (solid line) between the V-band light curve and the $J + H$ combined light curve on 2004 May 1 (UTC). The CCF peaks at 0.003 days, and the CCF centroid is estimated as $\tau_{\rm cent} = 0.005^{+0.011}_{-0.006}$ days, or $7.2^{+15.8}_{-8.6}$ minutes from the CCCD.

Peterson 1994). Since the number of V-band data points is larger and their photometric accuracy is better, the V-band light curve was interpolated. The lag of the CCF centroid $\tau_{\rm cent}$ was adopted to represent the lag between two light curves. The error of $\tau_{\rm cent}$ was estimated by a model-independent Monte Carlo simulation called the flux randomization/random subset selection (FR/RSS) method (Peterson et al. 2004). A cross-correlation centroid distribution (CCCD) was made based on the simulation of 10,000 realizations. Figure 2 shows the CCF and the CCCD between the V-band light curve and the combined near-infrared light curve on 2004 May 1 (UTC). The near-infrared lag time behind V is estimated from the CCCD as $\tau_{\rm cent} = 0.005^{+0.011}_{-0.006}$ days, or $7.2^{+15.8}_{-8.6}$ minutes. The intraday variations in the near-infrared (J, H) are almost synchronized with that in the optical within an accuracy of ~ 10 minutes. The short timescale of variation (a few hours) and the synchronization with the optical variation ($\sim$ 10 minutes) suggest that the intraday-variable component in near-infrared is an extension of the UV-optical power-law continuum emission that originates in the accretion disk, and these results can be explained by the X-ray reprocessing model, that is, the X-ray flux variation propagates with light velocity and drives the flux variation in optical and near-infrared wavelengths.

2.4. Discussion

The X-ray reprocessing model for the short timescale flux variations of NGC 4395 is indicated by the simultaneous monitoring observation in X-ray, UV, and optical wavebands more directly. Desroches et al. (2006) found that the optical flux variation lagged behind the X-ray flux variation by 44 ± 13 minutes, and lagged behind the UV flux variation by 24^{+7}_{-9} minutes, which is consistent with the X-ray reprocessing model. O'Neill et al. (2006) found that the X-ray and UV flux variations were simultaneous within ± 1 hour with a significance of $\sim$ 95 %, which is consistent with the view of the disk-corona model that the X-ray and UV fluxes are closely connected by reprocessing and/or Comptonization.

If the reprocessing model can be applied to the flux variation of the UV, optical, and near-infrared continuum emission, the lags between the variations at different wavelengths would be a direct measure of the extent of the accretion disk. In particular, the near-infrared emission from the accretion disk is expected to originate in its outermost region. Thus, the outer radius of the accretion disk would be indicated by the possible lag between the V-band and near-infrared intraday variations, and it is worthwhile to compare it with the size of the broad emission-line region (BLR).

Our measurement of the near-infrared lag time behind V is $\tau_{\rm cent} = 7.2^{+15.8}_{-8.6}$ minutes (2004 May 1). If we add the lag times of the V-band flux variations behind the UV or X-ray flux variations (2004 April 11) obtained by Desroches et al. (2006), the near-infrared lag time behind the UV continuum or X-ray flux that are considered to originate in the central part of the accretion disk would be $\tau_{\rm NIR} \sim 30 - 50$ minutes. Peterson et al. (2005) reported that the CIV emission-line lagged behind the UV continuum ($\lambda = 1350$ Å) by $\tau_{\rm CIV} = 48^{+24}_{-19}$ minutes (2004 April 10) and $\tau_{\rm CIV} = 66^{+24}_{-19}$ minutes (2004 July 3). A comparison of $\tau_{\rm NIR}$ and $\tau_{\rm CIV}$ indicates that the accretion disk is extended to just inside the BLR.

Next, we discuss the result that intraday flux variations in the K-band were not detected. Although a part of the K-band emission is contributed by power-law continuum emission from the accretion disk (Tomita et al. 2006; Kishimoto et al. 2008), it is usually dominated by thermal radiation from the dust torus. Thus, even if there was an intraday flux variation of the power-law continuum component in the K band, it would be veiled by the large amount of thermal radiation from the dust torus, because the dust torus is extended considerably so that short timescale variation of the incident flux is smeared out. The inner radius of the dust torus of NGC 4395 is estimated as $\sim$ 1 lt-day based on the correlation between the optical luminosity and the dust lag of AGNs (Minezaki et al. 2004), which is certainly much larger than the extent of the accretion disk.

3. Lag Between X-ray and Optical Flux Variations in NGC 5548

3.1. The correlation between X-ray and UV/optical flux variations in NGC 5548

Clavel et al. (1992) reported a UV lag of $\Delta t = 0 \pm 6$ days behind the X-rays by comparing the light curves in hard X-rays ($2 - 10$ keV) and UV (1350 Å) for NGC 5548. It

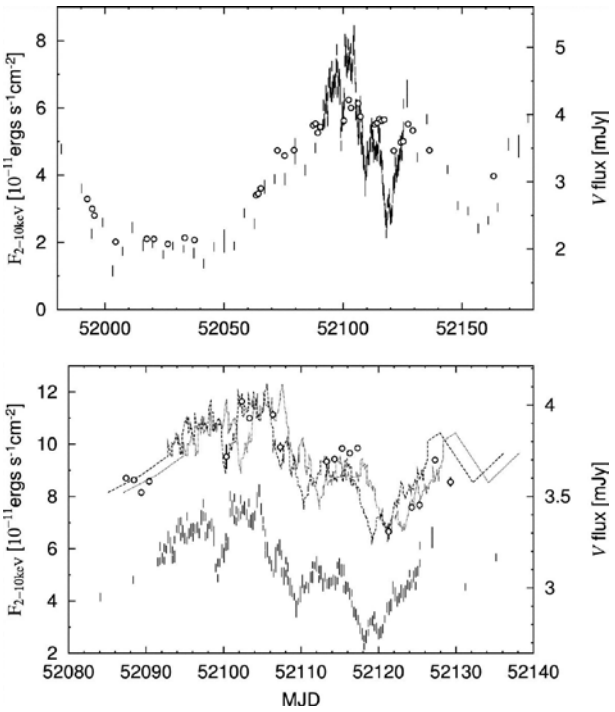

Fig. 3. Top: Observed light curves of NGC 5548 in the V band (open circles) and in the X-ray energy range of $2-10$ keV reported by Uttley et al. (2003). Bottom: Same as the top panel, but only for the active phase in 2001 (MJD $= 52,085-52,130$) when intensive X-ray satellite (RXTE) observations were done. The dashed line is the RXTE light curve shifted arbitrarily in the vertical direction and by $+1$ day in the horizontal direction; the dotted line is shifted by $+3$ days. Note that the scale for the optical flux is expanded in this panel.

is not easy to detect a clear correlation between X-ray and UV/optical variations on short timescales or the lag time between them because generally, the amplitude of UV/optical variation on a short timescale is small and difficult to observe.

From monitoring observations in the optical (5100 Å) and hard X-rays ($2-10$ keV) spanning for 6 years for NGC 5548, Uttley et al. (2003) reported a strong correlation in their long-timescale variations while only weakly restricting $\Delta t = 0 \pm 15$ days. Since the amplitude of such optical variation is found to exceed that of the hard X-rays, they argued that the X-ray reprocessing model is not the main driver of the long-timescale optical variation, at least for NGC 5548.

Thus, the problem yet to be answered is whether there is a clear correlation between X-ray and optical variations on short timescales.

3.2. Results and discussion

A long-term monitoring observation of NGC 5548 in optical and near-infrared wavebands was carried out by the MAGNUM project (Suganuma et al. 2006). It started in 2001 with a median sampling interval of ~ 3 days, and covered the period of the X-ray monitoring observation by the RXTE (Uttley et al. 2003). Then, the correlation and possible lag between the X-ray and optical flux variations were be examined.

The top panel of Figure 3 shows our V-band light curve and the X-ray ($2-10$ keV) light curve. These two light curves strongly correlate with each other, but the amplitude of the optical variation is much smaller than that of the X-rays. The bottom panel shows a portion of the light curves for a period of MJD $\approx 52,085-52,130$ with an expanded vertical scale for the optical flux. Although the optical data were not sampled as often as the RXTE data, we found that the optical flux variation clearly lagged behind the X-ray flux variation. The lag time is estimated as $\Delta t = 1.6^{+1.0}_{-0.5}$ days from the cross-correlation analysis of the two light curves.

The size of the X-ray–emitting region in AGNs is considered to be as small as a light-travel distance of hours, since a significant fraction of the X-ray flux varies on this timescale (Fig. 3). The observed correlated variability indicates that the optical emitting region in NGC 5548 is located at a light-travel distance of $1-2$ days from the X-ray–emitting region and favors the thermal reprocessing of X-rays by the optically thick accretion disk, rather than a nonthermal process that emits both X-ray and UV/optical fluxes from almost the same region. On the other hand, the long-timescale X-ray and optical variations might be generated by some other mechanisms, such as instabilities of the accretion disk itself.

Our result also shows a geometrical relationship between the accretion disk and the BLR. Korista et al. (1995) and Peterson & Wandel (1999) reported that the broad emission line of highest ionization in NGC 5548 gives the shortest lag of a few days. Therefore, the optical lag of $1-2$ days behind the X-ray indicates that the accretion disk is located just inside the BLR in NGC 5548.

References

Arevalo, P. et al. 2005, A&A., 430, 435
Clavel, J., et al. 1992, ApJ., 393, 113
Collier, S. et al. 1999, MNRAS., 302, L24
Desroches, L.-B., et al. 2006, ApJ., 650, 88
Filippenko, A. V., & Ho, L. C. 2003, ApJ., 588, L13
Filippenko, A. V., Ho, L. C., & Sargent, W. L. W. 1993, ApJ., 410, L75
Filippenko, A. V., & Sargent, W. L. W. 1989, ApJ., 342, L11
Gaskell, C. M., & Peterson, B. M. 1987, ApJS., 65, 1
Ho, L. C., & Peng, C. Y. 2001, ApJ., 555, 650
Ho, L. C., & Ulvestad, J. S. 2001, ApJS., 133, 77
Iwasawa, K. et al. 2000, MNRAS., 318, 879
Kishimoto, M. et al. 2008, Nature, 454, 492

Kobayashi, Y. et al. 1998a, Proc. SPIE, 3354, 769
Kobayashi, Y. et al. 1998b, Proc. SPIE, 3352, 120
Korista, K. T. et al. 1995, ApJS., 97, 285
Krolik, J. H. et al. 1991, ApJ. 371, 541
Kraemer, S. B. et al. 1999, ApJ., 520, 564
Lira, P. et al. 1999, MNRAS., 305, 109
Maoz, D., Edelson, R., & Nandra, K. 2002, AJ., 119, 119
Marshall, K. et al. 2008, ApJ., 677, 880
Mason, K. O. et al. 2002, ApJ., 580, L117
McHardy, I. M. 2008, this proceeding
Minezaki, T. et al. 2004, ApJ., 600, L35
Minezaki, T. et al. 2006 ApJ., 643, L5
Moran, E. C. et al. 2005, AJ., 129, 2108
Moran, E. C. et al. 1999, PASP., 111, 801
Nandra, K. et al. 2000, ApJ., 544, 734
O'Neill, P. M. et al. 2006, ApJ., 645, 160
Peterson, B. M., & Wandel, A. 1999, ApJ., 521, L95
Peterson, B. M., et al. 2004, ApJ., 613, 682
Peterson, B. M., et al. 2005, ApJ., 632, 799
Schlegel, D. J., Finkbeiner, D. P., & Davis, M. 1998, ApJ., 500, 525
Shemmer, O. et al. 2001, ApJ., 581, 197
Shemmer, O. et al. 2003, MNRAS., 343, 1341
Shih, D. C., Iwasawa, K., & Fabian, A. C. 2003, MNRAS., 341, 973
Skelton, J. E. et al. 2005, MNRAS., 358, 781
Suganuma, M. et al. 2006, ApJ., 639, 46
Tomita, H. et al. 2006, ApJ., 652, L13
Uttley, P. et al. 2003, ApJ., 584, L53
Uttley, P. 2006, Proceeding of AGN Variability from X-Rays to Radio Waves, ASP Conf. Ser. 360, 101
Vaughan, S. et al. 2005, MNRAS., 356, 524
White, R. J., & Peterson, B. M. 1994, PASP., 106, 879
Wrobel, J. M., Fassnacht, C. D., & Ho, L. C. 2001, ApJ., 553, L23
Yoshii, Y. 2002, in New Trends in Theoretical and Observational Cosmology, ed. K. Sato & T. Shiromizu (Tokyo: Universal Academy Press), 235

GAMMA-RAY BURSTS

GRB observations with MAXI

Motoko Suzuki,[1] and MAXI team

[1] Japan Aerospace Exploration Agency, 1-1, Sengen 2chome, Tsukuba, Ibaraki 305-8505, Japan
E-mail(MS): suzuki.motoko@jaxa.jp

Abstract

MAXI has an ability to distribute gamma-ray burst (GRB) alert promptly. For the prompt emissions, bursts in the MAXI field of view (1.5deg × 160deg × 2ways) will be observed. Based on latest results of observations, we simulate various prompt emissions and X-ray afterglows of GRBs. From the results of simulations we estimate sensitivity to these bursts. The positions of the bursts (excluding bursts with the angular distance to the sun of <30 deg) will be scanned by MAXI within about 70 minutes of the prompt emissions. GRB prompt emissions or other transient events will be searched by MAXI Nova Search system, and these information will be distributed to the world. In this document, the summary of the number of observable bursts and X-ray afterglows are presented,

Key words: X-rays: observations — gamma-rays: bursts — methods: simulations

1. Introduction

In studying gamma-ray bursts (GRBs), It is important not only analyzing prompt emissions but also investigating into afterglows and host galaxies with telescopes. Automatic system of the localization from prompt emissions and alert systems to distribute burst information enable the fast and complete follow-up observation. MAXI is a mission which has an ability of fast localization and distribution of alert.

MAXI covers 0.5-30keV energy range. This will provide unique capability to catch extremely soft bursts, called X-ray flashes (XRFs). The study of XRFs are advanced based on the data from BeppoSAX and HETE-2. After the end of HETE-2 operation, MAXI may be the first mission that is able to trigger GRBs or XRFs in energy range below 25 keV. Moreover, joint fit the data of the instruments sensitive to higher energy range, such as BAT on Swift, GBM and LAT on Fermi, and WAM on Suzaku, with MAXI will give more accurate low-energy index for soft bursts, and also accurate E_{peak}.

MAXI consists of two kinds of detectors, position sensitive gas-proportional counters for 2-30 keV X-rays (Mihara et al. 2008) and CCD cameras for 0.5-12 keV X-rays (Tomida et al. 2008). Among the two type of instruments of MAXI, the camera of gas-proportional counters (Gas Slit Camera: GSC) has relatively large effective area and field of view. Considering these properties, we can conclude GSC is more suitable for the detection of GRBs both prompt emissions and X-ray afterglow.

To study how much GRBs are in the MAXI field of view, and the quality of the data from MAXI, we use maxi simulator (Eguchi et al. 2008). First we describe the function of maxi simulator in section 2.1.. Details of models of prompt emissions and X-ray afterglows we simulated will be presented in section 2.2. and section 2.3. respectively. In section 3., the descriptions of method of processing and analyzing data from MAXI simulator are given. In section 4., we discuss the potentiality of MAXI for observations of GRBs, and in section 5. summarize conclusions.

2. Methods and parameters of simulation

2.1. Overview of MAXI simulator

MAXI simulator is a program which simulate MAXI instruments. We can input the list of X-ray sources, including variable sources. The spectra of the sources should be described in the parameter files. When we run the program, simulator considers orbits and attitude of ISS, and then select the sources in the field of view of the instruments. After the decision of the properties of photons coming into the detector, simulator calculates output pulse height using detector response function. Finally, it outputs the list of X-ray events. The format of the output is similar to the raw data from MAXI.

2.2. Simulations of prompt emissions

MAXI simulator accept fast rise exponential decay type "burst model" as a model of variable source light curve. The source flux F of the burst source is given by the following function,

$$F(t) = \begin{cases} 0 & (t < t_0) \\ \exp\left(-(t-t_0)/\tau\right) & (t \geq t_0) \end{cases}, \qquad (1)$$

where t_0 is the time of the peak and τ is the decay time of the burst. We take $\tau = 10$ seconds for burst sim-

ulation. MAXI will observe efficiently rather soft and bright GRBs. Therefore we decided to adopt the spectral parameters of GRB030329 (see Table 1), which is the most bright GRB in the field of view of HETE-2. In order to study the sensitivity of MAXI GSC to GRBs, we changed two parameters, the intrinsic flux and the incident angle of the bursts, both of which affect the intensity of the signal of the burst. The intrinsic peak flux of the burst was changed from 1/300 to 1 of the average flux of GRB030329. To express an incident angle on MAXI cameras, it is convenient to adopt the coordinate drawn in figure 1. Because collimator sheets are parallel to the x-z plane, an effective area to a point source determined mainly by azimuthal angle of a source. On the other hand, changes of elevation angle have little effect on effective area. In the simulations of GRBs, we have to take into account only a peaking time t_0 of a burst instead of azimuthal angle. This is because azimuthal angle changes, in contrast to elevation angle, during a scan of a source.

Figure 2 shows variation of effective area about a point source as a function of the time. As shown in the figure, we defined the offset time of a burst as a time from the peaking time of the effective area curve to the peaking time of the burst. If the burst precede the peak of the effective area curve, the offset takes negative value.

We set the offset time between -34 sec and $+26$ sec.

2.3. Simulations of X-ray afterglows

To simulate X-ray afterglows, first we defined "average" X-ray afterglow. According to comprehensive study of X-ray afterglows observed by Swift (for example Nousek et al. 2006, Sakamoto et al. 2008), X-ray afterglows generally follow the shape shown in the top panel of figure 3. In order to estimate the rate of X-ray afterglows observed with GSC, we should examine how long GSC can observe an X-ray afterglow. A rough estimate may be made considering the flux limit of a source with a scan, which is about 20 mCrab (Hiroi et al. 2008). This limit corresponds to 10^{-9} erg cm^{-2} sec^{-1} in the energy band of X-ray telescope on Swift, 0.3–10 keV. an average X-ray afterglow stays this flux level for only about 150 seconds. To confirm this estimation with simulator, we tested four cases: the peak of effective area curve comes 100, 150, 200, and 250 seconds after the burst (the lower panel of figure 3.) The spectral model of the afterglows in the simulations is set to the power-law function with the index -2.0.

Table 1. The spectral parameters of GRB030329 (Sakamoto et al. 2005). The spectral model is Band function (Band et al. 1993). The normalization is in the unit of 10^{-2} photons cm^{-2} s^{-1} keV^{-1} at 15keV.

model parameter	value
low-energy index α	-1.26
high-energy index β	-2.28
peak energy in νF_ν spectrum E_{peak} (keV)	67.8
normalization	146

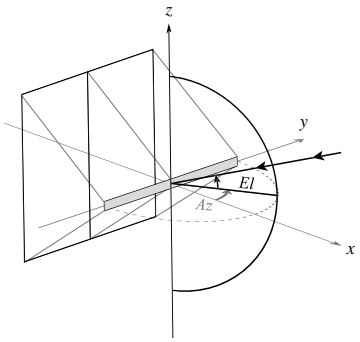

Fig. 1. Definition of the incident angle on GSC. The thin long box in gray is a slit plane of a camera. We define the slit coordinate system of Cartesian coordinate. The slit-normal axis is defined as an axis normal to the slit plane. The slit-long axis is an axis parallel to the long edge of the slit, and slit-short axis is an axis parallel to the short edge of the slit. A path of a photon is defined with two parameters, slit-elevation angle (El) and slit-azimuthal angle (Az). The slit-elevation angle is defined as an angle between the path of a photon and the plane of slit-normal and slit-long axes. The slit-azimuthal angle is an angle between the projection of the path of photon toward the plane of slit-normal and slit-long axes, and slit normal axis. is define as an angle between

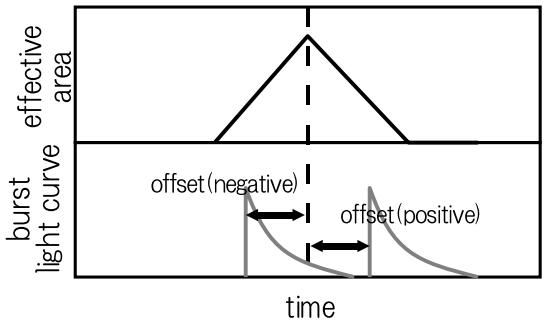

Fig. 2. A schematic picture of the definition of the offset time.

2.4. Simulations of X-ray and non X-ray background

One of the most important elements of the simulation is an estimation of background in the MAXI instruments. The estimation and simulation of backgrounds in the instruments are important, because we will discuss the detection and significance of the burst signal against the background. We generate photons of cosmic X-ray background assuming isotropic distribution in the sky. The spectrum and intensity of the background is set to the parameters in Boldt (1987). On the other hand, the

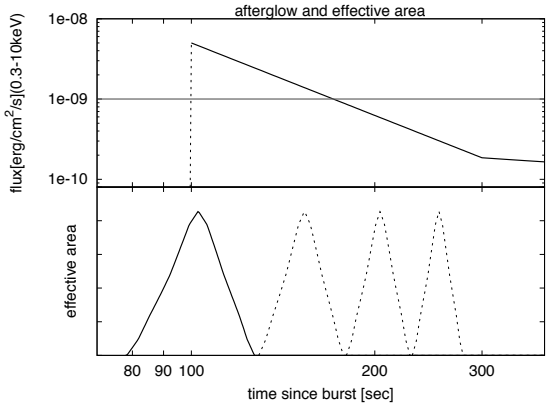

Fig. 3. An "average" light curve of X-ray afterglow, and effective area curve, which we tested.

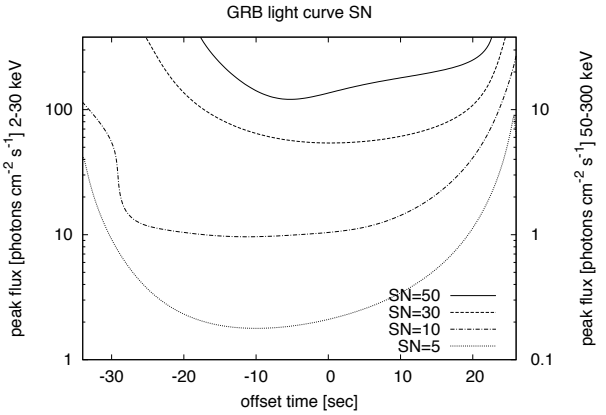

Fig. 4. The contour map of light curve S/N in the space of time offset of the burst and the flux of the burst. The horizontal axis is the offset time, which defined as shown in figure 2. The vertical axis is the flux of the burst. The contour of solid, dashed, dashed-dotted, and dotted line correspond to the S/N level of 50, 30, 10, and 5 respectively.

rate and spectrum of non X-ray background are estimated from the data of ground calibration or the data from other satellites. The count rate of non X-ray backgrounds are set to 10 counts per GSC counter per second. The energy and position distribution of non X-ray background are determined from the background templates, which is based on the data of ground calibration. Note that the rate of non X-ray background will vary with latitude, longitude, and altitude on earth. However, we do not take into account this effect in current simulation.

3. Process and analysis of simulated data

3.1. Processing procedure

The data from MAXI simulator is a series of ASCII format files. We process these files to create event files of standard fits format. Then we extract images, light curves, and spectra from event files using *xselect* [1] . To find prompt emission of the bursts, first we generate light curves of certain area of detector coordinate, because a point source stays at the same region in the detector coordinate during a scan. Then we examine these light curves to find excesses from the background rate.

3.2. Study of the rate

In order to study GRB and afterglow rate, first we have to decide the criterion of "detection" of the bursts. First we introduce the term "light curve S/N", which is defined as the ratio of the counts of the burst photons to the counts of background fluctuation in a time bin. We set the criteria that light curve S/N should be above 5.

3.2.1. The rate of prompt emissions

The observation rate of bursts is proportional to both observation time window and total rate above the sensitivity. Figure 4 shows the cntour of light curve S/N in the space of time offset and burst flux. From figure 4, we can observe the burst with the flux level of 0.4 photons cm^{-2} s^{-1} in 50–300 keV, when the time offset ranges from -25 to $+12$. Next, we have to consider the total rate of GRB. Stern et al. (2002, S02 hereafter) shows the combined BATSE and Ulysses GRB brightness distribution in 50–300 keV range. According to S02, the number of the burst, correspoinding to this flux limit, is about 400 events per year.

Combining the observable time offset range and total rate of the burst, we can calculate the rate of GRBs in the MAXI field of view $N_{\rm fov}$ as the following.

$$N_{\rm fov} = \eta \left(\frac{t_{\rm win}}{t_{\rm orbit}} \right) n_{\rm system} N_{\rm total}, \qquad (2)$$

where η is operation efficiency of the MAXI instruments, $t_{\rm win}$ is the observable time offset interval, $t_{\rm orbit}$ is the orbit period of the ISS, and $n_{\rm system}$ is number of camera system, and $N_{\rm total}$ is the total number of GRBs. The operation efficiency η should be about 0.65 due to the scheduled turn off when the sun in the field of view of the camera or at the South Atlantic Anomaly. The orbital period of the ISS $t_{\rm orbit}$ is about 5500 sec. The observable time offset interval $t_{\rm win}$ and the total number of GRBs depend on the flux level of the GRBs. In the case of 0.4 photons cm^{-2} s^{-1} in 50–300 keV, the numbers are

$$N_{\rm fov} \approx 3.5 \left(\frac{\eta}{0.65} \right) \left(\frac{t_{\rm win}}{37} \right) \left(\frac{5500}{t_{\rm orbit}} \right) \left(\frac{n_{\rm system}}{2} \right) \left(\frac{N_{\rm total}}{400} \right). \qquad (3)$$

3.2.2. The rate of afterglows

The observable rate of GRB afterglow in the GSC field of view is mainly determined with the length of X-ray af-

[1] http://heasarc.gsfc.nasa.gov/docs/software/lheasoft/ftools/xselect/index.html

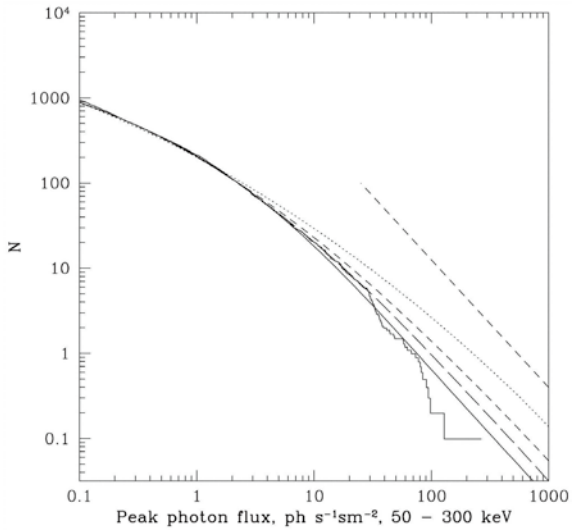

Fig. 5. The integral peak flux distribution of Ulysses/BATSE GRBs. This figure is from Stern et al. (2002).

terglow staying above the detection limit of a scan. From the result of our simulations, the average afterglow is too dim to detect with GSC even after 150 seconds after the prompt emission. It is necessary to scan the position of the afterglow within 100 seconds after the prompt emission. From the similar calculation to equation (3), we can estimate the rate of X-ray afterglows as

$$N_{\rm fov} \approx 2.4 \left(\frac{\eta}{0.65}\right) \left(\frac{f}{0.1}\right) \left(\frac{t_{\rm win}}{100}\right) \left(\frac{5500}{t_{\rm orbit}}\right) \left(\frac{n_{\rm system}}{2}\right) \left(\frac{N_{\rm total}}{1000}\right), \quad (4)$$

where f is indefinite fraction of bursts with bright X-ray afterglows.

4. Discussions

4.1. GRBs, afterglows, and other transients

It takes less than 50 seconds for a star to cross the MAXI field of view. In other words, the maximum exposure time of a star in a scan is less than 50 seconds. The first alert of MAXI bursts should be sent based on the data of this small exposure time. The following observation of the burst by MAXI itself must be delayed for 20 or 70 minutes. It is difficult to classify the transient event into burst, afterglows, or other class of events only from the information of such short exposure.

4.2. Uncertainty about the rate of soft bursts

As of now, the largest collection of the bursts is BATSE burst catalog (Paciesas et al. 1999). To calculate the burst rate in the MAXI field of view, we used S02, which contains the samples of Ulysses in addition to the BATSE samples. It should be noted that the rate in the S02 is the rate in 50 – 300 keV energy range. On the other hand, MAXI GSC covers 2 – 30 keV, which is an order of magnitude softer than BATSE's or Ulysses's band. We extrapolated the relation between the rate and the brightness in 2 – 30 keV band from the rate of S02 using the spectrum of the burst with intermediate hardness. According to Sakamoto et al. 2005, one third of the bursts emit more energy in X-ray (2 – 30 keV) band than gamma-ray (30 – 400 keV) band. Therefore some of the dim burst in 50 – 300 keV band should emit more energy in 2 – 30 keV, which may be easily detected with MAXI GSC.

4.3. Suggestion on the high redshift GRBs

Generally bursts originate from high redshift should have soft spectra and long duration. These properties are at advantages in observing high redshift GRBs with MAXI. As shown in equation (3), the burst rate in the MAXI field of view is proportional to the observable time window $t_{\rm win}$ within an orbit. This $t_{\rm win}$ heavily depends on the duration of the burst. Of course, the cameras with low energy sensitivity are also suitable to observe soft events. Moreover, the capability of imaging is unique to MAXI. It is difficult to trigger less variable source with a detector of coded mask type, which is common to WFC on BeppoSAX, WXM and SXC on HETE, and BAT on Swift.

5. Conclusions

MAXI will be able to detect 3.5 prompt emissions and 2.4 X-ray afterglows of GRBs per year. About prompt emissions, the uncertainty of the number mainly comes from the ambiguous extrapolation of the rate from gamma-ray to X-ray band. On the other hand, the uncertainty of the rate of the afterglows comes from uncertainty of the brightness distribution of the X-ray afterglows.

MAXI GSC has intrinsic capability of imaging and sensitivity in relatively low energy band. These properties will be advantages in detecting high redshift GRBs.

References

Band, D. et al. 1993, ApJ, 413, 281
Boldt, E. 1987, Observational Cosmology, 124, 611
Eguchi, S. et al. 2009, in this proceedings
Hiroi, K. et al. 2009, in this proceedings
Mihara, T et al. 2009, in this proceedings
Nousek, J. A. et al. 2006, ApJ, 642, 389
Paciesas, W. S. et al. 1999, ApJS, 122, 465
Sakamoto, T. et al. 2005, ApJ, 629, 311
Sakamoto, T. et al. 2008, ApJ, 679, 570
Stern, B. E. et al. 2002, ApJ, 578, 304
Tomida, H. et al. 2009, in this proceedings

Recent Results of GRB X-ray Afterglows

David N. Burrows[1]

[1] Dept. of Astronomy & Astrophysics, The Pennsylvania State University,
525 Davey Lab, University Park, PA 16802, USA
E-mail(DNB): burrows@astro.psu.edu

Abstract

I review recent results on GRB X-ray afterglows measured by the *Swift* X-ray Telescope (XRT). The XRT had observed over 290 X-ray afterglows of GRBs at the time of this meeting, obtaining > 80% of the world total of GRB X-ray afterglows and > 70% of the world total of GRBs with redshifts. I discuss general characteristics of X-ray afterglows as observed by *Swift*, and will then focus on a few of our most interesting discoveries. One of the most exciting of these was the recent "naked-eye" burst, GRB 080319B, with the brightest optical counterpart ever seen and one of the best-observed X-ray and optical light curves ever obtained. We interpret the bright prompt emission as the result of an extremely large bulk Lorentz factor, combined with a very narrow jet beamed directly at us, with Synchrotron Self-Compton emission from the UV/optical photons accounting for the γ-ray emission. The X-ray and optical afterglows are interpreted as the result of a two-component jet, with the wide jet accounting for the optical afterglow, while the X-ray afterglow is initially dominated by the narrow jet until that component fades following its jet break.

Key words: missions: Swift — GRBs: X-ray afterglows — GRB 080319B

1. Introduction

In the first 30 years since the discovery of Gamma-ray Bursts (GRBs) in 1967 (Klebesadel et al. 1973), GRBs had been found to have an isotropic distribution on the sky and a volume-limited distribution in distance (Meegan et al. 1992). It was also known that the distribution of GRB durations (typically defined as t_{90}, the time during which 90% of the fluence was detected) was bimodal (Fig. 1), with one peak at subsecond durations (generally referred to as "short" GRBs) and another peak at tens of seconds ("long" GRBs) (Kouveliotou et al. 1993). Little was known about the progenitors and hosts of GRBs, and there was debate about whether they represented a local population of objects or were distributed at cosmological distances. This debate was resolved in 1997 with the Beppo-SAX discoveries of the first GRB afterglows, their localization to arcminute accuracy, and the subsequent identification of associated optical transients (Costa et al. 1997; van Paradijs et al. 1997). Redshift measurements determined that GRBs were at cosmological distances (Metzger et al. 1997; Djorgovski et al. 1998). Subsequent associations of a few long GRBs with supernovae, together with the association of long GRBs with star forming regions of their host galaxies (Fruchter et al. 2006), provided evidence that long GRBs are produced during the collapse of massive stars and are probably associated with the formation of black holes. Although not localized to similar precision, short GRBs were thought to be associated with mergers of compact objects (Lattimer & Schramm 1976; Paczyński 1986; Eichler et al. 1989; Paczyński 1991).

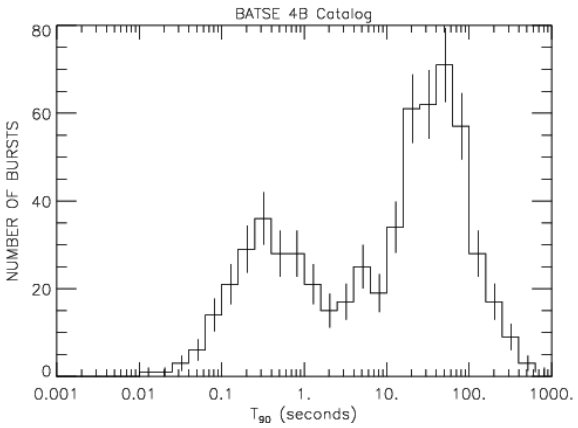

Fig. 1. Distribution of GRB durations measured by the BATSE instrument on the *Compton Gamma-Ray Observatory* (from *http://www.batse.msfc.nasa.gov/batse/grb/duration/*).

Observations of GRB afterglows in the optical and X-ray bands agreed well with the predictions of what has become the standard fireball model (Rees & Mészáros

1992; Mészáros & Rees 1993), in which a central engine releases an enormous amount of energy, producing a highly relativistic outflow in the form of a collimated jet. Internal shocks within this outflow are responsible for the prompt gamma-ray emission, while external shocks produced when the outflow encounters the surrounding medium produce a long-lived broadband afterglow.

The launch of the *Swift* satellite (Gehrels et al. 2004) on 20 November 2004 introduced a new era in GRB studies. Whereas *Beppo-SAX* typically required 6-8 hours to begin observing a GRB afterglow (de Pasquale et al. 2006), *Swift* is a highly autonomous robotic observatory, capable of automatically modifying its on-board observing program to incorporate observations of new GRBs and of slewing promptly to them, beginning observations of afterglows within 1-2 minutes after the burst in most cases. It carries 3 instruments: the Burst Alert Telescope (BAT, Barthelmy et al. 2005a), a coded aperture instrument with a 2 sr field of view (FOV) covering the energy band 15-350 keV; the X-ray Telescope (XRT, Burrows et al. 2005), an automated instrument covering the energy range 0.2-10 keV and capable of measuring positions accurate to about 2 arcseconds (Goad et al. 2007, Evans et al. 2008); and the UV/optical telescope (UVOT, Roming et al. 2005) covering the band 170-650 nm with subarcsecond position accuracy. GRB positions are determined on-board to arcminute and often to several arcsecond accuracy and distributed immediately to the Gamma-ray burst Coordinations Network. Subsequent ground processing generally produces arcsecond positions distributed within tens of minutes of the burst.

At the time of this conference, the *Swift* BAT had detected 339 GRBs (at a rate of about 100 per year), of which 88% have XRT followup observations. The XRT had observed 225 GRBs with prompt followup, typically beginning within $\sim$ 100 s after the burst and lasting for days or weeks. The XRT detection rate is 94% for observations of BAT-discovered GRBs for which XRT observations begin within 200 ks of the burst trigger. The detection rate for long GRBs is 97%, while XRT has detected 23 of 31 short GRBs (74%). The UVOT detects optical transients about 40% of the time, with ground-based observations adding another 20%. Roughly 1/3 of *Swift* GRBs have measured redshifts. The current redshift distribution for *Swift* long GRBs is shown in Fig. 2. The median redshift is now 2.0 with a mean of 2.2, down from 2.5 for the first 2 years of the mission (Jakobsson et al. 2006); for reasons we do not understand, no redshifts greater than 4.0 have been measured since GRB 060927. Because of uncertainties in the determination of redshifts for short GRBs, none of which has yet been measured in absorption against the optical transient, and for which host galaxy identification is often problematic, I do not show the distribution of short GRB redshifts, but they tend to be at lower redshifts than long bursts, with a mean redshift of about 0.5 for the best-determined cases.

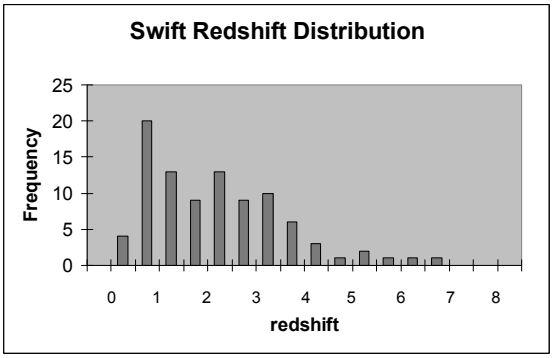

Fig. 2. Redshift distribution of long *Swift* GRBs through June 2008.

2. Key *Swift* Discoveries

Here I highlight some of the key discoveries made by *Swift* in its first three years of operation.

2.1. X-ray afterglows

With $\sim$230 prompt X-ray afterglows, the XRT has shown that the early behavior of X-ray afterglows is typically much more complex than the simple power laws observed at later times with *Beppo-SAX* (de Pasquale et al. 2006). X-ray afterglows exhibit a variety of non-power-law behavior in the first several hours, including steep decays generally attributed to the end of the prompt emission, flat plateau segments with very slow decays, and flares (Nousek et al. 2006; Zhang et al. 2006; Panaitescu et al. 2006a). Fig. 3 shows the light curve of GRB 060413, which displays all of these characteristics, and can be considered a prototypical, or "canonical", X-ray light curve. However, we note that X-ray light curves showing all these features are very rare: most X-ray light curves display only some of these phases.

An interesting point that has yet to be settled is the apparent absence of jet breaks at the expected times (Burrows & Racusin 2006; Liang et al. 2008; Racusin et al. 2009, in prep), combined with a related observation of fairly common chromatic behavior between the X-ray and optical bands (Panaitescu et al. 2006b). Some of this behavior may result from insufficient sensitivity to detect very late jet breaks (Curran et al. 2008; Racusin et al. 2009, in prep), while some of it may be due to more complex jet structure than the simple top-hat jet usually assumed (Racusin et al. 2009, in prep; de Pasquale et al. 2008). Further work is needed on this topic.

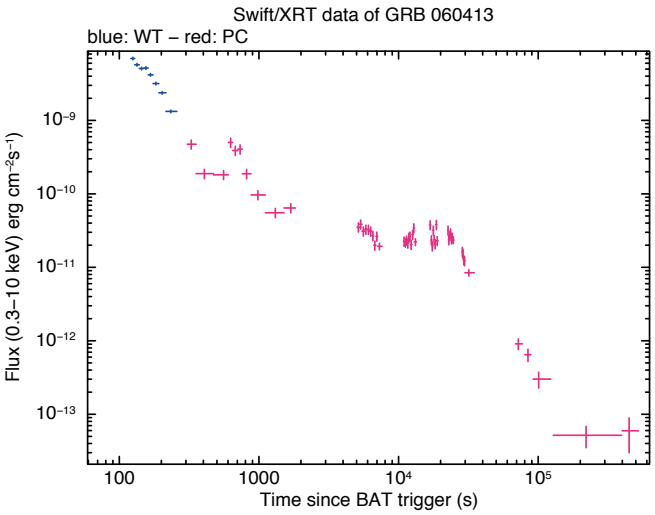

Fig. 3. XRT light curve for GRB 060413. Blue data points are in Windowed Timing mode, red data points are in Photon-Counting mode. This light curve shows all the "canonical" features, including a rapid decline, a flare, a plateau phase, and a normal decay phase (though the latter is unusually steep and may actually represent a post-jet break phase in this case).

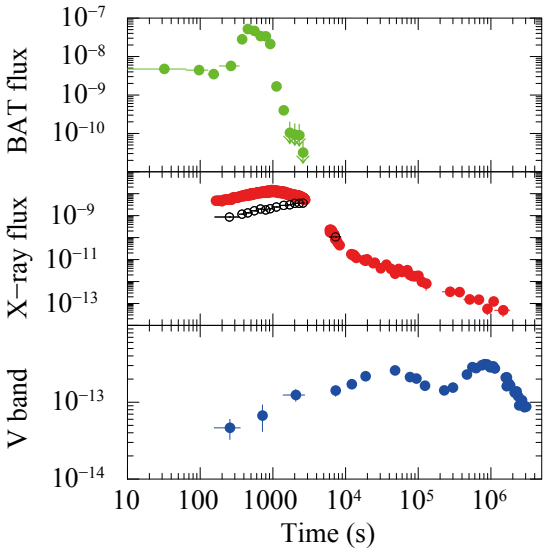

Fig. 4. Top: Swift BAT light curve of GRB 060218. Middle: Swift XRT light curve of GRB 060218. The open circles show the flux due to the black body component. Bottom: Swift UVOT v band light curve of GRB 060218. The first peak is due to the shock breakout, while the second peak is caused by the supernova.

2.2. Short GRB Localizations

One of the most important results from the *Swift* mission has been the localization of short GRBs by the BAT and XRT. At the time of this conference in June 2008, 23 short GRB X-ray afterglows had been localized to precision of several arcseconds. Early results provided dramatic evidence in support of a different origin for short GRBs than for long GRBs, with several cases of short GRB afterglows associated with elliptical galaxies with extremely low rates of star formation (Gehrels et al. 2005; Barthelmy et al. 2005b), in stark contrast to the environment of typical long GRB afterglows (Fruchter et al. 2006). A substantial fraction of the short bursts have been localized to directions with no obvious host galaxy, suggesting that they may have been ejected from their host. Finally, no supernova components have been found associated with short bursts, even when they are at low redshifts. All of these observations are consistent with expectations for compact mergers (NS-NS or NS-BH), which is the favored model for the majority of short GRBs (e.g. Lattimer & Schramm 1976; Paczyński 1986; Eichler et al. 1989; Paczyński 1991).

2.3. GRB 060218: First Detection of Shock Breakout

GRB 060218 was an unusual GRB at a very low redshift. The gamma-ray lightcurve was very smooth and extremely long, with $t_{90} = 2100 \pm 100$ s (Campana et al. 2006). The X-ray light curve was also very long and smooth, peaking at about T+2000 s (Fig. 4). The X-ray spectrum was just as unusual as the light curve: virtually all XRT afterglow spectra can be fit with an absorbed power law, but this spectrum required an additional soft component consistent with a black body spectrum, suggestive of shock breakout. The radius of the black body component increases in time, and its temperature drops, also consistent with expecteations for shock breakout. However, the radius was found to be significantly larger than expected for a Wolf-Rayet star, the expected progenitor of a GRB. We interpreted the event as a shock breakout from the dense stellar wind surrounding the WR star (Campana et al. 2006; Waxman et al. 2007), the first time that this long-predicted phenomenon has been observed.

3. GRB 080319B: the "Naked-Eye" GRB

19 March 2008 was a busy day for *Swift*, with four GRBs on that day and five GRBs in a 24 hour period! The 2nd of these, GRB 080319B, turned out to be one of the most interesting bursts ever seen (Racusin et al. 2008; Bloom et al. 2008; Kumar & Panaitescu 2008). The optical counterpart peaked at a visual magnitude of 5.3, by far the brightest optical GRB counterpart ever seen (the previous record was grb 990123 at about 9^{th} magnitude). What made this even more remarkable is that the redshift of this GRB is $z = 0.937$ (Vreeswijk et al. 2008). The gamma-ray emission was among the brightest ever observed, and the X-ray afterglow was the brightest seen the the XRT. I refer readers to Racusin et al. (2008) for details of the large set of radio, optical, X-ray and gamma-ray observations our team assembled, together with detailed discussion of the theoretical interpretation

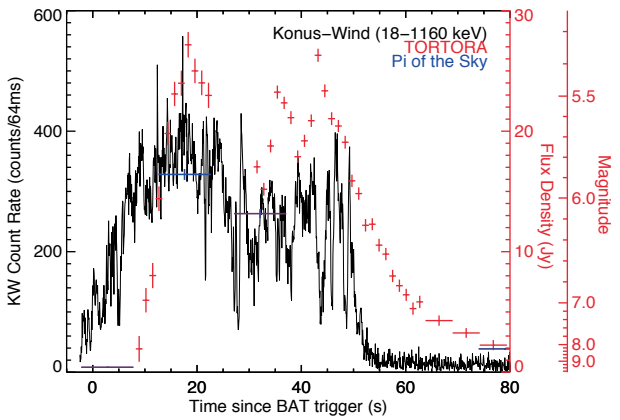

Fig. 5. Prompt light curve of GRB 080319B (Racusin et al. 2008). The black curve shows the Konus-Wind data in the 18 keV - 1.16 MeV energy range. The blue points show the Pi-of-the-Sky optical data, while the red points show the TORTORA optical data. The optical light curves have gaps corresponding to the times when the instruments slewed from GRB 080319A to GRB 080319B. The high resolution TORTORA data peaked at 5.3 magnitudes - by far the brightest optical GRB ever seen!

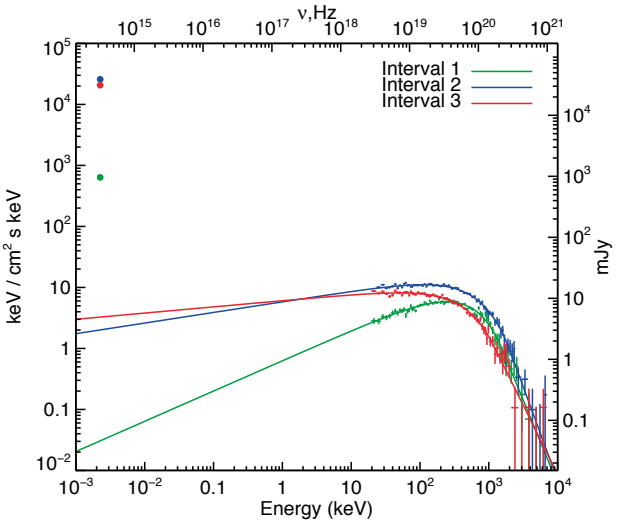

Fig. 6. Spectral Energy Distribution of the prompt emission in three time intervals (Racusin et al. 2008). The data points at about 2 eV represent the Pi-of-the-Sky flux density during these three time intervals. The high energy data points show the Konus-Wind spectrum during these same time intervals, with the curves showing the best-fit Band model extrapolated down to the optical regime. There is strong spectral evolution during the prompt emission, but in all three time intervals the optical flux density exceeds the extrapolation of the gamma-ray flux density by about 4 orders of magnitude, implying that a different spectral component is required to explain the optical flash.

of the data, which I briefly summarize here.

By a fortunate coincidence, GRB 080319B (19B hereafter) occurred only 27 minutes after GRB 080319A, and was located only 10 degrees away on the sky. As a result, 19B was in the field of view of the Pi-of-the-Sky, TORTORA, and RAPTOR optical instruments starting more than 20 minutes before it exploded. The *Swift* slew to 080319A was delayed by nearly 7 minutes due to an Earth limb constraint, but the BAT began collecting event data 1080 s before the burst and registered no precursors in that time period. Fig. 5 shows prompt gamma-ray data from the Konus-Wind instrument, along with prompt optical data from Pi-of-the-Sky and TORTORA.

It is important to note that the first Pi-of-the-Sky data point, which coincides with the BAT trigger, is significantly above the instrumental background and above the earlier data points. The optical flash therefore began within seconds of the gamma-ray burst itself. The optical and gamma-ray emissions clearly occur during the same time interval, though the rapid rise to the optical peak is slightly delayed with respect to the gamma-rays, and the optical decay is slower than the gamma-ray decay. The temporal coincidence of the optical and gamma-ray emission suggests that both bands are produced in the same spatial region. However, the spectrum clearly indicates that different spectral components are required (Fig. 6). A likely interpretation is that the optical emission is synchrotron while the gamma-ray emission is synchrotron self-Compton (Racusin et al. 2008; Kumar & Panaitescu 2008), in contrast to the usual interpretation of the gamma-ray emission being produced directly by synchrotron. An important prediction of this model is that GeV emission should result from 2nd order Compton scattering; unfortunately, the burst was not visible to the AGILE-GRID instrument and GLAST had not been launched yet, so we have no experimental confirmation of this.

The broad-band afterglow of this burst is shown in Fig. 7. The optical data points exhibit spectral evolution during the first few hours, and deviate strongly from the X-ray afterglow slopes. This strongly chromatic behavior requires a model more complex than a single jet, but can be explained quite well by the two component jet model shown in Fig. 8. In this model, the extremely high bulk Lorentz factor (~ 1000) of the narrow jet is responsible for the extremely bright optical and gamma-ray prompt emission, and the afterglow from this narrow jet dominates the X-ray light curve for the first ~ 12 hours after the burst. The optical afterglow, on the other hand, is dominated in the first hour by the reverse shock of the wide jet, and later by the forward shock of the wide jet. The chromatic behavior is thus explained by our conclusion that the optical and X-ray emission in the first 12 hours are dominated by different jet components. Once the narrow jet breaks, the X-ray emission also becomes

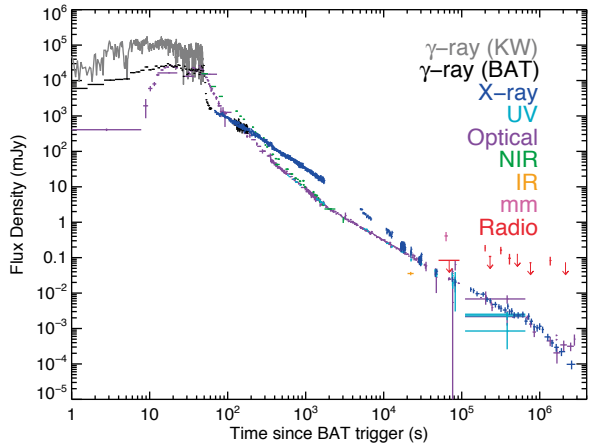

Fig. 7. Broad-band afterglow of GRB 080319B (Racusin et al. 2008). This is a rich data set from a large number of instruments and observing groups; please see Racusin et al. for the complete data list as well as the list of collaborators (co-authors). The prompt emission from *Swift*/BAT (extrapolated into the 0.3-10 keV band for comparison with the XRT data), Konus-Wind, Pi-of-the-Sky, and TORTORA are shown here, together with afterglow emission from *Swift*/XRT, *Swift*/UVOT, a number of ground-based optical telescopes, and several radio telescopes. The optical light curves are normalized to the UVOT v-band data between T_0+1500 s and $T_0+10,000$ s, and show clear evidence for spectral evolution during the first few hours (resulting in apparent discrepancies between different filters around several hundred seconds). The XRT/BAT data are scaled up by a factor of 45 to align the late-time X-ray light curve with the optical light curve, and the Konus-Wind data are scaled up by a factor of 10^4 for comparison with the optical flux densities during the prompt phase.

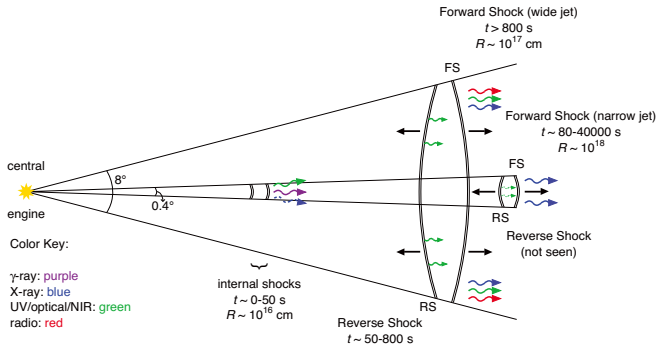

Fig. 8. Schematic diagram of the jet structure of GRB 080319B (Racusin et al. 2008; figure courtesy of J. D. Myers, NASA/GSFC). The chromatic behavior of the optical and X-ray light curves are a result of this complex jet structure. The prompt emission and early X-ray afterglow are dominated by a narrow jet pointed directly at us. The optical emission immediately after the prompt phase is dominated by the reverse shock of a much broader, concentric jet component. This fades rapidly, and by $T_0 + 1000$ s the optical emission is dominated by the wide jet's forward shock. The narrow jet breaks at about half a day, after which the X-ray afterglow is also dominated by the forward shock of the wide jet. Breaks in the X-ray light curve allow the opening angles of both jet components to be measured.

dominated by the forward shock of the wide jet. The two jet breaks seen in the X-ray light curve correspond to jet opening angles of about 0.4 and 8 degrees for the two jets. The energetics of this burst turn out to be comparable to typical GRBs, in spite of the unusual brightness, due to this narrow jet component. We were fortunate to see it - a simple probabilistic argument suggests that such events may be observable roughly once a decade.

4. The Future of *Swift*

The *Swift* observatory continues to work very well in its fourth year, and the team continues to improve calibration parameters and operating performance. Over the past two years *Swift* has shifted its emphasis from GRBs toward more Target of Opportunity (ToO) observations, and a substantial fraction of our time is now spent on ToOs (see paper by Gehrels in this volume). The success of the mission has been reflected in an extension of its funded operations until at least September 2011. This raises the prospect of exciting collaborative work with several other missions and experiments, in particular:

- GLAST: With the launch of GLAST during this conference, we are just entering the era of GLAST/*Swift* overlap. At the time of this writing, the GLAST Gamma-ray Burst Monitor instrument has already begun detecting bursts in coincidence with *Swift*. We anticipate exciting results stemming from simultaneous *Swift* and GLAST/Large Area Telescope GeV detectors of bursts that may indicate what role second-order Compton process such as that suggested above for GRB 080319B, or other extremely high energy processes, play in black hole formation and GRB explosions.

- LIGO: the gravitational inspiral "chirp" signature of a compact merger event in coincidence with a *Swift* detection of a short GRB would be the "smoking gun" needed to conclusively demonstrate that some fraction of these events originate in binary mergers. The chance of such a coincident detection is improved by the anticipated advent of Enhanced LIGO in 2009, which will double LIGO's detection range for these events. It is conceivable that *Swift* will still be operational when Advanced LIGO goes online, extending sensitivity to compact mergers out to 300 Mpc for NS-NS binaries and out to 650 Mpc for NS-BH binaries, and further improving chances for detection of gravitational wave events coincident with *Swift* bursts.

5. Beyond *Swift*

GRBs can now be exploited as bright background sources at high redshift in order to study star formation, galaxy

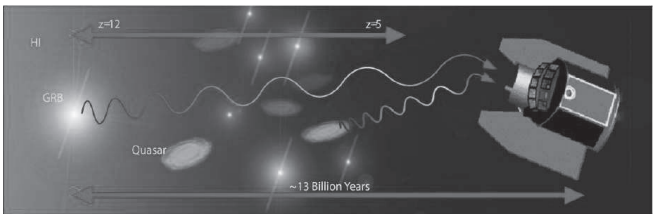

Fig. 9. The *JANUS* mission is designed to study high redshift GRBs and quasars.

evolution, and metal production in the high-z universe (e.g., Prochaska et al. 2007; Tejos et al. 2007; Penprase et al. 2008; Prochaska et al. 2008; Whalen et al. 2008; Fynbo et al. 2008). However, even in the *Swift* era the discovery rate for high-z GRBs is quite low; no burst with $z > 4$ has been found in the past two years, for example. In order to fully exploit this capability, new missions specifically designed to optimize the detection of high redshift bursts *and to measure their redshift directly* are required. One such mission is *JANUS* (Fig. 9), a NASA Small Explorer (SMEX) mission currently in Phase A. *JANUS* carries a wide-field X-ray monitor designed to detect high redshift bursts in the 1-20 keV band, and a Near IR Telecope with a grism designed to measure redshifts between 5 and 12. We expect to detect 25 GRBs per year with redshift greater than 5, providing positions and redshift measurements within 30 minutes of discovery to enable prompt NIR spectroscopy from the ground. *JANUS* will move GRBs beyond the realm of scientific curiosity to the role of an important cosmological tool for studies extending into the reionzation era.

Acknowledgements

This work was supported by NASA contract NAS5-00136. I acknowledge major contributions to the topics reviewed here from the entire *Swift*/XRT instrument team, as well as the contributions of our many collaborators to the investigation of the remarkable GRB 080319B.

References

Barthelmy, S. D., et al. 2005a, *Space Sci. Rev.*, 120, 143
Barthelmy, S. D., et al. 2005b, *Nature*, 438, 994
Bloom, J. S., et al. 2008, *Ap. J.*, submitted, *arXiv:0803.3215*
Burrows, D. N., et al. 2005, *Space Sci. Rev.*, 120, 165
Burrows, D. N., & Racusin, J. 2006, *Il Nuovo Cimento*, 121, 1273
Campana, S., et al. 2006, *Nature*, 442, 1008
Costa, E., et al. 1997, *Nature*, 387, 783
Curran, P. A., et al. 2008, *MNRAS*, 386, 859
de Pasquale, M., et al. 2006, *Astron. and Astrophys.*, 455, 813
de Pasquale, M., et al. 2008, *AIP Conf. Proc.*, 1000, 463
Djorgovski, S. G., et al. 2008, *Ap. J. (Letters)*, 508, L17
Evans, P. A., et al. 2008, *AIP Conf. Proc.*, 1000, 539
Fruchter, A. S., et al. 2006, *Nature*, 441, 463
Fynbo, J. P. U., et al. 2008, *Ap. J.*, 683, 321
Gehrels, N., et al. 2004, *Ap. J.*, 611, 1005
Gehrels, N., et al., 2005, *Nature*, 437, 851
Goad, M. R., et al. 2007, *Astron. and Astrophys.*, 476, 1401
Jakobsson, P., et al. 2006, *Astron. and Astrophys.*, 447, 897
Klebesadel, R. W., Strong, I. B., and Olson, R. A. 1973, *Ap. J. (Letters)*, 182, L85
Kouveliotou, C., et al. 1993, *Ap. J.*, 413, L101
Kumar, P., & Panaitescu, A. 2008, *MNRAS*, submitted, *arXiv:0805.0144*
Lattimer, J., & Schramm, D. 1976, *Ap. J.*, 210, 549
Meegan, C. A., et al. 1992, *Nature*, 355, 143
Metzger, M. R., et al. 1997, *Nature*, 387, 878
Nousek, J. A., et al. 2006, *Ap. J.*, 642, 389
Mészáros, P., & Rees, M. J. 1993, *Ap. J.*, 405, 278
Paczyński, B. 1986, *Ap. J.*, 308, L43
Paczyński, B. 1991, Acta Astron., 41, 257
Panaitescu, A., et al. 2006a, *MNRAS*, 366, 1357
Panaitescu, A., et al. 2006b, *MNRAS*, 369, 2059
Penprase, B. E., et al. 2008, *AIP Conf. Proc*, 990, 499
Prochaska, J. X., et al. 2007, *Ap. J.*, 666, 267
Prochaska, J. X., et al. 2008, *AIP Conf. Proc*, 1000, 479
Racusin, J. L., et al. 2008, *Nature*, in press, *arXiv:0805.1557*
Rees, M. J., & Mészáros, P. 1992, *MNRAS*, 258, 41P
Roming, P.W.A., et al., 2005, *Space Sci. Rev.*, 120, 95
Tejos, N., et al. 2007; *Ap. J.*, 671, 622
van Paradijs, J., et al. 1997, *Nature*, 386, 686
Vreeswijk, P. M., et al. 2008, *GCN Circ.*, 7444
Waxman, E., Mészáros, P., & Campana, S. 2007, *Ap. J.*, 667, 351
Whalen, D., et al. 2008, *Ap. J.*, 682, 1114
Zhang, B., et al. . 2006, *Ap. J.*, 642, 354

GRBCAT: Bursts from Vela to Swift

Lorella Angelini [1]

[1] GSFC/NASA, Code 661, Greenbelt, MD, 20771, USA
E-mail: lorella.angelini-1@nasa.gov

ABSTRACT

Gamma ray burst (GRB) astronomy started when the first event was recorded on July 2, 1967, by Vela 4a and 4b. Since then many missions have flown experiments capable of detecting GRBs. The events collected by these older experiments are mostly available in paper copy, each containing a few ten to a few hundreds bursts. No systematic effort in cataloging of these bursts has been available. In some cases the information is unpublished and in others difficult to retrieve. The first major GRB catalog was obtained by GRO with the BATSE experiment. It contains more than 2000 bursts and includes homogeneous information for each of the burst. With the launch of Swift, the first Gamma X-ray mission dedicated to the study of the GRBs and their afterglows, a wealthy of information is collecting by the Swift instruments as well as from ground based telescopes. This talked will describe the effort to create a comprehensive GRBCAT, its current status and future prospects.

1. Overview

On Jul 2 1967 with the first GRB detection by Vela (Fig.1) started the field of Gamma ray Bursts astronomy. Since then many missions with experiments capable to detected GRBs were flown. The events collected by most of these old experiments are published in paper copy. No systematic effort to cataloging these bursts has been available. Information in cases was unpublished or difficult to retrieve. The first major GRB catalog was obtained by GRO with the BATSE experiment, which contains more than 2000 events with homogeneous information. With the launch of Swift, the first mission dedicated to GRB and their afterglow a new wealthy of information is collected from Swift instrumentation and from ground based telescopes. GRBCAT is a cataloguing effort to create comprehensive catalogs of GRBs.

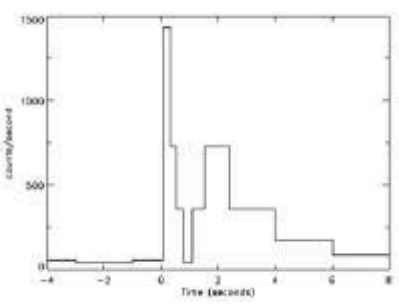

Fig.1. The first GRB with Vela 4a and 4b.

2. GRBCAT

GRBCAT contains currently GRB prior the Swift era. GRBCAT has been built including sources from paper published in the referee journal, unpublished papers (mostly provided from K.Hurley), events in PhD thesis and compilation of bursts already present in the HEASARC database. GRBCAT contains two kinds of information. There are basic parameters that characterized the detected event and for most recent bursts include information of their afterglow For each burst the literature and databases were searched for a number of information as

- Time of the trigger
- Duration
- Fluxes
- Fluence
- Position or the geometry of the region containing the position

The parameters of GRBCAT has been reported as they published in literature since there is no standards or single units of how these quantities has been reported. For example:

- Fluxes and/or fluence are reported either in different units or for individual one. Or more than one measurement are reported.
- Duration is not always the canonical T50 or T90.
- Time of the trigger arrival uses different time reference system or unspecified.

These quantities therefore are layout using several fields. For these older bursts one major problem was to obtain the accurate position.

- The GRO/BATSE has an accuracy of few degrees.
- Interplanetary GRB network exists since 1976. It uses the arrival time of these events as detected from different satellites. The positions reported in literature are from complicated regions. GRBCAT includes parameters to describe each of the regions.
- BeppoSAX GRBM working with the WFC was the first to get arcmin position.

GRBCAT currently contains 5814 unique GRBs from 1967 up to December 2004. Events were collected from over 23 satellites. If an event has been detected from more than one satellite, both are listed. Events are considered "different", if they occur in a time interval of 5 minutes apart. Note that SGR are not included.

The catalog is not complete and does not include events detected :

- by Ginga
- only by the BeppoSAX GRBM
- by HETE-2 and Integral after Dec 2004.

There is not a comprehensive publication for Ginga. For Integral and HETE-2 information were taken mainly from the GCN. BeppoSAX/GRBM or Ginga events are present only if other satellites have seen them.

Afterglow information is given for any bursts detected after May 11 1996 until Dec 2004. Afterglow information has been retrieved mainly for the GCN and includes: flux or level of detection and redshift. There are information for :

- 188 individual bursts follow up observations
- 108 detected or possible detected afterglows
- 80 with positive afterglow detections

A total of 2646 observations among radio, optical, infrared and X-ray are included:

- 32 detected in radio out of 52 observed.
- 43 detected in optical and IR out of 89 observed.
- 36 detected in X-ray EUV out of 46 observed.

The layout of GRBCAT is shown in Fig. 2. GRBCAT is not a single table but is composite of several tables of

- Mail Table : General and GRB duration
- Fluxes and Fluences
- Regions
- Afterglow

There is dedicated thematic web site

http://grbcat.gfsc.nasa.gov

Note that the beta version is currently populated and it is not searchable. Next will be to include the Swift GRB and complete the Integral, HETE-2, Suzaku, Agile and the IPN. It includes all source of information used to populated the catalog. Ready to go on-line within this month.

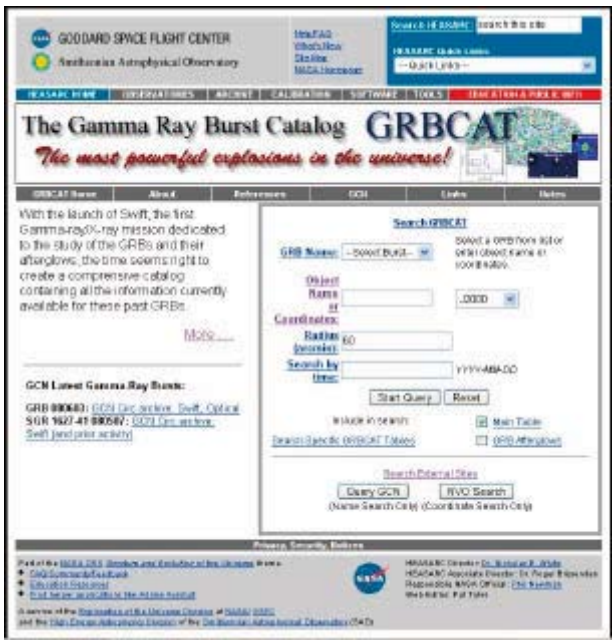

Fig.2. GRBCAT layout. http://grbcat.gfsc.nasa.gov

3. Swift GRB catalog

Current version of the Swift GRB catalog contains all GRBs up to GRB 070429B. The total is 259 bursts. They are all bursts discovered by Swift or discovered by others & followed by Swift. It is created by contribution of the Swift IT and mainly GCN circular. Several data products are associated with the catalog:

- Lightcurves and Images all three instruments & combine BAT XRT lightcurve
- Spectra (BAT and XRT)
- Informative tables listing parameters used in the processing
- HTML file to include all plots & link to files as well as information from the Swift GRB catalog

The Swift GRB catalog are generated by scripts using as much possible the current software. Addition routines will be included in the Swift software package. They run in automatic fashion (but for the XSPEC fitting of the XRT LC), and visually inspected and corrected if the automatic process fails.

The products will be linked to the Swift GRB catalog. We will start populating the archive by end of July from old bursts and it is expected to catch up with the latest burst within 6 months.

To each bursts associated several parameters :

- Position from the 3 instruments and best position
- If detected by the XRT or UVOT
- Time interval Swift followed the burst and first time on source
- Redshifts, galactic N_H, Galaxy association
- If follow up in the O R I and if detected
- Several measurements from the BAT, XRT and UVOT

The catalog is in the HEASARC develop area, but soon it will be moved in the public area.

4. Conclusion

GRBCAT and Swift GRB catalog are new resources, which will come on-line soon. The Swift GRB catalog will be ultimately part of GRBCAT. GRBCAT will be updates for not only Swift GRBs but also HETE-2, Integral, Suzaku, Agile, IPN and MAXI.

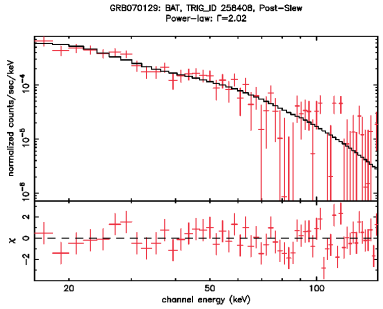

Fig.3. Example of the BAT GRB spectral plot.

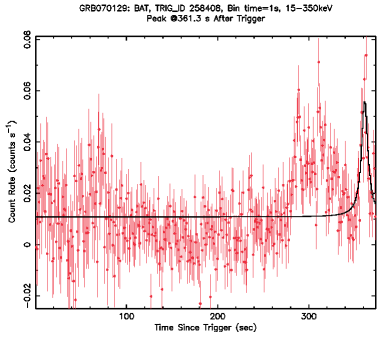

Fig.4. Example of the BAT GRB light curvel plot.

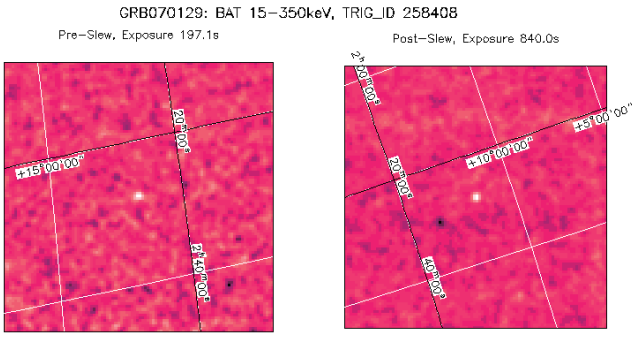

Fig.5. Example of the BAT GRB images.

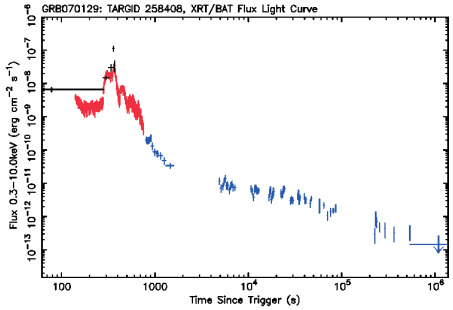

Fig.6. Example of XRT/BAT combined product

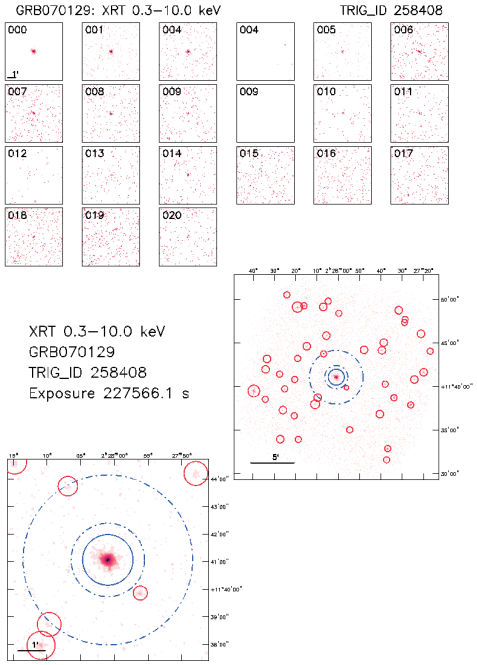

Fig.7. Example of XRT GRB image plot

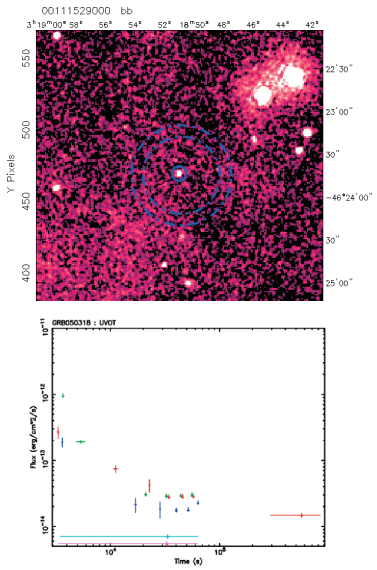

Fig.8. Example of UVOT GRB plot product

X-ray flashes

Luigi Piro [1]

[1] Istituto Astrofisica Spaziale Fisica Cosmica, Roma, INAF
E-mail(LP): luigi.piro@iasf-roma.inaf.it

Abstract

After their discovery with BeppoSAX and vigorous follow up programs with HETE2 and, more recently, with SWIFT, X-ray flashes are still puzzling phenomena. They are a very numerous class of soft GRB, making up about 40% of the total population. In this talk I will review the status of observations and discuss about different scenarios proposed to explain their origin. These include the off-axis jet scenario or sub-energetic GRBs. With its soft X-ray response and wide sky capability, we expect that MAXI will provide important observations to improve our understanding on these elusive phenomena.

X-ray Flashes

Luigi Piro

INAF/IASF Roma

Istituto di Astrofisica Spaziale e Fisica Cosmica - Roma

Summary

- Discovery
- A new class of GRBs
- Constrain on the origin from observations
- The puzzle remains open
- MAXI perspecitves

X-ray flashes

- **A New class discovered b BSAX and confirmed by HETE2: about 50% GRB with no or very faint or gamma-ray emission**
- **high redshift GRBs**
- **off-axis events**
- **Subenergetic events, mor numerous than normal GRBs**

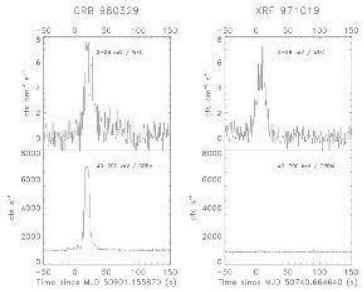

Heise et al 2001

XRF host galaxies

- 2 of XRF localized by BSAX and followed up by Chandra (Bloom et al 03)
- more redshift by SWIFT at z<3 (Gendre, Galli, LP, 2007)

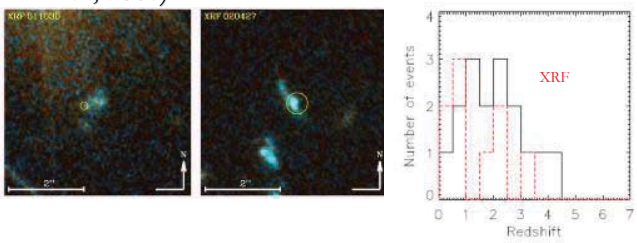

A class of GRBs

- HETE2 (Sakamoto et al 04)

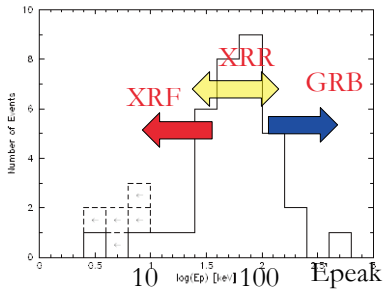

XRF vs GRB: HETE2+BSAX

- 54 XRF+XRR in a combined BeppoSAX and HETE2 (Sakamoto et al) sample (D'Alessio, LP, Rossi (A&A 2006,)
- H=S(2-30)/S(30-400 keV):
  - XRF:H>1
  - XRR: 0.32<H<1
  - GRB: H<1

XRF vs GRB: Prompt

- Spectral indexes are consistent
- <Epeak(XRF)>=35 keV
- <Epeak(GRB)>=165 keV

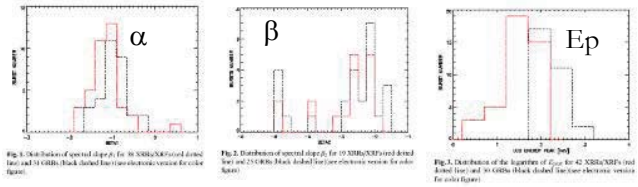

Collapsar model → Sub energetic X-ray flashes

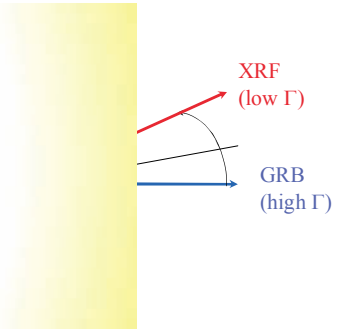

Woosley et al

Testing the unification scenario the off-axis jet

- GRB and XRF have the same intrinsic properties and z distribution
- The only difference is the viewing angle (analogous to the strong unification scenario for AGN)
- Derive average off-axis angle from the prompt (Epeak) for the two populations for homogeneous, gaussian and universal jet model, (dE/dΩ(θ), Amati relationship)
- Derive afterglow flux at 11 hrs/(1+z) corresponding to the two average off axis angles from model and compare with observations

D'Alessio, LP, Rossi (A&A 2006,)

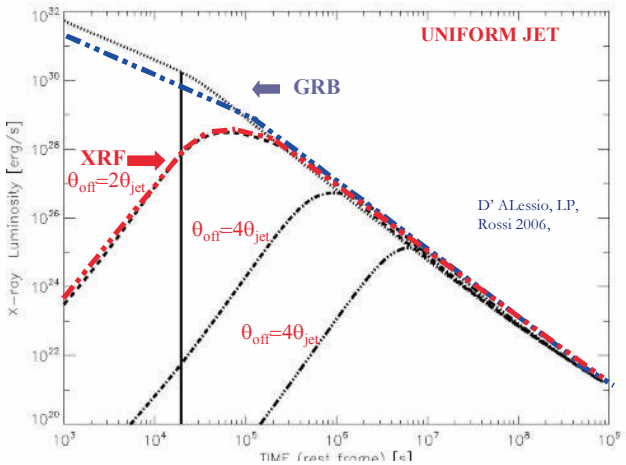

XRF vs GRB: afterglow data (I)

- Pre-SWIFT: The average X-ray flux (@ 11 hrs) in XRF is consistent with that of GRB (ratio GRB/XRF afterglow = 1.0+-0.8). Similar result for the optical afterglows

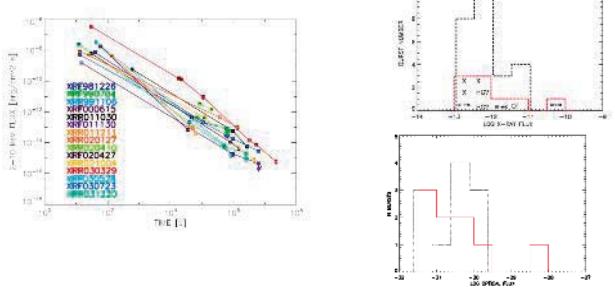

XRF vs GRB: afterglow data (II)

- SWIFT: X-ray Luminosity (z available)
- Results <Lx_{GRB}/Lx_{XRF}(@20ksec>=2.5+-2

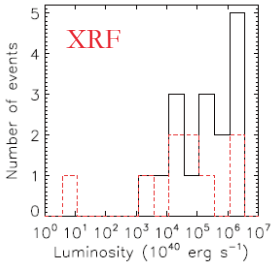

Gendre,Galli & LP 07

The puzzling origin of XRF

- XRF and GRB have similar X-ray afterglow luminosity
- Off-axis jet models, in their different incarnations (uniform, gaussian, universal) have severe difficulties in explaining this result
- The subenergetic scenario appears also problematic: the X-ray luminosity is a good proxy of the kinetic energy
- the high z scenario already excluded as a whole

Prospects with MAXI

- BSAX and HETE2 samples: XRF(+XRR):77%, GRBs(Ep>100 keV): 23%
- MAXI: about 10 GRB per year, most of the should be XRR-XRF
- Crucial to get the afterglow properties and redshift: SWIFT follow up

Suzaku Wide-band All-sky Monitor (WAM) Observations of High Energy Transients

Kazutaka Yamaoka, [1] Satoshi Sugita, [1] Makoto S. Tashiro, [2] Yukikatsu Terada, [2] Yuji Urata, [2] Kaori Onda, [2] Akira Endo, [2] Natsuki Kodaka, [2] Kouichi Morigami, [2] Takako Sugasawara, [2] Wataru Iwakiri, [2] Yasushi Fukazawa, [3] Takuya Takahashi, [3] Takeshi Uehara, [3] Chie Kira, [3] Yoshitaka Hanabata, [3] Kazuo Makishima, [4] Kazuhiro Nakazawa, [4] Ryohei Miyawaki, [4] Teruaki Enoto, [4] Tadayuki Takahashi, [5] Motohide Kokubun, [5] Masanori Ohno, [5] Motoko Suzuki, [6] Soojing Hong, [7] Toru Tamagawa, [8] Yujin E. Nakagawa, [8] Makoto Yamauchi, [9] Eri Sonoda, [9] Ryoji Hara, [9] Yuki Tanaka, [9] Hidenori Hayashi, [9] Kenta Kohno, [9] Norisuke Ohmori, [9] Toshio Murakami, [10], Tsuneyoshi Kamae, [11] Hiroyasu Tajima, [11] and the Suzaku WAM team

[1]Department of Physics and Mathematics, Aoyama Gakuin University, Kanagawa, Japan
[2]Department of Physics, Saitama University, Saitama, Japan
[3]Department of Physics, Hiroshima University, Hiroshima, Japan
[4]Department of Physics, University of Tokyo, Tokyo, Japan
[5]Division of High Energy Astrophysics, ISAS/JAXA, Kanagawa, Japan
[6]ISS project team, ISAS/JAXA, Ibaraki, Japan
[7]College of Science and Technology, Nihon University, Tokyo, Japan
[8]Institute of Physical and Chemical Research (RIKEN), Saitama, Japan
[9]Department of Applied Physics, University of Miyazaki, Miyazaki,Japan
[10]Department of Physics, Kanazawa University, Kanazawa, Japan
[11]Stanford Linear Accelerator Center (SLAC), CA, USA
E-mail(KY): yamaoka@phys.aoyama.ac.jp

Abstract

The wide-band all-sky monitor (WAM) is the secondary function of large BGO shields of the Hard X-ray Detector (HXD) on board the Suzaku mission. Owing to its large geometrical area of 800 cm^2 per side and wide field of view, the WAM is very powerful to study soft gamma-ray transients in the energy range of 50–5000 keV. The main scientific objectives are gamma-ray bursts (GRB), soft gamma-ray repeaters (SGR), solar flares, and black-hole binaries. 449 GRBs, 78 SGRs, and 171 solar flares confirmed by other satellites were detected during the three-years operation (August 2005 to September 2008). The GRB detection rate is more than 140 per year, which shows one of the highest in current GRB missions. High quality spectra and light curves can be obtained for bright GRBs, which enable us to investigate the time variability and the time resolved spectroscopy even for the short duration GRBs. Furthermore, the WAM detected a large flare from the black-hole binary Cygnus X-1 corresponding to TeV gamma-ray detections with MAGIC telescope on September 2006. In this paper, we will review the results obtained from the WAM, and report on the current status of the WAM observations of these high energy transients.

Key words: gamma-ray burst, Suzaku, gamma-rays

1. Suzaku Wide-band All-sky Monitor(WAM)

The Suzaku is the fifth Japanese X-ray astronomical satellite which was launched on July 10th, 2005 (Mitsuda et al. 2007). It is flown into a near-Earth orbit with the altitude of 570 km and the inclination angle of 31 degrees. It carries three scientific instruments: X-ray spectrometer (XRS), X-ray imaging spectrometer (XIS), and hard X-ray detector (HXD; Takahashi et al. 2007, Kokubun et al. 2007). Currently two instruments (XIS and HXD) are operational well, covering a broad energy range of 0.3–600 keV.

The Suzaku wide-band all-sky monitor (WAM) is a subsystem of the HXD utilizing 20 lateral BGO anti-coincidence shields (Figure 1). The main purpose of the WAM is background rejection to the main detectors (Si PIN diodes and GSOs), but owing to its large geometrical area of 800 cm^2 and its large field of view of a half sky, it can be an ideal gamma-ray burst detector with an energy range of 50–5000 keV. Furthermore, the on-axis effective area per one wall (of the four walls) is about

400 cm^2 at 1 MeV (Figure 2), which is much larger than those of other GRB missions. Hence, the WAM is expected to clarify the origin of radiation mechanisms of the GRB prompt MeV gamma-ray emissions with a high sensitivity. The WAM characteristics are shown in Table 1

In this paper, we present the current status of the Suzaku WAM over initial three years, focusing on observations of GRBs and hard X-ray sources related with the MAXI science. Details of design and its in-orbit performance of the Suzaku WAM are described in Yamaoka et al. (2009).

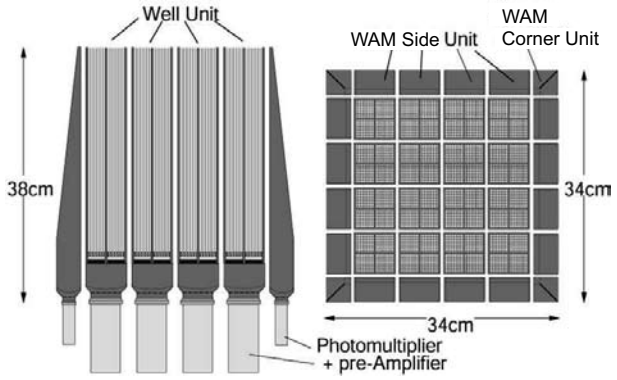

Fig. 1. Schematic view of the Hard X-ray Detector. Left panel: Cross-sectional view. Right panel: Top view. The WAM is a subsystem of the HXD which consists of the surrounding 20 BGO anti-coincidence shields.

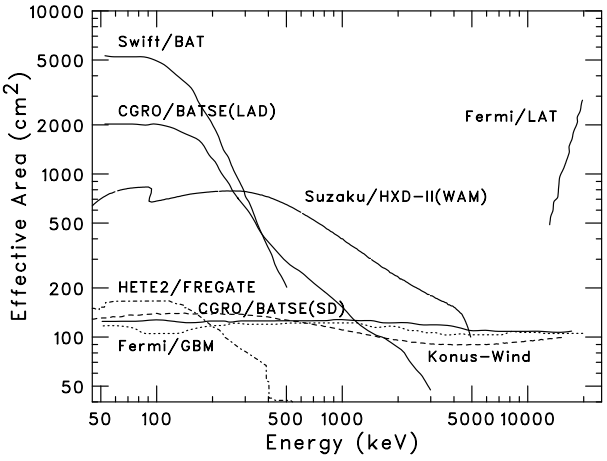

Fig. 2. On-axis effective area of the Suzaku WAM in comparison with previous and current GRB detectors. The Suzaku WAM has a very large effective area ∼400 cm^2 in the MeV range.

2. Current Status of Suzaku WAM

The WAM activation was completed on August 17, 2005. Since then, all the 20 WAM sensors have been working very well. There are also no problems in the

Table 1. Characteristics of the Suzaku wide-band all-sky monitor.

Sensors	20 BGO crystals + PMT
Number of detectors	4 (referred to as WAM 0–3)
Energy range	50–5000 keV (55 channels)
Geometrical area	800 cm^2 per side
Effective area	400 cm^2 per side @ 1 MeV
Energy resolution	∼ 30% @ 662 keV
Field of view	∼ 2 π
Time resolution	1/64s during 64 seconds (BST data)∗; every 1s (TRN data)
Telemetry rate	5 kbps
Response to GRBs	within a day (no alerts)
GRB localization capability	5–10 degrees (WAM alone), <1 degree (IPN)

∗ Since Mar. 20, 2006. 1/32 s during 128 seconds before this date.

WAM electronics including the data readout and GRB trigger system. Table 2 shows statistics of the WAM events from August 2005 to September 2008. 449 GRBs were confirmed by other satellites, while 298 GRB-like events were not confirmed and classified as possible GRBs. It means that the WAM has been detecting more than 140 GRBs per year. We have released 74 GCN circulars about the WAM spectral parameters and Inter-Planetary Network (IPN; IPN3 web site: http://ssl.berkeley.edu/ipn3/index.html) localization. The WAM sensitivity for 1-sec is estimated at ∼0.7 photons cm^{-2} s^{-1} in the 50−300 keV range. The funding for the Suzaku operation is approved for at least two more years, so the WAM will continue to detect GRBs at the same rate unless it does not work.

The energy-scale calibration is performed using the 511 keV line from surrounding activated materials on the satellite. We monitor the gain of all the units at once a day. The WAM absolute flux calibration is performed using GRBs which was simultaneously detected by Swift-BAT and Konus-Wind (Yamaoka et al. 2009 and Sakamoto et al. 2009). The current flux uncertainties above 120 keV are estimated at ∼30 % except for the XRS directions. Uncertainties for lower energy than 120 keV are at more than 40 %, probably due to additional absorptions from the satellite. Similar results have been obtained using Crab Nebula with the Earth-occultation technique. Further refinement of calibrations and study of GRB localization by the WAM alone are still under way. Absolute timing has been verified by measuring the time delay for position well-determined GRBs with IPN. Thus, the Suzaku WAM has been involved into the third IPNs and has played an important role as one of detectors in the low-Earth orbit.

Table 2. Statistics of the WAM events, through August 2005 to September 2008.

Category	Number (Trigger)
Confirmed GRBs	449 (274)
Swift/BAT	85 (44)
Fermi/GBM	27 (15)
INTEGRAL/IBIS	6
AGILE/superAGILE	6
Konus-Wind	364
Possible GRBs	298 (139)
Soft Gamma-ray Repeaters	78 (5)
Solar flares	171 (28)

3. WAM Observations of Gamma-ray Bursts

3.1. GRB Light Curves and Energy Spectra

The WAM can get the fine-time resolution light curve with 1/32 or 1/64 sec (BST data) in case a GRB trigger the WAM. We also continuously get the energy spectrum with 1-sec time resolution (TRN data). Figure 3 shows the light curve of the short-duration GRB 060317 in the four energy bands with 1/32 sec resolution. This GRB has a peak flux of 41±4 photons s^{-1} cm^{-2} in the 50-5000 keV range, and a very hard spectrum with $E_{\rm peak}$ ∼2 MeV (Ohno et al. 2008). Ohno et al. (2008) also estimated a lag between the 50–110 keV band and other three bands (110–240 keV, 240–520 keV, and 520–5000 keV), and found that all were consistent with zero, indicating that this GRB indeed belongs to the short-burst category. Thus, the WAM can produce high quality data for variability studies even in the highest energy range above 520 keV owing to its large effective area. The light curve data for confirmed GRBs are available at the web site: http://www.astro.isas.jaxa.jp/suzaku/HXD-WAM/WAM-GRB/

The T90 duration distribution for triggered bursts is shown in Figure 4. We have plotted it for confirmed GRBs and possible GRBs. The T90 duration was calculated as the time interval starting after 5% and ending after 95% of the counts in the 50–5000 keV range. The distribution of the BATSE sample in the 4th revised catalog (Paciesas et al. 1999) is also shown for comparison. We clearly observe a bimodal distribution for confirmed GRBs which peaks at 0.2 sec and 10 sec. This is almost consistent with the BATSE sample, but is quite different from the Swift distribution, which has relatively few short-duration GRBs (<2 sec) (Sakamoto et al. 2008).

An important feature of the WAM is its large effective area in the MeV range. Figure 5 shows time-averaged spectra in raw detector counts for six bright GRBs which were localized by the IPN. This sample includes two short GRBs: GRB 051103 and GRB 060317. All the

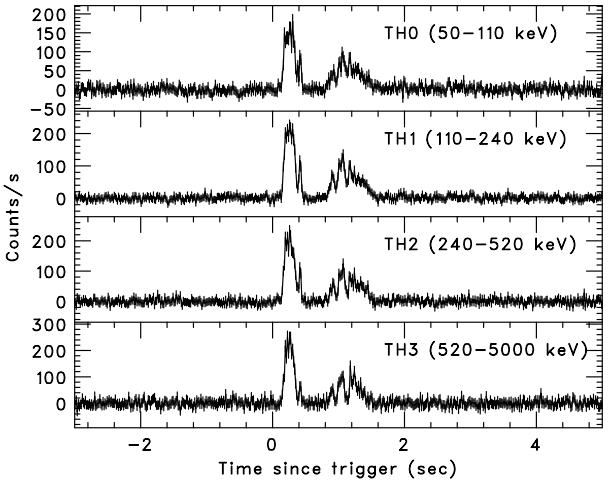

Fig. 3. Example of the bright short GRB 060317 in the four energy bands. High quality light curve can be obtained even in the highest energy band (>520 keV).

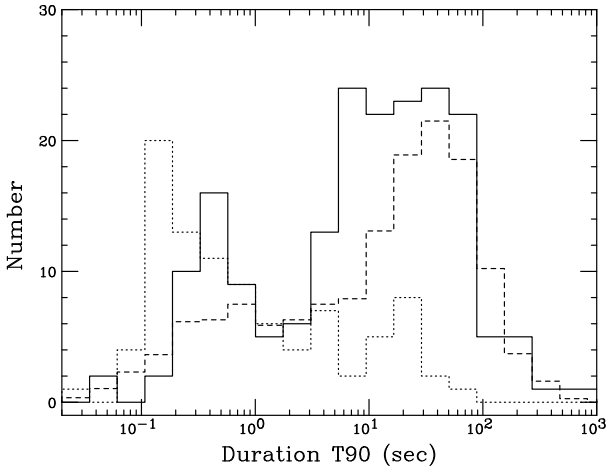

Fig. 4. T90 duration distributions of the WAM GRBs. Confirmed and possible GRBs are shown separately as solid and dotted lines, respectively. They are also compared with BATSE GRB sample (dashed line) with an arbitrary normalization.

bursts (even the short bursts) show clear signals above 1 MeV. High quality spectra can be obtained up to $\sim$ 5 MeV. This capability is a very powerful tool in determining the high energy photon index β and studying the connection between the low energy component, presumably due to synchrotron emission, and the poorly understood high energy component (> MeV) detected by EGRET/TASC (Gonzalez et al. 2002), which might be detected by Fermi and AGILE.

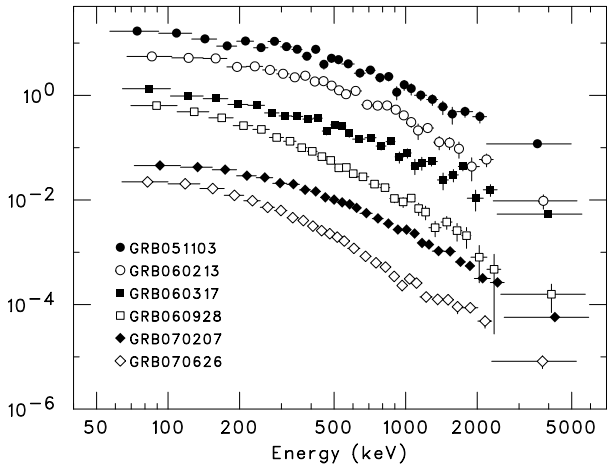

Fig. 5. Example of WAM count spectra for six bright GRBs. GRB 051103 and GRB 060317 are classified as short-duration bursts.

3.2. Joint Swift/BAT and Suzaku/WAM Spectral Analysis

Broadband spectral measurements of the GRB prompt emissions are important in understanding the GRB radiation mechanisms. In addition, several correlations among GRB spectral parameters such as peak energies ($E_{\rm peak}$) have been proposed and discussed. Some of them are used for redshift indicators and constraints on cosmological constants. Rapid localizations by Swift has enabled us to determine redshifts for many GRBS, however, only 14% of the Swift GRBs have $E_{\rm peak}$ due to the limited energy range of BAT (15−150 keV). Figure 6 shows an example of Swift-BAT and Suzaku-WAM $_{\nu}F_{\nu}$ spectra of the three Swift GRBs. The peaks of the spectra ($E_{\rm peak}$) is clearly visible in the 50 keV to 1 MeV range, so a combination of Swift/BAT (15−150 keV) and Suzaku/WAM (50−5000 keV) can be very powerful tool to determine GRB spectral parameters.

Since 2006 August, we are going to proceed joint spectral analysis project between Swift/BAT and Suzaku/WAM (Krimm et al. 2009). We have paid careful attention for the cross-calibration issue and analysis methods. 85 GRBs (44 WAM triggers and 41 untriggers) were detected by both instruments till September 2008, and 32 GRBs have known redshifts in their range of 0.089(GRB 060505) to 6.295 (GRB 050904; Sugita et al. 2009). All the bursts were jointly analyzed, and $E_{\rm peak}$ was determined for 51 GRBs. Figure 7 shows updated $E_{\rm p,i}$-$E_{\rm iso}$ correlations, so-called Amati relations, for BAT-WAM GRBs. Long GRBs satisfied with this relations within statistical errors, but there might be some bias to larger $E_{\rm peak}$. On the other hand, all the six short GRBs (GRB 051221A, 060801, 061006, 061210, 070714B and 071227) and sub-luminous GRB 060505 are outliers in the Amati relation. $E_{\rm peak} - L_{\gamma}$ (Ghirlanda relation; Ghirlanda et al. 2004) and $E_{\rm peak} - L_{\rm p}$ (Yonetoku relation; Yonetoku et al. 2004) are still under investigation.

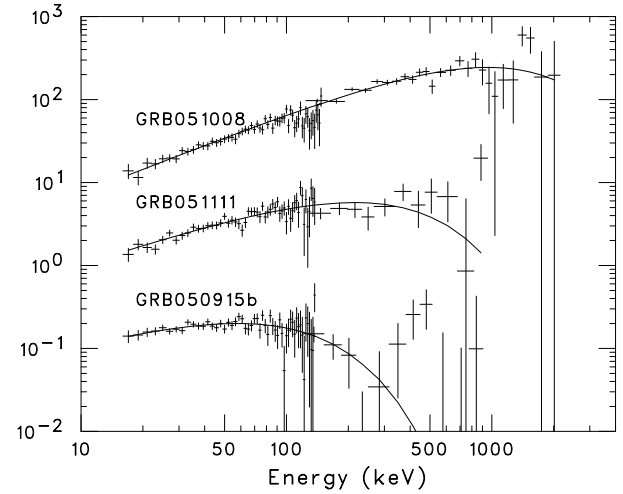

Fig. 6. Unfolded $_{\nu}F_{\nu}$ energy spectra of the three Swift GRBs (GRB 050915B, GRB 051111 and GRB 051008). A combination of Swift/BAT and Suzaku/WAM is very powerful to determine the peak energy ($E_{\rm peak}$) in the range of 50–1000 keV.

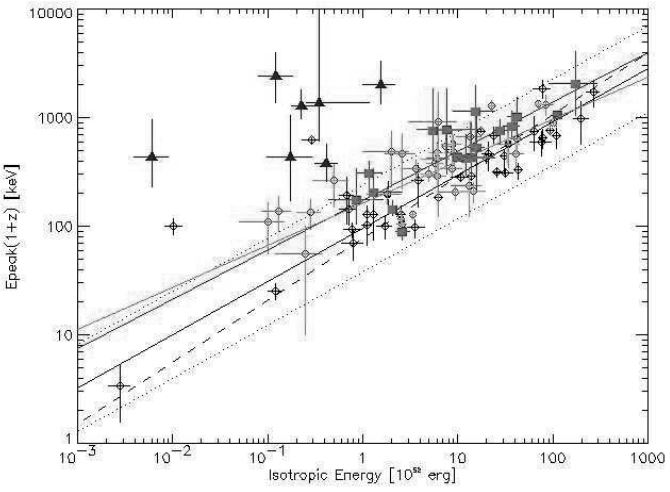

Fig. 7. Correlation between peak energy ($E_{\rm peak}$) and isotropic radiated energies ($E_{\rm iso}$) (Amati 2006). Short and log bursts are shown by triangles and squares, respectively.

Both Swift-BAT and Suzaku-WAM have a very large

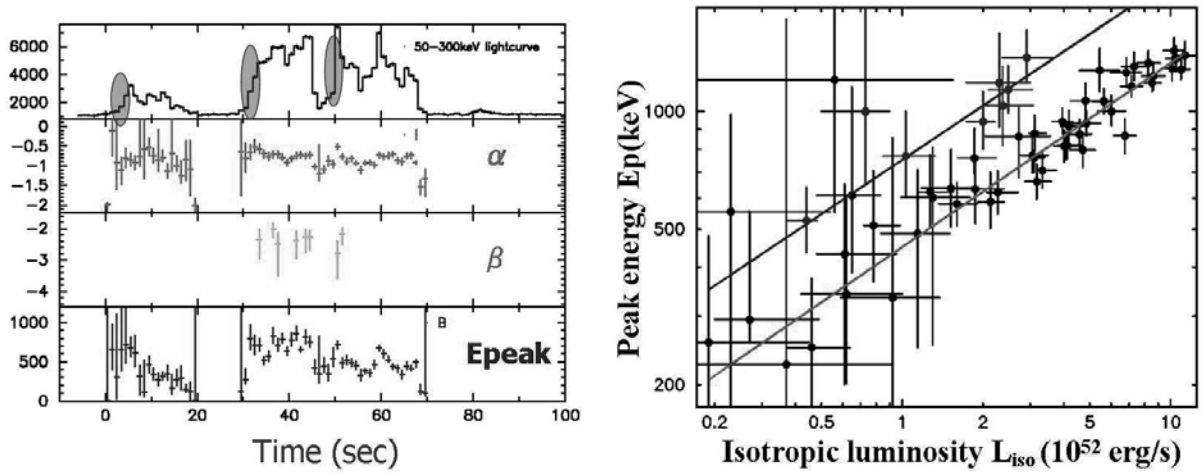

Fig. 8. Left:Time evolution the burst intensity and the spectral parameters of GRB 061007. The $E_{\rm peak}$ is variable with time. Right: Correlation between isotropic luminosity $L_{\rm iso}$ (10^{52} erg s^{-1}) and peak energy $E_{\rm peak}$ (keV) for individual 1-sec segments. Clear correlations are found except for the pulse rising phase (hatched region of left panel of the Figure).

effective area, so it is suitable for time-resolved spectroscopy of bright GRBs and verification of correlations between $E_{\rm peak}$ and $L_{\rm iso}$ (Yonetoku et al. 2004, and Liang et al. 2004). Long-duration GRB 061007 is the most brightest burst in the BAT-WAM sample with 1-sec peak flux of 14 photons cm^{-2} s^{-1} in the 100−1000 keV range (Ohno et al. 2009). We performed a joint spectral fitting with the Band function (Band et al. 2002) every 1 sec (minimum time resolution of the TRN data). Left panel of Figure 8 shows the time evolution of source intensity and spectral parameters (peak energy $E_{\rm peak}$, photon index α below $E_{\rm peak}$, photon index β above $E_{\rm peak}$). The burst shows typical hard-to-soft evolutions, and the $E_{\rm peak}$ is variable with the burst intensity. Right panel of Figure 8 shows correlation between $E_{\rm peak}$ and $L_{\rm iso}$ for 1-sec segment. A clear correlation between these two parameters is found as $E_{\rm peak} \propto L_{\rm iso}^{0.46\pm0.03}$ except for the initial rising phase of the burst pulse (see hatched regions of left panel of Figure 8). This relation is consistent with expected one from synchrotron shock model ($E_{\rm peak} \propto L_{\rm iso}^{1/2}$). Another possible correlation might be seen in the rising phase, suggesting that its origin is physically different (*e.x.* acceleration process) or it has different physical parameters (bulk Lorentz factor or/and shock radius) from other phases.

4. WAM Observations of Hard X-ray Sources

Bright hard X-ray sources with an intensity of ∼1 Crab can be monitored by the WAM using the Earth occultation methods developed by the CGRO/BATSE team (Harmon et al. 2002). This method measures the step in the flux contribution when the source rises above and sets below the Earth horizon. The WAM is an ideal detector for this purpose because its field of view is not limited. The current all-sky monitors are the RXTE/ASM, which operates in the 1.5–12 keV band and the Swift/BAT in the 15–50 keV range, so the WAM can provide unique opportunities to monitor sources in the range above 50 keV to fill the high energy end.

We have searched for the contributions from known sources expected at specific times based on the Suzaku orbital elements. Figure 9 shows the Earth-occultation step for the Crab Nebula. This was obtained by summing 16 orbits with the same satellite attitude. In addition to bright X-ray binaries such as Cygnus X-1 and GRS 1915+105, weak sources such as the radio galaxy Cen-A and the Seyfert galaxy NGC 4151 have been detected with the WAM. The sensitivity is estimated at about 300 mCrab and 30 mCrab in the 50–300 keV range for integrations of one-day and two-years, respectively.

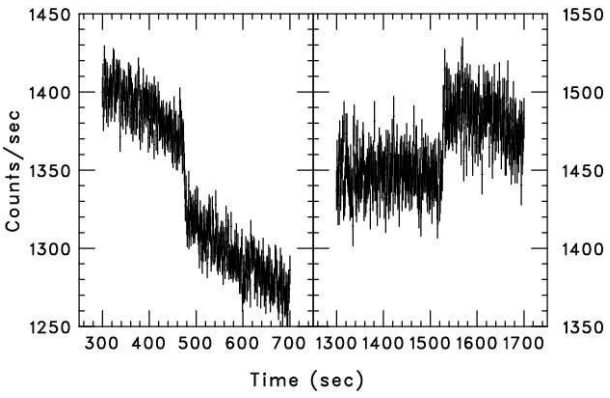

Fig. 9. Earth occultation step for the Crab Nebula observed by WAM 0 in the 50-300 keV range.

Figure 10 shows preliminary results of long-term light curve of the black hole binary Cygnus X-1 in the 100-300 keV range over two years. It is compared with publicly available data taken by Swift/BAT and RXTE/ASM. The WAM light curve is resemble with Two important events were seen from this light curve: 1) a possible state transition from the low/hard state to the high/soft state occurred on April 2006 (decrease of hard X-rays), and 2) a hard X-ray flare was observed in correspondence with MAGIC detection of very high energy gamma-rays on September 2006 (Albert et al. 2007). These data will be publicly available at the WAM web site. Details of the Earth occultation results are described in Kira et al. (2008).

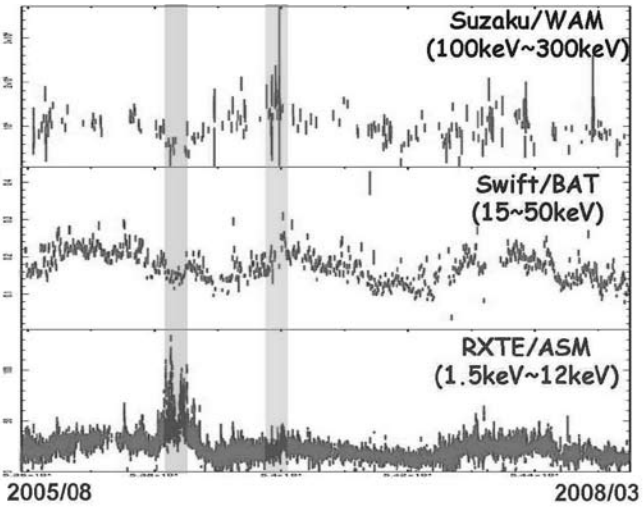

Fig. 10. Long-term Suzaku-WAM light curve of the black hole candidate Cygnus X-1 in comparison with Swift-BAT(15-50 keV) and RXTE/ASM (1.5-12 keV). We can see 1)possible state transition from the low/hard to the high/soft state on April 2006 and 2)a hard X-ray flare which corresponds to the MAGIC VHE gamma-ray detection on September 2006 (Albert et al. 2007).

5. Summary

We have presented current status of the Suzaku Wide-band All-sky Monitor (WAM) utilizing the anti-coincidence shield of the Hard X-ray Detector (HXD). The 20 BGO sensors and their electronics have been operating nominally since Suzaku launch. The WAM has been detecting 140 GRBs per year. and succeeded in detecting hard X-ray sources using the Earth occultation method. The different energy coverage of MAXI (0.3–30 keV) and Suzaku-WAM (50–5000 keV) will be complementary for both science.

References

Albert J. et al. 2007 ApJ., 665, L51
Amati L. 2006 MNRAS., 372, 233
Band D. et al. 1993 ApJ., 413, 281
Ghirlanda G. et al. 2002 A&A., 393, 409
Gonzalez M.M. et al. 2002 Nature, 424, 749
Harmon B.A. et al. 2002 ApJS., 138, 149
Kira C. et al. 2008, in this volume
Kokubun M. et al. 2007 PASJ., 59, S53
Krimm H. et al. 2009 ApJ., in preparation
Liang et al. 2004 ApJ., 606, 29
Mitsuda K. et al. 2007 PASJ., 59, S1
Ohno M. et al. 2008 PASJ., 60, S361
Ohno M. et al. 2009 PASJ., 62, accepted
Paciesas W.S. et al. 1999 ApJS., 122, 465
Sakamoto T. et al. 2008 ApJS., 175, 179
Sakamoto T. et al. 2009 PASJ., in preparation
Sugita S. et al. 2009 PASJ., submitted
Takahashi T. et al. 2007 PASJ., 59, S35
Yamaoka K. et al. 2009 accepted for PASJ. third Suzaku special issue
Yonetoku D. et al. 2004 ApJ., 609, 935

Spectral lag analysis of GRBs deteceted by HETE-2

Makoto Arimoto[1], Nobuyuki Kawai[1], Nicolas Vasquez Pazmino[1], and HETE2 members

[1]Tokyo Institute of Technology, Meguro, Tokyo, Japan
E-mail(MA): arimoto@hp.phys.titech.ac.jp

Abstract

Spectral lags of gamma-ray burst (GRB) become a valuable tool in the study of its radiation mechanism. We present the analysis of the spectral lags in a GRB sample from HETE-2 satellite. Using WXM and FREGATE on HETE-2, we can study the lags between the traditional gamma-ray band (30-400 keV) and the X-ray band (2-25 keV). We derive relations between peak lag, peak luminosity and duration in GRB pulses in the wide band of HETE-2. These results are consistent with those of BATSE and we verify that the BATSE correlations are still valid at lower energies (6−25 keV).

Key words: gamma-rays: bursts — X-rays: bursts

1. Introduction

Prompt emission of gamma-ray bursts (GRBs) should carry the key to clarify the emission mechanism and origin of the explosion.

One of the characteristics of GRB prompt emission is the spectral lag. It is the delay of the photons in the soft energy band with respect to the higher energy band in the GRB light curve. From the theoretical point of view, the spectral lag is important because it could be an indicator of the jet opening angle and of the Lorentz factor(Ioka & Nakamura 2001). Empirically from analyses of GRBs detected by BATSE, the spectral lags show correlation with both GRB peak luminosity and time history morphology; GRBs with shorter lags have higher variability and greater luminosities than long-lag, smooth bursts (Hakkila et al. 2007). Furthermore, Hakkila et al. 2008 derived a new peak lag versus peak luminosity relation in GRB pulses. This result shows that GRB spectral lags are pulse rather than whole burst properties, implying that most GRB pulses have similar physical mechanisms.

HETE-2 satellite has two scientific instruments, the Wide-field X-ray Monitor (WXM, 2−25 keV) and French Gamma-ray Telescope (FREGATE, 6−400 keV). We study the prompt emission of GRBs in a lower enegy band (2−25 keV) than that of BATSE instruments (25 keV −2 MeV). We examine if the correlations found in the BATSE gamma-ray bands also hold for the lower-energy bands.

2. GRB samples and spectral lag measurements

We study a sample of 16 pulses from 9 GRBs with known redshift (Table 1). Each pulse is fitted with a five-parameter pulse model (Norris et al. 1996)

Table 1. GRB samples

GRB	redshift
010921	0.45
020127	1.9
020819B	0.41
021004	2.33
021211	1.01
030528	0.78
040924	0.86
041006	0.45
050408	1.24

$$I(t) = A\exp\left(-|t-t_{max}|/\sigma_r\right)^{\nu} \quad t < t_{max}, \quad (1)$$
$$= A\exp\left(-|t-t_{max}|/\sigma_d\right)^{\nu} \quad t > t_{max}, \quad (2)$$

with background, where t_{max} is the time of the pulse's maximum intensity A, σ_r and σ_d are the rise ($t < t_{max}$) and decay ($t > t_{max}$) time constants respectively. ν is a measure of pulse sharpness (lower values imply a more peaked pulse). Pulses and background are fitted simultaneously over the whole burst using chi-square fitting routine ROOT (http://root.cern.ch/).

Spectral peak lags are defined as the difference between the maximum-intesity times (t_{max}) in different energy bands. Other measurable pulse properties include the pulse duration $w = (3^{\frac{1}{\nu}}\sigma_r + 3^{\frac{1}{\nu}}\sigma_d)$ defined as the time intervals where intesities equal to Ae^{-3}. We calculate the spectral lags between 6−25 keV and 50−400

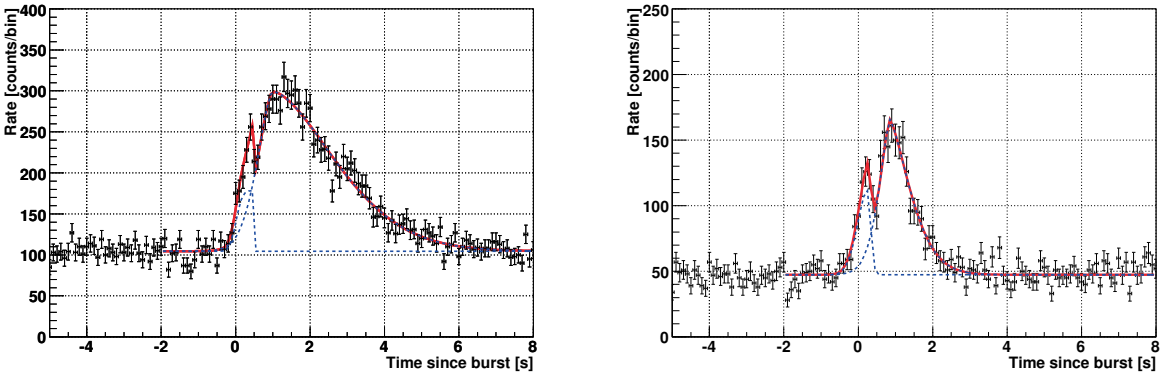

Fig. 1. Pulse-fitting result: GRB 021211 to 6−25 keV (left panel) and 50−400 keV (right panel).

keV using FREGATE light curve.

3. Discussion

We present an example of analysis procedures in 6−25 keV and 50−400 keV bands (GRB 021211, Fig. 1). GRB 021211 has two pulses: the first pulse has a lag of 0.246 ± 0.098s and the second one has a lag of 0.153 ± 0.094s. The durations w are 0.90 ± 0.26s and 2.53 ± 0.50s in the high-energy band, respectively. The spectral lag, pulse duration and pulse peak luminosity have been corrected to the GRB rest frame. In this case ($z = 1.01$ for GRB021211), the spectral lag becomes 0.122 ± 0.049s and 0.076 ± 0.047s, durations 0.45 ± 0.13s and 1.26 ± 0.25s and peak luminosity (1.26 ± 0.31) × 10^{52}erg/s, (0.48 ± 0.03) × 10^{52}erg/s, respectively. We do the same procedure for the other GRBs. The results are shown in Fig. 2 and Fig. 3. In Fig. 2, the pulse duration versus pulse lag is plotted and Fig. 3 shows the pulse luminosity versus pulse lag in the rest frame. We find that lag increases as pulse duration increases and pulse luminosity decreases. These correlations are most likely strong and we verify that similar correlations found in the BATSE gamma-ray bands also hold for the lower-energy bands. This implicates that each GRB jet emits X-ray photons with similar mechanisms in the X-ray band (6−400 keV). This result likely becomes a key to the energetics, jet structure, theoretical shock modeling and so on.

The analysis is done between 6−25 keV and 50−400 keV bands in the *observer* frame. In this situation, we cannot remove cosmological effect. To exclude the extrinsic effects, we need to do the analysis between two bands in the *rest* frame. The result of this analysis will be reported.

We thank the *HETE-2* team for their contributions. This work has been supoorted by Japanese Grant-in-Aid for Young Scientists (B) 20740102.

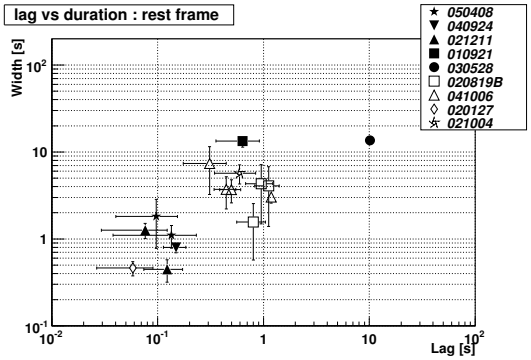

Fig. 2. Pulse duration vs. pulse lag for pulses between 6−25 keV and 50−400 keV. The same symbol represents the same GRB (16 pulses from 9 GRBs).

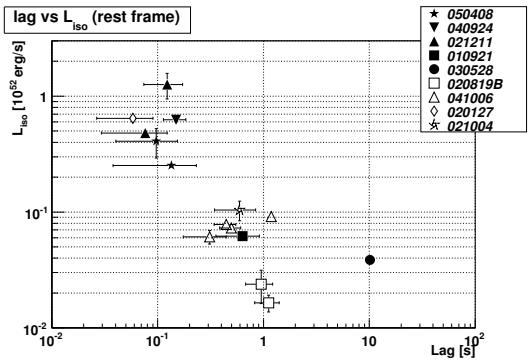

Fig. 3. Isotropic pulse peak luminosity vs. pulse lag for pulses between 6−25 keV and 50−400 keV.

References

Hakkila et al. 2007 ApJS., 169, 62
Hakkila et al. 2008 ApJ., 677, L81
Ioka & Nakamura 2001 ApJ., 554, L163
Norris et al. 1996 ApJ., 459, 393

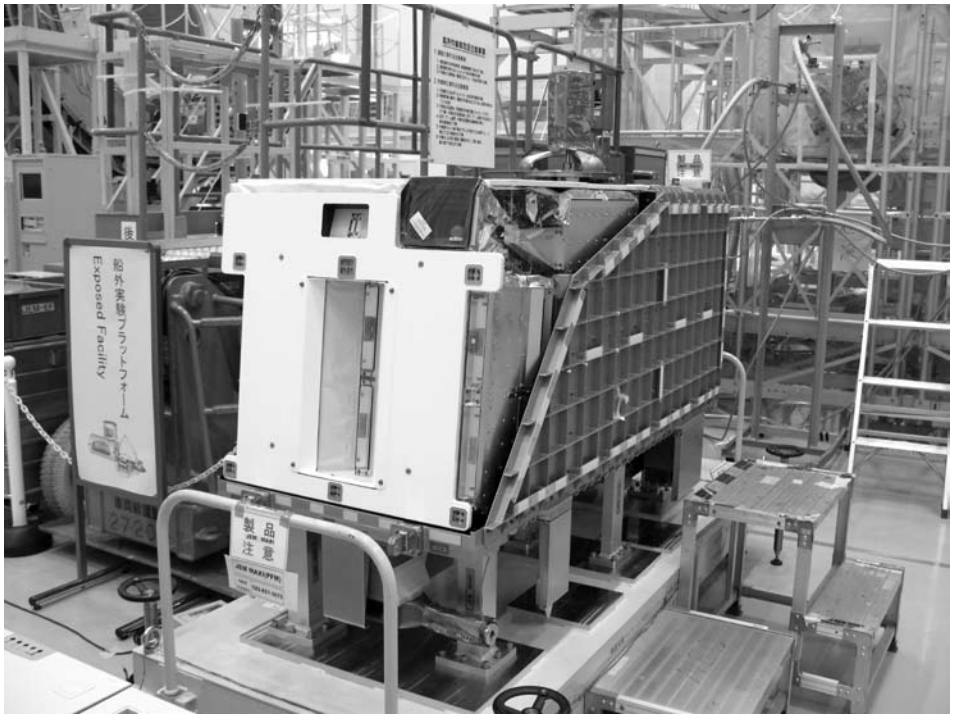

DIFFUSE EMISSION

The Diffuse Soft X-ray Sky

Dan McCammon
Physics Department, University of Wisconsin
Madison, WI 53706 U.S.A.
E-mail: mccammon@physics.wisc.edu

ABSTRACT

The MAXI experiment on the Japanese Experiment Module "Kibo" Exposed Facility (JEM-EF) is designed to provide high sensitivity to point sources and to observe each location often to track variability. However, the long total exposure time and all-sky coverage should permit gathering significant information on diffuse X-ray emission in favorable energy intervals. We speculate on the observational opportunities this might provide.

1. Introduction

MAXI is designed to monitor fluxes from a large number of point sources with high sensitivity. It covers most of the sky each orbit and is capable of detecting a few milli-Crab in one day and much fainter fluxes over longer intervals. Optimizing the instrument for point source sensitivity, unfortunately, also means minimizing its sensitivity to diffuse background X rays. This has been done rather well.

Despite this, MAXI's all-sky coverage and very long exposure times offer a rare view of the diffuse sky — the best available all-sky maps in the 2-20 keV range are still the ones made thirty years ago by *HEAO-I*. MAXI will also make the very first all-sky survey done with the energy resolution of CCD detectors. We therefore look first at some of the outstanding questions remaining about the large-scale diffuse background, and then at how useful the diffuse MAXI data might be in different parts of its bandpass.

2. The Current Situation

Figure 1 shows the best all-sky maps available in the 0.1–0.3, 0.5–1, and 2–9 keV energy bands. A quick look at the figure makes a convincing case that each of these bands is dominated by a different source, and more careful analyses have shown that each is itself a superposition of more than one. So there is a lot to figure out!

2.1 The 0.1–0.3 keV band

All of the soft X-ray sky surveys to date have been made with conventional proportional counters, with $E/\Delta E$ going from ~1 at 0.2 keV to ~8 at 10 keV. The 0.1–0.3 keV band is however well separated from higher energy bands by the detector window's carbon K edge at 0.284 keV. X rays in this band are thought to be produced largely by thermal emission from $\sim 1.0\times10^6$ K interstellar gas, which at these temperatures is almost entirely in characteristic lines of the partially ionized metals in the gas.

Most of the observed flux comes from hot gas in a "local hot bubble" of ~100 pc radius surrounding the Sun. This provides a fairly uniform intensity within 20° of the Galactic plane, but at higher latitudes is up to five times as bright in an irregular pattern that anti-correlates with H I column density, presumably due to a larger extent of the hot gas in these directions. Snowden et al (1998) and Kuntz and Snowden (2000) have shown that some intermediate and high latitude bright areas are due to intense emission from large clumps of hot gas in the Galactic halo, also at $\sim 1.0\times10^6$ K.

More recently, Cox (1998) has pointed out that charge exchange between highly ionized metals in the solar wind and interstellar neutral H and He passing through interplanetary space could be a significant contributor in this band. Lallement (2004) estimated that all of the 0.1–0.3 keV flux seen near the Galactic plane and an equal amount at other latitudes could be produced by this mechanism. Difficulties with fitting thermal emission models to detailed spectra in this energy range (Sanders et al 2001) lend credence to this possibility, but the atomic physics of the L lines that dominate this spectral region is complicated and there are no good predictions for how the charge exchange spectrum should be different from thermal emission. The solar wind models are also highly uncertain, so this important question remains unresolved.

2.2 The 0.5–1 keV band

In this band, the map is dominated by the North Polar Spur, part of the limb of the Loop I superbubble, and by a very bright region roughly 30° in radius surrounding the Galactic center and believed to lie at approximately this distance. This central emission is largely thermal with characteristic temperatures of $2–8\times10^6$ K. Stars must contribute some part of it, but is not known how much is truly diffuse. Resolved AGN provide up to ~60% of the observed intensity away from these areas and the Galactic plane, which is opaque to

extragalactic radiation in this band for about ±6°.

The origin of the remaining flux at high latitudes and in the plane is unknown. It has long been expected that the Galaxy might have a hot halo, and these have been observed in a few other galaxies, but there are currently no satisfactory global models that incorporate this. Koutroumpa and Lallement (2007) have postulated that all of this unexplained general emission may be produced by solar wind charge exchange within the solar system.

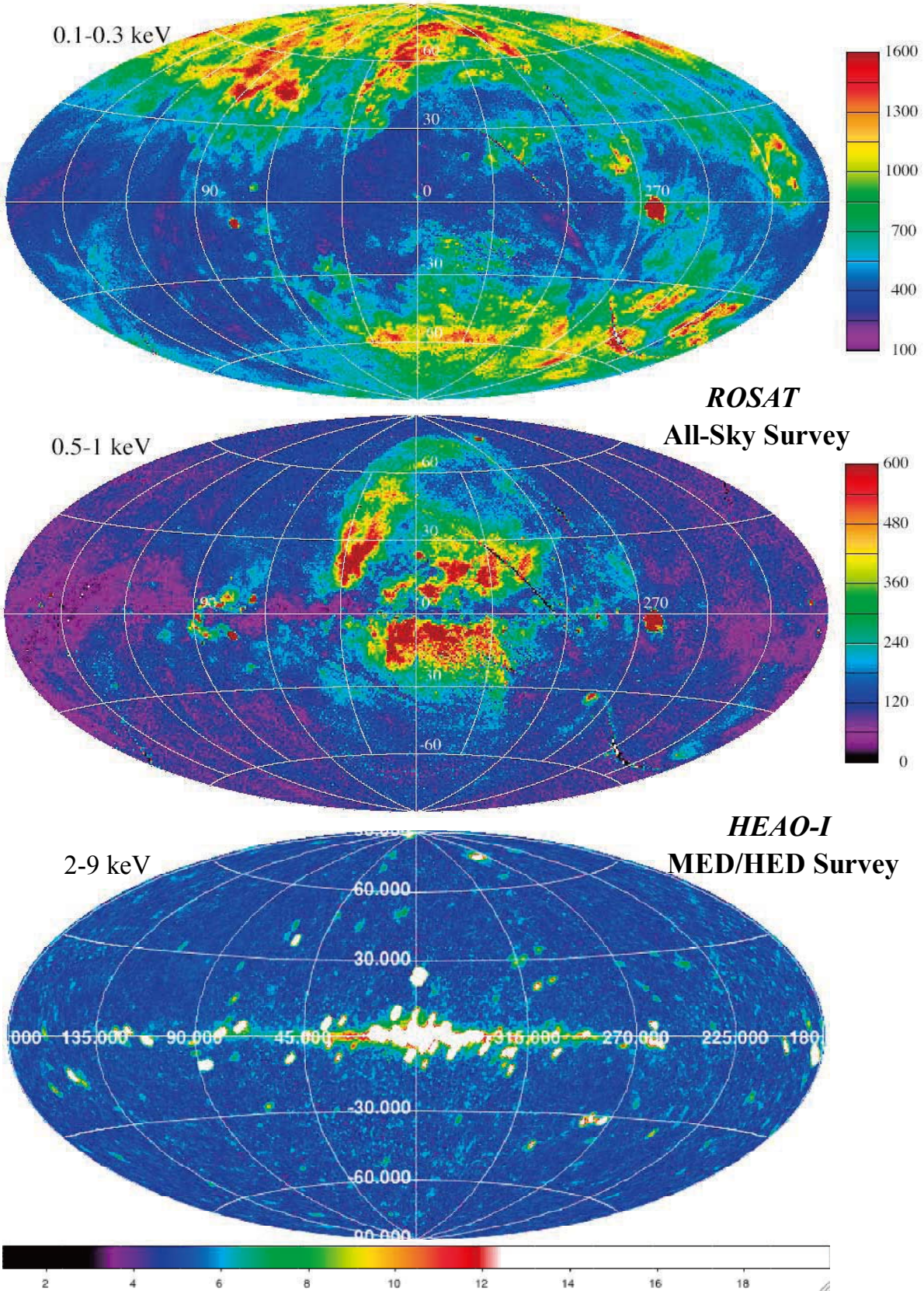

Fig. 1 Best all-sky diffuse background maps in the 0.1–9 keV region. *ROSAT* maps from Snowden et al. 1997. *HEAO-I* maps from Allen et al. 1994.

2.3 The 2–9 keV band

It is now generally thought that essentially all of the flux in this band is due to a superposition of extragalactic discrete sources, primarily AGN. The largest uncertainty in current estimates of the fraction that has been resolved, which ranges from ~1 at the low energy end to ~0.6 at 9 keV, is due to the questionable accuracy of normalization of the observed background spectrum. The best normalization from *HEAO-I* is ~35% lower than early rocket observations (McCammon & Sanders 1990, and references therein). Several more recent determinations have used various imaging telescopes. The throughput of these for a diffuse source is difficult to determine accurately, but these measurements seem to be converging on the higher normalization. Indeed, the background is somewhat over-resolved at the low energy end if the *HEAO-I* normalization is used.

In addition to the dominant extragalactic emission, there are at least two Galactic components. One is a narrow ridge confined to the Galactic plane with a scale height of about 1° (Worral et al. 1982). This has been studied extensively by a number of satellites, but it is still uncertain whether it is due entirely to stars or whether it has a truly diffuse component. The other has a scale height close to 30° (Iwan et al. 1982). It has similar spectral characteristics to the Galactic ridge emission, but has been little studied due to its much lower surface brightness and large extent.

3. MAXI, 0,1–0.3 keV

Figure 2 shows the MAXI CCD camera efficiency. It seems clear that there is no useful response below 0.3 keV.

4. MAXI, 0.5–1 keV

Here the response is small but useable, and the CCD energy resolution offers qualitative advantages over existing all-sky data. Spectral diagnostics for charge exchange are much better understood in this energy range, which is dominated by the K lines of O VII, O VIII, and Ne IX, as well as L lines of Fe XVII. However the best of these require resolving the helium-like triplets, so even CCD resolution doesn't help much.

All-sky maps in some of these lines would be of great benefit in untangling the existing problem. The brightest line is O VII, which unfortunately falls at a minimum in the response. We can calculate the total signal that might be obtained in this line: The CCD detectors total 200 cm^2 area, times 1.5° × 1.5° × 0.67 projected area factor × 5% efficiency ⇒ 0.0047 $cm^2 sr$ at 570 eV. The average O VII flux is ~3 line units (1 L.U. = 1 photon $cm^{-2} s^{-1} sr^{-1}$), giving 0.014 cts s^{-1}. We can estimate the background rate from the ASCA CCD rate 6×10^{-4} cts cm^{-2} s^{-1} keV^{-1} × 200 cm^2 × 0.1 keV ⇒ .012 cts s^{-1}, which assumes 0.1 keV FWHM spectral resolution. Two years observing with 70% efficiency would then give ~600 counts for every 5°×5° on the sky, with ~1:1 signal to background. The typical intensity in O VIII is a few

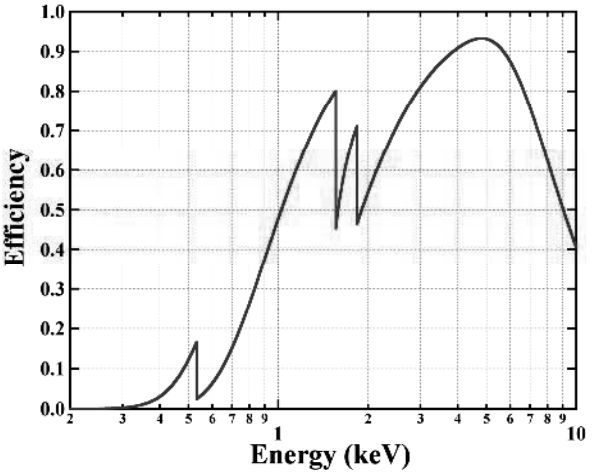

Fig. 2 MAXI CCD camera efficiency

times smaller, but the detector efficiency doubles at the higher energy, so comparable statistics could be achieved. These estimates are comparable to those presented by the MAXI team in October, 2007, based on ROSAT R45 band fluxes. The relatively high CCD operating temperature, radiation damage, and non-gaussian tails on the low energy side of the lines all tend to reduce the resolution and make the signal to noise ratio worse.

One problem with interpreting these results is that there are sporadic contributions to these oxygen lines from solar wind charge exchange in the Earth's geocorona that are up to several times larger than the quiet background that come and go on time scales of ~1 day, in addition to the more slowly varying interplanetary contribution, where the rapid variations in solar wind flux are averaged by the long transit time through the solar system. There are not enough counts to track these changes for individual directions in the sky, so cleaning up the data would require an independent understanding of the charge exchange contribution. It is possible that something useful could be obtained by summing the line fluxes over the entire sky. This would allow monitoring the total sky flux to a few percent with 1 day time resolution.

5. MAXI, 2–9 keV

In this energy range the primary camera would be the gas slit cameras. These are conventional proportional counters and do not have the high energy resolution of the CCDs, but they have much more effective area. We can estimate the counting rate: integrating the background spectrum gives ~7 photons cm^{-2} s^{-1} sr^{-1}. The cameras total 5000 cm^2 × 1.5° × 1.5° × 0.7 projected area factor ⇒ 2.4 $cm^2 sr$, giving about 17 counts s^{-1}. The background should be about 5×10^{-4} cts cm^{-2} s^{-1} keV^{-1} × 5000 cm^2 × 7 keV = 18 cts s^{-1}, so again we have about 1:1 signal to background ratio. Two years of observing with 70% efficiency then gives ~76,000 cts per 1.5°×1.5° pixel. This could give a fantastic improvement on the *HEAO-I* maps, but will require a very thorough understanding of the detector backgrounds. The 15 times per day coverage of each point over a two-year

period will provide much opportunity for studying these backgrounds, but it will be a major effort.

The payoff will be maps and spectral information that could provide much detailed information on the large scale height Galactic component of the diffuse background (the Galactic ridge will be far too source-confused), better measurements of X-ray background fluctuations due to nearby large scale structure in the Universe, and possibly a good measurement of the Compton-Getting effect in X-rays. If the solid angle of the collimators and counter efficiency are accurately calibrated, the uncertainties in the normalization of the background spectrum could be reduced. This would require careful evaluation of reflections from the collimator as a function of energy.

I thank Tatehiro Mihara and Emi Miyata for explaining many details of the MAXI cameras and their response.

6. References

Allen J. et al. 1994 Legacy, 5, 27
Cox D.P. 2008, Lecture Notes in Physics, 506, 121
Iwan D. et al. 1982, Ap.J.260, 111
Koutroumpa D. et al. 2007, A&A 475, 901
Kuntz K.D. & Snowden S.L. 2000, Ap.J. 195, 215
Lallement R. 2004, A&A, 418, 143
McCammon D.& Sanders W.T. 1990 ARA&A 28, 657
Sanders W.T. et al. 2001, Ap.J. 554, 694
Snowden S.L. et al. 1997 Ap.J. 485, 125
Snowden S.L. et al. 1998, Ap.J. 493, 715
Worrall D.M. et al 1982, Ap.J. 255,111

Diffuse Source Mapping with MAXI

Emi Miyata,[1] and MAXI team

[1] Department of Earth & Space Science, Graduate School of Science, Osaka University
1-1 Machikaneyama, Toyonaka, Osaka 560-0043, Japan
E-mail(EM): miyata@ess.sci.osaka-u.ac.jp

Abstract

MAXI, Monitor of All-sky X-ray Image, is an X-ray observatory on the international space station. MAXI carries two kinds of slit scanning camera; gas slit camera (GSC) and solid-state slit camera (SSC). In the course of one station orbit, MAXI can scan almost the entire sky with a precision of 1.5° and with an X-ray energy range of 0.5−30 keV. Major purpose of MAXI is monitor of known X-ray sources and detection of new serendipitous sources such as X-ray nova whereas diffuse X-ray emission in our galaxy is also an important target especially for SSC. The good energy resolving power of SSC enables us, for the first time, to map the entire sky with various line emission from O to Fe. Based on the previous observational data, we simulate MAXI data both for SSC and GSC. Large-scale structures in our galaxy such as supernova remnants, radio loop, superbubbles are possible targets for SSC. The Galactic ridge X-ray emission is important target both for GSC and SSC.

Key words: X-ray — all-sky survey — diffuse source — all-sky line map

1. Introduction

Over the past three decades, several X-ray all-sky monitors have been performed (e.g. Holt 1997). The major purpose of X-ray monitor is detection and localization of X-ray sources and monitor of their intensity variation. The high-sensitive soft X-ray survey was performed by Rosat in the 0.1−2.4 keV energy range (Trümper 1983). More than 100,000 sources were cataloged with the Rosat all-sky survey data (Voges et al. 2000). Since Rosat has high sensitivity for diffuse sources, high resolution (∼12′) X-ray map has been constructed for seven energy bands (Snowden et al. 1995, 1997). They revealed the global structure of diffuse X-ray emission for soft X-ray sky.

2. MAXI

MAXI, Monitor of All-sky X-ray Image, is an X-ray observatory on the Japanese experimental module (JEM) exposed facility (EF) on the international space station (Ueno 2009). MAXI is a slit scanning camera which consists of two kinds of X-ray detectors: one is a one-dimensional position-sensitive proportional counter with a total area of ∼ 5000 cm^2, the Gas Slit Camera (GSC; Mihara et al. 2002), and the other is an X-ray CCD array with a total area of ∼ 200 cm^2, the Solid-state Slit Camera (SSC; Katayama et al. 2005). GSC subtends a field of view with an angular dimension of 1.5°×160° while SSC subtends a field of view with an angular dimension of 1.5°×90°. In the course of one station orbit, MAXI can scan almost the entire sky with a precision of

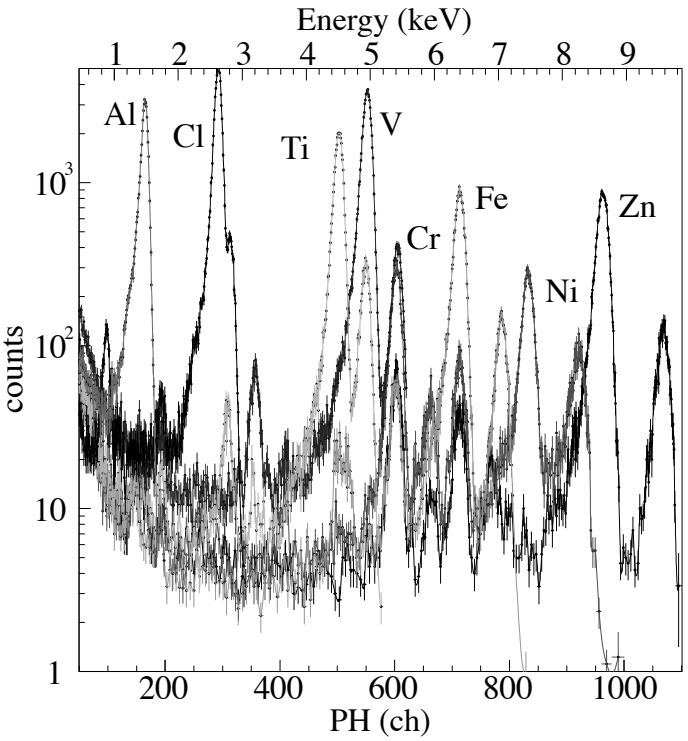

Fig. 1. Histogram of fluorescent X-rays from Al, Cl, Ti, V, Cr, Fe, Ni, and Zn obtained with SSC.

Table 1. Specifications of GSC and SSC.

	GSC	SSC
X-ray detector	12 units of position-sensitive proportional counter	32 chips of X-ray CCD
Energy range	2−30 keV	0.5−15 keV
Detector area	5350 cm^2	200 cm^2
Energy resolution	18% at 5.9 keV	2.5% at 5.9 keV
Field of view	1.5°×160°	1.5°×90°
Position resolution	1 mm	24 μm

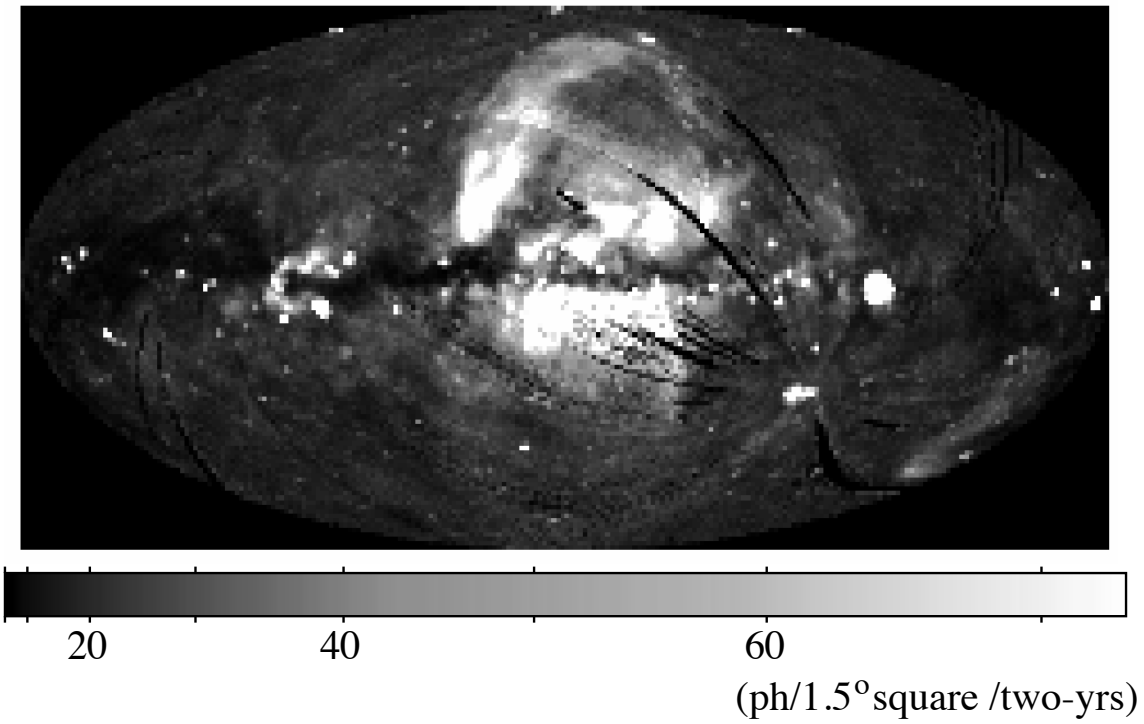

Fig. 2. O line map simulated for the two-yrs observation with SSC.

1.5° and with an X-ray energy range of 0.5−30 keV. Details of both detectors are summarized in Table 1. The mission life of MAXI is two yrs.

The moderate energy resolution of SSC shown in Table 1 enables us to resolve emission lines from heavy elements from O to Fe. Figure 1 shows the histogram of fluorescent X-rays from Al, Cl, Ti, V, Cr, Fe, Ni, and Zn obtained with SSC. Each emission line can be clearly resolved with SSC. SSC possesses the capability to map the entire sky with line emission from O to Fe for the first time. On the other hand, GSC can map the entire sky only with Fe whereas the effective area at Fe line is an order of magnitude larger than that of SSC. Such narrow-band imaging is a powerful tool for the long-term all-sky observation because this technique can be minimized the contamination of the non X-ray background originated in the detector.

3. Simulation Data for MAXI

In this section, we demonstrate the data simulated for MAXI.

3.1. O line map

O is one of the most abundant heavy elements in the universe. The full-width at half maximum energy resolution of SSC at O line is ∼80 eV. This resolution is limited by the relatively warm operating temperature of SSC (−50 ∼ −60°C). The separation of He-line O (O VII) and O Lyα is astrophysically important whereas it is difficult with SSC. These emission lines traces warm gas in our galaxy.

Based on the Rosat all-sky survey data, we simulated the O line map with the two-yrs observation of SSC. We employed 3/4 keV data since O line emission is dominant in this energy band. Figure 2 shows the O VII + O Lyα line map simulated for the two-yrs observation with SSC. As clearly demonstrated in this figure, we can expect to map the entire sky only by O lines with high statistics. The brightest object in this band is Puppis-A and the Vela supernova remnant (SNR). The Cygnus Loop is the second brightest object. Other large-scale structures are also possible targets for SSC such as Loop-I, Cygnus superbubble, Orion-Eridanus superbubble. X-ray emission from the Galactic bulge may be a good target.

3.2. Supernova remnants

The brightest target of SSC in the O band is Puppis-A and the Vela SNR. Figure 3 shows the O line map of Puppis-A and Vela SNR simulated for the two-yrs observation with SSC. The large apparent size of the Vela SNR (diameter of 8.3°; Aschenbach et al. 1995) enables us to study the spatially-resolved spectrum with SSC as shown in Figure 3. Since the Vela SNR is located far from the Galactic plane, the contamination of the Galactic diffuse emission can be negligibly small. This simulated image closely resembles the X-ray surface brightness map of the young SNR Cassiopeia-A observed with the ASCA SIS (Holt et al. 1994). We thus expect good scientific results of the Vela SNR with SSC similar to those of Cassiopeia-A with SIS.

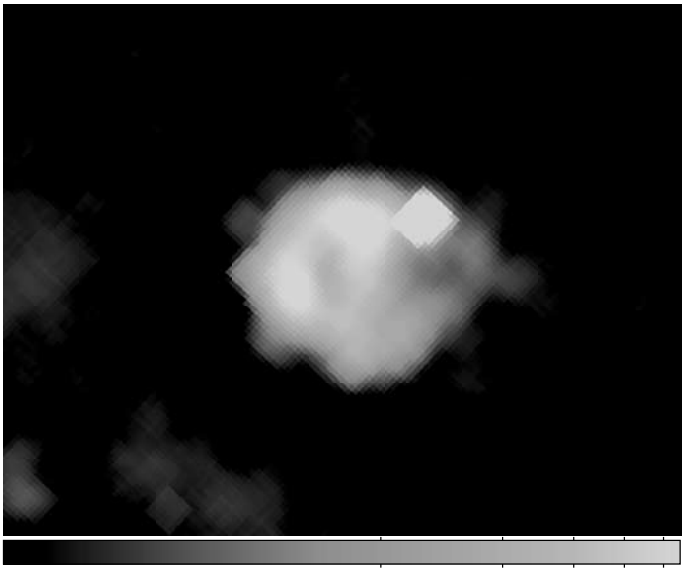

Fig. 3. O line map of Puppis-A and Vela SNR simulated for the two-yrs observation with SSC.

Since the beam size of SSC is 1.5° square, other SNRs are two small for SSC.

3.3. Loop I / North Polar Spur

Loop I is a Galactic giant radio loop of 58° radius centered at l=329° and b=17.5° (Egger & Aschenbach 1995). The brightest part of Loop I , in the north-east, has been called the North Polar Spur. The origin of Loop I is still unclear. Previous studies suggested that Loop I is an old, nearby SNR with a non-thermal shell, the remnant of a starburst, or explosion near the Galactic center (Miller et al 2008).

SSC enables us to observe the entire region of Loop I with the CCD resolution for the first time. Based on the spatially-resolved spectral analysis of Loop I, we can study its plasma diagnostics in detail. We can thus calculate the various physical parameters such as abundances of heavy elements, thermal energy, and thermal pressure for the first time. These parameters are clue to investigate the origin of Loop I.

3.4. Superbubbles

As shown in Figure 2, the Cygnus superbubble and the Orion-Eridanus superbubble can be mapped with SSC. Superbubbles are thought to be produced as large hot stars interact with the surrounding interstellar medium. The Cygnus superbubble and the Orion-Eridanus superbubble are large nearby superbubbles created by the

Cygnus OB2 association and the Orion OB1 association, respectively.

SSC enables us to observe the entire region of these superbubbles. Thanks to the good energy resolving power of SSC, we can study the plasma diagnostics and their spatial variation, resulting in the calculation of the total thermal energy and the thermal pressure. These parameters are key to study the evolution of warm and hot gas in our galaxy.

3.5. Galactic ridge X-ray emission

The X-ray sky along the Galactic plane exhibits many bright X-ray point sources (e.g. Warwick et al. 1985, 1988). Faint and unresolved X-ray emission is also observed with a half-thickness of 240 pc (Worrall 1982). Highly-ionized iron line (6.7 keV) is detected with the Tenma satellite (Koyama et al. 1986). This line emission together with the continuum emission suggested that the Galactic ridge X-ray emission (GRXE) is thermal radiation from optically thin plasma. So far most of X-ray satellites have spent significant amounts of their observing time to study GRXE, its origin has not yet been elucidated. Whether GRXE is truly diffuse emission or composed of numerous dim point sources remains inconclusive.

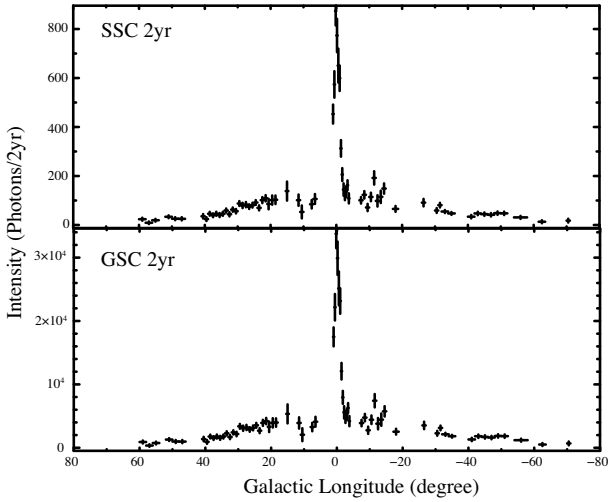

Fig. 4. Intensity profile of 6.7 keV line at the Galactic ridge simulated for GSC and SSC.

Based on the Ginga scanning observation (Yamauchi & Koyama 1993), we simulated the intensity profile of 6.7 keV line at the Galactic ridge for the two-yrs observation both with GSC and SSC, shown in Figure 4. As clearly shown in this figure, we can detect 6.7 keV line with high statistics not only at the Galactic center but also at the Galactic ridge. MAXI furthermore enables us to map the 6.7 keV line at the entire region of the Galactic ridge.

Recent Suzaku observation revealed that Fe line emission consists of three narrow Fe K-emission lines from low-ionized (6.41 keV), He-like (6.67 keV), and H-like (7.00 keV) (Ebisawa et al. 2008). Collisional ionization equilibrium plasma is the likely origin for the 6.67 keV and 7.00 keV lines; however, the origin of the 6.41 keV line, which is due to fluorescence from cold material, has not been elucidated.

With SSC, we can resolve three lines of Fe complex. Based on the Suzaku observational data, we estimated intensities of 6.41 keV, 6.67 keV, and 7.00 keV line to be 26 ph, 119 ph, and 26 ph at typical 1.5° square region for the two-yrs SSC observation, respectively. We can therefore study the spatial variation of these three lines at the Galactic ridge. Spatial variation of line intensity ratio of 6.67 to 7.00 keV allows us to investigate the temperature variation, which gives us an important clue to origin of hot gas; superposition of point sources or diffuse sources.

Origin of 6.41 keV is not also elucidated. Valinia et al. (2000) proposed interactions between the interstellar medium and cosmic supra/non-thermal electrons are responsible for 6.41 keV line. Revnivtsev et al. (2006) proposed that a superposition of numerous, different kinds of point sources may create iron line complex (e.g. cataclysmic variables). In both cases, the spatial variation of 6.41 keV is a key issue. With SSC, we expect 26 ph at 1.5° square region for 6.41 keV line. We can therefore investigate the spatial variation of 6.41 keV line at the entire region of the Galactic ridge. The correlation between 6.41 keV spatial distribution and the spatial distribution of CO or star may give us an important clue to the origin of 6.41 keV line.

It is known that GRXE has low-temperature component with $kT_{\rm e} \simeq 0.8$ keV (Kaneda et al. 1997; Ebisawa et al 2005). Highly-ionized emission lines from Ne, Mg, Si, S, Ar, Ca, and Fe-L are detected whereas its origin is also unknown.

Table 2. Intensities of emission lines from various ions for low-$kT_{\rm e}$ component of GRXE simulated for the two-yrs observation of SSC.

Emission line	ph/two-yrs/1.5° square
Fe XVII	29
Ne IX	44
Mg XI	48
Si XIII	60
Si XIV	14
S XV	54
S XVI	23
Ar XVII	24

We calculated the intensities of emission lines from various ions for low-$kT_{\rm e}$ component of GRXE observed

with SSC based on the Suzaku observation (Ebisawa et al. 2008). As shown in Table 2, we can detect various emission lines from the Galactic ridge at typical 1.5° square region with enough statistics to perform the plasma diagnostics. We therefore investigate the spatial structure of low-kT_e plasma. If nonequilibrium ionization condition is confirmed, SNR origin is most likely for low-kT_e component.

4. Conclusion

Major purpose of MAXI is monitor of known X-ray sources and detection of new serendipitous sources such as X-ray nova whereas diffuse X-ray emission in our galaxy is also an important target especially for SSC. The good energy resolving power of SSC enables us, for the first time, to map the entire sky with various line emission from O to Fe. We can study the Galactic large-scale structures such as supernova remnants, radio loop, superbubbles with SSC. The Galactic ridge X-ray emission is the important target both for GSC and SSC. In order to study the diffuse emission, we need to accumulate all X-ray data obtained during the whole mission life. Therefore, stable detector responses over the mission life are essential. We are also required a precise onboard calibration to achieve the good energy resolving power of the detector.

We would like to thank Drs. Ebisawa and Yamauchi for many useful comments and suggestions. EM is supported by Grant-in-Aid for Specially Promoted Research (16002004). Part of this research has made use of data obtained through the High Energy Astrophysics Science Archive Research Center Online Service, provided by the NASA/Goddard Space Flight Center.

References

Aschenbach B. 1995 Nature, 373, 587
Ebisawa K. et al. 2005 ApJ,635, 214
Ebisawa K. et al. 2008 PASJ, 60, S223
Egger R.J. & Aschenbach B. 1995 A&A, 294, L25
Holt S.S. 1994 PASJ, 46, L151
Holt S.S. 1997 Proc. All-Sky X-ray Observations in the Next Decade, 9
Kaneda, H. et al. 1997 ApJ, 491, 638
Katayama H. 2005 Nucl. Inst. and Meth. A, 541, 350
Koyama K. et al. 1986 PASJ, 38, 121
Mihara T. 2002 Proc. SPIE, 173, 186
Miller E.D. 2008 PASJ 60, S95
Revnivtsev, M. et al. 2006 A&A, 452, 169
Snowden S.L. et al. 1995 ApJ, 454, 643
Snowden S.L. et al. 1997 ApJ, 485, 125
Trümper J. 1983 Adv. Space Res., 2(4), 241
Ueno S. 2009 in these proceedings
Valinia A. et al. 2000 ApJ, 543, 733
Voges W. et al. 2000 IAUC, 7432
Worrall D.M. et al. 1982 ApJ, 255, 111
Warwick R.S. et al. 1985 Nature, 317, 218
Warwick R.S. et al. 1988 MNRAS, 232, 551
Yamauchi S. & Koyama K. 1993 ApJ, 404, 620

Hard X-ray Mapping of Galaxy Clusters

Yasushi Fukazawa,[1] Kazuhiro Nakazawa,[2]

[1] Department of Physical Sciences, Hiroshima University
[2] Department of Physics, University of Tokyo
E-mail(YF): fukazawa@hep01.hepl.hiroshima-u.ac.jp

Abstract

Hard X-ray emission from clusters of galaxies is important to probe the acceleration phenomena in the largest system in the universe. Here we presented Suzaku observations of A3376 and A3667. Upper limit of nonthermal hard X-ray emission gives a reasonable lower limit of intracluster magnetic field. Extremely hot gas component is found in A3667, indicating a suprathermal emission. We will suggest a possible hard X-ray mapping with MAXI to constrain the spatial distribution of hard X-ray emission.

Key words: Clusters: X-ray — Acceleration: hard X-ray

1. Introduction

Clusters of galaxis are the largest systems in the universe, but they are still evolving. The released gravitational energy will lead to particle acceleration of high energy particles up to 10^{16-17} eV, through such as shock wave around the mass inflow of intergalatic gas or hydromagnetic turbulence in the intracluster medium. Powerful jets from central dominant galaxies also cause particle acceleration. Therefore, clusters of galxies are now believed to be a possible particle acceleration site. At fact, radio synchrotron halo is often observed from clusters of galaxies, indicating that high energy electrons really exist in the intracluster space. Such nonthermal energy in high energy particles has a small entropy, and thus past information is expected to be preserved. Also if nonthermal energy is not negligible in comparison with thermal energy, it causes some important impacts, such that gravitational mass estimated from only thermal pressure will be modified. In addition, clusters of galaxies are possible sources of extragalactic cosmic rays.

Such high energy particles can be probed by nonthermal hard X-rays and gamma-rays. Gamma-ray survey with CGRO/EGRET did not find any significant emission from galaxy clusters (Reimer et al. 2003). Then, gamma-ray observatory *Fermi* is promising for exploring the gamma-ray view of galaxy clusters. On the other hand, recent hard X-ray survey has reported possible nonthermal emission from galaxy clusters. First reports were BeppoSAX/PDS detection of hard tail from the Coma cluster (Fusco-Femiano et al. 1999, 2000, 2001), but this is still under debate (Rossetti et al. 2007). Nevalainen et al. (2004) reported hard power-law component from 7 galaxy clusters above 3σ level. Hard X-ray from clusters has also been reported with RXTE (Rephaeli et al. 1999, 2003, 2006). Nonthermal X-ray emission from galaxy groups is also detected with ASCA (Fukazawa et al. 2001; Nakazawa et al. 2006). However, significance of detection is still very low and distinguishment from AGN emission is difficult now. Therefore, further confirmation with high sensitivity or imaging detectors is necessary, and Suzaku/HXD and MAXI are suitable for such studies.

2. Suzaku Observations of Nonthermal Emission

The HXD/PIN (Takahashi et al. 2007; Kokubun et al. 2007; Fukazawa et al. 2009) onboard Suzaku has a very low background in the 10–30 keV band than any past instruments. In addition, its narrow field of view ($34'\times34'$ FWHM), compared with the BeppoSAX/PDS (1.3° hexagonal FWHM) and RXTE/PCA (1° hexagonal FWHM), yields several advantages. First, the confusion from hard point sources is reduced, as is the contribution of the ICM thermal emission, and finally the nonthermal emission may be localized better. Suzaku/XIS also achieves the lowest background level of any previous X-ray CCDs, and it is useful to constrain the hard X-ray emission.

Abell 3376 is a nearby on-going merger cluster (z=0.046), and revealed to have a symmetric strong radio relic (Bagchi 2005, 2006). Significant hard X-ray detection is also reported with BeppoSAX/PDS (Navaleinen et al. 2004). Suzaku observed this cluster, focusing on the cluster center containing the diffuse radio emission to the east, and cluster peripheral region to the west. For both observations, we detect no excess hard X-ray emission above the thermal cluster emission (Kawano et

al. 2009). An upper limit on the non-thermal X-ray flux of 2.1×10^{-11} erg cm^{-2} s^{-1} (15–50 keV) at the 3σ level from a 34×34 arcmin^2 region, derived with the HXD/PIN, is similar to that obtained with the BeppoSAX/PDS. Using the XIS data, the upper limit on the non-thermal emission from the West Relic is independently constrained to be $< 1.1 \times 10^{-12}$ erg s^{-1} cm^{-2} (4−8 keV) at the 3σ level from a 122 arcmin^2 region. Assuming Compton scattering between relativistic particles and the cosmic microwave background (CMB) photons, the intracluster magnetic field B is limited to be $>0.03\mu$G (HXD) and $>0.10\mu$G (XIS).

Abell 3667 (z=0.056) is famous of its pair of radio relics (Roettgering e tal. 1997), which is the brightest and largest among the diffuse radio sources associated with galaxy clusters. Suzaku observed this cluster, focusing on the north radio relic. Nakazawa et al. (2009) reported that nonthermal hard X-ray is not detected with a HXD upper limit of 5.3×10^{-12} erg s^{-1} cm^{-2} in 10–40 keV for the entire cluster region and with an XIS upper limit of 7.3×10^{-13} erg s^{-1} cm^{-2} in 10–40 keV for the radio relic region. Combined with the radio flux, strong constraint on the magnetic field is obtained to be >1.6 μG. Interestingly, Suzaku detected an extremely hot thermal component from this cluster; the spectrum is well represented by two-temperature model of $\sim$5 keV and $>$ 13 keV. Such a hot component is possible suprathermal emission caused by the strong shocks. Similar extremely hot component has been also found in RX J1347.5-1145 with Suzaku (Ota et al. 2008).

3. MAXI Observation

X-ray emission of nonthermal and suprathermal electrons from clusters of galaxies may be extended over wide regions. Wide field of view (FOV) with large effective area above 10 keV is needed to search for them. MAXI with 1.5 deg FOV can resolve several nearby clusters, as well as Ginga scanning observations (Takano et al. 1989; Ikebe et al. 1992). In addition, MAXI monitoring observation is useful to eliminate variable point sources. Therefore, we can measure the hard X-ray emission to compare their profile with that of soft thermal emission; Is there any extraordinary hot component? Is there any hard power-law component? How extended is it, if it exist?

References

Bagchi, J., Durret, F., Lima Neto, G. B., Paul, S., & Chavan, S. 2005, Proceedings of the 29th International Cosmic Ray Conference.

Bagchi, J., Durret. F., Lima Neto. G. B., & Paul. S., 2006, Science, 314, 791

Fukazawa, Y., Nakazawa, K., Isobe, N., Makishima, K., Matsushita, K., Ohashi, T., & Kamae, T. 2001, ApJ, 546, 87

Fukazawa, Y. et al. 2009, PASJ, 61, in press

Fusco-Femiano,R., dal Fiume, D., Feretti, L., Giovannini, G., Grandi, P., Matt, G., Molendi, S., & Santangelo, A. 1999, ApJ, 513, 21

Fusco-Femiano, R. et al. 2000, ApJ, 534, 7

Fusco-Femiano, R., Dal Fiume, D., Orlandini, M., Brunetti, G., Feretti, L., & Giovannini, G. 2001, ApJ, 552, 97

Ikebe, Y. et al. 1992, ApJ, 384, L5

Kawano, N. et al. 2009, PASJ, 61, in press

Kokubun, M. et al. 2007, PASJ, 59, S53

Nakazawa, K., Makishima, K., & Fukazawa, Y. 2007, PASJ, 59, 167

Nakazawa, K. et al. 2009, PASJ, 61, in press

Ota, N. et al. 2008, astro-ph/0805.0500 (A&A 2008, in press)

Nevalainen, J., Oosterbroek, T., Bonamente, M., & Colafrancesco, S. 2004, ApJ, 608, 166

Reimer, O. et al. 2003, ApJ, 588, 155

Rephaeli, Y. et al. 1999, ApJ, 511, L21

Rephaeli, Y. et al. 2003, ApJ, 595, 137

Rephaeli, Y. et al. 2006, ApJ, 649, 673

Rossetti, M. and Molendi, S. 2007, astro-ph/0702417

Rottgering, H. J. A. et al. 1997, MNRAS 290, 577

Takahashi, T. et al. 2007, PASJ, 59, S35

Takano, S. et al. 1989, Nature, 340, 289

Light bending and the hard X-ray background

P. Gandhi

Institute of Physical and Chemical Research (RIKEN), 2-1 Hirosawa, Wakoshi, Saitama 351-0198, Japan
E-mail: pg@crab.riken.jp

Abstract

Light bending due to strong gravity has recently been invoked to explain variability and flux correlations between different bands in some accreting black holes. A characteristic feature of light bending is reflection-dominated spectra, especially if photon sources lie in the deepest parts of the gravitational potential within a few gravitational radii of the event horizon. We use the spectrum of the hard X-ray background in order to constrain the prevalence of such reflection-dominated sources. We first explore the broad-band properties of realistic spectra that incorporate light bending and then use these spectra, in conjunction with the observed 2–10 keV AGN luminosity functions in order to predict the hard X-ray background spectrum over 3–100 keV, and provide limits on the fraction of reflection-dominated sources, dependent on the flare height. Our results allow for a cosmologically- significant fraction of sources that incorporate strong light bending. The luminosity function based on intrinsic flare luminosities is derived. We discuss prospects for missions such as *NeXT* and *Simbol-X* that can image such sources as well as confirm the precise spectral shape of the background near its peak, important for constraining the universal relevance of light bending.

Key words: galaxies: active – X-rays: galaxies – X-rays: cosmic background radiations

1. Introduction

We pose a simple question: How common are active galactic nuclei (AGN) with extreme reflection fractions in X-rays? The motivation for this is the recent finding that incorporation of general relativistic light bending effects on photon propagation can have dramatic consequences for the spectra of accreting sources with peaked central emissivities. For isotropic photon sources (such as magnetic reconnection events/flares, a hot electron corona or the base of a jet) that lie within a few gravitational radii ($R_{\rm G} = GM_{\rm BH}/c^2$) of the BH, the cross-section of photon geodesics intercepting the accretion disk (or lost down the event horizon) can be very large, as compared to sources at much higher heights (h). For constant luminosity photon sources, the primary flux observed at infinity can vary dramatically with changing source height, while the reflected flux component remains relatively unchanged, resulting in reflection-dominated spectra for low h. This model has been shown to be capable of explaining the apparently dis-jointed variability patterns and flux-flux correlations observed between different bands in some Seyferts, Narrow Line Seyfert 1s, as well as Galactic BH candidates (e.g., Miniutti & Fabian 2004, Fabian et al. 2005, Rossi et al. 2005, Ponti et al. 2006).

The general importance of the light bending model is currently unclear, though evidence for sources with high reflection fractions (e.g. Panessa et al. 2008, Ueda et al. 2007) is increasing; as is evidence for the ubiquity of rapidly-spinning black holes with accretion disks extending down to the innermost stable circular orbits, where light bending should be strongest (Fabian et al. 2002, Volonteri et al. 2005, Wang et al. 2006).

In this work, we use the cosmological hard X-ray background (XRB) radiation to place constraints on the fraction of sources which are reflection-dominated. This is possible because the background is simply the integrated emission of AGN spread out in redshift, and its characteristic spectral shape irrefutably requires the presence of reflection. Full details have been published in Gandhi et al. (2007).

2. Reflection-dominated AGN spectra

As our base broad-band spectral energy distributions (SEDs), we use the ones of Suebsuwong et al. (2006; hereafter S06), who have carried out detailed Monte Carlo investigations that incorporate light bending to quantify changes in observed spectral properties, with the variables being inclination angle, source height, source size (either point-like or ring-like) and source distance from the rotation axis, assuming the proper Kerr space-time metric and no emission from the plunging region between the innermost marginally stable orbit of the accretion flow and the event horizon. The specific angular momentum of the BH is taken to be $a = 0.998$, implying that the innermost stable orbit lies at a distance

of 1.23 $R_{\rm G}$ from the BH. For simplicity, we consider only the case with on-axis point-like flares at height h above the accretion disk.

Fig. 1 shows the effect of increasing light bending from bottom-to-top. The 'PEXRAV' SED is taken to be the unabsorbed template SED used by Gandhi & Fabian (2003): a power-law with a photon-index (Γ) of 1.9 and a reflection component from a flat, infinite slab covering 2π steradians viewed at an inclination angle (i) of 60 degs, generated according to Magdziarz & Zdziarski (1995). An exponential power-law cut-off ($E_{\rm cut}$)=500 keV is used, in order to directly compare with the results of Ueda et al. (2003, hereafter U03). The spectra that incorporate light-bending are plotted for a range of source heights (S06 generate spectra at four discrete heights of $h = 2, 5, 10$ and 20 $R_{\rm G}$). For the present comparison, these spectra have been averaged over all viewing angles, and are normalized at 1 keV. Identical intrinsic Γ and $E_{\rm cut}$ values are assumed in all the spectra plotted in the figure, including the reflection-free power-law ('PL').

As source height decreases from bottom-to-top, more photons are bent towards the central object, and also impinge on the accretion disk, resulting in a larger reflection fraction. For the lowest height plotted ($h = 2$), the peak monochromatic flux is higher than that of the PEXRAV SED by a factor of 26 (6), for a normalization at 1 keV (over 2–10 keV). As h increases, the photon source is located in regions of shallower gravitational potential and the effect of light bending decreases until, for $h = 20$, the reflection fraction closely matches the PEXRAV 2π reflector model.

To summarize, the result of an increased reflection component is that the spectra become more 'peaky' in $EF_E(\equiv \nu F_\nu)$ units.

Fig. 2 shows a schematic illustration of the actual reflection model that we envision. Light bending enhances the disk reflection component, which may subsequently be obscured by the torus along the observed line-of-sight, depending on inclination angle. A more distant reflection component may be attributed to the inner torus walls and result in a narrow Fe emission line; this component is likely to be unabsorbed.

3. Distributions in luminosity and obscuring column

In order to simulate the X-ray background (XRB) spectrum, we require a distribution of sources in luminosity and obscuration parameter space. One of the best-determined X-ray luminosity functions (XLF) and $N_{\rm H}$ distributions is that of U03 over the 2–10 keV range, which we use here until more precise measurements become available above 10 keV from on-going *Swift* and *INTEGRAL* surveys. We use the luminosity-dependent density evolution (LDDE) in redshift model favoured by U03.

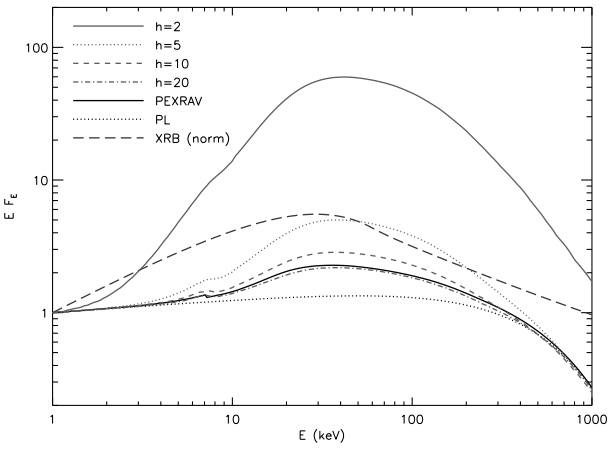

Fig. 1. Comparison of angle-averaged broad-band light-bending SEDs (source height as labelled) with a PEXRAV ($R = 1$; $\theta = 60$ degs; solid black) and simple cut-off power-law (PL; no reflection; lowest dotted black) SEDs. All spectra assume an incident power-law with $\Gamma = 1.9$ and an exponential cut-off $E_{\rm cut} = 500$ keV, and have been normalized at 1 keV. The observed XRB fit from Gruber et al. (1999), also similarly normalized, is shown as the blue long-dashed line.

A range of obscured reflection-dominated spectra were generated, with columns of cold gas ranging from log$N_{\rm H}$=20–22 for Sy 1s (intrinsic spectrum averaged over viewing angles of 0–50 degs) and log$N_{\rm H}$=22–25 (Sy 2s; averaged over 50–90 degs), for each height h. For Compton-thick sources, the effects of down-scattering (Wilman & Fabian 1999) were fully included.

Fits to the XRB are carried out over the 3–100 keV range by assuming that the *HEAO* error bars are normally-distributed, and computing a weighted sum of square deviations (an effective 'χ^2'). The difference in this fit parameter ($\Delta\chi^2$) is computed relative to the base U03 model (without inclusion of light bending). Given the uncertainty in the population size of Compton-thick sources, we allow the fractional contribution of Compton-thick AGN (log$N_{\rm H}$=24–25) to vary by a factor of $0 \leq r_{\rm CT} \leq 2$, where $r_{\rm CT} = 1$ represents an equal normalization between Compton-thick sources and Compton-thin ones with log$N_{\rm H}$=23–24, as assumed by U03. Finally, in order to account for uncertainties in the XLF (at least 5 per cent) as well as the shape and normalization of the XRB itself (e.g., Ajello et al. 2008), we allow a final variable normalization of between 0.95 and 1.05 applied to the overall spectrum.

Any realistic AGN population is likely to have a mixture of sources that readily show light bending, and those that do not. We thus assume that light bending is important in a certain fixed fraction (f) of all AGN, and we produce results for various values of f.

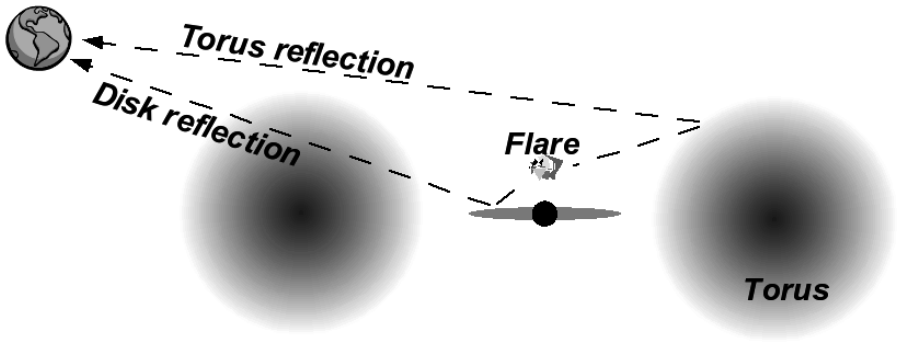

Fig. 2. Schematic picture showing the two reflection components in our AGN SEDs. Light bending strongly enhances the disk reflection component, for low heights h of flares above the event horizon. Depending on the angle of inclination, this component may be absorbed along the line-of-sight through the torus. Torus reflection is generically imagined to be unabsorbed.

4. Results

Although the torus reflection component is an integral part of our model, in order to clearly gauge the effect of the light bending, we separated our fits into two classes: those with a torus reflection component (so the overall SEDs have a fraction f of sources with PEXRAV+light bending included, and a factor $1 - f$ of PEXRAV only), and those without (i.e. a simple PL, instead of the torus PEXRAV). With respect to the schematic of Fig. 2, this is equivalent to determining the fraction of sources in which only light-bent disk reflection component contributes significantly to the overall SED, as opposed to the torus, or other reflection components.

Fig. 3 shows the improvement in χ^2 (with respect to the base model of U03) of the various fits to the XRB spectrum using the reflection-dominated SEDs. For spectra with a particular flare height h, various values of the light bending f were tried, and the maximum change in χ^2 is plotted. As an example, the XRB spectrum solution for one of the best models with $h = 5$ and a 30 % contribution of light bending ($f = 0.3$) is shown to reproduce the background data very well.

Compiling all our results, we are now immediately able to answer the question that we posed at the beginning. The overall prevalence of sources with light bending is shown in Fig. 4, as a function of source flare height.

5. Discussion

Our results show that the XRB allows for the existence of a significant fraction of sources with pronounced light bending. Assuming that light bending is important in a certain fraction (f) of sources, we derive broad constraints on f by fitting the hard X-ray background over 3–100 keV. f can be thought of as representing the distribution of sources with high effective reflection fractions ($R > 1$). Including both PEXRAV and light bending reflection components, we find values $f \leq 0.02, 0.1$ and 0.5 (decreasing with decreasing source height h [or equivalently, with increasing spectrum peakiness]; Fig. 3, *top*). Slightly larger values of f can be allowed if the peaky contribution of Compton-thick sources is neglected, though it is likely that a sizable fraction of Compton-thick AGN exists in the Universe. If light bending is the only source of reflection (the 'PL+light bending' scenario; Fig. 3, *middle*), then specific ranges of $f \approx 0.05 (h = 2), 0.1 - 0.3 (h = 5)$ and $0.3 - 0.8 (h = 10)$ are required, due to the fact that reflection-free SEDs under-predict the XRB peak. Fig. 4 has summarized all the allowed solutions in one place.

In Gandhi et al. (2007), a number of consequences of our findings have been discussed. These include the effects of ionized reflection (Ross & Fabian 2005) as may be expected within the innermost hot accretion flow regions, and the possibility of fitting the X-ray background without a significant Compton-thick population, if light-bent spectra can instead provide the peakiness required by the XRB spectrum. Here we discuss two other important aspects: that the total accretion power released in the Universe may have to be significantly increased, and the implied detectability of light-bent sources with upcoming missions.

5.1. Higher intrinsic flare luminosities

The U03 XLF involves the intrinsic 2–10 keV luminosity (L_{2-10}) and inherently assumes that this can be computed by correction of the observed source flux for obscuration and redshift effects only. On the other hand, one of the main conclusions of Miniutti & Fabian (2004) was that, under the light bending scenario, variations in the height of a flare of constant luminosity could cause the observed primary power-law emission to vary dramatically (while leaving the reflected component largely unchanged). For properly 'flux-calibrated' spectra determined by S06 (see their Figs. 6a and 15), the flux seen at infinity decreases with decreasing flare height (with

a dependence on the inclination angle) due to multiple reflections, scattering, gravitational redshifting and photons falling into the event horizon. If one knows the flux loss factor, then one can correct these to determine the intrinsic flare luminosities ($L_{\rm flare}$). For the modelled Monte Carlo light-bent spectra, it is possible to compute that for $h = 2, 5$ and 10, the inferred 2–10 keV luminosity at infinity is 0.02, 0.17 and 0.36 times $L_{\rm flare}$, due to the effect of light bending. Combining this flux loss per AGN with the best-fit light bending contribution (f), the XLF ($d\Phi/d\log L_{\rm flare}$) based on intrinsic flare luminosities can be computed. This is shown in Fig. 5.

Clearly, our corrections imply a larger number density (per cubic comoving Mpc) at the same luminosity, in the case of stronger light bending. This number density can exceed the XLF without light bending by a factor of between ~ 5 and 160 for the PEXRAV+light bending case shown (and even more for the PL+light bending case); the largest excess being at highest luminosities due to the steep slope of the XLF there. Since f is taken to be independent of z, similar behaviour is expected at higher redshift, with the exact deviation from the base XLF depending on its slope.

AGN Eddington fractions would then also be correspondingly increased (for a constant black hole mass). On a cosmological scale, using our results would imply that local Seyferts should have mean Eddington ratios larger by a maximum factor of $\sim 1.5 - 6$ (when averaged over all $\log L < 44.5$), while the corresponding increase for higher luminosity quasars should be $\sim 5 - 500$. The above increase in mean Eddington ratios is comparatively modest (at least for Seyferts), and has already been inferred for at least one source (Miniutti et al. 2007).

Interestingly, flux loss down the event horizon should also be strong enough to increase the local mass density in black holes by up to 14% in the case of extreme light bending (see details in Gandhi et al. 2007).

5.2. Predictions for hard X-ray missions

On-going surveys with *INTEGRAL* and *Swift* (Beckmann et al. 2006, Markwardt et al. 2005) should begin to detect sources in which light bending dominates, if these sources occur at low redshift and low-luminosity. Some will also definitely be detected by *MAXI* (e.g., Matsuoka et al. 2007), though measuring accurate reflection fractions may have to await telescopes such as *NeXT* and *Simbol-X*.

The large hard X-ray effective area design of *NeXT* will give a continuum sensitivity of several $\times 10^{-8}$ photons s^{-1} keV^{-1} cm^{-2} in 100 ks, or a point-source flux limit of $\sim 5.0, 1.7$ and 0.6×10^{-14} erg s^{-1} cm^{-2} over 8–80, 20–50 and 10–30 keV respectively, assuming a power-law source with a photon-index of 2 (the exact sensitivity depends on the final telescope configuration parameters, which are to be finalized in the near future). At these flux limits, 35, 39 and 68 per cent of the total XRB in the respective bands will be resolved, for the XRB normalization adopted by U03. If the original XRB normalization due to Gruber et al. is closer to the correct value, the above percentages will be increased by a factor of 1.26.

As an example, in Fig. 6 we show (as the thick lines) the cumulative XRB expected to be resolved by *NeXT* in the 8–80 keV band, along with the corresponding cumulative number counts as a function of flux. For this illustration, we chose one of the good solutions with the maximum allowed f value (in this case, $f = 0.3$ for $h = 5$ for the 'PL+light bending' scenario; cf. the bottom plots of Fig. 3) in order to show the effect of light bending. Compared to the currently resolved XRB level of $\sim 1\%$ over this energy range, the next generation of hard X-ray telescopes will enable us to make a quantum leap in knowledge.

6. Conclusions

Our results allow for a cosmologically-significant fraction of sources that are reflection dominated. The percentage of AGN in which strong light bending is occurring may be anywhere between 2 and 50% of all AGN, depending on source flare height. One of the important implications of this is that the total accretion energy density released in the Universe must be larger (on average, by a factor of a few) because only a fraction of the released accretion energy is actually observed at infinity. Such sources should be observable by the next generation of hard X-ray missions.

P.G. acknowledges a Fellowship of the Japan Society for the Promotion of Science during the course of this work. He warmly thanks the organizers for an interesting meeting.

References

Ajello M. et al. 2008 ApJ. in press, arXiv:astro-ph/0808.3377

Beckmann V., Gehrels N., Shrader C.R. & Soldi S. 2006 ApJ., 638, 642

Fabian A.C. et al. 2002 MNRAS., 335, L1

Fabian A.C., Miniutti G., Iwasawa K. & Ross R.R. 2005 MNRAS., 361, 795

Frontera F. et al. 2007 ApJ., 666, 86

Gandhi P. & Fabian A.C. 2003 MNRAS., 339, 1095

Gandhi P. et al. 2007 MNRAS., 382, 1005

Gruber D.E., Matteson J.L., Peterson L.E. & Jung G.V. 1999 ApJ., 520, 124

Matsuoka M. et al. 2007 in Society of Photo-Optical Instrumentation Engineers (SPIE) Conference, Vol.

6686, UV, X-Ray, and Gamma-Ray Space Instrumentation for Astronomy XV. Edited by Siegmund, Oswald H. Proceedings of the SPIE, Volume 6686, pp. 668611-668611-9 (2007)
Magdziarz P. & Zdziarski A.A., 1995, MNRAS., 273, 837
Miniutti G. & Fabian A.C. 2004 MNRAS., 349, 1435
Miniutti G. et al. 2007 MNRAS., 375, 227
Panessa F. et al. 2008 A&A., 483, 151
Ponti G. et al. 2006 MNRAS., 368, 903
Ross R.R. & Fabian A.C. 2005 MNRAS., 261, 74
Rossi S., Homan J., Miller J.M. & Belloni T. 2005 MNRAS., 360, 763
Suebsuwong T. et al. 2006 A&A., 453, 773 **(S06)**
Takahashi T., Mitsuda K., Kunieda H. 2006 in Turner M. J. L., Hasinger G., ed, Space Telescopes and Instrumentation II: Ultraviolet to Gamma Ray. Edited by Turner, Martin J. L.; Hasinger, Günther. Proceedings of the SPIE, Volume 6266, pp. 62660D (2006)
Ueda Y. et al. 2003 ApJ., 598, 886 **(U03)**
Ueda Y. et al. 2007 ApJ., 664, L79
Volonteri M., Madau P., Quataert E. & Rees M.J. 2006 ApJ., 620, 69
Wang J.-M. et al. 2006 ApJ., 642, L111
Wilman R.J. & Fabian A.C. 1999 MNRAS., 309, 862

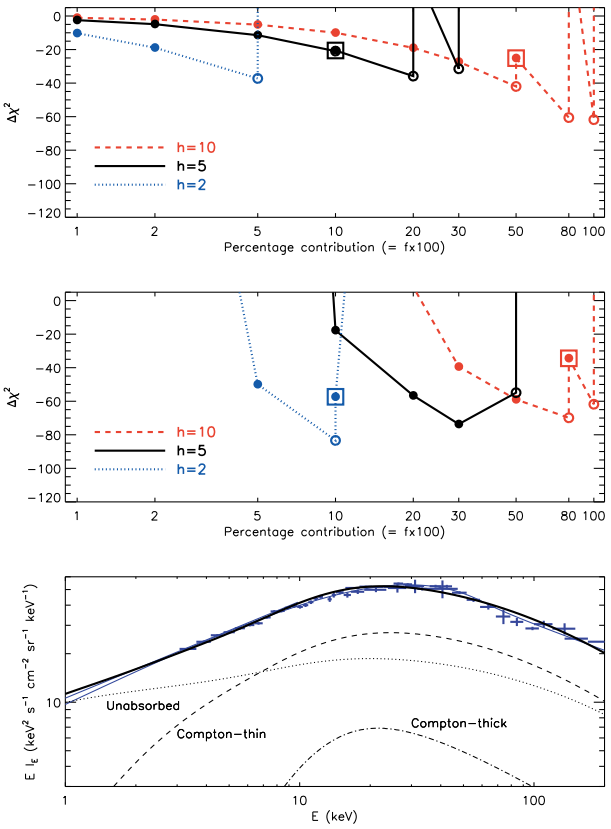

Fig. 3. **(***Top:)* $\Delta\chi^2$ for the acceptable models incorporating light bending with different percentage contributions ($f \times 100$) of light bending. The change in χ^2 is computed with respect to the base PEXRAV model with no light bending included. Empty circles represent solutions in which the best-fit fraction of Compton-thick sources ($r_{\rm CT}$) is small (< 0.5). In these cases, a secondary fit was carried out by forcing $0.5 \leq r_{\rm CT} \leq 2$ (boxed circles), which results in the apparent jaggedness of the otherwise-smooth $\Delta\chi^2$ curves. **(***Middle:)* Same as above, but with reflection-free (i.e. PEXRAV-free) power-law SEDs that incorporate different percentage contributions ($f \times 100$) of light bending. **(***Bottom:)* Best-fit modelled XRB spectrum for one of the solutions (h=5, f=0.3) incorporating PEXRAV-free power-laws+light-bending. The data is from Gruber et al. (1999).

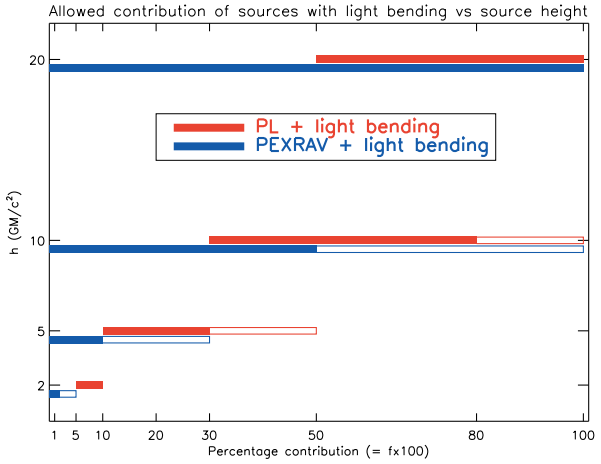

Fig. 4. Allowed combinations of (f, h) determined by fitting light-bent SEDs to the XRB, as described in the text. At each height h, the lower, blue bar denotes the 'PEXRAV+light bending' scenario (Fig. 3, *top*) and the red, upper bar is for the ' PL+light bending' scenario (Fig. 3, *middle*). Acceptable solutions that require a small Compton-thick fraction ($r_{\rm CT}$<0.5) are outlined by the empty bars, the rest being denoted by the filled bars. Though bars are drawn continuously for clarity, only the discrete f values of the previous figures were investigated.

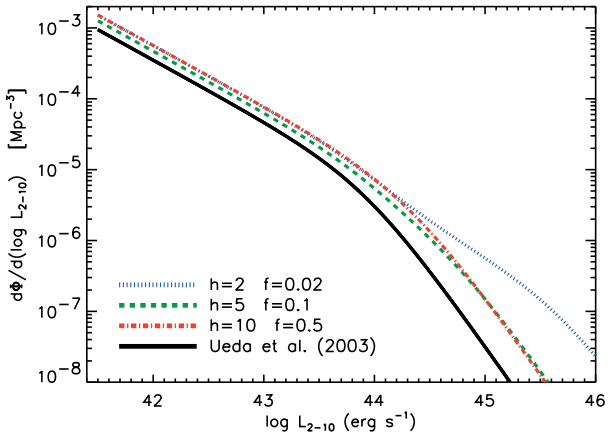

Fig. 5. Determination of XLFs based on *intrinsic*, rather than observed, flare luminosities. The black solid line shows the base 2–10 keV XLF from U03, i.e. without correction for light bending. The other lines show the XLF for $L_{2-10} = L_{\rm flare}$, using some maximum best-fit f values at each h for the case of *i)* PEXRAV + light bending scenario. The redshift of $z = 0.1$ is simply chosen as the 'local' example (cf. Fig 11 of U03). With increased light bending at low h, the correction to intrinsic luminosities goes up; or equivalently, the source number density at any given luminosity is increased.

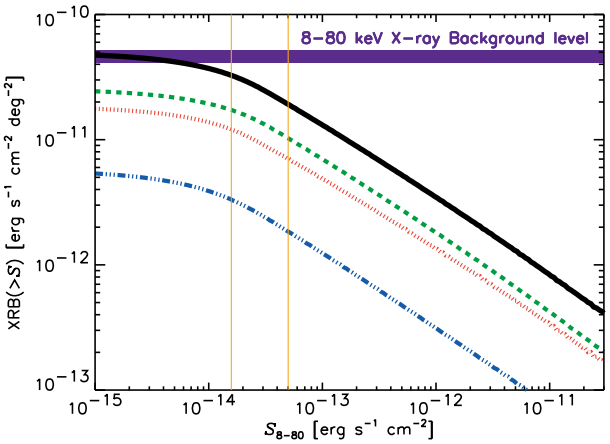

Fig. 6. The cumulative 8–80 keV XRB expected to be resolved by *NeXT*, as a function of flux. The width of the blue band near the top denotes the normalization uncertainty in the observed XRB: between 1 and 1.26 × the background level inferred from the fit of Gruber et al. (see discussion in U03). The thin yellow vertical lines are drawn at representative 100 ks and 1 Ms flux limits of 5 and 1.6 $\times 10^{-14}$ erg s^{-1} cm^{-2}. From top to bottom, the cumulative model XRB curves are i) the contribution of all sources (solid black); ii) that of Compton-thin obscured AGN (green dashed); iii) unobscured AGN (red dotted); and iv) Compton-thick AGN (blue dot-dashed).

Study of the Ejecta Distribution in the Vela SNR with MAXI

Hiroya Yamaguchi,[1] Satoru Katsuda,[2,3] Junko S.Hiraga,[1] Asami Hayato[1,4] and Toru Tamagawa[1,4]

[1] RIKEN, Wako, Saitama, Japan
[2] Osaka University, Toyonaka, Osaka, Japan
[3] NASA/GSFC, Greenbelt, MD, USA
[4] Tokyo University of Science, Shinjyuku, Tokyo, Japan
E-mail(HY): hiroya@crab.riken.jp

Abstract

The Vela supernova remnant (SNR) is a very ideal target for studying the detailed structure, since it has a quite large angular diameter ($\sim 8°$). In this proceeding, we first review the previous observations of several "shrapnels", the fragments of the ejecta protruding beyond the primary blast-shock front. Then, we report the preliminary results of shrapnel B with Suzaku. The elemental abundances are found to be significantly higher than the solar values for the first time, indicating the shrapnel originates from the supernova ejecta. Finally, we discuss the scientific significance of MAXI observations of the Vela SNR. The most part of the SNR has not yet been observed by the recent satellites, since it is too large to be covered with their limited exposure times. MAXI will be the first X-ray mission allowing us to study the ejecta distribution in the entire SNR as well as to search other ejecta fragments hiding inside the shell by the projection effect. Those information must become a key to solve the mechanism of the supernova explosions.

Key words: ISM: individual (Vela Supernova Remnant) — supernova remnants

1. Introduction

Mechanism of supernova (SN) explosions has not yet been understood completely. Therefore, we are motivated to study the distributions of the ejected nucleosynthesis products in supernova remnants (SNRs), because the information of them is essentially important to understand the explosion mechanism.

The Vela SNR is one of the brightest celestial soft X-ray sources. The origin of the SNR is considered to be Type II-P SN explosion of the progenitor star with the mass of < 25 solar mass (Gvaramadze 1999). Its age has been estimated to be $\sim 1.1 \times 10^4$ yr from the spin down rate of PSR B0833–45 (the Vela pulsar: Taylor et al. 1993). In such old SNRs, all ejecta had already been heated by reverse shock. Therefore, the evolved SNRs are suitable for the study of the global ejecta distribution, even though the emission from shocked interstellar medium (ISM) is dominantly strong. Furthermore, the Vela SNR has the largest angular size ($\sim 8°$: Aschenbach et al. 1995) among observable SNRs, and hence it is the most ideal target for studying the detailed structure.

2. Previous results

Figure 1 shows the X-ray image of the entire Vela SNR, obtained with the ROSAT all-sky survey (RASS). With the RASS observation, Aschenbach et al. (1995) discovered six ejecta fragments, named "shrapnels" A to F, which are protruding beyond the primary blast shock front. The opening angles of the shrapnels suggest supersonic motion in tenuous matter. The center line of each shrapnels can be traced back to the center of the SNR, which is close to the Vela pulsar. Therefore, they are considered to originate from clumps of SN ejecta.

Tsunemi et al. (1999a) observed shrapnel A with ASCA, and found a strong Si K-shell emission line with relatively weak emission from other elements. Using XMM-Newton, Katsuda & Tsunemi (2006) confirmed that the Si abundance was a few times higher than the solar value, while the abundances of the other elements were sub-solar values. Therefore, they concluded that shrapnel A originated from a deep (Si-rich) layer of the progenitor star. The XMM-Newton spectra of shrapnel A are shown in figure 2a. Katsuda & Tsunemi (2006) also found that the temperature increases toward the "head" region of the shrapnel, which is contrast to the temperature distribution generally seen behind the shock front of the blast wave.

Figure 2b shows the XMM-Newton spectra of shrapnel D, the brightest and largest of the ejecta fragments. Katsuda & Tsunemi (2005) found extreme overabundances of O, Ne, and Mg, while the abundance of Fe was consistent with the solar value. Therefore, they

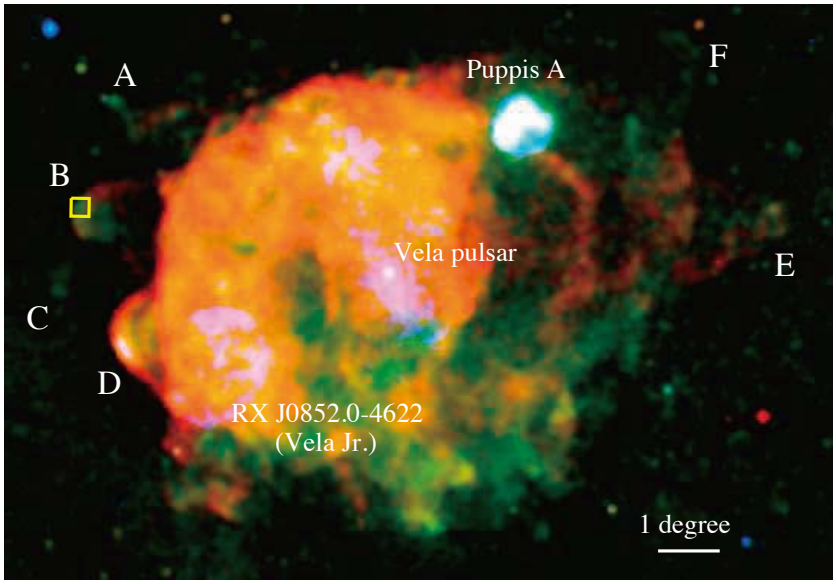

Fig. 1. ROSAT all-sky survey image of the entire Vela SNR. Red, green, and blue correspond to 0.1–0.5 keV, 0.5–1.3 keV, and 1.3–2.0 keV, respectively. The labels A–F indicate the "shrapnels" discovered by Aschenbach et al. (1995). The yellow square shows the field of view of Suzaku/XIS on Vela shrapnel B (see section 3).

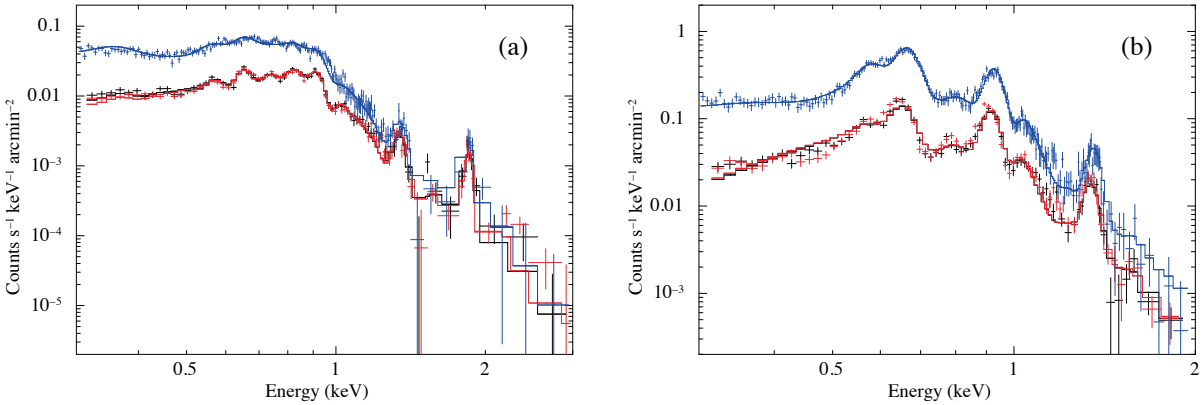

Fig. 2. XMM-Newton spectra of shrapnels A (a) and D (b). Black, red, and blue represent MOS1, MOS2, and PN, respectively.

concluded that shrapnel D is a fragment of ejecta from the shallow (O-Ne-Mg-rich) layer of the progenitor.

Recently, XMM-Newton observation of the northern part of the Vela SNR discovered the ejecta knots (Miceli et al. 2008), which are possible candidates of "new" shrapnels hidden inside the Vela main shell by the projection effect. The relative abundances of these knots were found to be quite similar to those observed in shrapnel D: O, Ne, and Mg were much more abundant than those of the other elements.

3. Suzaku preliminary results of Shrapnel B

Suzaku observed Vela shrapnel B on 2006 November 5 for $\sim$ 60 ksec. The field of view of XIS (Koyama et al. 2007) on board Suzaku is shown as the yellow square in the RASS image (figure 1). Although Tsunemi et al. (1999b) observed this shrapnel with ASCA, they could not determine the elemental abundances due to the poor photon statistics. Utilizing the good sensitivity of XIS, we investigated the detailed spectral properties of shrapnel B. Here, we present the preliminary results of our analysis. The more extended results will be reported in a future paper (Yamaguchi & Katsuda, in preparation).

Figure 3 shows the vignetting-corrected XIS image in 0.5–2.0 keV band. We extracted X-ray spectra from the brightest region indicated as the green ellipse. The result is shown in figure 4, where the non X-ray background are subtracted. These spectra are considered to include two of X-ray background components: the cosmic X-ray background (CXB) and the local hot bubble

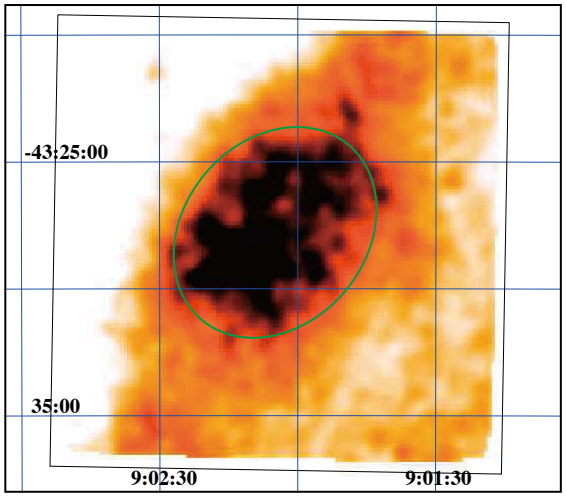

Fig. 3. XIS image of Vela shrapnel B in 0.5–2.0 keV band. The vignetting effect is corrected after the subtraction of non X-ray background. The coordinates (RA and Dec) refer to epoch J2000. The black square and green ellipse are respectively indicate the field of view of XIS and the spectrum extraction region.

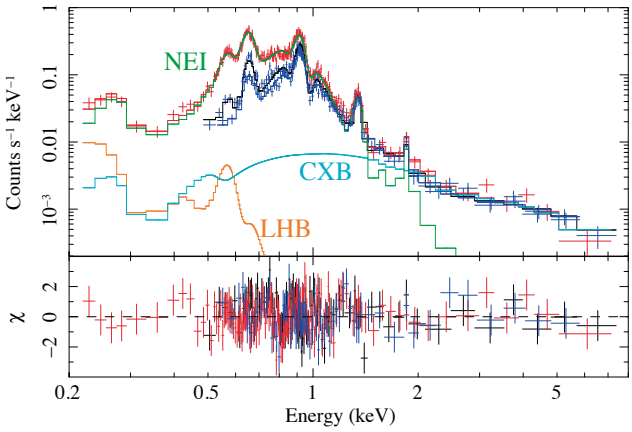

Fig. 4. NXB-subtracted XIS spectra extracted from the elliptical region shown in figure 3. The black, red, and blue data points represent XIS0, 1, and 3 spectra, respectively. The solid lines, colored green, light blue, and orange show the components of the NEI (emission from the shrapnel), CXB, and LHB.

(LHB), in addition to the emission from the shrapnel. As the CXB component, we introduced a power-law model with photon index of $\Gamma = 1.412$, following Kushino et al. (2002). As the LHB component, we assumed a thin-thermal plasma (an APEC model) with a temperature of 0.1 keV and an elemental abundances of the solar values. From the surface brightness in the ROSAT PSPC R1 and R2 bands, the emission measure of the LHB component around the Vela SNR was estimated to be 1.7×10^{16} cm^{-5}; we use this value in the following spectral analysis.

Since several strong emission lines can be clearly seen below 2 keV, we used a model of optically thin-thermal plasma at a non-equilibrium ionization (an NEI model) for the emission from the shrapnel. Then, the acceptable fit was obtained with χ^2/d.o.f. of 332/318. The best-fit parameters are listed in table 1, where the solar abundances are assumed to be those of Anders & Grevesse (1989). The 2–10 keV surface brightness of the CXB component was obtained to be $(5.3 - 6.2) \times 10^{-8}$ ergs cm^{-2} s^{-1} sr^{-1}, which is consistent with the value derived by Kushino et al. (2002).

The absolute abundances of heavy elements are found to be significantly enhanced from the solar values, for the first time. This fact suggests that shrapnel B is one of the ejecta fragments originating from an explosion of Vela SN, similarly to shrapnel A and D (Katsuda & Tsunemi 2005; 2006). The relative abundances of Ne/Fe and Mg/Fe are higher than those of the solar, which are similar to shrapnel D rather than A.

Table 1. Best-fit parameters for Vela shrapnel B

Parameter	Value
$N_{\rm H}$ (cm^{-2})	2.0 (1.3–2.7) $\times$ 10^{20}
kT_e (keV)	0.55 (0.52–0.62)
O (solar)	1.9 (1.6–2.5)
Ne (solar)	5.1 (4.3–7.4)
Mg (solar)	3.6 (2.8–4.7)
Si, S (solar)	3.2 (2.3–3.9)
Fe, Ni (solar)	1.6 (1.4–2.4)
$n_e t$ (cm^{-3} s)	4.9 (3.9–5.7) $\times$ 10^{10}
$\int n_e n_p \, dl$ (cm^{-5})	3.5 (3.2–3.9) $\times$ 10^{16}

4. Available results with MAXI

Although ROSAT observed the entire SNR, the global ejecta distribution had not been determined, because of its poor energy resolution. On the other hand, since the angular size of the Vela SNR is extremely large, observing the entire remnant with the recent pointing satellites (e.g., XMM-Newton, Chandra, or Suzaku) is difficult due to their limited exposure times.

Solid State Camera (SSC) on board MAXI has good energy resolution with the wide energy range of 0.5–10 keV (Katayama et al. 2005). Thus, it will be the first X-ray mission allowing us to study the ejecta distribution in the entire SNR, by spatially resolved spectroscopy. We will also be able to search other ejecta fragments hiding inside the shell by projection, similar to those found in the northern part of the SNR by the XMM-Newton observation. Those information will help us to understand the detailed mechanism of the core-collapse SN explosions.

References

Anders E. & Grevesse N. 1989 GeCoA., 53, 197
Aschenbach B. et al. 1995 Nature, 373, 587
Gvaramadze V. 1999 A&A., 352, 712
Katayama H. et al. 2005 NIM., A541, 350
Katsuda S. & Tsunemi H. 2005 PASJ., 57, 621
Katsuda S. & Tsunemi H. 2006 ApJ., 642, 917
Koyama K. et al. 2007 PASJ., 59, S23
Kushino A. et al. 2002 PASJ., 54, 327
Miceli M. et al. 2008 ApJ., 676, 1064
Taylor G.B. et al. 1993 ApjS., 88, 529
Tsunemi H. et al. 1999a PASJ., 51, 711
Tsunemi H. et al. 1999b hxra.conf., 310

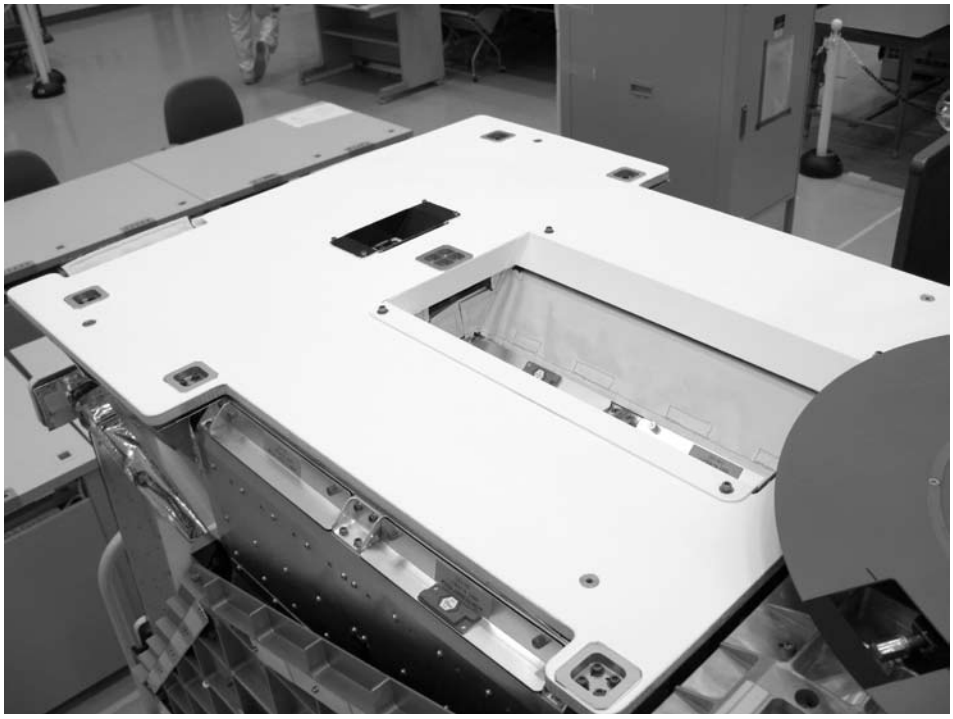

MULTIWAVELENGTH OPPORTUNITIES AND RESULTS

Hard X-Ray sources observed by INTEGRAL/IBIS and their science

Pietro Ubertini on behalf of the IBIS Survey Team

IASF-Roma, INAF, Via Fosso del Cavaliere 100, 00133 - Rome, Italy
E-mail: pietro.ubertini@iasf-roma.inaf.it

Abstract

After more than 5.5 years of in flight lifetime, the ESA space observatory INTEGRAL is depicting a new scenario in the soft gamma Ray domain. With the observation and discovery of more than 400 hard X-Ray sources has changed our view of a moderately crowded and dark sky basically populated by "peculiar" and erratic sources. The new high energy sky is also composed by a large variety of "normal" though very powerful objects, characterized by new accretion and acceleration processes. Among the 421 sources detected in the energy range 17-100 keV the 3^{rd} INTEGRAL/IBIS catalogue includes 41% galactic accreting system, 29% extragalactic objects, 8% of other types, and 26% not classified i.e. of unknown origin. If compared to to previous IBIS/ISGRI surveys it is clear that there is a continuous increase of the rate of discovery of HMXB, an increase in the number of AGN discovered, including a variety of distant QSOs, basically due to the increased exposure away from the Galaxy Plane, while the percentage of sources without an identification has remained constant. INTEGRAL, by the end of Y6, will complete the Core Programme observation due to provide an almost constant exposure of the whole Galaxy Plane and will be fully open to the scientific community for Open Time and Key Programme observations from the beginning of 2009. In this paper we shortly review the main outcome of the 3^{rd} INTEGRAL/IBIS catalogue (cat3) including an excursus of the INTEGRAL high energy sky with particular regard to sources emitting at high energy, including Low and High Mass X-Ray Binaries (LMXB & HMXB), Supergiant Fast X-Ray Transients (SFXT), Pulsar Wind Nebulae (PWN) and Active Galactic Nuclei (AGN).

Key words: Subject headings: Gamma-rays, observations, surveys

1. INTRODUCTION

The INTEGRAL ESA gamma-ray observatory has already carried out more than 5 years of Core, Key and Guest Observer Programme observations in the energy range from 5 keV - 10 MeV (Winkler et al. 2003). The IBIS coded mask imager is optimised for scientific observations over a wide field of view (∼1000 squared degree) with excellent imaging and spectroscopy capability (Ubertini et al. 2003), to provide survey type data, including detailed images of the whole sky, time profile and spectra of all the sources detected with a sensitivity better than 1 mCrab in the central radian.

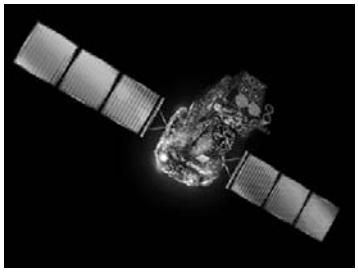

Fig. 1. The INTEGRAL Observatory (ESA Courtesy).

2. The INTEGRAL Observatory

The ESA INTEGRAL (International Gamma-Ray Astrophysics Laboratory) observatory was selected in June 1993 as the next medium-size scientific mission within ESA Horizon 2000 programme. INTEGRAL (Winkler et al. 2003), shown in Figure 1, is dedicated to the fine spectroscopy (2.5 keV FWHM @ 1 MeV) and fine imaging (angular resolution: 12 arcmin FWHM) of celestial gamma-ray sources in the energy range 15 keV to 10 MeV. While the imaging is carried out by the imager IBIS (Ubertini et al. 2003), the fine spectroscopy if performed by the spectrometer SPI (Vedrenne et al. 2003) and coaxial monitoring capability in the X-ray (3-35 keV) and optical (V-band, 550 nm) energy ranges in provided by the JEM X and OMC instruments (Lund et al. 2003; Mass-Hesse et al. 2003). SPI, IBIS and Jem-X, the spectrometer, imager and X-ray monitor are based on the use of coded aperture mask technique that is a key feature to prove images at energy above tens

of keV, where photons focusing become impossible using standard grazing technique. Moreover, coded mask feature the best background subtraction capability because of the possibility to observe at the same time the Source and the Off-Source sky. This is achieved at the same time for all the sources present in the telescope field of view. In fact, for any particular source direction, the detector pixels are split into two sets: those capable of viewing the source and those for which the flux is blocked by opaque tungsten mask elements. This very well established technique is discussed in detail by (Skinner & Connell 2004) and is extremely effective in controlling the systematic error in all the telescope observation, working remarkably well for weak extragalactic field as well for crowded galactic regions, such as our Galaxy Center. The mission was conceived since the beginning as an observatory led by ESA with contributions from Russia (PROTON launcher) and NASA (Deep Space Network ground station). INTEGRAL was launched from Baikonur on October 17^{th}, 2002 and inserted into an highly eccentric orbit (characterized by 9000 km perigee and 154000 km apogee). The high perigee in order to provide long uninterrupted observations with nearly constant background and away from the electron and proton radiation belts. Scientific observations can then be carried out while the satellite being above a nominal altitude of 60000 km, while entering the radiation belts, and above 40000 km, while leaving them. This strategic choice ensure about 90% of the time is used for scientific observations with a data rate of realtime,108 kbps science telemetry received from the ESA station of Redu and NASA station of Goldstone. The data are received by the INTEGRAL Mission Operation Centre (MOC) in Darmstadt (Germany) and relayed to the Science Data Center (Courvoisier et al. 2003) which provide the final consolidated data products to the observes and later archived for public use. The proprietary data become public one year after distribution to single observation PIs.

3. The INTEGRAL/IBIS sky

3.1. The Catalogue

In order to give maximum access to the whole scientific INTEGRAL/IBIS data set a catalogue, comprising all the detected high energy sources is generated roughly on an annual basis (Bird et al, 2004, 2006, 2007). The last of them (the 3^{rd}, namely THE 3^{rd} IBIS/ISGRI SOFT GAMMA-RAY SURVEY CATALOG) has been produced using all the IBIS data available up the and of May 2006 (40 Ms exposure time). It contains 421 sources, detected above 4.5σ in the energy range 18-100 keV; in Figure 2 is shown the distribution of the sources (top panel) and the INTEGRAL/IBIS Sky coverage evolution as per cat 1, 2 and 3; the bottom panel on the right is the coverage at the end of Y5. As expected the

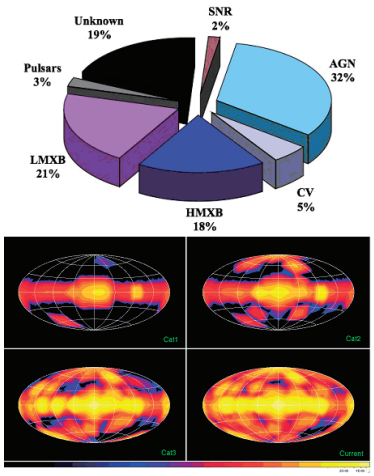

Fig. 2. Top:distribution of the high energy sources of the 3^{rd} IBIS Catalogue: for each source is also produced the spectrum and the light curve. Bottom: IBIS Sky coverage evolution vs time.

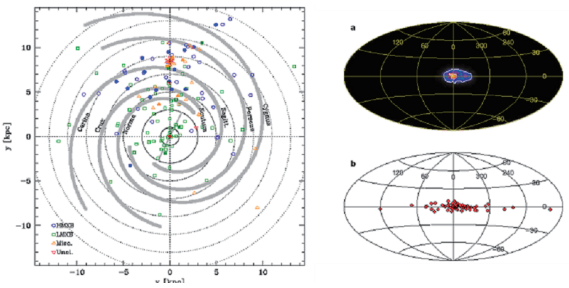

Fig. 3. Left: distribution of IBIS sources in the Galaxy. Right-top: discovery of asimmetric distribution of positron 511 keV annihilation in the Galactic disk. Right-bottom: IBIS LMXB distribution.

majority of the IBIS sources are located at low galactic latitudes, due to the basic fact that INTEGRAL is frequently observing in the Galactic Plane and the sky coverage is far for uniform, as shown in Figure 2. The source identification process is based on a multi wavelength approach, taking into consideration the Radio, IR, X-ray and higher energy archival data. A robust programme of optical and IR observation campaigns has been activated just after the INTEGRAL launch and had been very successful (Masetti et al. 2006a,b,c,d and 2008). Among the sources that have been firmly identified are 171 associated with galactic binary accreting systems (41%), 122 are extragalactic sources (29%), 15 belong to different classes of high energy emitters. As many as 113 (26%) are still not identified. The sources belonging to our Galaxy are sub-divided into 21 CV systems (9 of which are new detections with emission extending up to 100keV), 65 high-mass X-ray binaries (HMXB) and 78 low-mass X-ray binaries (LMHB). IBIS continues to detect Low Mass systems X-Ray Binaries even if the rate of discovery is much lower than for the high mass systems.

In particular, the High Mass Binary includes 19 new IBIS sources which have been identified with Be systems on the basis of their spectral characteristic and/or transient behavior. A distinct type of new objects, increasing regularly in the INTEGRAL/IBIS sample are the Super Giant fast X-ray transient (SFXT). Apart from the detailed and unbiased study related to the IBIS/ISGRI catalogue production several outstanding studies and results of wide astrophysical interest have been carried out with INTEGRAL/IBIS. An overview, even if superficial, is behind the scope of this short overview. Just as an example in Figure 3 (left panel) is shown the distribution of the IBIS sources in the Galaxy: circles are HMXB, squares are LMXB, triangles are Miscellaneous and inverted triangles are unclassified sources (Bodaghee et al., 2007). Of complete different nature the discovery of asimmetric distribution of positron annihilation in the Galactic disk based on the SPI outstanding spectroscopic capability and IBIS high angular resolution (Weidenspointner et al., 2008) as shown in Figure 3 (left panel): the IBIS LMXB distribution; (right panel) the SPI 511 keV emission. This result clearly demonstrate the SPI-IBIS complementarity.

3.2. The IBIS sky: E>100 keV

The data accumulated with INTEGRAL/IBIS at energies above 100 keV in the first 3.5 years of operative life, have been discussed in Bazzano et al. (2006). This data set provided the first IBIS sources catalog characterised by very hard spectral components, listing 49 sources detected with a significance above 4 in the 100-150 keV energy range of which only 14 seen above 150 keV. Black Holes and accreting Neutron Stars systems mainly populate the high energy sky but extragalactic source are also contributing with 20% of the sample. In the higher energy range (>150 keV) the main emitting sources are Black Hole candidates/microQSOs. A larger sample is due to be finalized and the sample consist now of about 100 sources. All classes are included with the majory being galactic sources. The IBIS sample is consistent with the SPI resolved point sources in the 100-200 keV band (Bouchet et al., 2008). Also, an indication of the possible association between the the observed asymmetry in the 511 keV line emission from the galactic disk with X-ray Binary, mainly LMXB, has been suggested by Weidenspointner et al., 2008 (cfr paragraph 3.1). It was also noticed by the same author that similar asymmetry is derived when taking into account the LMXB distribution as from the 3^{rd} IBIS catalog above 20 keV (Bird at al., 2007) and even more evident when using the sources above 100 keV. Finally, in Figure 4 is shown the AGILE High Energy Sky for E>100 MeV (Tavani et al. 2008), dominated by the Disk diffuse emission (left) and the IBIS soft gamma Ray sky, E>20 keV, dominated by discrete sources (right).

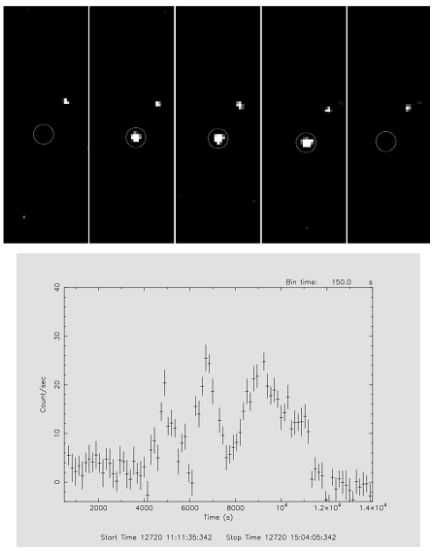

Fig. 5. Short time variability of XTE J1739-302.

3.3. The keV to TeV connection

Another significant class of sources strongly emitting in the soft gamma-ray range as well as at very high energies (>TeV) are the Pulsar and Pulsar Wind Nebulae (PWN). While there is no room in this short paper to properly address this topic, it is worth to mention that IBIS has detected more than 10 of those high energy sources, most of them associated with HESS/MAGIC high energy gamma ray emission (For a comprehensive review see Aharonian et al. 2005, Albert et al., 2007, Malizia et al. 2005, Ubertini et al. 2005, Dean et al. 2008, Ubertini et al., 2008 and references therein).

3.4. FXT sources and Supergiant HMXB

One of the two new class of high energy emitters discovered by INTEGRAL belong to the category of Fast Transient X-Ray sources (FXT), the other one correlated with strongly absorbed binary NS of which J16318-4848 is the archetype (Walter et al., 2006). Even if one of the most common characteristics of the high energy sky is the source variability (from ms to Ms), very little was known before the INTEGRAL launch on the class of sources that were identified as FXT. The basic information available were correlated with their location, off the Galaxy plane, and their seldom large outbursts lasting less than a day. The only un-biased survey of those class of objects was performed by BeppoSAX with the Wide Field Camera detectors, taking advantage of their large field of view (2×40×40 squared degree looking at 180 degree each other) and the total mission span along more than 6 years. BeppoSAX detected almost 50 different objects that exhibited a bimodal distribution in their duration. The first type is now known to be associated with the so-called X-Ray flashes, connected with

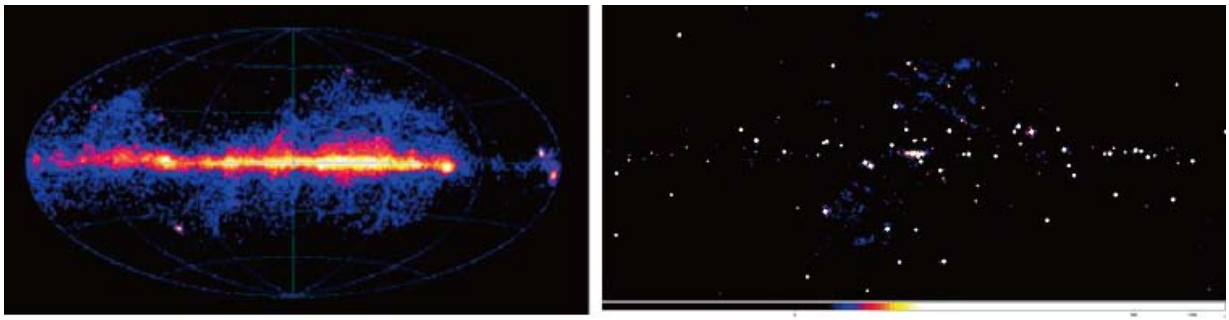

Fig. 4. The AGILE, E>100 MeV, High Energy Sky, dominated by the Disk diffuse emission (left) and the IBIS soft gamma Ray sky, E>20 keV, dominated by discrete sources.

Gamma-ray bursts type event (D'Alessio et al., 2006) and the second one, connected with active coronal star. More recently, INTEGRAL has changed the BeppoSAX scenario, thanks to the extended high energy response of the IBIS telescope, via the discovery of the so-called Supergiant Fast X-Ray Transient (Sguera et al., 2005, 2006, 2007, 2008; Neguerela et al., 2006). This new class of high energy emitters, SFXTs, has been optically identified with HMXB hosting an early type supergiant star. The surprise was that this kind of classical Supergiant HMXB (called SGXBs), discovered more than 40 years ago, were known to be persistent X-ray emitters with an emission ranging from $10^{36} - 10^{38} erg\ s^{-1}$. In fact, the SFXTs have a quiescent luminosity from 1000 to 1000,000 times smaller and therefore undetectable most of the time with current X-Ray monitoring experiment. Conversely, they occasionally have fast X-ray activity lasting from hours to a day (or more) with peak luminosity of the order of $10^{36} - 10^{37} erg\ s^{-1}$. INTEGRAL revealed flares characterized by short duration peaks (ten of minutes) and steep spectra above 20 keV, with photon power law index between 2-3. Alternatively, the spectra can be fitted with thermal bremsstrahlung models (kT comprised between 10 and 35 keV). In Figure 5 (top panel) is shown a "classical" detection of the IBIS telescope: the images are related to the detection of a fast X-ray outburst of XTE J1739−302 in the energy range from 20 to 30 keV. Each panel has a duration of about 2000s and the source is visible only in the 3 central panel, for a total flare duration of less that one hour. In the first and last half hour observation is well below the flux at the peak and was not detected at all. The stable serendipity source in the top part of the image is the BHC 1E 1740.7-2942. In the right panel is shown the IBIS/ISGRI light curve integrated over the energy range from 20 to 60 keV (Sguera et al., 2005). The emission processes responsible for the very low stable emission from SFXTs and the short hysteric flares are probably explained by very wide eccentric orbit (with a much longer period than classical SGXBs ∼15 days) and in turn, with a low amount of wind material available to accretion onto the compact companion. When the collapsed star is closer to the supergiant donor star, highly inhomogeneous, structured, wind clumps accretion can become efficient and hance flares detectable by INTEGRAL in the soft gamma ray range (Negueruela et al., 2005, In't Zand 2005). This scenario implies a periodicity of the fast outbursts as they should occur always relatively close to the periastron passage, but to date periodicity has been observed only from one source: IGR J11215−5952, with a period of ∼330 days (Sidoli et al., 2006, Romano et al., 2007). In the light of these new and exciting INTEGRAL results, the size of the population of SGXBs in our Galaxy could have been severely underestimated. An entire population of still undetected SFXTs could be hidden in our Galaxy, on top the 8 firm source already discovered. Ongoing observations with INTEGRAL are expected to provide new SFXTs discovery and permit a breakthrough in our understanding of the physical processes behind their fast X-ray transient behavior.

3.5. The extragalactic IBIS sky

The INTEGRAL observing programme has been initially focused on the Galaxy plane scanning and deep observation of the Galaxy center. In recent years more attention has been dedicated to the observation of the extragalactic sky, with particular attention to obtain a substantial number of deep extragalactic field via the so-called Key Programmes. The result is that from the third IBIS survey (Bird et al. 2007) has provided a significant improvement in the detection of extragalactic objects due to the larger sky coverage available and deep observations (>2-5 Ms). One of the main task was to have a better high energy picture of the close Universe, i.e. the one amenable for a "complete sample" observation with IBIS. In fact, quantifying the AGNs missing fraction

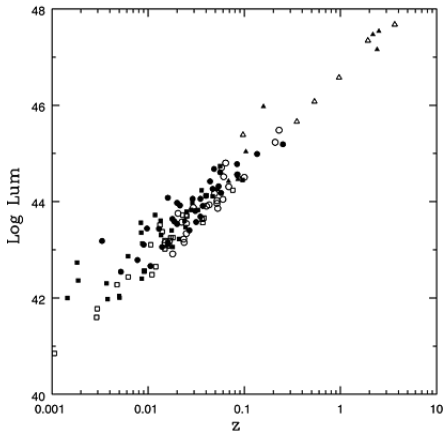

Fig. 6. Lum vs z for the IBIS AGN sample.

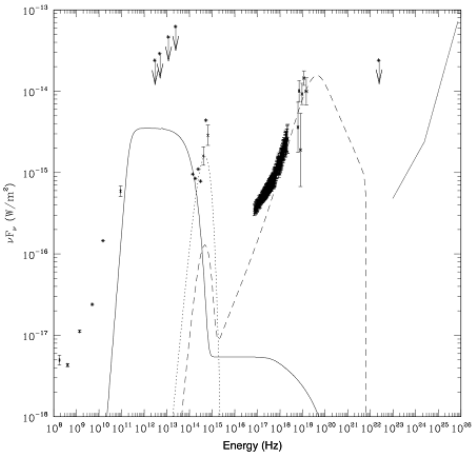

Fig. 7. SED of the QSO 4c04.42 (z=0.965) suggestive of Bulk Comptonisation.

due to absorption (especially in the classical X-Ray band Surveys) is necessary to fully understand the accretion evolution of the Universe (Bassani et al., 2007a). This is also a fundamental issue to understand the contribution of AGNs to the X-ray cosmic diffuse background (Churazov et al., 2008) and in order to test the current unified theories. This is only possible with a good knowledge of the spectral shape and column density distribution of the detected AGNs. Clearly, high energy observations, above 10 keV, are necessary to obtain an unbiased measurement of the column densities and of the high energy cut-off distributions of AGNs in the local Universe. Recently, this has been possible thanks to the extragalactic INTEGRAL/IBIS deep exposure and by the All Sky monitoring from SWIFT/BAT (Gehrels et al., 2004) providing new complementary information on hard X-Ray emitting AGNs. The list of cat3 AGNs has been obtained by the use of a large number of identification and classification being provided through optical spectroscopy and catalogue searches. Within the sample of optically classified objects (Masetti et al., 2006 a,b,c,d, 2008) about 120 are Seyfert galaxies and 13 are blazars; within the Seyfert sample 58 objects are AGN of type 1-1.5 (circles in Figure 6) while are 60 type 2 (squares), i.e. a ratio 1:1, which illustrates the power of gamma-ray surveys to find narrow line AGN and 13 are blazars (triangles), with about 10% of the sample being radio loud objects. The range of redshift probed by our sample is 0.001-3.668 while the 20-100 keV luminosities span from 10^{41} to 10^{48} erg s^{-1}. This, in turn, establish the limit sensitivity of the cat3 Survey, i.e. about $1.5{\times}10^{-11}$ erg cm^2 s^{-1}. This limit is improving with time in view of the largest exposure for extragalactic fields and the basic insensitivity of the IBIS observation to systematic error. The closest object detected is the Seyfert 1.8 galaxy NGC4395 with a z=0.001 (Panessa et al. 2006) and IGR J22517+2218 with a z=3.668 (Bassani et al., 2007b). The IBIS sensitivity to faint extragalactic objects is increasing with time providing, for the first time, the detection of the brightest Blazars, the most powerful objects in the observable Universe emitting from radio up to very high energy gamma-ray. In the X/gamma-ray range, hard spectra are shown by the highest luminosity objects (Fossati et al. 1998), and Flat Spectrum Radio Quasars (FSRQ) are the most luminous class of Blazars. The Spectral Energy Distribution (SED) of FSRQ exhibits two main peaks (one between the IR and soft X-ray frequencies and the other in the gamma-ray regime), disclosing the presence of two main components: it is widely believed that the low energy one is due to the Synchrotron radiation of relativistic electrons in a jet, while the high energy one is due to Inverse Compton scattering (IC) of the same electrons with a photon field (Ghisellini et al. 1998). IBIS is becoming sensitive to bright distant AGNs, and several of them are now becoming visible and amenable to spectral studies (Table I). As an example, in Figure 7 is shown the SED of the luminous QSO 4c04.42 at z=0.965 for which has been observed and excess of emission below 2 keV (in the observer frame) suggesting Bulk Compton motion (De Rosa et al., 2008).

Conclusion

After more than 5.5 years of observations, INTEGRAL is still performing a survey of the all sky and the deep monitoring of the Galactic Plane, monitoring more than 420 sources and spending several Ms observations in selected deep flieds; this is giving us exciting results about new high energy emitters and discovering new dozen of variable sources. The large field of view, the good angular resolution and the deep observations provide all

together a powerful tool to discovery highly variable sources, like new SFXTs, distant AGN flares, Blazar like IGR J22517+2218, the second most distant one detected above 20 keV. The main conclusions are: i) the number of INTEGRAL sources continue to increase dramatically (+> 200 sources in cat 4), ii) the HMXB numbers increasing faster than LMXB after initial GCDE campaign, iii) AGN numbers increased to ∼130 in cat3 and are almost doubled today, boosted by exposure and follow-up campaigns, iv) the SFXT have emerged as a new class: 14 (including candidates) have been observed when not in outburst, v) a significant numbers of CVs are now detected: almost exclusively IP sub-class, vi) PWN are now a distinct class of soft gamma ray emitters. The Sky above 100 keV is becoming more and more populated. Finally, a great expectation is due to the launch of the GLAST high energy observatory just placed in orbit the 11 June, 2008, during the MAXI Workshop. We have clearly entered a "golden age" for high energy astrophysics with contemporaneous in-flight operation of CHANDRA, XMM/Newton, INTEGRAL, SWIFT, SUZAKU, AGILE, now GLAST and MAXI hopefully to arrive soon.

Acknowledgement

The author wish a particular thanks to Prof. Masaru Matsuoka and Prof. Nobuyuki Kawai for the kind invitation to participate to the MAXI Workshop and for the invited talk on INTEGRAL. The author acknowledge financial contribution from Contracts ASI I/008/07/0 and a special thanks to Mrs. Catia Spalletta for the professional preparation of the manuscript.

Table 1. High-z INTEGRAL QSOs: the sample

Source	z	Reference
PKS1830-211	2.507	De Rosa et al. 2005, Zhang et al. 2008
Swift J1656.3-3302	2.4	Masetti et al. 2008
IGR J22517-2218	3.668	Bassani et al. 2007
QSO B0836-710	2.172	Bird et al. 2007
4C04.42	0.965	De Rosa et al. 2008
1RXS J19245	0.352	Bird et al. 2007
IGR J03184-0014	1.93	Bird et al. 2007
QSO B0212+735	2.367	Bird et al. 2007
PKS 2149-307	2.345	Bird et al. 2007
PKS 0537-286	3.104	Possibly detected in 20-200 keV
QSO 0723+679	0.884	Possibly detected in 20-200 keV

4. References

Aharonian F., et al. 2005, Science 307, 1938
Albert, J., et al., 2007, astro-ph0709.3763
Bassani, L., et al., 2007a astro-ph/0610455v1
Bassani, L. et al. 2007b Ap.J., 669,L1
Bazzano A., et al., 2006 ApJ, 649, L9
Bird, A.J., et al. 2004, ApJ, 607, 33
Bird, A.J., et al., 2006, ApJ, 636, 765
Bird, A.J., et al. 2007, ApJS, 170, 175
Bouchet, L. et al., 2008, ApJ, 679, 1315
Bodaghee A. et al., 2007, A&A, 467,585
Churazov E. et al., 2008 A&A, 467, 529
Courvoisier T., et al., 2003, A&A, 411 L49
D'Alessio, V., et al., 2006, A&A, 460, 653
De Rosa et al., MNRAS, 388, L54, 2008
Dean A. J., et al. 2008, MNRAS, submitted
Fossati, G., et al. 1998, MNRAS, 299, 433
Gehrels, N., et al. 2004, Ap.J., 611, 1005
Ghisellini, G., Celotti, A. et al., 1998, MNRAS, 301, 451
Lund N., et al. 2003, A&A, 411, L231
Malizia A., et al. 2005, ApJL, 630, 157,
Masetti, N., et al. 2006a, A&A, 448, 547 (Paper II)
Masetti, N., et al. 2006b, A&A, 449, 1139 (Paper III)
Masetti, N., et al. 2006c, A&A, 455, 11 (Paper IV)
Masetti, N., et al. 2006d, A&A, 459, 21 (Paper V)
Masetti, N., et al., 2008, astro-ph/0802.0988 (Paper VI)
Mass-Hesse M. et al. 2003, A&A, 411 L261
Negueruela, I. et al. 2005, ESA SP-604, 165
Panessa, F. et al. 2006 A.&A, 455, 173
Romano et al., 2007, atel 1151
Sguera, V., Barlow, E. J., et al., 2005, A&A, 444, 221
Sguera, V., Bazzano, A., et al., 2006, ApJ, 646, 452
Sguera, V., Bazzano, A., et al., 2007, as-ph/0704.2737
Sguera, V., et al., 2008, as-ph/0805.0496
Sidoli, L., et al., 2006, A&A, 450L, 9S
Skinner, G. & P.Connell 2003, A&A, 411, L123
Tavani et al., 2008, Cospar Symp.E12, in press
Ubertini P., et al. 2003, A&A, 411, L131
Ubertini P., et al. 2005, ApJL, 29, 109
Ubertini P., De Rosa, A., Bazzano, A., et al., 2008, Nucl. Instr.& Meth. A, 588, 63
Vedrenne G,. et al. 2003 A&A, 411, L63
Walter, R., et al. 2006, A&A, 453, 133
Weidenspointner G. et al., Nature, 451,159,2008
Winkler C. et al. 2003, A&A, 411, L1

Non-GRB Sources Observed with Swift

Neil Gehrels[1]
on behalf of the Swift Team

[1] NASA/GSFC
E-mail: Neil.Gehrels@nasa.gov

Abstract

The Swift mission has great synergy with MAXI. Operating together, the two missions will provide sensitive sky monitoring in both the soft and hard X-ray bands. Swift will also provide follow-up observations for sources detected by MAXI. This paper describes the non-GRB capabilities and science of Swift. The mission is made up of the BAT wide-field hard X-ray instrument and the XRT and UVOT focusing narrow-field X-ray and UV-optical telescopes. The BAT continuously observes the hard X-ray sky performing a sensitive survey in the 15 - 350 keV range. It is nearly uniform across the sky and is not affected by absorption for Compton-thin sources. At a sensitivity of 10^{-11} ergs cm^{-2} s^{-1}, it is has detected ∼580 sources in 22 months. The XRT performs observations in the 0.2 - 10 keV range of select source fields during GRB and non-GRB pointings. Sensitivities achieved are in the 10^{-15} to 10^{-14} erg cm^{-2} range. The UVOT observes UV and optical fields to a sensitivity of ∼23 magnitude. Valuable data are obtained from Target of Opportunity observations of transients. To date more that 500 such TOOs have been performed. This paper summarizes the non-GRB capabilities and science of Swift.

Key words: Swift

1. Introduction

Swift (Gehrels et al. 2004) is a first-of-its-kind autonomous spacecraft with on-board constraint checking and a 3-instruments multiwavelength payload. The wide-field Burst Alert Telescope (BAT) instrument (Barthelmy et al. 2005) surveys the sky for persistent and transient sources in the 15 - 350 keV band and positions them to arcmin accuracy (20 arcmin PSF). The narrow-field X-Ray Telescope (XRT) (Burrows et al. 2005) covers the 0.2 - 10 keV band in a 24 arcmin × 24 arcmin field of view. It has CCD spectroscopy and positions sources to few arcsec accuracy (18 arcsec PSF). The UV-Optical Telescope (UVOT) (Roming et al. 2005) covers the 170 - 600 nm optical/UV band in a 17 arcmin × 17 arcmin field of view. It has a filter wheel with 6 colors and 2 grisms (resolving power of 200 and 400) and position sources to subarcsec accuracy (1.9 arcsec PSF).

Gamma-ray bursts and other short transients are detected by the BAT which determines their position using on-board software. The position is provided to the spacecraft, built by General Dynamics, which then repoints to the burst location in less than 2 minutes to allow XRT and UVOT observations. Alert data from all three instruments are sent to the ground via NASA's TDRSS relay satellite. The full data set is stored and dumped to the Italian Space Agency's equatorial Malindi Ground Station. Source positions can also be sent up to the spacecraft for rapid (<1 hour turn around) target of opportunity (TOO) observations.

The Swift mission was built by an international team from the US, UK, and Italy. After five years of development it was launched form Kennedy Space Center on 20 November 2004. Full normal operations commenced on 5 April 2005.

2. Non-GRB Science

The Swift observing strategies have been changing as the mission matures with the fraction of time spent on non-GRB science increasing. This is shown in Figure 1 comparing 2005 and 2007. The time spent on TOOs observations of transient sources has increased from 8% to 20% and on scheduled "fill-in" observations of persistent sources from 18% to 25% (8 Ms per year). The reason for the change is both an increased interest in the non-GRB capabilities in the user community and a new strategy for GRBs where follow-up observations are terminate earlier for less interesting bursts.

Another indication of change in Swift is in the rate of TOO observations per year. Figure 2 shows the number of TOOs performed per year. It is seen to rise continuously since launch and is now at a rate of more than one

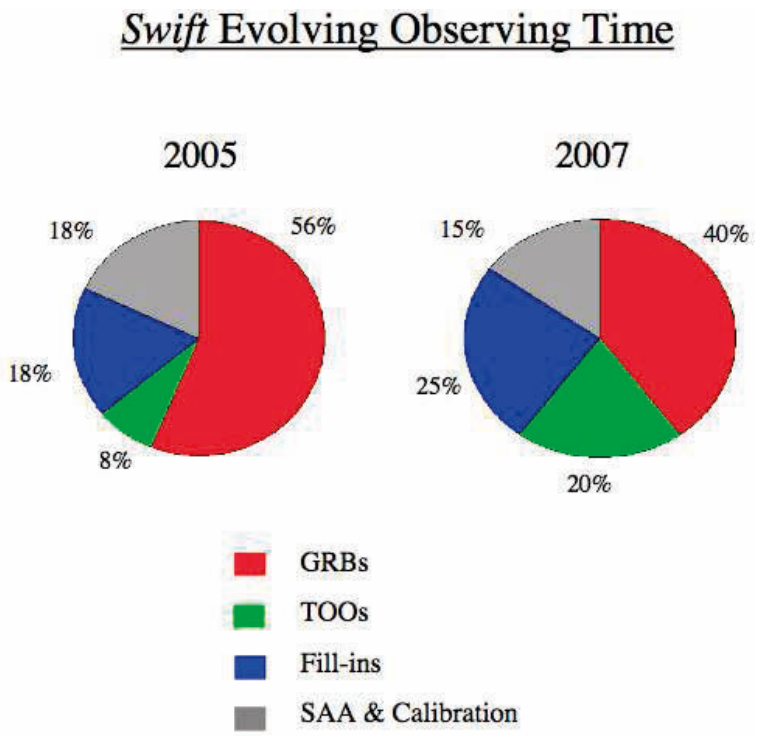

Fig. 1. Evolution of the Swift observing time fractions. More time is being spent on TOOs and fill-in observations than GRBs in 2007 than in 2005.

per day.

Key areas of Swift non-GRB science are BAT sky survey, transient monitoring, AGN studies, supernovae, and CVs/novae. These topics will now be addressed individually.

3. Hard X-ray Survey

Swift/BAT is performing the most sensitive hard X-ray (15 - 150 keV) all-sky survey ever (Markwardt et al. 2005). In its first 22 months, the BAT survey has reached a sensitivity of 0.8 mCrab over 80% of the sky (Figure 3), >15 times deeper than the 1978 HEAO-1 survey (Rothschild et al. 1983). It has detected ∼583 sources across the sky including 235 AGN (Tueller et al. 2008). Since hard X-rays are highly penetrating, this spectral band is unique in its complete coverage of AGN including the long-sought obscured population (Ueda et al. 2007). It is found in the BAT survey that ∼50% of the AGN are heavily absorbed ($N_H > 10^{22}$ cm^{-2}).

The BAT survey sensitivity is becoming more sensitive as the square root of observing time with no indication yet of limitation from systematic errors. The predict sensitivity for 4 years of data collection is 0.5 mCrab. The survey is complementary to that of INTEGRAL (Bird et al. 2007) which concentrates on the galactic plane. It will also complement of that of MAXI which will be in the X-ray band at comparable sensitivity to BAT.

4. Transient Monitoring

Swift's flexible observing schedule and the large BAT field of view make it an ideal monitor of high energy sources. The BAT observes ∼80% of the sky each day. The BAT Transient Monitor software autonomously searches for outbursts in known and new sources. Additional BAT transient detection is now being provided by the recently implemented BAT Slew Survey (Grindlay et al. 2008).

BAT light curves for over 500 galactic and extragalactic sources are available on a public web site (http://swift.gsfc.nasa.gov/docs/swift/results/transients). The daily exposure for a typical source is ∼9000 seconds, with a 1-sigma sensitivity of ∼7 mCrab. Of these, 65 are detectable in a day's observations or are periodic, and another 49 are transient. Through the transient monitoring the 8th known transient accretion-powered ms pulsar, SWIFT J1756.9-2508, was found with one of the lowest mass companions yet identified (Krimm et al. 2007).

5. AGN Observations

Due to its multiwavelength capacity and flexible observing schedule, Swift has become an important observatory for studies of Active Galactic Nuclei (AGN). Swift covers the critical optical/UV to X-ray range where most of the accretion power in an AGN is released. AGN are

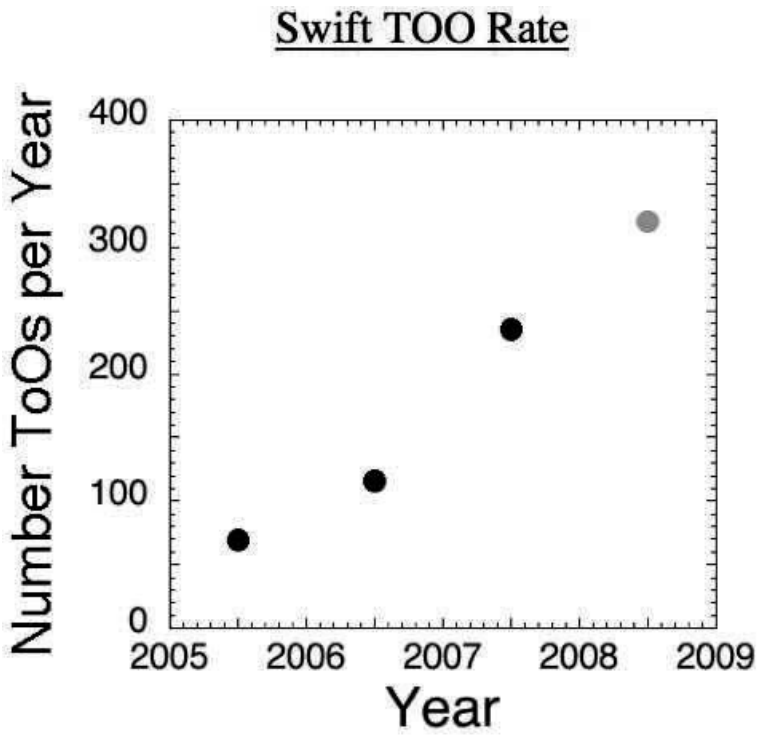

Fig. 2. The number of TOO observations per year is growing rapidly. The point for 2008 is an extrapolation to the full year from the TOOs observed in the first months.

highly variable, changing in their X-ray intensity by factors of 2-5 within a day and in the UV on time scales of days to weeks. Simultaneous observations at UV and X-ray energies are required to infer the physical conditions. The flexible schedule allows easy coordination with other observatories.

Swift studies of Big-Blue-Bump emission in 70 AGN clearly shows that UV and X-ray spectral slopes are correlated. Swift caught Mkn 335 in a historic low state (Grupe et al. 2007a) and detected hard X-ray photons in WPVS 007 (Grupe et al. 2007b), previously the softest X-ray AGN known.

Swift regularly monitors blazars in coordination with the Fermi and AGILE high energy gamma-ray telescopes and with the MAGIC, HESS, VERITAS and MILAGO TeV telescopes. These observations determine the flux and spectral slope of jet emission and constrain models for inverse Compton boosting of X-ray photons into the TeV range (Foschini et al. 2007). Swift observations of the blazar 3C454.3 in outburst coordinated with AGILE have sampled the broad-band spectrum during this historically brightest MeV-GeV emission state (Ghisellini et al. 2007).

6. Supernovae

The rapid response and flexible scheduling, and multi-wavelength capability of Swift provide unique observations of supernovae. Swift has now observed more than 60 SNe (Brown et al. 2008).

The interaction of outgoing SN shocks with material in their environments can create copious amounts of UV and X-radiation. Over the past 2 years, Swift has discovered X-ray emission from 8 core collapse SNe. Perhaps the most interesting case is SN 2006jc, a Type Ib SN whose progenitor ejected a shell of He-rich material in a Luminous Blue Variable eruption two years before the SN explosion. The X-ray data record the interaction of the SN blast wave with this dense shell of material, resulting in a brightening in X-rays over a period of 120 days, followed by a steep decline as the shock moved out of this shell (Immler et al. 2007a). Multi-epoch UVOT grism observations further showed the presence of a resonance MgII 2800 $\AA$ emission line as one of the main coolants in the SN 2006jc shell.

Utilizing the fast response of Swift, SN 2006bp (Type IIP) was observed less than two days after shock breakout. The observations showed that the SN was bright in X-rays even at such an early epoch, caused by the presence of substantial amounts of dense ($>10^6$ cm^{-3}) material from the progenitor's strong stellar wind (Immler et al. 2007b). Additional Swift XRT observations led to the detections of the two brightest SNe discovered in X-rays over the past three decades, SNe 2005kd and 2006jd (both Type IIn, $L_x > 10^{41}$ erg s^{-1}). UV obser-

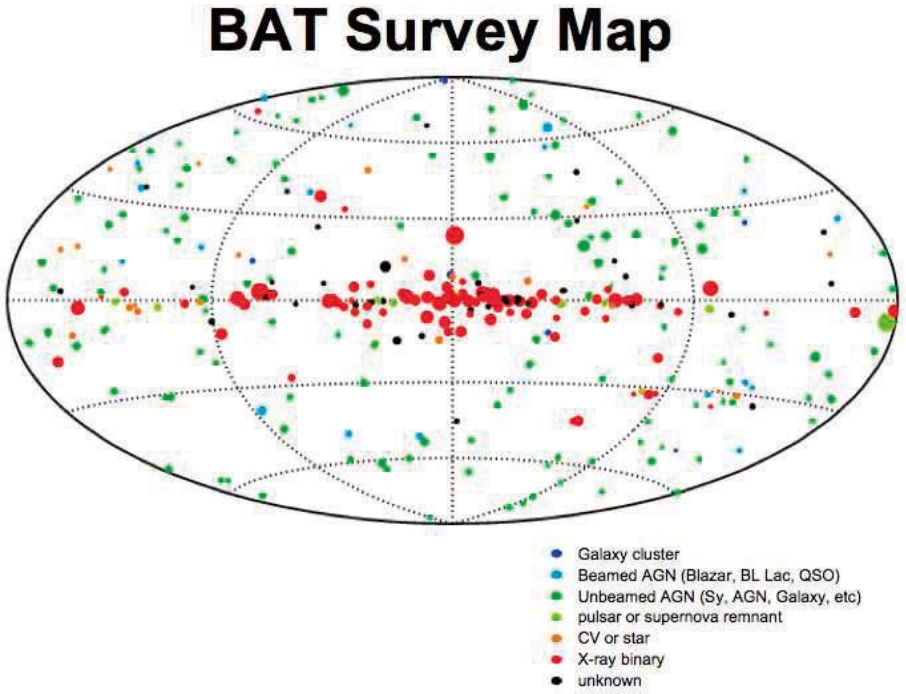

Fig. 3. Sources detected in the BAT all-sky hard X-ray survey. Based on 22 months of data. Color of dot shows sources type as indicated in the key and size of dot shows intensity.

vations of SN 2006bp and 2005cs (Type IIP; Brown et al. 2007), demonstrated the critical importance of these types of observations for constraining the extinction and evolving temperature/ionization structure in the photosphere of SNe II (Dessart et al. 2008). This greatly improves our ability to model Type II spectra and use them as independent distance indicators.

UVOT and XRT observations of thermonuclear (Type Ia) SNe permit a systematic study of SNe Ia in the UV and X-ray wavelength ranges. Beginning with observations of SN 2005am (Brown et al. 2005), the UV light curves of 13 SNe Ia observed to date have highly homogeneous light curve shapes, with peak dates similar to the peak dates in the U band. From these light curves a mean template has been generated. This template permits the peak date and magnitude to be determined with minimal dependence on sampling (Milne et al. 2007). These findings are important for cosmological utilization of SNe Ia as standard candles, and they afford insight into the thermonuclear explosion mechanism.

XRT observed an X-ray outburst signaling the shock breakout from the surface of a normal Type Ibc supernova (Soderberg et al. 2008). The object was discovered serendipitously on 9 January 2008 during scheduled observations of SN2007uy in NGC2770. This discovery raises the possibility that all core collapse supernovae have X-ray outburst from shock breakout.

7. Accreting White Dwarfs

Swift's rapid-response ToO capability has resulted in significant discoveries about the X-ray evolution of Cataclysmic Variables (CVs) in general, and Classical (CN) and Recurrent Novae (RN) in particular. X-ray observations are the best means to follow the evolution of the central nuclear-burning white dwarf during the outburst. Such observations constrain the mass, radius and composition of the white dwarf through model atmosphere fitting of the X-ray spectrum, determine the ejecta energy budget by measuring the hard X-ray shock temperature, and reveal the evolution of the later stages of the thermonuclear runaway by observing the flux variations.

These aspects were spectacularly demonstrated by Swift's high-density campaign on the 2006 outburst of the recurrent nova RS Oph (Figure 4, Osborne et al. 2007). There are two key results from the observations: 1) RS Oph was detected by the BAT showing unique hard X-ray emission, and 2) XRT observed turn-on of super soft emission 30 days after the optical turn-on, rare for such RNe and important for understanding the population and mix of supersoft sources in the Galaxy. There are other such RNe, with quiescent X-ray behavior different from RS Oph that are overdue for explosion and will be exciting targets for Swift. We have already made observations of over 20 other novae to date (Ness et al. 2007).

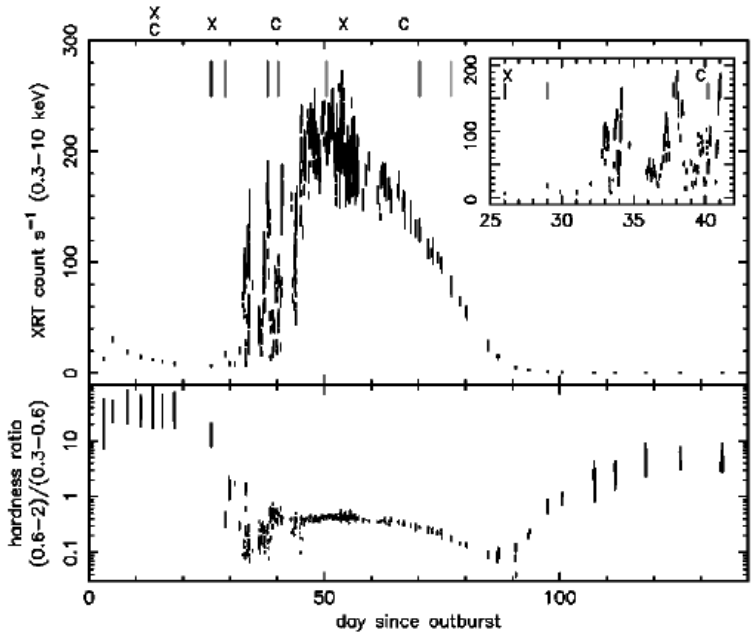

Fig. 4. Swift XRT light curve of RS Oph (Osborne et al. 2007). The dramatic flaring during the onset of the supersoft phase may be related to highly variable absorption. Note the marked change of hardness on day 35 indicating the onset of the super soft phase.

8. Conclusions

Swift is a versatile satellite with increasing observing time spent on non-GRB science areas. It is an excellent joint mission with MAXI, having complementary sky survey capabilities and the ability to perform TOO follow-up observations of source bound by MAXI.

Acknowledgement

I greatly appreciate the support of the Swift science team in operating the satellite and producing the scientific results presented here. I thank J.D. Myers for assistance in preparing this manuscript.

References

Barthelmy, S. D., et al. 2005, Sp Sci Rev, 120, 143
Bird, A. J., et al. 2007, ApJS, 170, 175
Brown, P. J., et al. 2005, ApJ, 635, 1192
Brown, P. J., et al. 2008, AJ, submitted (arXiv: 0803:1265)
Brown, P. et al. 2007, ApJ, 659, 1488
Burrows, D. N., et al. 2005, Sp Sci Rev, 120, 165
Dessart, L., et al. 2008, ApJ, accepted, arXiv:0711.1815
Foschini, L. et al. 2007, ApJL, 657, L81
Gehrels, N., et al. 2004, ApJ, 611, 1005
Ghisellini, G., et al. 2007, MNRAS, 382, L82
Grindlay, J. E., et al. 2008, ApJ, in preparation
Grupe, D., et al. 2007a, ApJ, 668, L111
Grupe, D., et al., 2007b, AJ, 133, 1988
Immler, S., et al. 2007a, ApJ, submitted, arXiv:0712.3290
Immler, S., et al. 2007b, ApJ, 664, 435
Krimm, H., et al. 2007, ApJ, 668, L147
Markwardt, C. B., et al. 2005, ApJ, 633, L77
Milne, P. A., et al. 2007, in Supernova 1987A: 20 Years After: Supernovae and Gamma-Ray Bursters. AIP Conference Proceedings, 937, 303
Ness, J.-U., et al. 2007, ApJ, 663, 505
Osborne, J. P., et al. 2007, ApJ, submitted
Roming, P. W. A., et al. 2005, Sp Sci Rev, 120, 95
Rothschild, R. E., et al. 1983, ApJ, 269, 423
Soderberg, A., et al. 2008, Nature, submitted (arXiv: 0802.1712)
Tueller, J. , et al. 2008, ApJ, submitted
Ueda, Y., et al. 2007, ApJ 664, L79

Science of Compact X-Ray and Gamma-ray Objects: MAXI and GLAST

D. J. Thompson,[1] on behalf of the GLAST LAT Collaboration
[1] NASA Goddard Space Flight Center, Greenbelt, MD 20771 USA
E-mail(DJT): David.J.Thompson@nasa.gov

Abstract

The Monitor of All-sky X-ray Image (MAXI) and Gamma-ray Large Area Space Telescope (GLAST) observatories will be surveying the sky simultaneously. Compact objects that may show variability will be excellent targets for coordinated multiwavelength studies. Gamma-ray bursts (and afterglows), pulsars, high-mass X-ray binaries, microquasars, and active galactic nuclei are all objects whose X- and gamma-ray relationship can be explored by such observations. Of particular interest will be variable unidentified gamma-ray sources, whose contemporaneous observations by MAXI may prove decisive in identifying the source of the high-energy emission.

Key words: X-rays — gamma rays — variability

1. Introduction

One of the clearest characteristics of the high-energy (X-ray and gamma-ray) sky is variability. Bursting, flaring, and periodic variability are seen on timescales ranging from milliseconds to years. Monitoring the changing cosmos therefore provides a valuable resource for scientific analysis and interpretation.

With the launch of GLAST, which took place during the MAXI workshop, and the upcoming launch of MAXI itself, the scientific community will have for the first time sensitive all-sky monitors covering a broad portion of the high-energy electromagnetic spectrum. The goal of this paper is to outline some of the scientific topics that can be addressed by cooperative efforts between these two missions.

2. GLAST Mission and Operating Plans

GLAST (Figure 1) is a successor to the successful Compton Gamma Ray Observatory (CGRO) that operated during the 1990's. GLAST is an international mission, involving the U.S. NASA and Department of Energy as well as contributions from many astrophysics and particle physics institutions and agencies in Japan, France, Germany, Italy, and Sweden. The GLAST Observatory (Michelson, 2003) includes two scientific instruments:

- The GLAST Burst Monitor (GBM) is a successor to BATSE on the Compton Observatory. It uses sodium iodide (NaI) and bismuth germanate (BGO) wide-field detectors to monitor the sky for transients in the 10 keV – 30 MeV energy range (Meegan et al 2008). The GBM field of view is large enough to view the entire sky except for the part occulted by the Earth.
- The Large Area Telescope (LAT) is a pair-production high-energy telescope successor to EGRET on CGRO. It uses a combination of detector subsystems (silicon strip tracker, cesium iodide calorimeter, plastic scintillator anticoincidence detector) to measure the properties of gamma-ray pair production events and to separate such events from the much larger background of charged particle cosmic rays (Atwood et al 2008).

Some important characteristics of the GLAST LAT are:

- Huge field of view (approximately 2.4 steradians).
- Broad energy range (20 MeV - >300 GeV, including the largely unexplored 10 - 100 GeV range).
- Good source location accuracy (1 arcmin for bright sources).
- Large effective area (factor >4 better than EGRET).
- Single photon absolute time accuracy better than 10 microseconds.

This combination of improvements results in a factor >30 improvement in sensitivity compared to EGRET, with an even larger factor at energies above 10 GeV.

GLAST was launched on June 11, 2008, into a 565 km circular orbit with inclination 25.5°. For comparison with MAXI, the most important operating feature

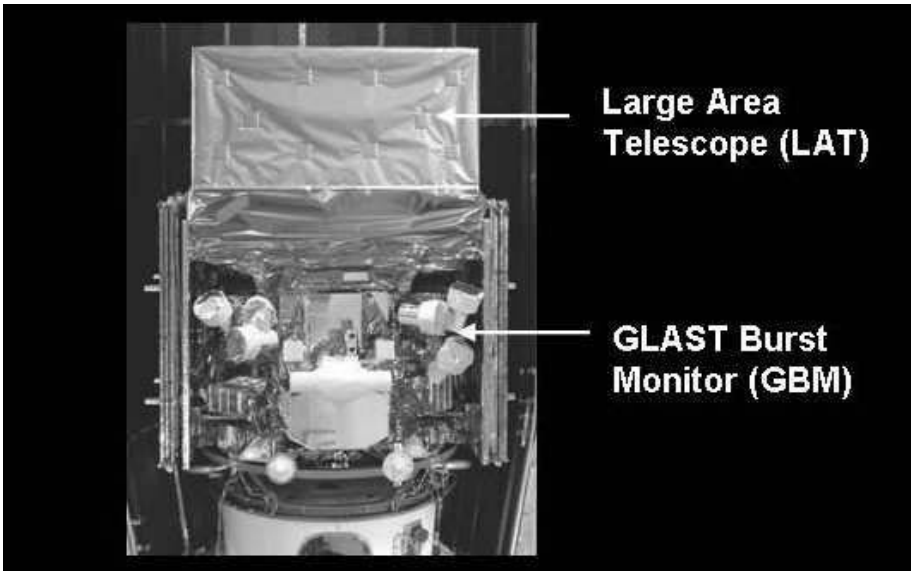

Fig. 1. GLAST on its launch vehicle.

of GLAST is its planned scanning mode. Taking advantage of the large instrument fields of view, the spacecraft will continually point away from the Earth. By rocking 35° north of the zenith for one orbit and 35° south of the zenith on the following orbit, both the LAT and the GBM will survey the entire gamma-ray sky every two orbits (192 minutes). For the first time, high-energy gamma-ray astrophysics will have an all-sky monitor.

Following a checkout period of about 60 days, GLAST will spend most of the next year in scanning mode, with a few exceptions for pointing mode operation triggered by unusual phenomena such as bright gamma-ray bursts. Results from bright sources and transients will be made public quickly, including Gamma-ray Burst Coordination Network (GCN) notices. At the end of approximately one year of normal science operations, all the data, including the first-year data, will become public as quickly as they can be processed. The GLAST Science Support Center (GSSC) at Goddard Space Flight Center (http://glast.gsfc.nasa.gov/ssc/) will be providing software and support for analysis of both GBM and LAT data.

3. GLAST, MAXI, and Multiwavelength Studies

Modern astrophysics has become a multiwavelength enterprise, reflecting the realization that many astrophysical sources reveal their properties across broad ranges of the electromagnetic spectrum. Gamma-ray telescopes, for example, provide little or no information about distances, composition, velocities, magnetic fields, or polarization of detected objects. Determining these other parameters requires identification and study at other wavelengths. For this reason, GLAST scientists are strongly interested in cooperative efforts with other observatories such as MAXI.

MAXI and GLAST have enough similarities that they have a particularly strong potential for working together:

- Both MAXI and GLAST survey the whole sky regularly.
- Both have good time resolution.
- Both cover a wide range of energies.

Two likely areas of cooperation between MAXI and GLAST are:

- Construction of broad-band Spectral Energy Distributions (SEDs) to help determine physical processes (such as particle acceleration and interaction) that are important in specific sources; and
- Study of correlated time variability to help examine relationships between the X-ray and gamma-ray emission processes.

4. Sensitivities and Potential Targets

Although MAXI and GLAST are in principle good candidates for cooperative efforts, the practical question is whether the time-dependent sensitivities of the two instruments are matched to potential sources. One way to address this question is shown in Figure 2, which plots the SED for the Crab along with the approximate energy ranges and sensitivities of the MAXI SSC, the MAXI GSC, and the GLAST LAT for a one week observation in their standard operating modes. These values are approximate because performance is estimated based

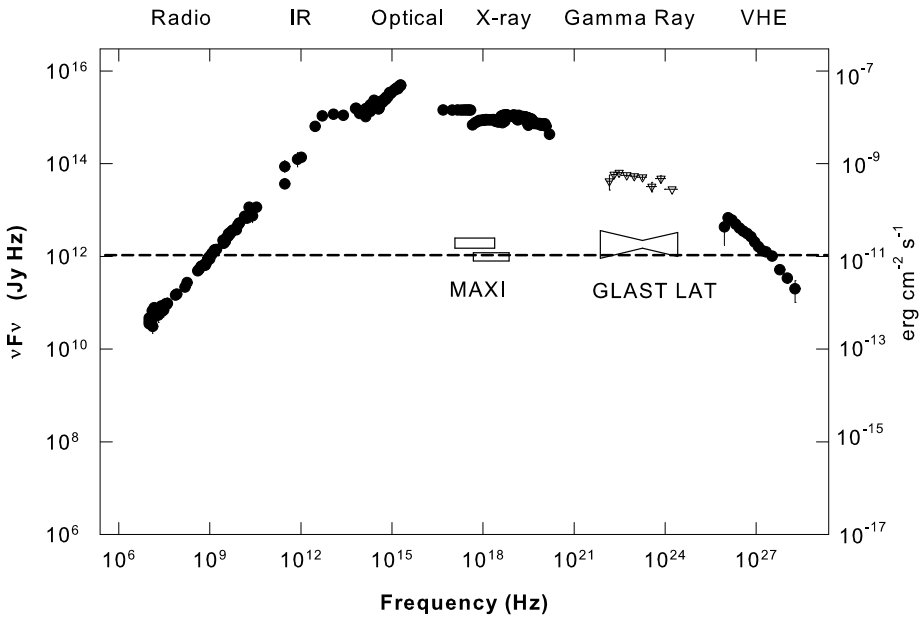

Fig. 2. Data points: Broadband energy spectrum of the Crab (nebula and pulsar). MAXI open rectangle upper left: SSC sensitivity in one week. MAXI open rectangle lower right: GSC sensitivity in one week. See other MAXI papers in these proceedings for details. GLAST LAT "bowtie": sensitivity in one week.

on pre-launch calibrations, not from in-flight conditions. The GLAST GBM is primarily sensitive to shorter transients and so is not shown on this figure. It is clear from this figure that a source like the Crab would be easily visible to both MAXI and GLAST in less than one week. Both telescopes can add data to gain sensitivity. For weaker sources, the integration time required for a measurement would be longer.

The horizontal dashed line on this figure provides a useful reference for comparing MAXI and GLAST LAT sensitivities. The level 10^{-11} erg cm^{-2} s^{-1} or 10^{12} JyHz is one that can be reached by either MAXI or GLAST LAT in one to two weeks.

Other than the Crab, what sorts of sources might be of interest to both MAXI and GLAST? Thermal sources are not good candidates; they might be visible to MAXI but not to GLAST. Conversely, nuclear sources would be more likely to be gamma-ray sources than X-ray sources. The best possibilities would seem to be nonthermal sources (involving accelerated particles) with some combination of synchrotron radiation (more likely in X-rays) and Compton radiation (more likely in gamma rays). Sources that combine both types of emission may yield information about the particle populations and acceleration processes, the magnetic fields, and photon fields in and around the source. Those with pronounced time variability (i.e. compact objects) are clearly of greatest interest, in order to take advantage of the monitoring capability of the two observatories. Some examples of potential astrophysical targets are discussed below.

4.1. Blazars and Other Active Galactic Nuclei

Active Galactic Nuclei (AGN), particular blazars, in which the jet is pointed toward the Earth, are primary targets for both X-ray and gamma-ray telescopes. They can have broad, nonthermal spectra and strong time variability. Figure 3 illustrates one example, blazar 3C279 as observed in 1993 during a moderately bright state. The data require time-dependent modeling, and this example from Hartman et al (2001) shows some possible components to the emission. If observed simultaneously, the MAXI data would constrain the synchrotron self-Compton component, while the GLAST LAT data would measure the Compton components arising from interactions of the same particles with external photon sources. Optical and radio observations would help constrain the synchrotron contribution, allowing a fairly complete model of the source as a function of time. Note that for this 1993 observation no X-ray data were available.

Blazars in particular are seen with a wide distribution of luminosities and spectra. 3C279 is a Flat Spectrum Radio Quasar with high luminosity and SED peaks at relatively low energies. High-Peaked BL Lac objects such as Mkn 421 have lower luminosities but SED peaks at higher energies. For such sources, MAXI would measure

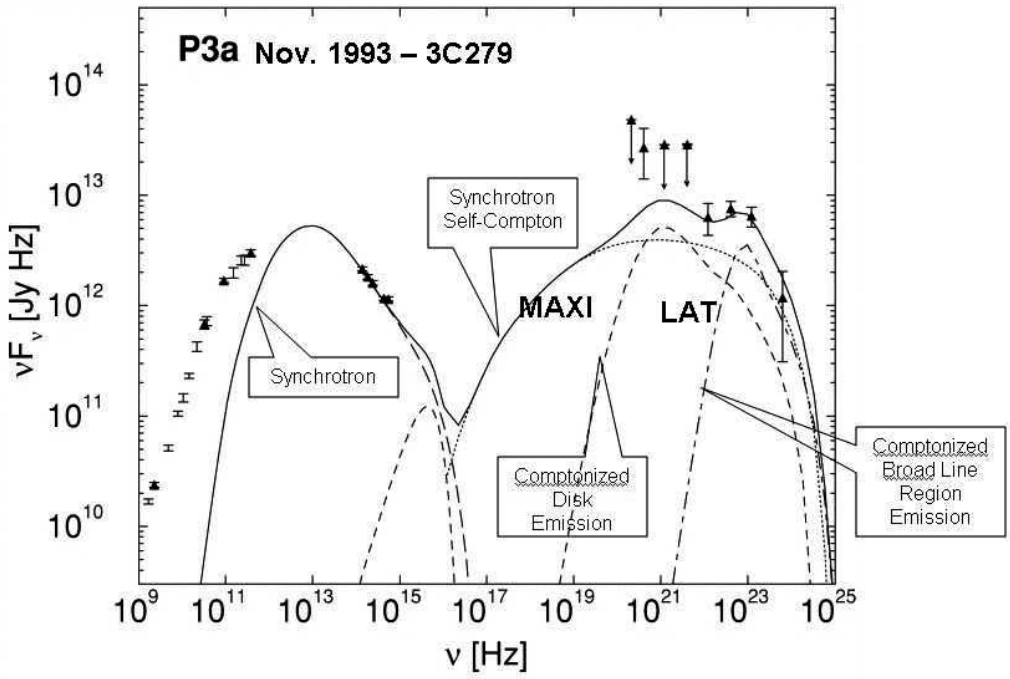

Fig. 3. Data and models for the 3C279 SED, adapted from Hartman et al (2001). The approximate one-week sensitivities of MAXI and GLAST LAT are shown by their names.

the synchrotron component directly, while GLAST LAT would measure the synchrotron self-Compoton component.

4.2. Gamma-ray Bursts

The GLAST GBM, along with other observatories such as Swift, will provide trigger information for gamma-ray bursts (GRBs). Both MAXI and GLAST LAT have some chance of seeing bursts directly, and both will be able to conduct afterglow studies. X-ray afterglows (e.g. Burrows et al 2005) are seen regularly from GRBs, potentially observable by MAXI for hours. Delayed high-energy gamma-ray emission was also seen for a small number of GRBs by EGRET on CGRO (e.g. Hurley et al 1994; Gonzales et al 2003), with components seen up to 90 minutes after the initial flash. The X-ray afterglows were not discovered until late in the CGRO mission, so that none of the EGRET-detected bursts had simultaneous X-ray measurements. MAXI and other X-ray telescopes will provide the first opportunity to determine the relationship, if any, between X-ray afterglows and delayed high-energy gamma-ray emission.

4.3. High-mass X-ray Binaries

Some high-mass X-ray binaries (HMXBs) have powerful winds that can accelerate particles and produce nonthermal emission, including both X-rays and gamma rays. An example is shown in Figure 4. LSI +61 303 has a 26 day period that produces a time-varying signal, although current studies are inconclusive about the nature of the emission. The summary of data and one possible model from Gupta and Böttcher (2006) illustrates the potential for coordinated study with MAXI and GLAST LAT. The X-ray range is likely synchrotron emission, while the gamma rays may be observing a transition between synchrotron and Compton radiation. Having simultaneous monitoring of this source and others like it will be important in resolving the processes important in this binary system.

4.4. Pulsars

Rotation-powered pulsars (as opposed to those powered by accretion) are particle accelerators. They can have nonthermal emission that provides insight into the strong gravitational, magnetic, and electric fields in the magnetospheres of these rotating neutron stars. The good timing capabilities of MAXI and GLAST LAT offer two particular possibilities for working together:

- Discovery of new X-ray and gamma-ray pulsars can be done by searching for short periodicities in sources. Most rotation-powered pulsars have been discovered in the radio band, but some have been found that are radio-quiet. Although MAXI and GLAST LAT have similar sensitivities in terms of energy, MAXI detects far more photons and therefore can potentially find pulse periods that could then be searched for in the LAT data. It is possible,

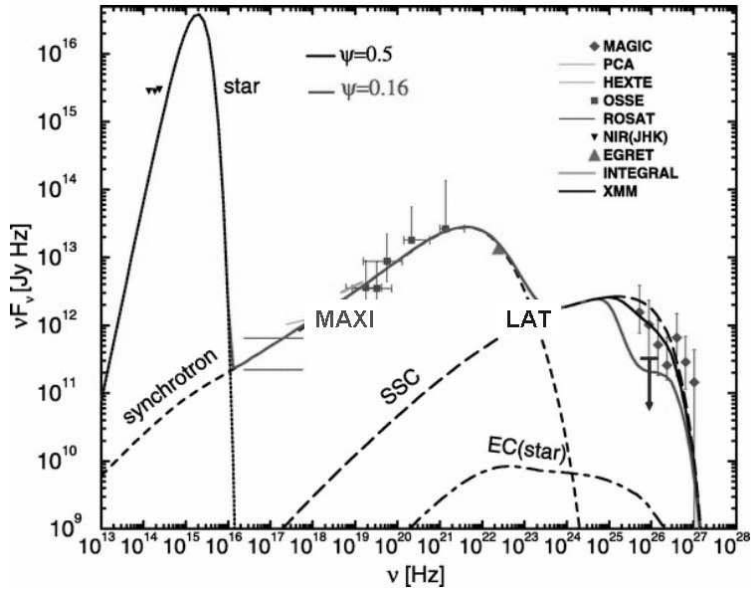

Fig. 4. LSI +61 303 SED, adapted from Gupta and Böttcher (2006). The approximate one-week sensitivities of MAXI and GLAST LAT are shown by their names.

too, that some pulsars could be discovered in the LAT data that MAXI might then search for; and

- For any pulsar seen in both energy bands, a comparison of light curves and energy spectra helps identify where and how the particle acceleration and interaction processes are taking place in the pulsar magnetospheres. An example is shown in Figure 5 (Thompson et al 1999). The X-ray and gamma-ray light curves differ in both shape and phase, suggesting different emission processes and locations.

4.5. Pulsar Wind Nebulae

Although pulsar wind nebulae (PWNe) are not by themselves compact objects, they are powered by pulsars and can exhibit time variability. The summary in Figure 6, from Nakamori et al (2008), shows why having simultaneous MAXI and GLAST LAT data will be valuable for PWNe studies. The X-rays seem well described as synchrotron radiation, implying high-energy electrons, but the gamma-ray origin is far less clear. Finding correlated time variability would be a strong argument in favor of a leptonic (inverse Compton) origin for the gamma rays rather than a hadronic (π°-decay) origin.

4.6. The Unknown - Source Identification and Study

Although the X-ray sky has been surveyed fairly thoroughly, the gamma-ray sky is far less understood. Over half the sources in the third EGRET catalog (Hartman et al 1999) remain unidentified. One of the major challenges for GLAST will be resolving the nature of these and other newly-discovered gamma-ray sources. Even with arcmin positions, spatial association is often inadequate to make a firm identification of a new source. Correlated variability, by contrast, is a high-confidence means of identification. The all-sky monitoring capabilities of MAXI and GLAST are extremely complementary for this type of identification.

5. Summary

With the launch of MAXI to the International Space Station next year and the continued operation of GLAST, astrophysics will have for the first time sensitive all-sky monitors in both both X-ray and gamma-ray bands. For nonthermal processes that are visible to both observatories, the opportunities for cooperation are extensive.

Acknowledgements

I extend thanks to B. Lott and the LAT team for the calculation of the one-week LAT sensitivity.

References

Atwood, W. B. et al. 2008 ApJ, submitted
Burrows, D. N. et al. 2005 Science, 309, 1833
Gonzales, M. M. et al. 2003 Nature, 424, 74
Gupta, S. and Böttcher, M. 2006 ApJ, 650, L123
Hartman, R. C. et al. 1999 ApJS, 123, 79
Hartman, R. C. et al. 2001 ApJ, 553, 683
Hurley, K. et al 1994 Nature, 372, 652
Meegan, C. A et al. 2008 ApJ, submitted
Michelson, P. 2003 Proc. SPIE, 4851, 1144
Nakamori, T. et al. 2008 ApJ, 677, 297
Thompson, D. J. et al. 1999 ApJ, 516, 297

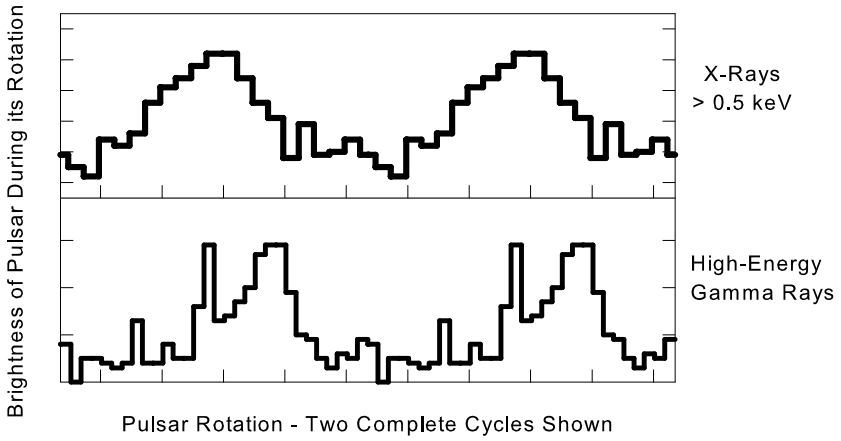

Fig. 5. X-ray and gamma-ray light curves (two cycles shown) of PSR B1055−52 (Thompson et al. 1999).

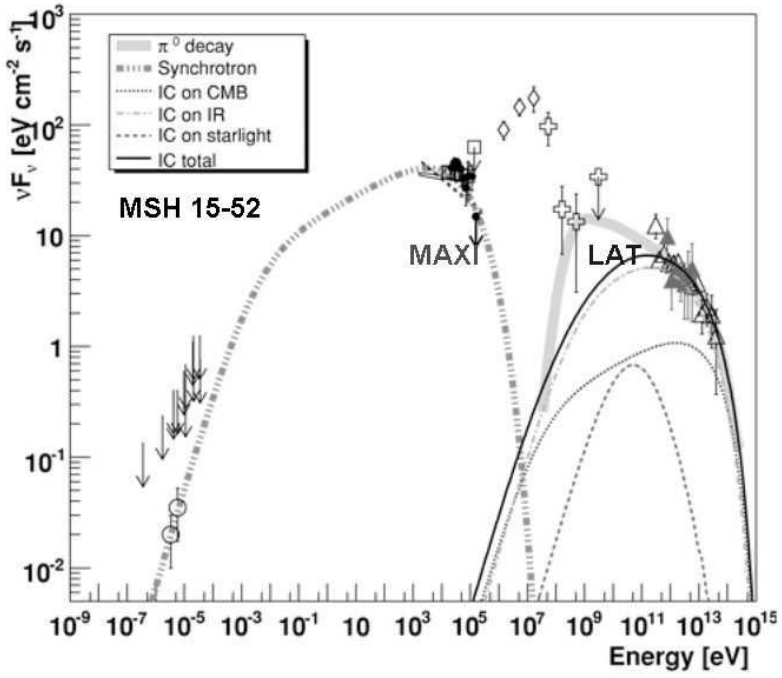

Fig. 6. MSH 15-52 SED, adapted from Nakamori et al (2008). The approximate one-week sensitivities of MAXI and GLAST LAT are shown by their names.

The challenge of identifying Galactic TeV sources

Olaf Reimer

W.W.Hansen Experimental Physics Lab & Kavli Institute for Particle Astrophysics and Cosmology, Stanford University, CA 94305, USA
E-mail: Olaf.Reimer@stanford.edu

Abstract

Since VHE gamma-ray observations made during the H.E.S.S. Galactic Plane Survey revealed for the first time the existence of dozens of extreme particle accelerators in our Galaxy, source identification became a crucial aspect in ground-based high-energy gamma-ray astronomy. Whereas the general problem resembles that of the unidentified EGRET sources, a low-threshold imaging Cherenkov telescope array's superior angular resolution and resulting imaging capability against a drastically reduced diffuse component enables different identification techniques. Given that IC photons at TeV energies originate from seed photons at keV energies, the wide field X-ray imaging capabilities and high duty cycle of the MAXI mission will provide contemporaneous X-ray observations to essentially all VHE gamma-ray observations to come, and might ultimately help to characterize the underlying particle population of these extreme Galactic gamma-ray emitter. Most particular, the so far sparsely probed domain of time dependent high-energy characteristics offered from all-sky monitoring by MAXI will add new perspectives to the exploration of VHE gamma-ray sources.

Key words: astrophyiscs: high-energy — observations: TeV, X-rays — source identification techniques

1. Galactic VHE gamma-ray astronomy

Since several decades space-based exploration of the gamma-ray sky we know that our Galaxy is rich of high-energy sources. The succession of more and more capable instruments operating at high MeV/low GeV energies, starting from SAS-2 (1972-1973) via COS-B (1975-1982) and EGRET (1991-2000) to AGILE and Fermi LAT in orbit now, can be directly seen in relation to our growing knowledge of energetic sources and particle acceleration in our Galaxy. What once started with observing excess emission broadly aligned with the equator of our Milky-way was followed by the discovery of gamma-ray point-sources. The first clue towards their nature was only a spatial location close to the Galactic plane. Meanwhile many dozens of gamma-ray point sources located at energies from 100 MeV to 10 GeV (Hartman et al. 1999) have been cataloged, yet the overwhelming majority of the galactic GeV sources evade their conclusive relation to an unique astrophysical object. These sources are commonly referred to as *Unidentified EGRET sources*. The only exception in the rather disappointing small fraction of cataloged gamma-ray sources compared against a multitude of possible interpretations regarding objects at other wavelengths, is the class of pulsars, which revealed their nature by providing a similar periodic gamma-ray as known from radio- or X-ray observations.

That VHE gamma-ray astronomy would be challenged with a similar severe identification problem was hinted by the HEGRA discovery of the source TEV J2032+4130 (Aharonian et al. 2002), a source located towards a dense stellar association in the Cygnus region (Cyg OB2), but slightly extended compared with the nominal telescope array's response to a celestial point-source. That the inherent quality of stereoscopic observations from observations of nearby AGN found its application also in Galactic TeV objects (Aharonian 1999), was perhaps most impressively documented by the discovery of Cas A (Aharonian et al. 2001) after dedicating 232 hours of observations on this source. Still, the puzzling source TEV J2032+4130 offered several alternatives in its astrophysical interpretation, and it can be seen as a precursor of what to expect from the next generation of ground-based Cherenkov facilities to come.

With the begin of operation of the vastly more sensitive current generation VHE gamma-ray experiments, the problem of Galactic source identification reached finally a scale comparable to what was encountered by satellite-based gamma-ray observations. Most notably, the accomplishments by the High Energy Stereoscopic System (H.E.S.S.) shaped the status of the field of Galactic VHE gamma-ray astronomy. With a dedicated science exploration towards searching for the sources of

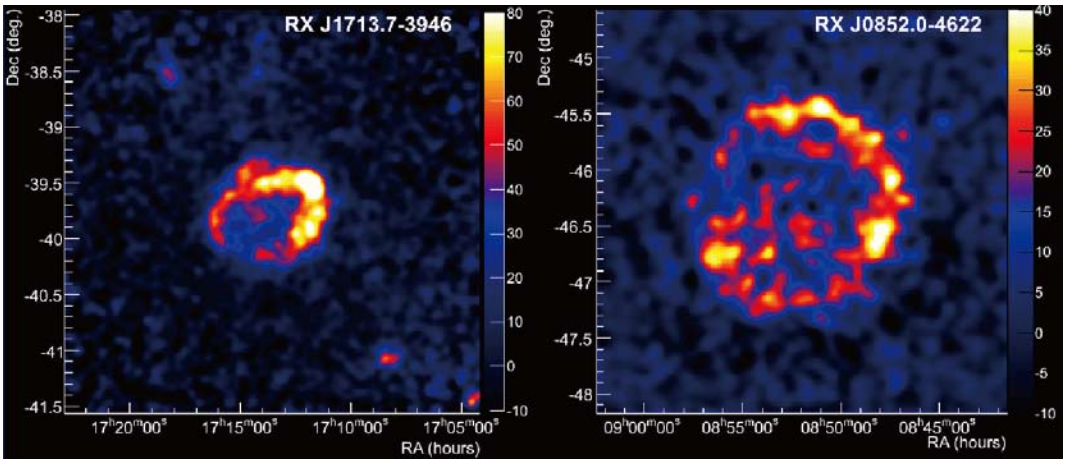

Fig. 1. Morphological resolved shell-type SNRs at VHE energies: RX J1713.7−3946 and RX J0852.0−4622. The observations were made with the H.E.S.S. telescope array. In such cases, the identification with the corresponding astronomical object is conclusive. [from Funk 2007]

Galactic cosmic rays and understanding the underlying acceleration processes, H.E.S.S. systematically scanned the inner part of our Galaxy in a multi-year observation program. With the capability of detecting a point source with flux $F_{\rm min}(> 100\,{\rm GeV}) \sim 4 \times 10^{-12}{\rm erg\,cm^{-2}s^{-1}}$ for a $5\,\sigma$ in 25 hrs, and a comparably wide-field imaging camera, the chance for success in scan-type observations were good, and this strategy paid off: The vast majority of the currently known Galactic VHE sources was discovered during this survey (Aharonian et al. 2005a, 2006a, 2008). The perhaps most striking result among the many Galactic discoveries can be seen in the sheer number and diversity among the newly found extreme particle accelerators, a diversity seen in their individual gamma-ray emission morphology (ranging from close resemblance of structures known from other wavebands to morphological features currently unmatched at other wavelengths), as well as in the diversity among their associated astronomical sources, which are presently Supernova remnants (SNRs), Pulsar Wind Nebulae (PWNe), and binary systems, but include also cosmic ray interactions in dense molecular environments, and stellar-wind related acceleration sites.

Whereas prominent young shell-type SNRs (Fig.1) have been identified through their resolved morphology, closely resembling those known from observations at (primarily) X-ray energies (e.g. RX J1713.7-3946, RX J0852./0-4622, RCW 86, SN1006), other VHE sources coincide spatially with known SNRs but cannot readily established as such, particular if their angular size is in the order of the instrumental point spread function or less (H.E.S.S.: approximately Gaussian with a 68% containment radius of 0.1°). For the latter, an inherent ambiguity in associating *unresolved* VHE gamma-ray sources with either the SNR or a PWN powered from a compact object within the SNR cannot be addressed solely from the perspective of VHE gamma-ray observations. Examples of such SNR-associations, now commonly referred to as *composite SNR*, are SNR G0.9+0.1/HESS J1747-281 (Fig.2 right) G348.5+0.1 (CTB 37A)/HESS J1714-385, or G29.7-0.3 (Kes75)/HESS 1846-029.

In a few cases, however, X-ray data argue favorable for a PWN scenario. G12.8-0.02/HESS 1813-178, or G338.3-0.0/HESS J1640-465, both unresolved at VHE energies, were subsequently targeted by XMM-Newton and Chandra, respectively. The deep X-ray observation revealed, unlike in the case of the morphological resolved SNRs, X-ray emission from a small region inside the shell of these SNRs, indicative rather for a central PWN than shell- or rim-associated SNR emission.

A different scenario is favored in middle-aged SNRs like IC443/MAGIC J0616+225 (Fig.2 left) or W28/HESS J1800-240, where gamma-ray emission is observed inside their, albeit deformed, shell structure, but in good correlation with overdensities in the molecular material traced through MWL observations. They are good candidates for gamma-ray emission interpreted by interactions with giant molecular clouds, and both density and filling factor for their target material constitute promising cases for π^0-decay related emission.

Leaving the domain where energetic particles are confined inside an astrophysical object (as in young shell-type or composite SNRs), accelerated particles can also diffuse out into the surrounding medium. Here, the size of the emitting region itself defines the spatial extent of the gamma-ray source; consequently, a variety of different source morphologies are seen among the class of VHE PWN (Fig.3). Preceded long since by the Crab Nebular, once more establishing itself as an unique cosmic laboratory through its exceptional broad coverage

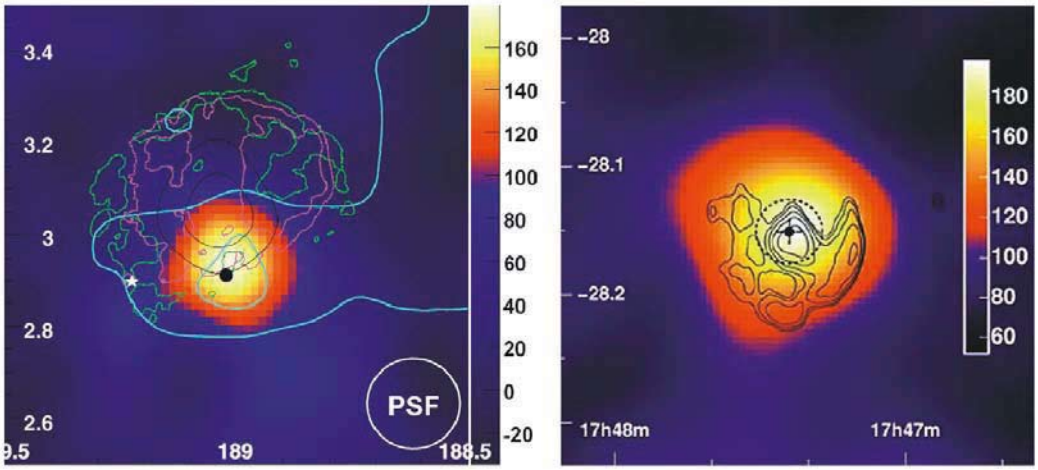

Fig. 2. Left: The case of a composite VHE SNR (G0.9+0.1/HESS J1747-281), where one cannot distinguish between resemblance of a SNR-morpholgy or conclude on a PWN inside an unresolved VHE source. [from Aharonian et al. 2005b] Right: The case of VHE emission seen well within the shell of a SNR (IC443/MAGIC J0616+225). The proposed scenario here is based on a connection of the VHE excess with overdensities in the molecular material inside the shell, traced by ^{12}CO emission (cyan). [from Albert et al. 2007]

over the entire electromagnetic spectrum, Pulsar wind nebulae meanwhile represent the numerically dominant class of Galactic VHE objects. The observed gamma-ray emission characteristics is manifold: spatially extended, and often asymmetric to the celestial location of the respective pulsar believed to be powering the PWN. Asymmetric PWN have been known from X-ray observations before, but on comparably smaller scales. Given the variety among their VHE gamma-ray emission size, orientation, and center-of-gravity, in some cases the identification with a PWN remains only suggestive, but not settled. Therefore population studies start to fill in the missing pieces, e.g. by systematically probing a connection between the energetics of the powering pulsar and the VHE-detected PWN (Carrigan et al. 2007). In case of observed energy dependent morphology change (e.g. HESS J1825-137), with its gamma-ray spectrum softening with the increasing distance to the PSR, a preference for a Inverse Compton scenario is indicated. But even a peculiar shaped high-energy spectrum as of Vela X (HESS J0835-455, Fig.4 left) does not offer a clear imprint of the underlying radiation processes, and both leptonic and hadronic emission scenarios are able to accommodate the data. The magnetic field strengths becomes the critical parameter in modeling the high-energy emission from a PWN, too.

For those Galactic VHE gamma-ray sources currently lacking a convincing MWL association, the situation for X-ray counterpart searches can become desperate. Many VHE gamma-ray sources are typically characterized by a ratio of VHE gamma-ray energy flux to X-ray energy flux in the order of unity. In case of HESS J1616-508 (Fig.4 right), the upper limit on the X-ray flux (Matsumoto et al. 2006) implies that at least 55 times more energy goes into gamma rays. For an electron accelerator and typical Galactic magnetic fields of about a few μG, one would expect a ratio around unity, ruling effectively out an electronic origin of the gamma-ray emission. However, in that case that synchrotron radiation is observed at energies of some keV their parent particle distribution is electrons at $\sim$100 TeV; yet the VHE gamma-rays are produced by lower-energy electrons in the 1 to 10 TeV range. Thus, if the electron energy spectrum has a sharp cutoff between 10 and 100 TeV, the two data sets could be reconciled. Additionally, pronounced levels of gamma-ray production relative to the X-rays are expected when intense target photon fields for Inverse-Compton scattering are required to be considered. Nevertheless, similar sources without a satisfying MWL connection are found in the Galactic VHE source catalog (Aharonian et al. 2008). If no steadily emitting X-ray source can be picked-up by even the most sensitive X-ray instruments, a different element offering some prospects of source identification needs to be pursued: persistent monitoring through an all-sky X-ray instrument like MAXI.

2. Where MAXI enters VHE gamma-ray source identification and characterization

Yet one class of Galactic VHE gamma-ray sources will unquestionably benefit from permanent X-ray monitoring, the gamma-ray binaries. At present, four such systems and one candidate have been established as VHE emitter. These objects show variability in the VHE band directly related to their orbital motion: PSR B1259-

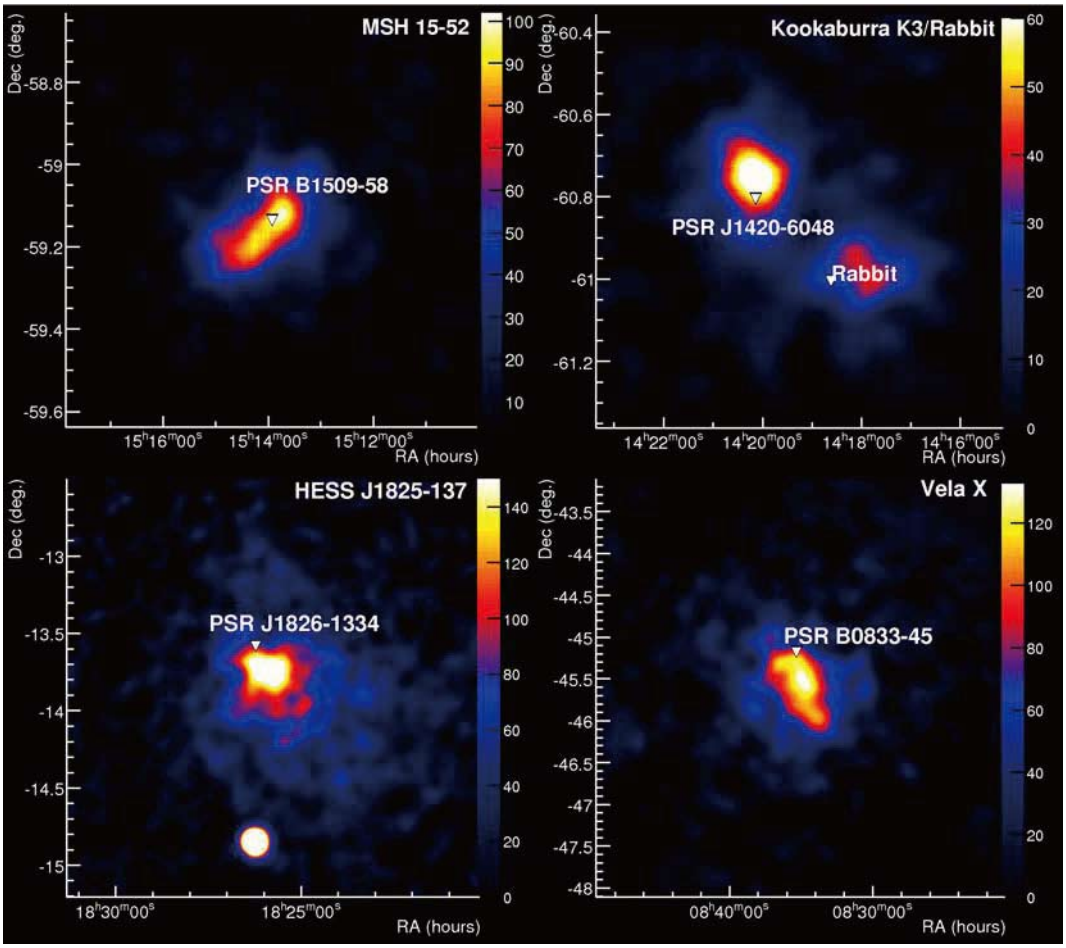

Fig. 3. VHE gamma-ray smoothed excess maps of MSH–15–5 (top left), the Kookaburra region showing the emission coincident with the two non-thermal wings of the Kookaburra (top right), HESS J1825–137 (bottom left) and Vela X (bottom right). Also shown are the energetic pulsars that are thought to power the PWNe. This ensemble documents the variety in the observed morphology in PWN at VHE energies. [from Funk 2007]

63/SS 2883 (Aharonian et al. 2005c), LS 5039 (Aharonian et al. 2005d), and LS I +61 303 (Albert et al. 2006), or transient emission as in the case of Cyg X-1 (Albert et al. 2007). Just recently, a candidate for a further gamma-ray binary was suggested based on its MWL characteristics (HESS J0632+057, Hinton et al. 2008). Since gamma-ray binaries are currently the only variable Galactic sources in the VHE sky, and their variabilty timescales range from fractions of their orbital cycle (3.9 days for LS 5039 up to 3.8 years for PSR B1259-63/SS 2883), their interpretation in terms of emission scenarios is consequently complex compared to that of non-variable Galactic VHE gamma-ray sources.

The pulsar PSR B1259-63 (P = 48 ms) is in a highly eccentric orbit around a Be-type companion star. VHE emission is predominantly produced around its periastron phase where the effects of adiabatic and radiative cooling due to the Inverse Compton process as well as synchrotron losses are strongest. The observed temporal behavior of the source during its 2004 periastron passage was quite different from what was predicted. Refined models including a more detailed treatment of Inverse Compton scattering in energetic and anisotropic radiation fields as well as adiabatic energy losses can reproduce the observed light curve and provide some crucial predictions to be probed with new observations, if possible over the full orbit. For all VHE observation dedicated to this system, MAXI will effortless obtain the needed contemporaneous X-ray data for MWL modeling. Perhaps even more interesting are the two systems LS 5039 and LS I +61 303 which are characterized by significantly shorter orbital periods of 3.9 and 26.5 days, respectively. Being considered as micro-quasars with a steady radio-jet feature, our understanding of these archetypal gamma-ray binaries is perhaps changing towards pulsar winds in interaction with the stellar outflow. Crucial for any considered emission scenario is the absorption of VHE photons due to pair-production in the

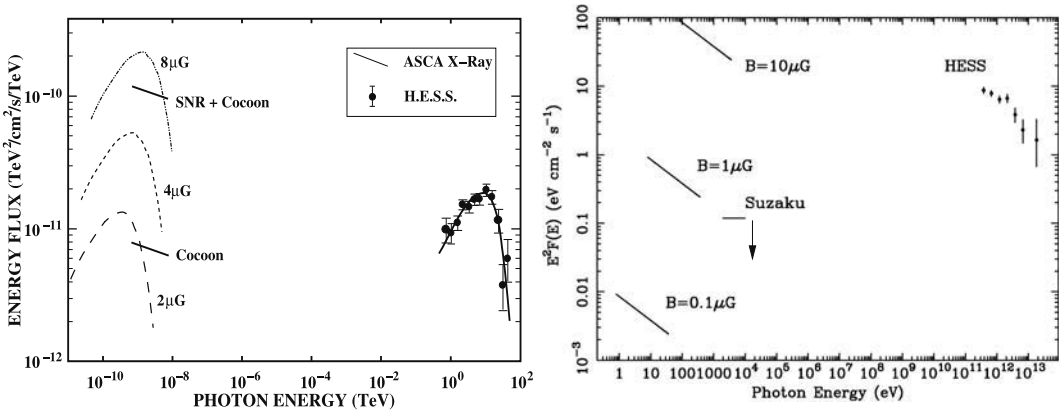

Fig. 4. Left: Spectral energy distribution (SED) of the Vela X (HESS J0835-455) Pulsa Wind Nebula. The broadband fit in an inverse Compton emission scenario is shown. The predicted synchrotron flux is shown for three possible magnetic field strengths, ranging between 2 μG and 8 μG. [from Aharonian et al. 2006b] Right: Spectral energy distribution of HESS J1616-508. The upper limit on the X-ray flux from the Suzaku XIS instrument is well below the measured gamma-ray flux. Assuming that a population of high-energy electrons is responsible for the gamma-ray emission, the expected X-ray level due to synchrotron radiation depends on the magnetic field in the source, as indicated by the lines. Typical interstellar fields are around 5 microGauss, a value for which X-ray energy flux and gamma-ray energy flux should be comparable. Here, we're not picking up the X-ray counterpart to the VHE gamma-ray source, leaving open the possibility of preference of hadronic vs. leptonic emission in a 'Dark Accelerator' [from Matsumoto et al. 2006]

photon field of the stellar companion. If the line-of-sight towards the VHE emission region passes closely of the companion star, absorption will produce notable effects over different orbital phase. To connect the only sporadic monitored flux modulation at VHE energies with regular monitoring through MAXI at keV and Fermi LAT at GeV energies will allow us to study regular or exceptional emission cases (spikes?/transients?) in those systems.
Finally, the detection of Cygnus X-1 at VHE energies has exemplified the need of regular X-ray monitoring. Not only different means of evaluation of mildly significant VHE gamma-ray excesses probably corresponding to a rapid emission state change can be accomplished once contemporaneous X-ray data exist, it also enables the chance to investigate e.g. similarities among the lightcurve during activity state changes, X-ray precursor activity to observed VHE outbursts, as well as enable us to pursue the ultimate quest for concluding about time-lags in the photons arriving in different wavebands.
Yet another perspective to significantly enhance the scientific return from VHE gamma-ray observations towards binary objects is anticipated: Given that regular monitoring of any microquasar, and black hole candidate binary system is granted, VHE observations can actively respond on alerts issued from MAXI observations in case of serendipitously emission phenomena, or on transitions in their activity states traced by X-ray observations.

3. Unidentified Galactic VHE sources

Most sources so far discussed have been conclusively identified or are at least associated with known astrophysical objects. However, a sizable number of objects at the Galactic VHE sky still remain to be identified. Among these objects, the Galactic Center source is certainly the most prominent. The central region of our Galaxy contains a super-massive black hole, and mm-, IR-, and X-ray sources associated with Sgr A* have been found to exhibit variability including flares and outbursts with a time-scale of hours. The point-like VHE gamma-ray source in the Galactic Center, seen by all major VHE experiments, needs to be discussed in the context of broadband emission near to the super-massive black hole. If indeed near Sgr A*, emission can be either produced in the high magnetic fields that are believed to be threaded in the accretion disk or from π^0-decay from energetic protons. Further away from Sgr A*, acceleration in a SNR as well as in stellar winds has been suggested. The accuracy of reconstruction in the position of the VHE-emitting point source has been improved to the level of the pointing accuracy of ~ 6 arc seconds and excludes the Sgr A East SNR (van Eldik et al. 2007). The error box for the VHE source still encompasses at least three possible candidates for VHE emission: Sgr A*, a low-mass X-ray binary system (LMXRB), the stellar system IRS 13, and the PWN G359.95-0.04. Albeit a typical X-ray flare was detected by Chandra during dedicated MWL observations of Sgr A* in summer 2005, the simultaneously taken H.E.S.S.-data lacked the imprint of variability even though the observed rate of VHE photons was sufficiently large to detect a flare of comparable strength as seen in the X-ray data. Given the complex interstellar radiation field and the variety of possible objects that may or may not be related to the observed

VHE gamma-ray emission, detection for correlated variability might offer a distinct way towards understanding the nature of this source.
Finally, the detection of VHE gamma-ray emission from the young stellar cluster Westerlund-2 (Aharonian et al. 2007) was a crucial step towards establishing the role of stellar wind driven cosmic ray acceleration. Whether or not the observed emission can be directly related to the prominent massive Wolf-Rayet binary system WR 20A, or a collective stellar wind emission scenario may be established only in the future through probing variability over timescales possible only by perpetual high-energy monitoring.

4. Beyond known VHE sources?

With extremely capable ground-based VHE gamma-ray observing facilities in regular operation now, one can also speculate about new classes of Galactic sources where MAXI might become critical to trigger subsequent VHE observations, or where VHE gamma-ray astronomy will benefit from supplementary data taken by MAXI. First and foremost we have to consider supernovae, expected to be part of any target-of-opportunity program in ground-based imaging atmospheric Cherenkov experiments. But also Galactic objects prone for sporadic but powerful outbursts like magnetars come to mind. Given the limited field-of-view and both site and night-time constraints for VHE gamma-ray observations, this community will critically depend on timely and reliable trigger mechanism from the instruments of high duty cycle and all-sky survey capability. X-ray observations at keV energies by MAXI will predictably find a place next to the Fermi LAT instrument operating at GeV energies in that regard.

I thank the organizers for inviting me to this workshop as well as for encountering profound interest in the field of VHE gamma-ray astronomy, which will certainly benefit from seeing the *Monitor of All-Sky X-ray Image* instrument in orbit soon.

5. References

Aharonian F., 1999 APh, 11 225
Aharonian F., et al.(HEGRA) 2001 A&A, 370 112
Aharonian F., et al.(HEGRA) 2002 A&A, 393 L37
Aharonian F., et al. (HESS) 2005a Science, 307 1938
Aharonian F., et al. (HESS) 2005b A&A, 432 L25
Aharonian F., et al. (HESS) 2005c A&A, 442 1
Aharonian F., et al. (HESS) 2005d Science, 309 746
Aharonian F., et al. (HESS) 2006a ApJ, 636 777
Aharonian F., et al. (HESS) 2006a A&A, 448 L34
Aharonian F., et al.(HESS) 2007 A&A, 467 1075
Aharonian F., et al.(HESS) 2008 A&A, 477 353
Albert J., et al.(MAGIC) 2006, Science 312 1771
Albert J., et al.(MAGIC) 2007a ApJ, 664 L87
Albert J., et al.(MAGIC) 2007b, ApJ 665 L51
Carrigan S., et al.(HESS) 2007, Proc. 30th ICRC, 493
Funk S., 2008 AdSpR, 41, 464
Hartman R.C., et al. 1999 ApJS, 123 79
Hinton J.A., et al. 2008, ApJ in print (arXiv0809.0584)
Matsumoto H., et al. 2006 PASJ, 59 199
van Eldik C., et al.(HESS) 2007, Proc. 30th ICRC, 286

Target of Opportunity Observations of Blazars with the MAGIC Telescope

Elina J. Lindfors[1], Daniel Mazin[2], Masaaki Hayashida[3], Pratik Majumdar[4], Masahiro Teshima[5]
On Behalf of the MAGIC Collaboration
and
Anne Lähteenmäki[6]

[1] Tuorla Observatory, Department of Physics and Astronomy, University of Turku, 21500 Piikkiö, Finland
[2] Institut de Fisica d'Altes Energies (IFAE), Barcelona, Spain
[3] KIPAC, Stanford Linear Accelerator Center, Menlo Park, CA 94025, USA
[4] DESY Deutsches Elektronen-Synchrotron D-15738 Zeuthen, Germany
[5] Max-Planck-Institut für Physik, D-80805 München, Germany
[6] Metsähovi Radio Observatory, Helsinki University of Technology TKK, 02540 Kylmälä, Finland

E-mail: elilin@utu.fi

Abstract

The MAGIC collaboration has been performing Target of Opportunity observations of blazars, when seen flaring in the optical by the Tuorla blazar monitoring program. In the past three years, there have been 5 optical alerts during good weather conditions and reasonable declination of the source. Three alerts have resulted in discoveries of VHE γ-rays from previously undetected sources. In this paper we discuss the discovered sources, MAGIC observations of BL Lac and 3C 279, and we give an outlook for ToO observations of blazars with MAGIC in the MAXI era.

Key words: gamma-rays:observations—galaxies:active

Fig. 1. The MAGIC telescope (right) and the MAGIC II telescope, to be inaugurated in September 2008.

1. Introduction

MAGIC is an Imaging Air Cerenkov Telescope (IACT) located on La Palma, Canary Islands. Due to its large collecting area and uniquely designed camera, MAGIC has reached a lower energy threshold (trigger threshold 50-60 GeV, with new trigger 25 GeV (Teshima et al. 2008a)) for γ-ray emission than any existing terrestial imaging γ-ray telescope. A more detailed introduction to MAGIC can be found in Albert et al. (2008a).

Blazars are the most extreme types of Active Galactic Nuclei (AGN). In these objects the dominant radiation component originates in a relativistic jet pointed nearly towards the observer. Blazars show variable flux in all wave bands from radio to very high energy (VHE, defined as E> 100 GeV) γ-rays. The relationship between the variability at different wave bands appears rather complicated.

The MAGIC collaboration is performing Target of Opportunity observations of sources in high flux state in the optical and/or X-ray band. Alerts of optical high state originate from the Tuorla Blazar Monitoring Program. Optically triggered observations have resulted in the discovery of VHE γ-rays from Mrk 180 (Albert et al. 2006), 1ES 1011+496 (Albert et al. 2007a), and most recently from S5 0716+714 (Teshima et al. 2008b). In addition, parts of the BL Lac data in 2005 (Albert et al. 2007b) and the 3C 279 data in 2006 (Albert et al. 2008b) were taken when the sources were in high optical state, and resulted in the discovery of VHE γ-rays from these sources. Interestingly Mrk 180, S5 0716+714, BL Lac and 3C 279 were also in high X-ray state during the MAGIC discoveries (for 1ES 1011+496 no simultaneous X-ray data exist).

In this paper we discuss the discovered sources, their multiwavelength behavior and the prospects of using X-ray triggers from MAXI.

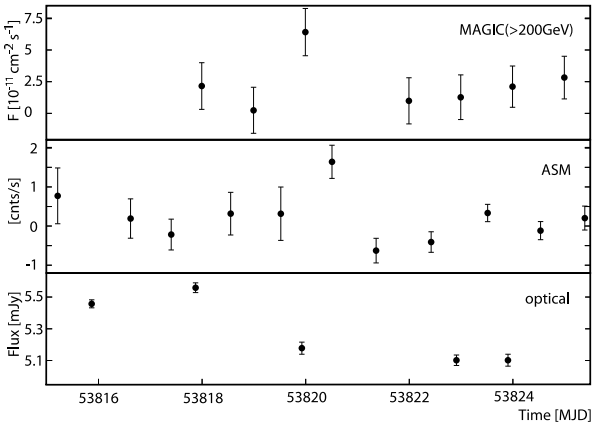

Fig. 2. Lightcurve of Mrk 180 for MJD= 53815-53825 (2006, March 21-31). *Upper panel*: VHE γ-rays measured by MAGIC above 200 GeV. *Middle panel*: ASM count rate, the highest count point corresponds to 3 σ detection of the source by ASM. *Lower panel*: Optical flux measured by KVA.

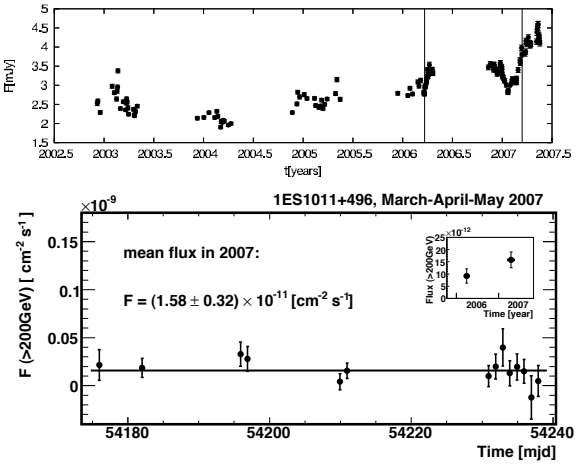

Fig. 3. Optical (top) and VHE γ-ray (bottom) light curves of 1ES 1011+496. The optical lightcurve shows five years of data from the Tuorla blazar monitoring program, and the vertical lines indicate the starting points of the MAGIC observations. The VHE γ-ray lightcurve shows two months of data from March 17th to May 18th 2007. The inset shows the yearly averages.

2. Optically triggered Target of Opportunity observations with MAGIC

The optical monitoring observations are performed with the KVA 35 cm telescope at La Palma, remotely operated from Finland, and the Tuorla 1m telescope. The observations are done in the R-band and the magnitudes are measured using differential photometry with calibration stars in the same CCD frame as the object. From the observed flux the host galaxy contribution is subtracted following Nilsson et al. (2007) to measure the flux of the core. If the core flux increases $\sim$ 50% (for some extremely variable sources 200%) the MAGIC observations are triggered. The lightcurves are updated to the project web page http://users.utu.fi/kani/1m/ on a daily basis.

In the past three years, there have been 5 optical alerts during good weather conditions and reasonable declination of the source. For two of the sources the MAGIC observations yielded in upperlimit of VHE γ-ray flux and the publication on these upperlimits is in preparation. Three of the alerts have resulted in the discovery of new VHE γ-ray emitting blazars and are discussed here below.

2.1. Mrk 180

Mrk 180 (1ES 1133+704) is a well-known high frequency peaked BL Lac (HBL) at a redshift of $z = 0.045$ (Falco et al. 1999). In March 2006 it underwent an optical outburst and was observed for 12.4 hours by MAGIC. During these observations VHE γ-ray emission was detected with a significance of 5.5 σ. An integral flux above 200 GeV of $(2.3 \pm 0.7) \times 10^{-11}\,\mathrm{cm}^{-2}\mathrm{s}^{-1}$ was measured, corresponding to 11% of the Crab Nebula flux. No significant flux variations were found. Earlier observations by other experiments have only set upper limits on the VHE γ-ray emission from Mrk 180. The upper limits are above the flux measured by MAGIC. It is therefore not possible to judge whether the detected VHE γ-ray flux level represents a flaring or a quiescent state of this AGN.

In X-rays the source is usually too weak to be detected with ASM, but at the epoch of the MAGIC observations there was a 3 σ detection of the source possibly indicating that the source was in high X-ray state.

2.2. 1ES 1011+496

1ES 1011+496 is an HBL object at a redshift of $z = 0.212$. The MAGIC observations were triggered by an optical outburst in March 2007, and the source was observed from March to May 2007. The 18.7 hours of data show an excess at 6.2σ significance with an integrated flux above 200GeV of $(1.58\pm0.32) \times 10^{-11}$ cm^{-2} s^{-1}. The source has been observed previously by MAGIC in March–April 2006 when the source was in a lower optical state. Those observations only showed weak evidence for a signal at 3.5σ (Albert et al. 2008c). Consequently, the VHE γ-ray flux was $> 40\%$ higher in March–May 2007 than in March–April 2006, indicating that the VHE emission state may be related to the optical emission state. The source is too weak in X-rays to be detected with ASM, so there is no information on the X-ray state of the source.

2.3. S5 0716+714

The BL Lac object S5 0716+714 has been studied intensively at all frequency bands. It is highly variable with rapid variations observed from the radio to X-ray

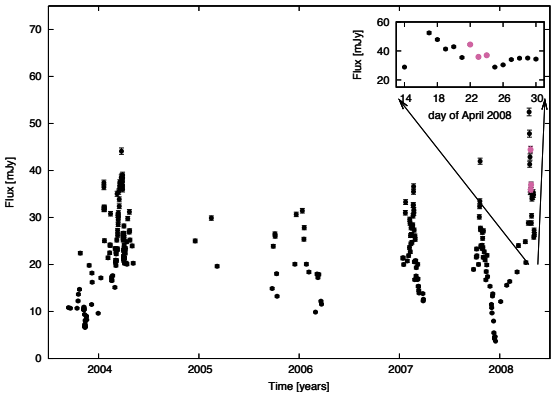

Fig. 4. Long term optical lightcurve of S5 0716+714. The inset shows the lightcurve from April 2008, the pink data points are simultaneous with MAGIC observations.

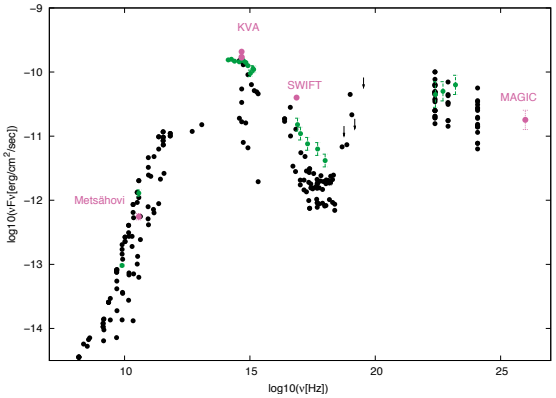

Fig. 5. The spectral energy distribution of S5 0716+714. The black data points are the historical SED from (Ostorero et al. 2006) and the green data points are from the high state of October 2007 (Villata et al. 2008, Giommi et al. 20008a). The pink data points are from April 2008: 37 GHz from Metsähovi Radio Observatory, optical from KVA, X-ray from SWIFT (Giommi et al. 2008b) and γ-ray from MAGIC (Teshima et al. 2008b)

bands (Wagner et al. 1996). It has therefore been target to several multiwavelength campaigns, the most recent one organized by the GLAST-AGILE Support Program in July-November 2007 (Villata et al. 2008, Giommi et al. 2008a). Due to the very bright nucleus which outshines the host galaxy, its redshift is still uncertain. The recent detection of the host galaxy suggests a redshift of 0.31 ± 0.08 (Nilsson et al. 2008) which is consistent with the redshift z=0.26 determined by spectroscopy for 3 galaxies close to S5 0716+714 (Stickel et al. 1993, Bychkova et al. 2006). It can therefore be concluded that z=0.26 seems to be a rather likely redshift for S5 0716+714, although considering the lack of lines in the optical spectrum (e.g. Rector et al. 2001), the ultimate proof for the redshift is still missing. S5 0716+714 has a synchrotron peak in the optical band and is therefore classified as LBL (Nieppola et al. 2006) or IBL (Padovani et al. 1995). S5 0716+714, discovered by MAGIC, is only the third LBL (BL Lac (Albert et al. 2007b); W Comae (Acciari et al. 2008)) that has been detected at VHE γ-rays. With a presumable redshift of $z=0.31 \pm 0.08$, S5 0716+714 is the most distant object of the three and the second most distant of all VHE γ-ray emitters (after 3C 279 with z=0.536).

In April 2008 the optical flux of S5 0716+714 almost doubled in three nights (14th of April: 29 mJy, 17th April: 52 mJy) reaching its historical maximum on April 17th (see Fig. 4). MAGIC started the observations 5 nights later (April 22nd), when the moon conditions allowed. The observations resulted in the discovery of VHE γ-rays from S5 0716+714, announced in an Astronomer Telegram on April 30th (Teshima et al. 2008b). A detailed paper on the MAGIC results is in preparation. Interestingly, the source was in an all time high state also in the X-rays during the MAGIC observations (Giommi et al. 2008b). The quasi-simultaneous spectral energy distribution of this high state in April 2008 is shown in Fig. 5.

3. Observations in high optical and X-ray state

In addition to optically triggered observations, MAGIC has observed two interesting blazars during high optical and X-ray states. Both observations resulted in the discovery of VHE γ-rays from the sources. The connection between X-ray high states and γ-ray high states is expected from theoretical models (e.g. Ghisellini et al. 1998) and correlated variability between X-rays and γ-rays has been observed in many sources (e.g. Fossati et al. 2008). MAGIC observations of BL Lac and 3C 279 give further confidence that X-ray triggers from MAXI would be highly useful for triggering MAGIC observations. In addition simultaneous radio-optical-X-ray and γ-ray observations can provide strong constraints on the models.

3.1. BL Lac

BL Lacertae (1ES 2200+420, z=0.069, Miller et al. 1978) is the prototype for a class of active galactic nuclei, the BL Lac objects. BL Lacertae was observed with the MAGIC telescope from August to December 2005 (22.2 hours) and from July to September 2006 (26.0 hours). A VHE γ-ray signal was discovered with a 5.1 σ excess in the 2005 data. BL Lacertae is the first low-frequency peaked BL Lac object for which a clear detection of VHE γ-ray signal below the previous upper limits has been obtained. The 2006 data contain no signal, which is interpreted as a lower VHE γ-ray emission state.

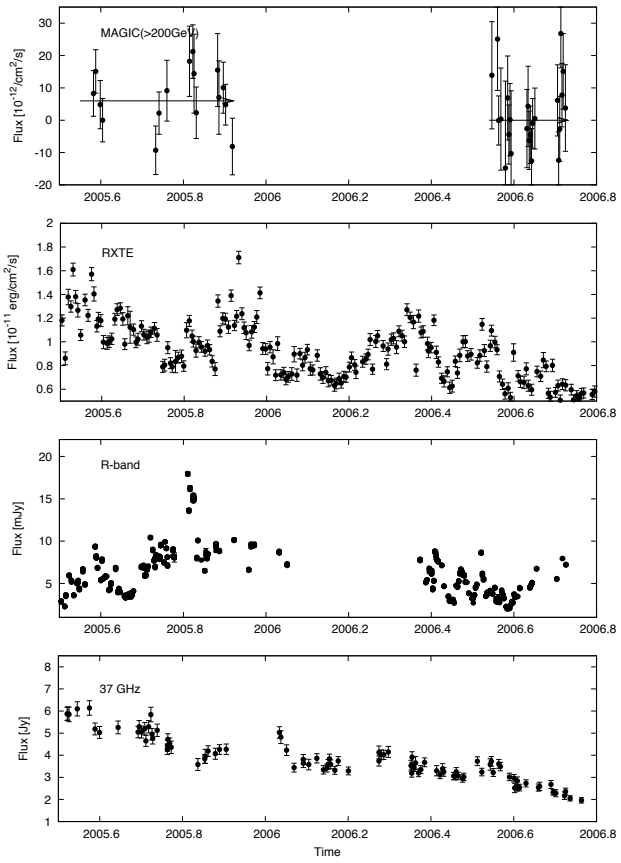

Fig. 6. Lightcurves of BL Lac at VHE γ-rays (top), X-rays, optical R-band and radio (bottom) from 2005.5 (beginning of July) to 2006.8 (end of September). VHE γ-ray (> 200GeV) lightcurve measured with MAGIC (Albert et al. 2007b, Hayashida et al. 2007) and the horizontal lines represents the average fluxes of the observing periods. X-ray data are from RXTE (Marscher et al. 2008). The optical R-band data are from the Tuorla blazar monitoring program, the host galaxy flux of 1.37 mJy (Nilsson et al. 2007) has been subtracted from the lightcurve. The 37GHz data are from Metsähovi Radio Observatory.

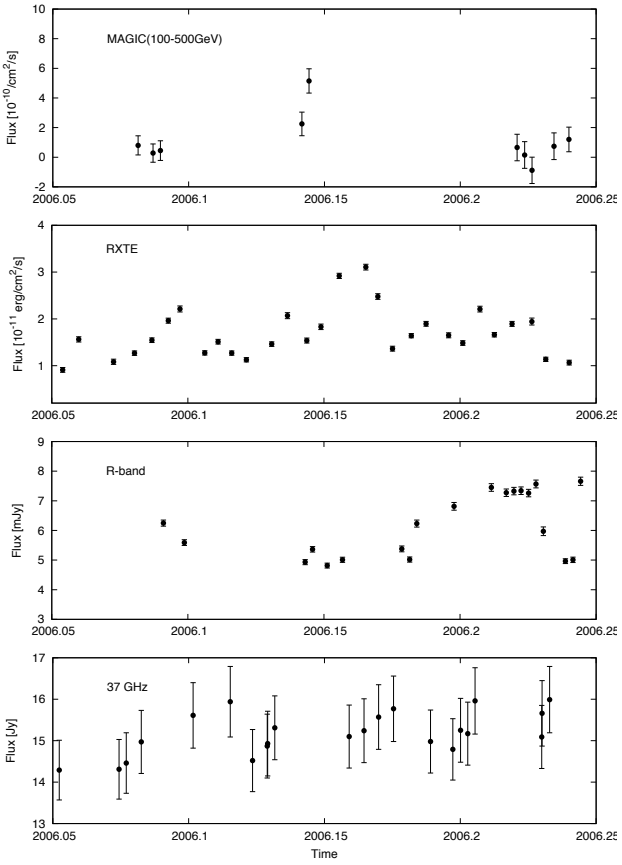

Fig. 7. Lightcurves of quasar 3C 279 at VHE γ-rays (top), X-rays, optical R-band and radio (bottom) from 2006.05 (January 18th) to 2006.25 (April 2nd). VHE γ-ray (100-500 GeV) data are measured with MAGIC (Albert et al. 2008b), and the two high points around 2006.15 (22th and 23rd of February) are the marginal and clear detections, respectively. The X-ray data are from RXTE (Chatterjee et al. 2008), optical from KVA telescope and the 37 GHz data from Metsähovi Radio Observatory.

The multiwavelength observations simultaneous to 2005 MAGIC observations show very interesting behavior from the X-ray to radio regime. The source was bright in all energy regimes, showing a two-peaked outburst in X-rays and optical and a 180 degree turn in polarization angle, but a single outburst in the radio regime. Marscher et al. (2008) interpreted this as a shock propagating down the jet along a spiral streamline, the first flare occurring during the last 240° twist of the streamline before the flow straightens and becomes turbulent. The passage of the feature through the millimetre-wave core stimulates the second flare. Marscher et al. (2008) also pointed out that the MAGIC lightcurve seems to agree with their scenario as the highly significant detections from 2005.819 to 2005.831 during the first X-ray flare implies that acceleration of electrons with sub-TeV energies was particularly efficient at this time. Although the MAGIC data from 2005 are statistically consistent with constant emission, in the data we find a marginal correlation between γ-rays and X-rays. Future simultaneous MAGIC-MAXI observations should be able to confirm this, as MAXI should be able to monitor BL Lac on a weekly basis (Tomida et al. 2008) and MAGIC-II will improve the MAGIC sensitivity so that monitoring observations of BL Lac become possible.

3.2. 3C 279

Flat Spectrum Radio Quasar 3C 279 (z=0.536) was the first blazar identified as a γ-ray source with the Compton Gamma Ray Observatory. It was observed with the MAGIC telescope over 10 nights between late January and April 2006 (total of 9.7 hours) and the VHE γ-ray

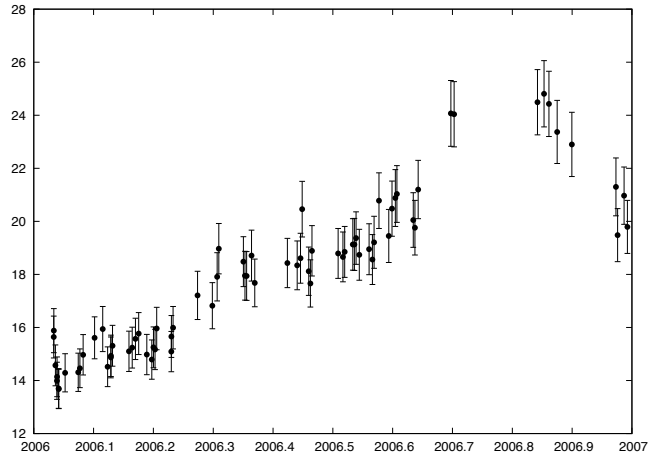

Fig. 8. 37 GHz lightcurve of 3C 279 from 2006 showing that during the MAGIC detections the radio flux was steadily increasing (see text).

signal was detected on the night of February 23rd with a significance of 6.1σ. Also data on the night before shows hint of signal.

During the MAGIC observations 3C 279 was in optical high state (low state being ~ 3 mJy), but the nights of MAGIC detections did not show any short time flaring activity in the optical regime. The actual optical flare occurred 15 days after the MAGIC detection. Also the long time X-ray lightcurves (Chatterjee et al. 2008) show that during the MAGIC observations, the source was in high state in the X-ray bands. It seems however that the flare reached its highest flux at the X-ray and optical band *after* the MAGIC observations, but the sampling of the MAGIC lightcurve is rather poor (see Fig. 7). Interestingly, it seems that radio flux was increasing during the MAGIC detection (see Fig. 8), in agreement with the findings of Lähteenmäki & Valtaoja (2003) and Lindfors et al. (2006) for γ-ray flares seen by EGRET, suggesting that the γ-ray flares in this source occur far away from the central engine well outside the BLR. As BLR is usually assumed to be origin for external photons to be scattered to γ-rays, this challenges the current models (e.g. Hartman et al. 2001) for emission of γ-rays in this source. Observations with Fermi Gamma-ray Space Telescope, simultaneous to X-ray with MAXI, VHE γ-ray, radio and optical observations should allow us to solve the mystery of the γ-ray emission site and mechanisms in 3C 279 as well as other blazars.

4. Discussion and Outlook

The optically triggered Target of Opportunity observations have resulted in the discovery of three new VHE γ-ray emitting blazars. The observation strategy has proved successful, although the ultimate proof for the connection between the optical and the VHE γ-rays is still missing. The optically triggered observations will be continued, and follow-up observations of discovered sources will be performed in order to further study the connection between the flaring in the optical and VHE γ-ray regimes.

The prospects for using X-ray triggers from MAXI are good. For the five sources discussed here, four were in high state in X-rays at the time of discovery of VHE γ-ray emission, and for one we have no simultaneous data. However, the information on high X-ray state was in all cases received after the MAGIC observations had already started. With fast alerts from MAXI we foresee X-ray triggered observations of several blazars. These observations will hopefully increase the number of known VHE emitting AGN (currently 23, see e.g. http://www.mppmu.mpg.de/∼rwagner/sources for up-to-date source list) and increase our knowledge of the population of γ-ray emitting blazars. The long-time X-ray lightcurves from MAXI in combination with lightcurves from other energy regimes will have a crucial role in answering the many open questions in the blazar field.

5. Acknowledgements

MAGIC enjoys the excellent working conditions at ORM and is supported by the German BMBF and MPG, the Italian INFN, the Spanish MCI-NN, ETH research grant TH 34/04 3, the Polish MniSzW Grant N N203 390834, and by the YIP of the Helmholtz Gemeinschaft. E.J.L wishes to acknowledge the support by the Academy of Finland grants 122352 and 121148. D.M's research was supported by a Marie Curie Intra European Fellowship within the 7th European Community Framework Programme.

References

Acciari, V. A. et al. (the VERITAS Collaboration) 2008, ApJL, accepted

Albert, J. et al. (the MAGIC Collaboration) 2006, ApJ, 648, L105

Albert, J. et al. (the MAGIC Collaboration) 2007a, ApJ, 667, L21

Albert, J. et al. (the MAGIC Collaboration) 2007b, ApJ, 666, L17

Albert, J. et al. (the MAGIC Collaboration) 2008a, ApJ, 674, 1037

Albert, J. et al. (the MAGIC Collaboration) 2008b, Science, 320, 1752

Albert, J. et al. (the MAGIC Collaboration) 2008c, ApJ, 681, 944

Bychova, V. S., Kardashev, N. S., Boldycheva, A. V. et al. 2006, Astronomy Reports, 50, 802
Chatterjee, R., Jorstad, S. G., Marscher, A. P. et al. 2008, ApJ, accepted
Falco, E. E. et al. 1999, PASP, 111, 438
Fossati, G., Buckley, J. H., Bond, I. H. et al. 2008, ApJ, 677, 906
Ghisellini, G., Celotti, A., Fossati, G. et al. 1998, MNRAS, 301, 451
Giommi, P., Colafrancesco, S., Cutini, S. et al. 2008a, A&A, submitted
Giommi, P., Perri, M., Verrecchia, F. et al. 2008b, ATel 1495
Hartman, R., Böttcher, M. et al. 2001, ApJ, 553, 683
Hayashida, M. et al. 2007, Proc. 30th Int. Cosmic Ray Conf., Merida, Mexico,
Lähteenmäki, A. & Valtaoja, E. 2003, ApJ, 590, 95
Lindfors, E., Türler, M., Valtaoja, E. et al. 2006, A&A, 456, 895
Marscher, A. P., Jorstad, S. G., D'Arcangelo, F. D. et al. 2008, Nature, 452, 966
Miller, J. S., French, H. B. & Hawley, S. A. 1978, ApJ, 219, L85
Nieppola, E., Tornikoski, M., Valtaoja, E. 2006, A&A, 445, 441
Nilsson, K., Pasanen, M., Takalo, L. O. et al. 2007, A&A, 475, 199
Nilsson, K., Pursimo, T., Sillanpää, A. et al. 2008, A&A, 487, L29
Ostorero, L., Wagner, S. J., Gracia, J. et al. 2006, A&A, 451, 797
Padovani, P., Giommi, P. 1995, MNRAS, 277, 1477
Rector, T. A. & Stocke, J. T. 2001, AJ, 122, 565
Stickel, M., Fried, J. W. & Kuehr, H. 1993, A&AS, 98, 393
Teshima, M. (MAGIC Collaboration) 2008a, ATel 1491
Teshima, M. (MAGIC Collaboration) 2008b, ATel 1500
Tomida, H., Matsuoka, M., Kawasaki, K. et al. 2008, this volume
Villata, M. Raiteri, C., Larionov, V. M. et al. 2008, A&A, 480, 339
Wagner, S. J., Witzel, A. Heidt, J. et al. 1996, AJ, 111, 2187

All Sky Observations with BATSE and GBM

Colleen A. Wilson-Hodge[1] for the GBM and BATSE teams

[1] NASA/MSFC, Huntsville, AL 35812, USA
E-mail(CAWH): Colleen.Wilson@nasa.gov

Abstract

The Burst and Transient Source Experiment (BATSE) on board the Compton Gamma Ray Observatory (CGRO) monitored the entire sky from 1991-2000. I will review highlights of BATSE observations including gamma ray bursts, black hole candidates, accreting pulsars, and active galaxies. On 2008 June 11, the Fermi Gamma Ray Space Telescope was launched. The Gamma ray Burst Monitor (GBM) on board Fermi continues the all-sky monitoring legacy started with BATSE. I will review early results and planned observations with GBM.

Key words: Fermi; GBM; Gamma Ray Bursts; X-ray binaries; Pulsars; Accretion; Earth occultation

1. Instrument Descriptions

1.1. BATSE

BATSE consisted of 8 detector modules positioned on the corners of the CGRO spacecraft. Each module consisted of two detectors, a large area detector (LAD) and a spectrocopy detector (SD), both of which were sodium idodide (NaI) scintillation crystals. Each LAD had a geometric area of 2025 cm^2, a thickness of 1.27 cm, and was sensitive from about 25 keV to 1.8 MeV. Each SD had a geometric area of 126 cm^2, a thickness of 7.62 cm, and depending on the gain settings, was sensitive from 8 keV - 10 MeV. The BATSE detectors viewed the entire unocculted sky at all times (Paciesas et al 1999).

1.2. GBM

GBM consists of 14 detector modules, 12 low-energy (8 keV-1 MeV) NaI detectors, and two high energy (150 keV- 30 MeV) bismuth germanate (BGO) detectors. Each NaI detector has a geometric area of 126 cm^2 and a thickness of 1.27 cm, while each BGO detector has a geometric area of 126 cm^2 and a thickness of 12.7 cm. The NaI detectors are arranged on the Fermi spacecraft to produce a 9 steradian field of view. Two detectors are positioned opposite each other looking 20 deg from the spacecraft zenith. Four detectors are evenly spaced around the spacecraft looking 45 deg from the spacecraft zenith. The remaining six detectors are evenly spaced around the spacecraft and are looking 90 deg from the spacecraft zenith. BGO detectors are positioned on the +X and -X sides of the spacecraft (Meegan et al 2007).

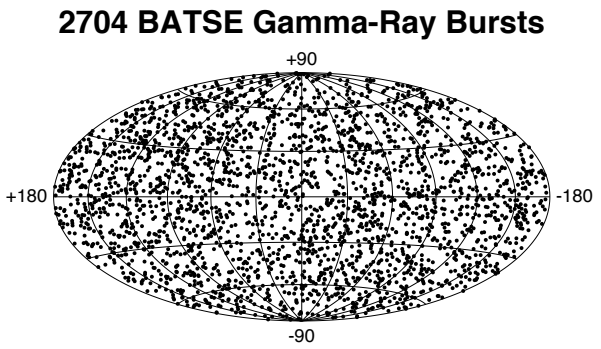

Fig. 1. The BATSE sky map, showing 2704 triggered gamma ray bursts over the 9 year mission, clearly illustrating the isotropy of gamma ray bursts.

2. Gamma Ray Burst Observations

2.1. BATSE

Before CGRO was launched, gamma ray bursts (GRBs) were believed to be galactic by many in the astronomical community. BATSE showed that these bursts had an isotropic angular distribution (Fig. 1), while the intensity distribution showed fewer weak bursts than expected from a homogeneous distribution of sources in Euclidean space. Because no observed galactic component had these spatial properties, BATSE provided the first clear indication that gamma ray bursts were of cosmological origin (Meegan et al. 1992).

BATSE triggered when it observed a change in count rate above a specified threshold (typically 5.5 σ) usually in the 50-300 keV band in either 64 ms, 256 ms, or 1.024 s timescales. In triggered mode, high rate data were accumulated for 573.4 s. During its 9 year mission, BATSE triggered a total of 8021 times. These

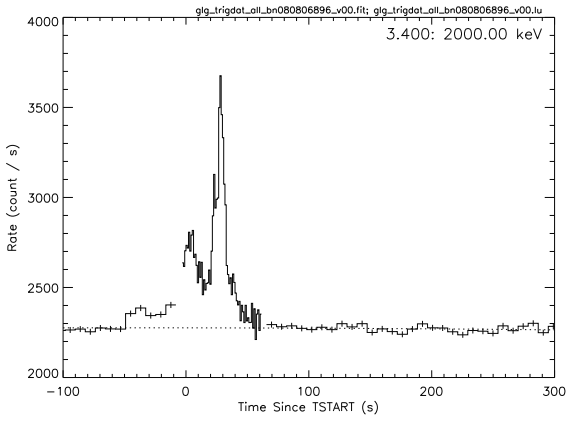

Fig. 2. The TRIGDAT light curve for a GRB observed with GBM on 2008 August 6 at 21:29:40 UT shows the combined count rates in all energy channels from GBM NaI detectors 1 and 2.

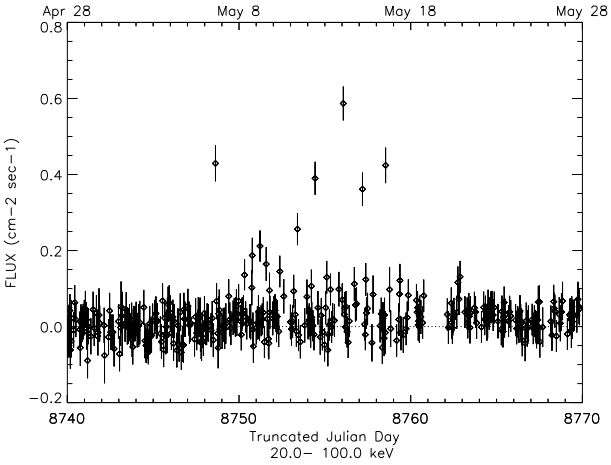

Fig. 3. From Paciesas et al. (1996). Single step Earth occultation measurements of GRS 1915+105 with BATSE in the 20-100 keV band during early May 1992. The high points on the plot are bright flares from GRS 1915+105 detected as large Earth occultation steps. For comparison, the flux from the Crab Nebula is ~ 0.3 ph cm^{-2}s^{-1} in this band

triggers included: 2704 GRBs, 1192 solar flares, 185 soft gamma repeaters, 2003 transient sources, 78 terrestrial gamma flashes, 1717 magnetospheric events, and 142 triggers that were phosphorescence spikes, accidental triggers, unknown events, or undetermined due to insufficient data (Paciesas et al. 1999, Briggs et al. in preparation).

2.2. GBM

GBM together with the Large Area Telescope (LAT) onboard Fermi will enable GRB observations over up to seven decades in energy. GBM continues the BATSE legacy and ties bursts observed with Fermi back to the well studied BATSE sample. GBM has 128 possible trigger algorithms, of which 62 are currently used. These algorithms contain combinations of energy bands and timescales from 16 ms - 4 s. Each trigger algorithm has an independently adjustable trigger threshold defined in terms of significance above background. GBM triggers when it detects a change in count rate above a specified threshold (typically 4.5-5.5 σ) in at least two NaI detectors. Thereafter, it immediately alerts the TDRS satellites to send information about the trigger, called TRIGDAT, to the ground to facilitate observations with other observatories through GCN notices. This information includes the triggered detectors, triggered algorithm, on-board sky location, the on-board classification (e.g. GRB, Solar Flare, SGR, etc.), the flux, fluence, and significance of the trigger. In addition, an immediate signal is sent to the LAT along with a repoint recommendation if the burst fits pre-defined intensity and hardness criteria. During trigger mode, time tagged event data are produced for 300 seconds, the 8 channel continuous timing (CTIME) data are sped up from nominal 256 ms to 64 ms resolution, the 128 channel continuous spectra (CSPEC) are sped up from nominal 4.096 s to 1.024 s, and a ring buffer of 500,000 pre-trigger events is transmitted (Meegan et al 2007). An example TRIGDAT light curve from a burst observed with GBM in 2008 August is shown in Figure 2.

From 2008 July 13 (when triggers were enabled) until 2008 October 6, GBM triggered a total of 129 times. Of these triggers, 63 are identified as Gamma Ray Bursts, 33 as soft gamma repeaters or anomalous X-ray pulsars, four galactic X-ray binaries, and four terrestrial gamma flashes. The remaining 25 triggers are either too weak to identify, due to background fluctuations, or magnetospheric events.

3. Earth Occultation

The intensity of a galactic or extra-galactic source can be measured by calculating the difference in observed count rate before and after the source is occulted by the Earth. This measurement is most easily made using a small window of data surrounding the calculated time when the source of interest enters or exits Earth occultation. Projections of the Earth's limb on the sky at the time of these occultation "steps" can be used to locate new astrophysical sources. This technique is required for BATSE and GBM because neither instrument has direct imaging capabilities.

3.1. BATSE

With BATSE, we made extensive use of the Earth occultation technique. We monitored a catalog of 179 sources including primarily X-ray binaries, plus representative samples of active galaxies, X-ray emitting stars, and supernova remnants. From this catalog, we detected 74 X-ray binaries, three supernova remnants, and six active

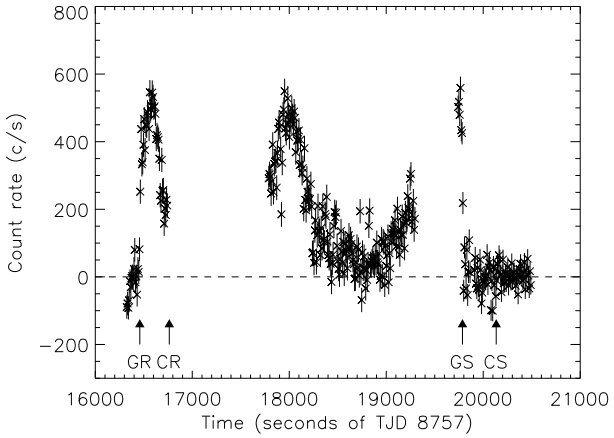

Fig. 4. From Paciesas et al. (1996). A flaring episode from GRS 1915+105 on 1992 May 15. Shown are background subtracted BATSE count rates with 8.192 s resolution in the 20-100 keV band summed over two detectors. GR, GS and CR, CS denote GRS 1915+105 and Cyg X-1 rise and set times, respectively. In this band, the Crab Nebula count rate is ~ 300 cts s^{-1}.

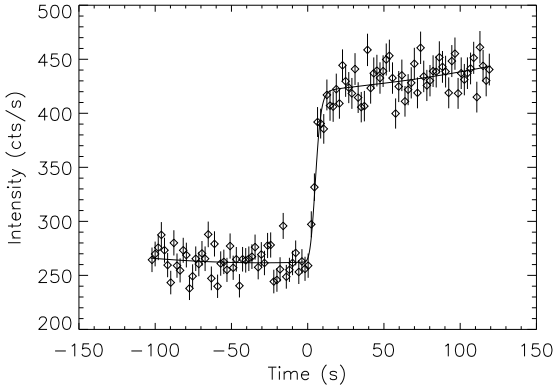

Fig. 5. An example Earth occultation step observed with GBM on 2008 September 21 from Sco X-1 in the 10-25 keV band. The diamonds denote the raw CTIME count rates measured with GBM plotted at 2 s resolution. The solid line denotes the fitting model which consists of a quadratic background plus an atmospheric transmission function convolved with predicted count rates for Sco X-1. The predicted count rates result from folding an assumed spectral model through the changing detector response function as the spacecraft moves.

galactic nuclei at 10 σ or better either over the entire 9 year mission or in at least one identifiable outburst. Our limiting sensitivity was 3.5-20 mCrab, due to sky dependent systematic errors, over the 20-430 keV band (Harmon et al. 2004).

Although this technique is less sensitive than imaging instruments, it has the advantage of monitoring the entire sky all of the time. This allowed us to observe unpredictable events such as black hole state changes in Cyg X-1, 1E 1740–29, GX 339-4, and Cyg X-3 (Harmon et al. 2004 and references therein) and to find pre-discovery emission in archival data. We discovered extremely bright flares, shown in Figures 3 and 4, from GRS 1915+105 from data prior to its discovery (Paciesas et al. 1996). In addition, BATSE data were very useful for studying long-term trends in source behaviors and were important components in several multiwavelength campaigns (e.g. Cyg X-3, McCollough et al 1999). With the BATSE Earth occultation technique, we discovered three new black hole transient systems, GRO J0422+32, GRO J1655–40, and GRO J1719–24=GRS 1716–249.

3.2. GBM

We have a guest investigation program (P.I. Wilson-Hodge) in place to implement the Earth occultation technique with GBM. Implementation of the technique is in progress. For GBM, the technique is complicated by the fact that Fermi is scanning the sky, rather than being intertially pointed like CGRO. This means the detector response is changing and must be taken into account. Figure 5 shows a rising Earth occultation step from Sco X-1 in GBM NaI #2. Figure 6 shows the estimated GBM sensitivity taking into account the expected backgrounds, which are consistent with observed rates. GBM

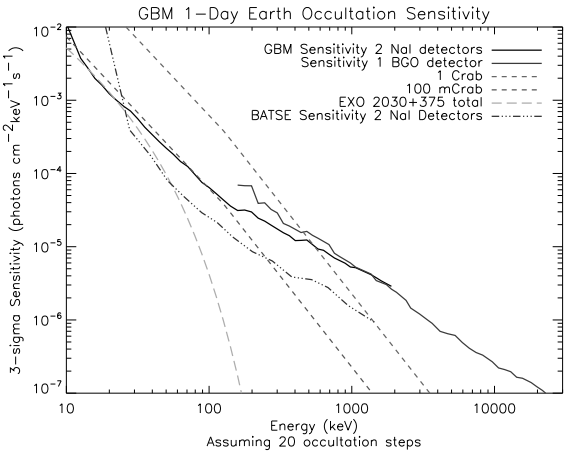

Fig. 6. The estimated 1-day Earth occultation sensitivity limits for two GBM NaI detectors and one GBM BGO detector for a source at moderate viewing angles. The BATSE sensitivity limit for 2 LADs is shown for comparison. Also shown are 1 Crab and 100mCrab spectra, as well as the spectrum of the accreting X-ray pulsar EXO 2030+375.

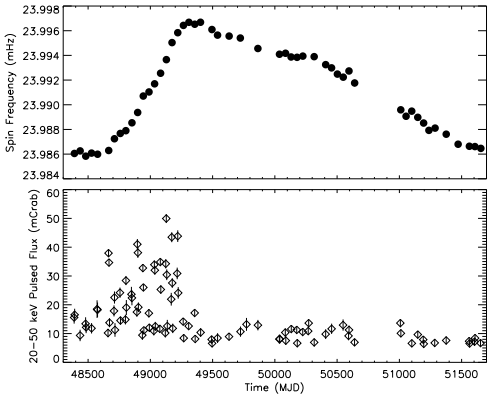

Fig. 7. *(top):* Barycentered, orbit corrected spin-frequency for EXO 2030+375 at each periastron passage where BATSE detected pulsations. *(bottom):* Corresponding 20-50 keV pulsed flux for these observations measured with BATSE.

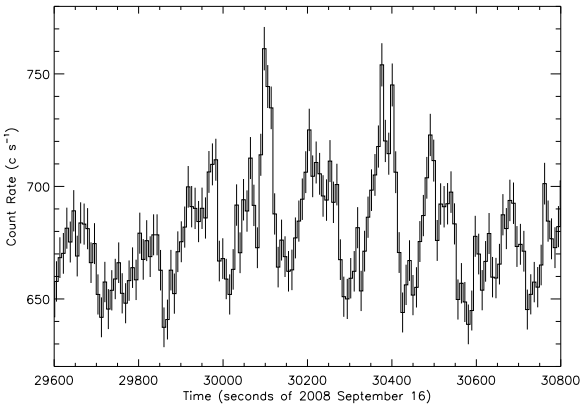

Fig. 8. An example of an accreting X-ray pulsar in the GBM data. This Figure shows 283-s pulses from Vela X-1 in the 12-52 keV energy band for GBM NaI 4.

has considerably better sensitivity from about 8-25 keV than BATSE because the GBM NaI detectors have only a Be window instead of the plastic scintillator, aluminum honeycomb, and aluminum window located in front of the BATSE detectors. The 1-day sensitivity limit for the Earth occultation technique with GBM assuming a source is viewed by two NaI detectors is about 90 mCrab below 100 keV (Case et al. 2007). The Japanese Monitor of All-Sky X-ray Image (MAXI), described in detail elsewhere in these proceedings and scheduled to be attached to the space station in 2009, has much better sensitivity, but only extends up to 30 keV. Earth occultation monitoring with GBM will provide the only all-sky capability above about 50 keV. Hence GBM will provide important complementary data for bright events observed with MAXI.

3.3. Accreting Pulsar Observations

Accreting X-ray pulsars consist of a magnetized neutron star ($B \sim 10^{12}$ G) orbiting a companion. Accretion in these systems occurs via either Roche lobe overflow, a stellar wind, or interaction with the circumstellar disk of a Be star near periastron passage. Recently, *INTEGRAL* has discovered a number of likely highly absorbed wind accreting X-ray pulsars (Walter et al. 2006).

3.4. BATSE

A large number of accreting pulsars were monitored daily with BATSE. For example, Figure 7 shows the spin-frequency history and the pulsed flux measured for the accreting Be/X-ray pulsar EXO 2030+375. Each point corresponds to a periastron passage in the system, when the source was typically detectable for 4-12 days. Monitoring of this particular pulsar led to the discovery that the infrared magnitudes showed a decline shortly before the pulsar began to spin down and the pulsed flux abruptly dropped (Wilson et al. 2002). This implied that the density of the disk around the companion star declined, making less material available for accretion onto the pulsar. Later, after CGRO deorbited, the infrared magnitudes again brightened accompanied by a brightening of the X-ray outbursts and a transition to spin-up observed with the Rossi X-ray Timing Explorer (Wilson et al 2005).

The techniques used to detect known accreting pulsars with BATSE are described in detail elsewhere (Bildsten et al. 1997, Finger et al. 1999). The basic idea is that the data, when the pulsar of interest was above the horizon, were fitted with a model consisting of a background plus a Fourier expansion in the pulse phase model which used an approximately known spin-frequency. This model was used to generate pulse profiles for short segments of data, short enough that the loss of power due to phase drift was small. These short segment profiles were then shifted using a grid in pulse frequency and sometimes frequency derivative. The shifted profiles were combined and the best frequency (and derivative) was selected from the grid using a modified Z_n^2 statistic. In addition to this technique, daily fast Fourier transforms of the BATSE data were performed to look for new periodicities in the data. Six new accreting pulsars were discovered with BATSE: GRO J1008–57, GRO J1948+32, GRO J1744–29, GRO J2058+42, GRO J1750–27, and GRO J1944+26 = XTE J1946+274.

3.5. GBM

We have a guest investigation program in place to monitor accreting pulsars using GBM (PI Finger). We expect that GBM should be able to detect most of the X-ray pulsars observed with BATSE, despite GBMs smaller area. This is because of the fortunate combination of a large number of photons in the 8-25 keV range from

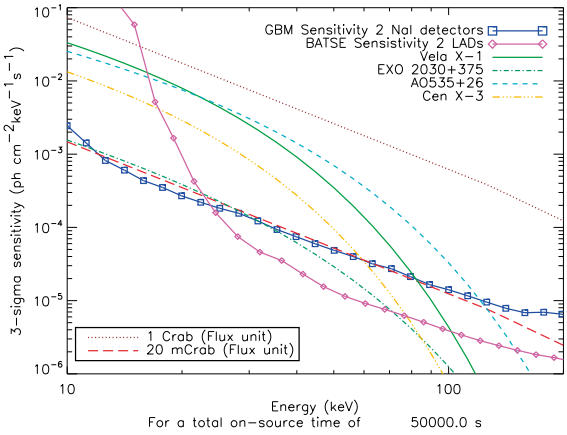

Fig. 9. Estimated GBM 3-σ root-mean squared (rms) pulsed flux sensitivity to accreting X-ray pulsars for 50 ks on-source. For comparison, we show BATSE's sensitivity and representative rms pulsed flux spectra for the accreting X-ray pulsars Vela X-1, EXO 2030+375, A 0535+262, and Cen X-3. One Crab and 20 mCrab flux units are also shown for reference.

most accreting pulsars combined with GBMs improved low-energy response over BATSE. For accreting pulsars, GBM will provide daily monitoring of spin-frequencies, while MAXI will provide precise flux measurements. Together these results will be excellent for studying correlations between pulsar spin-up rates and total flux. Figure 8 shows pulses from the 283-s wind-fed accreting X-ray pulsar, Vela X-1, that are visible in the raw data.

Figure 9 shows the result of our sensitivity calculation in terms of rms pulsed flux. Details of the calculation are given in Wilson-Hodge et al. (2007). For reference, we have also done the same calculation for the BATSE LADs using actual measured background rates and corresponding detector response matrices for two detectors. Typical rms pulsed flux spectra of 4 accreting pulsars are also shown that were detectable with BATSE and are expected to be detectable with GBM.

4. Conclusions

BATSE observed 2704 triggered GRBs and provided the first clear evidence that GRBs were cosmological. With BATSE, we monitored the sky using Earth occultation measurements in the 20-1800 keV band, providing important contributions to multiwavelength studies, long-term studies, and observations of unpredictable events such as state changes in black holes. We provided the only continuous monitoring of accreting pulsar spin-frequencies, including transitions from spin-up to spin-down. Most BATSE data are still available through NASA's High Energy Astrophysics Science Archive Research Center (http://heasarc.gsfc.nasa.gov) for archival studies.

Using GBM we will continue all-sky monitoring observations. It is still very early in the mission, but results so far look exciting. GBMs most important contributions will most likely be for GRBs where, combined with the LAT, we will provide the broadest spectral coverage ever achieved. Plus we will complement GRB observations from other instruments, such as Swift, providing higher energy coverage with our BGO detectors. Today, other all-sky monitors are also available such as the Burst Alert Telescope on-board Swift (15-150 keV, Barthemy et al. 2005) and in 2009, MAXI (0.5-30 keV). GBM data will complement these other monitors, providing additional time coverage in the 8-50 keV band, the only high energy source monitoring above about 50 keV, and the only near-continuous monitoring of accreting pulsar spin-frequencies.

References

Barthelmy, S.D. et al. 2005, Space Science Reviews, 120, 143
Bildsten, L. et al. 1997, ApJS, 113, 367
Case, G.L. et al. 2007, The First GLAST Symposium, AIP Conf. Proc. 921, eds. S.Ritz, P. Michelson, C. Meegan, (AIP: Melville), 538
Finger, M.H., et al. 1999, ApJ, 517, 449
Harmon et al. 2004, ApJS, 154, 585
McCollough, M.L. et al. 1999, ApJ, 517, 951
Meegan, C.A.et al. 2007, The First GLAST Symposium, AIP Conf. Proc. 921, eds. S.Ritz, P. Michelson, C. Meegan, (AIP: Melville), 13
Paciesas, W.S. et al. 1996, A&AS, 120, 205
Paciesas, W.S. et al. 1999, ApJS, 122, 465
Walter, R. et al. 2006, A&A, 453, 133
Wilson, C.A. et al 2002,ApJ, 570, 287
Wilson, C.A., Fabregat, J., Coburn, W. 2005, ApJ, 620, L99
Wilson-Hodge, C.A. et al. 2007, The First GLAST Symposium, AIP Conf. Proc. 921, eds. S.Ritz, P. Michelson, C. Meegan, (AIP: Melville), 229

Transients in the Local Universe

S. R. Kulkarni[1] and M. M. Kasliwal[1]

[1] California Institute of Technology
E-mail(SRK): srk@astro.caltech.edu

Abstract

Two different reasons make the search for transients in the nearby Universe (d$\lesssim$ 100 Mpc) interesting and urgent. First, there exists a large gap in the luminosity of the brightest novae (-10 mag) and that of sub-luminous supernovae (-16 mag). However, theory and reasonable speculation point to several potential classes of objects in this "gap". Such objects are best found in the nearby Universe. Next, the budding and nascent fields of Ultra-high energy cosmic rays, TeV photons, astrophysical neutrinos and gravitational waves (GW) are limited by $\sim$ 100-Mpc horizon either due to physical effects (GZK effect, photon pair production) or instrumental sensitivity (neutrino and GW). Here we describe a key project of a new facility – the Palomar Transient Factory (PTF) – aimed at a comprehensive study of transients in the Local Universe. PTF has recently achieved first light and we look forward to a synergistic program with MAXI.

Key words: Supernovae : Novae — Synoptic Surveys : Palomar Transient Factory — UHECR : TeV : Neutrino : Gravitational Wave Astronomy

1. Background

Variable objects have surprisingly played a major role in the history of astronomy. At the beginning of the previous century, the pulsating Cepheids showed that the Galaxy was much larger than had been assumed before. The empirical relation between the decay time and luminosities of novae yielded meaningful distances to the Andromeda galaxy. Supernovae touched upon the origin of cosmic rays, the synthesis of iron and higher-Z elements and the possibility of collapse of cores leading to the formation of neutron stars. It is worth noting that Zwicky's pioneering wide field optical program began at Palomar. Caltech provided $50,000 which resulted in the construction of the 18-inch Palomar Schmidt telescope[1]. The 18-inch Schmidt essentially started and laid the foundation of the field of supernovae. The success of this program led to the 48-inch Palomar Oschin Schmidt telescope, famous for the two Sky Surveys.

At the end of the previous century, supernovae came back into main stream. The first indication of a new constituent of the Universe, dark energy, was deduced from the dimming of Ia supernovae located at cosmological distances (Perlmutter et al. 1999, Reiss et al. 1998).

Over the last decade, a veritable explosion of progress took place in the field of gamma ray bursts. We now recognize that the GRB phenomenon can be traced to at least three separate classes: long duration bursts (associated with the deaths of certain but hitherto unidentified types of massive stars), short duration bursts with large hardness ratio (associated with the coalescence of compact objects) and short duration bursts with small hardness ratio bursts (traced to flares from magnetars). The first two classes are the most relativistic explosions known in Nature. In both cases a rapidly spinning black hole is expected. Astronomers eagerly await the use of long duration GRBs to probe the very young Universe, physicists regard short duration events as the prime targets for gravitational wave (GW) detectors and soft gamma-ray repeaters are truly Nature's most exotic and unique laboratory for electrodynamics.

Clearly, the study of transients has been a very fruitful endeavor. Here we focus on transients in the local Universe (distance, $d < 200$ Mpc). The rationale for this myopic view is given in §2., §3. and §4.. Our pilot program of searches in the nearest galaxies (10 Mpc) and the nearest clusters (Virgo, Fornax) is summarized in §5.. Next, in §6., we discuss the Palomar Transient Factory (PTF), a key goal of which is a systematic unveiling of transients in the local Universe. We conclude in §7. with a discussion of a possible MAXI-PTF program.

2. Rationale & Motivation: Events in the Gap

A plot of the peak luminosity versus a duration that is characteristic (based on physics or convention) is a convenient way to summarize explosive events. We first focus on novae and supernovae of the type Ia. As can

*[1] This venerable telescope can now can be found at the Palomar Museum

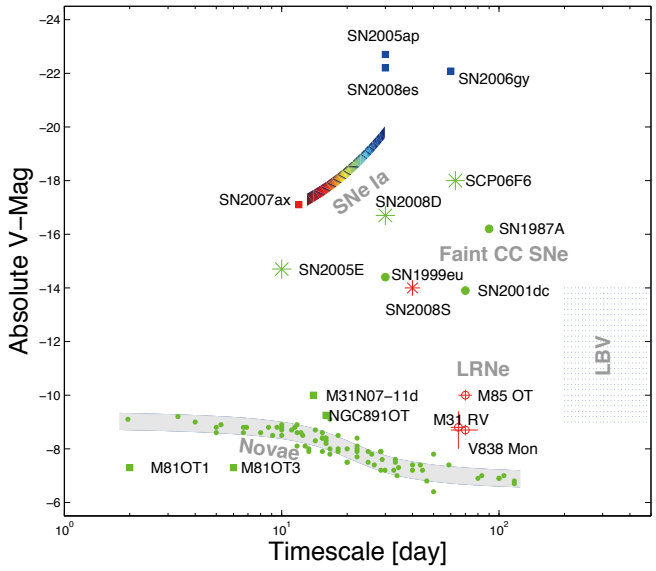

Fig. 1. Cosmic transients phase space (peak V-band luminosity as a function of duration, with color a measure of the true color at maximum). Shown are the known explosive (supernovae) and eruptive (novae, luminous blue variables [LBV]) transients. Also shown are new types of transients (and discussed in §4.): the peculiar transients M 85 OT2006-1, M31-RV and V838 Mon, which possibly form a new class of "luminous red novae,", the baffling transient with a spectrum of a red-shifted Carbon star, SCP 06F6, the shock-breakout X-ray transient (SN 2008D), a possible accretion induced collapse event SN 2005E and a peculiar eruptive event with an extremely red progenitor SN 2008S. Adapted from Kulkarni et al. 2007.

be seen from Figure 1 novae and supernovae of the Ia type form a distinctly different locus. Brighter supernovae take a longer time to evolve (the "Phillips" relation; Phillips et al. 1999) whereas the opposite is true of novae: the faster the nova decays the higher the luminosity (the "Maximum Magnitude Rate of Decline", MMRD relation; see, for example, Della Valle and Livio 1995).

The primary physical parameter in Ia supernovae is the amount of Nickel that was synthesized. There is almost a factor of 10 variation as we go from the brightest supernova ("1991bg-like") to the dimmest ("1991T-like"). The Phillips relation has been very quantified with high precision and the theory is well understood. In contrast, the MMRD does not enjoy the same quantity or quality of light curves as those of Ia supernovae. Fortunately, dedicated on-going nova searches in M31 and the P60-FasTING project described below (§5.) should vastly increase the number of light curves.

The large gap between the brightest novae (say $M_{\rm V} \sim -10$) and the faintest supernovae ($M_{\rm V} \sim -16$) is hard to miss. The gap beckons astronomers to search the heavens for new populations.

A discussion of potential new classes of events in the gap would benefit from a review of the basic physics of explosions. Here, we restrict to non-relativistic explosions. Given this restriction the assumption of spherical symmetry is not particularly restraining.

An explosion is a ball of matter and photons. An added but important complication is a potential heat source at the center: a hot white dwarf (novae) or gradual release of radioactive energy (supernovae). The primary physical parameters are: the mass of the ejecta ($M_{\rm ej}$), the velocity of the ejecta (v_s), the radius of the progenitor star (R_0) and the total energy of the explosion ($\mathcal{E}_0$). Two distinct sources of energy contribute to the explosive energy: the kinetic energy of the ejecta, $\mathcal{E}_{\rm k} \equiv (1/2) M_{\rm ej} v_s^2$ and the energy in the photons (at the time of the explosion), $\mathcal{E}_{\rm ph}$.

Approximating the explosion by a homogeneous sphere we can write the following equation to describe the gains and losses suffered by the store of heat (E):

$$\dot{E} = \varepsilon(t) M_{\rm ej} - L(t) - 4\pi R(t)^2 P v(t). \quad (1)$$

Here, $L(t)$ is the luminosity radiated at the surface and $\varepsilon(t)$ is heating rate (energy per unit time) per gram from any source of energy (e.g. radioactivity or a long-lived central source). P is the total pressure and is given by the sum of gas and photon pressure:

$$P = n_i (Z+1) kT + aT^4/3. \quad (2)$$

Here, n_i is the density of ions, n_e is the density of electrons and it is assumed that all the gas is hot enough to be fully ionized.

Next, we resort to the so-called "diffusion" approximation (see Arnett 1996; Padmanabhan 2000, volume II, §4.8),

$$L = E_{\rm ph}/t_{\rm d}, \tag{3}$$

where $E_{\rm ph} = aT^4V$ is the energy in photons [V is the volume of the sphere, $(4\pi/3)R^3$]

$$t_d = B\kappa M_{\rm ej}/cR \tag{4}$$

is the timescale for a photon to diffuse from the center to the surface. The pre-factor B in Equation 4 depends on the geometry and, following Padmanabhan (*ibid*), we set $B = 0.07$. κ is the mass opacity.

We will make one simplifying assumption: most of the acceleration of the ejecta takes place on initial hydrodynamic timescale, $\tau_h = R_0/v_s$. With this "coasting" approximation we have

$$R(t) = R_0 + v_{\rm s}t. \tag{5}$$

This simplification means that we need solve only one differential equation, namely the energy equation (Equation 1).

First, let us consider a "pure" explosion i.e. no subsequent heating, $\varepsilon(t) = 0$. If photon pressure dominates then $P = 1/3(E/V)$ and an analytical formula for $L(t)$ can be obtained (Padmanabhan, *op cit*):

$$L(t) = L_0 \exp\left(-\frac{t\tau_h + t^2/2}{\tau_h\tau_d}\right); \tag{6}$$

here, $\tau_d = B(\kappa M_{\rm ej}/cR_0)$ is the initial diffusion timescale and $L_0 = \mathcal{E}_{\rm ph}/\tau_d$.

The analytical formula allow us to get some insight into pure explosions. For strong explosions, $\tau_h \ll \tau_d$. In this case, the internal energy goes in to PdV work and is rapidly depleted on timescales of τ_h. However, the light curve decays on a much longer scale, thanks to the long diffusion timescale for photons.

The light curve be divided into two phases: a plateau phase which lasts until about $\tau = \sqrt{\tau_d\tau_h}$ after which the luminosity undergoes a (faster than) exponential decay. The duration of the plateau phase is

$$\tau = \sqrt{\frac{B\kappa M_{\rm ej}}{cv_s}} \tag{7}$$

and is independent of R_0. The plateau luminosity is

$$\begin{aligned} L_p &= \mathcal{E}_{\rm ph}/\tau_d \\ &= \frac{cv_s^2R_0}{2B\kappa}\frac{\mathcal{E}_{\rm ph}}{\mathcal{E}_{\rm k}}. \end{aligned} \tag{8}$$

As can be seen from Equation 8 the peak luminosity is independent of the mass of the ejecta but directly proportional to R_0. To the extent that there is rough equipartition[2] between the kinetic energy and the energy in photons the luminosity is proportional to the square of the final coasting speed, v_s^2.

Pure explosions satisfactorily account for supernovae of type IIp. Note that since $L_p \propto R_0$ the larger the star the higher the peak luminosity. SN 2006gy, one of the brightest supernovae, can be explained by invoking an explosion in a "star" which is much larger (160 AU) than any star (likely the material shed by a massive star prior to its death; see Smith & McCray 2007). Conversely pure explosions resulting from the deaths of compact stars (e.g. neutron stars, white dwarfs or even stars with radius similar to that of the Sun) can be not to be luminous. For such progenitors visibility in the sky would require some sort of additional subsequent heat input.

In the spirit of this discussion (namely, an open ended discussion of new transients) we also consider the case where the gas pressure could dominate over photon pressure. This is the regime of weak explosions. If so, $P = 2/3(E/V)$ and Equation 1 can be integrated to yield

$$L(t) = \frac{L_0}{(t/\tau_h + 1)}\exp\left(-\frac{\tau_h t + t^2/2}{\tau_h\tau_d}\right). \tag{9}$$

In this case the relevant timescale is the hydrodynamic timescale. This regime is populated by Luminous Blue Variables and Hypergiants. Some of these stars are barely bound and suffer from bouts of unstable mass loss and photometric instabilities.

We now turn to new classes of transients. This is an exciting area as judged by the number of speculative papers. The most fruitful ideas result from considerations of binary stars.

First we will consider "supernova"-like events i.e. events in which the resulting debris is heated by radioactivity. One can easily imagine a continuation of the Ia supernova sequence. We consider three possible examples for which we expect a smaller amount of radioactive yield and a rapid decay (timescales of days): coalescence of compact objects, accreting white dwarfs (O-Ne-Mg and Helium).

Following Li & Paczynksi (1998), Kulkarni (2005) considers the possibility of the debris of neutron star coalescence being heated by decaying neutrons. Amazingly (despite the 10-min decay time of free neutrons) such events (dubbed as "macronovae") are detectable in the nearby Universe over a period as long as a day, provided even a small amount ($\gtrsim 10^{-3}\,M_\odot$) of free neutrons released in such explosions.

Bildsten et al. (2007) consider a Helium nova (which arise in AM Cvn systems). For these events (dubbed

*2 This is a critical assumption and must be checked for every potential scenario under consideration. In a relativistic fireball most of the energy is transferred to matter.

".Ia" supernovae), not only radioactive Nickel but also radioactive Iron is expected.

The fate of O-Ne-Mg white dwarfs accreting matter from a companion continues to fascinate astronomers. Such systems exist and the issue is what happens once the mass of the accretor exceeds the Chandrashekar limit. The likely possibility is a neutron star but the outcome depends severely on the unknown effects of rotation and magnetic fields. One possibility is a weak supernova explosion (see Metzger et al. 2008 for a recent discussion and review of the literature). Only a small amount of radioactive Nickel is expected and thus the expectation is a sub-luminous supernova with decay on timescales of a day or so.

An entirely different class of explosive events are expected to arise in massive or large stars: birth of black holes (which can range from very silent events to GRBs and everything in between), strong shocks in supergiants (van den Heuvel 2008) and common envelope mergers. Equations 7 and 8 provide a guidance to the expected appearance of such objects. For the case of the birth of a black hole with no resulting radioactive yield (the newly synthesized material could be advected into the black hole) the star will slowly fade away on a timescale of $\min(\tau_d, \tau)$. Modern surveys are capable of finding such wimpy events (Kochanek et al. 2008).

3. Rationale & Motivation: New Astronomy

Four entirely different fields of astronomy are now being nurtured by physicists: ultra-high energy cosmic rays (UHECR), TeV astronomy, gravitational wave astronomy and neutrino astronomy. For these fields all that matters is transients in the local Universe.

Cosmic rays with energies exceeding 10^{20} eV are strongly attenuated owing to the production of pions through interaction with the cosmic micro-wave background (CMB) photons [the famous Greisen-Zatsepin-Kuzmin (GZK) effect]. Recently, the Pierre Auger Observatory (PAO 2007) has found evidence showing that such cosmic rays with energies above 6×10^{19} eV are correlated with distribution of matter in the local 75-Mpc sphere. Cosmic rays with higher energies are suppressed and their "horizon" is correspondingly smaller.

Similarly very high energy (VHE) photons (TeV and PeV) have a highly restricted horizon. The TeV photons interact with CMB photons and produces electron-positron pairs. A number of facilities are now routinely detecting extra-galactic TeV photons from objects in the nearby Universe (Veritas, MAGIC, HESS, CANGAROO).

Neutrino astronomy is another budding field with an expected vast increase in sensitivity. The horizon here is primarily limited by sensitivity of the telescopes. Large field-of-view (FOV) instruments like PTF are well suited to the expected localization of a few square degrees of these instruments.

The same two limitations (a small horizon and poor localization) apply to the exciting field of GW astronomy. The horizon radius is 45 Mpc for `enhanced` LIGO (eLIGO) and about 175 Mpc for `advanced` LIGO (aLIGO). However, the localization will remain poor (limited by the small baseline lengths, relative to the GW wavelength) – tens of square degrees (at best). There is wide spread agreement that the greatest gains will require electromagnetic localization of the event. Unfortunately, all sorts of foreground and background transients *will* be found within such a poor localization. Studying each of these transients will result in significant "opportunity cost". Addressing this opportunity cost is a significant motivation for PTF (see §6.).

Fortunately, the limited sensitivity-limited horizon of GW astronomy is a blessing in disguise. The opportunity cost can be reduced by restricting transients to those overlapping galaxies within the LIGO radius. Our simulations show that electromagnetic localization of LIGO events is quite feasible (Kasliwal et al., in prep).

4. Serendipitous Discoveries

Recent serendipitous discoveries give us comfort and confidence that a systematic investigation of the nearby Universe will be profitable.

In Kulkarni et al. (2007), we report a $M_R = -12$ transient in M85 (initially "rejected" by KAIT as too faint to be a supernova). This elusive group (dubbed Luminous Red Novae, LRNe; see Figure 2) has three other potential members: V838 Mon, M31 RV and V4332 Sgr. Suggested models to explain LRNe are diverse: common-envelope merger, a rare type of novae, low-luminosity tail of supernovae (and even a planet plunging into its parent star!).

Next, Barbary et al. (2008) announced the discovery of SCP 06F6, a transient with a nearly symmetric light curve, discovered during HST observations of a cluster. The transient has no detected host galaxy or star, an amplitude >7 mag and a spectrum oddly similar to a carbon star at z≈0.14 (Gansicke et al. 2008). Another intriguing fact is that the X-ray emission (detected at late times, 100 days) is brighter than the optical emission. It cannot be ruled that this was a primarily an X-ray transient with the optical being a side show. Soker et al. (2008) consider several explanations and favor tidal destruction of a CO white dwarf by an intermediate mass black hole. This object is truly intriguing. However, it cannot be too rare given that it was discovered in a WFPC (field-of-view of 5.7 square arcminutes!) study.

SN 2008S (in NGC6946) and NGC 300-OT had a peak absolute magnitude between $-13 > M_V > -15$. The explosion signature (light curve and spectrum) looks sim-

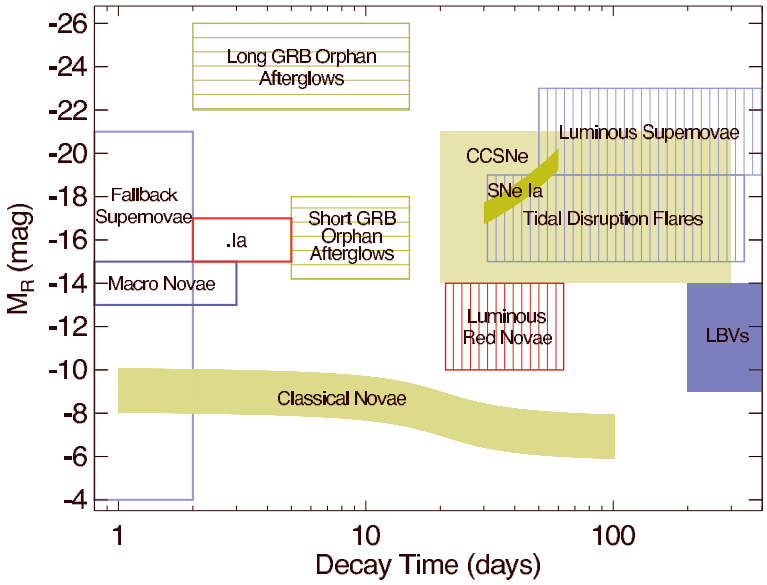

Fig. 2. R-band peak magnitude as function of characteristic decay timescale (typically the time to fade from peak by two magnitudes) for luminous optical transients and variables. Filled boxes mark well-studied classes with a large number of known members (classical novae, SNe Ia, core-collapse supernovae [CCSNe], luminous blue variables [LBVs]). Vertically hatched boxes show classes for which only few (< 4) candidate members have been suggested so far (luminous red novae, tidal disruption flares, luminous supernovae). Horizontally hatched boxes are classes which are believed to exist, but have not yet been detected (orphan afterglows of short and long GRBs). The positions of theoretically predicted events (fall back supernovae, macronovae, .Ia supernovae [.Ia]) are indicated by empty boxes. See text for references related to each science case. The brightest transients (on-axis afterglows of GRBs) and events detectable predominantly in the Milky Way (e.g., dwarf novae) are omitted for clarity (see Table 2 for a more complete list). Regions indicate the general location of each class and are not exclusive. The color of each box corresponds to the mean $g-r$ color at peak (blue, $g-r<0$ mag; green, $0<g-r<1$ mag; red, $g-r>1$ mag). From Rau et al. 2008b.

ilar to luminous blue variables (Smith et al. 2008) and hypergiants (Bond et al. 2009). However, this massive star progenitor hypothesis was put in question by the extremely reddened SED of the progenitor (not detected in optical to deep limits, only detected in mid-infrared, Prieto et al. 2008). Thompson et al. (2008) suggest that these two events and the luminous red nova in M85 form a new class of explosive events with very dusty progenitors with a large radius.

Tantalizing evidence of an accretion induced collapse comes from recent study of nebular spectra of SN 2005E (Perets et al. 2009). This transient had an absolute magnitude -14.7) and decayed on timescale of 12 days. It occurred in the halo of a galaxy (~ 30 kpc from nucleus of NGC 1032). Moreover, the measured total ejecta mass is only 0.18 $M_\odot$.

Another odd transient is SN 2008ha. It had a spectrum similar to the peculiar type Ia SN 2002cx but it has a very low absolute magnitude of -14. If this is indeed a Type Ia supernova, it would be fainter than the faintest Type Ia known so far (SN 2007ax; Kasliwal et al 2008) by two magnitudes.

All these discoveries (in the space of only two years) demonstrate that the gap is not empty and a new, systematic search has the potential to uncover novel astrophysical transients.

Finally, Soderberg et al. 2008 announced the discovery of a burst of X-rays from SN 2008D in NGC 2770 during an unrelated Swift/XRT observation ($M_V = -15$, uncorrected for 2 mags of extinction). The importance of this discovery is that the discovery was made in the classical X-ray band – a band well suited for all-sky monitors. The outburst may arise from the interaction with the shock with the outer layers of the star (or the circumstellar medium at stellar radius) and is an excellent proxy for the shock breakout emission. A deep, fast cadence search of the nearby Universe is clearly well suited to finding supernovae very early on the rise.

5. Pilot Programs

Our group has undertaken three pilot studies aimed to find transients located in the gap (faint and fast): P60-FasTING, CFHT-COVET and Fast transients in Fornax.

The "Fast Transients In Nearest Galaxies" program was undertaken at the Palomar 60 inch (whence, P60-FasTING). It targets about sixty of the nearest ($<$10 Mpc), brightest (<-18) galaxies to a depth of g$<$21 mag and cadence $<$1 day. Though started in 2007, major pipeline upgrades were made until April 2008. Thus far, P60-FasTING has independently discovered a score of novae, a supernova in M 61 (SN 2008in) and a

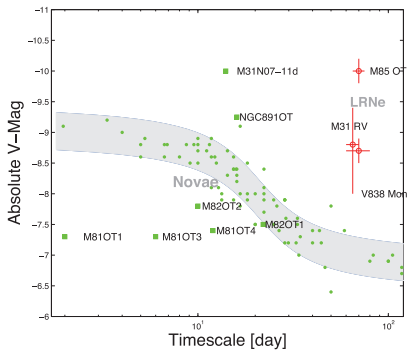

Fig. 3. A plot of the peak absolute magnitudes versus decay timescale of novae discovered by P60-FasTING. The shaded grey region represents the Maximum Magnitude Rate of Decline relationship bounded by $\pm 3\sigma$ (Della Valle and Livio 1995). The data that defined this MMRD are shown by green circles. [Data are preliminary results from Kasliwal et al. 2009b, in prep.]

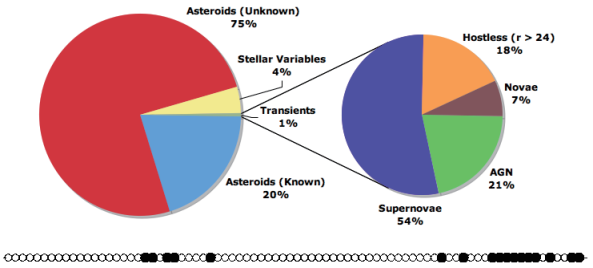

Fig. 4. Twenty eight COVET transients were discovered during our pilot run in 2008A (7 hours). Of these, two were novae in M60, and the remainder were background supernovae and AGN (classified spectroscopically where available and based on offset from host galaxy nucleus otherwise). Transients with no point source or galaxy host to a limiting magnitude of r>24 are classified as hostless. Of the total number of transient candidates, our pipeline automatically rejected 99% as solar-system or galactic. The line of dots (bottom of the figure) indicates which of the 80 nights we got data (filled circles) vs. not (empty circles). We have been granted 30 hours to search 10 fields daily in 2009A. Preliminary version from Kasliwal et al. 2009c, in prep.

luminous blue variable in NGC 925.

It is in the classical field of novae that P60-FasTING appears to have made some progress. In addition to a dozen novae in M 31, our search found five novae in M 81, two in the nearby starburst M 82, and one in NGC 891. As can be seen from Figure 3 several of these novae appear to be outliers on the canonical Maximum Magnitude Rate of Decline (MMRD; Downes and Duerbeck 2000, della Valle and Livio 1995) relation. Despite the photometric peculiarity, they are spectroscopically similar to regular novae.

The large scatter of the new novae suggests that in addition to the mass of the white dwarf, other physical parameters (such as accretion rate, temperature) also govern the photometric signature of novae and that novae are not viable standard candles. We note that this may in part be an observational bias as this search was designed to be more sensitive to fainter and faster novae than previous searches.

Second, we undertook a search of nearby clusters of galaxies with the 3.5-m Canada France Hawaii Telescope (CFHT) – "Coma and Virgo Exploration for Transients" (whence COVET). This search utilizes the MegaPrime Camera which has a field of view of one sq deg, pixel scale of $0.18''$ pix^{-1}, and is on the telescope every dark fortnight of the month. Given that our project requires searching for faint targets overlapping bright galaxies, the fine pixel scale is advantageous in measuring the convolution kernels for image subtraction (see Figure 3). Our real-time pipeline was designed to probe deep into the cores of bright galaxies with a high detection efficiency.

COVET's pilot project (2008A) targeted the rich nearby galaxy super-cluster, Virgo (16 Mpc) to a depth of r<22.5 and cadence of 1 day. Despite a modest total investment of 7 hrs of on-sky time in 2008A and non-optimal sampling, we discovered twenty eight transients – twenty six background supernovae/AGNs and two novae in M 60 (see Figure 4).

The primary lesson that we learnt is the extensive fore- and back-ground "fog". The primary foreground fog (99%) are asteroids and stellar variables. We rejected the former by looking for movement between two images (taken over the same night and separated by about 15 minutes in time) and the latter by looking for a known stellar counterpart in the SDSS archive. The background fog is composed of supernovae and AGNs in small, faint galaxies. Some had no stellar/galaxy counterpart to r >24. The only two transients of interest (i.e. located in VIRGO) discovered were the two novae in M60, an elliptical galaxy. In 2009A, we have been granted 30 hours to search Virgo (7 sq deg, 42% of cluster light) and Coma (3 sq deg, 60% of cluster light).

Third, a search for extremely fast hour-timescale transients was undertaken targeting twenty three members of the Fornax cluster (Rau et al. 2008a). This is the second richest close (17 Mpc) cluster. Galaxies were imaged with the Wide Field CCD Re-imaging Camera on the 2.5-m du Pont telescope at a cadence of 32 min on ten nights from October through December of 2006. Asteroids were eliminated via repeated imaging. Unlike COVET the B band was used for observations. Two previously known supernovae (both in NGC 1316, a galaxy in the Fornax cluster) and five uncataloged stellar variables (two flare stars, two W UMa-type eclipsing binaries and one δ Scuti). Clearly, this approach (blue band, high cadence) appears well suited to the discovery of foreground stellar variables.

Our pilot surveys highlighted the importance of understanding the overwhelming numbers of fore- and background transients. This experience is similar to that of the transients found in the Deep Lens Survey (Kulkarni & Rau; see also Rau et al. 2006, Rau et al. 2007 & Drake et al. 2008). We have come to appreciate the importance of a a well-defined follow-up strategy. Next, we also learnt the importance of a real-time, robust and efficient transient detection pipeline. Follow up is easy when the transient is bright!

6. The Palomar Transient Factory

The first author of this paper conceived the Palomar Transient Factory (PTF) in response to the scientific prospects discussed earlier: explosive events in the gap (§2.) and the urgent need for a thorough understanding of transients in the local Universe arising out of New Astronomy (§3.). PTF is now a multi-institution[3] program devoted to a comprehensive study of transient objects. A full description of the magnificent anticipated science returns from PTF can be found in Rau et al. (2008b).

PTF consists of two telescopes: the Palomar 48-inch Oschin Schmidt telescope (P48) equipped with a refurbished CFH12K camera[4] (Rahmer et al 2008), the automated Palomar 60-inch telescope (P60) equipped with a CCD photometer (Cenko et al. 2006) and the PAIRITEL near-IR 1.3-m telescope equipped with a JHK (simultaneous) imager (Bloom et al. 2006). The data are analyzed in near real time at the Lawrence Berkeley Laboratory. The classification engine is run at UC Berkeley and the final archive (post 1-day) is done by the Infrared Processing & Analysis Center (IPAC).

In contrast to other synoptic surveys (e.g. PanSTARRS, SkyMapper) PTF is designed with only one goal in mind: the study of transients. This translates to two key design requirements: (1) high throughput for transient object astronomy and (2) end-to-end follow-up planning. As explained below, these two demanding key design goals are met by the innovative multi-telescope strategy.

In the context of transient studies, high throughput means either large cadence (revisiting the same piece of sky many times) or a high sky coverage rate (as measured, say, by the number of square degrees surveyed per hour). For PTF, throughput is maximized by undertaking observations in only two bands, a green filter for dark time and a red filter for bright time. Relative to other efforts (which typically employ five to six filters) this stratagem immediately gives a factor of 2 to 3 increase in throughput. However, color information is valuable and here is where the multi-telescope strategy pays off. Color information for newly found transients are obtained by photometric observations on P60 and PAIRITEL. [In conventional approaches, e.g. SDSS, the same wide field imager obtains the color of all objects, transients or otherwise – but at the cost of throughput.]

Next, a transient that is not classified with some degree of certainty is a wasted transient. A transient without good followup is unlikely to result in a paper. In short, it is important to leave no transient behind.

The P60 and PAIRITEL multi-color data form the basis of rapid classification. Another important input is the presence or absence of a putative host galaxy. The `DeepSky`[5] data is efficient at identifying variable stars and variable AGN (for both of which quiescent emission is expected). Transients deemed as interesting are then broad-cast to the PTF collaboration for further spectroscopic follow up at Palomar, Lick, MDM, Keck and McDonald Observatories.

PTF is organized by key projects (Supernovae, Novae, Variable Stars, Flare Stars, Transients in the nearby Universe, Galactic Dynamics, Pre-main sequence Stars etc; see Rau et al. 2008). PTF has two main observing strategies designed to satisfy the needs of these key projects: Dynamic Cadence (`DyC`) aimed at studying the sky on timescales of minutes to days and the five Day Cadence (`5DC`) optimized for supernova searches (see Table 1).

Table 1. PTF Cadence.

Experiment	% Exposure	Cadences	Filter
`5DC`	41	5 d	R
`DyC`	40	1 min–3 d	g, R
`Orion`	11	1 min	R
`Full Moon`	8	–	Hα, [O III]

Notes: The % Exposure is the fraction of time devoted to the specific experiment.

6.1. Key Project: Transients in the Local Universe

A systematic search and study of transients in the local Universe ($d \lesssim 200$ Mpc), especially those in the gap (-10 to -16 mag) and fast transients (duration of few days), is one of the key projects of PTF. Our current knowledge and speculations relevant to this key project is summarized by the way of rates (some based on observations, other based on speculation) in Table 2.

*3 California Institution of Technology, Columbia University, Infrared Processing & Analysis Center, Lawrence Berkeley Laboratory, Las Cumbres Observatory Global Telescope, Weizmann Institute of Science & UC Berkeley.

*4 Built by the Canada-France-Hawaii Observatory and used on CFHT until a few years ago.

*5 The `DeepSky` project offers a simple access to all the wide field data collected by P48, over the past decade. The data have been fully reduced (i.e. photometric and astrometric calibration applied). These data provide a decade long, if irregular, history of the Palomar sky. This effort is a result of the efforts of Dr. Peter Nugent of the Lawrence Berkeley Laboratory.

Table 2. Properties and Rates for Optical Transients[a]

Class	M_R [mag]	τ^b [days]	Universal Rate (UR)	PTF Rate [yr^{-1}]
Dwarf Novae	9..4	3..20	$3 \times 10^{-5}\,pc^{-3}\,yr^{-1}$	100
Classical novae	$-5.. -10$	2..100	$2 \times 10^{-10}\,yr^{-1}\,L^{-1}_{\odot,K}$	60..150
Luminous red novae	$-10.. -14$	20..60	$> 1.5 \times 10^{-13}\,yr^{-1}\,L^{-1}_{\odot,K}$	>1.5
Fallback SNe	$-4.. -21$	0.5..2	$10^{-13}\,yr^{-1}\,L^{-1}_{\odot,K}$	1
Macronovae	$-13.. -15$	0.3..3	$10^{-4..-8}\,Mpc^{-3}\,yr^{-1}$	0.1
SNe .Ia	$-15.. -17$	2..5	$(4..10) \times 10^{-6}\,Mpc^{-3}\,yr^{-1}$	0.25..2
SNe Ia	$-17.. -19.5$	30..70	[c] $3 \times 10^{-5}\,Mpc^{-3}\,yr^{-1}$	500
Core-collapse SNe	$-14.. -21$	20..300	$5 \times 10^{-5}\,Mpc^{-3}\,yr^{-1}$	200

[a]Table from Rau et al. 2008b; see references therein.

[b]Time to decay by 2 magnitudes from peak.

[c]Universal rate at z< 0.12.

Our search strategy is two-fold. First, we will extensively follow-up all optical transients that are spatially coincident with galaxies known to be within 200 Mpc found in either the DyC or the 5DC experiment. We have compiled a detailed catalog of all galaxies known to be within this distance by synthesizing information from several different surveys. Based on this, we have selected the top hundred luminosity over-densities in the local universe which would be observed at a fast cadence with PTF (DyC). Targeting luminosity concentrations probes more star-light than random pointings by more than a factor of four. We note that the current catalog is incomplete[6]: fifty percent at 200 Mpc (Figure 5).

Second, to pursue transients that are in a galaxy not previously known to be within 200 Mpc, we will target fast-evolvers (timescale < 7 days) for follow-up spectroscopic observations and follow up imaging observations (to identify putative host galaxies). Fast transients lie in the least explored regime observationally and are least likely to be ordinary (routine Ia or routine core collapse) supernovae. Moreover, as extensively discussed in §2. theoretical models for transients in the gap also predict short lifetimes.

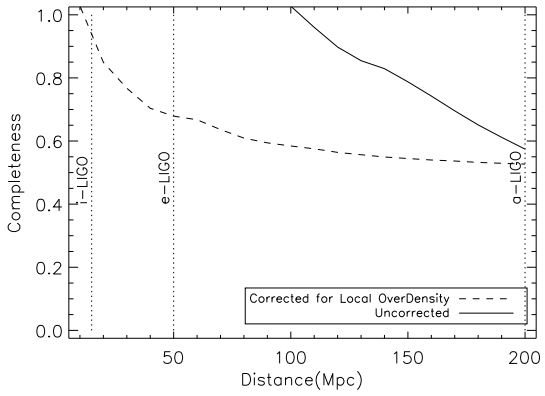

Fig. 5. Fraction of total theoretical light that is accounted for by galaxies in the catalog as a function of distance. A correction has been applied for the local overdensity by scaling the Schechter function by the observed luminosity brighter than L-star. This correction is applied every 10 Mpc and is a factor of three at 10 Mpc and one at 200 Mpc. From Kasliwal et al. 2009a, in prep.

7. PTF & MAXI

On Dec 13, 2008 PTF achieved first light. All indications are that the system is working as per specifications (except, as was determined in pre-commissioning lab tests, one of the twelve CCDs is dead; the effective solid angle is thus $7.79 \times 11/12 = 7.13$ square degrees). The on-sky performance will be reported shortly (Law et al. 2009).

The Japanese Space Station scientific module MAXI (Matsuoka et al. 2007) is expected to be in operational on the International Space Station (ISS) by May 2009. The field of view of MAXI is $2 \times 1.5 \times 160$ square degrees (Gas Slit Camera) and $2 \times 1 \times 90$ square degrees (Solid State Camera); the first factor of two refer to the horizontal and vertical sets. In one revolution period of ISS (about 91.3 minutes) almost 90% of the sky is scanned by the Gas Slit Camera system. For the minimum crossing time of 30 s, the 5-σ flux density is 7 mCrab $= 1.75 \times 10^{-10}\,erg\,cm^{-2}\,s^{-1}$ (2–10 keV band); see Ueno et al. (2004). We will refer to this as the one-orbit detection limit.

The MAXI one-orbit detection can be compared with the X-ray outburst of SN 2008D ($7 \times 10^{-10}\,erg\,cm^{-2}\,s^{-1}$; 0.3–10 keV band) and duration of 400 s (Soderberg et al. 2008). Clearly, MAXI is well positioned to detecting similar events out to 50 Mpc. The covering fraction of

*6 A long term goal of PTF is to comprehensively the sky for star-forming galaxies (through narrow band filter survey) and improve the completeness and thus increase the yield of the transients in the local Universe.

MAXI for such events is small, 0.006. Using Table 2 one such event is expected over a 5-year lifetime of MAXI.

Separately, the 5-σ luminosity at a distance of 50 Mpc is $5 \times 10^{43}\,\mathrm{erg\,s^{-1}}$ (1-orbit) and $5 \times 10^{42}\,\mathrm{erg\,s^{-1}}$ (100-orbit). Nearby versions of the slow transient SCP 06F6 (§4.), assuming that the prototype was located at a cosmological distance of $z \sim 0.1$ or about 400 Mpc, will be detected by MAXI. As can be gathered from Table 2 all events with a rate of few percent of the SN rate (Ia or core-collapse) should be seen by PTF.

The basic approach of our key project (correlating the position of transients to the catalog of nearby galaxies) is well suited to the 0.1-degree localization of MAXI. The nearly complete sky coverage of MAXI (every ISS orbit) and the expected rapid transmission of the data (Matsuoka et al. 2007) means that we will have nearly contemporaneous X-ray coverage. The detection of X-ray flux provides a critical discriminant between thermal and non-thermal/highly shocked sources. We eagerly await the launch of MAXI!

The program discussed here is the thesis topic of the second author. This program has benefitted from discussions and collaborations with L. Bildsten, E. Sterl Phinney & Lin-Qin Wen. We thank Eran Ofek for comments.

References

Arnett D. 1996, Supernova and Nucleosynthesis (Princeton University Press)
Barbary K. et al. 2008, ApJ, accepted, arXiv:0809:1648
Bildsten L. et al. 2007, ApJ, 662, 95
Bloom. J.S. et al. 2006, ASPC, 351, 751
Bond, H. E. 2009, astroph, arXiv:090.0198
Cenko S.B. et al. 2006, PASP, 118, 1396
Della Valle M. & Livio 1995, ApJ, 452, 704
Downes R.A. & Duerbeck 2000, AJ, 120, 2007
Drake, A. et al. 2008, astro-ph, arXiv:0809.1394
Fryer C. et al. 2007, ApJ, 662, 55
Gänsicke B.T. et al. 2008, ApJL, accepted, arXiv:0809:2562
Kasliwal, M. et al. 2008, ApJ
Kochanek, C. et al. 2008, ApJ, 684, 1336
Kulkarni S.R. 2005, astro-ph/0510256
Kulkarni, S. R. & Rau, A. 2006, ApJ, 644, L63
Kulkarni S.R. et al. 2007, Nature, 447, 458
Law, N. et al. 2009, in prep.
Li L. & Paczynski, B. 1998, ApJ, 507, 59
Matsuoka M. et al. 2007, SPIE, 6686, 32
Metzger B. et al. 2008, MNRAS, submitted, arXiv:0812:3656
PAO, Pierre Auger Observatory, http://www.auger.org
Padmanabhan P. 2000, Theoretical Astrophysics (Cambridge University Press)
Perets, H. et al. 2009, in prep.
Perlmutter S. et al. 1999, ApJ, 517, 565
Phillips M.M. et al. 1999, AJ, 118, 1766
Prieto, J. L. et al. 2008, ApJ, 681, L9
Rahmer, G. et al. 2008, SPIE, 7014, 163
Rau, A. et al. 2006, ApJ, 664, 474
Rau, A. et al. 2006, A&A, 449, 79
Rau A. et al. 2008b, PASP, submitted
Rau A. et al. 2008, ApJ, 682, 1205
Reiss A.G. et al. 1998, AJ, 116, 2009
Smith N. et al. 2007, ApJ, 671, L17
Smith N. et al. 2008, ApJL, submitted, arXiv:0811:3929
Soderberg A.M. et al. 2008, Nature, 453, 469
Soker N. et al. 2008, New Astronomy, submitted, arXiv:0812:1402
Thomspon T.A. et al. 2008, ApJ, submitted, arXiv:0809:0510
Ueno, S. et al. 2004, SPIE, 5488, 197
van den Heuvel E.P.J. 2008, Nature, 451, 775

Suzaku-WAM soft gamma-ray all-sky monitor by the earth occultation technique

C.Kira[1], Y.Fukazawa[1], T.Asano[1], T.Takahashi[1], T.Uehara[1], Y.Hanabata[1], H.Takahashi[1], K.Yamaoka[2], M.Tashiro[3], Y.Terada[3], T.Tamagawa[4], K.Makishima[4,5], K.Nakazawa[5], M.Ohno[6], T.Takahashi[6], M.Kokubun[6], and HXD-WAM team

[1] Hiroshima Univ., [2]Aoyama Gakuin Univ., [3]Saitama Univ.
[4]RIKEN, [5]Univ. of Tokyo, [6]ISAS/JAXA
E-mail(CK): kira@hep01.hepl.hiroshima-u.ac.jp

Abstract

Suzaku-WAM has detected many gamma-ray bursts and solar flares. In addition, thanks to its large field of view, WAM is able to monitor the bright soft gamma-ray sources by the earth occultation technique, as CGRO-BATSE. We have constructed the analysis system of the WAM earth occultation, performed calibration by using spectra of the Crab nebula, and then found that the response uncertainty is around 10–20%. As a result, WAM is an important all-sky monitor in 50keV–1MeV band. This is unique against the RXTE/ASM (1–10keV) and Swift/BAT (10–100keV). Here, we introduce the analysis process, Crab calibration, and preliminary results on the Galactic black hole binaries and AGNs.

Key words: workshop: soft gamma-ray — black hole binary — Suzaku-WAM — earth occultation

1. Introduction

It is believed that most of black holes are accompanied by jets. So as to investigate the mechanism of jet emission, it is important to study non-thermal components of jet origin in soft gamma-ray region. However, still the soft gamma-ray emission from black holes is not well understood. In low/hard state, is there a non-thermal component or 511keV line associated with the jet emission beyond the normal thermal-Compton components? In high/soft state, where is a cut-off for the power-law component? How about very high state? In order to give an answer to these questions, it is essential to study spectral changes at the state transition. Hence, it is very important to monitor black holes continuously, especially in several 100 keV bands, and catch the state transition. Here we introduce the Suzaku-WAM soft gamma-ray all-sky monitor by the earth occultation technique, and show preliminary results on the black hole binaries and AGNs.

2. WAM (Wide-band All-sky Monitor)

Suzaku-WAM (Wideband All-sky Monitor) is active shield of the HXD (Hard X-ray Detector) constructed from thick BGO scintillaters and photomultipliers (Fig.1; Yamaoka et al. 2009, PASJ in press). It surrounds four sides of HXD, and each side is called WAM0, WAM1, WAM2, and WAM3. WAM is also a detector with very large field of view (2π str), wide energy range (50–5000 keV), and large effective area (800 cm^2) to observe many gamma-ray bursts, soft gamma-ray repeaters, and solar flares. In addition, thanks to its large field of view, WAM can monitor bright soft gamma-ray sources of at least 50 mCrab with the earth occultation technique, as CGRO-BATSE (Ling et al. 2000, ApJS 127, 79). Current all-sky monitors are RXTE-ASM (1.5–12 keV) and Swift-BAT (15–150 keV). WAM is unique against such monitors for its high energy band, and enables us to monitor objects in wide energy band from 1keV to 600keV, by utilizing these three instruments. This is a great advantage to observe the hard tail of black hole binaries and search non-thermal components or 511keV line associated with

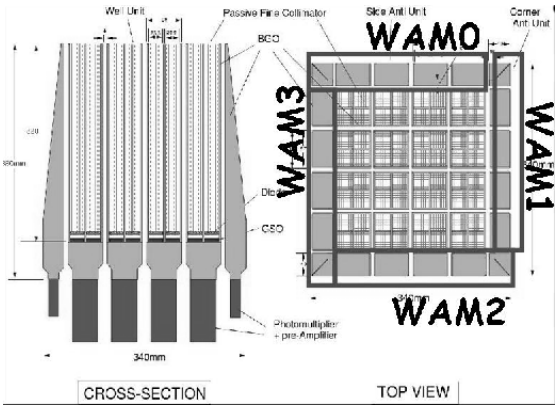

Fig. 1. Overview of Suzaku-WAM

the jet ejection.

3. Analysis Procedure

3.1. Calculate Occultation Time

At first, we selected the observations in which the incident angle of a target object to each WAM detector is smaller than 50 degrees, and calculate the time of occultation from target position and satellite orbit. There are about 15 occultations in one day, and each occultation is recognized by two steps of count rate at the begin and end of the occultation in the light curve. Fig.2 is an example of earth occultation of the Crab.

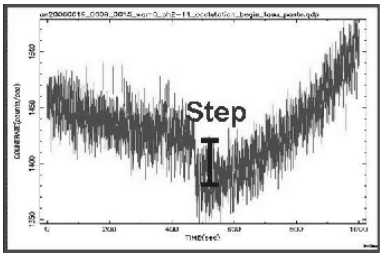

Fig. 2. Example of earth occultation step of the Crab

3.2. Extract Occultation Light Curve

We analyzed Suzaku-WAM TRN-data. TRN-data are light curves of 55 energy channels with a time resolution of 1 sec. Here, we treated the light curves of 1–27 ch in 50–1000 keV, and extracted the light curve before/after 500 sec for each occultation in each energy channel.

3.3. Sum over Light Curves

Since the earth occultation time calculated above is obtained without considering the atmospheric absorption, we must correct it before summing over the occultation light curves. The effect of atmosphere depends on the object track on the earth, seen from the satellite. Therefore, we obtained the relation between the real time of occultation and the duration of occultation. Using the obtained relation, we corrected the time from the duration of predicted occultation. We used only the data whose occultation duration time is longer than 1200 sec. We eliminated the occultation light curves containing SAA, background high-rate period, and calibration mode, and summing over the occultation light curves in one observation, one month, or three years for each energy channel to increase the statistics. WAM2 data are not in use because of its large calibration uncertainty

3.4. Quantify Occultation Step Count Rate

We fitted an occultation light curve in each energy channel by an appropriate function to quantify the step count rate (Fig.3). Here, occultation light curves at the begin and end are simultaneously fitted with the same step

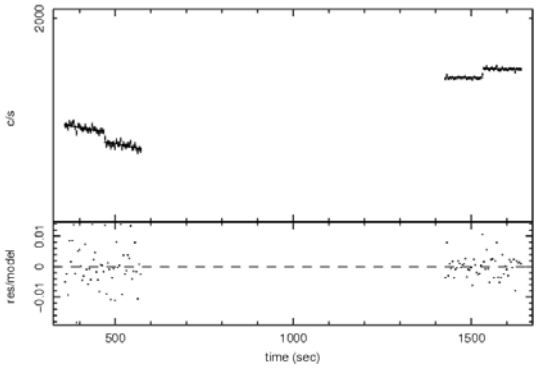

Fig. 3. Example of fitting earth occultation step of the Crab

count rate. We derived the spectrum of the object from the step count rates in each energy channel.

3.5. Calculate the Response Function

We calculated the response functions from the incident direction of the object to the WAM. The response is created for one observation, during which incident direction is the same. In the case of the occultation light curves summing over one month or three years, we averaged the responses too, weighted by number of occultations in each observation.

4. Current detection uncertainty

Detection is almost limited by the photon statistics of background events. We analyzed the step count rate of 11 dark objects for WAM in the same method as above, and derived the systematic uncertainty of detection by estimating the variance of the obtained step count rates for these dark objects(Fig.4).

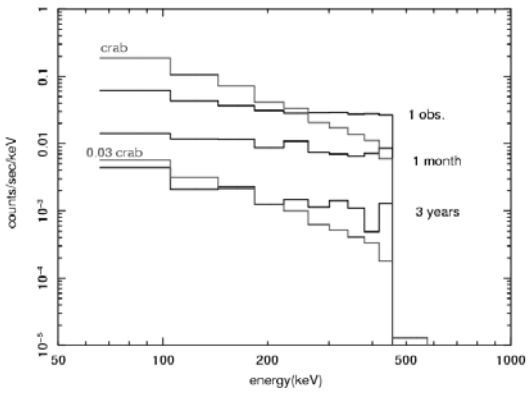

Fig. 4. Current detection uncertainty

Three-year integration gives systematic errors of 0.03 Crab at 100 keV. However, the analysis procedure is not yet polished well, and therefore the uncertainty is currently somewhat worse than the above.

5. Calibration by the Crab

The incident direction varies with the satellite attitude, and the WAM response function strongly depends on the incident direction due to the surrounding satellite body and other instruments. Therefore, we first calibrated the response function by the Crab for various incident directions. As shown in Fig.4, in three-year integration, Crab can be detected up to 300 keV in one observation integration, during which the satellite attitude is the same.

We fitted the spectrum of each observation by power-law model with a photon index fixed to 2.1, and obtained the flux in 100-800keV. We confirmed that the flux does not depend on the elapsed time from launch. On the other hand, it is significant that the flux depends on the incident angle to each WAM detector above 60 degrees. The flux obtained by WAM1 add WAM3 is found to be systematically different from that of WAM0 by several tens %, and thus we corrected the difference.

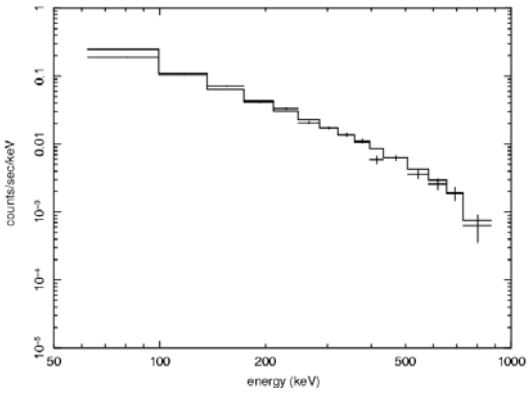

Fig. 5. Averaged spectrum of the Crab in three-year integration

In three-year integration, it can be detected up to 800 keV (Fig.5). The spectrum is well fitted by power-law model with a photon index of 2.1 and flux of 1.1×10^{-8} erg/sec/cm^2 (100–500 keV) with a 30% uncertainty. These are consistent with the INTEGRAL results (Sizun et al. 2004, astro-ph/0406052, Proc. of the 5th INTEGRAL Workshop).

6. Preliminary Results

6.1. Long-term Light Curve of Cyg X-1

The long-term light curve in one observation integration of Cyg X-1 is successfully obtained in 100–600 keV with WAM as shown in Fig.6. Together with light curves of RXTE-ASM and Swift-BAT, we can clearly see the different behavior between them. Noticeably, the bright phase in 2006 September (MJD≃53400) is coincident with a high energy gamma-ray detection at 0.1–1 TeV energies by MAGIC telescope (Albert et al. 2007, ApJ, 665, L51). This event was also reported by RXTE-ASM, Swift-BAT and INTEGRAL-IBIS and SPI (Malzac et al.

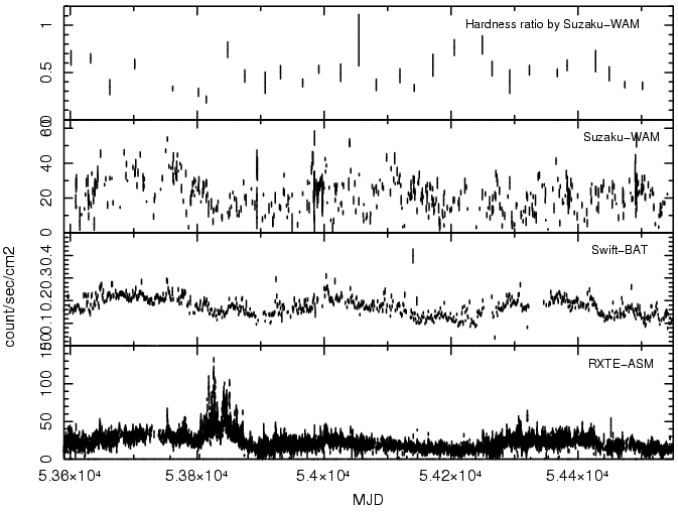

Fig. 6. Long-term light curve of Cyg X-1

2008, astro-ph/0805.4391v1). The next noticeable is a dark phase above 10 keV against a bright flare in 2006 April–May (MJD≃53830). Although there is no report that Cyg X-1 became high state in this period, it shows a typical high state feature.

6.2. Spectra of Cyg X-1 at Various Epochs

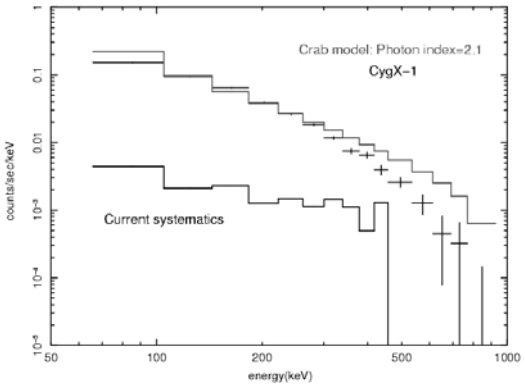

Fig. 7. Averaged spectrum of Cyg X-1 in three-year integration

Fig.7 shows the average spectrum in three-year integration of Cyg X-1, compared with the spectrum of the Crab with a photon index of 2.1. High energy cut-off is clearly seen. It is well fitted by cut-off power-law model with a photon index of 1.5 and a cut-off at 200 keV.

Time resolved spectra can be obtained up to 400–500 keV in each month as shown in Fig.8–11. Thus we can trace a spectral change of Cyg X-1. Fig.8 is a period during which Cyg X-1 seems like a high state in 2006 April (MJD≃53830), Fig.9 is a period of TeV gamma-ray flare in 2006 September (MJD≃53400), Fig.10 is a period of soft gamma-ray flare in 2007 Augast(MJD≃54300 ; Golenetskii et al. 2007, GCN CIRCULAR 6745), and

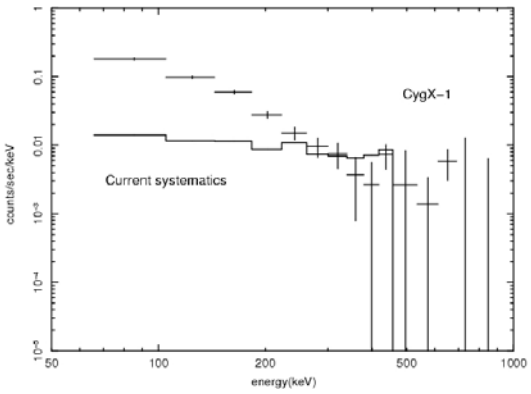

Fig. 8. Spectrum of Cyg X-1 (20060319–20060407)

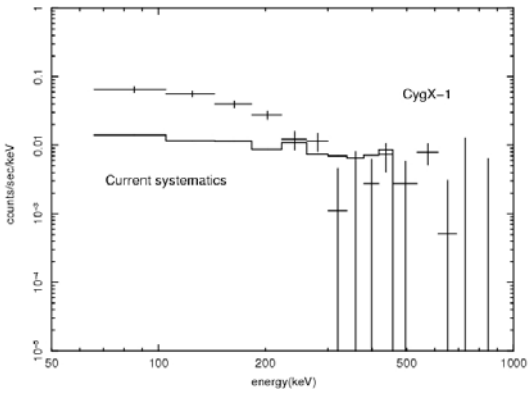

Fig. 10. Spectrum of Cyg X-1 (20070711–20070808)

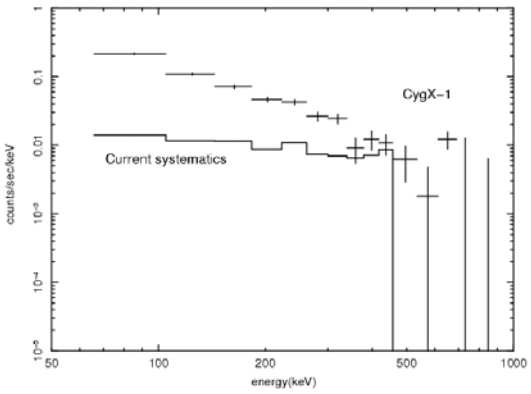

Fig. 9. Spectrum of Cyg X-1 (20060913–20061010)

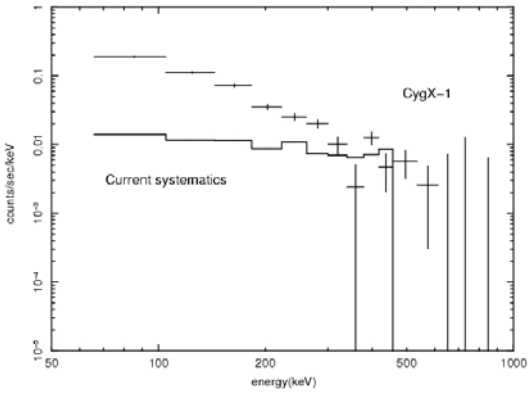

Fig. 11. Spectrum of Cyg X-1 (20080108–20080203)

Fig.11 is a period during which the flux is at the average level in 2008 January (MJD≃54480). Compared with Fig.11 or averaged spectrum (Fig.7), the spectrum in high-state-like period seems softer and that in the TeV flare period is harder.

6.3. Other Sources

We obtained a monthly light curve and spectrum of GRS 1915+105 as shown in Fig.12. While the count rate of Swift is almost the half of Cyg X-1, the flux above 100 keV is much smaller for GRS 1915+105, although the detection is significant. During the normal hard state before MJD≃54250, GRS 1915+105 was continuously detected. After entering the soft state, the detection becomes difficult. During the soft state, several outbursts occurred, and WAM detected one of them at 0.5 Crab level around MJD≃54380.

Fig.13 shows the average spectrum of GRS 1915+105 in three-year integration. It is detected up to 300 keV, and the photon index is around 2. Fig.14 shows the spectrum at the outburst at MJD≃54380. Even in only one-month integration, it is detected up to 300 keV. The spectral shape is not so different from the average. Other black hole binaries are also detected, such as GX 339-4, together with AGNs such as Cen A and NGC 4151.

References

Albert et al. 2007, ApJ, 665, L51
Golenetskii et al. 2007, GCN CIRCULAR 6745
Ling et al. 2000, ApJS 127, 79
Malzac et al. 2008, astro-ph/0805.4391v1
Sizun et al. 2004, astro-ph/0406052, Proc. of the 5th INTEGRAL Workshop
Yamaoka et al. 2009, PASJ in perss

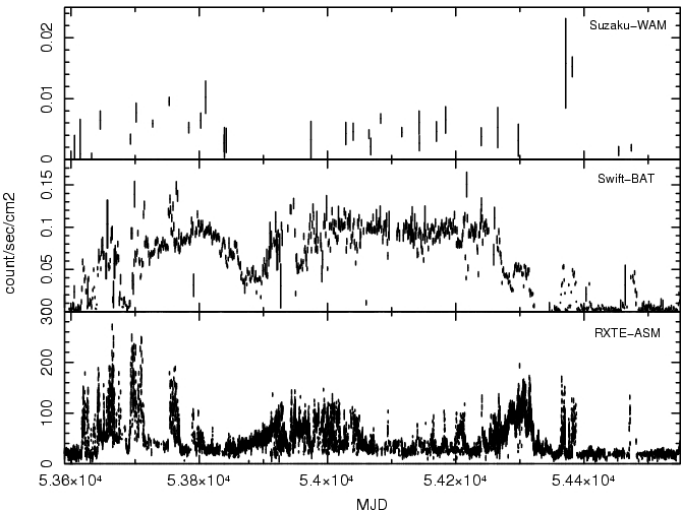

Fig. 12. Monthly light curve of GRS 1915+105

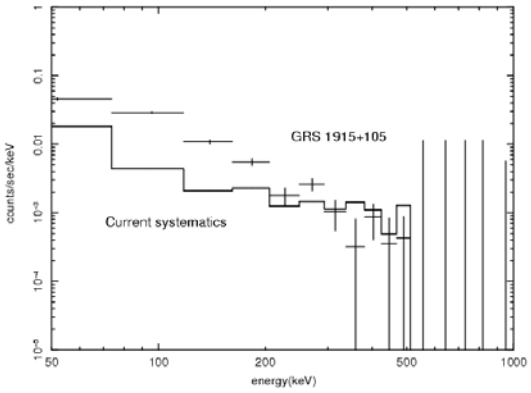

Fig. 13. Averaged spectrum of GRS 1915+105 in theree-year integration

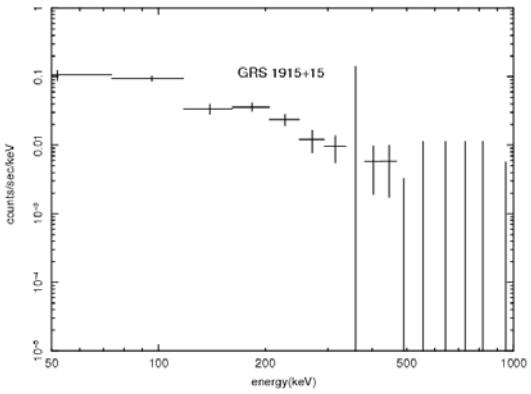

Fig. 14. Spectrum of GRS 1915+105 at flare period on MJD 54380

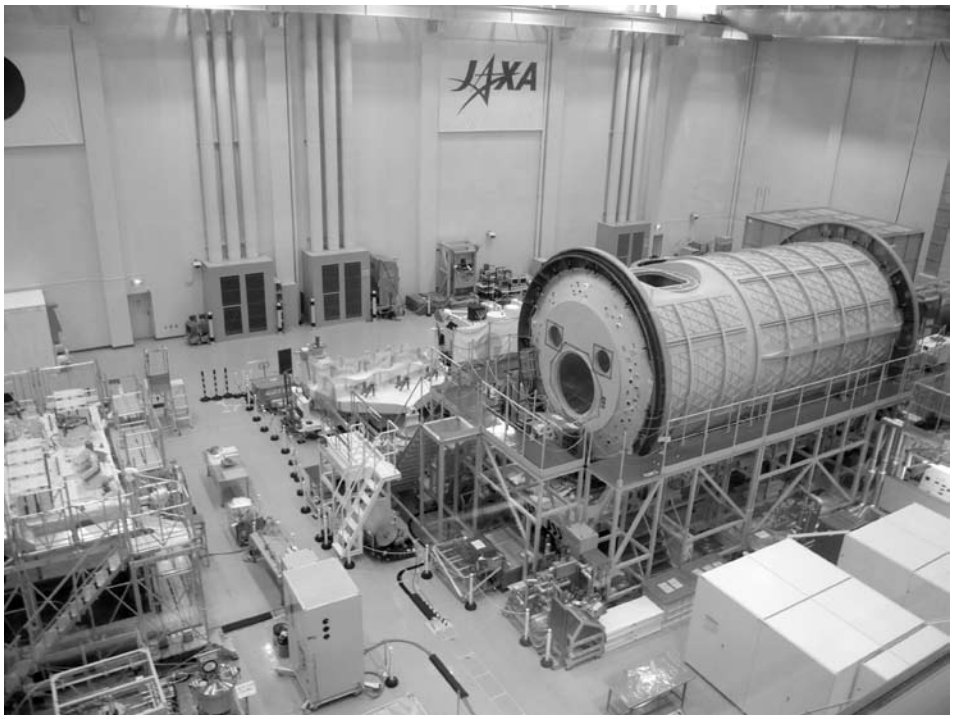

Optical—Infrared Observation of Astronomical Transients with the "KANATA" 1.5-m Telescope

Uemura, M.,[1] and the KANATA team

[1] Astrophysical Science Center, Hiroshima University, Kagamiyama 1-3-1, Higashi-Hiroshima, 739-8526, Japan
E-mail(MU): uemuram@hiroshima-u.ac.jp

Abstract

In the last decade, studies of astronomical transient phenomena entered a new era, in which we can promptly receive and send the information about transients and variables. On the other hand, large ground-based telescopes can provide only few observation times for them, which is insufficient to perform dense and long monitorings of transients. Here, we introduce our new observatory and telescope, which are developed exclusively for studies of various kinds of transients. Our 1.5-m telescope "KANATA" was installed at Higashi-Hiroshima Observatory in May 2006. We can study transients in near-infrared wavelengths, with polarimetry, and with high-speed photometry. These observation modes have revealed several new features of our targets, such as gamma-ray bursts, blazars, X-ray binaries, supernovae, and cataclysmic variables.

Key words: infrared:general — polarization — telescopes

1. Introduction

Astronomical transient phenomena have received much attention since ancient times. The situation of observations of them has recently experienced a revolution led by the development of the Internet. We can now send the information of variables and transients to general public, immediately receive them, and quickly start observations. On the other hand, the revolution was, in general, applied only to observations with small, 30-cm class telescopes, since only few observation times were allowed for transients in large telescopes. Most recently, however, the situation has been changing. Due to the growing number of > 3 m class telescopes, 1-m class telescopes are now regarded as "small" ones, having a plenty of flexible observation times. They have a great potential for observations of transients.

Here, we introduce our project, "Higashi-Hiroshima Observatory". We moved a 1.5-m telescope installed in Tokyo in 1995 by National Astronomical Observatory of Japan to Hiroshima, and rebuilt its driving system. In 2006 May, our new observatory opened, and the telescope was named "KANATA" (having a meaning of "far away"). KANATA is the telescope dedicated for astronomical transients. Owing to a plenty of observation times and an easy access to the observatory (20-min by car from our office), we have obtained several results for γ-ray bursts (GRBs), blazars, supernovae, X-ray binaries, cataclysmic variables, and others, which are shown below.

2. "KANATA" and Instruments

As a 1-m class telescope, KANATA is one of standard systems, having Ritchey-Chretien optics and three available focuses (one Cassegrain and two Nasmith), except for its high driving speed. The azimuth and altitude driving speeds are 5° and $2^\circ\,\mathrm{s}^{-1}$, respectively. This high motion is required to obtain very early light curves of GRBs and their afterglows.

At the Cassegrain focus, TRISPEC, developed by Nagoya University, is currently attached to KANATA (Watanabe et al. 2005). In TRISPEC, the incident light is divided into optical (0.45—0.90 μm) and two infrared lights (0.90—1.85 and 1.85—2.5 μm) by two dichroic mirrors. Each path has wheels including grisms and Wollaston prisms. As a result, TRISPEC works as a simultaneous optical and near-infrared imager, spectrograph, and polarimeter.

There are still only few observatory which can monitor variables in the near-infrared region, although it provides an important information for objects showing dust formation episodes and jets, for example, classical novae, blazars, and microquasars. Figure 1 shows the K_s-band light curve of a famous microquasar GRS 1915+105 obtained with TRISPEC/KANATA. Between JD 2454350 and 2454550, we can see a previously-unknown anti-correlation between the infrared and X-ray fluxes. During this period, the object was in its soft X-ray state. We consider that the infrared emission originated from the thermal accretion disk, which occasionally disappeared

or weakened when X-ray flares occured (Arai et al. 2008, in prep)

As well as infrared observations, polarimetric observations were also desired for transients and variables, for example, showing anisotropic explosions and synchrotron jets. Figure 2 shows the light curve and the temporal evolution of polarization parameters on the Stokes $Q-U$ plane of a blazar 3C 454.3, obtained with TRISPEC/KANATA. The polarization vector experienced clockwise rotation around the maximum of the giant flare in JD 2454300—2454350, as can be see in figure 2. Between JD 2454370 and 2454500, the object experienced repetitive short flares superimposed on a gradually brightening trend. On the $Q-U$ plane, we can see that these short flares have their specific polarization vectors, and furthermore, their vector was apparently rotating anticlockwise with time. These episodes of the rotation of the polarization vector may indicate a moving of the emitting region through a helical magnetic field in a jet (Sasada et al. 2008, in prep).

At the 1st Nasmith focus of KANATA, High Speed Camera is attached, as a collaboration with the Kyoto University team. It has a frame transfer CCD chip, enabling the fastest time-resolution of 0.03 s. We use this camera for X-ray binaries and cataclysmic variables, in which the gas rapidly rotates around compact objects. Its spectroscopic mode is now under development.

For the 2nd Nasmith focus, we are now developing a new instrument, "HOWPol" (Hiroshima One-shot Wide-field Polarimeter), which focuses on rapid variations of polarizations. The engineering first-light of HOWPol was performed in July 2008. A new infrared—optical camera is also under development. It will be the instrument to be replaced with TRISPEC.

3. Summary and Future Plan

KANATA can provide unique data of transients, in terms of infrared, polarimetric, and high speed observations. These observation modes, in particular, can be a great tool for studies of jet sources, as shown in figure 1 and 2. From August 2008, we are planning to perform observational campaign for blazars, collaborating with the *Fermi* satellite. Preliminary results of blazars and other transients are reported in our web site[1]

This work was partly supported by a Grand-in-Aid from the Ministry of Education, Culture, Sports, Science, and Technology of Japan (19740104).

References

Watanabe, M. et al., 2005, PASP, 117, 870

*1 http://kanatatmp.blogspot.com/

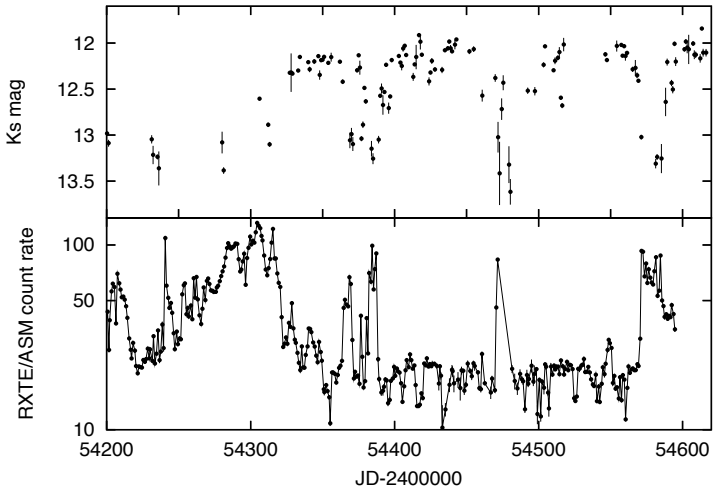

Fig. 1. K_s-band (upper panel) and X-ray (lower panel) light curves of GRS 1915+105..

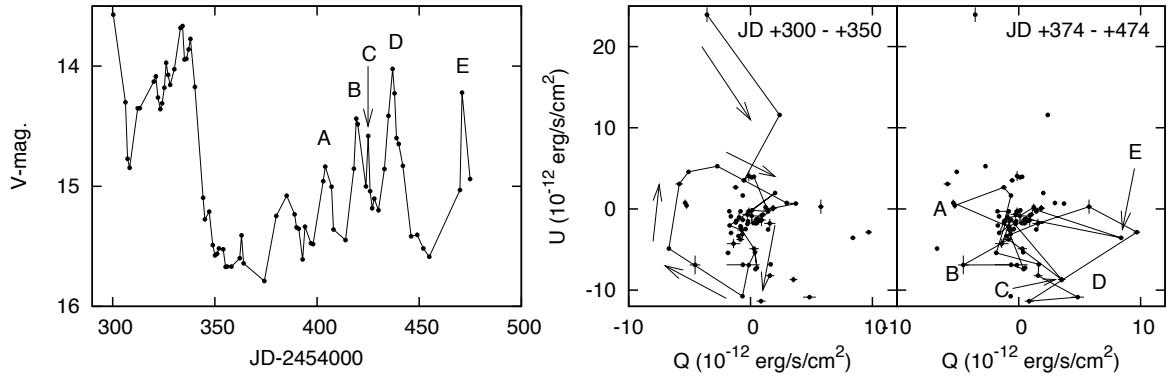

Fig. 2. (Left panel) Light curve of 3C 454.3 in 2007. (Middle and Right panels) Temporal variations of the polarization parameters on $Q-U$ plane. The directions of QU are not corrected to the standard north-east ones.

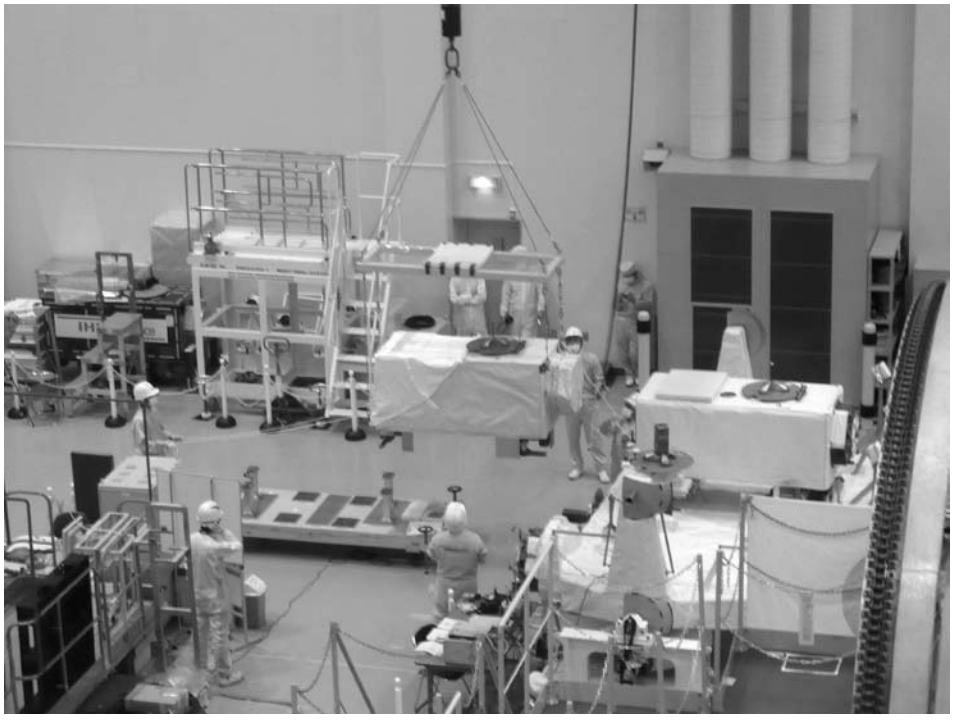

Optical Follow-up Observations of Transient Sources at Gunma Astronomical Observatory

Kinugasa,K.,[1] Hashimoto,O.,[1] Honda,S.,[1] Takahashi,H.,[1]
Taguchi,H.,[1] Nishihara,E.[1], and the GAO staff

[1] Gunma Astronomical Observatory, Takayama, Gunma, Japan
E-mail(KK): kinugasa@astron.pref.gunma.jp

Abstract

Gunma Astronomical Observatory (GAO) is a public observational facility founded in 1999 by Gunma Prefecture local government. GAO has a 1.5-m reflector, a 65-cm reflector, and other small telescopes. Moreover, there are some powerful instruments prepared for the 150 cm telescope such as a near infrared camera/spectrograph, a high resolution spectrograph and a low resolution spectrograph and imager for optical wavelength. The observatory is designed for both astronomical research and public use. We can flexibly operate it as an independent observatory, allowing us to observe time-limited transient sources. We proceed with optical follow-up observations of gamma-ray bursts, supernovae, and other variable objects and cooperate with some multi-wavelength observation campaigns of SS 433, GRS 1915+105 and so on. We introduce some GAO facilities and some scientific results from the optical follow-up observations of transient sources. We can carry out follow-up observations for new transient sources discovered by MAXI.

Key words: telescopes: instruments — transients: optical — follow-up

1. Gunma Astronomical Observatory and Its Facilities

Gunma Astronomical Observatory (GAO) was established by Gunma Prefectual local government in 1999. It is located in Takayama village about 140 km northwest of Tokyo (Lat. 36° 35′ 37″ N, Long. 138° 58′ 35″ E, and Alt. 885 m). It has many fine days in winter, but not so good in summer season. This observatory is designed for both astronomical research and public use. We have a 1.5-m reflector as its main telescope, as well as a 65-cm reflector and other small telescopes. Moreover, some powerful observational instruments are equipped on the telescopes. Characteristics of the telescopes and the instruments are summarized below.

1.1. 1.5-m telescope and its instruments

The main telescope of GAO is a 1.5-m reflector on an alt-azimuth mounting which provides pointing and tracking accuracies about 3.0" and 0.7", respectively. The telescope is the Ritchy-Chritien type reflector with F-ratio of 12.2. There are some powerful instruments attached to the telescopes, such as Gunma Infrared Camera and Spectrograph (GIRCS), GAO Echelle Spectrograph (GAOES) and Gunma LOW resolution Spectrograph and imager (GLOWS).

GIRCS is an infrared camera and spectrograph attached on the Cassegrain focus of the 1.5-m telescope. With an 1,024 × 1,024 pixels HgCdTe array (HAWAII), it covers a field of 6.8′ × 6.8′ with a spatial resolution of 0.4 "/pixel. The limiting magnitudes are 17.7 mag in J, 16.9 mag in H, and 16.3 mag in K_s with S/N=10 at 9 min exposure. A spectrograph mode with grisms can be used for J, H, K-bands with a spectral resolution of about 1,000.

GAOES is a high resolution spectrograph with an echelle grating set on the Nasmyth focus of the telescope. It provides an optical spectrum with spectral resolution up to 100,000 for a wavelength coverage of 360–1,000 nm. The whole optical system is enclosed in a vacuum chamber in order to avoid thermal instability and air turbulence in the optical system. The limiting magnitude is about 10 mag which is limitted by slit-viewer of GAOES.

GLOWS is an optical low-resolution spectrograph and imager on the bent-Cassegrain focus. It covers a field of 10.7′ × 11.7′ with a resolution of 0.56"/pixel using Andor DW432, an 1,152 × 1,250 pixels back-illuminated CCD camera, which cools down to − 70 degC controlled by electronics. It can be used as a grism spectrograph with a spectral resolution of 400-500 for wavelengths of 400-800 nm. Limiting magnitude of the spectrograph is about 17 mag with S/N=30 at 30 minutes exposure. It is useful for quick or time-critical observations of transient objects such as gamma-ray bursts (GRBs), supernovae (SNe), and novae.

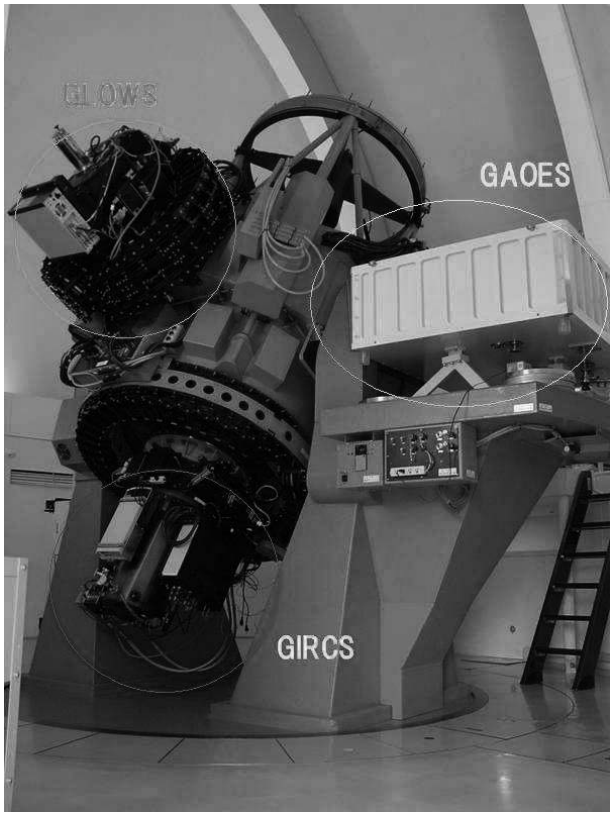

Fig. 1. 1.5-m reflector of GAO

1.2. 65-cm telescope and GETS telescope

Besides the 1.5-m telescope, we have a 65-cm telescope and other small telescopes.

The 65-cm telescope is the Cassegrain type reflector with F-ratio of 12. Some instruments can be attached on the classical Cassegrain focus of the telescope. One of them is Gunma Compact Spectrograph (GCS), which is an optical low-resolution spectrograph with a resolution of 500 or 2000. Others are optical imaging CCD cameras, such as Apogee Alta U6, which covers a field of $10' \times 10'$.

GETS (Gunma Experiment of optical Transient Search) is a robotic system which consists of a 25-cm robotic telescope and its enclosure. It can automatically point the telescope at GRBs following GCN (GRB Coordinate Network) alerts. The telescope is Meade LX200, a Schmidt-Cassegrain type with F-ratio of 6.3. Using CCD camera Apogee Alta U6, it covers a field of $50' \times 50'$. It mainly provides with sequential optical photometry for GRBs, dwarf novae, and so on.

There are other small telescopes with a diameter of 25-30 cm settled in sliding roof, which are mainly used by amateur astronomers.

Fig. 2. GETS consists of a 25 cm Schmidt-Cassegrain telescope and its enclosure.

2. Optical Follow-up Observations

GAO is designed not only for an astronomical research but also public education and popularization for astronomy. On the basis of the latter point of view, we must spare machine time of the telescopes for public star gazing in the evening. On the other hand, there are some definite advantages as well in the view of scientific research. Since GAO is operated independently from open use, we can make a flexible time allocation for ourselves to focus original scientific subjects. Take advantages of this point, we can carry out "time-critical" observations for transient sources. In this section, we describe some results from optical follow-up observations at GAO.

2.1. Gamma-ray bursts

We proceed with follow-up observations of GRB afterglows with a trigger of GCN alerts from Swift and INTEGRAL satellites. We mainly perform optical or infrared photometric observations with GETS and the 1.5-m telescope equipped with GLOWS or GIRCS. At first, we tried to observe an afterglow of GRB 011212. Since then, we have reported 21 observation results in GCN Circulars.

For GRB 030329, the monster GRB associated SN 2003dh, we intensively performed the follow-up observations with many instruments of GAO under a poor weather condition. We carried out infrared photometry with the 1.5-m telescope and GIRCS, optical photometry with GETS, and optical spectroscopy with the 65-cm telescope and GCS. As the results, we obtained optical-infrared light curve and SED in the early phase (Torii et al. 2003; Nishihara et al. in prep.). Early SED evolution of GRB 030329 is shown in figure 3.

For GRB 041006, we performed optical and infrared photometry with GETS and the 1.5-m telescope equipped with GIRCS. Obtained early optical and in-

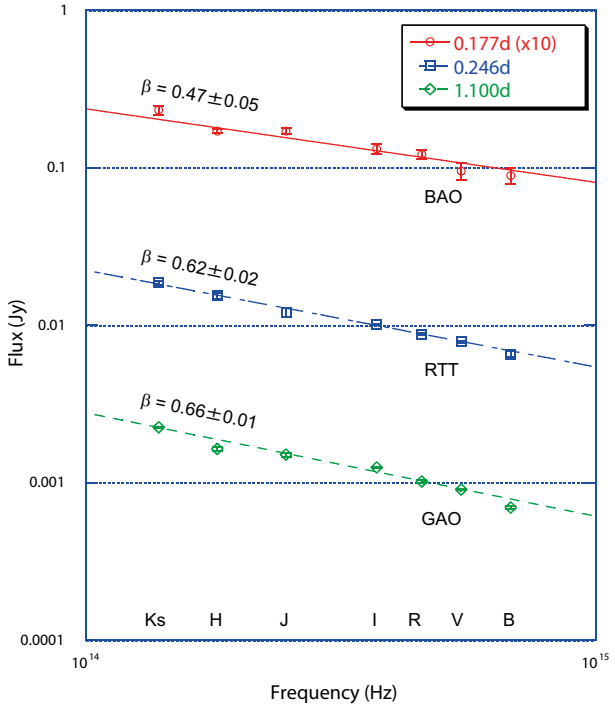

Fig. 3. The early Opt.-IR SED of GRB 030329 obtained with GAO, Bisei Astronomical Observatory, and RTT150 (Burenin et al. 2003).

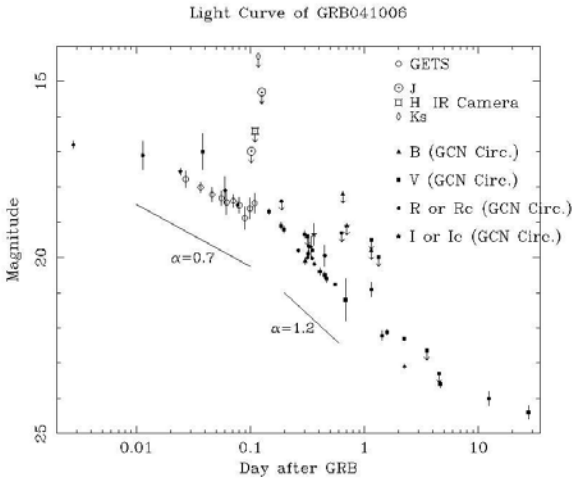

Fig. 4. The early light curve of GRB 041006 obtained with GAO and GCN Circ.

Fig. 5. M74 images before (left panel) and after (right panel) the appearance of SN 2002ap. The SN is marked with a dash line on light panel.

frared light curve is shown in figure 4.

Moreover, we caught an optical afterglow of GRB 060927, which is the second highest redshift GRB ever discovered (z∼5.47; Ruiz-Velasco et al. 2007). We started about 37 minutes after the burst with GLOWS attached on the 1.5-m telescope and detected it to be R∼ 20 mag. Even the high redshift GRB can be detected with small to middle-size telescopes if we can observe soon after the burst.

2.2. Supernovae

We proceed with the earliest spectroscopy program of relatively bright supernovae with GLOWS attached on the 1.5-m telescope and GCS on the 65-cm telescope. The objective is the early identification of the important events such as hypernovae according to spectroscopic observations to follow the discovery reports of IAU circular (IAUC) and CBET. We have reported 11 earliest observation results on the IAUC/CBET. If the target is important and enough bright to observe with our facilities, we will carry out continuous spectroscopic observations to trace the SN evolutions.

For example, we tried spectroscopic observations for SN 2002ap, which is a broad line SN Ic, so called hypernovae, with the 65-cm telescope and GCS to follow the discovery report (Nakano et al. 2002). We found a broad-line SN Ic feature from the obtained spectrum and reported these results as soon as possible (Kinugasa et al. 2002a). Our report was a trigger of much observations with larger telescopes in the world. As the results, many observation reports has been published so far. Therefore, SN 2002ap could be a very important event to study a connection between SN and GRB, although it was not accompanied with GRB. Moreover, the following sequential spectroscopic observations at GAO could reveal the early evolution and a variety of hypernovae (Kinugasa et al. 2002b). The image and spectral evolution of SN 2002ap in the early phase are shown in figure 5 and 6, respectively.

2.3. Novae and Dwarf Novae

In the same way as SNe, spectroscopic observations of novae and dwarf novae, have been performed to follow IAUC, CBET and VSNET. We can confirm and determine whether an observed object is a nova or a dwarf nova, and whether it is a FeII type or a He/N type nova.

Especially, we pay attention for WZ Sge-type dwarf novae, which is a subclass of SU UMa type. Their features are the large outburst amplitude over 6 mag, and

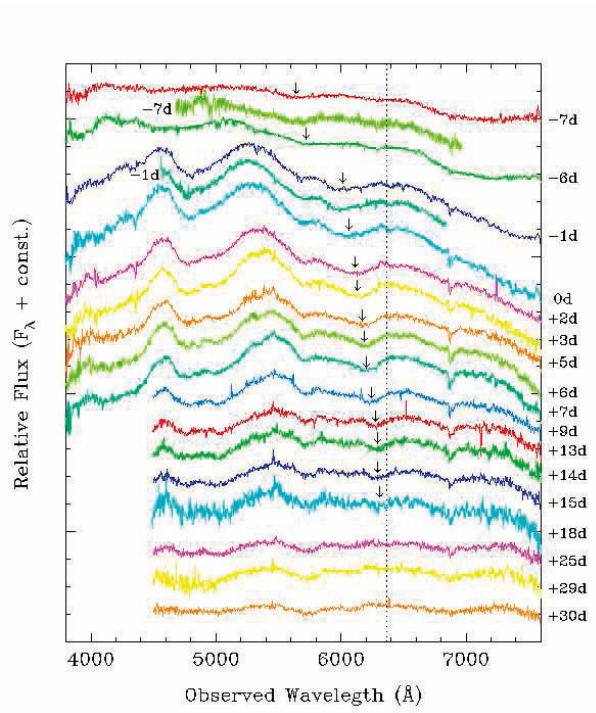

Fig. 6. Spectral evolution of SN 2002ap from -7 to +30 days relative to B-maximum. Arrows mark the absorption minima of SiII 6355. Dot line marks the rest wavelength of SiII (Kinugasa et al. 2002b).

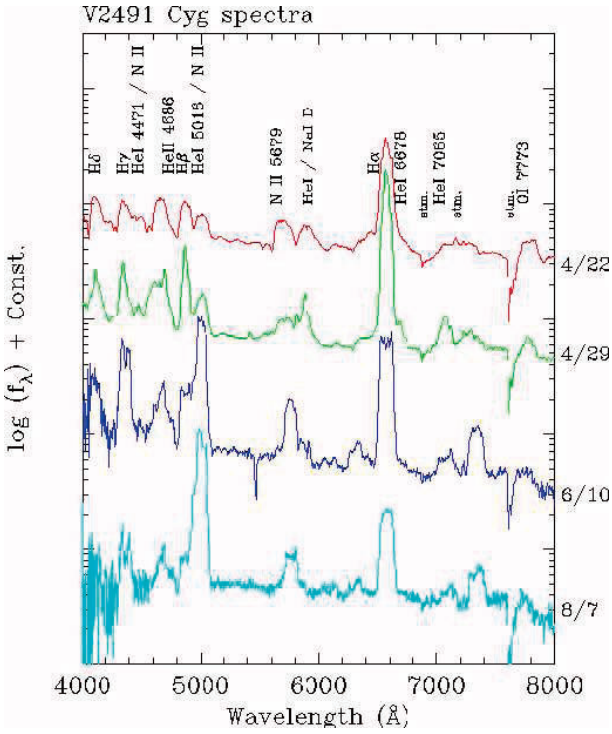

Fig. 7. Optical spectral evolution of V2491 Cyg in April to August 2008. Line identification and observed date are also shown.

the long recurrence cycle of the superoutburst (several year or more), and no (or few) normal outburst. These peculiar mechanisms are still in debate. We performed spectroscopic observations of two WZ Sge-type dwarf novae, GW Lib and V455 And, during their superoutbursts in 2007 (Nogami et al. 2008).

Recently, we also have interested in novae as soft X-ray emitters since these events sometimes has been observed by X-ray observatories, such as Swift and Suzaku. For example, we carried out the spectroscopic observations for V2491 Cyg, which was discovered in April 2008 (Nakano et al. 2008) and observed by Swift and Suzaku many times. These optical spectra obtained at GAO are shown in figure 7. The spectra clearly show prominent He emission lines at early phase. It is a He/N type nova.

We expect that SXC on board MAXI can discover these classical novae as soft X-ray emitters such as super soft sources. We will be able to perform spectroscopic observation of these targets with GLOWS attached on the 1.5-m telescope. These sources newly discovered by MAXI may be a new class of nova.

3. Cooperative Observations

Taking advantages of capability of the flexible time allocation from GAO operation, we can carry out not only follow-up observations but also some cooperative observations along with other facilities such as X-ray satellites.

3.1. SS 433

SS 433 is a microquasar with a precessing bipolar continuous jet with a velocity of 0.26c. Simultaneous optical spectroscopic observations along with X-ray satellites provide a precise direction of jets on the obtained X-ray data sets. Since it is important to study the jet physics, we performed spectroscopic observations when X-ray satellites observed SS 433 for several times.

So far, we carried out simultaneous observations along with ASCA in March – April 2000, Chandra in May and October 2001 (Namiki et al. 2003), and Suzaku in April 2006 (Kubota 2007). Moreover, in a flare of SS 433, the similar cooperative observations with XTE and RATAN-600 in November 2001 (Kotani et al. 2006) and December 2006 (Kotani et al. in prep.). The spectral variation of SS 433 during Suzaku observation campaign 2006 is shown in figure 8. These spectra clearly show moving Hα emissions labeled r (red) and b (blue), which represent directions of two jets.

3.2. GRS 1915+105 and other sources

We tried to investigate the correlation of multi-wavelength light-curve of GRS 1915+105 from simultaneous infrared photometric observations along with INTEGRAL in March 2003 and Suzaku October 2006. However, we could not observe due to bad weather con-

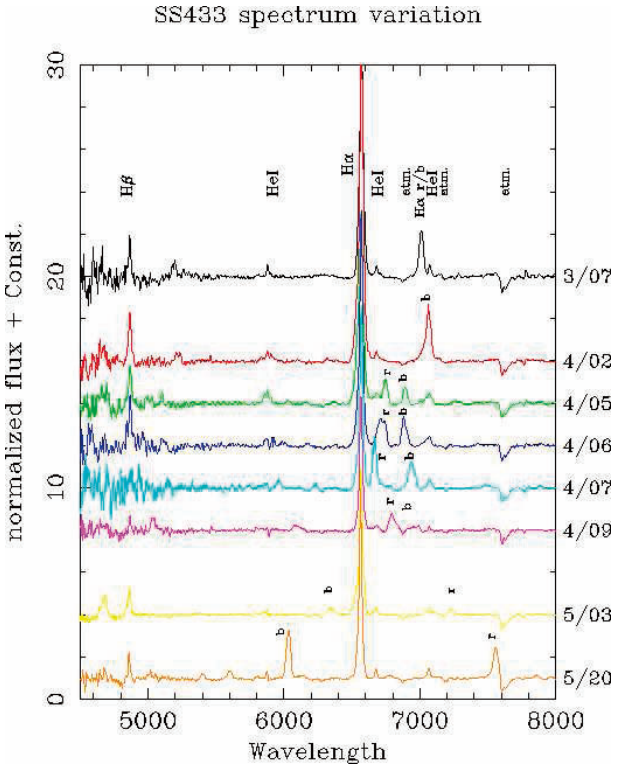

Fig. 8. Optical spectral variation of SS 433 during Suzaku observation campaign 2006. Two moving Hα emissions labeled r (red) and b (blue), represent the direction of each jet.

ditions.

Moreover, we sometimes carry out the cooperative observations of interesting variable stars along with other facilities. For example, low-resolution sequential spectroscopic observations along with other observatories were performed for Tago event, which is a nearby gravitational microlensing event, since discovery (Fukui et al.2007). A high resolution spectroscopy was performed for ζ Oph with MOST satellite to study the line-profile variations (Koubsky et al. 2007).

4. Summary

GAO is a public observational facility founded in 1999. GAO has a 1.5-m reflector, a 65-cm reflector, and other small telescopes. Moreover, there are some powerful instruments attached on the telescopes. The observatory is designed for both astronomical research and public use. Since GAO is operated independently from open use, we can make a flexible time allocation for ourselves to focus original scientific subjects. Take advantages of this point, we can carry out "time-critical" observations for transient sources. We proceed with optical follow-up observations of GRBs, SNe, and other variable objects and with cooperative observations such as multi-wavelength observation campaigns. Especially, we expect the first frequent soft X-ray survey by SXC on board MAXI can discover soft X-ray novae such as super soft sources. Although these sources may include classical novae, these will be a new class of novae. We will be able to carry out the follow-up observations for new transient sources discovered by MAXI.

References

Burenin R. et al. 2003 AstL., 29, 573
Fukui A. et al. 2007 ApJ., 670, 423
Kinugasa K. et al. 2002a IAUC., 7811, 1
Kinugasa K. et al. 2002b ApJ., 577, L97
Kotani T. et al. 2006 ApJ., 637, 486
Koubsky P. et al. 2007 ASP Conf. Ser., 361, 451
Kubota K. 2007 Master Thesis, Kyoto University
Nakano S. et al. 2002 IAUC., 7810, 1
Namiki M. et al. 2003 PASJ., 55, 281
Nogami D. et al. 2008 astro-ph, arXiv0807.2098
Ruiz-Velasco et al. 2007 ApJ, 669, 1
Torii K. et al. 2003 ApJ., 597, L101

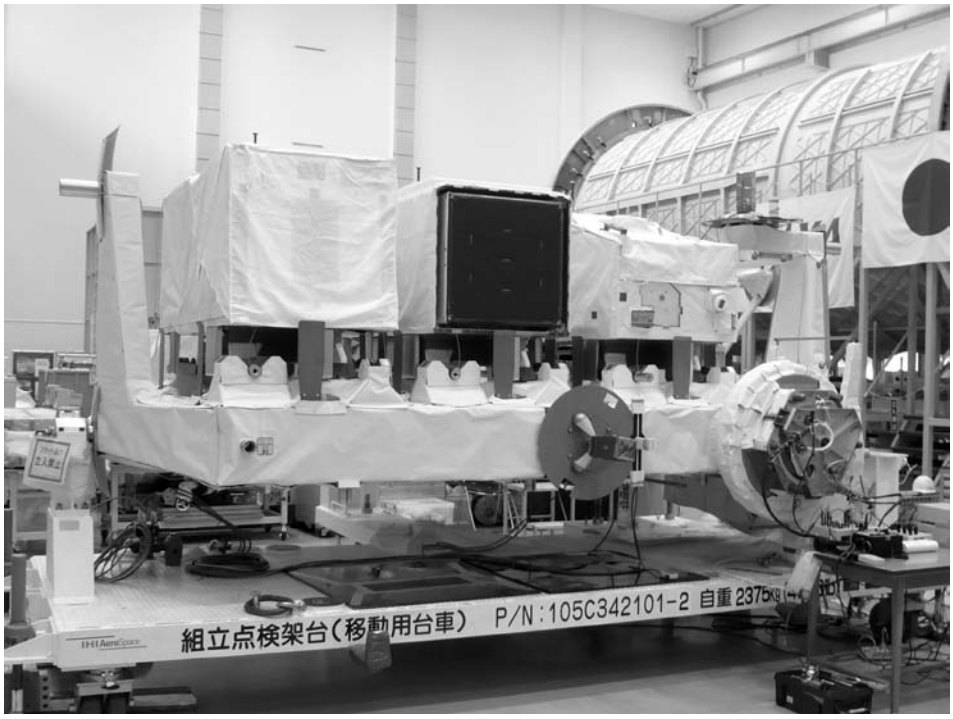

CANGAROO-III Search for TeV Gamma-rays from Two Clusters of Galaxies

R.Kiuchi[1], M.Mori[1], G.V.Bicknell[2], R.W.Clay[3], P.G.Edwards[4], R.Enomoto[1], S.Gunji[5], S.Hara[6], T.Hara[7], T.Hattori[8], S.Hayashi[9], Y.Higashi[10], Y.Hirai[11], K.Inoue[5], C.Itoh[6], S.Kabuki[10], F.Kajino[9], H.Katagiri[12], A.Kawachi[8], T.Kifune[1], H.Kubo[10], J.Kushida[8], Y.Matsubara[13], T.Mizukami[10], Y.Mizumoto[14], R.Mizuniwa[8], H.Muraishi[15], Y.Muraki[13], T.Naito[7], T.Nakamori[10], S.Nakano[10], D.Nishida[10], K.Nishijima[8], M.Ohishi[1], Y.Sakamoto[8], A.Seki[8], V.Stamatescu[3], T. Suzuki[11], D.L.Swaby[3], T.Tanimori[10], G.Thornton[3], F.Tokanai[5], K.Tsuchiya[16], S.Watanabe[10], Y.Yamada[9], E.Yamazaki[8], S.Yanagita[11], T.Yoshida[11], T.Yoshikoshi[1], and Y.Yukawa[1]

[1] Institute for Cosmic Ray Research, University of Tokyo, Kashiwa, Chiba 277-8582, Japan
[2] Research School of Astronomy and Astrophysics, Australian National University, ACT 2611, Australia
[3] School of Chemistry and Physics, University of Adelaide, SA 5005, Australia
[4] Narrabri Observatory of the Australia Telescope National Facility, CSIRO, Epping, NSW 2121, Australia
[5] Department of Physics, Yamagata University, Yamagata, Yamagata 990-8560, Japan
[6] Ibaraki Prefectural University of Health Sciences, Ami, Ibaraki, 300-0394, Japan
[7] Faculty of Management Information, Yamanashi Gakuin University, Kofu, Yamanashi 400-8575, Japan
[8] Department of Physics, Tokai University, Hiratsuka, Kanagawa 259-1292, Japan
[9] Department of Physics, Konan University, Kobe, Hyogo 658-8501, Japan
[10] Department of Physics, Kyoto University, Sakyo-ku, Kyoto 606-8502, Japan
[11] Faculty of Science, Ibaraki University, Mito, Ibaraki 310-8512, Japan
[12] Department of Physical Science, Hiroshima University, Higashi-Hiroshima, Hiroshima 739-8526, Japan
[13] Solar-Terrestrial Environment Laboratory, Nagoya University, Nagoya, Aichi 464-8602, Japan
[14] National Astronomical Observatory of Japan, Mitaka, Tokyo181-8588, Japan
[15] School of Allied Health Sciences, Kitasato University, Sagamihara, Kanagawa 228-8555, Japan
[16] National Research Institute of Police Science, Kashiwa, Chiba 277-0882, Japan
E-mail (MM): morim@icrr.u-tokyo.ac.jp

Abstract

As accretion and merger shocks in clusters of galaxies may accelerate particles to high energies, clusters are candidate sites for the origin of ultra-high-energy (UHE) cosmic-rays. Recently, a prediction was presented for gamma-ray emission from a cluster of galaxies at a detectable level with modern imaging atmospheric Cherenkov telescopes. The gamma-ray emission was produced via inverse Compton upscattering of cosmic microwave background (CMB) photons by electron-positron pairs generated by collisions of UHE cosmic rays in the cluster. We have observed two clusters of galaxies, Abell 3667 and Abell 4038, searching for very-high-energy gamma-ray emission with the CANGAROO-III atmospheric Cherenkov telescope system in 2006. The analysis showed no significant excess around these clusters, yielding upper limits on the gamma-ray emission. By comparing the upper limit for the north-west radio relic region of Abell 3667 with the model prediction, we can derive a lower limit of the magnetic field of the region of $\sim 0.1\mu$G. This shows the potential of gamma-ray observations in studies of the cluster environment. We also discuss the upper limit from cluster center regions with a model of gamma-ray emission from neutral pion produced in hadronic collisions of cosmic-ray protons with the intra-cluster medium (ICM). The derived upper limit of the cosmic-ray energy density within this framework was one order higher than that of our Galaxy.

Key words: galaxies: clustrs – gamma-rays: observations

1. Introduction

Existence of non-thermal particles is suggested by observations of clusters of galaxies at various wavelengths (i.e. radio, optical, X-ray, and etc.) (e.g. Giovannini and Feretti 2004 and references therein). Cluster accretion and merger shocks could produce such high-energy particles, however accretion shocks may be more effective than merger shocks in particle acceleration due to their high Mach numbers (Miniati et al. 2000, Ryu et al. 2003). Cosmic ray electrons accelerated directly by these shocks may produce gamma-ray emission via inverse Compton (IC) scattering of the cosmic microwave background (CMB) (Totani and Kitayama 2000, Miniati 2003, Gabici and Blasi 2004). On the other hand, the accelerated cosmic ray protons can interact hadronically with the intra-cluster medium (ICM), and gamma-rays may be produced via π^0-decay (Völk et al 1996, Berezinsky et al. 2007, Pfrommer and Enßlin 2004) as well as IC emission by secondary electron/positron pairs from $\pi^{\pm}$-decay (Blasi and Colafrancesco 1999).

Observationally, no evidence of gamma-ray emission has been reported from clusters of galaxies (Reimer et al. 2003), though there is suggestive evidence (Totani and Kitayama 2000, Kawasaki and Totani 2002, Sharf and Mukherjee 2002). If a gamma-ray flux is observed from clusters of galaxies, it would be a direct measurement of the energy density of non-thermal particles. In the past, observations in TeV gamma-rays with atmospheric imaging telescopes yielded only upper limits (Hattori et al. 2003, Fegan et al. 2005, Perkins et al. 2006, Kiuchi et al. 2007, Domainko et al. 2007).

Recently, Inoue, Aharonian and Sugiyama (2005) discussed the following mechanism of gamma-ray emission from Coma-like clusters of galaxies: protons could be accelerated up to $10^{18} \sim 10^{19}$ eV in the cluster accretion shocks, and secondary electron-positron pairs would be produced in the $p - \gamma$ interaction with the cosmic microwave background photons, and then the electron-positron pairs could boost up those photons into the TeV range by the inverse Compton process. The predicted gamma-ray flux could be at the detectable level for the Coma cluster, for example, depending on mainly the strength of magnetic field in the cluster of galaxies.

Here we report preliminary results from our observations of two clusters of galaxies at TeV energies with CANGAROO-III, an array of imaging atmospheric Cherenkov telescopes. We have selected targets whose characteritics are similar to those of the Coma cluster from the southern Abell catalog (Abell, Corwin Jr. and Olowin 1989): Abell 3667 is one of the brightest X-ray sources in the southern sky, and is also known to show huge diffuse radio emission around the cluster (Röttgering, Wieringa and Hunstead 1997). The location of its center is centered at $(\alpha, \delta) = (20^h12^m27.4^s, -56°49'36")$ (J2000), and its refshift is $z = 0.055$ (Sodré et al. 1992). Since the radio relics around Abell 3667 might be a site of particle acceralation (Knopp et al. 1996), it could be a good TeV gamma-ray candidate, however, the distance is a little farther than the Coma cluster ($z = 0.023$). Abell 4038, formerly known as Klemola 44, is an rich southern cluster with $z = 0.028$ with a cD galaxy at $(\alpha, \delta) = (23^h47^m45.1^s, -28°08'26")$ (J2000) (Slee et al. 2001).

2. Observation

We observed two clusters of galaxies, Abell 4038 and Abell 3667, with the CANGAROO-III telescopes (Mori et al. 2007) in 2006. Three telescopes (we call them as T2, T3 and T4) were used for these observations, and the data were recorded when any two telescopes were triggerd (Nishijima et al. 2005). The observation of each cluster consists of ON-source runs and OFF-source runs: for each run we adopted wobble mode, in which the pointing direction was shifted in declination $\pm 0.5°$ from the tracking position every 20 minutes. The total observation time are 25 hours (ON) and 24 hours (OFF) for Abell 4038, and 32 hours (ON) and 29 hours (OFF) for Abell 3667.

3. Analysis

We basically followed analysis procedure explained in detail in Enomoto et al. (2006), so here we give a brief description.

First, we selected shower events from the data by applying clustering cuts, and we calculated the image moments: *width* and *length* (Hillas 1985). The typical shower rate is ~ 7 Hz, and we cut the data when the shower rate was lower than 5 Hz. The effective observation time for ON and OFF source after this selection is 18.7 hours and 17.7 hours for Abell 4038, and 28.7 hours and 23.7 hours for Abell 3667, respectively. After this shower image selection for each telescope, we selected only three-fold coincident events and also require that none of the shower images should be in the outermost layer of the cameras in order to avoid image truncation.

Next, for gamma-ray/hadron sepataion, we adopted the Fisher Discriminant method (Fisher 1936) as described elsewhere (Enomoto et al. 2006). Briefly stating, we made a linear combination of image parameres for each event (hereafter we call it FD) as expressed by:

$$FD = \alpha_1 W_1 + \alpha_2 W_3 + \alpha_3 W_4 + \alpha_4 L_2 + \alpha_5 L_3 + \alpha_6 L_4$$

where W_i and L_i are *width* and *length* observed by telescope i (Ti), and calculated the coefficients ($\alpha_1 \sim \alpha_6$) so that the difference of FD distributions between

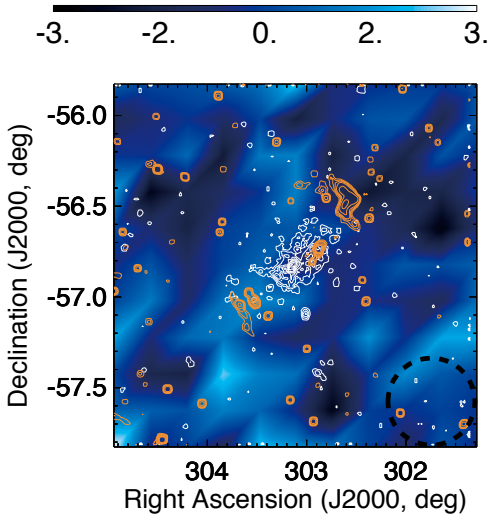

Fig. 1. Two-dimensional significance map of gamma-ray excess counts around Abell 3667. The map center is the cD galaxy, and contors of X-ray (ROSAT hard band: Voges et al. 1999) and radio (SUMSS 843 MHz: Mauch et al. 2003) intensities are overlaid.

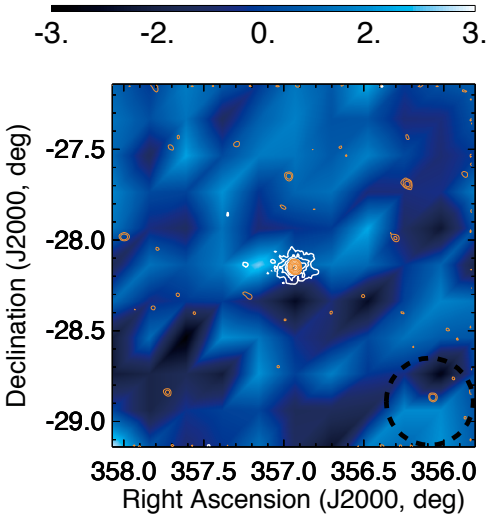

Fig. 2. Two-dimensional significance map of gamma-ray excess counts around Abell 4038. The map center is the cD galaxy, and contors of X-ray (ROSAT hard band: Voges et al. 1999) and radio (VLA 1.4 GHz: Condon et al. 1998) intensities are overlaid.

the gamma-ray events and hadron events was maximized. In this calculation, we used Monte Carlo simulation for gamma-ray events, and OFF-source run for hadron events. Since FD value has a small dependence on zenith angle due to the image size dependence on the same parameter, we corrected this effect by using OFF-source run distributions. We extracted gamma-ray events from fitting procedure of the ON-source FD distribution with background (OFF-source) distribution plus a scaled gamma-ray distribution (Enomoto et al. 2006). In our Monte Carlo simulation, the overall light collecting efficiency (reflectivity of mirrors, quantum efficiencies of photomultiplier etc.) was estimated from a muon ring analysis (Enomoto et al. 2006), and we assumed the power-law index of $\Gamma = -2.1$ for the incident gamma-ray spectrum.

4. Results

4.1. Two dimensional morphology and θ^2 distribution

With the procedures described in the previous section, we calculated two-dimensional (2D) significance maps around the cluster centers. We divided the regions (as the ON region) into $0.2^\circ \times 0.2^\circ$ square bins, and calculated the gamma-ray like excesses and their errors with the FD fitting method. Each background (OFF-source) bin was taken so that its position on the field-of-view would correspond to that of the bin of the ON region, but the areae was extended to 3×3 neighboring bins, to improve statistical accuracy. Fig. 1 and Fig. 2 show the resulting 2D significance maps of gamma-ray like excesses for Abell 3667 and Abell 4038, respectively. Since the gamma-ray acceptance falls off toward the outer part of the field-of-view, we limit the map to within 1 degree from the cluster centers. The significance distributions from all bins in 2D maps were well approximated by standard normal distributions for both regions, and we found no significant gamma-ray signals.

Next, the incident direction of each Cherenkov image was calculated and the space angle, θ, between the event and the assumed source position was assigned. Fig. 3 shows the θ^2 distributions for Abell 4038 (upper panel) and Abell 3667 (lower panel), after subtracting background distributions obtained from OFF-source runs. Also shown are the solid histograms of Monte Carlo simulation results for a Crab-like gamma-ray point source at each cluster center. These plots show no hint of gamma-ray excess to appear toward $\theta^2 = 0$ if there is a point-like gamma-ray source in the cluster centers. Although there are some deviations in the θ^2 distributions, there are not statistically significant, considering our point spread function $\theta^2 < 0.06$ degree^2. In summary, there were no detectable point sources in the cluster fields.

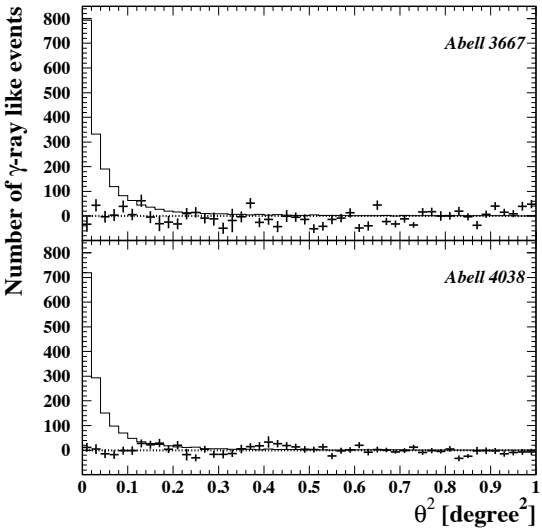

Fig. 3. θ^2 distribution of excess counts around the center of Abell 3667 (upper panel) and Abell 4038 (lower panel). The solid histograms show Monte Carlo simulation results for a Crab-like point source at each cluster center.

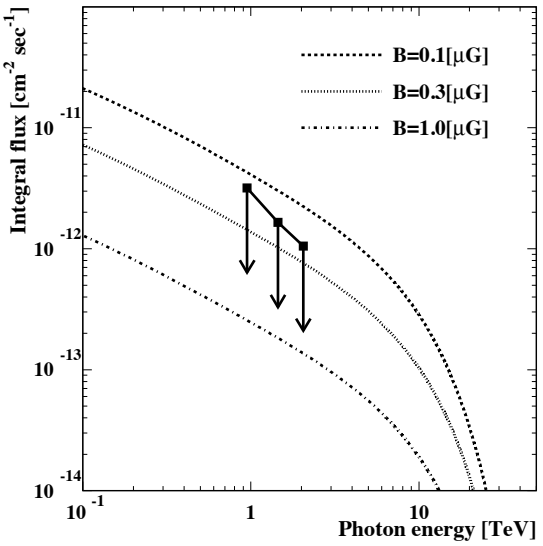

Fig. 4. Derived gamma-ray flux upper limits from NW Relic region of Abell 3667 (filled squares) with the prediction by Inoue, Aharonian and Sugiyama (2005). The model was scaled with the mass and the distance of Abell 3667.

4.2. Gamma-ray emission profiles and upper limits

We also adopted several gamma-ray emission profiles in the cluster fields, and searched the diffuse gamma-ray signals. First, we defined two circular regions (hereafter *NW/SE Relic* region) which cover the prominent radio relics around Abell 3667, since they may represent a shock morphology. The center coordinates (R.A. & Dec. in J2000) and their radii were defined as follows: $(20^h10^m24^s, -56^\circ27'00'')$ and 0.30° for *NW Relic* region, $(20^h14^m36^s, -57^\circ03'00'')$ and 0.24° for *SE Relic* region.

We may expect that gamma-ray emission via π^0-decay might be concentrated toward the cluster center regions. It is well known that many clusters have a diffuse X-ray morphology at their centers which may trace thermal components bounded by the gravitational potential of clusters. We thus assume that the gamma-ray emission profile would trace the X-ray morphology of clusters. We looked at the *ROSAT* PSPC data for the X-ray morphology. The peak positions of the X-ray brightness are almost coincident with the cD galaxies of the clusters, which were the tracking points of our observations. We then defined two regions (hereafter *Cluster Core* regions) such that their centers were at the position of the cD galaxies and the radii were equal to the point where the S/N of the *ROSAT* data fell below ~ 3, which was 0.40° for Abell 3667 and 0.26° for Abell 4038, as described in Table 2 of Mohr et al. (1999). In our Monte Carlo simulation, gamma-rays were generated uniformly within the defined area with a power-law spectrum of index $\Gamma = -2.1$.

The gamma-ray excess count for each region was calculated by the *FD* fitting method as before. The *FD* distribution of each region fitted with that of OFF-source region and that of gamma-ray events from Monte Carlo simulation are compared, but, there are no significant excesses which exceed 3σ. Therefore, we calculated the 2σ upper limits on the gamma-ray integral fluxes from these regions. The obtained flux upper limits are shown in Fig. 4 for *NW Relic* region of Abell 3667 and Fig. 5 for *Cluster Core* region of Abell 4038.

5. Discussion

The theory by Inoue, Aharonian and Sugiyama (2005) predicts gamma-ray emission at accretion shocks around a massive cluster. We searched for gamma-ray emission from the radio relics of Abell 3667, assuming that they might trace the accretion shock (Enßlin et al. 1998), although it has also been suggested that the relics are the results of a major merger (Röttigering et al. 1997) in which case the particle acceleration would not be as strong as assumed in the accretion model. However, we found no evidence of gamma-ray emission from either region. Since the magnetic field of Abell 3667 was estimated for the area of the cluster center and the northwest relic so far (Johnston-Hollitt, 2003), we compared the derived upper limits from *NW Relic* region with the

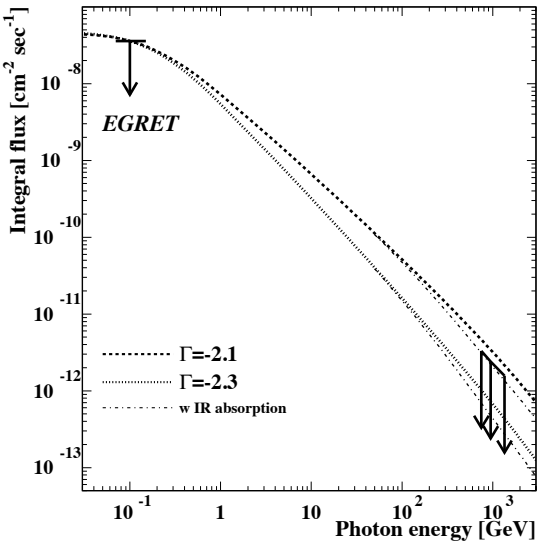

Fig. 5. Derived gamma-ray flux upper limits from the *Cluster Core* region of Abell 4038 with the gamma-ray emission spectrum via π^0-decay process, normalized to the EGRET upper limits (Reimer et al. 2003). The gamma-ray absorption effect by extragalactic infrared photons are shown by dot-dashed lines, where the P0.4 model given in Aharonian et al. (2006) is adopted.

model prediction in Fig. 4. The model assumes a proton luminosity of one tenth of the kinetic energy flux through strong accretion shocks, which depends on the cluster mass in the form of $\propto M^{5/3}$ (see Eq.(2) in Inoue, Aharonian and Sugiyama (2005)), and we scaled the predicted gamma-ray flux according to the mass (M) and distance (d) of Abell 3667 from the parameters (Coma-like cluster) used in their model ($M = 2{\times}10^{15} M_\odot$, $d = 100\,\mathrm{Mpc}$). The mass of Abell 3667 has been estimated using the Virial relation (Sodré et al. 1992, Girardi et al. 1998), and here we adopt $M = 2{\times}10^{15} h^{-1} M_\odot$. The scaled fluxes are shown in Fig. 4 with lines assuming magnetic fields of 0.1μG, 0.3μG, and 1.0μG.

Fig. 4 indicates that we can set a lower limit for the magnetic field in these clusters to be $\sim 0.1\mu$G, within the framework of the model by Inoue, Aharonian and Sugiyama (1995). This value is not a strong constraint on the magnetic field when it is compared with the other estimation, e.g., a few μG from Faraday rotation measurements (see Johnston-Hollitt (2003) for other results), however, this is the first example to show the potential of TeV gamma-ray observations to study physical parameters of the cluster environment. Note that the above flux upper limits also provide a constraint on the gamma-ray emission via primary electron IC which is assumed to appear at the cluster shocks (Miniati 2003).

We also searched for gamma-ray emission from the *Cluster Core* regions, deriving flux upper limits. The gamma-ray flux via π^0-decay, produced in the hadronic collisions of the high-energy protons with the ICM, is thought to be the brightest at the cluster centers, and its flux level is usually discussed from the aspect of the effective confinement of cosmic-rays inside the cluster during a Hubble time. Here we consider the total cosmic-ray energy stored inside the cluster centers. We plotted the flux upper limits from the Abell 4038 *Cluster Core* region together with the EGRET upper limit (Reimer et al. 2003) in Fig. 5. Völk and Atoyan (2005) assumed that the high-energy protons were accumulated in a cluster through supernova explosions and predicted a proton spectrum in the power-law forn of an index $\Gamma = -2.1$ with an energy cutoff of $E_{\max} = 200\,\mathrm{TeV}$. We adopted their parameters, and the gamma-ray absorption effect by the extragalactic background infrared radiation (P0.4 model in Aharonian et al. (2006)) was also incorporated. The gamma-ray spectra were represented by lines in Fig. 5, which were scaled to be consistent with the EGRET upper limits.

As shown in Fig. 5, the EGRET and CANGAROO-III results for Abell 4038 gave almost the same constraint on the gamma-ray emission for the case of $\Gamma = -2.1$, and the total cosmic-ray energy to explain our flux upper limits is $1.2{\times}10^{63}\,\mathrm{erg}$, using an ICM density of 10^{-3} cm^{-3}, which is a typical value for cluster centers (Blasi et al. 2007). We then derived the upper limit of the cosmic-ray energy density within the *Cluster Core* region of Abell 4038, as $\sim$40 eV cm^{-3}, assuming a spherical symmetry with the radius we defined for this region. This value is one order of magnitude higher than that of our Galaxy, $\sim 1\,\mathrm{eV\,cm^{-3}}$, however, it opens the door to discussions of the non-thermal component in the clusters. The same estimation was made for the *Cluster Core* region of Abell 3667 as well, though we obtain a higher upper limit than that for Abell 4038.

6. Summary

We observed two clusters of galaxies, Abell 3667 and Abell 4038, searching for very-high-energy gamma-ray emission with the CANGAROO-III atmospheric Cherenkov telescope system in 2006. No significant excess was detected from both clusters, and flux upper limits on the gamma-ray emission were obtained. By comparing the upper limit for the north-west radio relic region of Abell 3667 with a model prediction, we can derive a lower limit for the magnetic field of the region of $\sim 0.1\mu$G. We also discussed the flux upper limit from cluster center regions with a gamma-ray emission model via the decay of π^0 produced in hadronic collisions of cosmic-ray protons with the ICM. The upper limit of the cosmic-ray energy density stored within the Abell 4038

cluster center was estimated to be $\sim$40 eV cm^{-3} by imposing some assumptions, such as the ICM density, and this value is one order higher than that of our Galaxy. These estimations show the potential of gamma-ray observations in studies of the cluster environment.

Acknowledgements

We thank Dr. Susumu Inoue for discussions and suggestions on the gamma-ray emission from clusters of galaxies. This work is supported by the Grant-in-Aid for Scientific Research, Ministry of Education, Culture, Science and Technology of Japan, and Australian Research Council.

References

G. O. Abell, H. G. Corwin Jr., and R. P. Olowin 1989, Astrophys. J. Suppl. 70, 1–138
F. Aharonian et al. 2006, Nature 440, 1018
V. S. Berezinsky, P. Blasi and V. S. Ptuskin 1997, Astrophys. J. 487, 529
P. Blasi and S. Colafrancesco 1999, Astropart. Phys., 12, 169
P. Blasi et al. 2007, Int. J. Mod. Phys. A22, 681
J.J. Condon et al. 1998, Astron. J. 115, 1963
W. Domainko et al. 2007, in Proc. 30th International Cosmic Ray Conference, OG2.3, id 535 (Merida, Mexico)
R. Enomoto et al. 2006, Astrophys. J. 638, 397–408
T. A. Enßlin et al. 1998, Astron. Astrophys. 332, 395
S.J. Fegan et al. 2005, Astrophys. J. 624, 638
R. A. Fisher 1936, Annals of Eugenics, 7, 179
S. Gabici and P. Blasi 2004, Astropart. Phys., 20, 579
M. Girardi, A. Biviano, F. Mardirossian, G. Giuricin, and M. Mezzetti 1995, Astrophys. J. 438, 527–538
G. Giovannini and L. Feretti 2004, J. Korean Astro. Soc., 37, 323
T. Hattori et al. 2003, In Proc. 28th International Cosmic Ray Conference, volume 5, pages 2659–2662 (Universal Academy Press, Inc. Tokyo, Japan)
A. M. Hillas 1985, In 19th International Cosmic Ray Conference, volume 3, pages 445–448 (NASA/Goddard Space Flight Center, NASA)
S. Inoue, F. A. Aharonian, and N. Sugiyama 2005, Astrophys. J. 628, 9–12
M. Johnston-Hollitt 2003, in Proc. The Riddle of Cooling Flows in Galaxies and Clusters of Galaxies, ed. T. Reiprich, J. Kempner and N. Soker
W. Kawasaki and T. Totani 2002, Astrophys. J. 576, 679–687
R. Kiuchi et al. 2007, in Proc. 30th International Cosmic Ray Conference, OG2.3, id 829 (Merida, Mexico)
G. P. Knopp, J. P. Henry and U. G. Briel 1996, Astrophys. J. 472, 125–130
T. Mauch et al. 2003, MNRAS 342, 1117
J. J. Mohr et al. 1999, Astrophys. J. 517, 627
F. Miniati, D. Ryu, H. Kang, T. W. Jones, R. Cen and J. P. Ostriker 2000, Astrophys. J. 542, 608
F. Miniati 2003, MNRAS 342, 1009
M. Mori et al. 2007, In Proc. 30th International Cosmic Ray Conference, OG2.7, id 166 (Merida, Mexico)
K. Nishijima et al. 2005, In Proc. 29th International Cosmic Ray Conference, volume 5, pages 327–330 (Tata institute of Fundamental Research, Mumbai, India)
C. Pfrommer and T.A. Enßlin 2004, Astron. Astrophys. 413, 17 (erratum: 426, 777)
O. Reimer, M. Pohl, P. Sreekumar, and J. R. Mattox 2003, Astrophys. J. 588, 155–164
H. J. A. Röttgering, M. H. Wieringa, R. W. Hunstead, and R. D. Ekers. 1997, Mon. Not. R. Astron. Soc. 290, 577–584
J. S. Perkins et al. 2006, Astrophys. J. 644, 148–154
O. Reimer et al. 2003, Astrophys. J. 588, 155
D. Ryu, H. Kang, E. Hallman and T. W. Jones 2003, Astrophys. J. 593, 599
C.A. Sharf and R. Mukherjee 2002, Astrophys. J. 580, 154–163
O. B. Slee et al. 2001, Astron. J. 122, 1172–1193
L. Sodré et al. 1992, MNRAS 259, 233
T. Totani and T. Kitayama 2000, Astrophys. J. 545, 572–577
W. Voges et al. 1999, Astron. Astrophys. 349, 389
H. J. Völk, F. A. Aharonian and D. Breitschwert 1996, Space Sci. Rev. 75, 279
H. J. Völk and A. M. Atoyan 2000, Astrophys. J. 541, 88

The state of development and observation of MITSuME telescope

Y. Kudo[1], N. Kawai[1], T. Shimokawabe[1], N. Vasquez[1], Y. A. Mori[1]
M. Yoshida[2], K. Yanagisawa[2], S. Nagayama[2], H. Toda[2], Y. Shimizu[2]
D. Kuroda[2], J. Watanabe[3], H. Fukushima[3], M. Mori[4]

[1] Department of Physics, Tokyo Institute of Technology, 2-12-1 Ookayama, Meguro-ku,Tokyo 152-8551, Japan
[2] Okayama Astrophysical Observatory, Natiocal Astronomical Observatory Japan,
3037-5 Honjyo, Kamogata, Asakuchi, Okayama 719-0232, Japan
[3] Natiocal Astronomical Observatory Japan, 2-21-1 Oosawa, Mitaka, Tokyo, Japan
[4] Institute for Cosmic Ray Research, University of Tokyo, 5-1-5 Kashiwa, Chiba 277-8582, Japan
E-mail(YK): kudou.y.ab@m.titech.ac.jp

Abstract

MITSuME (Multicolor imaging telescopes for survey and monstrous explosions, or which means three-eyed monster in Japan) consists of three robotic telescopes designed for gamma-ray burst (GRB) afterglow observations. Two 50 cm optical telescopes, located in Okayama (OAO/NAOJ) and in Yamanashi (Akeno Observatory/ICRR) are equipped with tri-color CCD cameras that perform simultaneous imaging in the g′, Rc and Ic bands. We hove performed follow-up observations of 28 GRBs since April 2007 unitil May 2008 with MITSuME Akeno Telescope, and detected five afterglows. The telescope is automatically pointed to the GRB coordinates when a GCN notice is received. The images are automatically reduced, combined, and analyzed to detect uncatalogued objects in the field. While waiting for GRB alerts, the telescope perform patrol of pre-selected objects, such as variable active galactic nuclei (AGNs). The photometry of these patrolled objects is also performed automatically. In this paper, we report the results of the GRB afterglow observations at Okayama / Akeno MITSuME Telescopes. We also present the automatic observation and the analysis system.

Key words: gamma-ray - optical/NIR afterglows

1. GRBs

GRBs are the most energetic explosions in the Universe. Their origin and emission mechanism are at last starting to be revealed with the coordination of astronomy satellites and ground-based observations. Majority of long GRBs are now believed to be associated with death of massive stars. Their prompt emission, and their afterglows have been successfully explained by a synchrotron emission from relativistic shocks.

2. THE MITSUME PROJECT

The *MITSuME* projectis conducted and supported by Tokyo Institute of Technology, the National Astronomical Observatory of Japan (NAOJ) and the Institute of Cosmic Ray Research (ICRR). *MITSuME* stands for *Multicolor Imaging Telescopes for Survey and Monstrous Explosions*. The objective of the project is multicolor photometry from K_s to g' of GRB afterglows within tens of seconds, which allows the photometric redshift measurements up to $z \approx 10$. We built two 50 cm optical robotic telescopes at Akeno Observatory of the ICRR and at Okayama Astrophysical Observatory (OAO) of NAOJ. Each telescope has a *Tricolor Camera* capable of simultaneous photometry in g', R_c, and I_c bands[1,2,3]. The specification of the two optical telescopes is shown in Table 1. In addition, we have started GRB observations with Tricolor Camera at Ishigakijima Astronomical Observatory in a southern island of Japan. In addition, an existing 91 cm telescope at OAO is being converted to a NIR telescope, which is designed to have a wide field of view of $56' \times 56'$ and perform K_S, H, J, and y photometry[4].

3. OBSERVATION SYSTEM

Our observation system has been designed to observe afterglows of GRBs automatically. This system can respond to notifications distributed by the Gamma-Ray Burst Coordinate NetWork(GCN). After receiving a GCN notice, our telescopes immediately slew to the GRB position and then start to take series of three color bands images simultaneously. These images that taken with both Akeno and OAO telescopes are processed by the analysis pipeline and transfered to the database at Tokyo Institute of Technology. Our images

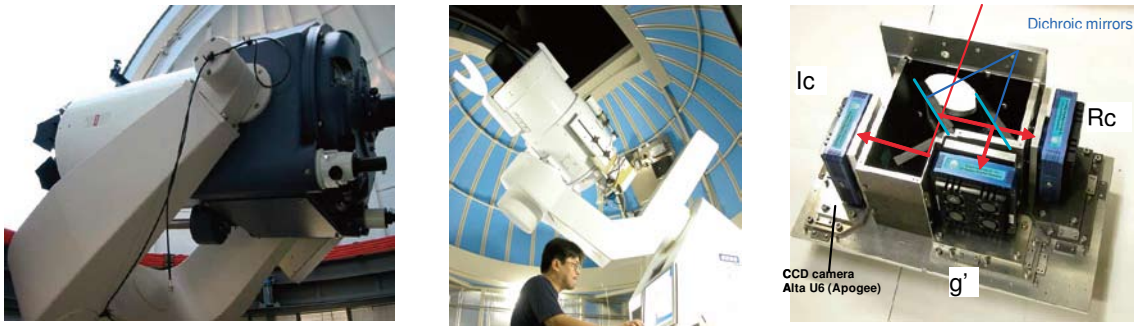

Fig. 1. Akeno 50 cm Telescope (left), OAO 50 cm Telescope (center), and Tricolor Camera (right). Each telescope has a Tricolor Camera. The light led in the camera from above is divided into three bands with two dichroic mirrors and districuted to three *Alta U6* CCDs.

Table 1. Properties of *MITSuME* telescopes

	Akeno 50 cm	*OAO 50 cm*
Mirror Diameter	500 mm	500 mm
Focal Length	3040 mm	3250 mm
F Number	6.0	6.5
FOV	$28^{'} \times 28^{'}$	$26^{'} \times 26^{'}$
Bands	$g^{'}$, R_c, I_c	$g^{'}$, R_c, I_c
Limiting Mag.	$g^{'} = 18.4$	$g^{'} = 18.4$
(10 min, S/N=10)	$R_c = 18.4$	$R_c = 18.5$
	$I_c = 17.7$	$I_c = 17.7$
Slew speed	9 deg.s^{-1}	4 deg.s^{-1}
Location	Akeno Observatory/ICRR	OAO/NAOJ
	Akeno, Yamanashi, Japan	Kamogata, Okayama, Japan
	138°30$^{'}$E, 35°47$^{'}$N, 900 m ASL	133°35$^{'}$E, 34°34$^{'}$N, 372 m ASL

are available through *Subaru Okayama Kiso Archive system (SMOKA)*[1] . We have started scheduled observations for variable and transient objects including supernovae and active galactic nuclei(AGNs) when we do not observe GRBs. If we observe other objects, we can point the telescope at GRBs at the maximum time of 20 seconds.

4. ANALYSIS PIPELINE

The analysis pipeline of *MITSuME* is an automatic system that processes images taken with the multiband telescopes. It allows us to find early optical afterglow of GRBs. The process flowchart is shown in Figure 2. First, sources are found in raw images we take and they are matched to star catalogs. Based on this catalog matching, sky coordinate called the world coordinate system (WCS) is mapped to the image pixels. Second, the photometric measurements are performed for all the sources in the images.GRB afterglow cordinates are those than are not present in the USNO-B 1.0 and NOMAD[2] catalogs, and are detected in more than one images and cross comparison of the source is carried out. Our analysis pipeline allows us to pick up a real GRB by eliminating as hot pixels and pixels hit by cosmic rays. The automatic detection worked well for observations of GRB061121 and GRB070920A. Finally, all images are registered to the database. We can easily access all data in the database through a web interface, which provides information of the images and displays their thumbnail images.

5. RECENT OBSERVATIONS

Recent observation of GRBs by *MITSuME* telescopes are shown in Table 2. From April 2007 to June 2008, we performed follow-up observation of 28 GRBs with the MITSuME Akeno Telescope, and detected five afterglows.

6. PATROL OBSERVATION

Telescope motion and operation of the CCD are under the computer control, allowing automated obser-

*1 http://smoka.nao.ac.jp/index.jsp

*2 http://www.nofs.navy.mil/data/fchpix/

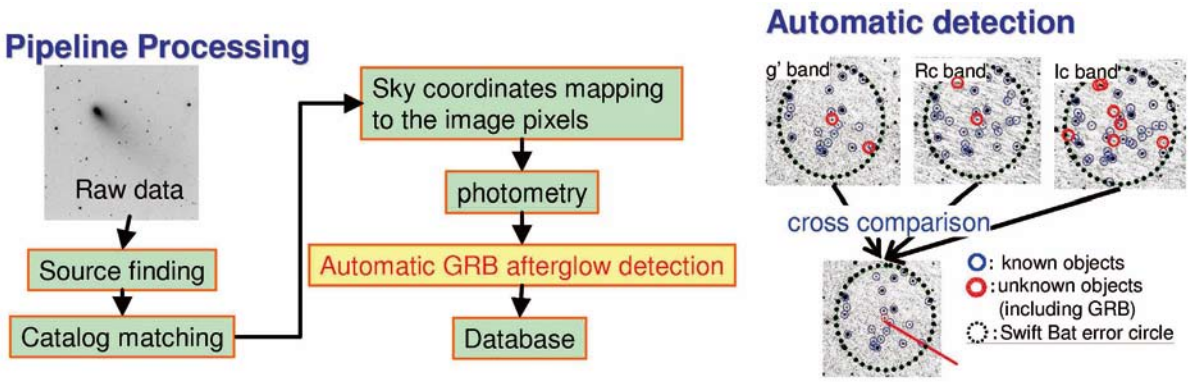

Fig. 2. The pipeline processing and the automatic detection. In the automatic detection, more than one images are compared and only a real GRB is picked up.

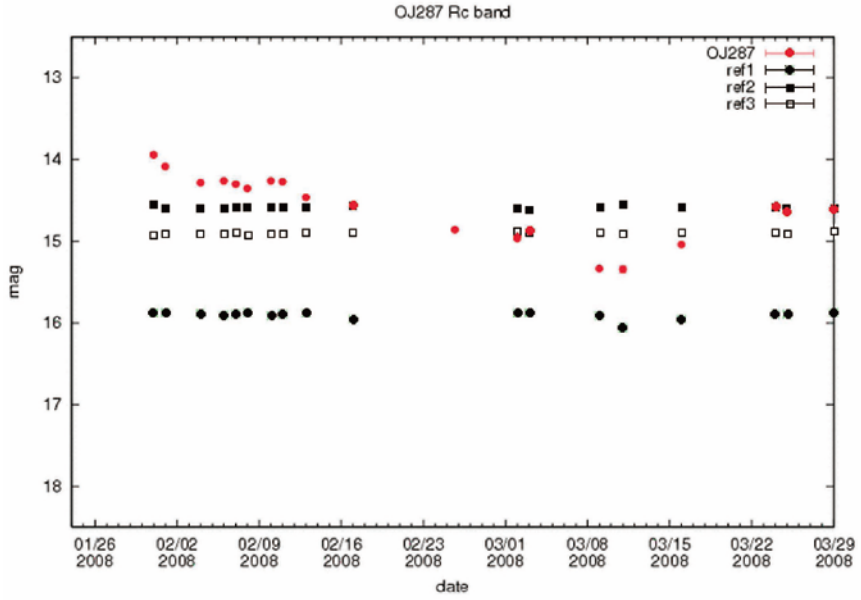

Fig. 3. Light curve of OJ287 at Rc-band.

vations for long-term monitoring of AGNs and transients, contributing to multiwavelength observation in the GLAST/MAXI era. We automatically image ∼10 AGNs and update their light curves every night [ex. Fig.3].

References

1. H.L.Johnson, *Astrophysical Journal* **141**,923-+(1965).
2. A.W.J.Cousins,*Monthly Notes of the Astronomical Society of South Africa* **37**,8-+(1978).
3. J.A.Smith, D.L. Tucker, S. Kent, M.W. Richmond, M. Watanabe, A.Tolea, A. Henden, J. Annis, J.R. Pier, T.A. McKay, J.Brinkmann, B. Chen, J. Holtzman, K. Shimasaku, and D.G. York, *Astron. J.* **123**, 2121-2144(2002), arXiv:astro-ph/0201143.
4. K. Yanagisawa, "Wide-field Monitoring of the Galactic Plane in the K- and the H-band",in *The Proceedings of the IAU 8th Asian-Pacific Regional Meeting, Volume II*, edited by S. Ikeuchi, J. Harnshaw, and T. Hanawa, Astronomical Society of Japan, Tokyo, 2002, p.83.
5. T. Ishimura, T. Shimokawabe, Y. Mori, Y. Kudou, N. Vasquez, Y. Yatsu, and N. Kawai, *GRB Coordinates Network* **7087**, 1-+(2007).
6. T.Kotani, N. Kawai, K. Yanagisawa, J. Watanabe, M. Arimoto, H. Fukushima, T. Hattori, M. Inata, H. Izumiura, J. Kataoka, H. Koyano, K. Kubota, D. Kurota, M. Mori, S. Nagayama, K. Ohta, T. Okada, K. Okita, R. Sato, Y. Serino, Y. Shimizu, T. Shimokawabe, M. Suzuki, H. Toda, T. Ushiyama, Y. Yatsu, A. Yoshida, and M. Yoshida,*Nuovo Cimento C Geophysics Space C* **28**, 755-+(2005), arXiv:astro-ph/0702708.

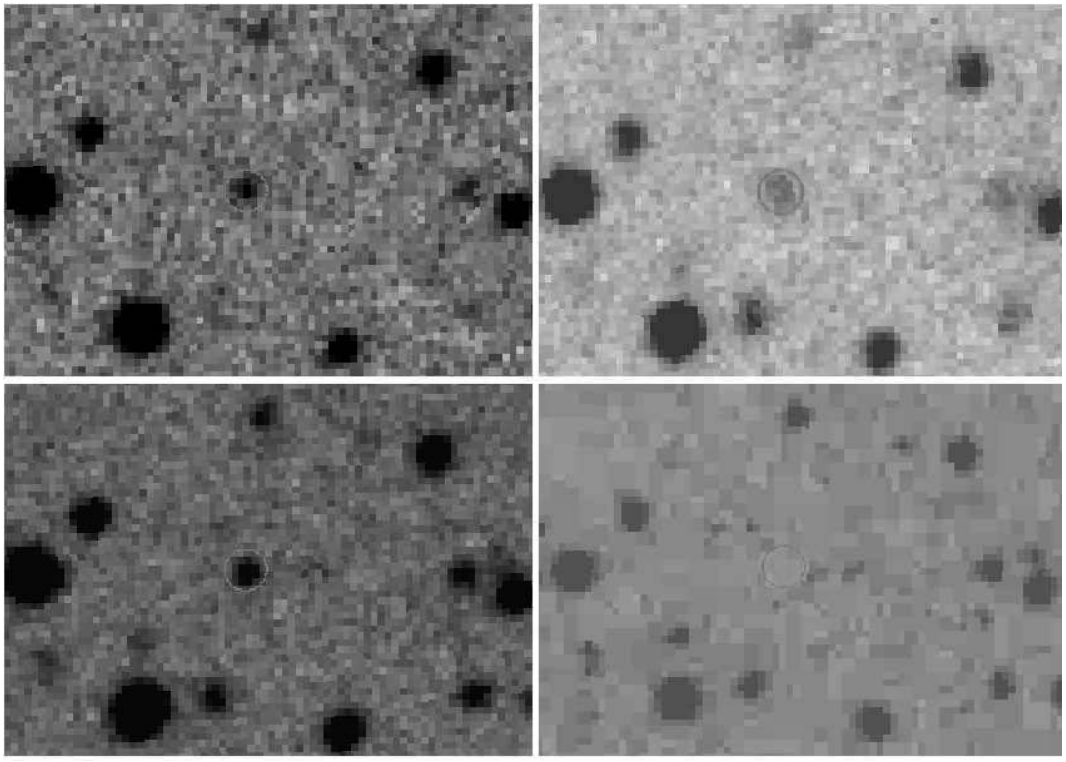

Fig. 4. GRB afterglow of GRB080506. $g^{'}$-band(upper left), I_c-band(upper right), R_c-band(under left), DSS catalog(under right)

Table 2. Recent observations by *MITSuME* telescopes

GRB	$g^{'}$[mag]	R_c[mag]	I_c[mag]	Site	Burst time
080604	>20.0	>19.2	18.6±0.4	OAO	5h 12min
080506	-	17.5±0.1	16.2±0.2	Akeno	1min 57s
080310	20.0±0.2	19.7 ±0.3	19.1±0.2	OAO	6h 31min
080205	>20.9	>20.9	19.6±0.3	Akeno	1h 20min
071118	>18.9	-	-	Akeno	7min
071112C	17.3±0.4	17.3±0.3	-	Akeno	1min
071011	-	19.0±0.3	18.2±0.4	OAO	9m 53s
071011	-	20.1±0.2	18.6±0.2	Ishigakijima	24m 02s
070612A	-	>16.7	17.1±0.3	OAO	8h41min
070419A	20.9±0.2	>21.5	> 19.4	OAO	54min

Possible coordinate observations by MAXI and the AROMA wide-field optical monitor

I. Takahashi,[1] T. Uehara,[1] O. Yamazaki,[1] T. Shiraki,[1] T. Kojima,[1] A. Yoshida,[1] Y. E. Nakagawa[2]

[1] Department of Physics and Mathematics, Aoyama Gakuin University, 5-10-1 Fuchinobe, Sagamihara, Kanagawa 229-8558, Japan.
[2] Institute of Physical and Chemical Research, 2-1 Hirosawa, Wako, Sait ama 351-0198, Japan.
E-mail(IT): itakahashi@phys.aoyama.ac.jp

Abstract

In order to observe the early optical afterglows of GRBs, we have developed and operated the automatic telescope Aoyama Gakuin University Robotic Optical Monitor for Astrophysical objects (AROMA). It currently consists of amateur-oriented astronomical instruments to conduct immediate and automatic follow-up observations and analyses of the GRB optical afterglows. In order to expand the scope of AROMA, a development of an observation system using multiple digital single-lens reflex cameras (AROMA-W) is underway. The new function of AROMA can achieve simultaneous observations in multiple optical bands with a wide field of view. The software which analyzes massive amounts of imaging data automatically was also under development. Finally we aim at discoveries of the optical transients by monitoring all the stars which are visible in an AROMA-W view. We report a developmental status of AROMA-W and a possibility of the simultaneous observation to the X-ray transients (e.g., X-ray nova, Supernova) discovered with MAXI.

Key words: Optical, GRB, Transients

1. Introduction

Monitor of All-sky X-Ray Image (MAXI) can monitor a short time scale X-ray variability and spectra of various X-Ray objects (e.g., Black Hole Candidates, AGNs, Gamma-Ray Bursts (GRBs), X-Ray Novae). Among them, GRB is the most energetic transient with an isotropic energy up to $E_{\rm iso} = 10^{52}$ ergs. The initial X-ray and gamma-ray emission is often referred to as prompt emission. The prompt emission is typically followed by emission from radio to X-ray, so-called afterglows. In a few cases, the afterglows last several months (e.g., GRB 030329). Many observations and studies give important results such as an association between long duration GRBs and hypernovae (e.g., GRB 030329). An emission mechanism of optical afterglows is still unclear, because a very rapid flux decreasing $t^{-\alpha}$ ($\alpha \sim$ 1-2) discourages detailed studies. Therefore, a quick follow-up observation in multiple wavelengths is important for a detailed research of the optical afterglows.

2. AROMA-N

Aoyama Gakuin University Robotic Optical Monitor for Astrophysical objects with Narrow field of view (AROMA-N) is a rapid follow-up telescope for astronomical transients that we have built in the Sagamihara Campus of Aoyama Gakuin University (Latitude = 35.566 ° and Longitude = 139.403 °).

For GRB optical afterglows, this system autonomously make rapid follow-up observations within several tens of seconds based on positional informations from satellites such as *Swift*. AROMA-N currently consists of amateur-oriented astronomical instruments; a Schmidt-Cassegrain telescope of 30.5 cm diameter (MEADE LX200GPS-30), a cooled CCD camera (SBIG ST9-XE), and a filter wheel equipped with multiple band pass filters (B, V, R and I). Figure 1 shows overview images of AROMA-N and its dome. A limiting magnitude is typically about 16-17 magnutude in R-band (100 s integration with 3σ level), and it can reach to 18 magnutude in the best sky condition. Automatic analysis programs are developed in order to search an optical afterglow soon after a determination of a GRB position.

AROMA-N has made follow-up observations for 29 GRBs since it started a steady operation in April of year 2006. Unfortunately, it was cloudy for 17 out of 29 GRBs and there is no useful data for them. Although sky conditions for the other 12 GRBs were fine, any optical transient could not be found. Among 12 GRBs, we here report observational results of two GRBs 060502B and 060923C, because AROMA succeeded in observation at an early phase ($t < 180$ s). Observations of

GRB 060502B were started 85 s after the burst. Despite a very quick follow-up observation, no new source was found. A limiting magnitude is estimated as R $\sim$ 16.1 with 3σ confidence. Observations of GRB 060923C were started 164s after the burst. For this GRB, we succeeded the fastest follow-up observations among all telescopes in the world. However, no new source was found. A limiting magnitude was turned out to be R $\sim$ 15.4 with 3σ confidence.

However, there are two problems in observation by telescopes. The first problem is a time-lag. There has been rapid follow-up observations of GRB optical afterglows by telescopes containing the AROMA-N. Figure 2 shows light curves of the GRB optical radiation (235 GRB events). What seems to be lacking is optical observations before and during prompt emission because of a time delay in the follow-up observations. The time-lag from GRB alert to ground based observations exists. In order to observe a GRB optical variablity in earliest stage, we always have to monitor the field of view of the satellites. The second problem is a pointing accuracy of the satellites. Although It is expected that GLAST Burst Monitor (GBM) on the GLAST which launched in June, 2008 detects 200 GRBs for every year, the pointing accuracy of the GBM/GLAST is 8 degrees. Since the field of view of the conventional telescope systems are a few degrees, they cannot cover an error circle at once. Therefore, the system which always observes a large view is needed to solve these problems. In order to correspond to the GRB follow-ups which reaches the whole sky by MAXI and GBM/GLAST, the largest possible field of view should be taken.

3. AROMA-W

We are developing an large view observation system AROMA-Wide (AROMA-W) using multiple digital single-lens reflex cameras to achieve the optical observations before and during the prompt emission. This implies that an optical flash (e.g., GRB 990123, GRB 080319B) can be observed by this system. Figure 3 shows an overview image of AROMA-W prototype. Similar systems are operated at various locations (e.g., Pi of the Sky, RAPTOR, TORTORA). In GRB 080319B, the brightest prompt optical emission that peaked at a visual magnitude of 5.3 was discovered by these systems during ths burst.

3.1. Instrument

The AROMA-W consists of multiple digital single-lens reflex cameras (DSLR), and an equatorial. Control of the cameras and an equatorial telescope is operated remotely. The cameras to be used are Canon EOS 5D, EOS kiss DN (EOS D Rebel) etc.. The lens which have various focal lengths attached to those cameras. Now, as a test, we are observing with the two cameras on an equatorial. In the future, we will apply about ten cameras to the mount for exclusive use. The shutters of the cameras are controlled by the pulse from the DIO board in the Personal Computer (PC), and these cameras simultaneously make exposures. The acquired data are transferred to the PC by every frame via USB. The equatorial is controlled by the PC and follows the field of view of the GRB observation satellites (eg. *Swift*, GLAST).

3.2. Field of view

AROMA-W sees the large field of view by arranging the field of view of the multiple cameras to make a mosaic image. For example, when a EOS 5D and a EF200mm F2.8 lens are combined, the field of view which amounts to $10.2^\circ \times 6.8^\circ$ can be secured. Since this system is designed for the purpose of constant observations to cover 50% of a *Swift* field of view, continuous observations before and after the prompt emission can be achieved. Figure 4 shows an example of the AROMA-W field of view, the BAT/*Swift* field of view and the GBM/GLAST error circle. .

3.3. Multiple bands Observation

The optical filter is placed along with a bayer arrangement on the image sensor of a camera (here we call R', G' and B' to distinguish AROMA filters). Simultaneous multiple bands observations can be achieved with a wide field of view by reading the data of these filters individually. Since the digital cameras employs R', G' and B' filters which differ a little from AROMA (R, V and B), a relation between the new system filters and the AROMA filters should be investigated. Then, a relative photometry in each filter was performed and magnitude relations (i.e., R-R', V-G' and B-B') are investigated. For example, the relations for EOS5D are well fitted by a linear function; R = (0.88 ± 0.02)R'$-(3.1 \pm 0.3)$, B = (0.93 ± 0.02)B'$-(0.2 \pm 0.3)$ and V = (0.90 ± 0.01)G'$-(2.8 \pm 0.2)$, where the quoted errors are 68.3% confidence levels.

3.4. Limiting Magnitude

Limiting magnitudes for all digital cameras were investigated in each filter. The 3σ limiting magnitude of EOS5D (10 times 20 s exposure), for example, were R = 12.8, V = 13.8 and B =14.1. This implies that our new system can observe an optical flash like GRB 990123 with $\sim$ 9 magnitude and GRB 080319B with $\sim$ 5.3 magnitude. Table 1 shows a summary of limiting magnitute in various cases.

3.5. Data Reduction System

The data obtained by observation will be analyzed in parallel and automatically with multiple PCs. Basic processes of the programs are as follows. First, basic data reductions such as dark count subtraction, flatfielding

Table 1. A summary of limiting magnitute in various cases (3σlimit)

Camera	EOS 5D		EOS kiss DN		EOS 5D
Exposure	20sec		20sec		20sec×10
Lens (mm)	200	100	200	200 (no IR)	200
B	13.5	12.7	13.4	13.1	14.1
V	12.8	12.0	12.3	12.2	13.8
R	12.1	10.9	11.9	12.4	12.8

and image conbine are performed. Second, astronomical objects are detected and compared with star catalogs (mainly USNO B1.0). 3000 to 5000 objects are detectable from the data of one camera (EOS 5D). The light curves of magnitude and flux ratio are obtained about all the objects within the AROMA field of view from the acquired data. These processes are done almost simultaneously with observation. By always monitoring the light curves, variable stars and transient objects (GRB, SNe, X-ray nova etc.$\cdots$) should become detectable. And unexpected brightening and variability also may be also detectable. When strong brightening and variability are detected by AROMA-W, AROMA-N will make rapid follow-up observations autonomously. Figure 5 shows a prospective schematic view of AROMA-W and AROMA-N.

4. Possible coordinate observations with MAXI

This section describes about targets and time schedule of the coordinate observation by MAXI and AROMA.

4.1. Observable objects

The targets of the coordinate observation by MAXI and AROMA are SNe and X-Ray Novae besides GRB. Multiple bands simultaneous observation is enabled by X-ray light curves and spectra of the MAXI and the optical light curves of the AROMA. Their generating mechanism and environment should be presumed from the correlation and the time delay of the light curves or spectrum variability.

We verify whether each object can be observe by AROMA below. As for supernovae, optical light and X-rays become very bright. Sence the time scale of them variability is tens of days, and the peak of brightening in optical is about 12∼13 mag (V band) when it is brightest, it can be observed from an early stage also by AROMA-W. Figure 6 shows a light curve of SN 2007sr (Brightest SN in 2007) with the limiting magnitudes of AROMA-W and AROMA-N. As for X-ray novae, part of them become brighter in optical with their brightening in X-ray. Some they can be observed also by the sensitivity of AROMA-W. Generally, after an X ray nova is detected with X ray detectors, such as MAXI, it is observed by visible light, but if a full-time, an extensive view observation like AROMA-W is performed, it may be able to be detected in optical before being detected with X-rays. For example, V4641 Sgr become bright almost every year and it become bright to 9 magnitude in September, 1999. Figure 7 shows a light curve of V4641 Sgr in 2003 with the limiting magnitudes of AROMA-W and AROMA-N.

4.2. Time Schedule

AROMA-W prototype (1∼2 DSLR) operation has started in July, 2008. AROMA-W will start the main operation in November, 2008. Since *Swift* and GLAST are already launched and MAXI will be launched in March, 2009, AROMA-W start the coordinete observations with various satellites (e.g., MAXI, *Swift*, GLAST) in 2009.

5. Conclusion

In order to observe optical afterglows of GRBs, SNe, X-Ray novae, and variable star etc., we are developing the full-time wide-field observation system using multiple digital single-lens reflex cameras. AROMA-W was designed for the purpose of constant observations to covercover 50% of a BAT/*Swift* field of view. Limiting magnitude of AROMA-W is 13∼14 magnitude. AROMA-W can monitor light curves of all the stars which are visible in its field of view. AROMA-W will soon start the simultaneous observation of the transients (e.g., GRBs,X-ray novae, Supernovae) discovered with various detectors, such as MAXI.

References

Costa, E. et al. 1997 *Nature*, **387**, 783–785
Gehrels, N. et al. 2007 *NJP.*, **85**, 37–
Kawabata, K. S. et al. 2003 *ApJ*, **593**, L19–L22
Matsuoka, M et al. 2007 *SPIE*, **6686E**, pp/668611-1-9
Mazzali, P. A. et al. 2003 *ApJ*, **599**, L95–L98
Meegan, C ea al. 2008 *AIPC* **1000**, 573–576
Monet, David G. et al. 2003 *ApJ*, **125**, 984–993
Racusin, J. L. et al 2008 arXiv:0805.1557
Sari, R., & Piran, T. 1999 *ApJ*, **517**, L109–L112
Tamagawa, T. et al. 2005 emphNCimC, **28**, 771–774
Uemura, M. et al. 2004, emphPASJ, **56**, 823–
Van Paradijs, J. et al. 1997 *Nature*, **386**, 686–689
Volvach, A. er al. 2003 *GCN*, **2424**
Wozniak, P. R. et al. 2006 *AIPC*, **836**, 345–348

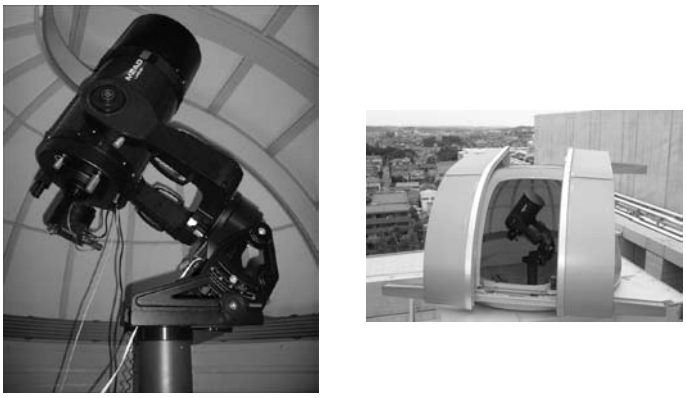

Fig. 1. Overview images of AROMA-N and its dome.

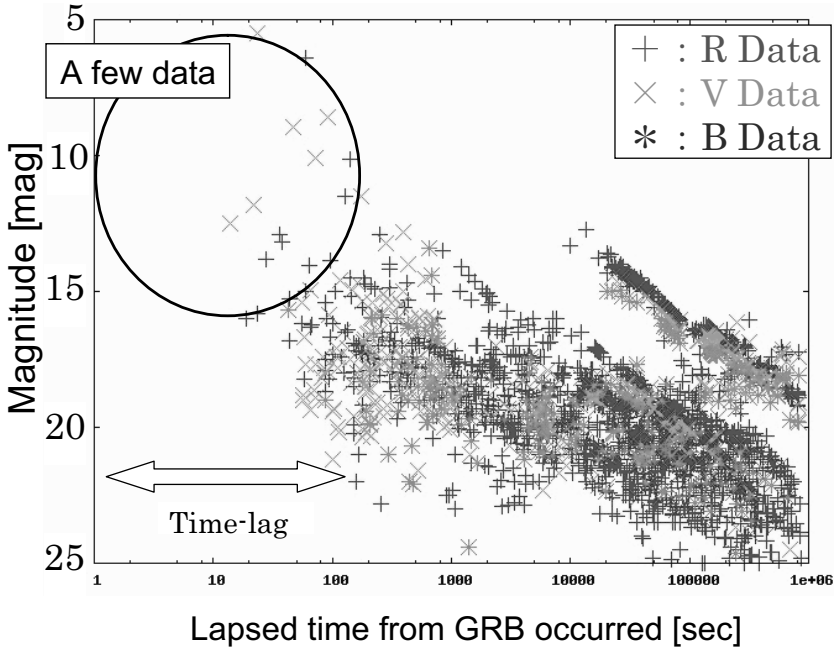

Fig. 2. Light curves of the GRB optical radiation (235 events)

Fig. 3. An overview image of AROMA-W prototype.

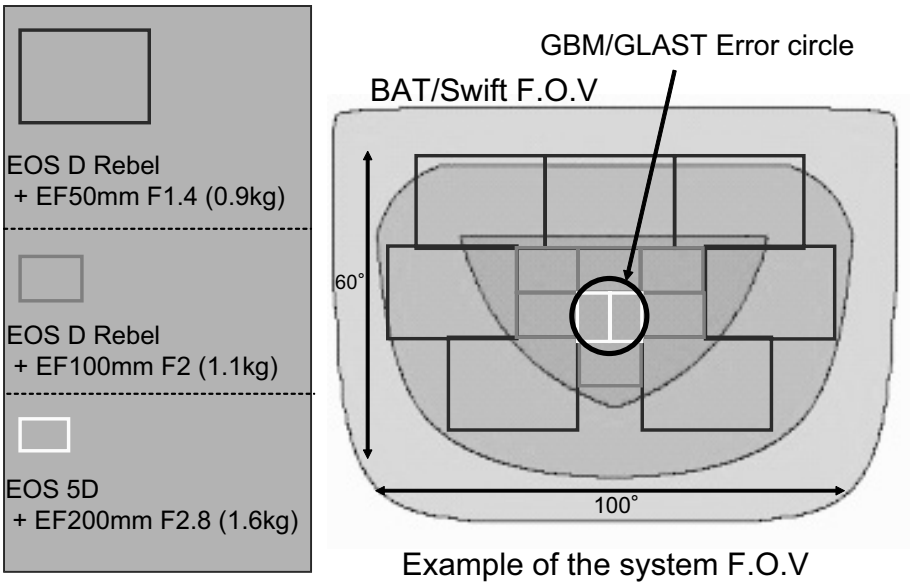

Fig. 4. An example of the AROMA-W field of view, the BAT/*Swift* field of view and the GBM/GLAST error circle

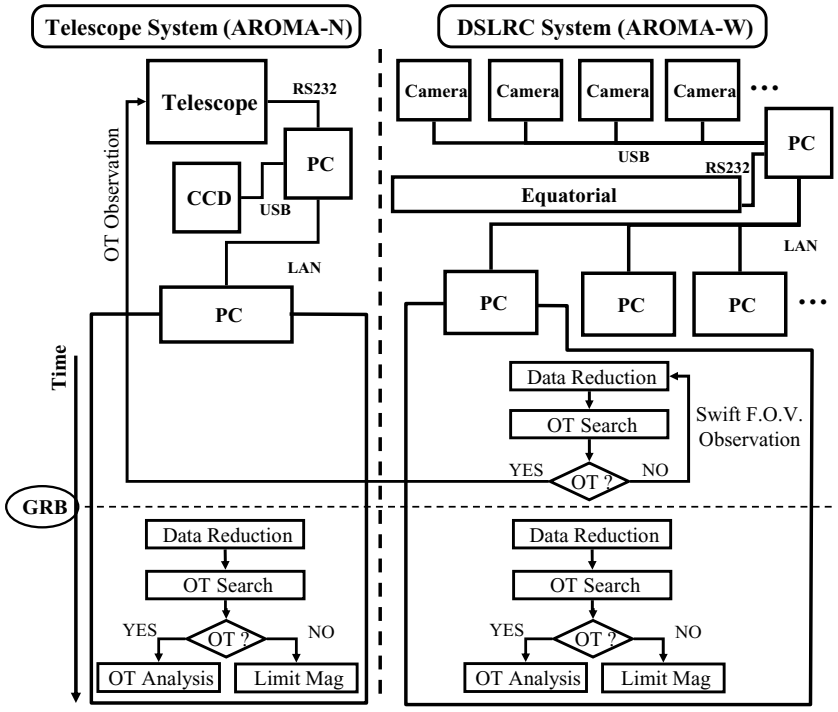

Fig. 5. A prospective schematic view of AROMA-W and AROMA-N

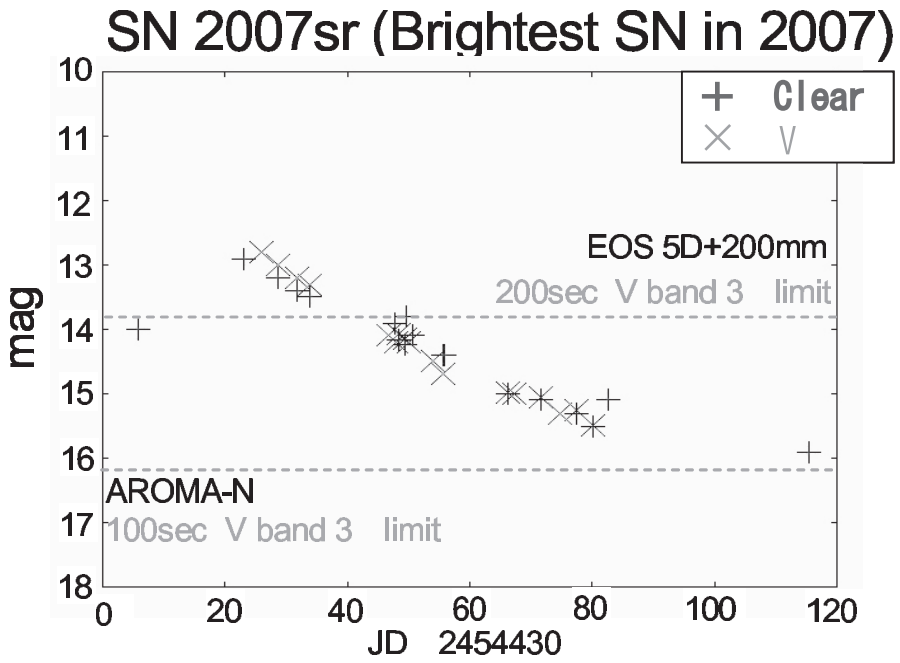

Fig. 6. A light curve of SN 2007sr (Brightest SN in 2007) with the limiting magnitudes of AROMA-W and AROMA-N.

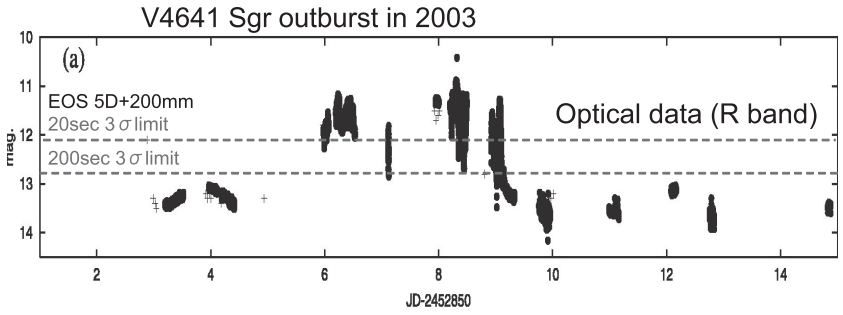

Fig. 7. A light curve of V4641 Sgr in 2003 with the limiting magnitudes of AROMA-W and AROMA-N.

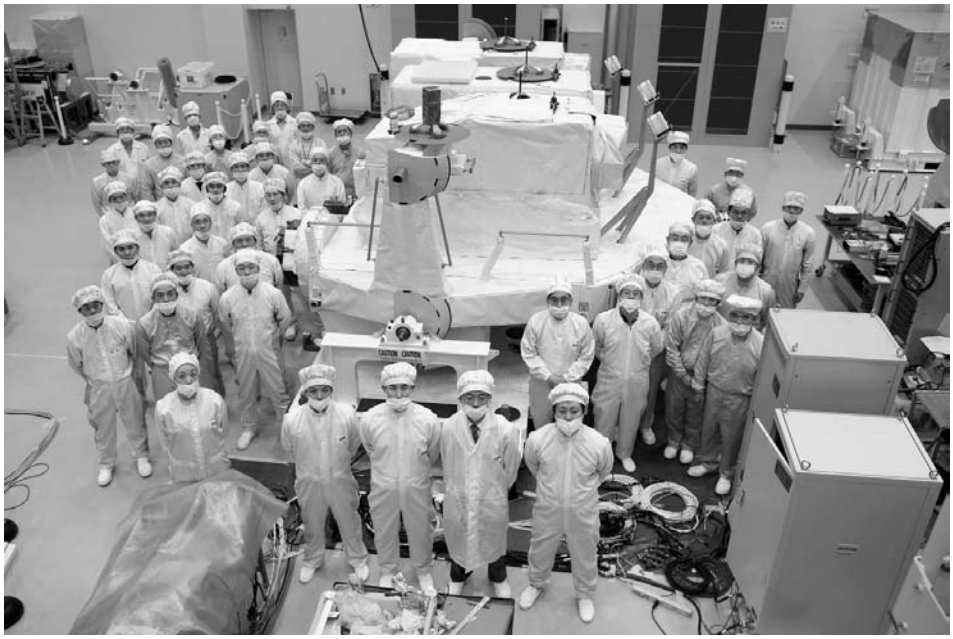

FUTURE MISSIONS

The ASTRO-H Mission

Tadayuki Takahashi[a], Richard Kelley[b], Kazuhisa Mitsuda[a], Hideyo Kunieda[c], Robert Petre[b], Nicholas White[b], Tadayasu Dotani[a], Ryuichi Fujimoto[d], Yasushi Fukazawa[e], Kiyoshi Hayashida[f], Manabu Ishida[a], Yoshitaka Ishisaki[g], Motohide Kokubun[a], Kazuo Makishima[h], Katsuji Koyama[i], Greg M. Madejski[j], Koji Mori[k], Richard Mushotzky[b], Kazuhiro Nakazawa[h], Yasushi Ogasaka[c], Takaya Ohashi[g], Masanobu Ozaki[a], Hiroyasu Tajima[j], Makoto Tashiro[l], Yukikatsu Terada[l], Hiroshi Tsunemi[f], Takeshi Go Tsuru[i], Yoshihiro Ueda[m], Noriko Yamasaki[a], Shin Watanabe[a] and the ASTRO-H team

[a]Institute of Space and Astronautical Science (ISAS), JAXA, Kanagawa, 229-8510, Japan;
[b]NASA/Goddard Space Flight Center, Greenbert, MD 20771, USA;
[c]Department of Physics, Nagoya University, Nagoya, 338-8570, Japan;
[d]Department of Physics, Kanazawa University, Kanazawa, 920-1192, Japan;
[e]Department of Physical Science, Hiroshima University, Hiroshia , 739-8526, Japan;
[f]Department of Earth and Space Science, Osaka University, Osaka, 560-0043, Japan;
[g]Department of Physics, Tokyo Metropolitan University, Tokyo, 192-0397, Japan;
[h]Department of Physics, University of Tokyo, Tokyo, 113-0033, Japan;
[i]Department of Physics, Kyoto University, Kyoto, 606-8502, Japan;
[j]KAVLI Institute, Stanford University, Menlo Park, CA 94025, USA;
[k]Department of Applied Physics, Miyazaki University, Miyazaki, 889-2192, Japan;
[l]Department of Physics, Saitama University, Saitama, 338-8570, Japan;
[m]Department of Astronomy, Kyoto University, Kyoto, 606-8502, Japan
E-mail(TT): takahasi@astro.isas.jaxa.jp

Abstract

ASTRO-H , the new Japanese X-ray Astronomy Satellite following Suzaku, is an international X-ray mission which is currently planed for launch in 2013. ASTRO-H is a combination of wide band X-ray spectroscopy (3–80 keV) provided by multi-layer coating, focusing hard X-ray mirrors and hard X-ray imaging detectors, and high energy-resolution soft X-ray spectroscopy (0.3–10 keV) provided by thin-foil X-ray optics and a micro-calorimeter array. The mission will also carry an X-ray CCD camera as a focal plane detector for a soft X-ray telescope and a non-focusing soft gamma-ray detector. With these instruments, ASTRO-H covers very wide energy range from 0.3 keV to 600 keV. The micro-calorimeter system will be developed by international collaboration lead by ISAS/JAXA and NASA. The simultaneous broad bandpass, coupled with high spectral resolution of ΔE ∼7 eV by the micro-calorimeter will enable a wide variety of important science themes to be pursued.

Key words: X-ray, Hard X-ray, gamma-ray, X-ray Astronomy, Gamma-ray Astronomy

1. Introduction

ASTRO-H, which was formerly called as NeXT, has been studied as the next key X-ray astronomy mission of Japan, which will be developed under international collaboration (Takahashi et al. 2008). It has completed the pre-phase A study in 2006 and entered into Phase A since June 2007. A Request For Proposal (RFP) for the spacecraft was released by ISAS/JAXA to Japanese industry in November 2007 and NEC was selected. System Definition Review, which is required before entering Phase B, was completed in May, 2008 . After the We anticipate that ASTRO-H will enter Phase B in the middle of 2008 for the planned launch year of 2013. More recently, NASA has selected the US participation in ASTRO-H as a mission of opportunity. Under this program, the NASA/Goddard Space Flight Center will collaborate with ISAS/JAXA on the implementation of an X-ray microcalorimeter spectrometer (SXS Proposal NASA/GSFC, 2007).

The ASTRO-H mission objectives are to study the evolution of yet-unknown obscured super massive Black Holes (SMBHs) in Active Galactic Nuclei (AGN); trace the growth history of the largest structures in the Universe; provide insights into the behavior of material in

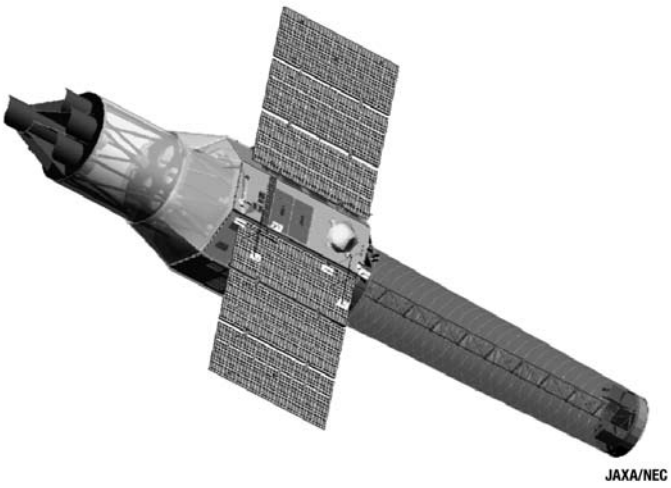

Fig. 1. Artist's drawing of the ASTRO-H satellite. The focal length of the Hard X-ray Telescope (HXT) is 12m, whereas the Soft X-ray Spectrometer (SXS) and Soft X-ray Imager (SXI) will have a focal length of 6 meters.

extreme gravitational fields; determine the spin of black holes and the equation of state of neutron stars; trace particle acceleration structures in clusters of galaxies and SNRs; and investigate the detailed physics of jets.

In this paper, we will summarize the scientific requirements, the mission concept and the current baseline configuration of instruments of ASTRO-H.

2. Science Requirements

By comparison with the soft X-ray band, where the spectacular data from the previous X-ray satellites are revolutionizing our understanding of the universe below 10 keV, the sensitivities of hard X-ray missions flown so far have not dramatically improved over the last decade. The imaging capabilities at high X-ray energies open the completely new field of spatial studies of non-thermal emission above 10 keV. This will enable us to track the evolution of Active Galaxies with accretion flows which are heavily obscured, in order to accurately assess their contribution to the cosmic X-ray background over cosmic time. It will also allow us to map the spatial extent of the hard X-ray emission in diffuse sources, tracing the sites of particle acceleration structures in clusters of Galaxies and supernova remnant (Koyama et al. 1995, Uchiyama et al. 2007, Aharonian 2004). Observing the hard X-ray synchrotron emission gives the maximum electron energy produced by the particle acceleration mechanism in SNR, while the high resolution SXS data on the gas kinematics of the SNR constrains the energy input into the accelerator.

In order to study the energy content of non-thermal emission and to draw a more complete picture of the high energy universe, observations by both a spectrometer with an extremely high resolution capable of measuring the bulk plasma velocities and/or turbulence with the resolution corresponding to the speed of a few $\times$ 100 km/s and an arc-min imaging system in hard X-ray, with the sensitivity two-orders of magnitude better than previous missions, are required. In clusters, X-ray hot gas is trapped in the gravitational potential well and shocks and/or turbulence are produced in this gas, as smaller substructures with their own hot gas halo fall into and merge with the dominant cluster. Large scale shocks can also be produced as gas from the intracluster medium falls into the gravitational potential of a cluster. Here there is a strong synergy between the hard X-ray imaging data and the high resolution (several eV) soft X-ray spectrometer which allows us to study the gas kinematics (bulk motion and turbulent velocity) via the width and energy of the emission lines. The kinematics of the gas provides unprecedented information about the bulk motion; the energy of this motion is in turn responsible for acceleration of particles to very high energies at shocks, which is in turn manifested via non-thermal processes, best studied via sensitive hard X-ray measurement.

On the smallest scales, many active galactic nuclei (AGN) show signatures from the innermost accretion disk in the form of broad "relativistic" Fe K emission lines. These broad lines were discovered using ASCA in the early 1990s and have been confirmed by XMM-Newton and Suzaku (Tanaka et al. 1995, Reeves et al. 2007). There is, however, a complex relationship between the Fe K line properties, the underlying continuum, and the signatures of cold and/or partially ionized material near the AGN. Precise measurements of the complex Fe K line and absorption components require high spectral resolution. Changes in the X-ray emission and absorption spectral features on the orbital time scale of black holes in AGN, enable characterization of the velocity field and ionization state of the plasma closest to the event horizon. The optically thick material that produces the broad fluorescent Fe K line also creates a Compton peak at $E > 20$ keV detectable with hard X-ray and soft gamma-ray detectors, providing multiple insights into the physics of the disk. In order to understand the evolution of environments surrounding super massive black holes, we need high signal-to-noise measurements of the broad lines of hundreds of AGN up to, at least, $z\sim2$. This requires high spectral resolution and bandpass extending to at least $\sim$40 keV. These observations will provide the first unbiased survey of broad Fe K line properties across all AGN.

Precision cosmology uses astronomical observations to determine the large-scale structure and content of the Universe. Studies of clusters of galaxies have provided in-

dependent measurements of the dark energy equation of state and strong evidence for the existence of dark matter. Using a variety of techniques (including the growth of structure, the baryonic fraction in clusters, and the Sunyaev-Zel'dovich effect) a well-constructed survey of clusters of galaxies, with the necessary supporting data (Rapetti et al. 2008), can provide precise measurements of cosmological parameters, including the amount and properties of dark energy and dark matter. The key is to connect observables (such as flux and temperature) to cluster mass. In the next few years, cluster surveys will be carried out by eROSITA, the South Pole Telescope, the Planck mission, and other Sunyaev-Zel'dovich Effect telescopes. To reduce the systematic uncertainties on the masses inferred from the coarser data from these surveys, a training set of precise cluster masses must be obtained. Measurements of bulk motion of cluster of galaxies and amounts of non-thermal energies going to cosmic-ray acceleration could reduce the "... substantial uncertainties in the baryonic physics which prevents their use at a high level of precision at the present time" (Dark Energy Task Force, Albrecht et al. 2006). Line diagnostics with energy resolution <7 eV greatly reduce the uncertainties in the baryonic physics by determining the velocity field, any deviations from thermal equilibrium, and an accurate temperature for each cluster. Information about the non-thermal particle content of the cluster can be determined via measurements of their Compton upscattering of the CMB: this is best studied via hard X-ray imaging, providing additional clues about the physical state of the cluster gas.

3. Spacecraft and Instruments

ASTRO-H is designed to perform leading edge science with cutting edge technology. ASTRO-H will carry two hard X-ray telescopes (HXTs) for the hard X-ray imager (HXI), and two soft X-ray telescopes (SXT), one with a micro-calorimeter spectrometer array with excellent energy resolution of ∼7 eV, and the other with a large area CCD. In order to extend the energy coverage to soft γ-ray region, a Soft Gamma-ray Detector (SGD) will be implemented as a non-focusing detector. With these instruments, ASTRO-H will cover the bandpass between 0.5 keV to 600 keV. The conceptual design of each instrument is shown in Fig. 2 and the specifications of instruments based on the base-line design are summarized in Table. 1 and Table 2 in our previous paper (Takahashi et al. 2008).

Both soft and hard X-ray mirrors are mounted on top of the fixed optical bench. Two focal-plane detectors for soft X-ray mirrors are mounted on the base plate of the spacecraft, while two hard X-ray detectors are mounted on the extensible optical bench to attain 12 m focal length.

ASTRO-H is in many ways similar to Suzaku in terms of orbit, pointing, and tracking capabilities, although the mass is larger; the total mass at launch will be 2400 kg. ASTRO-H will be launched into a circular orbit with altitude 500–600 km, and inclination 30 degrees or less. Science operations will be similar to that of Suzaku, with pointed observation of each target until the integrated observing time is accumulated, and then slewing to the next target. A typical observation will require 40–100 ksec integrated observing time, which corresponds to 1–2.5 days of clock time. All instruments operate simultaneously.

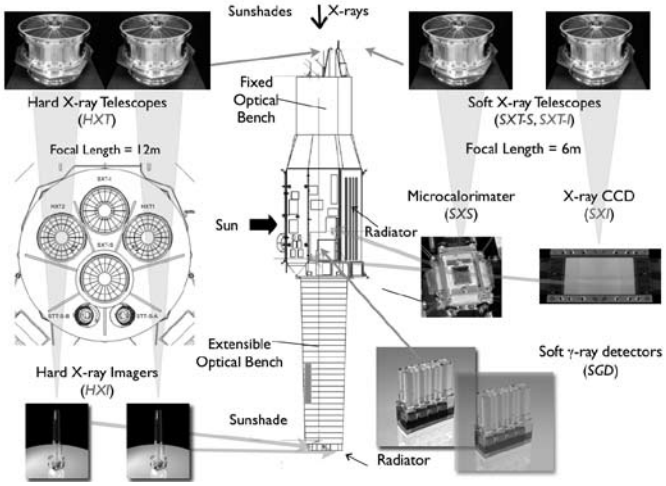

Fig. 2. Configuration of the ASTRO-H satellite

3.1. Hard X-ray Imaging System

The hard X-ray imaging system onboard ASTRO-H consists of two identical mirror-detector pairs (Hard X-ray Telescope (HXT) and Hard X-ray Imager (HXI)). The HXT has conical-foil mirrors with graded multilayer reflecting surfaces that provide a 5–80 keV energy range[**?**]. The effective area of the HXT is maximised for a long focal length, with current design value of 12 m giving an effective area of ∼300 cm^2 at 30 keV. A depth-graded multi-layer mirror reflects X-rays not only by total external reflection but also by Bragg reflection. In order to obtain high reflectivity up to 80 keV, the HXT's consist of a stack of multi-layers with different sets of periodic length and number of layer pairs with a carbon/platinum coating.

The HXI consists of four-layers of 0.5 mm thick Double-sided Silicon Strip Detectors (DSSD) and one layer of 0.5–1 mm thick CdTe imaging detector (Kokubun et al. 2008). In this configuration, soft X-ray photons will be absorbed in the Si part (DSSD), while hard X-ray photons go through the Si part and are detected by the newly developed CdTe double strip detector.The DSSDs cover the energy below 30 keV while

the CdTe strip detector covers the 20-80 keV band. The DSSD has a size of 3×3 cm^2 and a thickness of 0.5 mm, resulting in 2 mm in total. A CdTe strip detector has a size of ∼2×2 cm^2 and a thickness of 0.5 mm. In addition to the increase of efficiency, the stack configuration and individual readout provide information on the interaction depth.

3.2. Soft X-ray Spectrometer System

The Soft X-ray Spectrometer (SXS) is based on Suzaku-XRS (X-Ray Spectrometer) technology, which is the lowest risk option for implementing the capabilities needed for the SXS. The SXS consists of the Soft X-ray Telescope (SXT-S), the X-ray Calorimeter Spectrometer (XCS) and the cooling system (Mitsuda et al. 2008).

The XCS is a 32 channel system with an energy resolution of ≤7 eV between 0.3–12 keV. Micromachined, ion-implanted silicon is the basis of the thermistor array, and 8-micron-thick HgTe absorbers provide high quantum efficiency across the 0.3–12 keV band. With a 6-m focal length, the 0.83 mm pixel pitch corresponds to 0.48 arcmin, giving the array a field of view of 2.85 arcmin on a side. The detector assembly provides electrical, thermal, and mechanical interfaces between the detectors (calorimeter array and anticoincidence particle detector) and the rest of the instrument.

The XCS cooling system must cool the array to 50 mK with sufficient duty cycle to complete the SXS scientific objectives, requiring extremely low heat loads. To achieve the necessary gain stability and energy resolution, the cooling system must regulate the detector temperature to within 2 μK rms for at least 24 hours per cycle. As with Suzaku, the array will be cooled using an Adiabatic Demagnetization Refrigerator (ADR). This device is straightforward to construct, has no moving parts or sensitivity to gravity, and has strong flight heritage established by the XRS. The ADR and detector assembly will be developed, integrated, and tested together at GSFC, prior to installation into a redundant dewar system developed by ISAS. The ADR Controller (ADRC) electronics control and monitor the ADR performance.

For SXS, ISAS/JAXA will provide a redundant dewar system utilizing closed-cycle mechanical coolers that are not limited by expendables. This design is based on coolers developed for space-flight missions in Japan (Suzaku, Akari, and the SMILES instrument to be deployed on the ISS) that have achieved excellent performance with respect to cooling power, efficiency and mass. The 20 K thermal stage consists of a pair of redundant two-stage Stirling-cycle coolers. To provide the sub-2K heat-sink stage for the ADR, there is a hybrid, one-fault-tolerant system consisting of a LHe tank and a 3He Joule-Thomson (JT) refrigerator operating at 1.8 K.

The key properties of SXS are its high spectral resolution for both point and diffuse sources over a broad bandpass (≤7 eV FWHM throughout the 0.3–12 keV band), high sensitivity (effective area of 160 cm^2 at 1 keV and 210 cm^2 at 7 keV), and low non-X-ray background (1.5×10^{-3} cts $s^{-1}keV^{-1}$). These properties open up the full range of plasma diagnostics and kinematic studies of X-ray emitting gas for thousands of targets, both Galactic and extragalactic. SXS improves upon and complements the current generation of X-ray missions, including Chandra, XMM-Newton, Suzaku and Swift.

3.3. Soft X-ray Imaging System

X-ray sensitive silicon charge-coupled devices (CCDs) are a key device for the X-ray astronomy. The low background and high energy resolution achieved with the XIS/Suzaku clearly show that the X-ray CCD will also play very important role in the ASTRO-H mission. Soft X-ray imaging system consists of an imaging mirror and a CCD camera (Soft X-ray Telescope (SXT-I) and Soft X-ray Imager (SXI)) (Tsunemi et al. 2008).

In order to cover the soft X-ray band below 10 keV, the SXI will use next generation Hamamatsu CCD chips with a thick depletion layer, low noise, and almost no cosmetic defects. The SXI features a large FOV and covers 35×35 $arcmin^2$ region on the sky, complementing the smaller FOV but much higher spectral resolution of the SXS calorimeter. A mechanical cooler ensures a long operational life at −120 °C. The overall quantum efficiency and spectral resolution is better than the Suzaku XIS. The imaging mirror has a 6-m focal length, and a diameter no larger than 45 cm.

3.4. Soft Gamma-ray Detector (SGD)

Highly sensitive observations in the energy range above the HXT/WXI bandpass are crucial to study the spectrum of accelerated particles. The SGD is a non-focusing soft gamma-ray detector with a 10–600 keV energy range and sensitivity at 300 keV, more than 10 times better than the Suzaku HXD (Hard X-ray Detector). It outperforms previous soft-γ-ray instruments in background rejection capability by adopting a new concept of narrow-FOV Compton telescope (Takahashi et al. 2004).

In order to lower the background dramatically and thus to improve the sensitivity as compared to the HXD of Suzaku, we combine a stack of Si strip detectors and CdTe pixel detectors to form a Compton telescope. The telescope is then mounted inside the bottom of a well-type active shield. Above ∼50 keV, we can require each event to interact twice in the stacked detector, once by Compton scattering in a stack of Si strip detectors, and then by photo-absorption in the CdTe part (Compton mode). Once the locations and energies of the two interactions are measured, the Compton kinematics allows us to calculate the energy and direction (as a cone in

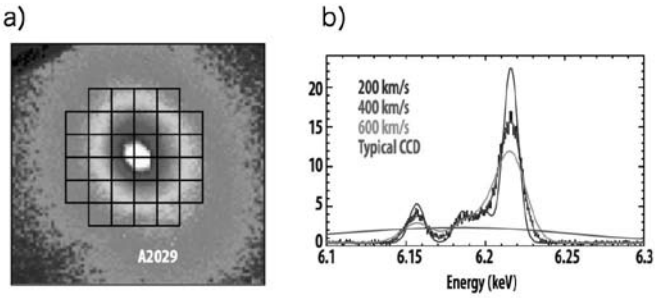

Fig. 3. A portion of a simulated spectrum from the cluster A2029, assuming 400 km/s turbulence, and models assuming 200, 400, and 600 km/s, clearly showing the capability of SXS to measure cluster dynamics. The simulation is for 100 ksec.

the sky) of the incident γ-ray by following the Compton equation,

4. Expected Performance

With ASTRO-H, we expect to achieve an area of about $300\,\mathrm{cm}^2$ at 30 keV with a typical angular resolution of 60" (HPD). Fig. 4 shows Detection limits of the SXT-I/SXI and HXT/HXI for point sources and for sources with of 60' × 60' extension. By assuming a background level of $\sim 1{\times}10^{-4}$ counts/s/cm^2/keV, in which the non X-ray background is dominant, the source detection limit in 1000 ksec would be roughly $10^{-14}\,\mathrm{erg\,cm^2\,s^{-1}}$ in terms of the 10–80 keV flux for a power-law spectrum with a photon index of 2. This is about two orders of magnitude better than present instrumentation, so will give a breakthrough in our understanding of hard X-ray spectra. With this sensitivity, 40-50 % of hard X-ray Cosmic Background would be be resolved (Ueda et al. 2003).

In addition to the imaging observations below 80 keV, the SGD will provide a high sensitivity in the soft γ-ray region to match the sensitivity of the HXT/HXI combination. The extremely low background brought by the new concept of a narrow-FOV Compton telescope adopted for the SGD will provide sensitive γ-ray spectra up to 600 keV, with moderate sensitivity for polarization measurements.

SXS spectroscopy of extended sources can reveal line broadening and Doppler shifts due to turbulent or bulk velocities (Fig. 3). This capability enables the spectral identification of cluster mergers, SNR ejecta dispersal patterns, the structure of AGN and starburst winds, and the spatially dependent abundance pattern in clusters and elliptical galaxies. SXS can also measure the optical depths of resonance absorption lines, from which the degree and spatial extent of turbulence can be inferred. Additionally, SXS can reveal the presence of relatively rare elements in SNRs and other sources through its high sensitivity to low equivalent width emission lines. The low SXS background ensures that the observations of almost all line rich objects will be photon limited rather than background limited.

Table 1. ASTRO-H Mission

launch date	2013 (planned)
launch vehicle	JAXA H-IIA
orbit	550 km circular, <30 degree

XMM-Newton and Suzaku spectra frequently show time-variable absorption and emission features in the 5–10 keV band. If these features are due to Fe, they represent gas moving at very high velocities with both red and blue shifted components from material presumably near the event horizon. CCD resolution is too low and the required grating exposures are too long to properly characterize the velocity field and ionization of this gas and determine whether it is from close to the black hole or from high velocity winds. SXS, in combination with HXI, provides a dramatic increase in sensitivity over Suzaku, enabling measurements that probe the geometry of the central regions of ∼50 AGNs on the orbital timescale of the Fe producing region (for an AGN with a $3{\times}10^7 M_\odot$ black hole, this is $\sim 60\ GM_\odot/c^2 = 10$ ksec).

Acknowledgement

The authors are deeply grateful for on-going contributions provided by other members in the ASTRO-H team in Japan and the US: L. Angelini, N. Anabuki, K. Arnaud, H. Atsukade, H. Awaki, A. Banba, M. Bautz, G. Brown, K.-W. Chan, J. Cottam, J. P. Doty, Y. Ezoe, A. Furusawa, F. Furusawa, M. Galeazzi, K. Gendreau, Y. Haba, K. Hamaguchi, I. Harrus, T. Hashimoto, J. Hiraga, A. Hornschemeier, U. Hwang, N. Isobe, M. Itoh, T. Kallman, H. Katagiri, J. Kataoka, M. Kawaharada, N. Kawai, C. Kilbourne, S. Kitamamo, T. Kohmura, M. Kokubun, A. Kubota, J. Lochner, M. Loewenstein, Y. Maeda, H. Matsumoto, D. McCammon, K. Matsumoto, T. Mihara, E. Miyata, T. Mizuno, H. Mori, K. Mori, K. Mukai, H. Murakami, M. Murakami, T. Murakami, Y. Nakagawa, H. Nakajima, M. Nakajima, M. Nomachi, T. Numasawa, T. Okajima, N. Ohta, F. S. Porter, I. Sakurai, R. Sambruna, K. Sato, A. Senda, P. Serlemitsos, K. Shinozaki, R. Smith, Y. Soong, H. Sugita, M. Suzuki, A. Szymkowiak H. Takahashi, T. Tamagawa, T. Tamura, T. Tanaka, Y. Tawara, Y. Terashima, H. Tomida, Y. Uchiyama, S. Ueno, S. Uno, Y. Urata, K. Yamaoka, H. Yamashita, M. Yamauchi, S. Yamauchi, D. Yonetoku, and A. Yoshida.

References

Takahashi, T. et al. 2008 SPIE, 7011, 70110O-1

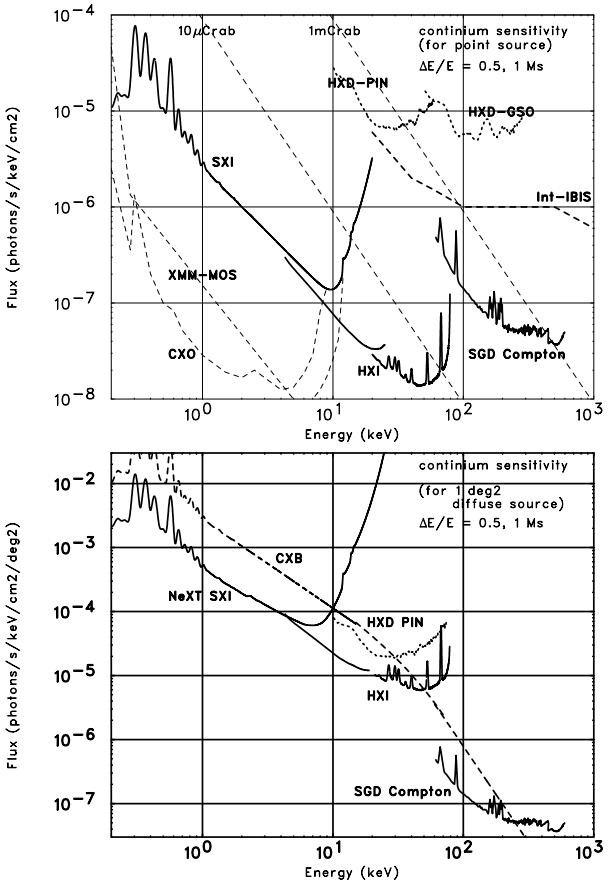

Fig. 4. Detection limits of the SXT-I/SXI and HXT/HXI for (a) point sources and (b) for sources with of 1×1 deg^2 extension (bottom) as functions of X-ray energy, where the spectral binning with $\Delta E/E = 0.5$ and 1000 ksec exposure are assumed. Detection limits for the XMM-Newton, Chandra, Suzaku and Integral observatories are shown for comparison for the sensitivity for point sources.

Koyama, K. et al. 1995, Nature, 378, 255
Uchiyama, Y. et al. 2007, Nature, 449, 576
Aharonian, F. 2004, World Scientific
Tanaka, Y. 1995, Nature, 375, 659
Reeves, J.N. et al. 2007, PASJ, 59S, 301
Rapetti, D. , Allen, S. , Mantz, A. 2008, MNRAS in press.
Ogasaka, Y. et al. 2008, SPIE, 7011, 70110P-1
Kokubun, M. et al. 2008, SPIE, 7011, 70110R-1
MItsuda, K. et al. 2008, SPIE, 7011, 701102K-1
Tsunemi, H. et al. 2008, SPIE, 7011, 70110Q-1
Takahashi, T. et al. 2004, SPIE, 5488, 549
Ueda, Y. et al. 2003, ApJ, 598, 886

ASTROSAT-LAXPC observations of MAXI transient sources

B. Paul
(on behalf of the LAXPC team)

Raman Research Institute, Sadashivanagar, C. V. Raman Avenue, Bangalore 560 080, India
E-mail(BP): bpaul@rri.res.in

Abstract

ASTROSAT is an astronomy satellite being made for a launch in 2009. It is designed for simultaneous multi-wavelength studies with five payloads in the optical/UV and a broad X-ray energy range. One of the instruments, a set of three large area xenon proportional counters (LAXPC) will enable high time resolution X-ray measurements in the 2-80 keV band with moderate energy resolution. There are two imaging X-ray spectrometers, one in the soft and one in the hard X-ray band. Two telescopes will provide multi-band imaging in three optical/UV channels. An X-ray sky monitor onboard ASTROSAT, that is similar in concept to the RXTE-ASM will be used to study long term intensity variations of bright X-ray sources. This instrument will also facilitate timely X-ray observations of transient and variable sources with the LAXPC and other payloads. Here we discuss the salient features of the LAXPC and its advantage of previous large area X-ray astronomy instruments. A very large effective area for hard X-rays with good energy resolution will allow the LAXPC to probe certain properties of X-ray sources with unprecedented detail. The main science issues to be addressed with the LAXPCs are discussed here with some simulated results. We particularly mention the science topics related to variable and transient X-ray sources for which the ASTROSAT observations will benefit from the all sky monitoring with MAXI.

Key words: Stars: neutron – (Stars:) pulsars: – X-rays: stars – (Stars:) binaries: general – X-rays: binaries

1. Introduction

ASTROSAT is a multi-wavelength astronomy satellite scheduled to be launched in 2009 (Agrawal 2006). It will carry five astronomy payloads covering a wide energy range from optical to hard X-rays and will provide a unique platform to make simultaneous multi-wavelength observations. The satellite will be placed in a near-equatorial orbit at an altitude of 650 km and the mission is expected to be functional for over five years.

The scientific payloads of ASTROSAT, in increasing order of energy are:

- Ultraviolet Imaging Telescopes (UVIT) with a pair of 40 cm diameter primary mirrors with three imaging instruments in the Optical, Near-UV and Far-UV bands.
- A Soft X-ray Telescope (SXT) in the energy band of 0.3-8.0 keV and effective area of 200 cm^2 at 1 keV. The SXT is made of an assembly of conical foil mirrors and an X-ray CCD in the focal plane.
- A Scanning Sky Monitor (SSM) in the the energy band of 2-12 keV. The SSM consists of three position-sensitive proportional counters with coded masks.
- Large Area Xenon Proportional Counter (LAXPC) array of three detectors. The LAXPC detectors will work in the energy band of 3-80 keV with an effective area in excess of 6000 cm^2 at 10 keV and timing resolution of 10 microsecond.
- A Cadmium-Zinc-Telluride coded-mask imager (CZTI). The CZTI, with an effective are of 100 cm^2 will work in the hard X-ray band of 10-150 keV.

2. LAXPC Characteristics

The LAXPC consists of three large area proportional counter detectors, each with a geometric area of 3,600 cm^2 and an effective area in excess of 2,000 cm^2. Compared to the previous generation large area proportional counter detectors for X-ray astronomy (EXOSAT-ME, GINGA-LAC and RXTE-PCA) the LAXPC detectors have a large depth of 15 cm, and gas pressure of 2 atm which makes it a very sensitive X-ray timing and continuum spectroscopic instrument in a wide energy band of 3-80 keV. In the 20-80 keV energy band, the LAXPC

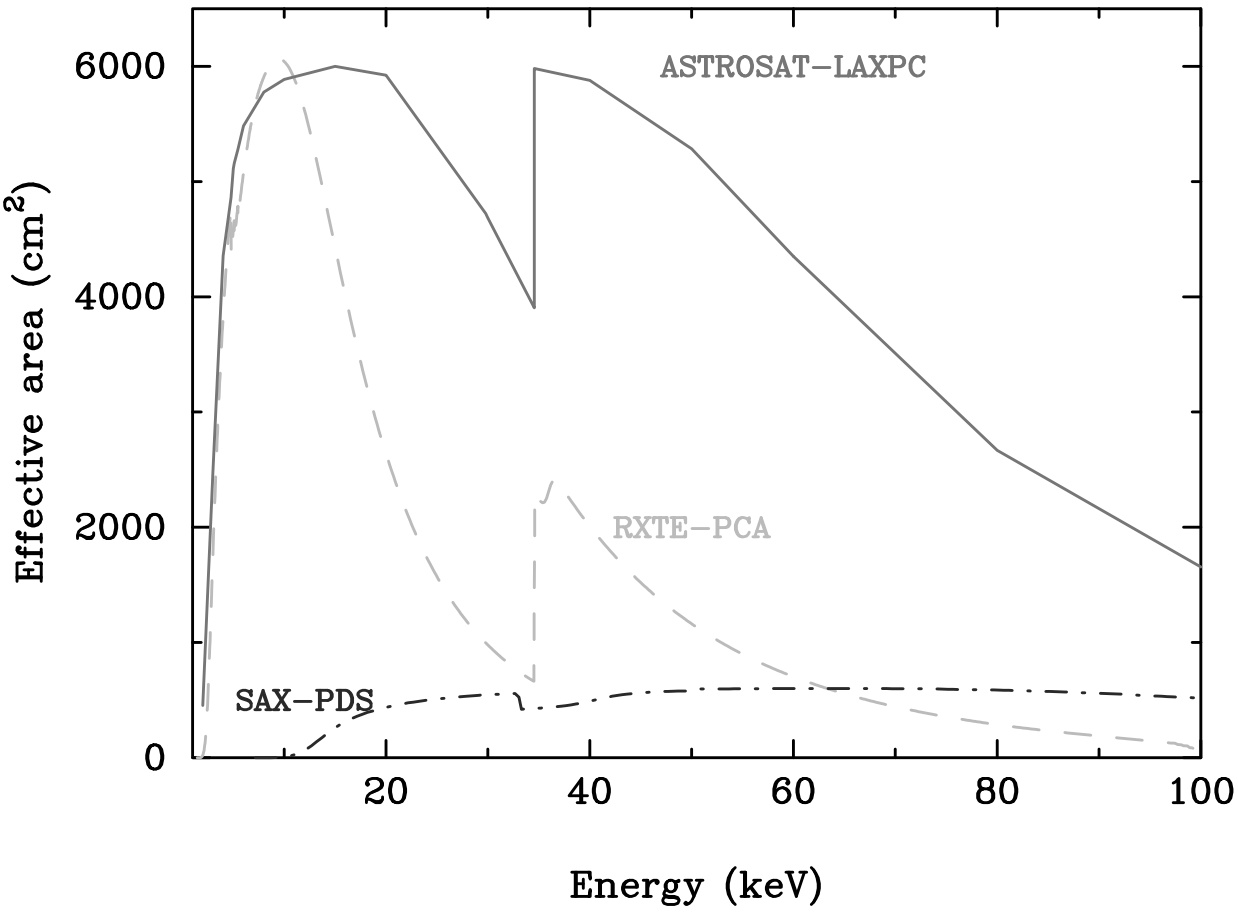

Fig. 1. The effective area of ASTROSAT-LAXPC is shown here along with the effective area of RXTE-PCA and BeppoSAX-PDS. The steps near 34 keV in the top two curves are the K-shell absorption edge of Xe. In the 20-80 keV band, LAXPC effective are is several times larger than that of the PCA.

detector array will have an effective area that is about 3-5 times larger than that of the previous largest instruments in this energy band, the PCA detectors onboard the Rossi X-ray Timing Explorer (RXTE) and the PDS detector onboard Beppo-SAX. A comparison of the LAXPC effective area with the RXTE-PCA and SAX-PDS is shown in Figure 1.

Important features of the LAXPC are:

- Total effective are in excess of 6000 cm^2. Detection efficiency of about 50% at 80 keV.
- Time resolution of 10 microsecond and similar absolute timing accuracy.
- Signal processing to be done separately for the three detectors.
- The LAXPC has multiple modes of operation and data formatting. Upto three data modes can be operated simultaneously for each detector. Different detectors can be operated in different modes.
- For every X-ray photon detected, the electronics dead time, only for its processing unit, is about 35 microsecond. For more accurate photon counting, in one of the datamodes that is applicable to bright sources, the dead time is reduced to 10 microsecond per X-ray photon.
- Energy resolution of 10-12 % achieved across the 20-80 keV band. Some calibration spectra are shown in Figure 2.
- A large fraction of the fluorescence emission from the xenon atoms are recaptured in the detector gas. These double events provide important clue to understand the detector characteristics and helps to improve the spectral resolution.
- Spectral leakage, due to escape of fluorescence emission from the xenon atoms is less compared to the RXTE-PCA. This will lead to greater reliability of continuum spectral measurement.
- Low and stable background level is expected due to

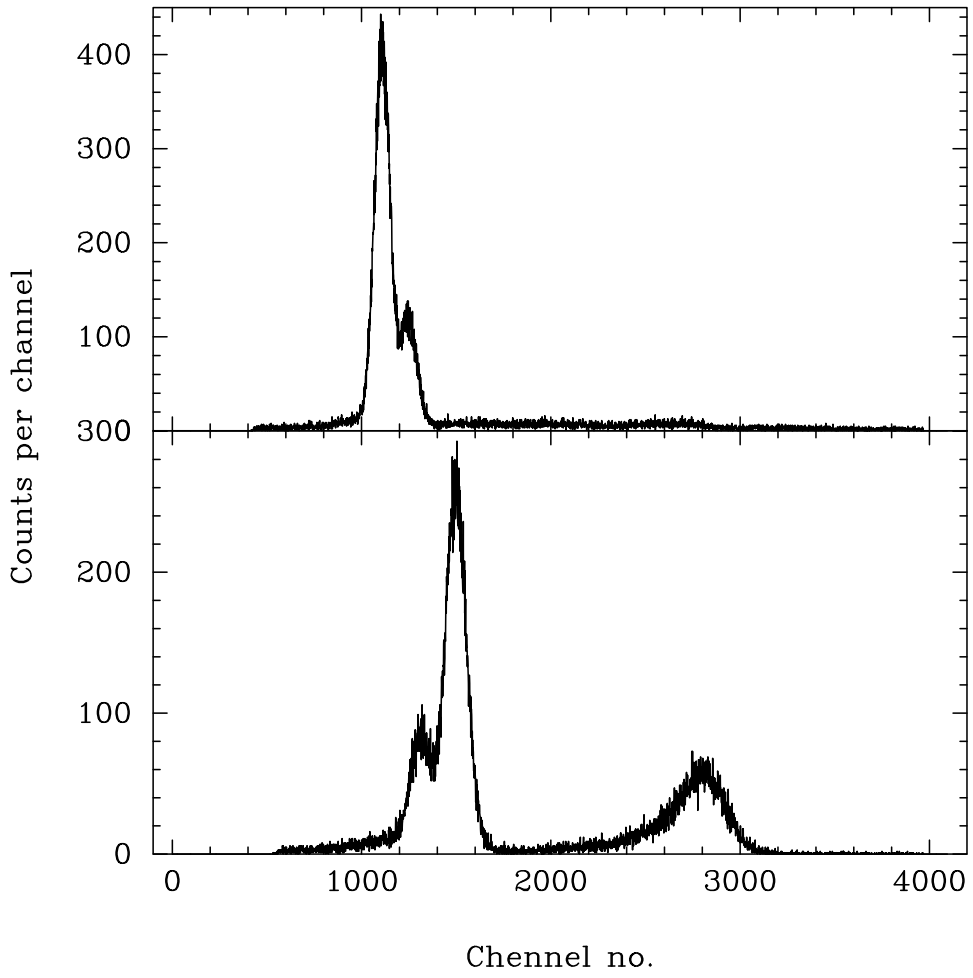

Fig. 2. Spectral response of one of the tests units of LAXPC is shown here. Response to 22 and 25 keV photons are shown in the top panel while response to 60 keV X-ray photons are shown in the bottom panel. A slight asymmetry in the response, with a low energy tail can be seen here. The 30 and 26 keV peaks in the bottom panel are due to energy loss associated with K_α and K_β fluorescence emission from the xenon atoms. The response, shown here for one of the layers of LAXPC shows a large fraction of escape events. However, many of the escape photons get absorbed in other layers of the detector. Since the LAXPC processing electronics is designed to process the double events as genuine X-ray events, the effective spectral leakage will be much smaller.

a near-equatorial orbit of the ASTROSAT.

- Field of view of 1° for energy above 20 keV and 0.7° below 20 keV.

- ASTROSAT has large data storage capacity in the onboard data recorder. For X-ray sources with brightness upto about 1 Crab, it will be possible to store event data in LAXPC with complete detail except for three continuous satellite passes every day when data download to ground station will not be possible.

3. Scientific Objectives

The combination of the LAXPC array, with its unprecedented sensitivity in the hard X-ray band and the SXT with its low energy sensitivity and the CZTI with its better energy resolution in the hard X-ray band will make ASTROSAT an unique observatory.

One of the major scientific objectives of ASTROSAT is broad band X-ray spectroscopic studies of binary X-ray sources, AGNs and other Galactic and extragalactic X-ray sources. With broad band spectroscopy, multiple spectral components in the X-ray spectra, like thermal and non-thermal components, will be decoupled to understand the energy generation and dissipation mechanisms.

Some of the most interesting scientific topics to be pursued in the initial stage of the operation of LAXPC are briefly mentioned here.

Measurement of magnetic field strengths of accretion powered X-ray pulsars will be performed through detection of cyclotron resonance scattering features. The sensitivity of the LAXPC array for this measurement is

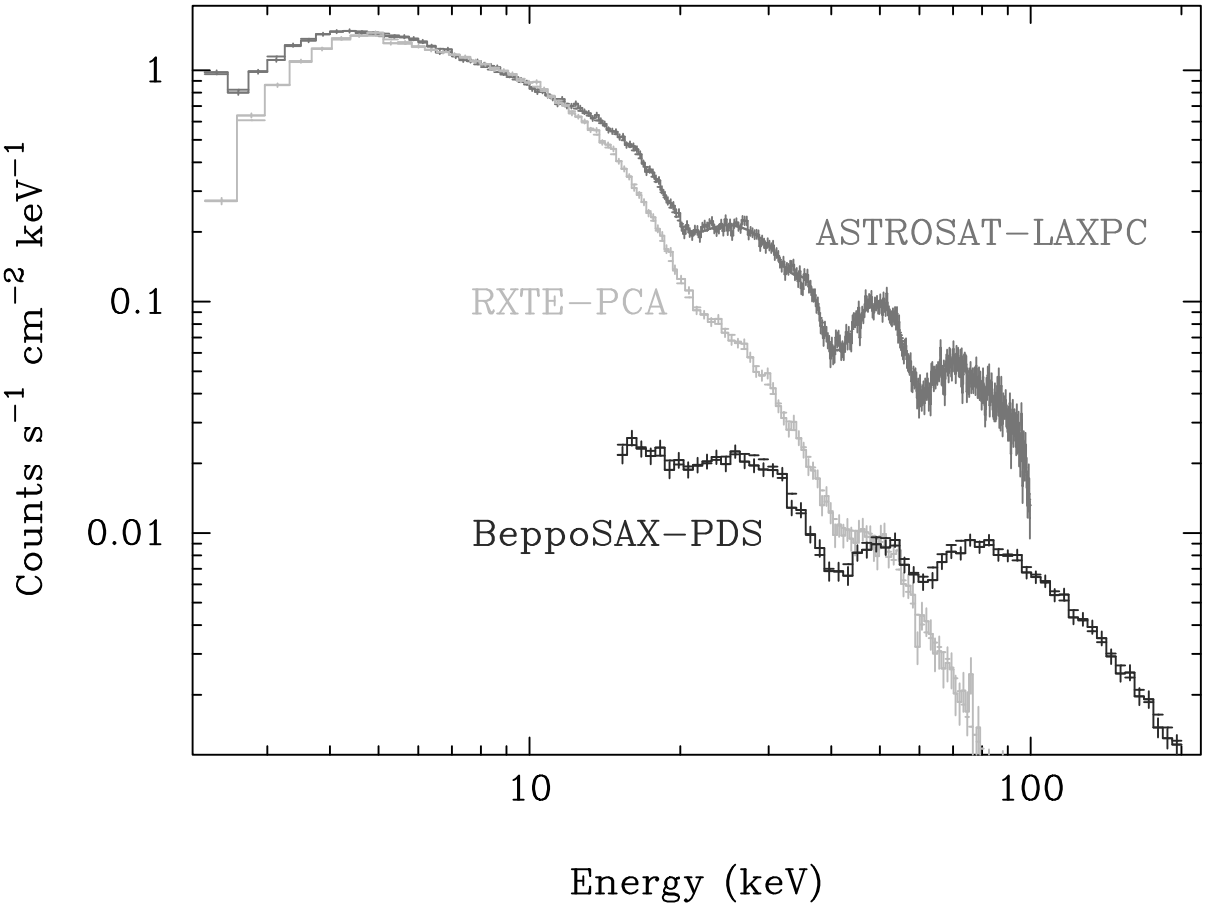

Fig. 3. X-ray spectra of an accretion powered pulsar with multiple cyclotron features simulated with the energy response matrices of ASTROSAT-LAXPC, RXTE-PCA and BeppoSAX-PDS are shown here.

unmatched compared to any other existing or upcoming experiment. LAXPC, SXT and CZTI spectra will also be very useful to characterise the broad band spectrum of the accreting binary X-ray pulsars extending from below 1 keV to more than 100 keV, this has so far been limited only to a handful of bright sources. Pulse phase resolved measurement of the cyclotron features will enable detailed realistic modeling of the pulsar magnetic filed structure. We will also measure the energy of the cyclotron feature as a function of X-ray luminosity in many transient X-ray pulsars that has been done for a few sources with GINGA, RXTE and SUZAKU observations during the decay of the X-ray outbursts (Nakajima et al 2006). Early detection of the onset of transient outbursts with MAXI will enable us to track the evolution of the cyclotron feature even during the rise of the X-ray outbursts. Simulated X-ray spectra of an accretion powered pulsar with multiple cyclotron features are shown in Figure 3 for ASTROSAT-LAXPC, RXTE-PCA and BeppoSAX-PDS.

SXT, LAXPC and CZTI observations together will be suitable to characterise the broad band X-ray spectrum of a large number of galactic and extragalactic black hole sources. Presence of the reflection component in the X-ray spectrum of black hole sources and its connection with the iron emission line profile and line strength will be investigated with ASTROSAT observations. MAXI detections of new transient sources and variability studies of AGNs will enable timely observations of these sources with ASTROSAT in different intensity states. Among the other type of transient sources, temporal and spectral measurements of X-ray emission from new micro-quasars will be performed with the LAXPC. Detection of high frequency QPOs from BHCs will give us a way of measuring the mass and spin of the black holes. In black hole sources, and the low mass X-ray binaries, the rms fraction of high frequency QPOs strongly increases with energy. LAXPC observations will be suitable for easier detection of the high frequency QPOs.

We expect discovery of several new accreting millisecond X-ray pulsars' by LAXPC follow-up observations of the faint transient X-ray sources that will be discovered with the MAXI. Often, the outbursts of these objects last only for a few days to few weeks. However, the outbursts

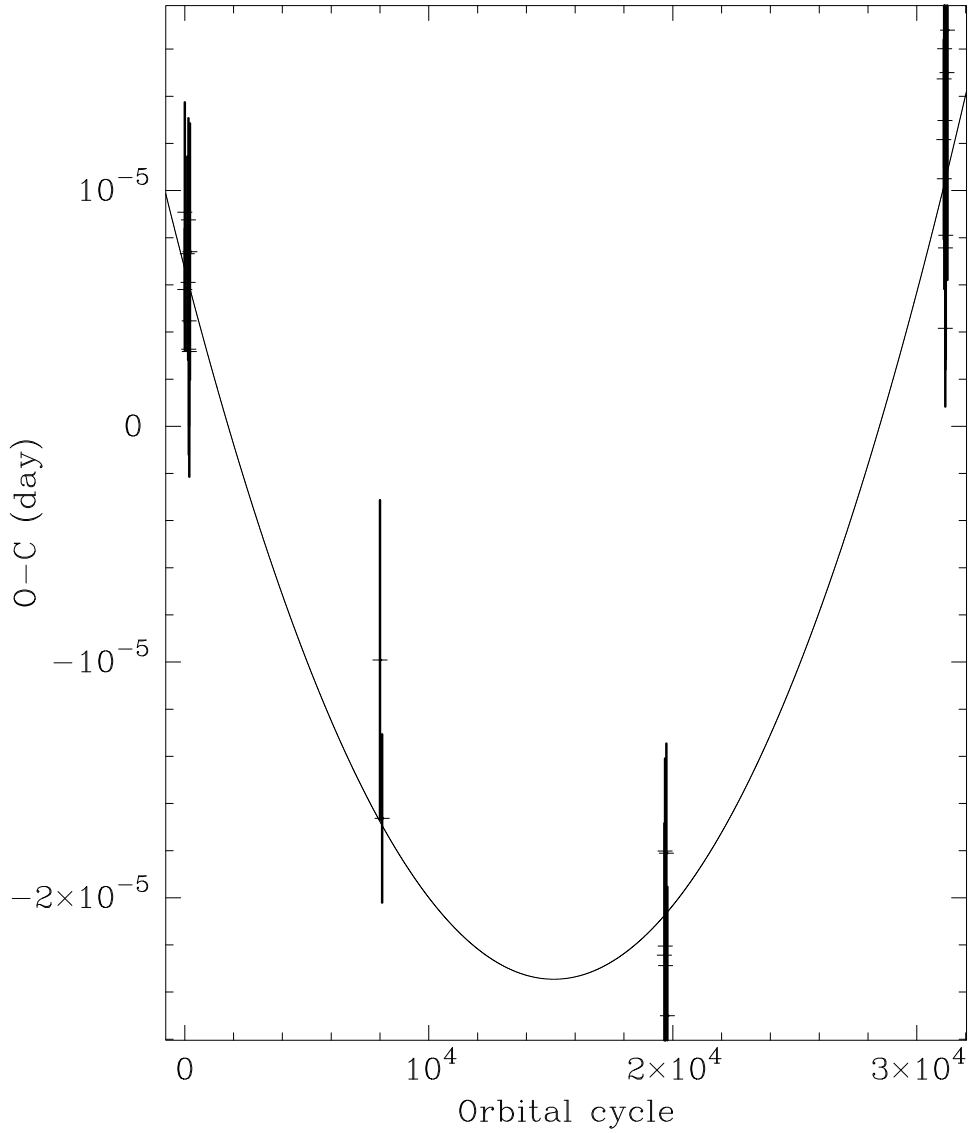

Fig. 4. Orbital evolution of the millisecond accretion powered X-ray pulsar is shown here.

of the presently known eight such sources were discovered with SAX, RXTE, SWIFT or INTEGRAL observatory. If there is an underlying population of fainter outbursts of such sources, MAXI will be able to detect those outbursts and LAXPC observations will be able to reveal their true nature. From observations of the known sources during their future outbursts, it will be possible to measure the spin and orbital evolution of these sources. Orbital evolution measurement of the first known accretion powered millisecond X-ray pulsar SAX J1808-5634, made with the RXTE-PCA observations (Jain, Dutta & Paul 2008) is shown in Figure 4.

Nonthermal emission component in the cluster of galaxies is an unresolved mystery (Nevalainen et al. 2004). Observation of several clusters of galaxies with the LAXPC will allow study of the Compton upscattering of the cosmic microwave radiation in the clusters by non-thermal electron population. This will lead to measurement of the magnetic field strength in the galaxy clusters and also the energy density of the non-thermal electrons.

References

Agrawal, P. C. 2006, AdSpR, 38, 2989

Jain, Chetana, Dutta, Anjan, & Paul, Biswajit 2008, JApA, 28, 197

Nakajima, M., Mihara, T., Makishima, K., & Niko, H. 2006, ApJ, 646, 1125

Nevalainen, J., Oosterbroek, T., Bonamente, M., & Colafrancesco, S. 2004, ApJ, 608, 166

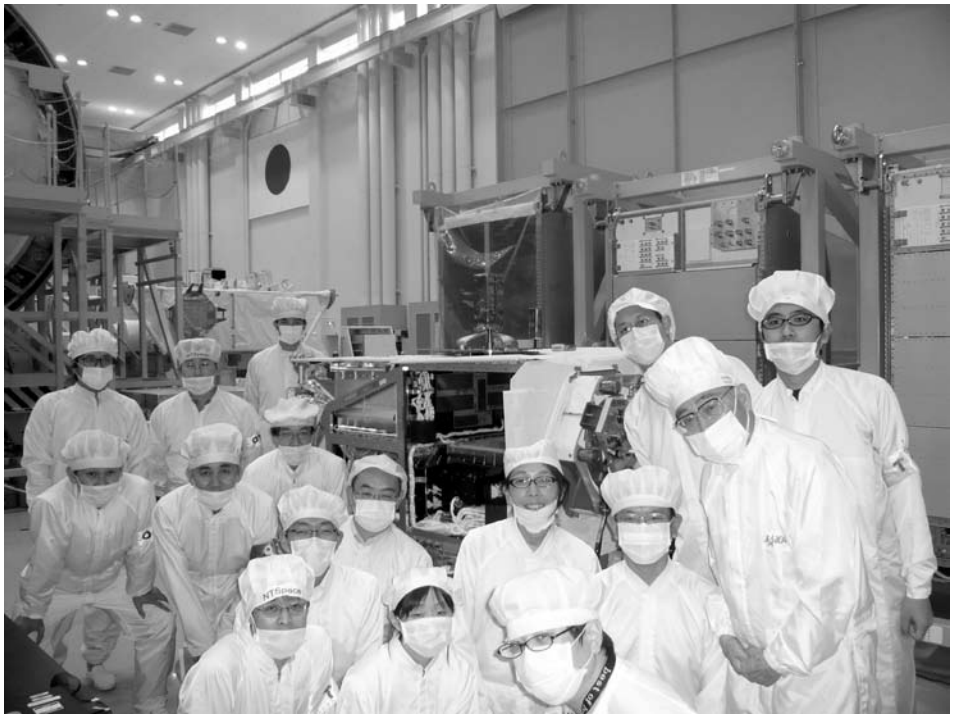

The Hard X-ray Modulation Telescope (HXMT) Mission

Lu FangJun[1], Zhang Shu[1], Wu BoBing[1], Chen Yong[1], Cao XueLei[1],
Zhang Zhi[2], Deng JingKang[2], Zhang ShuangNan[2] and Li TiPei[1,2]

[1] Key Laboratory for Particle Astrophysics, Institute of High Energy Physics, Beijing 100049, China
[2] Center for Astrophysics, Tsinghua University, Beijing 100084, China
E-mail(ZS): szhang@mail.ihep.ac.cn

ABSTRACT

HXMT is an X-ray astronomy satellite consisting of three slat-collimated instruments, the High Energy X-ray Instrument (HE), the Medium Energy X-ray Instrument (ME), and the Low Energy X-ray Instrument (LE). HE is sensitive in 20-250 keV. It contains 18 individual cylindrical NaI(Tl)/CsI(Na) phoswich modules, each with an area of 283.5 cm^2 and a field of view (FOV) of $5.7°\times1.1°$ (FWHM) each. ME is sensitive in 5-30 keV. It contains 3 individual Si-PIN detector arrays with an FOV of $5.7°\times1.1°$ each, and the total collection area is 952 cm^2. LE uses the Swept Charge Device as the detector which is sensitive in 1-15 keV. LE also contains 3 individual detector arrays each with two kinds of FOVs, $5.7°\times1.1°$ and $5.7°\times2.2°$, so as to study the cosmic X-ray background in this energy band. The total collecting area of LE is 384 cm^2. HXMT will perform a broad band (1-250 keV) X-ray all-sky imaging survey with both high sensitivity and high spatial resolution, as well as making pointed observations of X-ray sources to study their broadband spectroscopic and multi-wavelength temporal properties in details. The 3-σ continuum sensitivity of HXMT is about 0.5 mCrab (@100 keV, 10^5s). HXMT was proposed in 1994 and is scheduled to be launched around 2010. The designed lifetime of HXMT is 4 years.

KEY WORDS: HXMT: LE, ME, HE

1. Project History

In 1994 HXMT was first proposed in China. In 2000, the feasibility and technical demonstration study of HXMT was selected as a project under the Major State Basic Research Development Program in China. This project entered its full design phase in October 2005, and passed the technical feasibility review in September 2007.

2. Scientific Objectives

HXMT will perform an all-sky survey and sensitive pointed observations in 1-250 keV. It is anticipated that in the survey about 1,000 hard X-ray sources will be detected, while with the pointed observations the short time scale hard X-ray variability of some sources can be studied in details. Specifically, HXMT has the following scientific objectives:

Cosmic hard X-ray background: The origin of the cosmic X-ray background (CXB) has been a mystery since 1960's. Setti & Woltjer (1989) proposed that CXB is contributed by weak AGNs. This was further confirmed and developed by Madau et al. (1994), Comastri et al. (1995) and Ueda et al. (1998). Recently, Chandra and XMM-Newton resolved most of the CXB into isolated AGNs (Mushotzky et al. 2000; Hasinger et al. 2001). However, both Chandra and XMM-Newton show that a fraction of CXB remains unresolved yet, and this fraction increases with energy (Worsley et al. 2004). This suggests that there are some AGNs which are highly obscured by their respective dust tori. These AGNs are very dim in the soft X-ray band (¡10 keV) but bright in the energy band higher than 10 keV, for which the tori become almost transparent. A deep hard X-ray survey is thus essential to detect the highly obscured AGNs and to reveal the nature of the CXB.

The unified model of AGNs: AGNs are divided into a few types with their observational properties. The unified model proposed that all the AGNs are intrinsically the same and the various observational properties are actually the results of different obscuring geometry of the dust tori. HXMT will detect hundreds of various types of AGNs and obtain the X-ray spectra of some of them, which can be used to constrain the geometry of the various components in the unified model. In particular, with the combination of HE, ME, and LE, HXMT is also powerful for the study of the reflection components in AGN spectra.

Hard X-ray Quasi-Periodic Oscillation (QPO) in X-ray binaries: The study of QPOs in energy bands harder

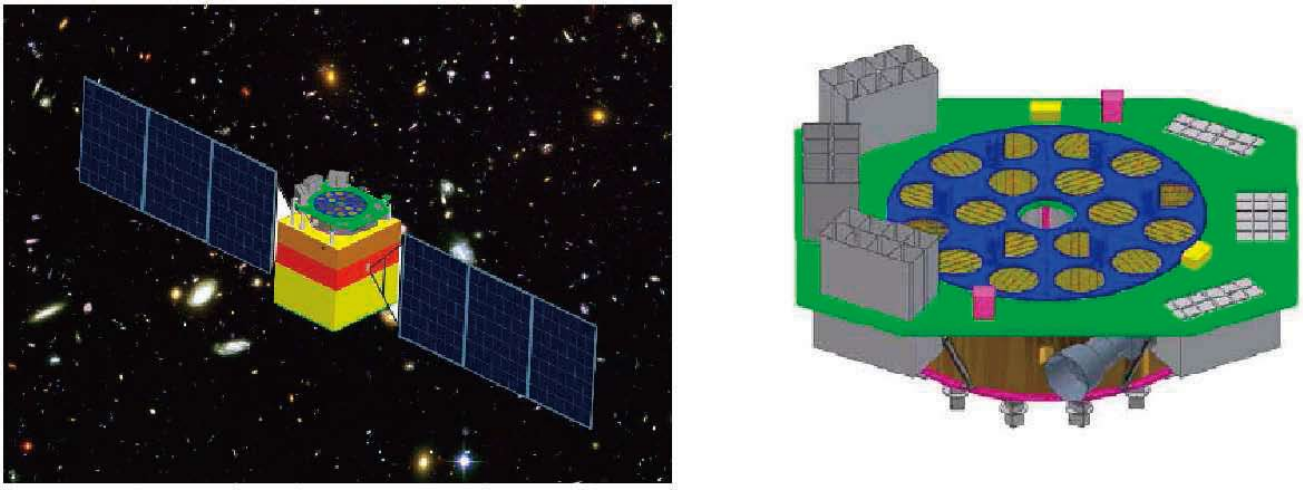

Fig. 1. An artist's illustration of HXMT in space (left panel) and the main payloads onboard HXMT (right panel). The 18 cyclindrical NaI/CsI detectors in the center belong to the High Energy X-ray Instrument (HE), the three detector boxes on the left with solar buffers are the Lower Energy X-ray Instrument (LE) and the three detector boxes on the right are the Medium Energy X-ray Instrument (ME).

than 20 keV remains almost an unexplored area. However, there is evidence that the low frequency QPOs become more significant with increasing energy (Cui et al. 1999). HXMT can study the QPO phenomena in the energy range of 1-250 keV, especially in the range higher than 20 keV.

Origin of the hard X-ray emission from X-ray binaries: The mechanism of hard X-ray emission of X-ray binaries is not well understood. It might be non-thermal process (such as synchrotron radiation or inverse Compton scattering in the jet) or Comptonization from the hot corona. With HXMT there are several ways to investigate the properties of the hard X-ray emitting regions: (1) For dipping sources, we can get information of the geometry with the eclipsing hard X-ray light curves, and (2) for these with relativistic jets, we can determine whether the hard X-ray emission is from the jets or corona by comparing their hard X-ray spectra in different states with and/or without jets; (3) the large sensitive area of the HE will allow sensitive timing diagnostics of the accretion dynamics close to the black hole horizon; (4) the broadband spectroscopy will allow accurate description of the accretion disk properties by detecting their reflection components.

Cyclotron resonance features (CRF) and the magnetic fields of X-ray pulsars: Since there exists strong magnetic field on pulsar surface, it is predicted theoretically and confirmed observationally that there exists CRFs in the hard X-ray spectra of pulsars, and the positions of the CRFs represents the magnetic field strength on the pulsar surface (e.g., Truemper et al. 1978). HXMT will study the CRFs and the magnetic field strength with sensitivity a few times better than the previous experiments.

Hard X-ray emission properties in cluster of galaxies: Evidence for hard X-ray emission from two galaxy clusters, Coma and Abell 2256, was found by BeppoSAX (Fusco-Femiano et al. 1999). But this detection is still under debate. The hard X-ray emission mechanism is probably inverse Compton scattering. However, the source of the high energy electrons remains unknown. It is probably related to the star formation activities, AGNs, or merging in these galaxy clusters. HXMT will quantify the hard X-ray flux of some nearby clusters of galaxies. Together with the radio emission of these clusters, the HXMT observations can be further used to investigate the origin of the relativistic electrons as well as the magnetic field in clusters.

Supernova remnants: It is widely believed that cosmic rays with energies up to the knee are accelerated by Galactic supernova remnants, which is strongly supported by the detection of non-thermal synchrotron emission from supernova remnant shells (e.g., Koyama et al. 1995). HXMT will observe the hard X-ray emission (of supernova remnants), in which the thermal contribution is negligible, and study the acceleration of cosmic rays.

3. Overview of the Observatory

3.1. Characteristics of the HXMT mission

The configuration of the satellite is shown in Figure 1 (left panel) and the key parameters of the mission are listed in Table 1.

3.2. Working mode

1, Scan survey mode: In this mode, the satellite attitude is in the three-axis stabilized state with the telescopes

Fig. 2. The configuration of HE.

pointed in the plane perpendicular to the Sun. The optical axis of the telescopes scans a great circle of constant ecliptic longitude in one orbital period.

2, Pointed observation mode: After the all-sky survey phase, HXMT will start the second phase, i.e., pointed observations of some objects and deep imaging observations of selected sky regions. In this phase the attitude of the satellite is controlled in the 3-axis stabilized mode with respect to stars in the sky. For pointed observations, we will only choose sources whose continuous visibility is higher than 30 minutes and the longer the continuous visibility is the higher the priority will be. The imaging of selected small regions will be realized by pointed observations with pointing directions distributed uniformly in the region.

4. On Board Instruments

4.1. Overall Configuration

Figure 2 (right panel) shows the schematic view of the payloads. HE is the central assembly consisting of 18 cylindrical detectors, ME contains the three boxes on the right side, and the 3 boxes with sun buffers on the left side are the detectors of LE.

4.2. The High Energy Instrument (HE)

HE has a cylindrical structure, consisting of 18 phoswich modules and their collimators (see Figure 2). The collection area of each detector is 283.5 cm^2, and its collimator defines $5.7° \times 1.1°$ field of view (FOV). The orientations of the 18 FOVs are different, with a step size of 10°.

Each detector unit is a cylindrical NaI(Tl)/CsI(Na) phoswich scintillation detector with a diameter of 19 cm. The thickness of the NaI, the main detector, is 3.5 mm, while that of the shielding CsI(Na) is 40 mm.

Because the sensitivity of the telescope is directly related to its background, shielding is an important measure to reduce the background induced by the diffused X-ray/γ-ray and high energy particles. Besides the collimator that defines the FOV of the telescope, both the active shielding and passive shielding are used on HXMT.

The background of the detectors contains mainly four sources: aperture incidence, shielding leakage, particle induced background, and albedo. The first source is dominant in the low energy band, while the latter three are more important in the high energy band.

4.3. The Medium Energy Instrument (ME)

ME contains three detector boxes, and three units in one detector box. Every unit contains six modules, which have 36 Si-PIN detector pixels. The 36 Si-PIN detector pixels are read out by one RENA-3 chip and each module works almost independently. Such a modularized design improves the overall reliability and makes the detectors easier to be installed.

The pixel size of the detectors is 7 mm×7 mm, with a 1.5 mm border and a guard ring. The size of a module that contains 36 pixels is 57.5 mm×57.5 mm, which gives

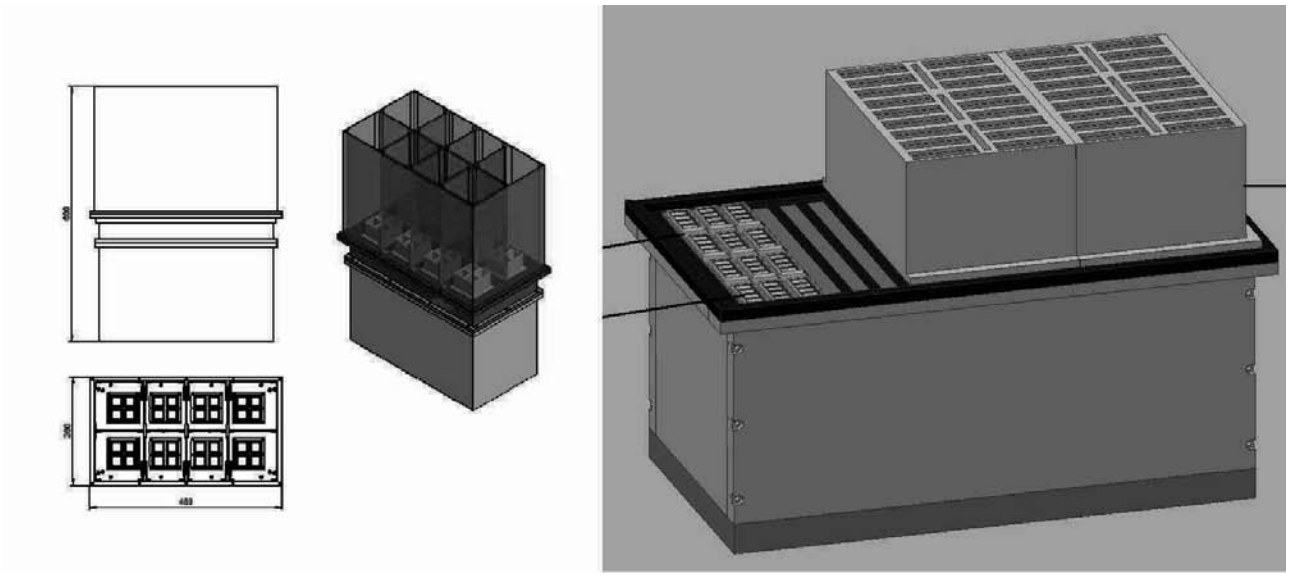

Fig. 3. The sketch map of the LE detector module (left panel) and the ME detector module (right panel).

a total area of 33.1 cm^2 and a sensitive detection area of 17.64 cm^2. ME contains 3 detector boxes and each box contains 18 modules. The total detecting area is 952.5 cm^2 and the total geometrical area is 1869 cm^2. See the architecture of ME in Figure 3 (right panel).

We can estimate the sensitivity of LE as 2.6×10^{-5} cts /cm^2/s/keV, where an energy range of 2 keV (the required spectral resolution), significance of 3σ, and observing time of 10^5s are used.

4.4. The Low Energy Instrument (LE)

LE is one of the three main payloads onboard the HXMT, covering the energy band of 1.0-15 keV. It uses the Swept Charge Device (SCD) as the detector so as to achieve a high time resolution.

LE contains three detector boxes with a sun buffer each. The buffer could also be used as the radiator to cool the detectors. One detector box contains two modules and each module contains 16 SCD chips (CCD236), and every four CCD236 detectors share one collimator. The total detecting area of each module is 64 cm^2. See the sketch map of the LE detector model in Figure 3 (left panel).

We estimate the sensitivity of LE as 4.4×10^{-5} cts/cm^2/s/keV, where an energy range of 450 eV (the required spectral resolution), significance of 3σ, and observing time of 10^5s are used.

5. Participants

The implementation of the HXMT mission is a collaboration between the Chinese Academy of Sciences (CAS) and Tsinghua University.

6. Acknowledgements

This work was subsidized by the National Natural Science Foundation of China, the CAS key Project KJCX2-YW-T03, NSFC-10325313, 10733010, and 973 Program (2009CB824800).

References

Comastri A. et al., 2002, ApJ., 571, 771
Cui W. et al., 1999, ApJ., 512,L43
Fusco-Femiano R., 1999, ApJ, 513, L21
Hasinger G. et al., 2001,A&A, 365,L45
Koyama K. et al., 1995, Nature, 1995, 378,255
Madau P., Ghisellini G., Fabian A.C., 1994, MNRAS, 270, L17
Mushotzky, R.F. et al., 2000, Nature, 2000, 404, 459
Setti G., Woltjer L., 1989, A&A, 224, L21
Truemper J. et al., 1978, ApJ., 219,L105
Ueda Y. et al., 1998, Nature, 391,866
Worsley M.A. et al., 2004, MNRAS, 352, L28

Table 1. The main specifications (goals) of the HXMT mission

Detectors	LE: SCD, 384 cm^2 ME: Si-PIN, 952 cm^2 HE: NaI/CsI, 5000cm^2
Energy Range	LE: 1-15 keV ME: 5-30 keV HE: 20-250 keV
Time Resolution	LE: 1 ms ME: 20μs HE: 25μs
Energy Resolution	LE: 8% @ 6 keV (goal 2.2%) ME: 15% @ 20 keV (goal 5%) HE: 19% @60 keV (goal 17%)
FOV of one module	LE: 5.7°×1.1°, 5.7°×2.2° ME:5.7°×1.1°, 5.7°×2.2° HE: 5.7°×1.1°
Angular Resolution (20 σ source)	$< 5'$
Source Location (20 σ source)	$< 1'$
Sensitivity (3 σ, in 10^5s)	LE: 4.4×10^{-5} cts/cm^2/s/keV (@6keV) ME: 2.6×10^{-5} cts/cm^2/s/keV (@20keV) HE: 3.0×10^{-7} cts/cm^2/s/keV (@100keV)
Orbit	Altitude: $\sim$ 550 km
Attitude	Inclination: $\sim$43° Three-axis stabilized
	Control precision: $\pm$ 0.1°
	Measurement accuracy: $\pm$0.01°
Data Rate	LE: 3 Mbps ME: 3 Mbps HE: 300 kbps
Payload Mass	$\sim$ 1000 kg
Nominal Mission Lifetime	4 years
Working Mode	Scan survey, pointed observation

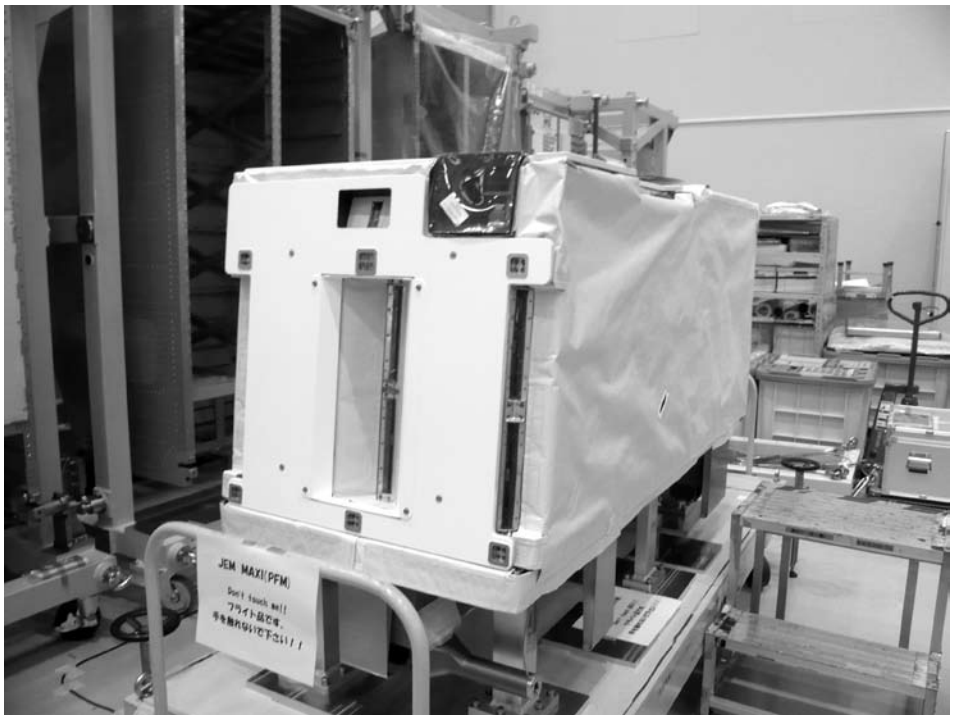

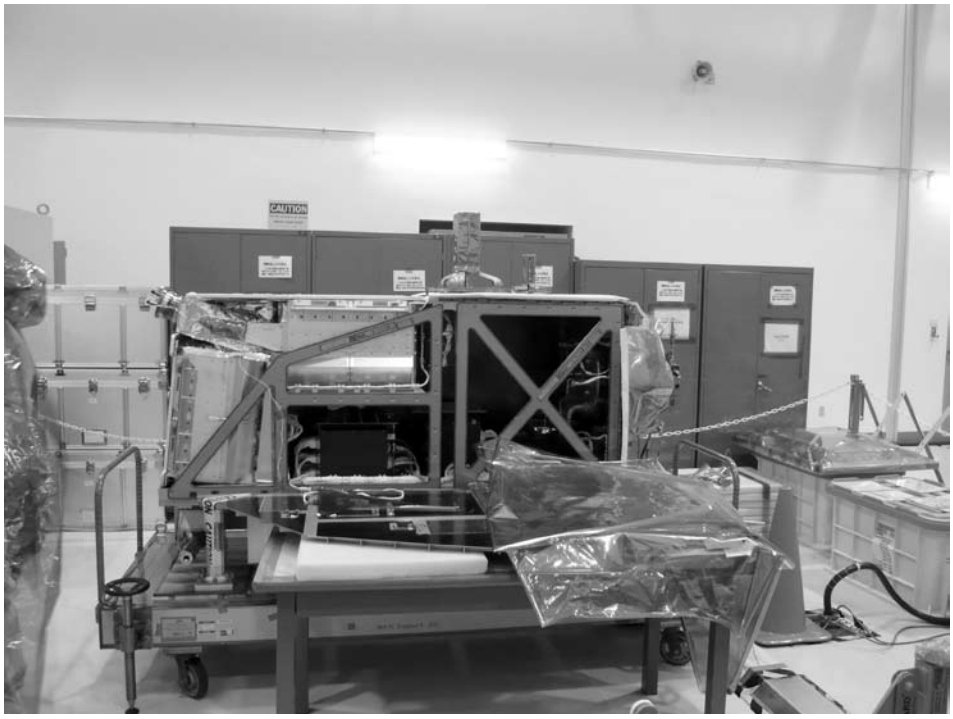

The CALET Project for All-Sky Gamma-Ray and Electron Observations on JEM-EF of ISS

Kenji YOSHIDA,[1] Shoji TORII,[2] for the CALET collaboration *

[1] Department of Electronic Information Systems, Shibaura Institute of Technology, Saitama, Japan
[2] Research Institute for Science and Engineering, Waseda University, Tokyo, Japan
E-mail(KY): yoshida@shibaura-it.ac.jp

Abstract

The CALorimetric Electron Telescope, CALET, is a new all-sky gamma-ray and electron observatory being developed for the Exposure Facility of Japanese Experiment Module on the International Space Station. The mission goal is to investigate high-energy universe by observing cosmic-ray electrons in 1 GeV – 10 TeV, gamma rays in 20 MeV – 10 TeV, and protons, heavier nuclei in several 10 GeV – 1 PeV. The main instrument consists of an imaging calorimeter of scintillating fibers, IMC, and a total absorption calorimeter of BGO, TASC. CALET has a unique capability to observe electrons and gamma rays over 1 TeV with a hadron rejection power larger than 10^5 and an energy resolution better than a few % above 100 GeV. This capability enables us to search for nearby cosmic-ray sources, dark matter and so on. With an auxiliary detector, CALET will also monitor gamma-ray bursts.

Key words: ISS:JEM-EF — cosmic rays:electrons — gamma rays

1. Introduction

We are developing CALorimetric Electron Telescope (CALET) for all-sky gamma ray and electron observations on the Japanese Experiment Module Exposure Facility (JEM-EF) of the International Space Station (ISS). The mission goal is to investigate the high-energy phenomena in the universe by observing electrons in 1 GeV – 20 TeV, gamma rays in 20 MeV – several TeV, and protons, heavier nuclei in several 10 GeV – 1 PeV.

Since 1993, we have developed an imaging calorimeter of the BETS (Balloon-borne Electron Telescope with Scintillating fibers) for balloon experiments, and successfully observed cosmic-ray electrons of 10 GeV – 100 GeV (Torii et al. 2001) and atmospheric gamma rays in a few GeV – several 10 GeV (Kasahara et al. 2002). In 2004, by using the Polar Patrol Balloon in Antarctica, we also carried out the observations of high-energy electrons in 100 GeV – 800 GeV for 13 days (Torii et al. 2008). The CALET is designed on the basis of the BETS instrument to observe higher energy electrons and gamma rays up to ∼10 TeV on the ISS.

In this paper, we will discuss the science, technique, observation and current status of the CALET project.

2. CALET instrument

2.1. Detector concept

The CALET detector consists of the IMaging Calorimeter (IMC), the Total AbSorption Calorimeter (TASC), the SIlicon pixel Array (SIA), and the Anti-Coincidence Detector (ACD). In addition, the Gamma-ray Burst Monitor (GBM) is put together. The total detector weight is $\sim 1.45 \times 10^3$ kg. Figure 1 and 2 present an overview of the CALET at JEM-EF on the ISS and a

* S.Torii,K.Kasahara, S.Ozawa, S.Udo, N.Hasebe, M.Hareyama, N.Yamashita, S.Kodaira, S.Kobayashi (Waseda University), M.Takayanagi, S.Ueno, H.Tomida, J.Nishimura, T.Yamagami, Y.Saito, H.Fuke, K.Ebisawa (JAXA/ISAS), T.Tamura, N.Tateyama, K.Hibino, S.Okuno (Kanagawa University), A.Yoshida, K.Yamaoka, T.Kobayashi, T.Kotani (Aoyama Gakuin University), Y.Shimizu, T.Yuda, M.Takita (ICRR, University of Tokyo), K.Yoshida, A.Kubota, E.Kamioka (Shibaura Institute of Technology), Y.Katayose, M.Shibata (Yokohama National University), S.Kuramata, M.Ichimura (Hirosaki University), T.Terasawa, Y.Tsunesada (Tokyo Institute of Technology), Y. Uchihori , H.Kitamura (National Institute of Radiological Sciences), H.Murakami (Rikkyo University), Y.Komori (Kanagawa University of Human Services), K.Mizutani (Saitama University), K.Munakata (Shinshu University), A.Shiomi (Nihon University), J.W.Mitchell, A.J.Ericson, T.Hams, A.A.Moissev, J.F.Krizmanic, M.Sasaki (NASA/GSFC), M.L.Cherry, T.G.Guzik, J.P.Wefel (Louisiana State University), W.R.Binns, M.H.Israel, H.S.Krawzczynski (Washington University in St Louis), J.F.Ormes (University of Denver), P.S.Marrocchesi, M.G.Bagliesi, G.Bigongiari, A.Cardaroe, M.Y.Kim, R.Cesshi, P.Maestro, V.Millucci , R.Zei (University of Siena and INFN), O.Adriani, P.Papini, L.Bonechi, L.E.Vannuccini (University of Florence and INFN), C.Avanzini, T.Lotadze, A.Messineo, F.Morsani (University of Pisa and INFN), J.Chang, W.Gan, J.Yang (Purple Mountain Observatory, Chinese Academy of Science), Y.Ma, H.Wang, G.Chen (Institute of High Energy Physics, Chinese Academy of Sciences)

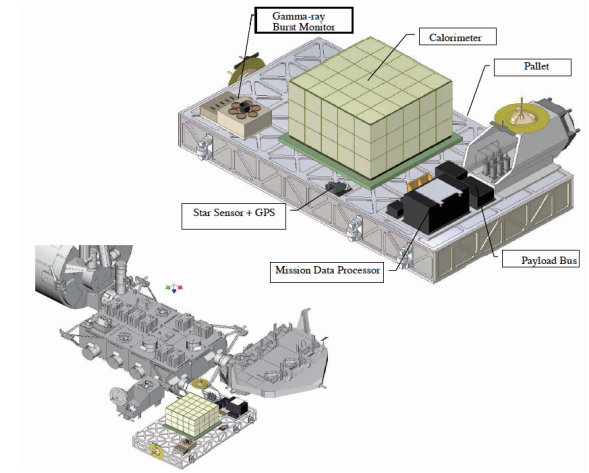

Fig. 1. Overview of the CALET at JEM-EF on the ISS.

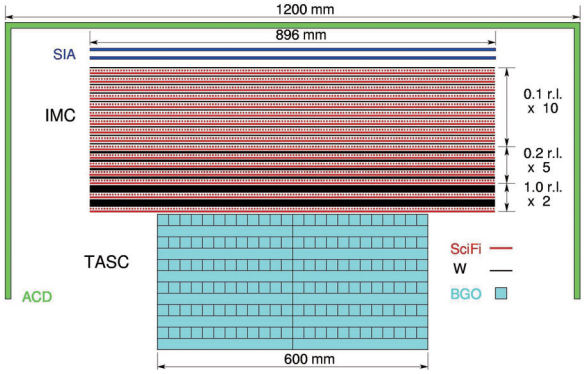

Fig. 2. Schematic side view of the CALET detector.

schematic structure of the CALET detector, respectively.

The IMC is a tracking-type calorimeter using scintillating fibers and tungsten plates. The scintillating fibers with a 1 mm cross section are used to observe particles in pre-shower stage. The IMC has 36 layers of scintillating fiber belts which are set in right angle alternately to observe the projected shower profile in x and y direction. The dimensions of IMC are 89.6 cm × 89.6 cm. While the total thickness of the tungsten plates is 4 radiation lengths (r.l.) and about 0.13 mean free paths (m.f.p.) for proton nuclear interactions, the first 10 tungsten plates are placed with 0.1 r.l. each, followed by 5 plates with 0.2 r.l. each and finally 2 plates with 1 r.l. each. This provides the precision necessary to separate the incident particle from backscattered particles, precisely determine the starting point for the electromagnetic shower, and identify the incident particle. The readout for the scintillating fiber layers is planned to consist of multi-anode photomultiplier tubes (MA-PMT), such as the Hamamatsu R5900. The front-end electronics for the IMC are based upon a high density ASIC such as the 32 channel Viking (VA32HDR2) chip (Tamura et al. 2007). Figure 3 shows an exploded view of the IMC.

The TASC measures the development of the electromagnetic shower to determine the total energy of the incident particle and separate electrons and gamma rays from hadrons. The TASC is composed of 12 layers of BGO logs where each log has dimensions of 2.5 cm × 2.5 cm × 30 cm and there are 48 such logs in each layer. Alternate layers are oriented 90° to each other to provide an x, y coordinate for tracking the shower core. The total area of TASC is $3.6{\times}10^3$ cm^2 and the vertical thickness is 32 r.l. and 1.6 m.f.p. Each BGO log is read by a photodiode for measuring in a high dynamic range (Katayose et al. 2007). Figure 4 shows an exploded view of the TASC.

At the top of IMC, the SIA is placed to improve the charge resolution of incident particles and eliminate effectively the back-scattered particles. The ACD also covers the whole detector to reject charged particles for low energy gamma-ray observations.

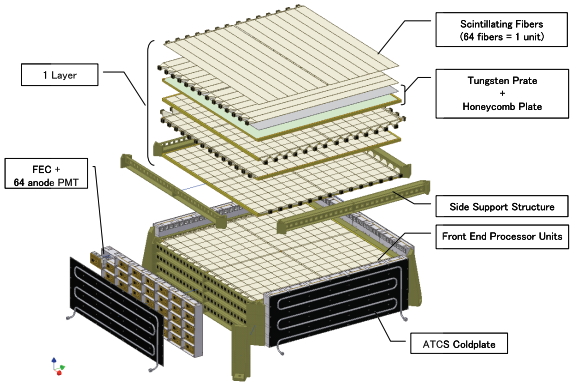

Fig. 3. Exploded view of the IMC.

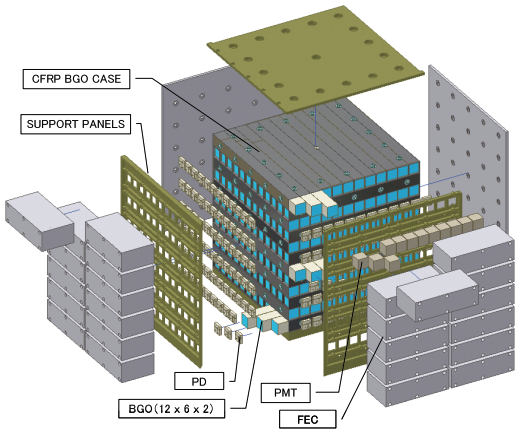

Fig. 4. Exploded view of the TASC.

2.2. Beam test and balloon experiment of the proto-type detectors

We have carried out a beam test in 2003 by use of CERN-SPS for the prototype detector, which consists of the IMC of 512 scintillating fibers with 4 r.l. lead plate and the TASC of 26 BGO logs with 23 r.l. in thickness (Katayose et al. 2005). The performance of the prototype detector has been studied on the rejection power against protons, the energy resolution, the angular resolution, and so on. These results were consistent with the Monte-Carlo simulations.

We have also carried out a balloon observation of cosmic rays with a 1/64 scale model of the CALET detector, so-called bCALET-1, at Sanriku Balloon Center of JAXA in 2006 (Shimizu et al. 2007). The bCALET-1 consists of 1024 scintillating fibers with tungsten plates for the IMC and 24 BGO scintillator logs for the TASC. The area of IMC is 12.8 cm × 12.8 cm. We used 8 MA-PMTs to read out the scintillation light of each scintillating fiber, and developed a front-end circuit with an analog ASIC chip, VA32HDR14, for the readout of the MA-PMTs. We optimized the VA32HDR14 to read out the MA-PMTs to obtain a higher dynamic range of a few thousands. As for the TASC, BGO logs were read out with photo-diodes. The observation was carried out at an altitude between 35 and 37 km for about 3.5 hours. We measured the energy spectrum of electrons from 600 MeV to 20 GeV, verifying the front-end circuits and the detector. We are planning a series of balloon experiments with larger-scale detectors and longer-duration flights, which includes one-month observation by a super-pressure balloon.

2.3. Performance of CALET

We have studied the detector performance by the balloon experiments, accelerator beam tests of the proto-type detector, and Monte-Carlo simulations.

As shown in Fig. 5, the CALET can observe electrons and gamma rays with the energy resolution of a few % at 100 GeV and better for higher energies due to the thick radiation lengths of the TASC. Figure 6 shows the angular resolution as a function of gamma-ray energy. The angular resolution for one photon is ∼0.1 degree above several 10 GeV with the IMC. The angular resolution for one electron is ∼0.06 degree above several 10 GeV, which is better than gamma rays (Akaike et al. 2008). The CALET also has an excellent capability of the proton rejection power larger than 10^5 with the TASC, which is necessary to select electrons and gamma rays in the TeV region. As for the separation of electrons and gamma rays, below 10 GeV, we separate by the anti-coincidence system. Over 10 GeV region, electrons and gamma rays are separated by the IMC, since gamma rays have no tracks at the incident position to the IMC except for back-scattered particles. Gamma-ray rejection power for the electron observation is larger than 5×10^2, and electron rejection power for the gamma-ray observation is larger than 10^5.

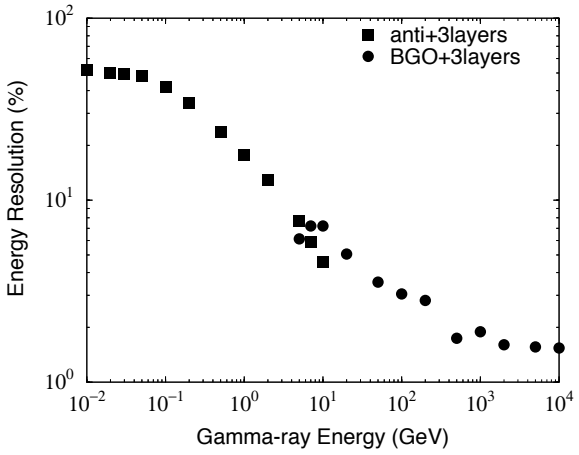

Fig. 5. The energy resolution as a function of gamma-ray energy.

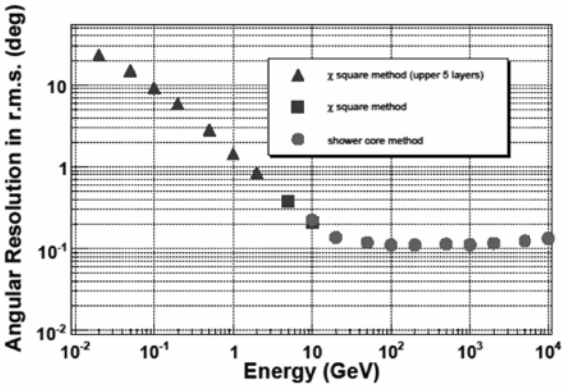

Fig. 6. The angular resolution as a function of gamma-ray energy.

The event trigger will be performed in the following three modes: gamma rays in 20 MeV - 10 GeV by anti-coincidence and tracking of shower particles in the IMC, electrons and gamma rays over 10 GeV by shower trigger in the IMC, and protons over 1 TeV by shower trigger in the TASC. The electrons in 1 GeV - 10 GeV are observed only for the limited term by reducing the threshold of the shower trigger in the IMC. The trigger rates estimated by simulations are ∼51 Hz for 20 MeV - 10 GeV gamma rays (∼37 Hz for albedo gamma rays), ∼40 Hz for electrons and gamma rays over 10 GeV, in which almost triggered events are protons and heliums as background, and <0.1 Hz for protons over 1 TeV.

3. Expected scientific results

The JEM-EF on the ISS gives us an excellent opportunity to carry out the high-energy electron and gamma-

ray observation for a long exposure. The CALET has a wide field of view of 0.5 – 1.8 sr, and a large area of ∼0.8 m^2. The CALET can perform all sky gamma-ray and electron survey without attitude control of the instrument by using the ISS orbit, observing gamma-ray point sources for ∼40 – 50 days.

3.1. Gamma-ray observations

The EGRET instrument performed the first complete sky survey with gamma rays in the energy range of 20 MeV to 30 GeV (Hunter et al. 1997). EGRET revealed that the high-energy gamma-ray sky is surprisingly dynamic and diverse, and found many unidentified sources. The GLAST, being a successor of EGRET, was launched in 2008 to study the high-energy universe by the observations of gamma rays in the 20 MeV – 300 GeV (The GLAST team 2008). CALET will continuously survey the gamma-ray sky up to higher energies and with better energy resolution than GLAST.

Figure 7 presents the expected point source sensitivity of CALET, compared to the other experiments. For air Cherenkov telescopes on the ground, the sensitivities are derived for a 50 hour exposure on a single source. For CALET, EGRET, AGILE, and GLAST, the sensitivities are shown for one year of all sky survey. As presented in Fig. 7, for individual point sources, air Cherenkov telescopes on the ground have a higher sensitivity over 100 GeV. However, since the ground based telescopes have limitations such as low duty cycles (10 %), a small field of view (< 5 deg), and incapability of rejection of the background electrons, CALET has a better sensitivity for observations of diffuse gamma-rays such as the Galactic and extra-galactic diffuse emission. Figure 8 presents the CALET detection limit of Galactic diffuse gamma rays for 4 years.

In addition, CALET can derive wide-band energy spectra of gamma-ray bursts (GRB) over an unprecedented 9 order of energy from a few keV to a few TeV by a combination of the CALET calorimeter and the GBM (Nakahira et al. 2008).

3.2. Electron observations

Evidences of non-thermal X-ray emission and TeV gamma-rays from supernova remnants (SNRs) reveal that high energy cosmic ray electrons and/or protons are accelerated in SNRs.

High-energy electrons lose energy via synchrotron and inverse Compton processes during propagation in the Galaxy. Since the energy loss rate by these processes is proportional to the square of energy, TeV electrons released from SNRs at distances larger than ∼ 1 kpc, or times older than ∼10^5 yr, cannot reach the solar system. Kobayashi et al. (2004) suggested that some nearby SNRs in space ant time, such as Vela, Cygnus Loop, or Monogem, could leave unique signatures in the

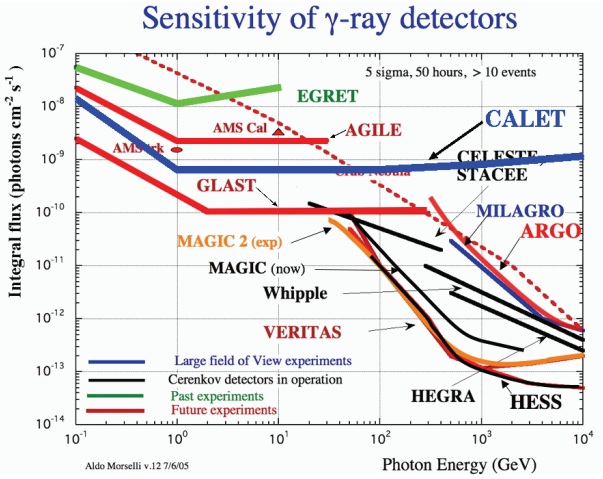

Fig. 7. Gamma-ray point source sensitivity of CALET, compared to the other instruments.

form of identifiable structure in the energy spectrum of TeV electrons, and show increases of the flux towards the sources. Thus, the primary electron component of the Galactic cosmic rays is of fundamental importance to identify cosmic-ray sources, providing acceleration and propagation mechanisms.

In the case of one of the calculations by Kobayashi et al. (2004), a diffusion coefficient of $D_0 = 2 \times 10^{29}$cm^2/s at 1 TeV, a cut-off energy of E_c=20 TeV for the electron source spectrum, and the burst-like release at $\tau = 5\times10^3$ yr after the supernova explosion, we simulated the energy spectrum observed with the CALET, as shown in Fig. 9. This figure presents that the CALET has a capability to identify the unique signature in the energy spectrum with high statistical precision, especially originated from the Vela SNR.

Because the rate of energy loss due to radiation is much higher for electrons than for nuclei, the degree of anisotropy of high-energy cosmic ray electrons is expected to be higher than that of the nuclear component (Shen et al. 1971). Figure 10 shows the electron intensity distribution along Galactic longitude in the case of a diffusion coefficient of $D_0 = 2\times10^{29}$cm^2/s at 1 TeV and a cut-off energy of E_c=20 TeV for the prompt release after the explosion ($\tau = 0$). The maximum intensity is in the direction of Vela at $(\ell, b) = (263°.9, -3°.3)$. As shown in this figure, CALET has a capability of the detection of anisotropy toward the nearby SNR.

3.3. Dark matter search

Although the nature and origin of the dark matter are one of the most important unresolved problem in astrophysics, we do not know what the dark matter is made of. The most predominant candidates of dark matter are some weekly interacting massive particles (WIMPs). WIMPs are, perhaps, the most plausible class of can-

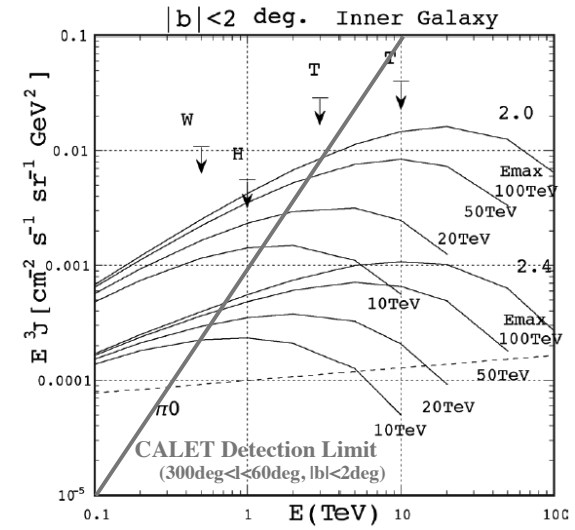

Fig. 8. The CALET detection limit of Galactic diffuse gamma rays above 0.1 TeV for 4 years, compared with the calculated energy spectra (Tateyama 2006).

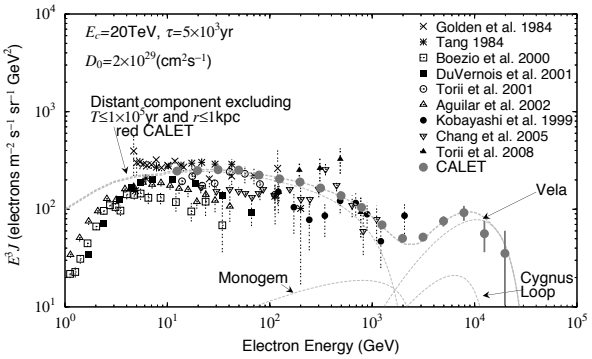

Fig. 9. Simulated electron energy spectrum of the CALET compared with previous data (Kobayashi et al. 2004 and references therein).

didates for dark matter. Among these, neutralino, χ, of the lightest stable supersymmetric (SUSY) particle is the most well motivated. Models with extra dimensions can also provide an alternative candidate for dark matter. In particular, the lightest Kaluza-Klein particle (LKP) in models of universal extra dimensions may be stable and can be a dark matter candidate. The most natural LKP is the first Kaluza-Klein excitation of the hypercharge gauge boson, $B^{(1)}$. This state is referred as Kaluza-Klein particle. These WIMPs are expected to annihilate and/or decay into gamma rays, e^+e^-, and so on. Hence, the indirect observations of dark matter is possible by the detection of these products.

There are many calculations of neutralino gamma-ray signals from accreting Galactic halo dark matter. By using the result of a calculation of Bergström et al. (2001), we estimated the possibility of detection of a

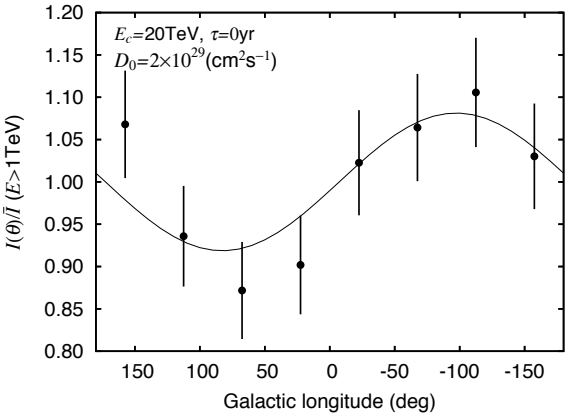

Fig. 10. Electron intensity distribution along the Galactic longitude with the simulated distribution of CALET.

neutralino annihilation. In the case of the annihilation rate σv of 7.5×10^{-29} cm^{3}s^{-1} with the gamma-ray energy of 690 GeV, the gamma-ray line flux is estimated to be 1.7×10^{-8} (cm^{-2} s^{-1} sr^{-1}) in a field of $44^\circ\times5^\circ$ along the Galactic plane in the direction of Galactic center. Figure 11 shows the simulated energy spectrum of a gamma-ray line at 690 GeV from neutralino annihilation for the four years observations, including the background of the Galactic diffuse emission. As shown in Fig. 11, the CALET has the excellent energy resolution less than a few % above 100 GeV that is suitable to observe line features in the gamma-ray energy spectrum. Thus, the CALET has a possibility to detect a gamma-ray line in the GeV - TeV region from dark matter annihilations.

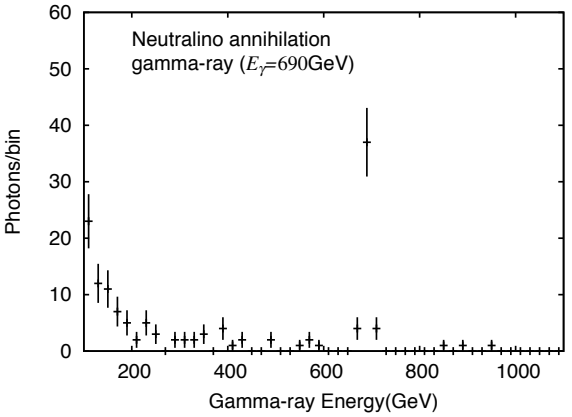

Fig. 11. Simulated energy spectrum of a gamma-ray line at 690 GeV from neutralino annihilation toward the Galactic center with CALET.

Although the direct annihilation to e^+e^- is suppressed for neutralino in the SUSY theory, Kaluza-Klein dark matter directly annihilates to e^+e^- with a large fraction of $\sim$20 %. Although the produced mono-energetic

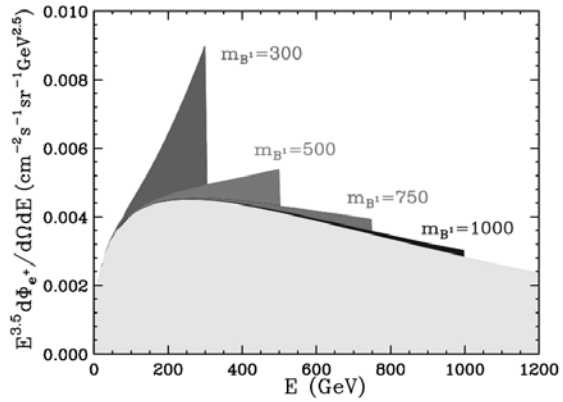

Fig. 12. Predicted positron signals from annihilation of Kaluza-Klein dark matter candidates from Cheng et al. (2002).

e^+e^- lose energy during the propagation in the Galaxy, the observed spectrum would still have a distinctive feature. Figure 12 shows the predicted positron signals for possible Kaluza-Klein particle masses with the estimated background flux of purely secondary positrons (Cheng et al. 2002).

In the case of Kaluza-Klein dark matter for the 300 GeV mass, we simulated the electron + positron spectrum observed with the CALET for the four years observations. The "background" continuum spectrum is the power-law with an index of -3.26 that well represents the observed cosmic-ray electron + positron spectra over a few 10 GeV (Kobayashi et al. 2002). Although the CALET cannot separate electrons and positrons, the high precise measurements of electrons + positrons enable us to detect the distinctive features from dark matter annihilation in the Galactic halo, as shown in Fig. 13.

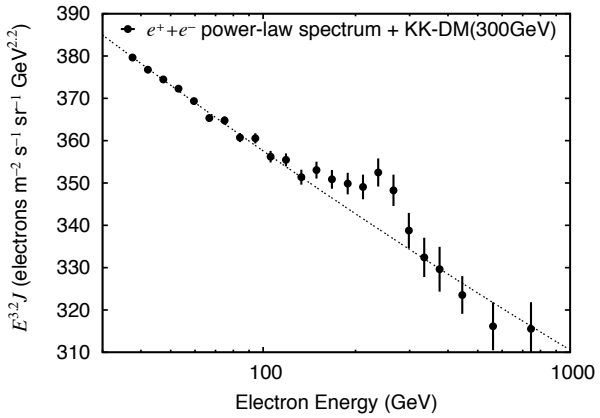

Fig. 13. Simulated energy spectrum of the electron, $e^+ + e^-$, power-law spectrum with Kaluza-Klein dark matter annihilation for 300 GeV mass.

4. Summary and future prospects

We have successfully been developing the CALET instrument for JEM-EF on ISS from the experience of balloon experiments. CALET would provide the first direct identification of cosmic-ray sources by the measurements of the TeV electrons. No other current of planned electron detector has the high-energy reach of CALET. This makes CALET a unique window into the high-energy universe. CALET will also continuously survey the gamma-ray sky up to higher energies with better energy resolution than GLAST. GRB measurements are complementary to those of GLAST and SWIFT but at substantially higher energies. In particular, CALET offers two separate channels by which dark matter candidates may be sought. Neutralinos could annihilate to produce a high-energy gamma ray emission line, or Kaluza-Klein particles could produce high-energy electrons that would show up above the background.

We have already completed a pre-phase A study within last 6 years by a support of JAXA (JSF) budget. International collaboration team (Japan, US, Italy, China) has successfully been established with an allocation of sub-component development. JAXA has selected CALET as one of three mission candidates in May, 2007 for concept study and definition of mission instrument (∼phase A). CALET will be launched around 2013 if it will be approved by the next selection expected within one year.

References

Akaike Y. et al. 2008, submitted to JPSJ Suppl. (International Workshop on Advances in Cosmic Ray Science)
Bergström L. et al. 2001, Phys. Rev.D, 63, 083515
Cheng H.C. et al. 2002, Phys. Rev. Lett., 89, 211301
The GLAST team 2008, http://glast.gsfc.nasa.gov/
Hunter S.D. et al. 1997, Astrophys. J., 418, 205
Kasahara K. et al. 2002, Phys. ReV. D, 66, 052004
Katayose Y. et al. 2005, proc. of 29th ICRC (Pune), 3, 325
Katayose Y. et al. 2007, proc. of 30th ICRC (Merida), in press
Kobayashi T. et al. 2002, Uchuken Houkoku SP, 44, 99
Kobayashi T. et al. 2004, Astrophys.J., 601, 340
Nakahira S. et al. 2008, in this proceeding
Shen C.S. et al. 1971, Astrophys. Lett., 9, 169
Shimizu Y. et al. 2007, proc. of 30th ICRC (Merida), in press
Tamura T. et al. 2007, proc. of 30th ICRC (Merida), in press
Tateyama N. 2006, PhD Thesis
Torii S. et al. 2001, Astrophys. J., 559, 973
Torii S. et al. 2008, submitted to Astropart. Phys.

Observation of Polarization in Hard X-Ray Region with PHENEX Polarimeter

Kishimoto Y.[1], Gunji S.[1], Ishikawa Y.[1], Takada M.[1], Toukairin N.[1], Tanaka Y.[1], Tokanai F.[1], Sakurai H.[1], Mihara T.[2], Sato T.[2], Hayashida K.[3], Anabuki N.[3], Ota M.[3], Tsunemi H.[3], Narita T.[4], Saito Y.[5], Kohama M.[6], Suzuki M.[6], Kishimoto S.[7]

[1] Yamagata University, Yamagata, Yamagata, Japan
[2] RIKEN, Wako, Saitama, Japan
[3] Osaka University, Toyonaka, Osaka, Japan
[4] College of the Holy Cross, Massachusetts, USA
[5] JAXA/ISAS, Sagamihara, Kanagawa, Japan
[6] JAXA/ISAS, Tsukuba, Ibaraki, Japan
[7] KEK, Tsukuba, Ibaraki, Japan
E-mail(KY): kishimo@ksprite.kj.yamagata-u.ac.jp

Abstract

On X-ray and hard X-ray astronomy, the polarization is the last key. It is very useful to understand the radiation mechanism of gamma-ray bursts and pulsars, magnetic structure of supernova remnants, space-time curvature near black hole, and so on. However, the observation for the polarization has been rarely carried out for about 30 years since the observation of the Crab Nebula in X-ray region. It is because of the difficulty for development of the polarimeter with high sensitivity. We have been developing a hard X-ray polarimeter with high sensitivity, called as a PHENEX (Polarimetry for High ENErgy X rays) polarimeter. The PHENEX polarimeter is Compton scattering type polarimeter sensitive to the energy range from 40 keV to 200 keV and is constructed assembling several detectors called as "unit counter". The unit counter is a detector utilizing Compton scattering and it has a modulation factor of 53% and a detection efficiency of 20% at 80keV. We constructed prototype PHENEX polarimeter with four unit counters and carried out a preliminary observation of the Crab Nebula on Jun. 13th 2006 as a balloon-borne experiment. Though we confirmed that the PHENEX detected hard X rays from the Crab Nebula with significance of 8σ, the degree and the direction of the polarization could not be determined with high accuracy because the attitude control system does not function correctly.

Now we are improving the performance of the ACS and the polarimeter to realize the observation of the Crab Nebula with higher accuracy in the next balloon-borne experiment. In this paper, we will present the follows: 1) summary of the PHENEX polarimeter and preliminary observation of Crab Nebula; 2) fix of the ACS trouble; 3) improvement of the PHENEX polarimeter; 4) expected performance for the next observation.

Key words: hard X ray, polarimeter, PHENEX

1. Introduction

In X-ray astronomy, the information on energy spectrum, timing, and imaging has been utilized to understand the nature of the universe. Left out of these measurements to date is polarimetry, yet the observation of polarization brings us invaluable information such as space-time curvature near black hole, radiation mechanisms in pulsars, and the magnetic structure of supernova remnants (P. A. Connors et al. 1980)(J. Dyks et al. 2004). Further, it is also useful for understanding the radiation mechanism in gamma-ray bursts (W. Coburn et al. 2003). Despite its potential usefulness, no significant x-ray polarization measurement has been carried out for about 30 years since the observation of the Crab Nebula (M. C. Weisskopf et al. 1978)(J. P. Hughes et al. 1984). This is because of the difficulty of developing an X-ray polarimeter with high sensitivity. Since the origin of the polarization is often due to non-thermal radiation processes such as synchrotron radiation, observations in the hard-X-ray region are possibly more important than that for the soft-X-ray region; it is expected that the degree of polarization in the hard X-ray region would be higher than

that at lower energies (F. Lei et al. 1997). For the above reasons, we have been developing a hard X-ray polarimeter with high sensitivity (S. Gunji et al. 1994)(H. Tomita et al. 1996), called PHENEX (Polarimetry for High ENErgy X rays) polarimeter (T. Suzuki et al. 2006)(Y. Kishimoto et al. 2007).

The PHENEX polarimeter is Compton-scattering-type polarimeter sensitive in the energy range from 40 keV to 200 keV and is constructed in a modular fashion with an array of "unit counters". After we measured the performance of one unit counter using the highly polarized beam of BL14A in KEK, we have constructed the PHENEX polarimeter with four unit counters and then carried out balloon-borne experiment on June 13, 2006 to observe the Crab Nebula.

In the following sections, we present summaries of the PHENEX polarimeter and preliminary observation of Crab Nebula in 2006. Moreover, we also explain the status of the preparation for the next observation and show the expected performance for it.

2. Unit Counter

The unit counter consists of 36 (6×6) pieces of plastic scintillator surrounded by 28 pieces of CsI(Tl) scintillator. These 64 pieces of the scintillator are read out by one multianode photomultiplier (MAPMT) with 64 channels developed by HAMAMATSU Photonics Inc. Fig. 1 shows a schematic view for the unit counter. The pixel size of the multianode photomultiplier is 6.0×6.0 mm^2 and the size of scintillators is 5.5×5.5×40 mm^3. As incident hard X ray enters into one of the plastic scintillator, Compton scattering occurs and then the scattered hard X ray is absorbed by one of the surrounding CsI(Tl) scintillators. The azimuthal scattering angle depends on the polarization direction of the incident hard X rays as shown in Eq. 1. Since these scintillators are segmented, the 2-dimensional scattering direction can be measured and hence the information on the polarization of the incident hard X rays can be obtained (Fig. 2). The instrument field of view is constrained to 4.8 degrees (FWHM) by a collimator made of molybdenum (1 mm thickness). The side of the unit counter is covered by graded passive shields made of Pb (2mm thickness) and Sn (1mm thickness). Each energy deposit in the plastic and CsI scintillators is read out by the MAPMT, and the signals of each pixel are fed through charge-sensitive preamplifiers and shaping amplifiers to an Analog to Digital Conversion (ADC) system for digitization.

$$\frac{d\sigma}{d\Omega} = \frac{r_0^2}{2}\frac{k^2}{k_0^2}\left(\frac{k_0}{k} + \frac{k}{k_0} - 2\sin^2\theta\cos^2\phi\right) \quad (1)$$

r_0 : classical radius of electron
θ : scattering angle for incident direction
ϕ : azimuthal scattering angle for polarization vector
k_0 : energy of incident hard X ray
k : energy of scattered hard X ray

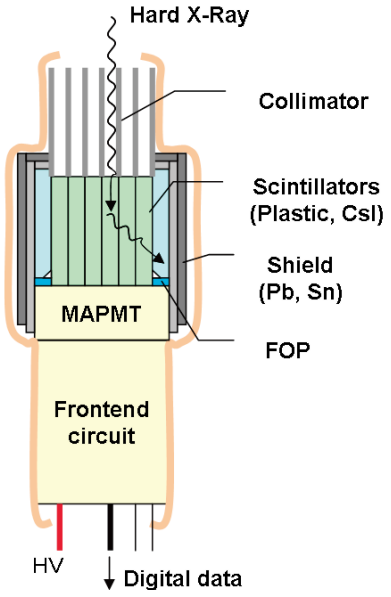

Fig. 1. The schematic view of the unit counter. An incident hard X ray is scattered by one of plastic scintillator and absorbed by one of CsI(Tl) scintillator, respectively.

The unit counter performance has been investigated in detail using a polarized hard X-ray beamline (Beam Line 14A) in KEK, and it has been recognized that the unit counter has a modulation factor of 53% and a detection efficiency of 20% at 80keV. In Table 1, the basic parameters of the unit counter are summarized.

Sensitive area [cm^2]	11
Field of view(FWHM) [degree]	4.8
Size [cm^3]	6×6×25
Sensitive energy range [keV]	40 to 200
Detection efficiency [%]	20 (80keV)
Modulation factor [%]	53 (80keV)

Table 1. Basic parameters of the unit counter.

3. PHENEX Polarimeter

In 2006, we constructed a balloon-borne flight model, PHENEX, with four unit counters to observe the Crab Nebula. The instrument configuration for this flight is shown in Fig. 3. In the center of the four symmetrically-arranged unit counters, the counter with CsI(Tl) scintillator (34×34×10 mm^3) is installed to monitor the flux from the Crab Nebula and then is called "monitor counter". The monitor counter has the same collimator

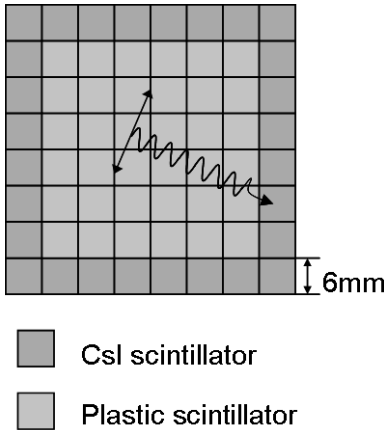

Fig. 2. The top view of scintillators. The solid arrow and the wavy arrow represent the direction of polarization of an incident X ray and the direction of the scattered X ray, respectively.

as that of the unit counters and is co-aligned with them. It can be also used to confirm the correct function of attitude control system. The monitor counter and the four unit counters are all installed inside CsI(Tl) active shields and the whole assembly is housed in a pressure vessel and can rotate along the line of sight. This rotation is necessary to permit removal of systematic effects such as spurious modulation due to individual differences in the scintillators.

Initiated by a trigger signal from any of the four unit detectors or the monitor counter, the signals of all 266 channels (64×4 channels), the monitor counter (1 channel), and active shields (9 channels) are all digitized by the front-end circuits. The information is processed by a VME-based data acquisition system and it is saved in data storage (USB memory) with timing information from GPS system. A data-flow diagram is shown in Fig. 4.

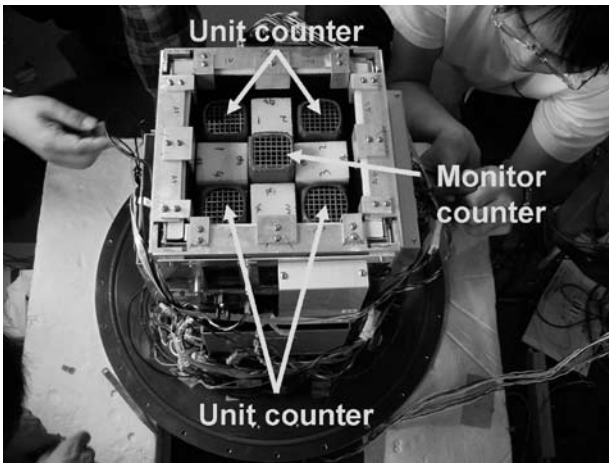

Fig. 3. The flight detector system. Four unit counters and one monitor counter are installed inside CsI(Tl) active shields.

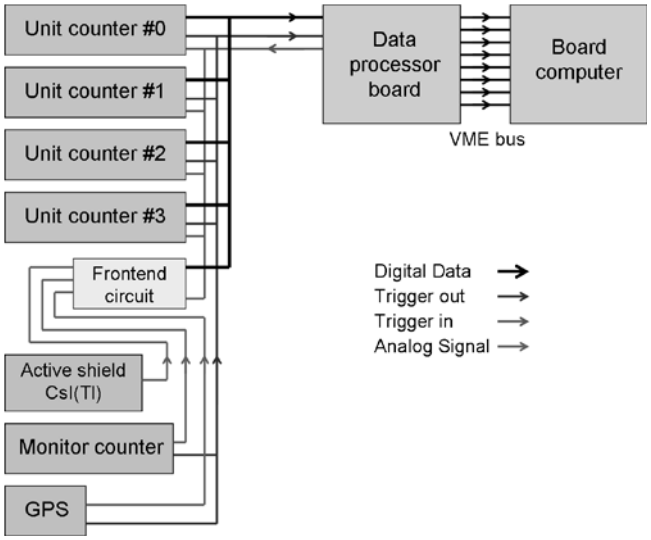

Fig. 4. The data flow diagram of the detector system. When one of the unit counters or the monitor counter generates a trigger signal, the signals of CsI(Tl) active shields are read out by the data processor board at the same time.

During flight, a sun sensor was used for the monitor and control of the line of the sight for the PHENEX polarimeter. The sun sensor is a pinhole camera with a two-dimensional position-sensitive photodiode. Its field of view is about 30°×30° and it can determine the attitude of the polarimeter to an accuracy of about 1 degree. The attitude control system (ACS) has the ability to track the Crab Nebula automatically using the output signal from the sun sensor.

4. Balloon Experiment

The balloon-borne experiment was carried out on June 13th, 2006 to observe the Crab Nebula after launch from the Sanriku Balloon Center. We achieved a level flight for 6 hours at the altitude of about 38 km. The detector system operated well without any serious problem over the duration of the flight and the data were saved safely. However, the ACS did not function correctly and hence the line of sight unfortunately wandered around the Crab Nebula. However, as the sun sensor operated well, we can obtain the necessary information about the pointing direction of the PHENEX polarimeter as a function of time. After all, we succeeded in observing the Crab Nebula for about one hour and also a blank region of the sky for about one hour. The region of the blank sky corresponds to the same elevation and azimuth as that of the Crab Nebula during its observation period. From the data, we confirmed that PHENEX polarimeter detected hard X rays from the Crab Nebula with a significance of 8σ. Then, we carried out polarization analysis and the result of it is shown in Fig. 5. As shown in this figure, the degree and the direction of the polarization can not be

determined with high accuracy. However, it is important advance for polarimetry in hard X-ray region taking into account that the polarization of the Crab Nebula had not been observed in hard X-ray region.

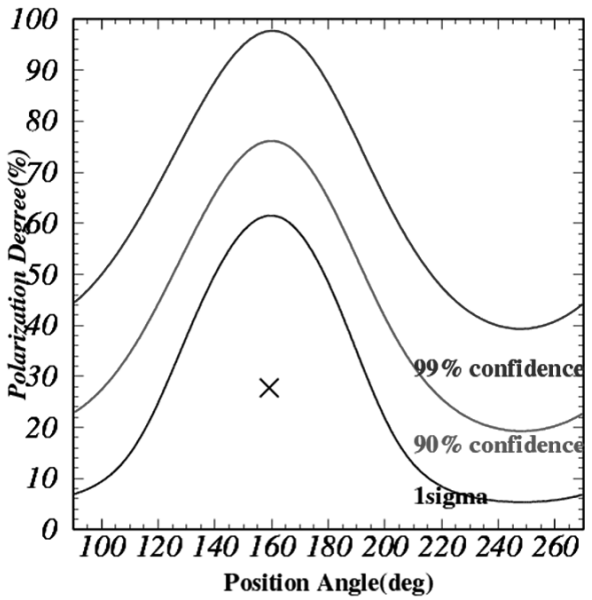

Fig. 5. The result of polarization analysis. The X-axis and Y-axis correspond to the polarization direction and degree, respectively. These lines show contour lines for three error levels (1σ, 90% confidence, 99% confidence).

5. Preparation for the Next Balloon Experiment

To determine the degree and the direction more accurately on the next balloon-borne experiment, it is important to fix the trouble of ACS and to improve the performance of the PHENEX polarimeter.

5.1. Fix of the Trouble on the ACS

First, we investigated the problem on ACS, and found that one of the important parameters used in the computer program of the ACS was not set to correct value. After the set to correct parameters, we investigated the performance of the pointing in use of computer simulation. Fig.6 is a typical result of the simulation. The x-axis and y-axis correspond to the elapsed time from the beginning of the control and the angular difference between the direction of the target object and the pointing direction, respectively. Though the gondola wobbles around the target object for about 3 minutes, the difference gradually converges. Finally it is stabilized to less than 0.1 degrees. Although we tried the simulation with some patterns of parameters, the behavior was basically similar to the above example. Conseqently, we recognized that the bug-fixed ACS can point the target object with the accuracy below 0.1 degrees in a few minutes. Now we are investigating the detail performance using the actual ACS.

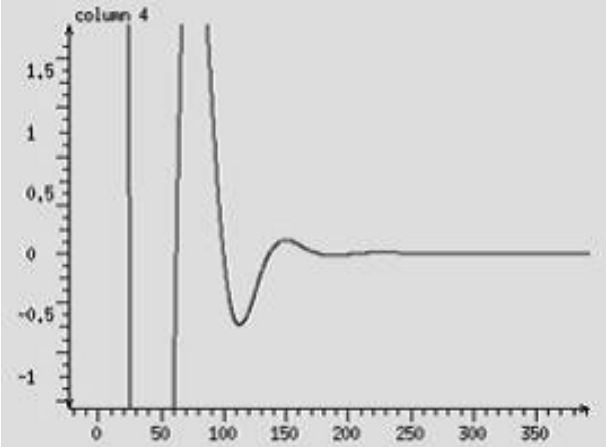

Fig. 6. A result of the simulation for our ACS. The X-axis shows the elapsed time since the beginning of the simulation. The Y-axis corresponds to the difference of azimuthal angle between the gondola and the target object. In this simulation, the initial angular difference between the gondola and the target object is set to 90 degrees, and we assume that the target object moves at the speed of 1 degree/sec constantly.

5.2. Improvement of the PHENEX Polarimeter

In parallel, we are improving the PHENEX polarimeter now. In the first place, we are manufacturing four more unit counters to install eight unit counters to the PHENEX polarimeter (Fig.7). It enlarges the detection area of the PHENEX polarimeter and achieves the effective area of two times more than previous one. Thus, statistical advantage for the determination of the polarization degree and direction can be obtained. Furthermore, this improvement also has another merit that signal-to-background ratio goes up. This merit is derived from the following. The previous version of the PHENEX polarimeter has empty slots as shown in Fig.3 to install more unit counters. Through the space, external background could hit the unit counters. Because this improvement fills the space with unit counters and the unit counter can also work as active shields for neighboring ones, much reduction of background should be realized and then signal-to-background ratio goes up. From the data on previous balloon-borne experiment and preliminary computer simulations considering the hard X-ray flux of the Crab and the background, it is expected that the signal-to-background ratio will go up to 1.0:0.6.

Secondly, we also improved the unit counter itself. Although the front-end circuit adopted for unit counter is compact and very useful for reading the MAPMT signals of 64 channels simultaneously, detection efficiency

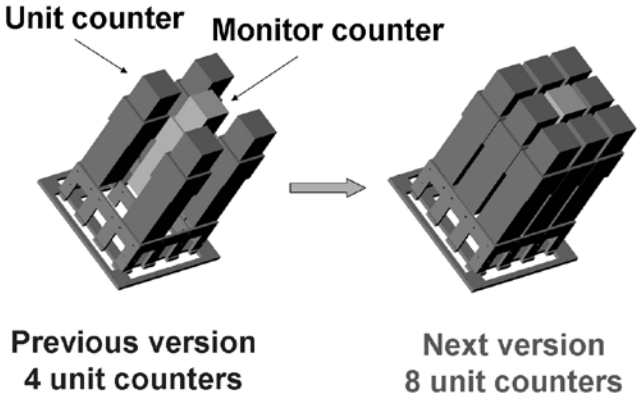

Fig. 7. Improvement of the PHENEX polarimeter. The number of unit counters will be doubled and the empty space in the previous version is also filled with unit counters. These have two merits as follows: 1) enlargement of the detection area; 2) improvement of the signal-to-background ratio. 2) is because that the unit counter can also work as active shields for neighboring ones.

around threshold is somewhat low. This caused deterioration of detection efficiency around 40keV in the balloon-borne experiment in 2006. Therefore, we optimized the gain of the circuit and the applied voltage to the MAPMTs to improve the detection efficiency around 40keV. In the result, detection efficiency at 40keV was improved to be about 4 times. Furthermore, we will enhance the passive shield around unit counter to reduce the background level as shown in Fig. 8.

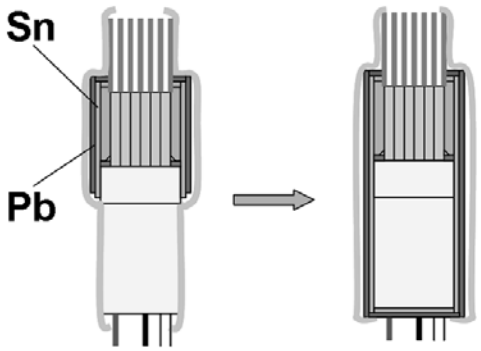

Fig. 8. Reinforcement of passive shield around unit counter. We will enhance passive shield and enclose unit counter wholly with it except incident window.

6. Expected Performance

So we estimated the expected performance for the enlarged PHENEX polarimeter by Eq. 2 of MDP (Minimum Detectable Polarization). For this, we took the following assumptions into consideration : 1) 3 hour's observation of the Crab Nebula at the level flight with enlarged PHENEX polarimeter (8 unit counters); 2) 1.0:0.6 as signal-to-background ratio calculated from a preliminary computer simulation using GEANT4; 3) 0.1cps as signal rate per one unit from the data on previous balloon-borne experiment. As the result, the minimum detectable polarization is estimated to be 11% for next observation. Furthermore, we calculated by another computer simulation the accuracy of the determination for the degree and the direction of the polarization. So we recognized that the degree and the direction of the polarization can be determined with accuracy of about $\pm 4\%$ and ± 9degrees respectively if the polarization degree in hard X-ray region is 30%. In above calculations, we have not yet considered the effects of the follows: 1) improvement of detection efficiency around 40 keV due to the optimization of the circuit gain and the voltage applied to MAPMT; 2) improvement of signal-to-background ratio due to the reinforcement of passive shield. Therefore, more higher performance will be expected if we include these effects in the calculations.

$$MDP = \frac{429}{A\eta SM}\sqrt{\frac{A\eta S + B}{T}} \tag{2}$$

A	:	Detection area [cm^2]
S	:	Signal Count Rate [sec^{-1}cm^{-2}]
η	:	Detection efficiency
M	:	Modulation factor
B	:	Background Count Rate [sec^{-1}]
T	:	Observation time [sec]

7. Conclusion and Future Works

We have been developing a hard X-ray polarimeter with high sensitivity, called as a PHENEX (Polarimetry for High ENErgy X rays) polarimeter. We carried out preliminary observation for the polarization of the Crab Nebula in June 2006 with the polarimeter. Although the PHENEX polarimeter detected hard X rays from the Crab with a significance of 8σ, the degree and the direction of polarization with high accuracy could not be determined in this observation.

Now we are improving the performance of the ACS and the polarimeter to realize the observation of the Crab Nebula with higher accuracy for the next balloon-borne experiment. First, we has fixed the bug of ACS and are performing laboratory experiments to demonstrate that it can point the target object with the accuracy below 0.1 degrees. Secondly, we are also improving the PHENEX polarimeter. In particular, we are constructing the PHENEX polarimeter with eight unit counters to enlarge the detection area as twice and to

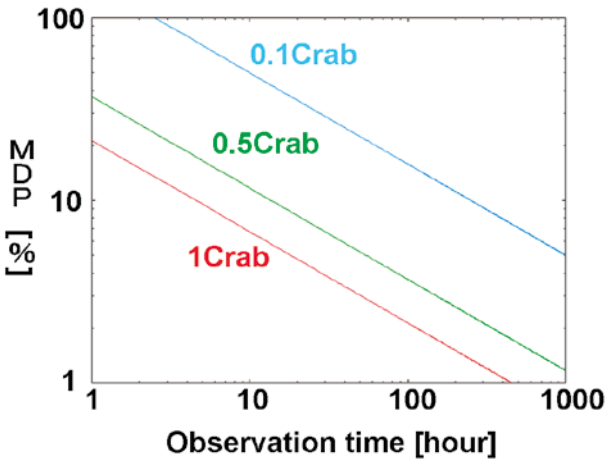

Fig. 9. Expected MDP for next version of PHENEX polarimeter. This is calculated on the following assumptions: 1) 3 hour's observation of the Crab Nebula at the level flight with enlarged PHENEX polarimeter (8 unit counters); 2) 1.0:0.6 as signal-to-background ratio calculated from a preliminary computer simulation using GEANT4; 3) 0.1cps as signal rate per one unit from the data on previous balloon-borne experiment.

improve signal-to-background ratio. Moreover, we already have developed the new version of unit counter with higher detection efficiency around 40 keV due to the optimization of the circuit gain and the voltage applied to MAPMT. Moreover, we will also enhance the passive shield of unit counter to go up signal-to-background ratio. We estimated the expected performance for the next observation assuming 3 hour's observation with enlarged PHENEX polarimeter and the signal-to-background ratio estimated from computer simulation. As the result, it was recognized that the polarization of Crab Nebula was detectable with the significance of 3 sigma if Crab Nebula was polarized more than 11%. Furthermore, we calculated by another computer simulation the accuracy of the determination for the degree and direction of the polarization. As the result, it was recognized that these can be determined with accuracy of about $\pm 4\%$ and ± 9degrees respectively if the polarization degree in hard X-ray region is 30%.

Now we are preparing for the next observation in 2009. After that, we will observe some sources that are bright in hard X-ray region. If long-duration-flight balloon is put to practical use, the MDPs for sources brighter than 0.5 Crab and 0.1 Crab will go up to a few percent and about 10%, respectively. Moreover, we are planning to load a modified PHENEX polarimeters to a small satellite named "POLARIS" as a focal-plane detector of a hard X-ray mirror.

References

F. Lei et al. 1997 SSR., 82, 309-388
H. Tomita et al. 1996 IEEE TNS., 43, 1527-1532
J. Dyks et al. 2004 ApJ., 606, 1125-1142
J. P. Hughes et al. 1984 ApJ., 280, 255-258
M. C. Weisskopf et al. 1978 ApJ., 220, 117-121
P. A. Connors et al. 1980 ApJ., 235, 224-244
S. Gunji et al. 1994 IEEE TNS., 41, 1309-1312
T. Suzuki et al. 2006 JJAP., 45, 274-278
W. Coburn et al. 2003 Nature, 423, 415-417
Y. Kishimoto et al. 2007 IEEE TNS., 54, 561-566

Recent Development Status of PoGOLite

K. Kurita[1], Y. Kanai[1], M. Ueno[1], J. Kataoka[1], N. Kawai[1], Y. Umeki[2], H. Yoshida[2], T. Tanaka[2], H. Takahashi[2], T. Mizuno[2], Y. Fukazawa[2], H. Tajima[3], T. Kamae[3], G. Madejski[3], G. Varner[4], M. Kiss[5], P. Carlson[5], W. Klamra[5], M. Pearce[5], F. Ryde[5], S. Larsson[5], H.-G. Florén[6], G. Olofsson[6], G. Bogaert[7], T. Takahashi[8], S. Gunji[9], for the PoGOLite Collaboration

[1]Tokyo Institute of Technology, Meguro, Tokyo, Japan
[2]Hiroshima University, Higashi-Hiroshima, Hiroshima, Japan
[3]Stanford Linear Accelerator Center, Menlo Park, CA, USA
[4]University of Hawaii, Honolulu, HI, USA
[5]Royal Institute of Technology (KTH), Stockholm, Sweden
[6]Stockholm University, Stockholm, Sweden
[7]École Polytechnique, Palaiseau, France
[8]ISAS/JAXA, Sagamihara, Kanagawa, Japan
[9]Yamagata University, Kojirakawa, Yamagata, Japan
E-mail(K. Kurita): kurita.k.aa@m.titech.ac.jp

Abstract

The light-weight Polarized Gamma-Ray Observer (PoGOLite) experiment is designed to measure the linear polarization of celestial soft gamma-rays in the 25 keV − 80 keV energy range. Polarized gamma-rays are expected from a wide variety of sources including rotation-powered pulsars, accreting black holes and neutron stars, and jet-dominated active galaxies. Polarization has never been measured at soft gamma-ray energies where non-thermal processes are likely to produce high degrees of polarization. The polarization is derived from the azimuthal distribution of Compton scattering angles in the sensitive volume of the instrument. The scattering angle will be measured by detecting coincident Compton scattering and photo-absorption sites in an array of 217 phoswich detectors. The PoGOLite experiment is being developed by groups in USA, Sweden, France and Japan.

We present the status of recent PoGOLite developments, including results from a polarized X-ray beam test performed at the KEK Photon Factory in Feburuary 2008.

Key words: Polarimetry, Soft Gamma-Rays, Balloon Experiment

1. Introduction

Polarization measurements in the X-ray and gamma-ray energy range provide crucial information about astrophysical objects such as isolated pulsars, jet-dominated active galaxies, accreting black holes and neutron starts. Strong X-ray and gamma-ray polarization can arise from synchrotron emission in an ordered magnetic field, photon propagation through extremely strong magnetic fields (magnetic field B $\geq 10^{12}$ Gauss) and anisotropic Compton scattering (Lei, F., A. Dean, J. & Hills, G. L. 1997). In all cases, the orientation of the polarization plane depends on the direction of the magnetic fields or the matter distribution, hence it probes the source geometry and emission mechanism.

Despite the potential importance of polarization measurements, the Crab Nebula has been the only source outside of the Solar system from which polarization has been detected significantly: the OSO-8 satellite viewed the Crab at 2.6 and 5.2 keV and measured the polarization using Bragg diffraction (Weisskopf, M. C. et al. 1978). Other sources including the Crab pulsar are below the sensitivity of past measurements (Silver, E. H. et al. 1978) and no systematic study of X-ray and gamma-ray polarization has been performed. Today many objects in high-energy astrophysics still await polarization study (Kataoka, J. et al. 2005).

The light-weight Polarized Gamma-Ray Observer (PoGOLite) is a new balloon-borne instrument capable of detecting 10% polarization from a 200 mCrab source in the 25∼80 keV energy range in a single 6-hour flight for the first time. In order to detect the polarization, PoGOLite measures the azimuthal angle asymmetry of Compton scattering and the subsequent photoabsorption in an array of detectors. This array consists of 217 well-type phoswich detector cells (PDCs) and 54 side anticoincidence shield (SAS) detectors made of bismuth germanete

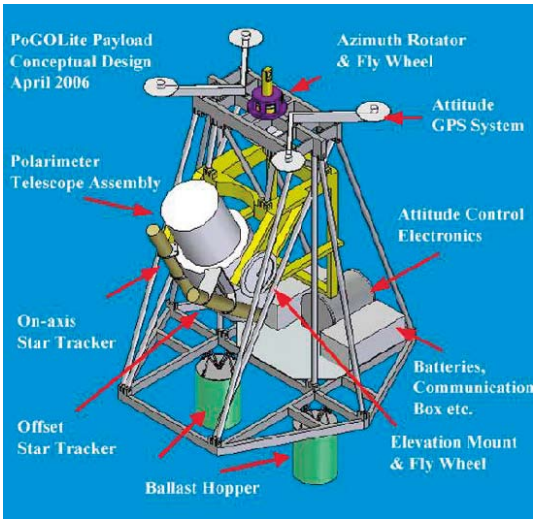

Fig. 1. PoGOLite payload. The dimension will be 2.5×2.5 m^2 in footprint and 3.5 m in height.

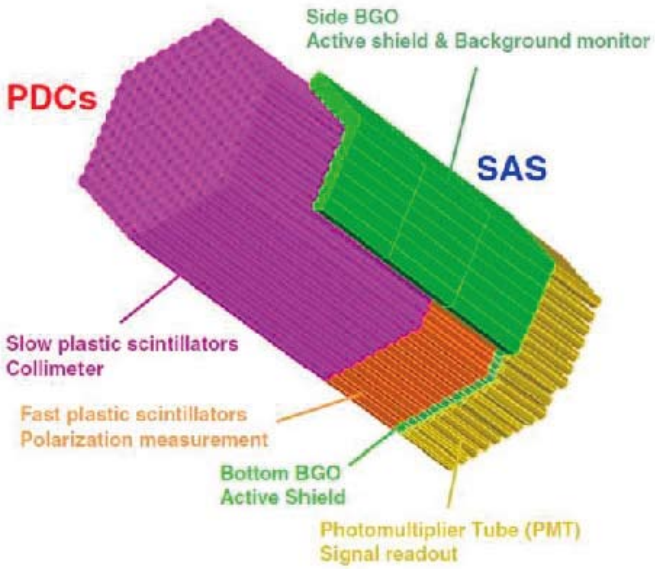

Fig. 2. PoGOLite detector design.

oxide (BGO) scintilators (Kamae, T. et al. 2008). The adoption of a well-type phoswich detector provides a narrow field-of-view (1.25 msr), a large effective area (∼228 cm^2 at 40 keV), a high modulation factor (more than 25 %) and the low background (∼ 100 mCrab) required to conduct high-sensitivity polarization measurements.

PoGOLite is scheduled for launch in 2010 (engineering flight) and will observe polarization from astrophysical objects above 25 keV for the first time.

2. PoGOLite Payload and Detector Configuration

2.1. Payload

The PoGOLite payload, shown schematically in Fig. 1, consists of a polarimeter telescope assembly, a data acquisition system, and a precision pointing gondola. The telescope assembly is covered by a wall of polyethylene (except for the field-of-view), enclosed in an aluminum structure and mounted on an offset pivot to allow full-sky viewing. The pointing accuracy will be better than ∼10% of the field-of-view (or 0.2°) which maximizes the effective area during observation. The assembly can monitor the angular distribution of cosmic-rays and rotate around its viewing axis: these features will allow us to minimize possible bias in observed polarization.

The PoGOLite payload and attitude control system have been designed various flight possibilities in mind: they include long-duration flights in the mid and high latitude regions of the northern and southern hemispheres, and, target-of-opportunity flights to catch long-lasting flares and outbursts.

2.2. Detector Configuration

The PoGOLite detector consists of 217 well-type phoswich detector cells (PDCs) to measure energy spec-

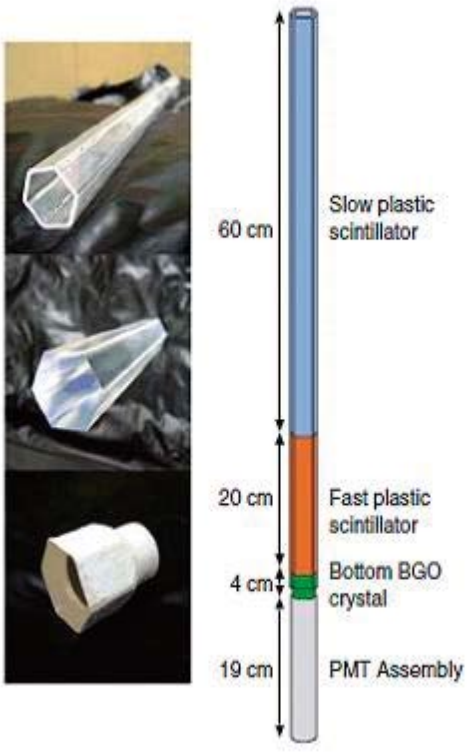

Fig. 3. Phoswich Detector Cell: (right) drawing; and (left) photos of a slow, fast, and bottom BGO scintillators before being glued together.

trum and polarization from azimuth angle asymmetry and 54 side anticoincidence shield (SAS) to reduce the background (Fig. 2). The arrangement of the PDCs is detailed in Fig. 3.

Each PDC is composed of hollow tube of slow plastic schintilatpr at the top (length 60 cm, decay time $\sim$ 285 ns), a solid rod of fast plastic scintilator (length 20 cm, decay time $\sim$ 2 ns), and a bottom BGO crystal (length 4 cm, decay time $\sim$ 300 ns), all viewed by one photomultiplier tube (PMT).

The slow scintillator tube acts as an active collimator, limiting the feld of view to about 1.25 msr ($2.0^\circ \times 2.0^\circ$). Photons or charged particles entering the instrument from the rear are detected in the bottom BGO crystals. The fast scintillator is the detector component where Compton scatterings and photoelectric absorptions take place. The three components are viewed by a single PMT, and by using pulse shape discrimination based on the scintillation decay times of the materials, signals from the different components can be distinguished (Kamae, T. et al. 2008). With the active collimator and BGO shields, background will be considerably reduced (e.g. $\sim$ 10 mCrab at 40 keV, $\sim$ 100 mCrab at 80 keV).

3. Photomultiplier Tubes

PoGOLite is designed to minimize the background by an improved phoswich configuration, which enables a detection of 10 % polarization in a 200 mCrab source in a 6$\sim$8 hour observation. To achieve such high sensitivity, low energy response of the detector is important because the source count rate is generally dominated by the lowest energy photons. We have developed new PMT assemblies specifically designed for PoGOLite to read-out weak scintillation light of one photoelectron level. The PMT assembly consists of PMT R7899EG (1 inch diameter, high QE type; Hamamatsu), a divider circuit, and a built-in DC/DC converter (improved C4900-51; Hamamatsu). The DC/DC converter operates on +12 V power supply. It amplifies the input control signal (0$\sim$5 V) by a factor of 250, and provides an output of an arbitrary high voltage in the range 0 $\sim$ +1250 V to each PMT. Note that lengthy HV cables can be eliminated completely in the PoGOLite flight system, since only +12 or +5 V (MAX) signal to each PMT assembly is required. Power consumption of each PMT ASSY is $\sim$ 300 mW, and total power amounts to 81 W for 271 units. This is within an acceptable range of the power budget of PoGOLite (Kataoka, J. et al. 2005).

4. Readout Electronics

To handle 271 PMT output signals with high flexibility and high throughput, we have been developing a new Data Acquisition (DAQ) system. This system consists of two types of SpaceWire boards, an flash analog to digital converter (FADC) board and a digital I/O board, controlled and read by a SpaceCube (Fig. 4). SpaceWire is a new global standard of the communication interface for scientific missions under development by ESA, ISAS/JAXA, Osaka University and other institutions and companies (Takahashi, T. et al. 2004). SpaceCube is a microcomputer to control instruments, and to process and transfer the data in the SpaceWire system (Takahashi, T. et al. 2007).

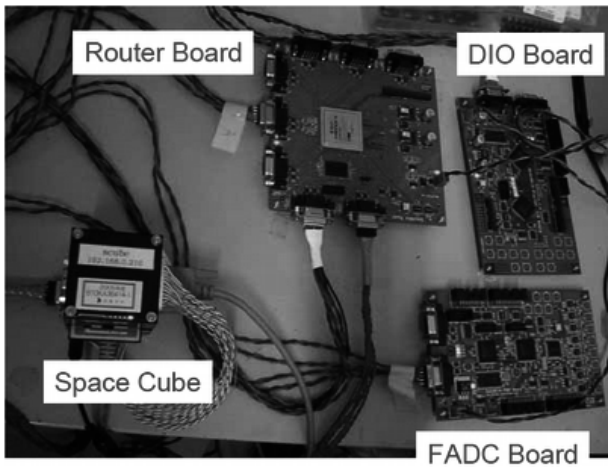

Fig. 4. Prototype SpaceWire boards for the PoGOLite DAQ system.

The PoGOLite FADC board consists of 8 fast Charge Sensitive Amplifier (CSA), 8 channel pipelined FADC, 8 channel digital to analog converter (DAC) to control high voltage supply in PMT assemblies and two Field Programmable Gate Arrays (FPGA) (Xilinx Spartan-3). One of two FPGAs is used for the inter-board interface (SpaceWire), and the other is used for the processing of PMT output signals digitized by the FADC. Therefore, each FADC board can handle up to 8 PMT signals, and 31 and 7 FADC boards will be used for the PDC and the SAS, respectively, in the flight model DAQ system. The network among the boards and the SpaceCube is constructed by using a SpaceWire router.

In our system, all signals from the last dynode of PMTs are fed into an individual fast CSA and then immediately digitized by the FADC. Therefore, most of the signal processing is done by digital circuits in the FPGA, enabling the reduction of the mass, the volume and the power consumption of the DAQ system. We also note that the front-end electronics are common between the PDC and the SAS, and the same FADC board can be used for either system only by changing the onboard FPGA firmware.

The digital I/O board consists of 2 FPGAs and digital I/O interface. This board collects trigger signals from the PDC FADC boards and veto signals from the

Fig. 5. The 19-unit prototype polarimeter used in the 2008 KEK beam test. The prototype was rotated azimuthally in 30 deg steps.

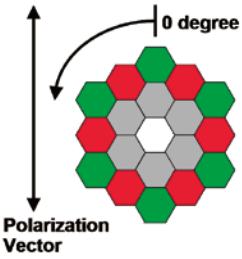

Fig. 6. Arrangement of the 19-PDC prototypes. We defined gray is group1, red is group2 and green is group3.

SAS FADC boards, and figures out if the event is consistent with the valid events or the background. It then send a global data recording trigger to each FADC board (Tanaka, T. et al 2007).

5. Event Selection

Candidates for Compton-scattered events will be selected in the off-line analysis using waveforms in three steps.

Step 1: Select the PDC where photo-absorption took place by requiring the waveform to be compatible with a clean hit in the fast scintillator with energy deposition greater than 15 keV.

Step 2: Waveforms of all neighboring PDCs (up to two layers or 18 PDCs) will be searched for a Compton scattering signal. This threshold was about 0.3 photo-electrons in the 2007 and 2008 KEK beam tests. We conservatively assumed the threshold for detecting Compton scattering to be 1.0 photo-electron in all computer simulations presented in this proposal.

Step 3: Compton-scattering events are selected through the two energy depositions at the photoabsorption site and the Compton-scattering site.

We determine the azimuthal angle of scattering for each event, correct it for the pointing axis and rotation of the Polarimeter Telescope Assembly, and derive the modulation curve. Fitting the modulation curve with computer simulated modulation curves determines the polarization (Kamae, T. et al. 2008).

6. KEK Beam Test 2008

We performed a beam test for a prototype polarimeter in February 2008. The prototype PoGOLite detector used in the test is constructed with 19 PDC units (Fig. 5), all of them were read-out by a flight-design DAQ consisting of three FADC boards and a digital I/O board. Each FADC board is equipped with 8 individual CSA with a time constant of 1 μs and digitizes CSA output to 12 bit accuracy and 36 MHz sampling rate. FPGAs onboard

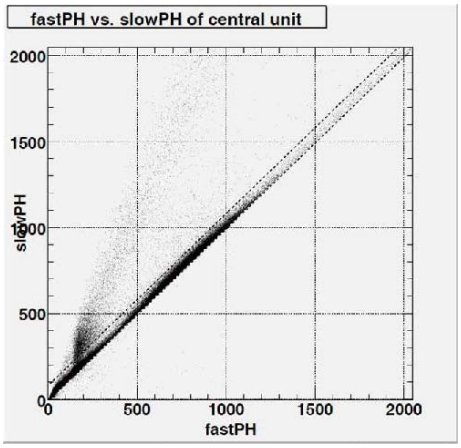

Fig. 7. Two dimensional plot of pulse heights integrated with a short time interval (∼110 ns) and a long one (∼ 420 ns), obtained under the irradiation of 50 keV beam on the central unit. Two dotted lines indicate the region to select clean fast scintillator signal.

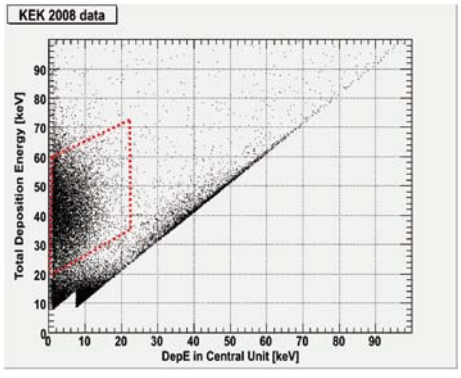

Fig. 8. Relation of the deposit energy in the central unit (Compton site) and the total energy deposition to 50 keV beam. Event selection region is given in red dotted lines. An edge at around 8 keV corresponds to the trigger threshold.

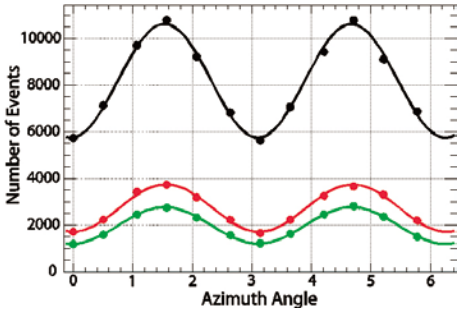

Fig. 9. The measured modulations at a ∼89.7% polarized 50keV beam in the 2008 KEK test for the 3 PDC sets group1 (black), group2 (red) and group3 (green) shown in Fig. 6. The beam entered at the center PDC of Fig. 6.

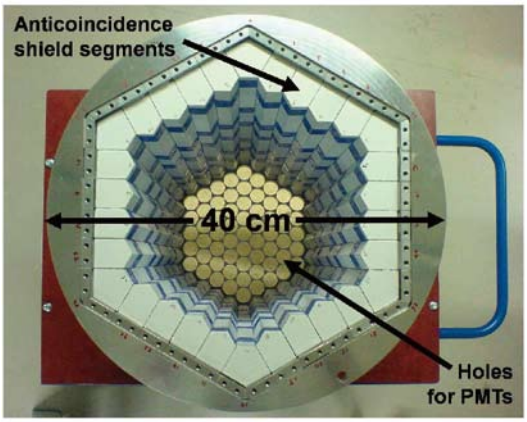

Fig. 10. Top view of the detector array mechanics of the PoGOLite Pathfinder currently under construction in Stockholm

check for each transient signal and issue trigger signals for events compatible with an energy deposition in the fast scintillator above ∼8 keV. Digital I/O boards collects trigger signals from three FADC boards and sends a global trigger signal. An onboard computer, the SpaceCube, controls these two types boards and records waveform data of 19 PDC units for offline analysis.

The experiment was carried out at station A of beam line 14 (BL14A) at KEK Photon Factory in Tsukuba, Japan. The beamline delivers a vertically plane-polarized X-rays via two Si(533) monochromator crystals. The beam polarization was ∼ 89.7%. We irradiated 50 keV beam to the central PDC unit and thereby the unit acted as an active scatterer with other 18 units absorbing the scattered photons.

To select a clean fast scintillator signal, waveform data are processed in the following way: the charges from PMTs are integrated over the fast (∼ 110 ns) and slow (∼ 420 ns) intervals and are compared. As illustrated in Fig. 7, clean fast scintillator signals fall in a narrow diagonal region and slow/BGO scintillator signals from the upper branch. By selecting events between two dashed lines in the figure, clean fast signals is obtained from each PDC unit.

We studied the distribution of the sum of any two energy depositions versus the energy deposition at the central unit (Fig. 8). Events enclosed by the dashed lines are valid Compton events, first Compton scattered in the central unit and then photoabsorbed in one of the other units.

Distributions of valid Compton events along the azimuth angle are shown in Fig. 9 separately for the 3 PDC groups, group1, group2 and group3 (see Fig. 6). The modulation depended on the distance between the Compton scattering site and photoabsorption site as predicted by our Geant4-based simulation program. We detected average modulation factor (MF) 31.3±0.4 %, which agrees in 5 % compared with data and simulation.

7. PoGOLite Pathfinder

A 61-unit proof-of-principle instrument, the PoGOLite "Pathfnder", is currently under construction in Stockholm (Fig. 10). It is scheduled for its frst flight from the Esrange ballooning facility in Northern Sweden in August 2010. The instrument will be used to measure polarization from the Crab nebula and Cygnus X-1, as well as to assess in-flight background in preparation for the flight of the full-size instrument.

The spin axis of the Crab system has been predicted to be at about 124°-126° based on observations with the Chandra X-Ray Observatory (Ng, C.-Y. et al. 2004). X-ray emission from the Crab is believed to be synchrotron emission from high-energy electrons trapped in toroidal magnetic structures around the system (Aschenbach, B. & Brinkmann, W. 1975), and if this model is correct, the polarization angle of the X-ray emission is expected to be parallel with the spin axis of the system (Kamae, T. et al. 2008). However, using an instrument on-board the OSO-8 satellite, the polarization angle at 2.6 keV and 5.2 keV was measured (Weisskopf, M. C. et al. 1978), and was found to be rotated relative to the spin axis by about 30°. If a 19% polarization degree, as measured on-board OSO-8, is assumed in the PoGOLite energy range, the Pathfinder instrument will be able to measure the polarization degree of the Crab nebula with a 7σ significance and determine the polarization angle with a precision of about 5° in a single six-hour flight. Such a measurement will not only reveal whether the polarization degree remains constant with energy, but also determine if the polarization angle aligns with the spin axis at higher energies, thus testing the paradigm that the X-ray emission from the system is synchrotron emission from electrons trapped in magnetic torii around the pulsar (Kamae, T. et al. 2008).

For Cygnus X-1 in the hard state, the PoGOLite Pathfinder will be able to measure as low as 10% polar-

ization. This enables the predicted energy dependence of the polarization to be tested against measurements (Axelsson, M. et al. 2007).

8. Summary

PoGOLite is a balloon-borne soft gamma-ray polarimeter designed to enhance the signal-to-noise ratio and secure a large effective area for polarisation measurement ($\sim$228 cm^2 at 40 keV) by limiting the field of view of individual pixels to 1.25 msr (FWHM) based on well-type phoswich detector technology. Thick neutron and gamma-ray shields have been added to reduce background to a level equivalent to $\sim$100 mCrab between 25$\sim$50 keV. PoGOLite can detect a 10% polarisation from a 200 mCrab object in a 6 hour balloon flight and will open a new observational window in high energy astrophysics. In February 2008, we performed a synchrotron beam test at KEK Photon Factory, and we detected average modulation factor (MF) 31.3$\pm$0.4% polarization with PDC 19 units and the MF agree in 5% compared with data and simulation. An engineering flight is scheduled for launch in 2010 and will observe polarization from astrophysical objects above 25 keV.

References

Aschenbach, B. & Brinkmann, W. 1975 A&A. 41. 147
Axelsson, M. et al. 2007 Astroparticle Physics 28, 327
Kamae, T. et al. 2008 accepted for publication in Astroparticle Physics.
Kataoka, J. et al. 2005 Proc. SPIE, vol. 5898, 133
Lei, F., A. Dean, J. & Hills, G. L. 1997 Space Sci. Rev. 82, 309
Ng, C.-Y. et al. 2004 ApJ. 601. 479
Silver, E. H. et al. 1978 ApJ. 225, 221
Takahashi, T. et al. 2004 The second Space Wire Working Group meeting, ESA/ESTEC, November 11th 2004
Takahashi, T. et al. 2007 "Space Cube 2 - an Onboard Computer based on Space Cube Architecture"
Tanaka, T. et al 2007 IEEE Nuclear Science Symposium Conference Record Vol. 1, 445
Weisskopf, M. C. et al. 1978 ApJ. 220, L117

Wide-band Gamma-Ray Burst Monitor

– GBM for the CALET Mission –

Satoshi Nakahira[1], Kazutaka Yamaoka[1], Atsumasa Yoshida[1], Taro Kotani[1], Kei Suzuki[1], Takaaki Doshida[1], Takuya Oyama[1], Satoshi Sugita[1], Hiroshi Tomida[2], Yujin E. Nakagawa[3], Shoji Torii[4] and the CALET team

[1]Department of Physics and Mathematics, Aoyama Gakuin University, Japan
[2]ISS Science Project Team, Institute of Space and Astronautical Science (ISAS), Japan Aerospace Exploration Agency (JAXA), Japan
[3]Riken, Wako, Japan
[4]Research Institute for Science and Engineering, Waseda University Japan
E-mail(SN): nakahira@phys.aoyama.ac.jp

Abstract

We are developing the gamma-ray burst monitor for the CALET(CALorimetric Electron Telescope) experiment which is proposed and studied (in phase A) to be a next experiment for the JEM/Exposure Facility of the ISS. The CALET GRB Monitor (CALET-GBM) is planned to measure wide-band energy spectra from GRB prompt emissions over nine decades in energy (from a few keV to a few TeV) together with the CALET Imaging Calorimeter (IMC) and the Total Absorption Calorimeter (TASC). To fulfill this requirement, we are planning to employ six $LaBr_3$(Ce) crystals for the range from a few keV to about 1 MeV together with a thick BGO detector covering from several tens of keV to about 20 MeV. Since the light yield of $LaBr_3$(Ce) is about twice as large as that of NaI(Tl), it is very attractive material. However it has not been yet used as a detector for long exposure in space. Therefore its radiation hardness and induced background due to trapped protons in the geomagnetic field are not fully understood. To evaluate its performance in high radiation environment in the ISS orbit,we carried out proton irradiation tests. Proton-induced radio-activation were measured from a few minutes after irradiation over a period longer than two months by a Germanium detector, and most of radioactive nuclei induced by protons are identified. We have manufactured a proto-type model, 3 inch in diameter $\times$ 0.5 inch thick with the entrance window of 220 μm beryllium. In preliminary measurements, 6.4 keV Fe Kα fluorescence line is clearly detectable. We can expect that the lower energy threshold can be around 4 keV or even lower.

Key words: Scintillation detectors, GRB, XRF, Gamma-rays, X-rays, Radiation-damage

1. introduction

Gamma-ray burst(GRB) is one of the biggest explosions in our universe. The total radiation energy release is estimated to be 10^{51} erg, and more than 50% of the energy is usually emitted in the hard X-ray to the soft gamma-ray range (20-1000 keV). Although the long-GRBs were considered to be associated with the death of massive stars and related to Ic supernovae. However detailed physics remain unclear even the initial energy source "fireball" model. Well-studied energy range of GRBs by typical detectors is 15 keV$\sim$10 MeV. By extending it to the lower energy side, Ginga, Beppo-SAX, and HETE-2 brought us a discovery of X-ray rich GRBs (XRR) and X-ray flashes (XRF) whose emitted energy is dominant in not gamma-rays but more in X-rays (10 keV)[1]. In the higher energy side than $\sim$10 MeV, two important discoveries were made by CGRO/EGRET observations[2]. One is a presence of the delayed GeV emissions from the GRBs, and the other is a presence of the high energy excess component [3]. In order to understand the radiation mechanisms of the GRB prompt emissions, it is essential to study wide-band spectra and their variability over the keV to GeV band. For this purpose, we propose to have a gamma-ray burst monitor (GBM) in the CALET experiment[4] on the International Space Station (ISS).

2. Components of the CALET

2.1. IMaging Calorimeter and Total AbSorption Calorimeter

The CALET (CALorimetric Electron Telescope) mission is aimed to study high energy electrons and gamma-rays. It is proposed for the second public advertisement of an experimental payload attached to the Japan Experimental Module/Exposure Facility of the ISS targeting the launch of 2013.

CALET main detector consists of an imaging calorimeter (IMC), total absorption calorimeter (TASC). The IMC is used for identification of the incident particle and energy measurement below 10 GeV, while the TASC is for total energy measurement above 10 GeV. The IMC consists of 17 layers of lead plates and scintillating fiber (SciFi) belts, and the dimension is about 90 cm × 90 cm. The readout for the SciFi is multi-anode photomultiplier tubes. The TASC is composed of 12 layers of BGO logs which has dimensions of 2.5 cm × 2.5 cm × 30 cm. There are 12 layers and 48 such logs in each layers, and has the size of 60 cm × 60 cm × 30 cm. Total weight of CALET instruments is ∼ 1450 kg and the effective geometrical factor is ∼ 7000 cm^2sr. The schematic structure is shown in Fig.1.

[4]

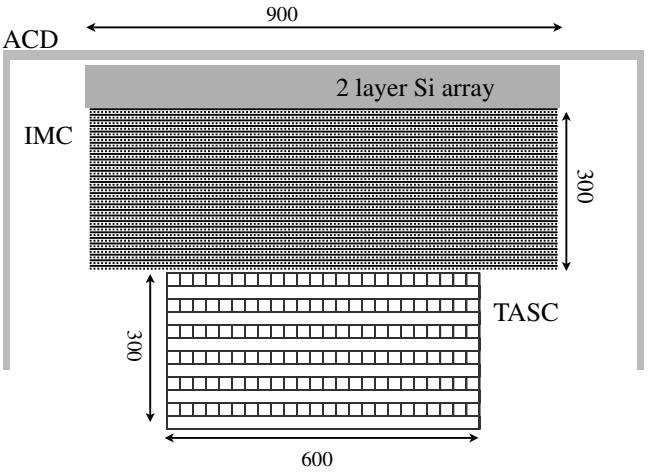

Fig. 1. image of CALET detectors.

The CALET is sensitive to electrons from 1 GeV to 20 TeV. With 3 years observation, CALET can observe about two thousands of galactic TeV electron events, and we can clearly identify local acceleration cites in the galaxy such as Vela from the energy spectrum and the anisotropy. Furthermore, the most exotic and interesting objective is a feature due to the decay of SUSY or Kaluza-Klein dark matter. The CALET also has sensitivity to gamma-rays from 20 MeV to several TeV, owing to the background rejection with the anti coincidence shield. The scientific target of the gamma-ray observation is Galactic and extra-Galactic diffuse component, supernova remnants, pulsars, AGNs, and gamma-ray bursts.

2.2. Gamma-Ray Burst Monitor

The CALET-GBM is designed to see the energy band lower of the CALET calorimeters (20 MeV), fulfilling a observational band of nine decades from several keV ∼ TeV together with the CALET IMC and TASC. The CALET-GBM employs two types of detector, Soft Gamma-ray Monitor (SGM) and Hard X-ray Monitors (HXM), shown in Fig.2). They consists of inorganic scintillators and photomultiplier tubes, it is basically same as Ginga/GBD, HETE-2/FREGATE and Suzaku/WAM. SGM is consist of a 5 inch ϕ × 3 inch thick BGO crystal with a large stopping power, and sensitive from several tens of keV to 20 MeV. HXM is consist of six 4 inch ϕ × 0.5 inch thick $LaBr_3$(Ce) crystals to achieve excellent energy resolution.

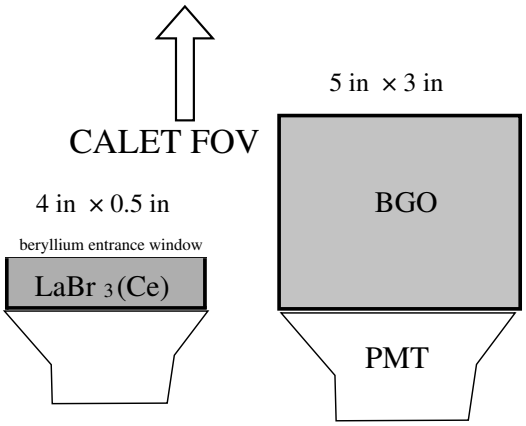

Fig. 2. image of CALET GBM

Because of deliquescent of $LaBr_3$(Ce) crystal, the air-tight housing is required. In order to have a sensitivity for X-rays, we will use 220 μm beryllium for the entrance window. All the detectors are co-aligned with CALET calorimeters to get a high sensitivity for the FOV events. Current characteristics of SGM and HXM are summarized in Table1, and effective area of them are shown in Fig.3.

2.3. scientific objectives of the GBM together with the CALET IMC and the TASC

The CALET-GBM is expected to observe in total 100 events per year assuming logN-logP distributions from the BATSE catalog. The FOV events will be expected to be 40 per year, while out of FOV events could be 60 events per year. More detailed background study is necessary taking mass distribution around CALET into account.

The scientific objectives ares as below.

Table 1. Current Design of the CALET-GBM.

	HXM	SGM
Scintillator Crystal	$LaBr_3(Ce)$	BGO
Number of Detector	6	1
Diameter (inch)	4	5
Thickness (inch)	0.5	3
Geometrical Area (cm^2)	486	127
Energy Range (keV)	∼7-600	∼100-20000
Energy resolution (662keV)	∼3%	11%
Weight (kg)	6.9	7.5

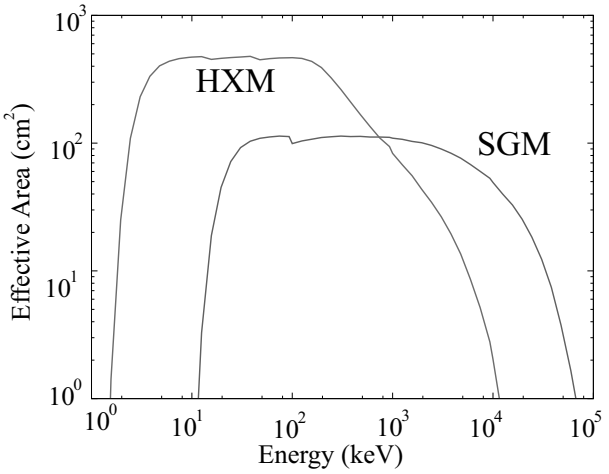

Fig. 3. Effective area of a SGM and six HXMs.

- Gamma-ray bursts (GRBs)
  - search for the spectral cutoff which reflects electron acceleration in the shock.
  - origin of the high energy excess (10 MeV) from the possible synchrotron emissions.
  - origin of delayed GeV emissions.
  - Ep distribution based on wide band $\nu F\nu$ spectra.
  - broadband time-variability study such as pulse widths and lags
  - search for possible emission/absorption line features.
- Soft gamma-ray repeaters (SGRs)
  - a detailed study of the broadband spectrum.
  - for flares with various intensities(short to giant).
  - origin of the non-thermal hard tail above 100 keV.
- Solar Flares
- hard X-ray transients from NS or BH system.

3. Evaluation of $LaBr_3(Ce)$ scintillator

The $LaBr_3(Ce)$ with a high light output, therefore an excellent energy resolution, a fast decay time and a high thermal stability[5] is very attractive material for our detector, nevertheless has not been used in space so far. Hence, we are studying its

- basic performances such as energy resolution
- basic performances and uniformity in larger 3 inch ϕ crystal
- lower energy threshold of the detector with a thin beryllium window
- intrinsic backgrounds
- radiation hardness for gamma-rays and protons
- proton induced background

3.1. performance

We have tested commercially available $LaBr_3(Ce)$ crystal of 0.5 inch × 0.5 inch thick. The crystal is covered by aluminum housing and light-guide glass, and it is coupled by the photomultiplier tube through the glass. Signals from a charge sensitive pre-amplifier are processed in a shaping amplifier, then recorded in a pulse-height analyzer.

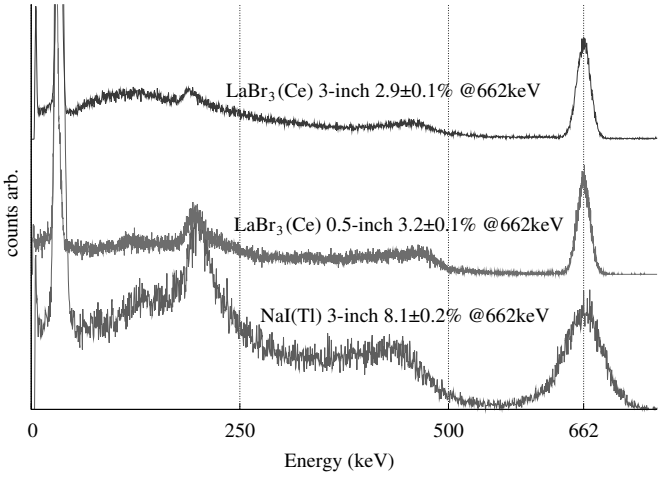

Fig. 4. ^{137}Cs 662 keV spectrum of $LaBr_3(Ce)$ crystal in comparing with NaI(Tl).

FWHM energy resolution of 662 keV gamma-rays from ^{137}Cs was measured, 3.2%±0.1% with $LaBr_3(Ce)$ while 8.2% ± 0.2% with NaI(Tl) (Fig.4).

The current technology of $LaBr_3(Ce)$ crystal growth is capable of being scaled up to 200 mm diameter crystals[6]. We obtained larger 3 inch diameter × 0.5 inch thickness $LaBr_3(Ce)$ single crystal as a proto-type of CALET-GBM, which has a 220μm beryllium entrance

window for a sensitivity to the lower energy. We tested it using 662 keV gamma-ray from ^{137}Cs and 14.4 keV, 122 keV, 136.5 keV gamma-ray, and 6.4 keV Fe-Kα from ^{57}Co for the lower energy. In the experiment, energy resolution at 662 keV was 2.9%±0.1%: comparable to smaller crystals (2.8∼3.2% typically).

For the lower energy, down to 6.4 keV X-ray were can be seen (Fig5). The achieved lower energy threshold was less than 4 keV. We expect that the lower energy threshold can be around 4 keV or even lower.

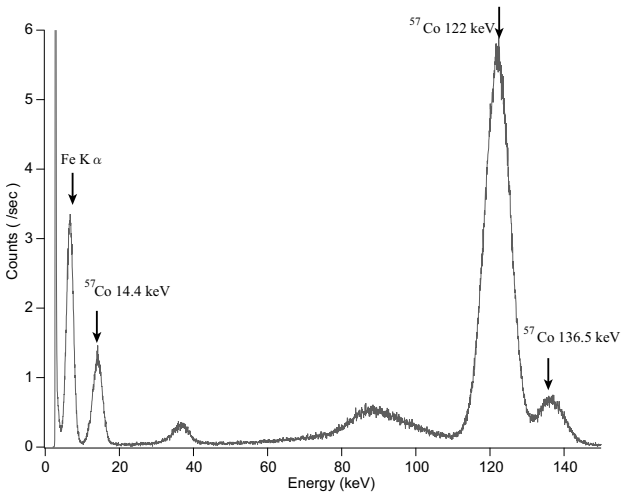

Fig. 5. ^{57}Co spectrum taken by of the 3 inch ϕ detector with a beryllium entrance window. The energy resolution was quite excellent. 6.4 keV Fe Kα X-ray and 14.4 keV 57Co gamma-ray were clearly resolved.

Naturally occurring lanthanum includes 0.09% of ^{138}La, which has a 1.05×10^{11} yr half-life and two different decay schemes shown Fig.6. 66.4% are EC (Electron Capture) decay with a 1435.6 keV gamma-ray and the rest with the broading ratio of 33.6% are β- decay emitting 788.7 keV gamma-ray and β- particle (β_{max}=254 keV).

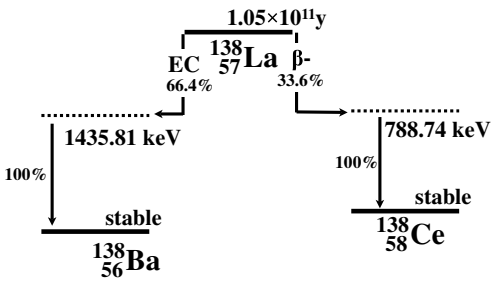

Fig. 6. Decay scheme of ^{138}La, which has EC decay and β- decay.

Measured spectrum using 3 inch ϕ × 0.5 inch thick crystal and Photomultiplier Tube is shown in Fig.7. There are broad component of β particle under 254 keV and sum of 788.7 keV gamma-ray and β component, and 1436 keV line are interfered with ^{40}K 1460.8 keV gamma-ray from the room background. Above 1435.6 keV peak, you can see broad triple peak caused by alpha particles due to ^{227}Ac contamination. The count rate of its intrinsic background was ∼1.2-1.3 counts s^{-1} cm^{-3}.

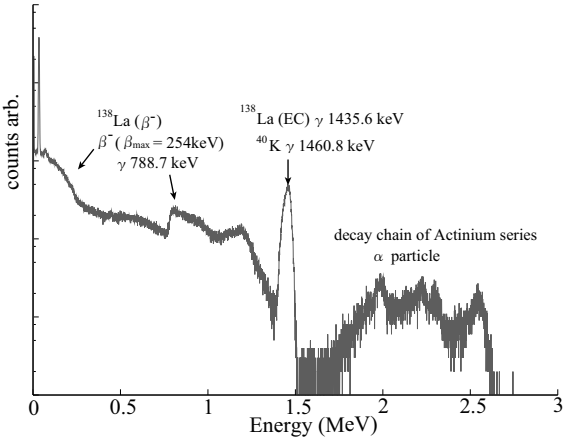

Fig. 7. Measured intrinsic background of 3 inch ϕ × 0.5 inch thick crystal and PMT. It is caused by naturally occurring radioactive ^{138}La and contaminated ^{227}Ac.

3.2. degradation by radiation damage

The International Space Station rotates around the Earth sixteen times a day, and passes through the South Atlantic Anomaly at a half of its passages. The proton dose in the ISS orbit is estimated to be 10^9 cm^{-2} per year. In such a radiation environment, degradation of properties of the detector by radiation damage is not negligible, and the induced background is considerably higher than that on the ground. Thus investigations for its radiation hardness and possible induced background is necessary. We carried out proton irradiation test on December 2007 at the Wakasa-Wan Energy Research Center, Fukui, Japan. We investigated degradation of its gain and energy resolution after irradiation by protons with their kinetic energy 140 MeV as a function of their dose ranging from 10^5 to 10^{11} protons cm^{-2}. By irradiation of 10^{11} protons cm^{-2} (corresponding to about 100 years on ISS orbit), the energy resolution degraded from 3% to 4% and the light yield looked to have decreased by 30%(Fig.8). However, for a few 10^9 protons cm^{-2} that corresponds to the flux on the actual duration of the mission, there were little degradations.

We noticed that the light-guide glass and/or $LaBr_3$(Ce) crystal was colored slightly in reddish-brown after 10^{11} protons cm^{-2} irradiation. So, we tested glass itself and measured permeability in optical ∼ near-UV range. Permeability spectrum was taken by a spectrometer Hamamatsu C10082CAH and light source L10290. The spectrum is shown in Fig.9, in 380 nm (peak wavelength of $LaBr_3$(Ce) fluorescence) permeability was de-

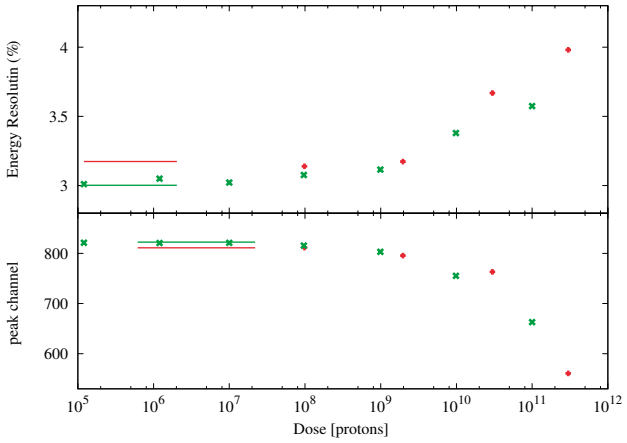

Fig. 8. Energy Resolution and peak channel using ^{137}Cs source was measured as a function of their dose. As a result, $10^9 \sim 10^{10}$ cm^{-2} caused a degradation. The lines shows a properties of before irradiation.

creased more than 70 %. The result shows that the color centre induced in the glass by the irradiation caused a degradation, nevertheless it is not clear if the $LaBr_3(Ce)$ degraded or not. So, we need a little more investigations doing well with its deliquescence.

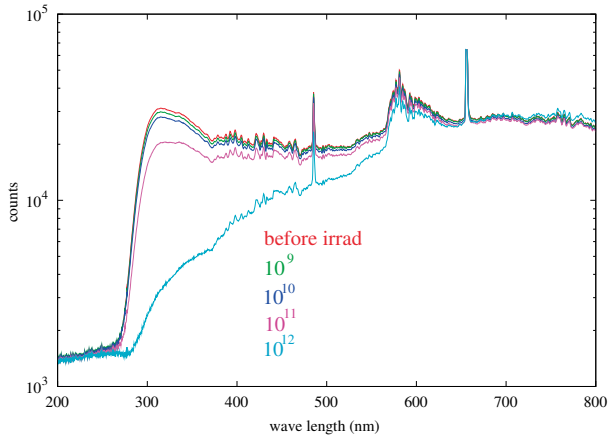

Fig. 9. Measured spectrum , with a dose of 10^9, 10^{10}, 10^{11} and 10^{12} protons cm^{-2}. The structure (such as the peak in 485 nm, 655 nm) reflects a characteristics of the light source.

3.3. proton-induced background

The nuclei with short lifetime of several minutes and long life-time of years gives different effects on the background. Proton-induced radioactive gamma-rays were monitored soon after irradiation by an external Germanium detector.

- 3×10^9 and 3×10^{10} protons cm^{-2} with kinetic energy 140 MeV were irradiated to each of two crystals.
- induced gamma-rays were investigated from a few minutes after irradiation for both one.

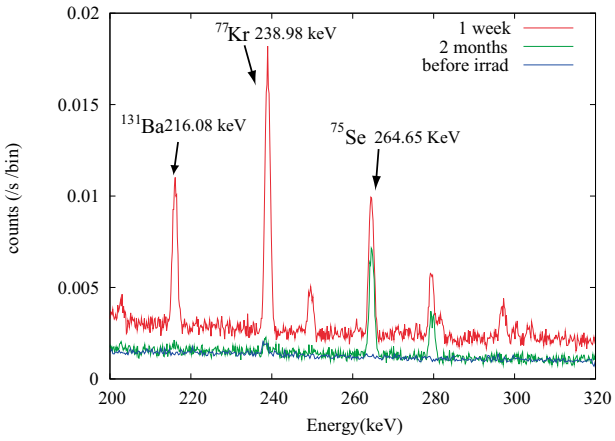

Fig. 10. Radio-activated background spectrum (partial) measured by Germanium detector: before irradiation, 1 week after proton beam irradiation, and after 2 months.

- especially for 3×10^{10} one, the measurement was continued for a longer period than two months.

Table 2. Summary of identified nuclei

5 min∼1 hour	^{74m}Br,^{77m}Br,^{77}Kr,^{130}La,^{131}La and more (lifetime:several minutes to a few hours)
1 week	^{75}Se(119 d),^{77}Br(57 h),^{131}Ba(11.5 d)
2 months	^{75}Se(119 d)

By the analysis on the data, most of radio-active nuclei induced by proton beam were identified. An example of proton induced background spectrum measured by the Germanium detector is shown in Fig.10, and the list of identified radio-active source is summarized in Table2. Considering the long-term background, ^{75}Se that has a 119 day half-life is dominant.

4. conclusion

The CALET experiment will provide an unique capability for detecting GRBs on a wide band, with the gamma-ray burst monitor(CALET-GBM).The GBM in currently designed to have a sensitivity in the energy range from 7keV to 20 MeV, covering >2 str. all the sky.

We have been investigating new scintillator: $LaBr_3(Ce)$ that has higher light output, better energy resolution and faster decay-time than NaI(Tl). We are testing its basic performance, radiation hardness and induced background anticipated on the ISS orbit, $LaBr_3(Ce)$ shows excellent performances as we expected. Although $LaBr_3(Ce)$ has several times as higher naturally occurring background as other inorganic scintillators.It is not

a considerable problem for our purpose: not pointing observation but burst monitoring.

Acknowledgments
We are grateful to S. Hatori, K. Kume and T. Hasegawa of the Wakasa Wan Energy Research Center for their important contributions to the proton beam irradiation experiments.

1) T. Sakamoto et al. ApJ, **629**, (2005) 311.
2) K. Hurley et al. Nature, **372**, (1994) 652.
3) M.M. Gonzalez et al. Nature, **424**, (2003) 749.
4) S.Torii for the CALET Collaboration : Nuclear Physics B **166** (2007) 43.
5) M. Moszyńnski et. al.: Nucl. Inst. meth. A **568** (2006) 739.
6) Peter R. Menge et. al.: Nucl. Inst. meth. A **579** (2007) 6.

X-ray polarimetry small satellite TSUBAME

Takahiro Toizumi[1], Takeshi Nakamori[1], Jun Kataoka[1], Yoshihiro Tsubuku[1], Yoichi Yatsu[1], Makoto Arimoto[1], Takashi Shimokawabe[1], Nobuyuki Kawai[1], Kuniyuki Omagari[2], Hiroki Ashida[2], Saburo Matsunaga[2] et al.

[1] Department of Physics, Faculty of Science, Tokyo Tech, Meguro, Tokyo, Japan
[2] Department of Mechanical and Aerospace Engineering, Tokyo Tech, Meguro, Tokyo, Japan
E-mail(TT): toizumi@hp.phy.titech.ac.jp

Abstract

TSUBAME is a university-built small satellite mission to measure polarization of hard X-ray photons (30-100 keV) from Gamma-ray bursts (GRBs) using azimuthal angle anisotropy of Compton-scattered photons. Polarimetry in the hard X-ray and soft γ-ray band plays a crucial role in the understanding of high energy emission mechanisms and the distribution of magnetic fields and radiation fields. TSUBAME has two instruments: the Wide-field Bust Monitor (WBM) and the Hard X-ray Compton Polarimeter (HXCP). The WBM determines on board the direction of the burst occurrence with an accuracy of 10 degrees, then using a high speed attitude control device, the HXCP is pointed to the GRB within 15 seconds after the burst occurrence to promptly detect polarized X-ray photons from the GRB.

Key words: gamma-ray bursts — Polarimetery

1. Introduction

In the study of GRBs and other X-ray and γ-ray sources, analyses of their spectra and time variability are common. But the information extracted from these observations may not be sufficient to identify the dominant emission mechanism. In some cases, measurements of thepolarization can clarify the emission mechanism and the orientation of the polarization plane will provide an idea of the distribution of magnetic field, radiation field and matter around the sources such as rotation powered pulsars, accreting black holes and AGNs. The reliable polarimetry in X-ray band has been done only once at the energies 2.6 and 5.2 keV using Bragg reflection [1]. Furthermore, for GRBs, only a few observations of X-ray polarimetry has been done [2], and these results were disputable because of a low level of significance [3]. In such situations, new observatories having a high sensitivity of X-ray polarimetry for GRBs have been long-awaited.

2. TSUBAME Mission Overview

TSUBAME, meaning a bird swallow in Japanese, is a small satellite that will measure the polarization of astronomical objects. The dimensions of TSUBAME are 300 mm $\times$ 300 mm $\times$ 300 mm and the total mass is $\sim$30 kg. TSUBAME is planned to be launched as a piggyback on the HIIA rocket. The main target of TSUBAME is GRBs. A rapid observation in the study of GRBs is needed because the duration of prompt emission is generally short (2 $\sim$ 100 sec). A schematic observation sequence is shown in Fig. 1, when a GRB occurs, TSUBAME localizes the coordinates of the GRB on board using the localization detector WBM. By slewing promptly using the rapid maneuvered system ($\sim$90 deg within 15 sec), the HXCP is pointed to the position of the GRB and starts the observation in 15 s after the burst occurrence. The WBM consists of 5 sets of a CsI scintillator connected to APDs. These CsI scintillators are attached to each corner of the observatory, shown in Fig. 2. Using the count rates of 5 detectors, GRBs will be localized with an accuracy of $\sim$10 degrees. FOV of the WBM is 2π str (half of the whole sky).

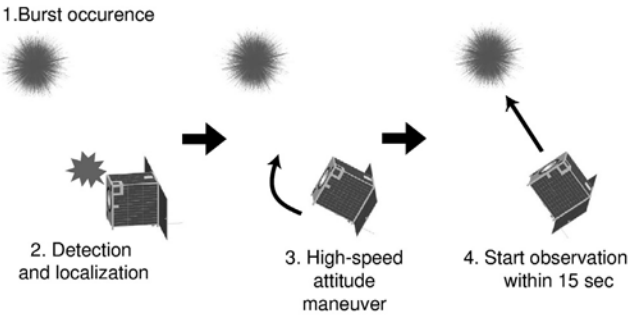

Fig. 1. TSUBAME observation sequence.

The polarimeter HXCP will measure the polarized photons in the 30 $\sim$ 200 keV band using the azimuthal angle anisotropy of Compton scattered photons, and consists of 8 $\times$ 8 plastic scintillators (scatterers) connected

to a MAPMT R8900-M16-UBA and 36 CsI scintillators (absorbers), each connected to an APD S8664-55 [5] surrounding the 8 × 8 scatterers, shown in Fig. 2. The effective area is ∼ 5 cm^2 and its field of view is 25 deg^2.

Now we assume to mount two HXCPs in TSUBAME. One with a collimator and the other without a collimator. The HXCP without collimator has large field of view but the background level is high, another HXCP with a collimator has lower background level but narrow field of view. TSUBAME aims to detect polarization from not only GRBs but also bright galactic diffuse sources (e.g., Crab Nebula), binary systems (e.g., Cyg X-1) and flares from blazars or soft gamma-ray repeaters. If the objects are very bright (≥ 1 Crab), TSUBAME can detect the polarization from these objects significantly with the HXCP with a collimator.

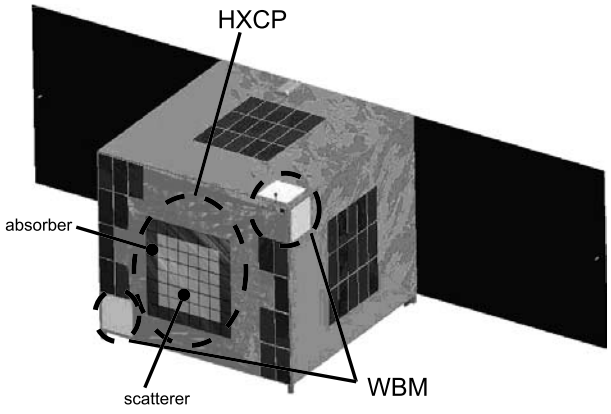

Fig. 2. TSUBAME configuration. HXCP is centered at the observatory. The HXCP consists of 8 × 8 plastic scintillators as a scattering site and 32 CsI scintillators as a photoelectric absorption site surrounding scatteres. Counters of the WBM are attached to each corner of the observatory.

3. HXCP Simulation

We performed a Compton simulation to determine the signal and background levels of HXCP, using Geant4 and the detectability of the polarization from GRBs. We use a modulation factor as a indicator of the performance of HXCP. Modulation factor is defined as the relative amplitude of te modulation curve (i.e. number of Compton-scattered phton s as a function of the azimuthal scatter angle) for 100 % polarized photons.

3.1. GRB021206

We simulate a GRB event; GRB 021206 which had a flux of 3.2 × 10^{-5} ergs/cm^2/s and a duration of 5.5 s. This event was a very bright GRB for which a strong polarization was reported(Coburn et al. 2003).

In this simulation, we assume that the burst photons are 100 % polarized and the energy range is 30 ∼ 200 keV. Here, the dominant γ-ray background are CXB and atmospheric γ-ray. The γ-ray background flux models have been developed based on observation data(Mizuno et al. 2004) and we generate the CXB and atmospheric γ-ray, representative of the satellite environment. We find that the background induced by high-energy charged particles can be easily rejected because the charged particles deposite very large signals(out of energy range) through the scintillators.

3.2. Design study

We optimized the design of the HXCP scintillators, *i.e.* number, pixel size and length of scintillators. To determine these parameters, we obtained the value of the modulation factor (MF), the effective area, and the minimum detectable polarization (MDP) by simulations. In conclusion, we obtained a best result with a plastic scintillator array of 64 pixels, CsI scintillator of 32 pixels, and the pixel size of the plastic scintillator of 7.5 mm × 7.5 mm, and the length of the scintillator of 50 mm. The effective area is, then, ∼5 cm^2, the MF is 47.6 ± 1.2 %, the MDP is 8.1 %. One of the simulation results are shown in Fig. 4 and Fig. 5. Fig. 4 shows the spectra of incident GRB photons, the Compton scattered photons detected, and the background.

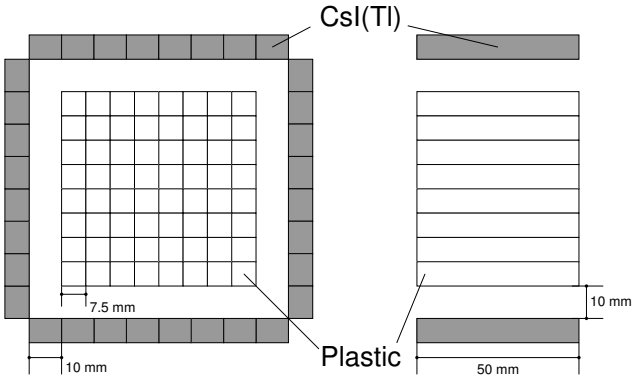

Fig. 3. Detctor design of HXCP(left: top view, right : side view)

3.3. Fine collimator

A fine collimator can improve the dtection efficiency for the polarization. in the previous section, scintillator design is fixed to the optimum value. Using this value, the fine collimator design was optimized. We obtained that the best collimator lenngth is 55 mm, tickness is 500 μm and the number of collimator grid is 4 × 4 or 8 × 8. With this collimator, we can make the polarimetry of the Crab Nebula wiht MDP ≤ 20 %.

4. Development of photon detector for scatterer

4.1. Performance of malti anode PMT (MAPMT) of UBA

In the TUSBAME mission, the MAPMTs are used to detect the position where the Compton scattering occurs.

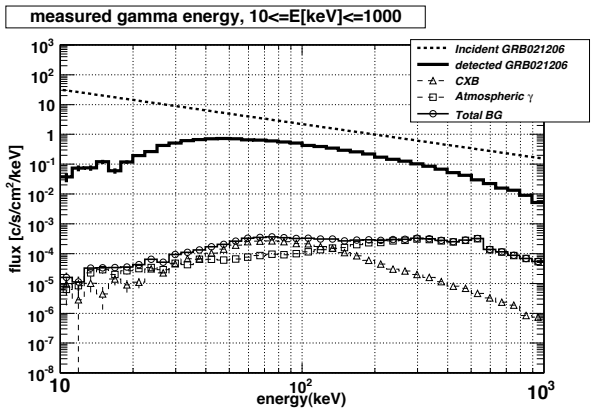

Fig. 4. Spectrum of GRB021206. Energy vs. flux. Energy range is 30 $\sim$ 200 keV. The flux of GRB021206 is more significant than total background.

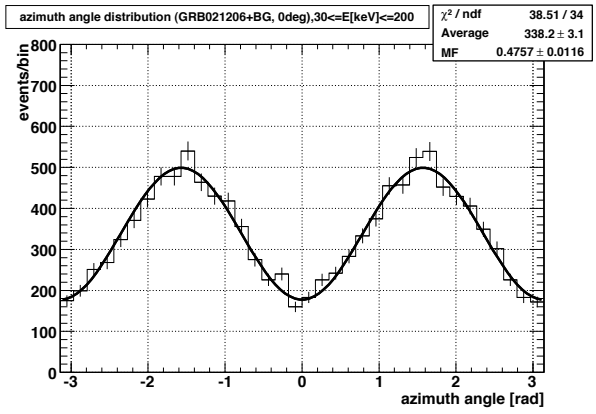

Fig. 5. Aimuthal modulation curve of GRB021206. MF = 47.6 %, MDP = 8.1 %.

These MAPMTs reuires high sensitivity for scintillation phtons because the light yield of the plastic scintillator of HXCP is low (5 photons/keV). In addition, it is necessary to apply a vibration test to them before the launch.

MAPMT-R8900-M16-UBA has 16 anodes and ultra bialkali (UBA) photo cathode. It is compact and require low voltage ($\sim$ 800 V) compared to other PMTs ($\sim$ 1500 V). The quantum efficiency of UBAs is more than 40 %, doubled form the bialkari (BAs). Although it is usually diffcult to become rugged for vibration because the configuration of dynodes is complicated, with HPK(Hamamatsu Photonics K.K.), we have developed the raggedness to survive.

4.2. Spectrum of ^{241}Am and single photoelectron

Fig.7 shows the spectrum irradiated with a ^{241}Am source γ-ray photons obtained with the MAPMT-R8900-M16-UBA and plastic scintillators. In this spectrum, we can cleanly see not only the 59.5 keV peak but also a lower energy peak ($\sim$ 20 keV).

Fig.8 shows the spectrum of single photoelectrons.

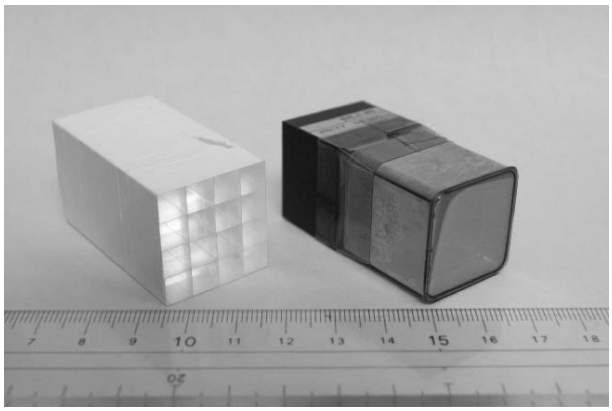

Fig. 6. MAPMT-R8900-M16-UBA and 16 pixel plastic scintillator array.

Single photoelectron peak corresponds to 0.96 keV by comparing with the 59.5 keV peak in the spectrum of ^{241}Am.

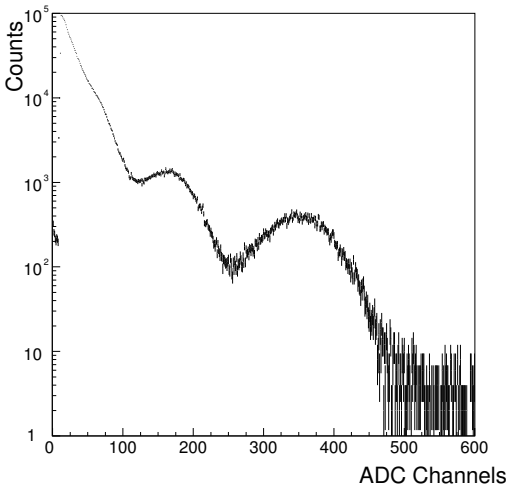

Fig. 7. The spectrum of ^{241}Am by the plastic scintilator and the MAPMT with UBA. This spectrum shows not only 59.5 keV peak but also lower energy peak. At 59.5 keV peak, energy resolution is 29.9 %.

4.3. UBA performance for polarimeter

By improving the quantum efficiency of MAPMT, it becomes possible to detect the low energy ($\geq$ 0.96 keV) Compton scatterings photons in the plastic sintillators. This is a significant improved over BA, which show single photoelectron peak of 2.7 keV. With this improvement, we shold be able to detect Compton scattering with small energy deposit. That is, number of events for the polarized X-ray detection increase, and the possibility that the polarization can be detected rises.

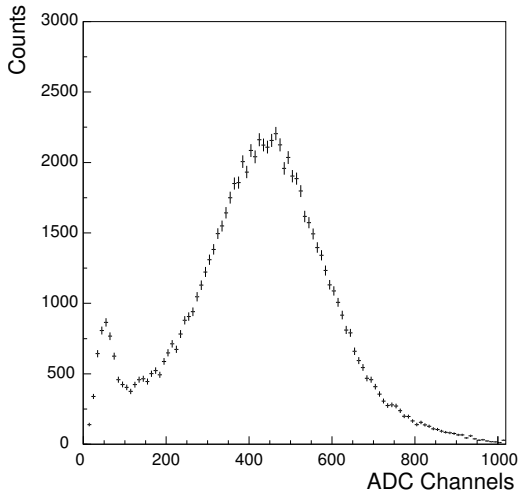

Fig. 8. The spetrum of single photoelectron. ADC channel vs. Counts.

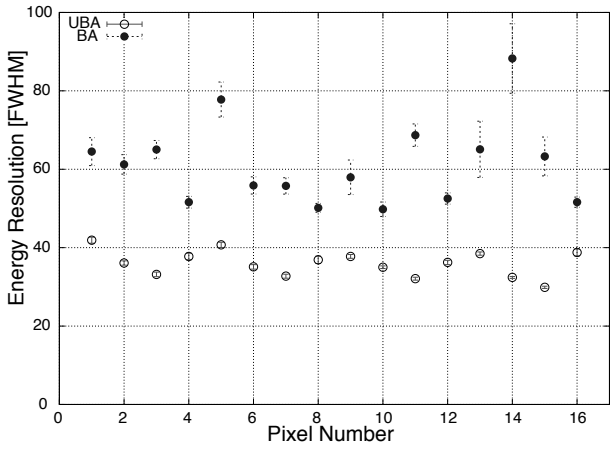

Fig. 9. Deference of energy resolution comparing UBA with BA. UBA has better resolution than BA in all pixels. Anode pixel number vs. energy resolution.

4.4. Vibration test

Standard MAPMTs lack improved tolerance and are not completely reliable against vibration impact when launching a rocket. The R8900-200-M16MOD-UBA offers improved tolerance to vibration in possible launching vehicles. Prior to delivering the MAPMTs to us, Hamamatsu Photonics K.K. tested 10 samples units using random levels of vibration up to 15 G_{rms}, and a shock level of 60 G. We continued detailed vibration testing on each MAPMT to confirm tolerance to random vibration that is 1.5 times that of the HIIA profile and determine the maximum vibration that each unit can withstand. The dynode represents the weak point relative to vibration. When the dynode is damaged, the MAPMT loses gain. Therefore, we examined variations in gain caused by vibration. In testing vibration for the MAPMT, we used a vibration generator (IMV i230/SA2M). The frequency profile was random vibration based on the HIIA profile as listed in Table 1. Random vibration was applied to three axes (X, Y, and Z). The duration of vibration for each axis was two minutes.

We initially tested at 12 G_{rms}. Before and after this test, we examined the MAPMT gain by using single photoelectron spectra.

We then accelerated the vibration and examined the gain after each test. Vibration was accelerated from 5 G_{rms} to 17 G_{rms} in increments of 3 G_{rms}. After vibratin at 12 and 17 G_{rms}, no significant change in signal output was noted. Therefore, The MAPMT was considered to withstand vibration even at double the conditions of the HIIA rocket profile.

Table 1. Characteristics of the frequency profile used in the vibration test. The duration of vibration was 120 sec.

Frequency range(Hz)	Vibration profile
$20 \sim 200$	+3.0 dB/oct
$200 \sim 2000$	0.032 G^2/Hz (for 7.8 G_{rms})

5. Future Plan for TSUBAME

We plan to estimate the performance of the prototype of the HXCP includeing plastic scintillators coupled MAPMTs and CsI scintillators coupled to APDs using a synchrotron X-ray beam line. In addition to WBM to localize GRBs position, we need to estimate its localization ability using Monte Carlo simulating. Based on the optimized the design, we will develop the engineering model of WBM.

References

[1] Weisskopf, M. C., et al. 1976, ApJL, 208, L125
[2] Coburn, W. & Boggs, S. E. et al. 2003, Nature, 423, 415
[3] McGlynn, S., et al. 2007, A&A, 466, 895
[4] Ikagawa, T., et al. 2003, NIMA, 515, 671
[5] Mizuno, T. et al. 2004, Apj, 614, 1113
[6] Kawasaki, Y. et al. 2006, NIMA, 564, 378
[7] Arimoto, M. et al. 2007, AIP, Proceedings of the Santa Fe Conference pp. 607

The Neutron star Interior Composition Explorer

Keith Gendreau[1], Zaven Arzoumanian[1,2], and the NICE Team

[1]NASA/GSFC, Greenbelt, MD USA
[2]USRA, Greenbelt, MD USA
E-mail(KJ): Keith.c.gendreau@nasa.gov

Abstract

The Neutron star Interior Composition Explorer (NICE) will be a Mission of Opportunity dedicated to the study of neutron stars, the only places in the universe where all four fundamental forces of nature are simultaneously in play. NICE will explore the exotic states of matter within neutron stars, revealing their interior and surface compositions through rotation resolved X-ray spectroscopy. Absolute time-referenced data will allow NICE to probe the extreme physical environments associated with neutron stars, leveraging observations across the electromagnetic spectrum to answer decades-old questions about one of the most powerful cosmic accelerators known. Finally, NICE will definitively measure stabilities of pulsars as clocks, with implications for navigation, a pulsar-based timescale, and gravitational-wave detection. NICE will fly on the International Space Station, while GLAST is on orbit and post-RXTE, and will allow for the discovery of new high- energy pulsars and provide continuity in X-ray timing astrophysics.

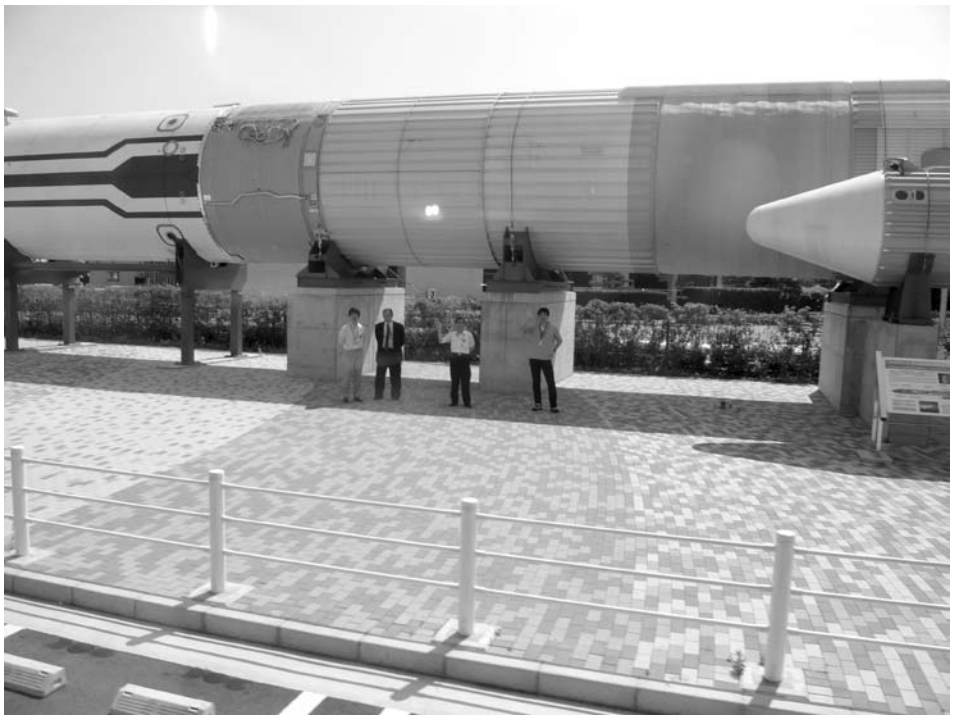

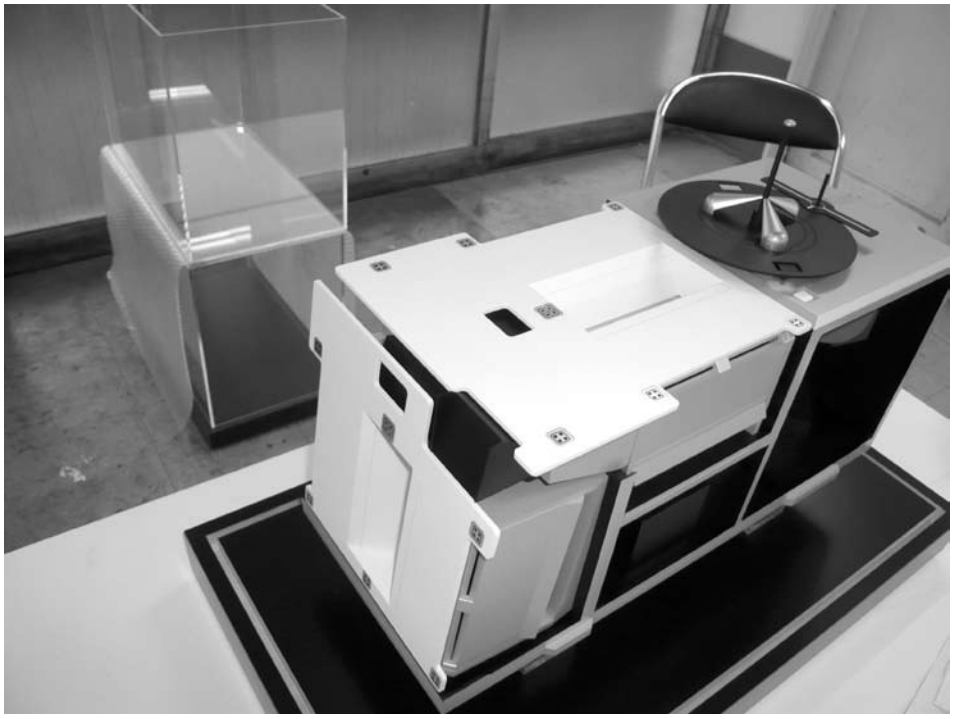

Concluding Remarks

Nobuyuki Kawai[1,2]

[1] Department of Physics, Tokyo Institute of Technology, 2-12-1 Ookayama, Meguro-ku, Tokyo 152-8551 Japan,
and
[2] Cosmic Radiation Laboratory, RIKEN, 2-1 Hirosawa, Wako, Saitama 351-0198, Japan
E-mail(NK): nkawai@phys.titech.ac.jp

Abstract

The scientific issues discussed at the 3rd MAXI Workshop "The Astrophysics with All-Sky X-Ray Observations" are summarized. MAXI will contribute to the science of Galactic compact X-ray sources, GRBs, AGN, and diffuse X-ray emission from the entire sky. Importance of follow-up observations with focusing X-ray telescopes and multiwavelength coverage are particularly noted.

Key words: MAXI — X-ray transients — X-ray surveys

1. The MAXI mission

At the 3rd MAXI Workshop "The Astrophysics with All-Sky X-Ray Observations" held on June 10–12 at RIKEN, 41 oral papers and 42 poster papers were presented with subjects pertinent to the X-ray all-sky observations with MAXI. The MAXI team members presented the mission concepts, instrument design, science objective, and the data release plan. The characteristics of the MAXI mission and its policies are outlined as follows.

- MAXI has improved sensitivities over the preceding all-sky X-ray monitor missions such as RXTE ASM.
- Most of the sky is covered at least once every 94 minutes with ∼10 mCrab sensitivity.
- There is no intentional bias in the sky coverage. It is limited only by avoidance of the SAA and the direct illumination of the sun.
- Detection of outbursts of X-ray sources will be notified to the community in near real time when ISS has contact with the ground.
- The light curves, and spectra of catalogued sources and the X-ray source map will be made public regularly.
- MAXI has modest position resolution of ∼1.5°. Its localization accuracy for bright X-ray sources is ∼0.1°.
- MAXI's instantaneous field of view is ∼1/60 of the sky, limiting to its capabilities short transient events like gamma-ray bursts.
- MAXI will perform the first all-sky survey since HEAO-1 in the traditional X-ray band of 2–15 keV, down to a confusion limit of ∼0.5 mCrab in <1 year.

With the understanding of the characteristics of the MAXI observations, papers were presented to discuss the scientific issues that can be addressed by MAXI. I highlight some scientific subjects discussed in the workshop, though it is by no means the complete summary of papers and discussions at the workshop.

2. Science of X-ray binaries and compact Galactic sources

Accreting X-ray binaries show a huge variety of phenomena on various time scales, thus constitute prime targets for MAXI. Recent progress in understanding the accretion phenomena onto black holes and neutron stars was discussed.

Their X-ray spectral states, which MAXI will monitor, are correlated with the X-ray power spectra (red noise and QPO's) and fluxes in other wavebands, and are related to the activities of jets and accretion disks. MAXI is expected to provide very quick alerts for outbursts and state changes of black hole binaries and other microquasars, so that timely TOO observations can be triggered for multiwavelength coverage and pointed X-ray observation with higher time resolution. Coordination with ground-based observatories in radio, optical/IR, and UHE gamma-rays, in-orbit X-ray and gamma-ray observatories is essential. (related talks: Makishima, Matsumoto, Fender, Ebisawa, Trushkin, Thompson, Paul, Takahashi, Ubertini, Kuiper)

There are also scientific topics that can be addressed mostly by MAXI alone. Detection of periodicities in the light curves provides direct evidence for spin and/or orbital motion. Slow-rotating X-ray pulsars, either accreting pulsars or magnetars, may be discovered solely by MAXI. Long-term super-orbital periodicities hint the third-body effects or disk precession. Aperiodic vari-

ations (red noise and QPO) have information on the physics of accretion, and possibly the mass of the accreting black holes (or neutron stars). (Zdziarski, Morii, Hayashida, McHardy)

MAXI is also expected to detect number of new X-ray transients. Identification of new source may require precise location, which calls for prompt TOO observations using X-ray telescopes such as on Swift, followed by multiwavelength ground coverages. (Negoro, Wijnands, Reimer, Gehrels, Kulkarni, Uemura)

3. Active galactic nuclei

The discussions on the AGN studies with MAXI may be categorized into three topics: (1) measurements of power spectra of X-ray variability, (2) multiwavelength variability study, and (3) population study.

In unbeamed AGN, it was argued that the frequency of break or QPO in the power spectrum density is related to the central black hole mass, and we can learn the accretion physics by studying PSD over decades of time scales. MAXI will be useful for longer time scale ($>$ days), and should be complemented by other X-ray missions like Suzaku or XMM to cover the shorter time scales. In this respect, desire for long operation of MAXI of 4–5 years or more was strongly expressed by participants. (McHardy, Hayashida, Sakano, Yuan)

For beamed AGN, multiwavelength obervations over the entire electromagnetic spectrum from radio to TeV gamma rays are important to understand emission mechanism, jet production, and its relation with the accretion. Rapid notification of outbursts by MAXI is highly expected. For unbeamed AGN, the reverberation analysis of the X-ray and optical/IR light curves will provide insights on the structure, the luminosity, and the mass of the source. (Madejski, Wagner, Minezaki, Lindfors)

MAXI will be also useful as a survey machine. MAXI will reach its confusion limit (a fraction of milliCrab) within a year, and at this level, MAXI will detect more absorbed (type 2) AGN than any other mission flown. The MAXI catalog of bright AGN, both absorbed and non-absorbed will be unique and valuable. (Ueda, Geherls)

4. Gamma-ray bursts

Although MAXI is not an ideal instrument to monitor GRBs, handful of them are expected to occur within it field of view that covers $\sim$1/60 of the sky at any given time. The number of detection is yet uncertain. A simulation of MAXI observations of GRBs, in particular the soft class of GRBs called X-ray flashes, with realistic combination of flux, spectra, and burst profile in the X-ray range is required for accurate estimation of the GRB detection rate. While the locations will be disseminated in real time, the coordinate in the direction of scan has intrinsic uncertainty due to the burst profile modifying the triangular collimator response. Rapid, coordinated follow-up observation by Swift is highly desirable. In addition to the prompt emission of GRBs, some of the early X-ray afterglows will be detected if scanned within $\sim 10^3$ s of the burst. The challenge would be how to identify these "orphan" events. If a transient X-ray emission is detected only at a single scan at a position of no known X-ray source, it may be a GRB afterglow. However, it could also be an AGN flare on a very short time scale or a stellar object in the Galaxy. Follow-up observations with high-sensitibity X-ray telescopes and in other wavelengths would be eagerly desired for these events. (Wilson-Hodge, Angelini, Piro, Burrows, Yamaoka, Suzuki)

5. Survey and mapping

In both Galactic and extragalactic sciences, the MAXI catalog will be valuable, but it will be more useful with accurate positions. It is even more necessary for transient new sources, for which the follow-up observations, in particular by Swift, is expected to play crucial role. (Gehrels)

MAXI can also contribute to the sceince of diffuse emission. With SSC, MAXI will be the first X-ray mission that covers most of the sky with the energy resolution of CCD. Earlier observations with rockets and ROSAT indicate that there are extended "thermal" emission associated with the galactic disk and isotropic emission presumably associated with the local hot bubble or charge exchange processes in the solar system. The repeated mapping of the sky with the emission lines of characteristic X-rays from O, Ne, Si, etc. will provide constraints on their origin, and give us clearer view of the solar system and the Galaxy. (McCammon, Miyata)

5.1. Action items before the launch

In order to start producing useful science immediately after the launch, we will need better characterization of the instruments: sensitivity, localization accuracy, and alert latency.

As discussed repeatedly in the workshop, good follow-up plans of the MAXI-detected transients are necessary. There should be close coordination with space missions like Suzaku, Swift, and also with ground-based UHE gamma-ray observatories and optical monitoring projects. Preparation for TOO observing proposals at big facilities such as VLBI should be made.

The MAXI team needs inputs from the wide community of the high-energy astrophysics., and will be collecting advice from the advisers and from the MAXI users forum.

Astrophysics with All-Sky X-Ray Observations
-- 3rd International MAXI Workshop --

RIKEN Symposium, June 10-12 2008
Suzuki Umetaro Hall, RIKEN, Wako, Saitama, Japan

Tuesday, June 10

9:00	Registration		
10:00	**Session 1 -- Opening; Black-hole binaries (Chair: Atsumasa Yoshida)**		
10:00	[O-01] M. Matsuoka	(12)	Welcome to the third MAXI Workshop
10:15	[O-02] K. Makishima	(30)	Suzaku Observations of Black-Hole Binaries and ULXs
10:50	Coffee Break / Poster Viewing		
11:20	**Session 2 -- Accretion variability (Chair: Luigi Piro)**		
11:20	[O-03] A. Zdziarski	(30)	Long-term and super-orbital variability of X-ray binaries
11:55	[O-04] R. Matsumoto	(30)	Variability Science in Accretion Disk Theory
12:30	Lunch / Poster Viewing		
14:00	**Session 3 -- MAXI mission; Galactic sources (Chair: Tadayasu Dotani)**		
14:00	[O-05] S. Ueno	(15)	MAXI Mission Overview and Schedule
14:20	[O-06] H. Tomida	(15)	The X-ray cameras of MAXI mission : Gas Slit Camera (GSC) and Solid-state Slit Camera (SSC)
14:40	[O-07] M. Sugizaki	(12)	Response Functions of X-ray Slit Cameras Onboard MAXI and Simulator
14:55	[O-08] H. Negoro	(30)	MAXI nova alert system and black hole transients
15:30	[O-32] D. J. Thompson	(30)	Science of compact X- and gamma-ray sources: MAXI and GLAST
16:05	Coffee Break / Poster Viewing		
16:35	**Session 4 -- Galactic sources; MAXI data (Chair: Masahiro Teshima)**		
16:35	[O-10] R. Fender	(30)	Relativistic jets from X-ray binaries
17:10	[O-11] K. Ebisawa	(30)	Galactic Transient Sources with MAXI
17:45	[O-12] R. Wijnands	(12)	Discovering and monitoring sub-luminous X-ray binaries using MAXI
18:00	[O-13] S. Trushkin	(12)	Active flaring states of GRS 1915+105 and Cyg X-3 in radio/X-ray monitoring
18:15	[O-14] M. Kohama	(12)	MAXI data distribution and the archive System

Astrophysics with All-Sky X-Ray Observations
-- 3rd International MAXI Workshop --

RIKEN Symposium, June 10-12 2008
Suzuki Umetaro Hall, RIKEN, Wako, Saitama, Japan

Wednesday, June 11

9:30	**Session 5 - GRBs (Chair: Hiroshi Tsunemi)**		
9:30	[O-15] C. Wilson-Hodge	(30)	All-sky observations with BATSE and GBM: X-ray sources and GRB
10:05	[O-16] L. Angelini	(15)	GRB Catalog : Bursts from Vela to Swift
10:25	[O-17] L. Piro	(15)	X-ray flashes
10:45	Coffee Break / Poster Viewing		
11:15	**Session 6 - GRBs (Chair: Takaya Ohashi)**		
11:15	[O-18] D. Burrows	(30)	Recent results of GRB X-ray afterglows
11:50	[O-19] K. Yamaoka	(12)	Suzaku Wide-band All-sky Monitor (WAM) Observations of High Energy Transients
12:05	[O-20] M. Suzuki	(12)	GRB observations with MAXI
12:20	Conference Photo		
12:35	Lunch / Poster Viewing		
14:00	**Session 7 -- Multiwavelength transients; AGNs (Chair: Takeshi Tsuru)**		
14:00	[O-09] O. Reimer	(30)	The challenge of identifying Galactic TeV sources
14:35	[O-22] E. J. Lindfors	(12)	Target of Opportunity Observations with the MAGIC telescope
14:50	[O-23] S. Wagner	(30)	Multiwavelength observations of Blazars
15:25	[O-24] I. McHardy	(30)	X-Ray Variability of AGN
16:00	Coffee Break / Poster Viewing		
16:30	**Session 8 -- Multiwavelength transients; AGNs (Chair: Kazuhisa Mitsuda)**		
16:30	[O-25] M. Uemura	(12)	Optical---Infrared Observation of Astronomical Transients with the "KANATA" 1.5-m Telescope
16:45	[O-26] G. Madjeski	(30)	MAXI and GLAST studies of jets in active galaxies
17:20	[O-27] W. Yuan	(12)	A search for large amplitude X-ray variables with the XMM-Newton Serendipitous Survey
17:35	[O-28] K. Hayashida	(12)	Relation between BH Mass and X-ray Variabilty: Expectations to the MAXI
17:50	[O-29] T. Minezaki	(12)	Near-Infrared Intraday Variations in AGN
18:30	Banquet		

Astrophysics with All-Sky X-Ray Observations
-- 3rd International MAXI Workshop --

RIKEN Symposium, June 10-12 2008
Suzuki Umetaro Hall, RIKEN, Wako, Saitama, Japan

Thursday, June 12

9:30	**Session 9 -- Compact hard X-ray/gamma-ray sources (Chair: Tatehiro Mihara)**		
9:30	[O-30] L. Kuiper	(30)	Hard X-ray/soft γ-ray characteristics of magnetars
10:05	[O-31] M. Morii	(12)	Suzaku observation of the AXP 1E 1841-045 and the future observation in the MAXI era
10:20	[O-21] S. Kulkarni	(30)	New Transients in the Optical and Radio Sky
10:55	Coffee Break / Poster Viewing		
11:25	**Session 10 -- Compact hard X-ray/gamma-ray sources (Chair: Hideyo Kunieda)**		
11:25	[O-33] P. Ubertini	(30)	The Hard X-ray sources observed by INTEGRAL/IBIS and their science
12:00	[O-34] N. Gehrels	(30)	Non-GRB X-ray and Hard X-ray Sources Observed with Swift
12:35	Lunch / Poster Viewing		
14:00	**Session 11 -- Source population; Diffuse emission (Chair: Masaki Mori)**		
14:00	[O-35] M. Sakano	(12)	The 2XMM catalogue and variability of X-ray sources
14:15	[O-36] Y. Ueda	(15)	Extragalactic survey with MAXI
14:35	[O-37] D. McCammon	(30)	Diffuse soft X-ray sky
15:10	[O-38] E. Miyata	(30)	Diffuse Source Mapping with MAXI
15:45	Coffee Break / Poster Viewing		
16:00	**Session 12 -- Future missions; Closing (Chair: Dave Thompson)**		
16:00	[O-39] T. Takahashi	(15)	NeXT
16:20	[O-40] B. Paul	(12)	ASTROSAT observations of variable X-ray sources: together with MAXI
16:35	[O-42] N. Kawai	(12)	Concluding Remarks

Friday, June 13

9:30-15:30	MAXI Tour to Tsukuba Space Center

List of Participants

Ababakr Karim	*Ministry of Education*
	karim_astronomy@yahoo.com
Adachi Yasuki	*JAXA/TKSC ISS*
	adachi.yasuki@jaxa.jp
Angelini Lorella	*gsfc/nasa*
	Lorella.Angelini-1@nasa.gov
Arimoto Makoto	*Tokyo Institute of Technology*
	arimoto@hp.phys.titech.ac.jp
Asami Fumi	*Tokyo University of Science*
	asami@crab.riken.jp
Asano Katsuaki	*Tokyo Institute of Technology*
	asano@phys.titech.ac.jp
Burrows N. David	*Penn State University*
	burrows@astro.psu.edu
Chujo Hirotaka	*RIKEN*
	chujo@crab.riken.jp
Dogiel Vladimir	*ISAS/JAXA (on leave P.N.Lebedev Institute)*
	dogiel@lpi.ru
Dotani Tadayasu	*ISAS/JAXA*
	dotani@astro.isas.jaxa.jp
Ebisawa Ken	*JAXA/ISAS*
	ebisawa@isas.jaxa.jp
Eguchi Satoshi	*Kyoto University*
	eguchi@kusastro.kyoto-u.ac.jp
Fender Rob	*University of Southampton*
	rpf@phys.soton.ac.uk
Fujimoto Shin-ichiro	*Kumamoto National College of Technology*
	fujimoto@ec.knct.ac.jp
Fukazawa Yasushi	*Hiroshima University*
	fukazawa@hep01.hepl.hiroshima-u.ac.jp
Gandhi Poshak	*RIKEN*
	pg@crab.riken.jp
Gehrels Neil	*NASA-GSFC*
	gehrels@milkyway.gsfc.nasa.gov
Gendreau Keith	*NASA/GSFC*
	Keith.c.gendreau@nasa.gov
Haru Tatuhito	*Systems Engineering Consultants Co. LTD. (SEC)*
	haru@sec.co.jp
Hayasaki Kimitake	*Yukawa Institute for Theoretical Physics Kyoto University*
	kimitake@yukawa.kyoto-u.ac.jp
Hayashida Kiyoshi	*Osaka University*
	hayasida@ess.sci.osaka-u.ac.jp
Hayato Asami	*RIKEN*
	hayato@crab.riken.jp

Hiraga S. Junko	RIKEN jhiraga@crab.riken.jp
Hiroi Kazuo	*Kyoto University* hiroi@kusastro.kyoto-u.ac.jp
Horike Naoko	*NEC Aerospace Systems Ltd.* n-horike@pb.jp.nec.com
Hotta Kazuhiro	*Systems Engineering Consultants Co. LTD. (SEC)* hotta@sec.co.jp
Ichibakase Atsushi	*Systems Engineering Consultants Co. LTD. (SEC)* ichibakase@sec.co.jp
Iida Manabu	*Systems Engineering Consultants Co. LTD. (SEC)* iida@sec.co.jp
Imada Akira	*Kagoshima University* imada@astro.sci.kagoshima-u.ac.jp
Inada Naohisa	*RIKEN* inada@crab.riken.jp
Inoue Yoshiyuki	*Kyoto University* yinoue@kusastro.kyoto-u.ac.jp
Ishida Manabu	JAXA/ISAS ishida@astro.isas.jaxa.jp
Ishikawa Masaki	*JAXA/TKSC* ishikawa.masaki@jaxa.jp
Ishino Yukiko	*Kyoto university* ishino@kusastro.kyoto-u.ac.jp
Ishiwata Ryoji	*Nihon University CST* ishiwata@cygnus.phys.cst.nihon-u.ac.jp
Itoh Masayuki	*Kobe University* mitoh@kobe-u.ac.jp
Iwahashi Takanori	*RIKEN* iwahashi@crab.riken.jp
Kai Masakazu	*Space Engineering Development Co. LTD. (SED)* kai.masakazu@sed.co.jp
Kanemaru Takehiro	*RIKEN* kanemaru@crab.riken.jp
Karim Mahmood Ababakr	*Ministry of Education-Erbil-Iraq* karim_astronomy@yahoo.com
Kasiko Dennis	*Kyambogo University* youthypc@yahoo.com
Kato Yoshiaki	*JAXA/ISAS* kato.yoshiaki@isas.jaxa.jp
Kawaharada Madoka	*RIKEN* kawahard@crab.riken.jp
Kawai Nobuyuki	*Tokyo Tech* nkawai@phys.titech.ac.jp

Kawanaka Norita	*RESCUE University of Tokyo*
	norita@resceu.s.u-tokyo.ac.jp
Kawasaki Kazuyoshi	*JAXA/TKSC*
	kawasaki.kazuyoshi@jaxa.jp
Kawashima Tomohisa	*Chiba University*
	kawashima-t@astro.s.chiba-u.ac.jp
Kawate Tomoko	*Kyoto Univ.*
	kawate@kusastro.kyoto-u.ac.jp
Kawauchi Masanori	*NEC Corporation*
	m-kawauchi@bq.jp.nec.com
Kinugasa Kenzo	*Gunma Astronomical Observatory*
	kinugasa@astron.pref.gunma.jp
Kira Chie	*Hiroshima University*
	kira@hep01.hepl.hiroshima-u.ac.jp
Kishimoto Yuji	*Yamagata University*
	kishimo@ksprite.kj.yamagata-u.ac.jp
Kohama Mitsuhiro	*RIKEN and JAXA/TKSC*
	kohama@crab.riken.jp
Kohmura Takayoshi	*Kogakuin University*
	tkohmura@map.kogakuin.ac.jp
Kojima Toru	*Aoyama Gakuin University*
	tkojima@phys.aoyama.ac.jp
Konami Saori	*Tokyo University of Science / RIKEN*
	konami@crab.riken.jp
Kotani Taro	*Aoyama Gakuin University*
	kotani@phys.aoyama.ac.jp
Kubota Kaori	*Kyoto University*
	kaori.k@kusastro.kyoto-u.ac.jp
Kudo Yusuke	*Tokyo Tech*
	kudou.y.ab@m.titech.ac.jp
Kuiper Lucien	*SRON-The Netherlands*
	L.M.Kuiper@sron.nl
Kulkarni Shri	*California Institute of Technology*
	srk@astro.caltech.edu
Kuramata Naoyuki	*Space Engineering Development Co. LTD. (SED)*
	kuramata.naoyuki@sed.co.jp
Kurita Kouhei	*Tokyo Institute of Technology*
	kurita.k.aa@m.titech.ac.jp
Lindfors Elina Johanna	*Tuorla Observatory University of Turku*
	elilin@utu.fi
Machida Mami	*NAOJ*
	mami@th.nao.ac.jp
Madejski Greg	*SLAC and KIPAC*
	madejski@slac.stanford.edu
Magara Moses	*LUNGUJJA INSTITUTE OF SCIENCES*
	rwadtechinstitute@yahoo.com

Makishima Kazuo	*RIKEN / University of Tokyo*
	maxima@riken.jp
Matsumoto Ryoji	*Chiba University*
	matumoto@astro.s.chiba-u.ac.jp
Matsuoka Masaru	*JAXA/TKSC*
	matsuoka.masaru@jaxa.jp
Matsuoka Toshiyuki	*aoyama gakuin university*
	tmatuoka@phys.aoyama.ac.jp
McCammon Dan	*University of Wisconsin*
	mccammon@wisp.physics.wisc.edu
McHardy Ian	*University of Southampton*
	imh@astro.soton.ac.uk
Mihara Tatehiro	*RIKEN*
	mihara@crab.riken.jp
Minezaki Takeo	*Institute of Astronomy University of Tokyo*
	minezaki@ioa.s.u-tokyo.ac.jp
Mitsuda Kazuhisa	*ISAS/JAXA*
	mitsuda@astro.isas.jaxa.jo
Miyamoto Kenji	*Yokohama National University*
	d07gd232@ynu.ac.jp
Miyata Emi	*Osaka University*
	miyata@ess.sci.osaka-u.ac.jp
Miyoshi Sho	*Nihon University*
	miyoshi@cygnus.phys.cst.nihon-u.ac.jp
Mizobuchi Satoko	*Systems Engineering Consultants Co. LTD. (SEC)*
	mizobuchi@sec.co.jp
Mizutani Kohei	*Saitama University*
	kohei0303@nifty.com
Moradi AmirMohsen	*joosh kam pars co.*
	amirmohsenm@yahoo.com
Mori Masaki	*Institute for Cosmic Ray Research University of Tokyo*
	morim@icrr.u-tokyo.ac.jp
Mori Yuki	*Tokyo Institute of Technology*
	ymori@hp.phys.titech.ac.jp
Morihara Kumiko	*Kobe University*
	morihana@radix.h.kobe-u.ac.jp
Morii Mikio	*Rikkyo University*
	mmorii@rikkyo.ac.jp
Nagase Masayuki	*Systems Engineering Consultants Co. LTD. (SEC)*
	nagase@sec.co.jp
Nakagawa Yujin	*RIKEN*
	yujin@crab.riken.jp
Nakahira Satoshi	*Aoyama Gakuin University*
	nakahira@phys.aoyama.ac.jp

Nakajima Hideya	*Tokyo Tech*
	nakajima.h.aa@m.titech.ac.jp
Nakajima Motoki	*Nihon Univ.*
	mnakajima@phys.cst.nihon-u.ac.jp
Nakamori Takeshi	*Tokyo Institute of Technology*
	nakamori@hp.phys.titech.ac.jp
Nakamoto Hiroyuki	*Systems Engineering Consultants Co. LTD. (SEC)*
	nakamoto@sec.co.jp
Namugambe Hadijja Najemba	*LUNGUJJA INSTITUTE OF SCIENCES*
	rwadtechinstitute@yahoo.com
Negoro Hitoshi	*Nihon University CST*
	negoro@phys.cst.nihon-u.ac.jp
Oda Hiroshi	*Chiba University*
	oda@astro.s.chiba-u.ac.jp
Ohashi Takaya	*Tokyo Metropolitan University*
	ohashi@phys.metro-u.ac.jp
Ohsuga Ken	*RIKEN*
	ohsuga@crab.riken.jp
Oka Harumi	*Iscene*
	harumi@iscene.co.jp
Omar Kurtanidze	*Abastumani Observatory*
	blazar_ao@yahoo.com
Paul Biswajit	*Raman Research Institute*
	bpaul@rri.res.in
Petre Robert	*NASA / GSFC*
	robert.petre-1@nasa.gov
Piro Luigi	*Istituto Astrofisica Spaziale Fisica Cosmica Roma INAF*
	luigi.piro@iasf-roma.inaf.it
Quimby Robert	*California Institute of Techonology*
	quimby@astro.caltech.edu
Reimer Olaf	*Stanford University*
	olr@stanford.edu
Sakamoto Seiichi	*JAXA/ISAS*
	sakamoto.seiichi@jaxa.jp
Sakano Masaaki	*University of Leicester*
	mas@star.le.ac.uk
Sato Tetsuya	*RIKEN*
	tetsuya@crab.riken.jp
Satomi Rintaro	*MEISEI Electric Co. LTD. (MEC)*
	satomir@meisei.co.jp
Sawachi Hideo	*MEISEI Electric Co. LTD. (MEC)*
	sawachih@meisei.co.jp
Shibazaki Noriaki	*Rikkyo University*
	shibazak@rikkyo.ac.jp
Shimokawabe Takashi	*Tokyo Institute of Technology*
	shimokawabe@hp.phys.titech.ac.jp

Shiraki Takayuki	*Aoyama Gakuin University*
	tshiraki@phys.aoyama.ac.jp
Sudou Hiroshi	*Gifu University*
	sudou@gifu-u.ac.jp
Sugita Satoshi	*Aoyama Gakuin University*
	sugita@phys.aoyama.ac.jp
Sugizaki Mutsumi	*RIKEN*
	sugizaki@crab.riken.jp
Suzuki Motoko	*JAXA/TKSC*
	suzuki.motoko@jaxa.jp
Takahashi Ichiro	*Aoyama Gakuin University*
	itakahashi@phys.aoyama.ac.jp
Takahashi Rohta	*RIKEN*
	rohta@riken.jp
Takahashi Tadayuki	*JAXA/ISAS*
	takahashi@astro.isas.jaxa.jp
Takei Dai	*Rikkyo University*
	takei@stu.rikkyo.ne.jp
Tamagawa Toru	*RIKEN*
	tamagawa@riken.jp
Tamunang Gregory Chungong	*SUSTAINABLE RESOURCE DEVELOPMENT FORUM-CAMEROON*
	sustainableresource@yahoo.com
Tanaka Isao	*MEISEI Electric Co. LTD. (MEC)*
	tanakai@meisei.co.jp
Teshima Masahiro	*Max-Planck-Institute for Physics*
	mteshima@mppmu.mpg.de
Thompson David	*NASA Goddard Space Flight Center*
	David.J.Thompson@nasa.gov
Thompson Kira	*Towson University*
	David.J.Thompson@nasa.gov
Toizumi Takahiro	*Tokyo Institute of Technology*
	toizumi@hp.phys.titech.ac.jp
Toma Kenji	*NAOJ*
	kenji.toma@nao.ac.jp
Tomida Hiroshi	*JAXA/TKSC*
	tomida.hiroshi@jaxa.jp
Tomoda Motoyasu	*Systems Engineering Consultants Co. LTD. (SEC)*
	tomoda@sec.co.jp
Torii Shoji	*Waseda University*
	torii.shoji@waseda.jp
Trushkin Sergei	*Special Astrophysical observatory RAS Russia*
	satr@sao.ru
Tsuchiya Harufumi	*RIKEN*
	harufumi@crab.riken.jp

Tsunemi Hiroshi	*Osaka university*
	tsunemi@ess.sci.osaka-u.ac.jp
Tsuru Takeshi	*Kyoto University*
	tsuru@cr.scphys.kyoto-u.ac.jp
Ubertini Pietro	*IASF-Roma/INAF*
	pietro.ubertini@iasf-roma.inaf.it
Ueda Yoshihiro	*Kyoto University*
	ueda@kusastro.kyoto-u.ac.jp
Uemura Makoto	*Hiroshima University*
	uemuram@hiroshima-u.ac.jp
Ueno Shiro	*JAXA/TKSC*
	ueno.shiro@jaxa.jp
Urayama Fumitaka	*Space Engineering Development Co. LTD. (SED)*
	urayama.fumitaka@sed.co.jp
Wagner Stefan	*Landessternwarte Heidelberg*
	swagner@lsw.uni-heidelberg.de
Wijnands Rudy	*Astronomical Institute 'Anton Pannekoek' University of Amsterdam*
	rudy@science.uva.nl
Wilson-Hodge Colleen	*NASA/MSFC*
	colleen.wilson@nasa.gov
Yamaguchi Chikara	*Iscene*
	chikara@iscene.co.jp
Yamaguchi Hiroya	*RIKEN*
	hiroya@crab.riken.jp
Yamamoto Takayuki	*NIHON.U/RIKEN*
	tyamamot@crab.riken.jp
Yamaoka Kazutaka	*Aoyama Gakuin University*
	yamaoka@phys.aoyama.ac.jp
Yoshida Atsumasa	*AGU*
	ayoshida@phys.aoyama.ac.jp
Yoshida Kenji	*Shibaura Institute of Technology*
	yoshida@shibaura-it.ac.jp
Yoshii Rie	*Tokyo University of Science*
	yoshii@crab.riken.jp
Yuan Weimin	*Yunnan Astronomical Observatory*
	wmy@ynao.ac.cn
Zdziarski Andrzej	*N. Copernicus Astronomical Center*
	aaz@camk.edu.pl
Zhang Shu	*Institute of High Energy Physics*
	szhang@mail.ihep.ac.cn

Author index